frontiers | Research Topics

Exploration, exploitation, and utilization of coal-measure gas into the future

Edited by
Mingjun Zou, Chongtao Wei, Reza Rezaee, Junjian Zhang
and Zhenzhi Wang

Published in
Frontiers in Earth Science

ISSN 1664-8714
ISBN 978-2-8325-2571-5
DOI 10.3389/978-2-8325-2571-5

About Frontiers

Frontiers is more than just an open access publisher of scholarly articles: it is a pioneering approach to the world of academia, radically improving the way scholarly research is managed. The grand vision of Frontiers is a world where all people have an equal opportunity to seek, share and generate knowledge. Frontiers provides immediate and permanent online open access to all its publications, but this alone is not enough to realize our grand goals.

Frontiers journal series

The Frontiers journal series is a multi-tier and interdisciplinary set of open-access, online journals, promising a paradigm shift from the current review, selection and dissemination processes in academic publishing. All Frontiers journals are driven by researchers for researchers; therefore, they constitute a service to the scholarly community. At the same time, the *Frontiers journal series* operates on a revolutionary invention, the tiered publishing system, initially addressing specific communities of scholars, and gradually climbing up to broader public understanding, thus serving the interests of the lay society, too.

Dedication to quality

Each Frontiers article is a landmark of the highest quality, thanks to genuinely collaborative interactions between authors and review editors, who include some of the world's best academicians. Research must be certified by peers before entering a stream of knowledge that may eventually reach the public - and shape society; therefore, Frontiers only applies the most rigorous and unbiased reviews. Frontiers revolutionizes research publishing by freely delivering the most outstanding research, evaluated with no bias from both the academic and social point of view. By applying the most advanced information technologies, Frontiers is catapulting scholarly publishing into a new generation.

What are Frontiers Research Topics?

Frontiers Research Topics are very popular trademarks of the *Frontiers journals series*: they are collections of at least ten articles, all centered on a particular subject. With their unique mix of varied contributions from Original Research to Review Articles, Frontiers Research Topics unify the most influential researchers, the latest key findings and historical advances in a hot research area.

Find out more on how to host your own Frontiers Research Topic or contribute to one as an author by contacting the Frontiers editorial office: frontiersin.org/about/contact

Exploration, exploitation, and utilization of coal-measure gas into the future

Topic editors
Mingjun Zou — North China University of Water Conservancy and Electric Power, China
Chongtao Wei — China University of Mining and Technology, China
Reza Rezaee — Curtin University, Australia
Junjian Zhang — Shandong University of Science and Technology, China
Zhenzhi Wang — Henan Polytechnic University, China

Citation
Zou, M., Wei, C., Rezaee, R., Zhang, J., Wang, Z., eds. (2023). *Exploration, exploitation, and utilization of coal-measure gas into the future*.
Lausanne: Frontiers Media SA. doi: 10.3389/978-2-8325-2571-5

Table of contents

frontiers | Frontiers in Earth Science

TYPE Original Research
PUBLISHED 29 August 2022
DOI 10.3389/feart.2022.1000520

Influence of geological structures on the occurrence of coalbed methane in Sima coal mine, China

Hongyang Liu[1,2], Boyang Zhang[3]*, Xuelong Li[1]*, Chengwei Liu[2], Chen Wang[4], Feng Wang[1], Zhenhua Cui[3,5] and Deyou Chen[1]

[1]College of Energy and Mining Engineering, Shandong University of Science and Technology, Qingdao, China, [2]School of Mining and Mechanical Engineering, Liupanshui Normal University, Liupanshui, Guizhou, China, [3]School of Civil Engineering, Henan Polytechnic University, Jiaozuo, Henan, China, [4]School of Mining, Guizhou University, Guiyang, China, [5]Lu'an Group Sima Coal Industry Limited Company, Changzhi, Shanxi, China

EDITED BY
Mingjun Zou,
North China University of Water Resources and Electric Power, China

REVIEWED BY
Shumin Liu,
Chongqing University, China
Peng Chen,
North China University of Science and Technology, China

*CORRESPONDENCE
Xuelong Li,
lixlcumt@126.com
Boyang Zhang,
zhangboyangzzdq@126.com

SPECIALTY SECTION
This article was submitted to Economic Geology,
a section of the journal
Frontiers in Earth Science

RECEIVED 22 July 2022
ACCEPTED 04 August 2022
PUBLISHED 29 August 2022

CITATION
Liu H, Zhang B, Li X, Liu C, Wang C, Wang F, Cui Z and Chen D (2022), Influence of geological structures on the occurrence of coalbed methane in Sima coal mine, China.
Front. Earth Sci. 10:1000520.
doi: 10.3389/feart.2022.1000520

Geological structures of Sima coal mine in Shanxi Province were analyzed to understand the control effect of the geological structures on the occurrence of coalbed methane (CBM) in coal seam #3 of Sima coal mine. The CBM contents in the districts #2 and #3 of Sima coal mine were tested, and the effects of buried depth, fault and collapse column on the distribution of coalbed methane content are studied. The research results showed that: 1) The average content of CBM has a linear relationship with buried depth and overburden thickness, but in the smallscale range of buried depth, the dispersion between CBM and buried depth is very large. 2) Faults and collapse columns significantly affect the content of local CBM nearby, but from the largescale range such as the whole mining area, the average value of CBM content at a certain buried depth will not be affected by faults and collapse columns. 3) In the hanging wall of F29 normal fault, it is roughly estimated that the average escape rate of CBM near the fault is 13.9%, while in the footwall of F29 normal fault, this value is 0.7%–1.1%. The results show that there is a significant difference in the influence of the fault on the CBM content in the hanging wall and footwall. 4) The control effect of collapse column on CBM occurrence is related to the development height of collapse column, the cementation degree of collapse column, groundwater runoff conditions and other factors. It can be divided into three categories: aggregation action, escape action (such as collapse column X8) and no obvious effect (such as collapse column DX7).

KEYWORDS

occurrence of coalbed methane, geological structure, buried depth, FAULT, collapse column

1 Introduction

With the rapid development and in-depth adjustment of the economy, the pattern of energy supply and demand has undergone profound changes, and the task of energy transformation and upgrading is arduous. CBM, as a clean and unconventional natural gas resource, has been generally valued by major coal-producing countries (Moore, 2012; Li et al., 2020). Moreover, CBM is one of the main disasters restricting the safe production of coal mines, and its efficient mining is a fundamental measure for mine disaster management (Zheng et al., 2019; Zhou et al., 2019; Zou Q. L. et al., 2020) and resource utilization. Meanwhile, CH_4, the main component of CBM, is used as a greenhouse gas (Wang et al., 2019; Li et al., 2021a). Its greenhouse effect is 21–25 times that of CO_2, which has a huge impact on the environment and climate. Therefore, it is vital to carry out CBM exploration and development work.

In 2020, China's underground CBM extraction production reached 14.7 billion m^3, accounting for 72% of the country's total CBM production (Zou et al., 2015). The geological conditions of the CBM storage areas should be clarified to ensure the efficient extraction of CBM underground. CBM is gradually formed in the long-term complex geological evolution process (Wang and Du, 2020; Zou M. J. et al., 2020; Zhou et al., 2021), so its occurrence is affected by structural evolution, depositional environment, buried depth, roof and floor lithology, coal seam thickness, hydrogeology, and magmatic activity (Xie et al., 2018; Zou et al., 2018a; Zhang C. L. et al., 2020; Kong B. et al., 2021; Zhang C. L. et al., 2021). Tectonic evolution is the key factor controlling the generation, migration, and occurrence of CBM (Zou et al., 2018b; Zhang K. Z. et al., 2020; Zhou et al., 2022).

Many scholars have studied the geological occurrence of CBM. Qin summarized the characteristics of CBM accumulation and coal reservoirs controlled by geological factors such as sedimentation, structure, coal rank, and hydrology in nine major basins in China, including Qinshui, Ordos, Junggar, Western Guizhou, Erlianhot, Hailar, etc. (Qin et al., 2018; Liu et al., 2020). Wang used mathematical statistics, literature analysis, well logging, hydrochemical analysis, and other methods to summarize the research status and development trend of the influence of hydrogeology on CBM (Wang K. et al., 2020). Ye analyzed the relationship among the structure (Pan et al., 2019), micro-pores (Liu X. F. et al., 2022), micro-cracks (Zhang et al., 2021a), and CBM content (Ma Y. K. et al., 2020; Lu et al., 2021), which is of great significance for the optimal selection of CBM production areas (Niu et al., 2019; Ye et al., 2019; Zhou et al., 2021). Sinha took a mine in India as an example to study the geological model of the CBM-enhanced recovery process (Sinha and Gupta, 2021). Fu analyzed the potential evaluation of CBM and developed sweet-spot prediction based on the developed geological conditions in the Yangjiapo block in the eastern Ordos Basin (Zou et al., 2018c). Hamilton explained the gas content trend of the Wallonia Group in the eastern part of the Surat Basin in Queensland, Australia from a geological point of view (Zhou et al., 2021). However, the existing studies rarely discuss the influence of faults and collapsed columns on the occurrence of CBM. Existing studies have shown (Zhang et al., 2005; Wang et al., 2016; Ma C. D. et al., 2020; Wang C. et al., 2020; Yu et al., 2021; Yuan et al., 2021; Liu H. Y. et al., 2022) that geological structures inevitably change the nearby ground stress field and reservoir properties (Feng et al., 2020; Feng et al., 2021; Li et al., 2021b; Shen et al., 2021; Zhang et al., 2021b), thereby affecting the occurrence of CBM (Zhang R. et al.,

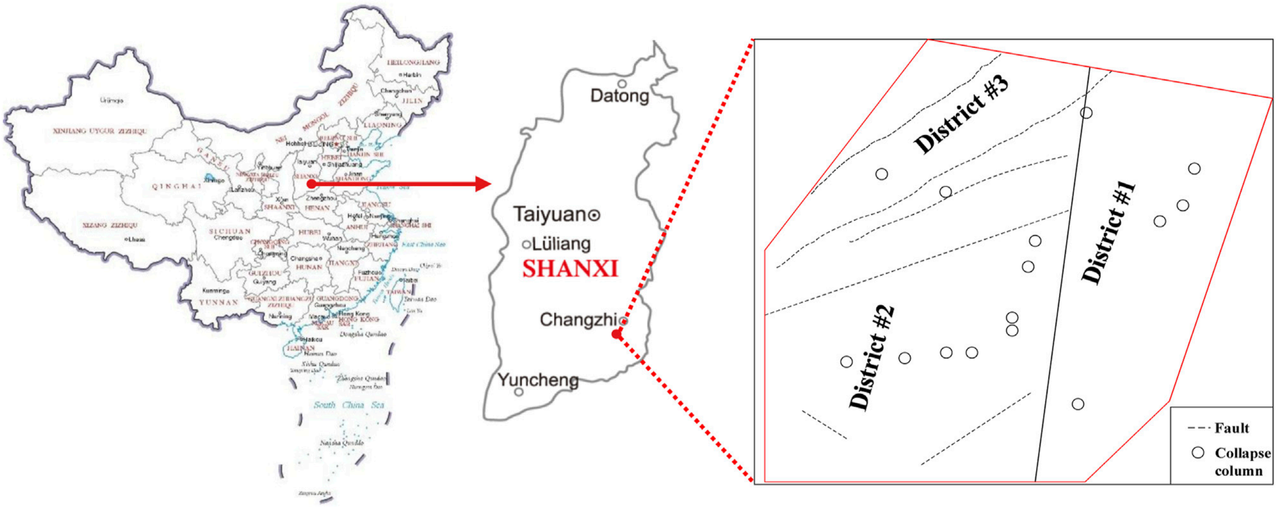

FIGURE 1
Survey of Sima coal mine.

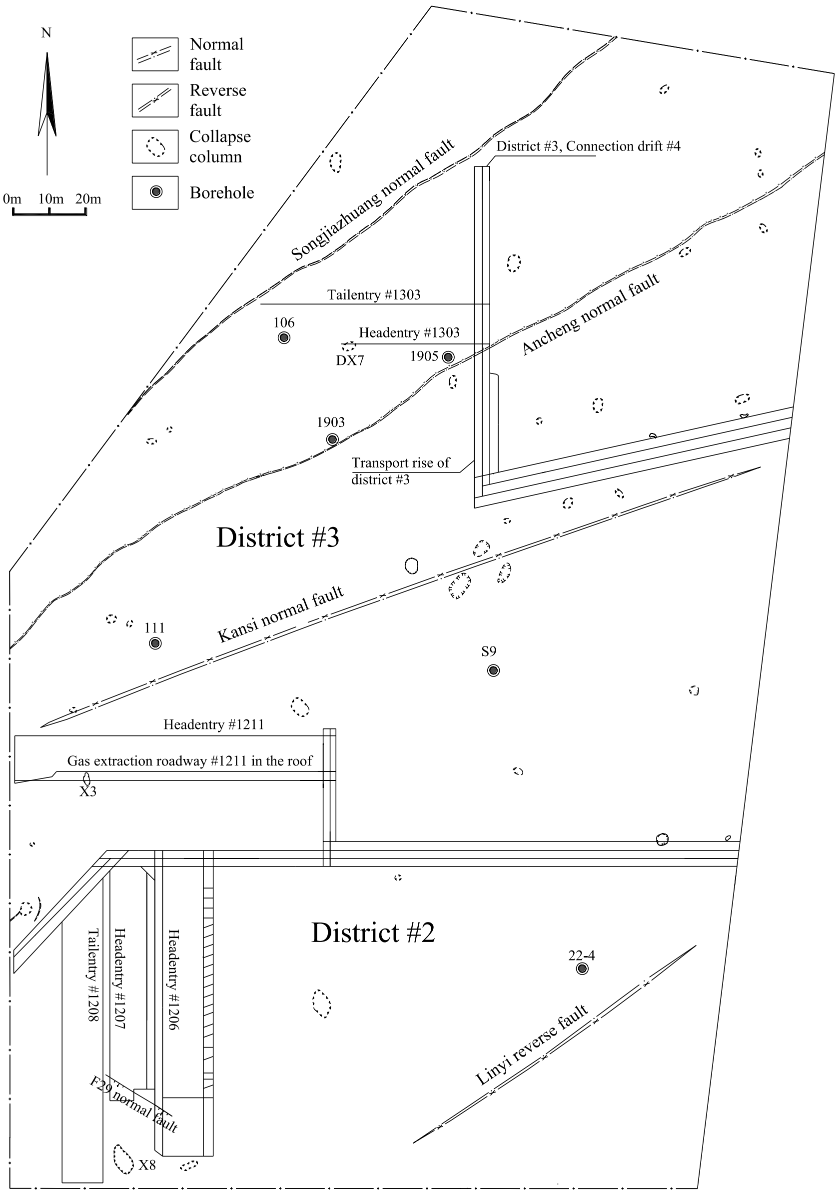

FIGURE 2
Roadway layout and main structure distribution.

2020; Kong et al., 2021a; Kong et al., 2021b). Therefore, it is necessary to study in this direction.

Shanxi Province is a major province with CBM resources in China, and the proven CBM resources are about 25.52*10^{12} m^3, accounting for 1/3 of the country's total resources (Su, 2016). The work took Sima coal mine in Changzhi County, Shanxi Province as an example to analyze the occurrence laws of CBM around geological structures such as folds, faults, and collapse columns based on the field measurement of the CBM content. On this basis, this paper studied the control effect of different geological structures on the occurrence of coalbed methane in Sima Coal Mine, especially expounded three different types of control effect and control mechanism of collapse column on the occurrence of coalbed methane, which could provid a theoretical basis for efficient underground drainage of CBM.

2 Geological structures of the coal mine

Sima coal mine is located in Shangdang District, Changzhi, Shanxi, China (see Figure 1), with a minefield of about

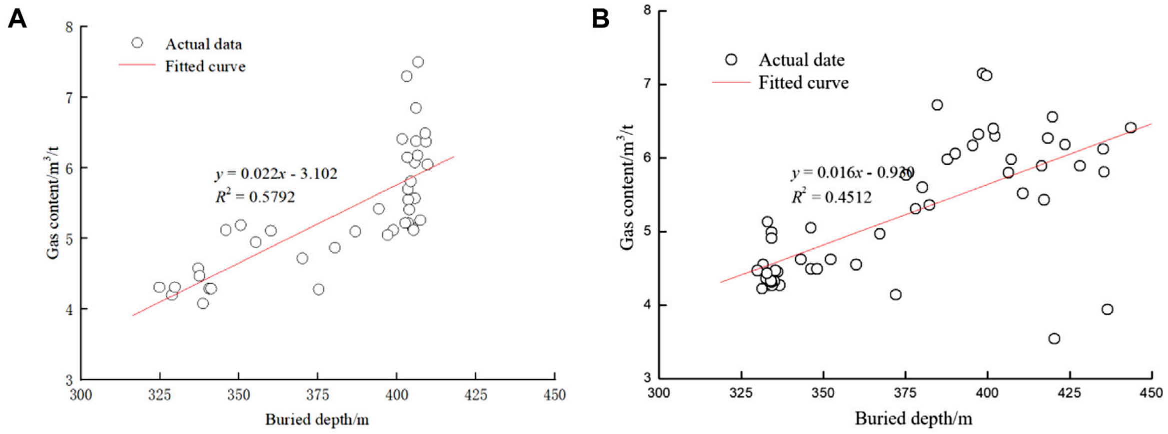

Headentry #1211

Gas extraction roadway #1211 in the roof

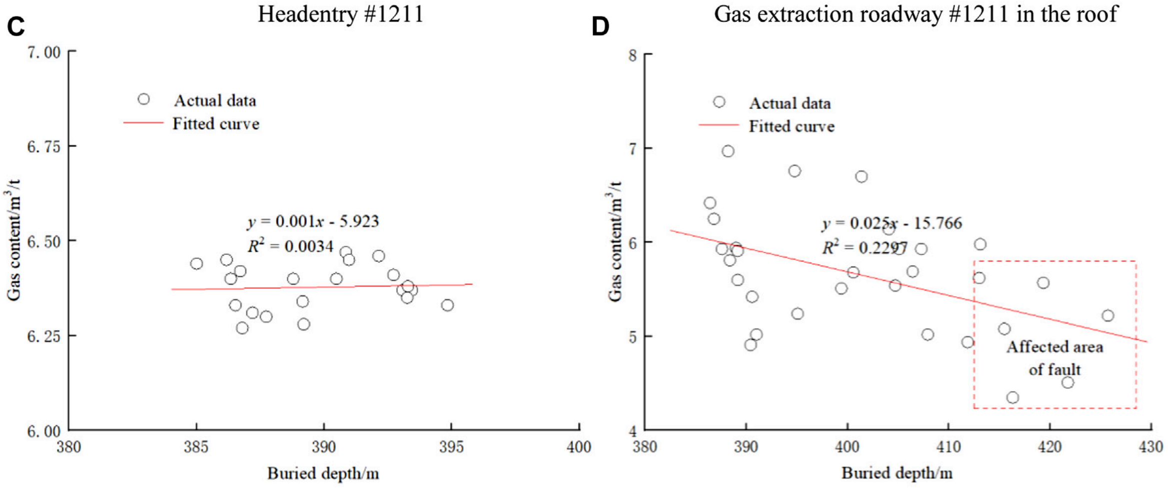

Headentry #1206

Headentry #1207

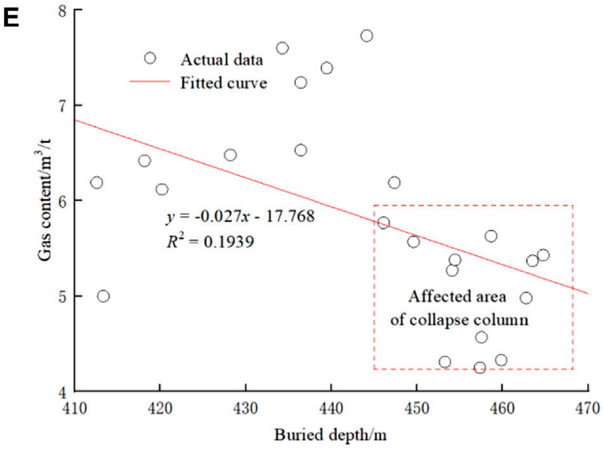

Tailentry #1208

FIGURE 3
Gas content scatter with fitting curve with the increased buried depth at each panel in district #2.

TABLE 1 Linear regression relationship between the gas content and buried depth.

Location	Linear fitting results	Correlation degree R^2	Geological structure description
Headentry #1211	$y = 0.022x - 3.101$	0.5791	
Gas extraction roadway #1211 in the roof	$y = 0.016x - 0.930$	0.4512	
Headentry #1206	$y = 0.001x + 5.923$	0.0034	The variation range of buried depth is small
Headentry #1207	$y = 0.025x - 15.766$	0.2297	There is a fault nearby
Tailentry #1208	$y = 0.027x - 17.768$	0.1939	There is a collapse column nearby

29.494 km^2 and a recoverable reserve of 96.56 Mt. The mineable coal seams are mainly #3 and 15, and coal seam #3 is currently the main mining. The minefield is mainly divided into three districts, and the stoping of coal seam #3 in district #1 has been completed.

2.1 Structural-control characteristics of the mining area

Shanxi Province is located inside the ancient North China plate, which is a typical intraplate structure. The Lu'an mining area of the Sima coal mine is located in the middle section of the Zhanshang-Wuxiang-Yangcheng NNE-trending concave fold belt in the eastern part of the Qinshui block depression of the Lvliang-Taihang fault block in North China. On the west side of the fault zone, the main part is superimposed on the new rift of Changzhi. Qinshui Basin, a compound syncline coal-bearing one, is a compound syncline formed in the Yanshanian period under the background of Mesozoic compression of the North China Plate and is generally distributed in the NNE direction. The edge is surrounded by the widely exposed Paleozoic erathem, and the interior of the basin is covered by Triassic (Liu et al., 2021).

The main geological structures in the mining area is fault structure. According to its directions, it is divided into three groups of NEE-NE, NNE-SN, and NW. The first group is the most developed, with Xichuan faults, south Wenwangshan, and north faults in the north of the mining area, the south and north Ergangshan faults in the south, and Anchang and Zhonghua faults in the middle. The mining area is separated by faults, which serve as the natural boundary. The second group is followed, and the third group is mainly small faults with a drop of several meters to more than 10 m exposed by the operating mines in the east, most of which are in the NNE-SN direction. The regional tectonic pattern has gone through the stages of formation of Paleocontinental crust plate from Archean to Early Proterozoic, stable development of plate from Late Proterozoic to Early Permian, and intraplate deformation since Jurassic. The regional structure is mainly formed in the third stage—the intraplate deformation stage since the Jurassic (Cui and Jia, 2011).

2.2 Geological structure of the mine

The strike of the fold in the minefield can be divided into near SN and NEE directions. There are faults with different drop sizes along the strike and inclination. The strike of the fault can be divided into NW and NNE-NE directions, and most of them are tensile normal faults. The collapse columns in the minefield are relatively developed, and 15 collapse columns are directly exposed, concentrated in district #2. Figure 2 shows the layout of roadways in districts and the distribution of main geological structures in the mine.

3 Influence of structures on the occurrence of CBM

3.1 Influence of buried depths on the occurrence of CBM

At present, the stoping of the coal seam #3 in district #1 of Sima coal mine is completed. Meanwhile, the CBM content in district #1 is generally low, and it is of no practical significance to discuss the occurrence of CBM in district #1. Therefore, the influence of the geological structure of the districts #2 and #3 of Sima Coal Mine on the occurrence of CBM is studied.

3.1.1 District #2

The layout of the panel in the district #2 has been completed, and the CBM test points are mainly distributed at panels #1206, 1207, 1208, and 1211. Figure 3 shows the scatters with fitting curves of the CBM contents at panels #1206, 1207, 1208, and 1211 with the increased buried depths. Figures 3A,B illustrate that in the headentry and gas extraction roadway in the roof of panel #1211, the CBM content increases with the increased buried depth. The variation range of the buried depths of the headentry of panel #1206 is only about 10 m, which is far less than the variation range of the buried depths above 100 m of the panel #1211. Within a relatively small variation range of burial depth, the CBM content is highly dispersed with the burial depth, showing a slight increase trend as a whole, as shown in Figure 3C. In Figures 3D,E, the CBM contents of the headentry #1207 and

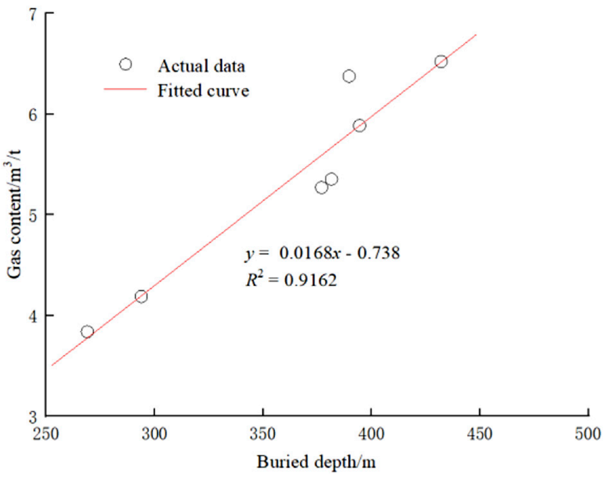

FIGURE 4
Gas content scatter with fitting curve with the increased buried depth in district #2.

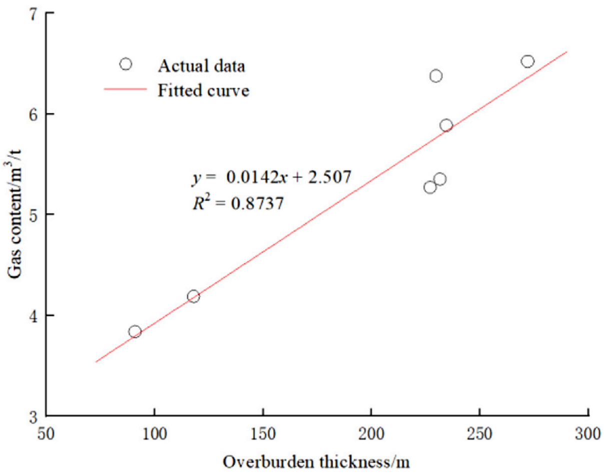

FIGURE 5
Gas content scatter with fitting curve with the overburden thickness in district #2.

tailentry #1208 decrease with the increased buried depth, what is inconsistent with conventional understanding. This result is due to the existence of F29 fault and collapse column near the headentry #1207 and tailentry #1208 respectively (Figure 2), and the CBM content is affected by the fault and collapse column. At the same time, it also shows that the influence of fault and collapse column on CBM content is significantly greater than that of buried depth.

For a unified explanation, the regression analysis method is used to establish the regression relationship between the CBM content and the buried depth of the coal seam. The linear relationship between the CBM content (y) and coal seam depth 10) is obtained to establish the following mathematical model.

Regression equation:

$$y = ax + b$$

where y represents the CBM content; x represents the buried depth of the coal seam; a and b represent the undetermined coefficients.

Table 1 shows the linear regression relationship between the CBM content and buried depth at panels #1206, 1207, 1208, and 1211.

Due to the influence of the small variation range of buried depth or the influence of faults and collapse columns, the CBM content of panel #1206, #1207 and #1208 have no significant linear relationship with buried depth. However, combined with the test data of CBM observation holes #9 and #22–4 in the district #2, we calculated the average value of CBM content at each measurement point, and plotted the variation curve of the average content of CBM with the increase of buried depth (Figure 4).

Figure 4 shows that the average CBM content increases with the increase of buried depth. The correlation degree (R^2) of the linear fitting is 0.9162, which is much greater than the linear fitting correlation of the test results of each panel. This shows that: 1) In the small-scale range of buried depth, the dispersion between CBM and buried depth is very large. It is meaningless to discuss the relationship between CBM content and buried depth. 2) Faults and collapse columns significantly affect the content of local CBM nearby, but from the large-scale range such as the whole mining area, the average value of CBM content at a certain buried depth will not be affected by faults and collapse columns.

In the linear relationship in Figure 4, b = −0.738, that is, when the buried depth is 0, the CBM content is negative, which has no practical significance. When calculating the buried depth of a measuring point, we used the same elevation of the ground to calculate the difference value, which is not rigorous enough. Considering the change of terrain and replacing the buried depth of a measuring point with the thickness of overburden, we get the variation relationship between the average content of CBM and the thickness of overburden, and the linear fitting parameter b becomes 2.507, as shown in Figure 5. Therefore, it is of more practical significance to discuss the relationship between CBM content and overburden thickness.

3.1.2 District #3

At present, only the main roadway and the headentry and tailentry of panel #1303 have been excavated in district #3 of Sima coal mine. Table 2 shows the basic parameters of CBM in the tailentry of panel #1303, and the maximum CBM content is about 4.5 m^3/t. The test results of CBM content of panel #1303, boreholes #111, #106, #1903, #1905, connecting entry #4 and belt roadways in the District #3 are comprehensively analyzed, and the variation curve of average CBM content with the increase of buried depth is drawn

TABLE 2 Test results of basic parameters of CBM in tailentry #1303.

Distance between measuring position and roadway exit/m	CBM content of raw coal/(m^3/t)	Distance between measuring position and roadway exit/m	CBM content of raw coal/(m^3/t)
5.6	4.3901	584.4	4.1096
49.3	4.4087	633.3	3.9290
97.9	4.4779	682.4	3.7528
142.4	4.3374	731.1	3.7647
192.3	4.4002	779.6	3.8316
241.6	4.2651	828.6	3.7937
290.4	4.0892	877.3	3.8076
339.6	4.1124	926.7	3.8311
388.3	3.9184	975.3	3.9661
437.8	4.1154	1024.0	4.223
486.4	4.2138	1072.9	4.4407
535.6	4.1257		

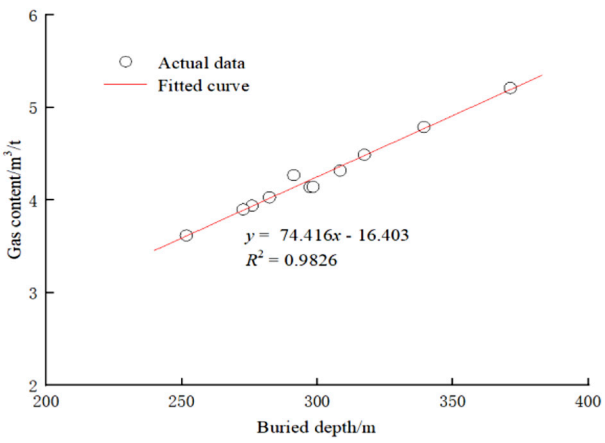

FIGURE 6
Gas content scatter with fitting curve with the increased buried depth in district #3.

(Figure 6). The fitting results are good, and the correlation coefficient reaches 0.9826. This further shows that the average value of CBM content is highly linear with the buried depth.

3.2 Influence of faults on the occurrence of CBM

Faults destroy the continuity and integrity of coal seams. The influence of faults on the occurrence of CBM mainly depends on its openness or sealing. The fault strike of Sima Coal Mine can be divided into NW direction and NNE-NE direction. Most of them are tensile faults with good permeability, which is conducive to the emission of CBM (Figure 7). This is because pores and fissures are widely developed in tectonic rock and two-wall rock in the fault zone of tensional or tensional shear normal fault, which provides a good channel for gas escape. On the one hand, it reduces the risk of CBM outbursts during coal mining. On the other hand, it is not conducive to the formation of CBM resources in Sima coal mine, which is difficult for the centralized mining of CBM.

Kansi normal fault and F29 normal fault were taken as examples to illustrate the control effect of Sima coal mine fault on CBM.

3.2.1 Kansi normal fault

The largest fault in the Sima coal mine is the Kansi normal fault, which is also the boundary between districts #2 and #3. Figure 8 shows the CBM content and seamfloor elevation in some areas around the Kansi normal fault. Obvious differences exist in the CBM content on both sides of the Kansi normal fault at the same elevation. At the same coal seam-floor elevation of 580 m, the CBM content of district #3 on the north side of Kansi fault is between 6.1–6.4 m^3/t, while that of district #2 on the south side of Kansi fault is 5.5–5.8 m^3/t. At the same elevation, there are obvious differences in the CBM content between the north and south sides of Kansi fault, indicating that Kansi fault is a barrier to migrating CBM.

3.2.2 F29 normal fault

F29 normal fault is located in panel #1207, and the outer edges of both sides reach panels #1208 and #1206. The fall of F29 normal fault is 3.3 m. Compared with Kansi fault, the scale and fall of F29 normal fault are much smaller, but there are still significant differences in gas content between hanging wall and footwall of the fault, as shown in Figure 9. This further shows that

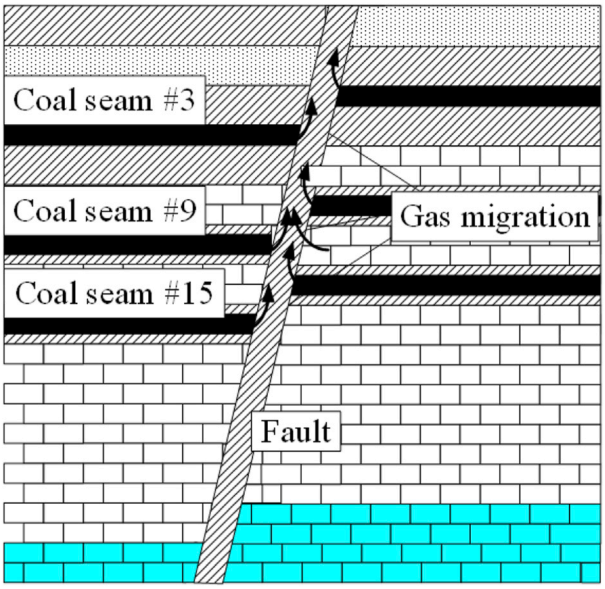

FIGURE 7
Control effect of faults in Sima coal mine on CBM.

no matter the size of the fault, it can obstruct the occurrence of CBM.

The CBM content at the headentry and setup entry of panel #1207 on the hanging wall of F29 normal fault is between 4.35 and 5.57 m^3/t, with an average value of 4.96 m^3/t. The corresponding buried depth of the measuring points is 411–425 m, with an average of 417.8 m. From the previous analysis, we know that although the fault can affect the occurrence of CBM in a certain range nearby, it will not change the average CBM content in a certain buried depth in a large-scale range. The buried depth of the headentry and setup entry of panel #1207 changes little as a whole. The average CBM content of all measuring points in the headentry and setup entry of panel #1207 is 5.64 m^3/t. Based on this, we can roughly estimate that the escape rate of CBM in the hanging wall of F29 normal fault is (5.64–4.96)/4.96 = 13.9%.

The CBM content of each measuring point in the headentry and setup entry of panel #1207 on the hanging wall of F29 normal fault is less than the overall average of the CBM content of the two roadways. The distance between these measuring points and F29 normal fault is 8.9–98.6 m (Figure 9). It shows that the influence radius of CBM escape in the hanging wall of F29 normal fault should be more than 100 m.

The CBM content of all measuring points in tailentry of panel #1207 at the foot-wall of F29 normal fault is 6.33–6.47 m^3/t, with an average of 6.40 m^3/t. The buried depth of all measuring points is 385–394m, with an average of 389.5 m. The CBM content of the three measuring points closest to F29 normal fault is 6.33–6.35 m^3/t, with an average of 6.34 m^3/t, and the buried depth is 389–394 m, with an average of 392 m. Compared with the overall average CBM content, the CBM content at these three points decreased by 0.7, 1.1, and 0.9% respectively.

The above results show that there is a significant difference in the influence of the fault on the CBM content in the hanging wall

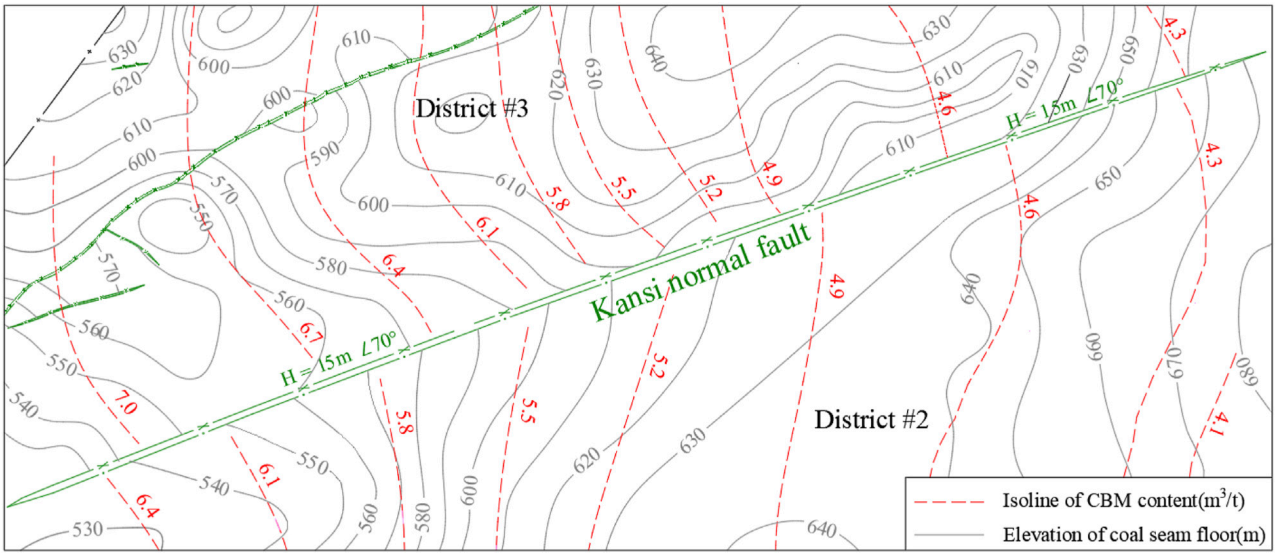

FIGURE 8
Gas content and elevation of the coal seam floor around Kansi fault.

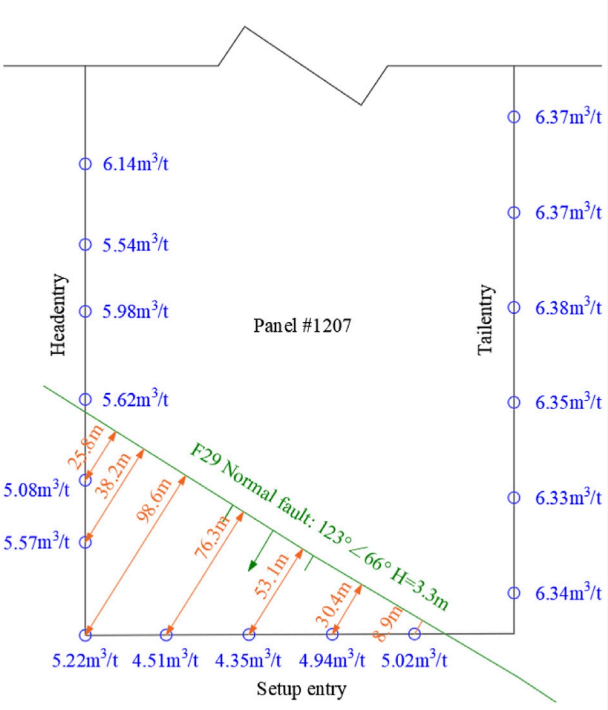

FIGURE 9
The CBM content near F29 normal fault.

and footwall, which needs to be analyzed in combination with the lithology, structural stress and other factors of the two walls.

3.3 Influence law of collapse columns on the occurrence of CBM

3.3.1 Types of controlling effect of collapse column on CBM occurrence

Collapse column is the collapse phenomenon of soluble rocks such as limestone and dolomite in the lower part of coal measure stratum under the action of groundwater and gravity. In the process of studying the formation mechanism of collapse columns, experts and scholars have formed theories such as "karst cave theory", "paste dissolution theory" and "vacuum suction collapse theory". Although there is no unified theory at present, it is generally believed that the development of collapse columns is controlled by three factors: karst conditions, hydrodynamic conditions and tectonic action. Sima Coal Mine has sufficient hydrodynamic conditions, fully developed karst, well-developed structural conditions in the process of geological evolution, and has the basic conditions for the development of collapse columns, resulting in the distribution of collapse columns in all areas of Sima Coal Mine.

The controlling effect of collapse column on CBM occurrence is related to the development height of collapse column, the cementation degree of collapse column, groundwater runoff conditions and the positional relationship between collapse column and other fault structures, which can be mainly divided into the following three categories:

3.3.1.1 Aggregation action

The minable coal seams in Sima coal mine are mainly 3 layers, coal seams #3, #9 and #15. The top of the collapse column may develop to the roof of coal seam #3 or only to the floor of coal seam #3. If the top of the collapse column develops to the roof of coal seam #3, the internal cementation is very poor and is not connected with other fault structures, the collapse column will become the vertical migration channel of coalbed methane. In general, the CBM content in deep coal seams is high and the pressure is high. The CBM existing in coal seams #9 and #15 migrate to coal seam #3 along the collapse column, and the CBM accumulation area is formed around the collapse column (Figure 10A).

3.3.1.2 Escape action

When the collapse column penetrates coal seams #3, #9 and #15, if the water barrier capacity inside the collapse column is very poor, Ordovician limestone water or water from the roof and floor of the coal seam may enter the working face through the collapse column, resulting in increased water inflow of the working face and even mine water damage. At this time, under the pressure of water, the CBM in the rock gap gradually precipitates and the CBM escapes (Figure 10B). At the same time, the flow of water will dissolve a small part of the CBM on the one hand and accelerate the CBM escape on the other hand. In addition, if the collapse column is connected with other fault structures to form a CBM drainage channel, the CBM content will also be reduced and the CBM will escape.

3.3.1.3 No obvious effect

When the collapse column does not penetrate into the floor of coal seam #3, and there is a thick and complete rock stratum with poor permeability between the floor of coal seam #3 and the collapse column, the existence of the collapse column will not have a significant impact on the CBM content of the coal seam #3 (Figure 10C). In addition, if the internal cementation of the collapse column is good and the mechanical and seepage indexes of the complete rock sample have been basically reached, and the top of the collapse column develops to the roof of the coal seam #3 in time, the existence of the collapse column will also not cause significant changes in the CBM content of the coal seam #3.

3.3.2 Collapse column X8

Collapse column X8 is located on the east side of tailentry #1208 (Figure 11), and the minimum distance from the tailentry is about

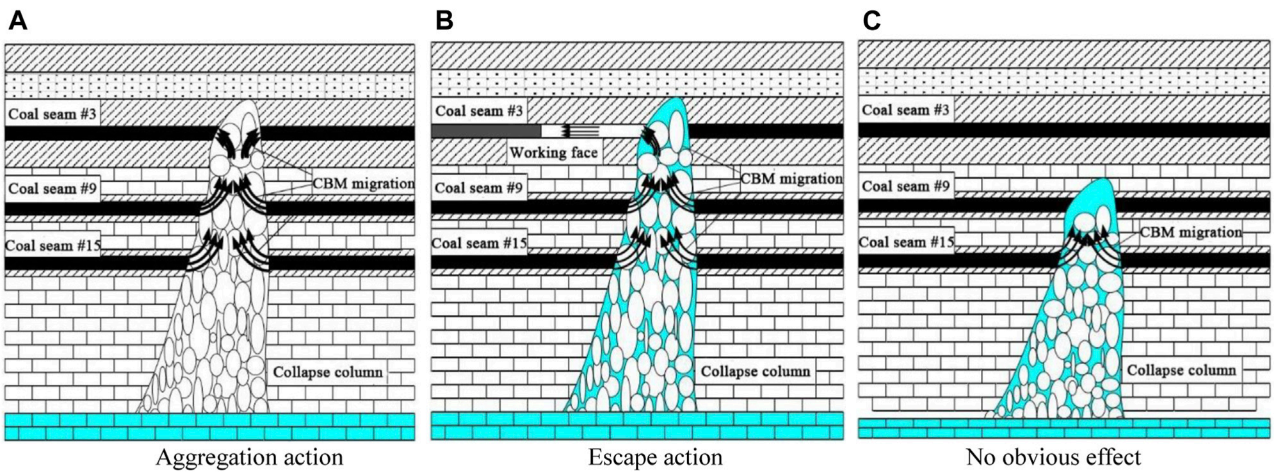

FIGURE 10
Different control effects of collapse column on the occurrence of CBM.

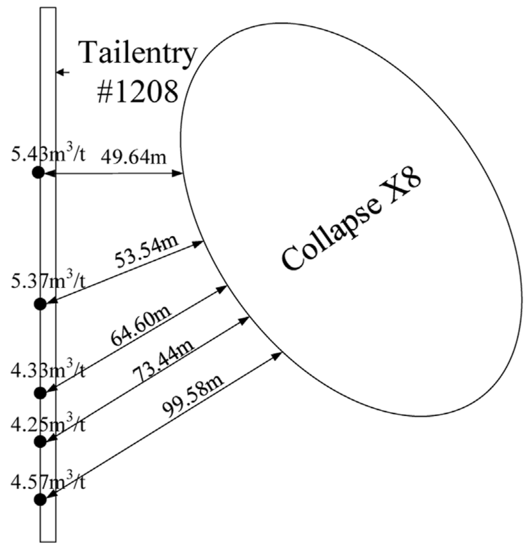

FIGURE 11
Gas occurrence rule around collapse column X8.

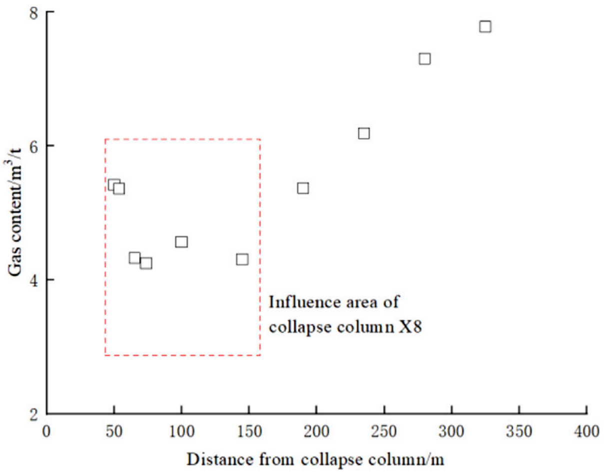

FIGURE 12
Influence radius of collapse column X8.

50 m, with the diameter of its major axis of 150 m and that of its minor axis of 50–60 m. Panel #1208 does not directly expose collapse column X8, and the drilling results show that collapse column X8 is more likely to exist.

The CBM measurement points around collapse column X8 are mainly located in tailentry #1208. If the calculation is carried out according to the linear relationship between the fitted CBM content and the buried depth in Figure 4, the gas content in the area where collapse column X8 is located should reach more than 6.50 m^3/t under the action of buried depth only. According to this calculation, the content of CBM near the collapse column X8 decreased by 16.4%–34.6%, with an average of 26.3%. This shows that collapse column X8 plays a major role in the escape of CBM.

Figure 12 shows that the CBM content within 150 m around collapse column X8 decreases significantly, and the minimum CBM content reaches 4.25 m^3/t. In the range of 150–300 m, the CBM content shows a gradual increase, and when the distance reaches about 300m, the CBM content reaches more than 6.50 m^3/t. So, It can be judged that the significant influence

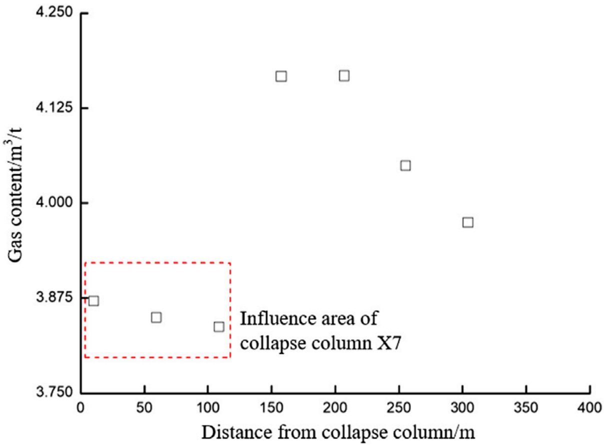

FIGURE 13
Influence radius of collapse column DX7.

radius of collapse column X8 is about 150 m, and the maximum influence radius may reach 300 m. The fractures in the formation process of collapse column provide a channel for coalbed methane transportation. The larger the fracture range is, the larger the gas escape range is.

3.3.3 Collapse column DX7

Collapse column DX7 is located at 595–650 m in headentry #1303 of Sima coal mine, with a major-axis diameter of about 70 m and a minor-axis diameter of about 40 m. Headentry of panel #1303 directly exposes and diagonally passes through collapse column DX7. Since panel # 1303 is the first working face in district #3, the CBM measurement points around collapse column DX7 are mainly distributed in headentry #1303.

It can be seen from Figure 13 and Table 3 that the CBM content around collapse column DX7 is not significantly reduced, and the CBM content within 50 m around collapse column DX7 is only reduced by about 7%. On the one hand, the scale of collapse column DX7 is small, and the cracks around it are not developed, which is not conducive to CBM escape; On the other hand, according to the field observation, the collapse column DX7 is well consolidated, and some areas are cemented and diagenesis again, which can not provide a good channel for CBM escape. Therefore, the CBM dissipation effect of collapse column DX7 is not obvious, and the maximum influence radius of CBM dissipation is only about 50 m.

4 Conclusion

Based on the actual measurement results of the occurrence of CBM in districts #2 and #3 of Sima coal mine, the effects of buried depth, fault and collapse column on CBM occurrence are analyzed. The control effect of different structures on the occurrence of CBM can provide a theoretical basis for efficient underground CBM drainage. The main conclusions are as follows:

1) The variation law of CBM content with buried depth is analyzed. The results show that: (1) In the small-scale range of buried depth, the dispersion between CBM and buried depth is very large. It is meaningless to discuss the relationship between CBM content and buried depth. (2) Faults and collapse columns significantly affect the content of local CBM nearby, but from the large-scale range such as the whole mining area, the average value of CBM content at a certain buried depth will not be affected by faults and collapse columns. (3) The average content of CBM has a linear relationship with buried depth and overburden thickness, and it is more practical to analyze the influence of overburden thickness on the average content of CBM.
2) In the hanging wall of F29 normal fault, it is roughly estimated that the average escape rate of CBM near the fault is 13.9%, while in the footwall of F29 normal fault, this value is 0.7%–1.1%. The results show that there is a significant difference in the influence of the fault on the CBM content in the hanging wall and footwall, which needs to be

TABLE 3 Test results of basic parameters in headentry #1303.

Distance between measuring position and roadway exit/m	CBM content of raw coal/(m^3/t)	Distance between measuring position and roadway exit/m	CBM content of raw coal/(m^3/t)
8.6	4.7543	289.6	3.9742
23.4	4.9372	338.6	4.0488
34.6	4.3518	387.1	4.1672
49.2	4.3657	436.4	4.1663
95.4	4.2045	485.3	3.8370
144.3	4.0503	534.7	3.8493
192.9	4.0206	583.9	3.8712
242.0	3.9648	632.6	3.7401

analyzed in combination with the lithology, structural stress and other factors of the two walls.

3) The control effect of collapse column on CBM occurrence is related to the development height of collapse column, the cementation degree of collapse column, groundwater runoff conditions and other factors. It can be divided into three categories: aggregation action, escape action (such as collapse column X8) and no obvious effect (such as collapse column DX7).

Data availability statement

The original contributions presented in the study are included in the article/supplementary material, further inquiries can be directed to the corresponding authors.

Author contributions

HL data curation and formal analysis, BZ and XL funding acquisition and investigation, CL, CW, and FW methodology, project administration and resources ZC and DC software, supervision and validation.

Funding

This work was supported by the National Natural Science Foundation of China (52104204, 51778215, 52174072), the Education Department of Guizhou Province Fund (Qianjiaohe KY Zi [2017] 265, Qianjiaohe KY Zi [2017] 266, Qianjiaohe KY Zi [2019] 073, Qianjiaohe KY Zi [2020] 050, Qianjiao XKTJ [2020] 23), the Science and Technology Department of Guizhou Province Fund [Qiankehe Platform Talent (2019) 5620, Qiankehe Platform Talent-YSZ (2021) 001], the Natural Science Foundation of Shandong Province (ZR2021QE170), the Liupanshui Science and Technology Bureau fund (52020-2018-04-08).

Acknowledgments

We would like to thank the Lu'an Group Sima Coal Industry Limited Company for providing part of research data for this study.

Conflict of interest

Author ZC was employed by Lu'an Group Sima Coal Industry Limited Company

The remaining authors declare that the research was conducted in the absence of any commercial or financial relationships that could be construed as a potential conflict of interest.

Publisher's note

References

Cui, H. Q., and Jia, B. S. (2011). The research on gas geology rule and gas outburst danger zone prediction at sima coal mine. *J. Henan Polytech. Univ. Nat. Sci.* . 30 (2), 131–136. (in Chinese with English abstract). doi:10.16186/j.cnki.1673-9787.2011.02.022

Feng, J. J., Wang, E. Y., Huang, Q. S., Ding, H. C., and Ma, Y. K. (2020). Study on coal fractography under dynamic impact loading based on multifractal method. *Fractals* 28 (1), 2050006. doi:10.1142/S0218348X20500061

Feng, F., Chen, S. J., Wang, Y. J., Huang, W. P., and Han, Z. Y. (2021). Cracking mechanism and strength criteria evaluation of granite affected by intermediate principal stresses subjected to unloading stress state. *Int. J. Rock Mech. Min. Sci. (1997).* 143 (7), 104783. doi:10.1016/j.ijrmms.2021.104783

Kong, B., Liu, Z., and Yao, Q. G. (2021). Study on the electromagnetic spectrum characteristics of underground coal fire hazardous and the detection criteria of high temperature anomaly area. *Environ. Earth Sci.* 80 (3), 89–11. doi:10.1007/s12665-021-09380-5

Kong, X. G., Li, S. G., Wang, E. Y., Ji, P. F., Wang, X., Shuang, H. Q., et al. (2021a). Dynamics behaviour of gas-bearing coal subjected to SHPB tests. *Compos. Struct.* 256, 113088. doi:10.1016/j.compstruct.2020.113088

Kong, X. G., Li, S. G., Wang, E. Y., Wang, X., Zhou, Y. X., Ji, P. F., et al. (2021b). Experimental and numerical investigations on dynamic mechanical responses and failure process of gas-bearing coal under impact load. *Soil Dyn. Earthq. Eng.* 142, 106579. doi:10.1016/j.soildyn.2021.106579

Li, X. L., Cao, Z. Y., and Xu, Y. L. (2020). Characteristics and trends of coal mine safety development. *Energy Sources Part A Recovery Util. Environ. Eff.* 2020, 1–19. doi:10.1080/15567036.2020.1852339

Li, X. L., Chen, S. J., Liu, S. M., and Li, Z. H. (2021a). AE waveform characteristics of rock mass under uniaxial loading based on Hilbert-Huang transform. *J. Cent. South Univ.* 28 (6), 1843–1856. doi:10.1007/s11771-021-4734-6

Li, X. L., Chen, S. J., Wang, S., Zhao, M., and Liu, H. (2021b). Study on *in situ* stress distribution law of the deep mine taking Linyi mining area as an example. *Adv. Mater. Sci. Eng.* 2021, 5594181–5594211. doi:10.1155/2021/5594181

Liu, S. M., Li, X. L., Wang, D. K., and Zhang, D. M. (2020). Investigations on the mechanism of the microstructural evolution of different coal ranks under liquid nitrogen cold soaking. *Energy Sources Part A Recovery Util. Environ. Eff.* 2020, 1–17. doi:10.1080/15567036.2020.1841856

Liu, X. F., Nie, B. S., Guo, K. Y., Zhang, C. P., Wang, Z. P., and Wang, L. K. (2021). Permeability enhancement and porosity change of coal by liquid carbon dioxide phase change fracturing. *Eng. Geol.* 287, 106106. doi:10.1016/j.enggeo.2021.106106

Liu, H. Y., Zhang, B. Y., Li, X. L., Liu, C. W., Wang, C., Wang, F., et al. (2022). Research on roof damage mechanism and control technology of gob-side entry retaining under close distance gob. *Eng. Fail. Anal.* 138, 106331. doi:10.1016/j.engfailanal.2022.106331

Liu, X. F., Wang, L. K., Kong, X. G., Ma, Z. T., Nie, B. S., Song, D. Z., et al. (2022). Role of pore irregularity in methane desorption capacity of coking coal. *Fuel* 314, 123037. doi:10.1016/j.fuel.2021.123037

Lu, J. X., Li, H., Shi, S. L., Huang, B. X., Lu, Y., Li, M., et al. (2021). Microwave-induced microstructure evolution of coal and its effects on the methane adsorption characteristic. *Energy fuels.* 35 (5), 4081–4090. doi:10.1021/acs.energyfuels.0c04363

Ma, C. D., Li, X. B., Chen, J. Z., Zhou, Y. N., and Gao, S. (2020). Geological core ground reorientation technology application on *in situ* stress measurement of an over-kilometer-deep shaft. *Adv. Civ. Eng.* 2020, 1–13. doi:10.1155/2020/8830593

Ma, Y. K., Nie, B. S., He, X. Q., Li, X. C., Meng, J. Q., and Song, D. Z. (2020). Mechanism investigation on coal and gas outburst: An overview. *Int. J. Min. Metall. Mater.* 27, 872–887. doi:10.1007/s12613-019-1956-9

Moore, T. A. (2012). Coalbed methane: a review. *Int. J. Coal Geol.* 101, 36–81. doi:10.1016/j.coal.2012.05.011

Niu, Q. H., Pan, J. N., Jin, Y., Wang, H. C., Li, M., Ji, Z. M., et al. (2019). Fractal study of adsorption-pores in pulverized coals with various metamorphism degrees using N_2 adsorption, X-ray scattering and image analysis methods. *J. Pet. Sci. Eng.* 176, 584–593. doi:10.1016/j.petrol.2019.01.107

Pan, J. N., Lv, M. M., Hou, Q. L., Han, Y. Z., and Wang, K. (2019). Coal microcrystalline structural changes related to methane adsorption/desorption. *Fuel* 239 (1), 13–23. doi:10.1016/j.fuel.2018.10.155

Qin, Y., Moore, T. A., Shen, J., Yang, Z. B., Shen, Y. L., and Wang, G. (2018). Resources and geology of coalbed methane in China: a review. *Int. Geol. Rev.* 60 (5-6), 777–812. doi:10.1080/00206814.2017.1408034

Shen, W. L., Shi, G. C., Wang, Y. G., Bai, J. B., Zhang, R. F., and Wang, X. Y. (2021). Tomography of the dynamic stress coefficient for stress wave prediction in sedimentary rock layer under the mining additional stress. *Int. J. Min. Sci. Technol.* 31, 653–663. doi:10.1016/j.ijmst.2021.04.003

Sinha, S. K., and Gupta, S. D. (2021). A geological model for enhanced coal bed methane (ECBM) recovery process: A case study from the jharia coalfield region, India. *J. Pet. Sci. Eng.* 201, 108498. doi:10.1016/j.petrol.2021.108498

Su, Y. F. (2016). Three gases Co-exploration and Co-mining of sea-land transition phase coal measures in Shanxi province, CNKI:SUN:ZGMC.0.2016-06-002. *China Coalbed Methane* 13 (6), 8–11. (in Chinese with English abstract).

Wang, K., and Du, F. (2020). Coal-gas compound dynamic disasters in China: a review. *Process Saf. Environ. Prot.* 133, 1–17. doi:10.1016/j.psep.2019.10.006

Wang, C., Xiong, Z. Q., Wang, C., Wang, Y. L., and Zhang, Y. H. (2020). Study on rib sloughage prevention based on geological structure exploration and deep borehole grouting in front abutment zones. *Geofluids* 2020, 1–12. doi:10.1155/2020/7961032

Wang, Z. Q., Yan, E. C., and Ji, H. B. (2016). *In-situ* stress field and geological tectonic analysis at Huangdao water-sealed underground oil carven site. *J. Eng. Geol.* 24 (1), 136–141. (in Chinese with English abstract). doi:10.13544/j.cnki.jeg.2016.01.017

Wang, C., Song, D. Z., Zhang, C. L., Liu, L., Zhou, Z. H., and Huang, X. C. (2019). Research on the classification model of coal's bursting liability based on database with large samples. *Arab. J. Geosci.* 12 (13), 411. doi:10.1007/s12517-019-4562-2

Wang, K., Yang, P., Yu, G. M., Yang, C., and Zhu, L. Y. (2020). 3D numerical modelling of tailings dam breach run out flow over complex terrain: A multidisciplinary procedure. *Water* 12 (9), 2538. doi:10.3390/w12092538

Xie, W. D., Wang, M., and Hou, X. W. (2018). Study on enrichment zones and enrichment regularity of coalbed methane in Hebei province. *J. Henan Polytech. Univ. Nat. Sci.* . 37 (182), 22–30. (in Chinese with English abstract). doi:10.16186/j.cnki.1673-9787.2018.03.003

Ye, Z. N., Hou, E. K., Duan, Z. H., and Li, Z. J. (2019). Coal reservoir characterization in a tectonic setting and the effects of tectonism on the coalbed methane (CBM) content. *Adv. Mater. Sci. Eng.* 2019, 1–11. doi:10.1155/2019/7974628

Yu, S. J., Liu, J. Y., Bai, P., Xu, H. T., He, R. S., Wang, Y. S., et al. (2021). Geological structure exploration of karst collapse column and evaluation of water insulation properties of the mud part. *Geofluids* 2021, 1–9. doi:10.1155/2021/2071333

Yuan, B. X., Li, Z. H., Chen, Y. M., Ni, H., Zhao, Z. Q., Chen, W. J., et al. (2021). Mechanical and microstructural properties of recycling granite residual soil reinforced with glass fiber and liquid-modified polyvinyl alcohol polymer. *Chemosphere* 268, 131652. doi:10.1016/j.chemosphere.2021.131652

Zhang, C. L., Wang, E. Y., Xu, J., and Peng, S. J. (2020). Research on temperature variation during coal and gas outbursts: Implications for outburst prediction in coal mines. *Sensors* 20 (19), 5526. doi:10.3390/s20195526

Zhang, C. L., Wang, E. Y., Xu, J., and Peng, S. J. (2021). A new method for coal and gas outburst prediction and prevention based on the fragmentation of ejected coal. *Fuel* 287, 119493. doi:10.1016/j.fuel.2020.119493

Zhang, X. M., Li, J. W., Han, B. S., and Dong, M. T. (2005). Division and formation mechanism of coalbed methane reservoir in Huainan Coalfield, Anhui Province, China. *Chin. Sci. Bull.* 50 (S), 7–17. doi:10.1007/BF03184077

Zhang, Z. B., Liu, X. N., Zhang, Y. H., Qin, X. Y., and Khan, M. (2021a). Comparative study on fracture characteristics of coal and rock samples based on acoustic emission technology. *Theor. Appl. Fract. Mech.* 111, 102851. doi:10.1016/j.tafmec.2020.102851

Zhang, Z. B., Wang, E. Y., Liu, X. N., Zhang, Y. H., Li, S. J., Khan, M., et al. (2021b). Anisotropic characteristics of ultrasonic transmission velocities and stress inversion during uniaxial compression process. *J. Appl. Geophy.* 186, 104274. doi:10.1016/j.jappgeo.2021.104274

Zhang, K. Z., Wang, L., Cheng, Y. P., Li, W., Kan, J., Tu, Q. Y., et al. (2020). Geological control of fold structure on gas occurrence and its implication for coalbed gas outburst: Case study in the Qinan coal mine Huaibei Coalfield, China. *Nat. Resour. Res.* 29, 1375–1395. doi:10.1007/s11053-019-09511-7

Zhang, R., Liu, J., Sa, Z. Y., Wang, Z. Q., Lu, S. Q., and Lv, Z. Y. (2020). Fractal characteristics of acoustic emission of gas-bearing coal subjected to true triaxial loading. *Measurement* 169, 108349. doi:10.1016/j.measurement.2020.108349

Zheng, C. S., Jiang, B. Y., Xue, S., Chen, Z. W., and Li, H. (2019). Coalbed methane emissions and drainage methods in underground mining for mining safety and environmental benefits: A review. *Process Saf. Environ. Prot.* 127, 103–124. doi:10.1016/j.psep.2019.05.010

Zhou, Y. B., Li, Z. H., Zhang, R. L., Wang, G. Z., Yu, H., Sun, G. Z., et al. (2019). CO_2 injection in coal: Advantages and influences of temperature and pressure. *Fuel* 236 (1), 493–500. doi:10.1016/j.fuel.2018.09.016

Zhou, Y. B., Li, H. S., Huang, J. L., Zhang, R. L., Wang, S. J., Hong, Y. D., et al. (2021). Influence of coal deformation on the Knudsen number of gas flow in coal seams. *Energy* 233, 121161. doi:10.1016/j.energy.2021.121161

Zhou, X. M., Wang, S., Li, X. L., Meng, J., Li, Z., Zhang, L., et al. (2022). Research on theory and technology of floor heave control in semicoal rock roadway: Taking longhu coal mine in Qitaihe mining area as an Example. *Lithosphere* 2022 (11), 3810988. doi:10.2113/2022/3810988

Zou, M. J., Wei, C. T., Huang, Z. Q., and Wei, S. (2015). Porosity type analysis and permeability model for micro-trans-pores, meso-macro-pores and cleats of coal samples. *J. Nat. Gas. Sci. Eng.* 27, 776–784. doi:10.1016/j.jngse.2015.09.025

Zou, M. J., Wei, S. M., Huang, Z. Q., Lv, X., and Guo, B. (2018). Simulations on recoverability performances for a coalbed methane field in SE edge of Ordos basin, China. *Fuel* 233, 354–360. doi:10.1016/j.fuel.2018.06.071

Zou, M. J., Wei, C. T., Zhang, M., and Lv, X. (2018). Quantification of gas and water transfer between coal matrix and cleat network during drainage process. *J. Energy Resour. Technol.* 140, 032905–032919. doi:10.1115/1.4038044

Zou, M. J., Lv, X. C., Huang, Z. Q., Wei, S., Zhang, M., and Sun, C. (2018). Modeling and prediction for gas production during coalbed methane drainage based on two indirect reservoir parameters. *Energy Explor. Exploit.* 36 (6), 1424–1437. doi:10.1177/0144598718777105

Zou, M. J., Liu, Y. Z., Huang, Z. Q., Zhang, M., and Zhang, P. (2020). Geological control of irreducible water within the coal matrix and its quantified evaluation model. *ACS Omega* 5, 9540–9549. doi:10.1021/acsomega.0c00782

Zou, Q. L., Liu, H., Zhang, Y. J., Li, Q. M., Fu, J. W., and Hu, Q. T. (2020). Rationality evaluation of production deployment of outburst-prone coal mines: A case study of nantong coal mine in chongqing, China. *Saf. Sci.* 122, 104515. doi:10.1016/j.ssci.2019.104515

frontiers | Frontiers in Earth Science

TYPE Original Research
PUBLISHED 01 September 2022
DOI 10.3389/feart.2022.999516

OPEN ACCESS

EDITED BY
Junjian Zhang,
Shandong University of Science and Technology, China

REVIEWED BY
Junqiang Kang,
China University of Mining and Technology, China
Fangkai Quan,
China University of Mining and Technology, China

*CORRESPONDENCE
Xin Li,
lixinwaxj@xju.edu.cn

SPECIALTY SECTION
This article was submitted to Economic Geology,
a section of the journal
Frontiers in Earth Science

RECEIVED 21 July 2022
ACCEPTED 08 August 2022
PUBLISHED 01 September 2022

CITATION
Qin Q, Li X, Peng R, Peng S, Liu Y, Zhou X and Yang J (2022), Coalbed methane reservoir dynamic simulation comparisons using the actual steeply inclined model and ideal steeply inclined model.
Front. Earth Sci. 10:999516.
doi: 10.3389/feart.2022.999516

Coalbed methane reservoir dynamic simulation comparisons using the actual steeply inclined model and ideal steeply inclined model

Quanling Qin[1,2], Xin Li[1,2]*, Rendong Peng[2], Shiqi Peng[2], Yipan Liu[2], Xiang Zhou[2] and Jingwen Yang[2]

[1]School of Safety Science and Engineering, Henan Polytechnic University, Jiaozuo, China, [2]College of Geology and Mining Engineering, Xinjiang University, Ürümqi, China

Numerical simulation is an efficient method to quantitatively describe the reservoir dynamics of coalbed methane (CBM) reservoirs. The ideal steeply inclined model (ISIM), assumed to be a steeply inclined plate, has been widely applied in steep coalbed methane reservoir modeling, although the ISIM cannot accurately reflect the actual reservoir geological conditions. In this paper, the dynamics of CBM production and reservoirs using the ISIM and actual steeply inclined model (ASIM) were compared, taking the steep coal in the Fukang mining area located in northwestern China as an example, with the purpose of revealing the differences and applicability of the ASIM and ISIM. The ASIM and ISIM were established by Petrel software, and CBM production was matched and predicted by Eclipse software. Data reflecting reservoir dynamics, such as water saturation, reservoir pressure, and gas content, were extracted. The dynamic changes in the reservoir physical properties of the ASIM and ISIM were also compared. The results showed that: 1) multiple gas production peaks occurred in both ASIM and ISIM. The maximum daily gas production of ASIM occurred earlier than the maximum daily gas production of ISIM. The peak gas production and cumulative gas production of ASIM were both greater than the peak gas production and cumulative gas production of ISIM. 2) Due to the variations in grid shape and dip angle with each grid in the ASIM, the production effect of the ASIM was better than the production effect of the ISIM in the third stage (4–10 years) of drainage. 3) In the third stage (4–10 years) of drainage, the decrease rate of reservoir pressure of ASIM was larger than the decrease rate of reservoir pressure of ISIM because of the relatively better production performance of ASIM. 4) Differentiation of gas and water dominated the variation trend of gas content, and in the third stage (4–10 years) of drainage, the ASIM has higher recovery efficiency compared with ISIM. Compared with ISIM proposed by previous scholars, the ASIM was more helpful to monitor the dynamic behavior of coal reservoirs, and ASIM can provide a more reliable basis for guiding coalbed methane development.

KEYWORDS
coalbed methane, numerical simulation, reservoir pressure, gas content, dynamic

1 Introduction

As an important part of unconventional natural gas resources, coalbed methane (CBM) has great potential for easing the scarcity of conventional natural gas, and its development is rising rapidly worldwide (Zou et al., 2019). Since the 1980s, China's CBM resources have been studied extensively (Shao et al., 2015; Qin et al., 2018). In 2020, China's surface production of CBM reached 5.767 billion m^3, accounting for 3.07% of the total natural gas production, indicating that China has entered the early stage of CBM development, but improvement of production is encouraged to realize large-scale development (Qin et al., 2022). The southern Junggar Basin is the main battlefield for the CBM development of low rank coal reservoirs in China. The strike, dip and dip angles of coal reservoirs formed in this area vary sharply and are very different from the strike, dip, and dip angles of most coal-bearing basins, such as the Powder River Basin in the United States, the Surat Basin in Australia, the Albert Basin in Canada, and the Qinshui Basin in China. Replicating the *in situ* geological conditions of complex coal reservoirs of the southern Junggar Basin using physical experiments is very difficult, while numerical simulation can be used as an efficient tool to study CBM production characteristics by considering actual geological conditions.

Reservoirs usually undergo three processes during CBM production, namely, desorption, diffusion, and seepage. Under the action of a pressure difference, CBM desorbs from the surface of the coal matrix, diffuses into large fractures under the action of a concentration difference, and penetrates the wellbore under the action of flow potential energy (Senthamaraikkannan et al., 2016; Tang et al., 2018; Dong et al., 2020; Duan et al., 2020). To simulate the seepage process of CBM, it is necessary to include these three processes in a reservoir model. At present, many simulators have been used in CBM numerical simulations, providing a reference for formulating reasonable production systems and optimization schemes for CBM drainage under different conditions (Ibrahimet and Nasr-El-Din, 2015; Sayyafzadeh et al., 2015; Sun et al., 2017). Wan et al. (2016) determined the desorption range and pressure drop area of CBM with the method of numerical simulation and proved that critical analytical pressure, well spacing and permeability are the factors that affect the desorption area of CBM. Yarmohammadtooski et al. (2017) analyzed the production data for gas water flow with a numerical model and found that fracture compression and matrix shrinkage affected reservoir permeability at different production times, consistent with the actual production. Karacan et al. (2014) evaluated the CBM migration capacity of the Illinois Basin in the United States through multiwell historical fitting, providing the real distribution of reservoir parameters and contributing to the effective management of CBM development. Coal seams in China are characterized by multi-layer superposition, and the changes of reservoir physical properties are more complex in the process of coalbed methane multi-layer combined production. It was difficult to analyze physical properties completely based on actual production data. Therefore, numerical simulation has become main method to analyze interlayer interference of methane co-production (Quan et al., 2022a; Quan et al., 2022b).

The coal seams of the southern Junggar Basin are highly heterogeneous, and the previous ideas cannot be completely applied to numerical research in this area. Numerous scholars have studied the dynamic characteristics of the physical properties of inclined coal reservoirs during CBM production by numerical simulation. The scholars found that different burial depths of reservoirs led to differences in variations in physical properties, resulting in different rules of gas production. Meanwhile, with the increase in the coal seam dip angle, the difference in gas production gradually increased. (Fu et al., 2018; Kang et al., 2018; Kang et al., 2019; Kang et al., 2020; Liang et al., 2020). However, previous studies have greatly simplified the coal reservoir in the process of CBM simulation, which may distort the actual reservoir, and the reliability of the simulation results has been relatively low. However, previous studies on steeply inclined coal reservoir production simulation have greatly simplified the reservoir as an ideal steeply inclined model (ISIM), which may be distorted for the actual reservoir, and the reliability of the simulation results needs to be reconsidered.

The foundation of numerical simulation is the construction of a geological model, and the degree of coincidence between the simulated geological model and an actual geological model determines the reliability of the production simulation. In the previous numerical simulation of CBM production of steeply inclined coal reservoirs, most scholars usually set up ISIM to simulate the actual drainage process. However, there may still be a certain gap in guiding actual production. In this paper, a coal reservoir located in the Fukang mining area of the southern Junggar Basin was selected as the research subject. Xinjiang, an actual steeply inclined model (ASIM), was constructed by combining the seismic data using the model construction method in Petrel software of Schlumberger, and numerical simulation software was used to restore the CBM production process. Compared with the ISIM proposed by previous scholars, the ASIM was found to predict higher gas production, better drainage, pressure reduction, and higher recovery. The proposed ASIM model is more objective and vivid than the ISIM model.

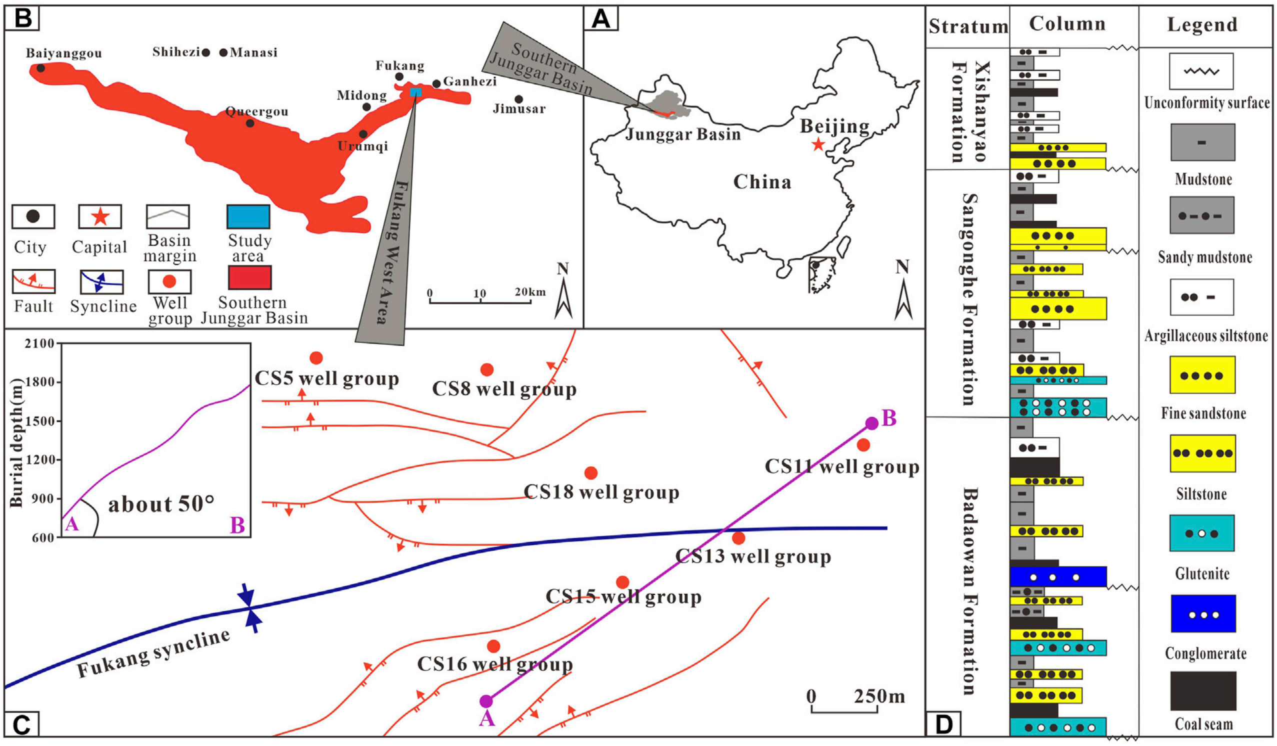

FIGURE 1
(A) Location map of the southern Junggar Basin. **(B)** Geological structure of the southern Junggar Basin. **(C)** Structural outline and well location distribution in the Fukang west area. **(D)** Coal-bearing stratum.

This work can provide guidance for CBM development where steep inclined coal reservoirs are found.

2 Geological setting

The southern Junggar Basin is located in northwest China, with an area of approximately 1.8×10^3 km^2 (Figure 1A). The CBM resource in the southern Junggar Basin is half the CBM resource in Xinjiang, which is an important area for CBM development (Liu et al., 2014; Ge et al., 2018). The southern Junggar Basin experienced Hercynian, Indosinian, Yanshanian and Himalayan movements, and a series of NW thrust faults formed (Guo et al., 2014) (Figure 1B). The Fukang mining area is located in the eastern part of the southern Junggar Basin (Zhang et al., 2021). Since the Mesozoic, the Fukang mining area has been influenced by the uplift of the Northern Tianshan and Bogda Mountains, resulting in a complex system of folds and faults under the action of Yanshanian and Himalayan movements (Fu et al., 2016). The southern limb of the Fukang syncline has a dip angle of 45°–70°, and the faults are mainly high-angle thrust faults (Zhang et al., 2021). Seven CBM well groups (CS5, CS8, CS11, CS18, CS13, CS15 and CS16) were drilled in the two limbs of the Fukang syncline (Figure 1C).

The coal-bearing strata in the study area are mainly the Xishanyao Formation of the Middle Jurassic (J_2x) and the Badaowan Formation of the Lower Jurassic (J_1b), with the Lower Jurassic Sangonghe Formation located between those two formations (Figure 1D) (Li et al., 2018). The lithology contains mudstone, sandy mudstone, argillaceous siltstone, fine sandstone, siltstone, glutenite, and coal, with small amounts of conglomerate. The thickness of the coal seam in the Badaowan Formation is more than 0.3 m, and the average total thickness is 68.48 m, which is the main CBM production layer (Zhang et al., 2021).

3 Model construction

3.1 Assumptions

A coal reservoir containing both a coal matrix and fracture is regarded as a dual porosity and single permeability model in this study (Liu et al., 2021). At present, most researchers generally believe that as drainage proceeds and when the reservoir pressure reaches below the critical desorption pressure, CBM desorbs from the coal matrix surface and diffuses into the fracture system according to Darcy's law

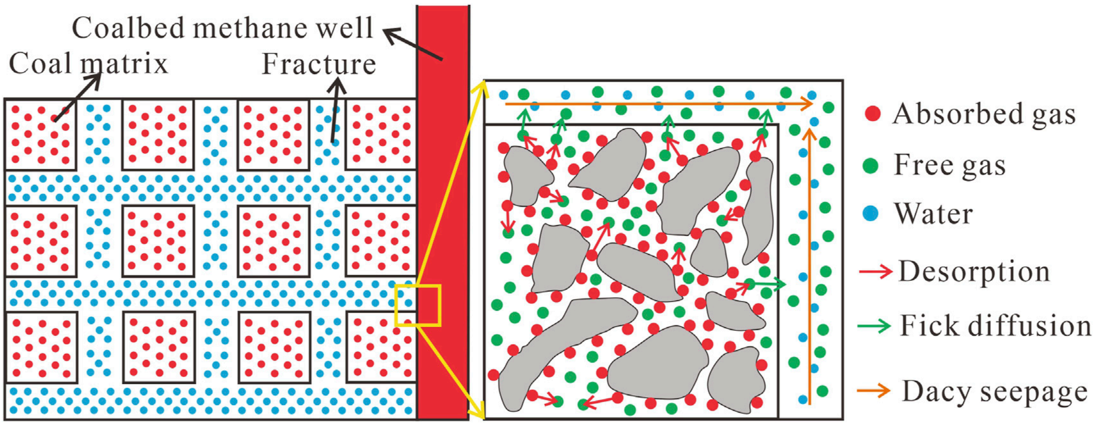

FIGURE 2
Theoretical model of the dual porosity and single permeability model (Qin et al., 2020).

TABLE 1 Parameters of the simulation using the ASIM and ISIM models.

Parameters	Value/Function	Unit	Parameters	Value/Function	Unit
Burial depth in bottom	1143	m	Porosity gradient	$2e^{(-0.005*H)}$	/
Initial reservoir pressure	11.8	MPa	Permeability gradient	$1000e^{(-0.005*H)}$	mD/m
Well diameter	0.24	m	Gas content gradient	96.864*H/(339.03+H)	$(m^3/t)/m$
Skin factor	0.5	/	Reservoir pressure gradient	$0.0103*H-3 \times 10^{-14}$	MPa/m
Gas content in bottom	10.01	m^3/t	Temperature	28	°C
Porosity in bottom	0.659	%	Langmuir pressure	3.5	MPa
Permeability in bottom	3.296	mD	Langmuir volume	13.38	m^3/t
Rock compressibility	$/5 \times 10^{-4}$	/MPa	Critical water saturation	30	%
Gas diffusion coefficient	1	m^2/d	Initial water saturation	100	%

(Figure 2). In the process of CBM production simulation of this work, the following assumptions were made: 1) the adsorption of CBM occurs in the matrix unit, and the flow occurs in the fracture unit, which is the dual porosity and single permeability model; 2) the adsorption and desorption of methane follows the Langmuir isothermal adsorption equation (Eq. 1), and all methane is adsorbed in the matrix unit by default in the initial state; 3) the diffusion of methane follows Fick's diffusion law (Eq. 2). When the reservoir pressure drops below the critical desorption pressure, methane is desorbed quickly and diffuses into the fracture unit for Darcy seepage (Eq. 3); 4) the software automatically initializes reservoir pressure according to the law of reservoir pressure variation as burial depth varies in the research area (Table 1); 5) shrinkage and expansion of the coal matrix are not considered.

In the initial state, all CBM was adsorbed on the surface of the coal matrix, following the Langmuir isothermal adsorption equation (Eq. 1). When the gas pressure was lower than the critical desorption pressure, CBM was desorbed from the matrix:

$$V = \frac{V_L P}{P + P_L} \tag{1}$$

where V is the volume of gas adsorbed by the solid under pressure P; V_L is Langmuir volume (m^3/t); P_L is Langmuir pressure (MPa); and P is the gas pressure (MPa).

The gas concentration difference between the matrix and the fracture makes methane diffuse into the fracture unit, following Fick's diffusion law (Eq. 2);

$$Jv = -D\frac{dX}{dr} \tag{2}$$

where Jv is the gas volume flux in a coal matrix; D is the diffusion coefficient; X is the gas content per unit volume of coal; and r is the radius of the coal particles.

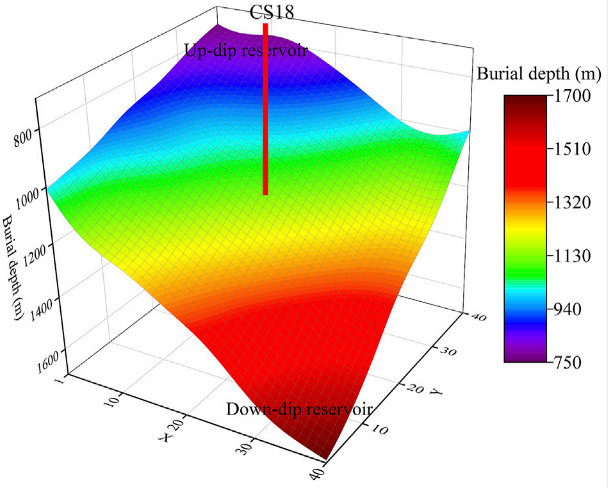

FIGURE 3
Actual steeply inclined model (ASIM).

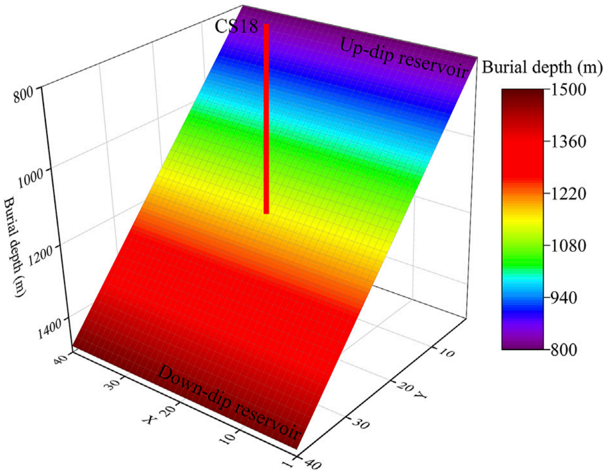

FIGURE 4
Ideal steeply inclined model (ISIM).

The pressure differential between the fracture and the wellbore causes the methane to flow into the wellbore, following Darcy's law (Eq. 3);

$$Jv = -K\frac{dP}{dr} \tag{3}$$

where Jv is the gas volume flux in a coal matrix, K is the permeability coefficient, P is the square of gas pressure, and r is the radius of coal particles.

3.2 Model construction

The ASIM and ISIM were constructed by corner grid. The former is the *in situ* reservoir model, which considers the topographic characteristics of the coal reservoir, and the latter is the coal reservoir assumed to be a 45° plate model. The length, width, and height of the two models were set as 1000 m × 1000 m × 17.6 m, and the number of grids was 40 × 40 × 3. The actual size of each grid is 25 m × 25 m × 5.87 m. The CS18 well is located in the center of the model. Details of those two models are illustrated below:

3.2.1 Actual steeply inclined model

Based on the coal seam interpreted by seismic data, the ASIM of the coal reservoir of the study area was constructed by Petrel (Figure 3). The dip angle of the model grid ranged between 0 and 61°, the dip direction was different due to the topographic fluctuation and geological structure variation, and the burial depth ranged from 765.74 m to 1691.51 m. The reservoir was divided into up-dip reservoirs and down-dip reservoirs, with CBM wells located at the center.

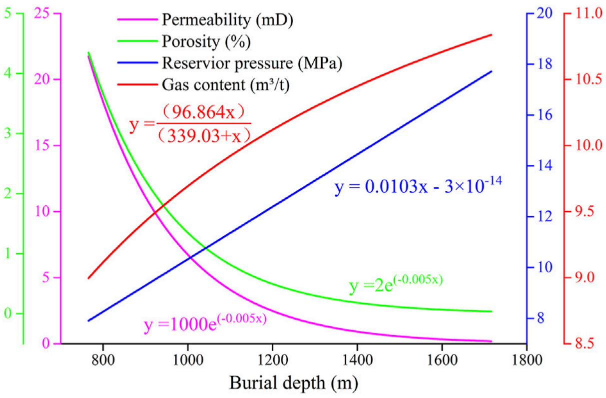

FIGURE 5
Parameters of permeability, porosity, pressure, and gas content in the ASIM and ISIM models.

3.2.2 Ideal steeply inclined model

Previous CBM researchers usually set the reservoir as a horizontal plate or an inclined plate with a certain dip angle when constructing the numerical model. Such a reservoir is homogeneous in reservoir parameters, and the degree of reservoir heterogeneity description is weak. Additionally, the influences of the actual terrain on the simulation results lack deep discussion. According to the research ideas of previous scholars, a plate coal reservoir model with a dip angle of 45° was constructed by using the CBM template provided by Eclipse. The burial depth of the model ranged from 801.28 m to 1493.52 m. The reservoir was divided into up-dip reservoirs and down-dip reservoirs, with the CS18 well located at the center (Figure 4).

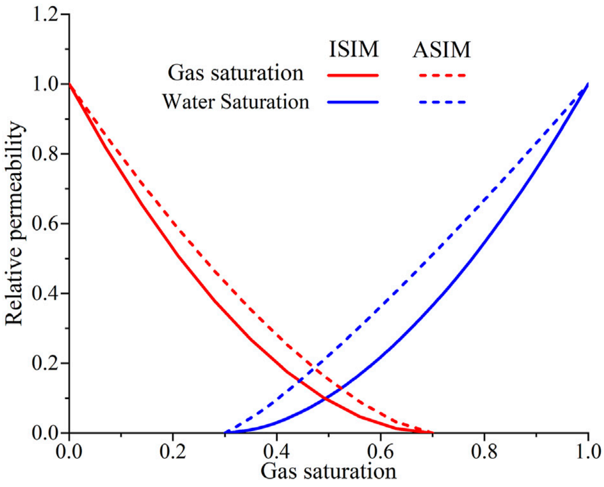

FIGURE 6
The relative permeability curves of gas and water in the ASIM and ISIM models.

4 Simulation parameters

Attribute assignment and historical matching were carried out for the above two models. Burial depth was the main factor controlling the reservoir pressure, porosity, permeability, and gas content; thus, those four parameters were assigned by using the fitting relationship function between those four parameters and burial depth, and some parameters were based on Kang et al. (2019) (Figure 5). Related studies have shown that initial gas content and reservoir pressure are positively correlated with burial depth, while permeability and porosity are negatively correlated with burial depth (Shi et al., 2018; Hu, 2019; Wang et al., 2020; Zhao and Chi, 2020). Coal seams have porosities and permeabilities typically ranging between 0.5 and 2.5% and 0.1–100 mD, respectively (Karimpouli et al., 2020; Mostaghimi et al., 2017). With the continuous progress of coalification and physical compaction, the porosity of coal rock will decrease exponentially as burial depth increases (Xin et al., 2019). Therefore, when setting the porosity and permeability, the burial depth was taken as the independent variable to decrease exponentially. The modeling region is located at the Fukang syncline tip, where stress release results in increased permeability. The CS11 well group, located approximately 900 m adjacent to the CS18 well group, has a maximum well test permeability of 16.64 mD (Pu et al., 2021). The production process of CBM can be divided into a single-phase water flow stage, gas-water flow stage and single-phase gas flow stage; thus, the relative permeability curves of gas and water were used to describe the relative flow capacity of gas and water in fractures. The relative permeability curves of gas and water were fitted by the classical Corey equation (Corey, 1954). The relative permeability curves fitted by the ASIM and ISIM are shown in Figure 6. Simulation parameters are shown in Table 1, and relevant parameters of each grid in both the ASIM and ISIM models were based on the parameters of the reservoir located in the wellbore position.

5 Results

5.1 History matching

The rising stage of gas production in the CS18 well was selected for historical matching, and the declining stage of gas production was selected to test the validity of the model. The depletion development mode to describe the bottom hole pressure decrease was selected for simulating the CBM production (595 days) of the CS18 well (Figure 7A). By adjusting the porosity, permeability, gas content gradient, and relative permeability curves of gas and water, historical fittings matching the gas production data using ASIM and ISIM were carried out (Figure 7B). For 0–250 days, the ASIM matching degree was better than the matching degree of ISIM; for 250–450 days, the ASIM matching degree was better than the matching degree of ISIM; and for 450–595 days, the matching degree of both ASIM and ISIM was better. In general, the matching results of the ASIM and ISIM were acceptable.

5.2 Productivity prediction

Based on the historical matching results, the 10-year gas production characteristics of the CS18 well using ASIM and ISIM were predicted. To prevent stress-sensitive reservoir damage caused by excessive pressure reduction, a constant bottom hole pressure (1.3 MPa) was adopted for 3–10 years. The results show that the first peak value of gas production of ASIM was 9292.95 m^3/d, occurring on the 600th day, and the second peak value of gas production was 19120.01 m^3/d, occurring on the 3100th day. The 10-year cumulative gas production of ASIM was 3.48×10^7 m^3. For ISIM, the first peak of daily gas production appeared on approximately the 600th day (9116.05 m^3/d) and the second peak of daily gas production occurred on the 3300th day (15406.85 m^3/d). The 10-year cumulative gas production of ISIM was 3.17×10^7 m^3 (Figure 8A). The first peak of ASIM was maintained for approximately 100 days, and the ISIM was maintained for approximately 400 days. The cumulative gas production of ISIM was higher than the cumulative gas production of ASIM during the first 3000 days and lower than the cumulative gas production of ASIM after 3000 days (Figure 8B).

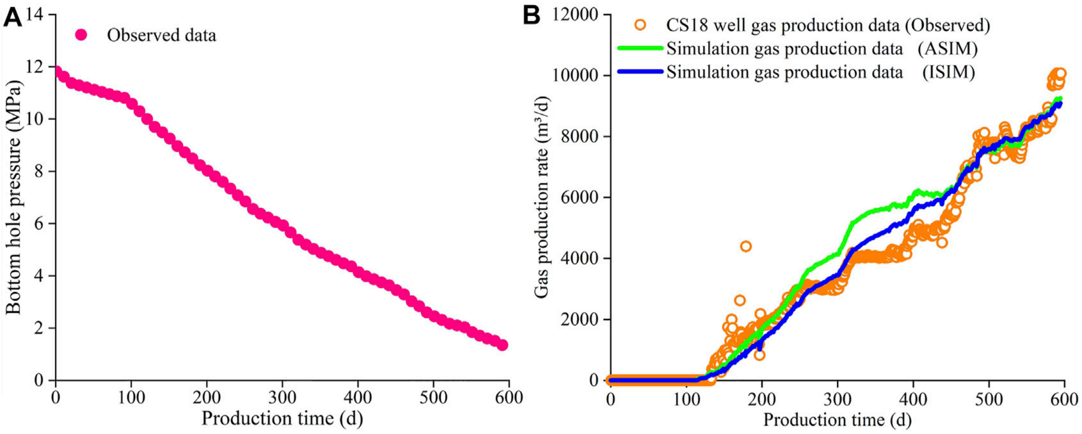

FIGURE 7
(A) Bottomhole pressure of ASIM and ISIM. **(B)** History matching results of ASIM and ISIM.

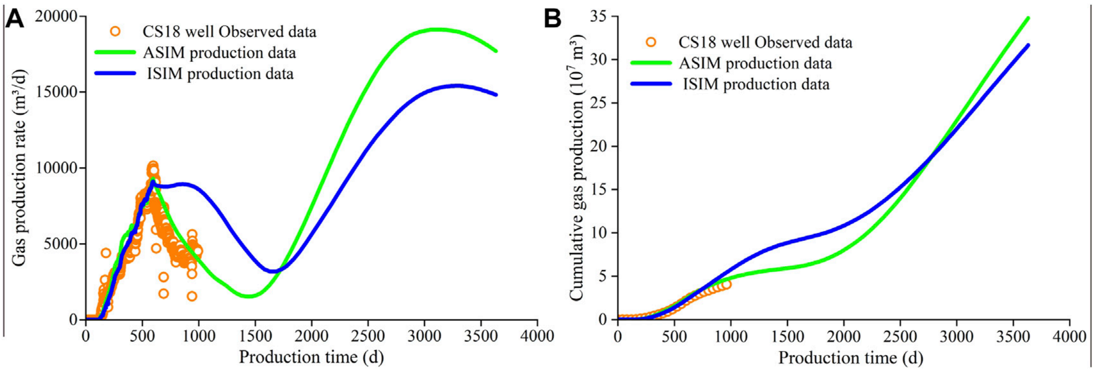

FIGURE 8
(A) Gas production rate of ASIM and ISIM. **(B)** Cumulative gas production of ASIM and ISIM.

5.3 Reservoir physical property dynamics

5.3.1 Water saturation dynamics

After completion of the simulation, the water saturation spatial distribution maps of the ASIM and ISIM at the initial state and at 1, 2, 3, 4 and 10 years were extracted (Figure 9; Figure 10). In both the ASIM and ISIM, reservoir water saturations in the up-dip direction decrease preferentially. For ASIM, in 0–1 year of drainage, the water saturations were generally high, with only a few grids being reduced to the lowest at this stage (57%) (Figure 9B). In the subsequent 9 years, as drainage proceeded, the water saturation of the up-dip reservoir grid gradually decreased to irreducible water saturation (Figures 9C–F). For ASIM, the decrease rates of water saturation in different grids with varied burial depths changed heterogeneously. For ISIM in 0–1 year of drainage, the water saturation around the wellbore decreased preferentially, reaching a value of 91% (Figure 10B). As the drainage process proceeded, the water saturation basically decreased symmetrically in the center of the wellbore in the strike direction. However, in the dipping direction, the water saturation of the reservoir in the up-dip direction with shallow burial depth first decreased to the critical water saturation (Figures 10C–F). The water saturation of the ASIM decreased by 0.68% in 0–1 year, 3.53% in 1–2 years, 3.55% in 2–3 years, 4.66% in 3–4 years, 23.33% in 4–10 years, and 33.34% in 0–10 years. For ISIM, the overall water saturation decreased by 1.08% in 0–1 year, 3.99% in 1–2 years, 2.92% in 2–3 years, 2.47% in 3–4 years, 22.73% in 4–10 years, and 30.22% in 0–10 years (Table 2).

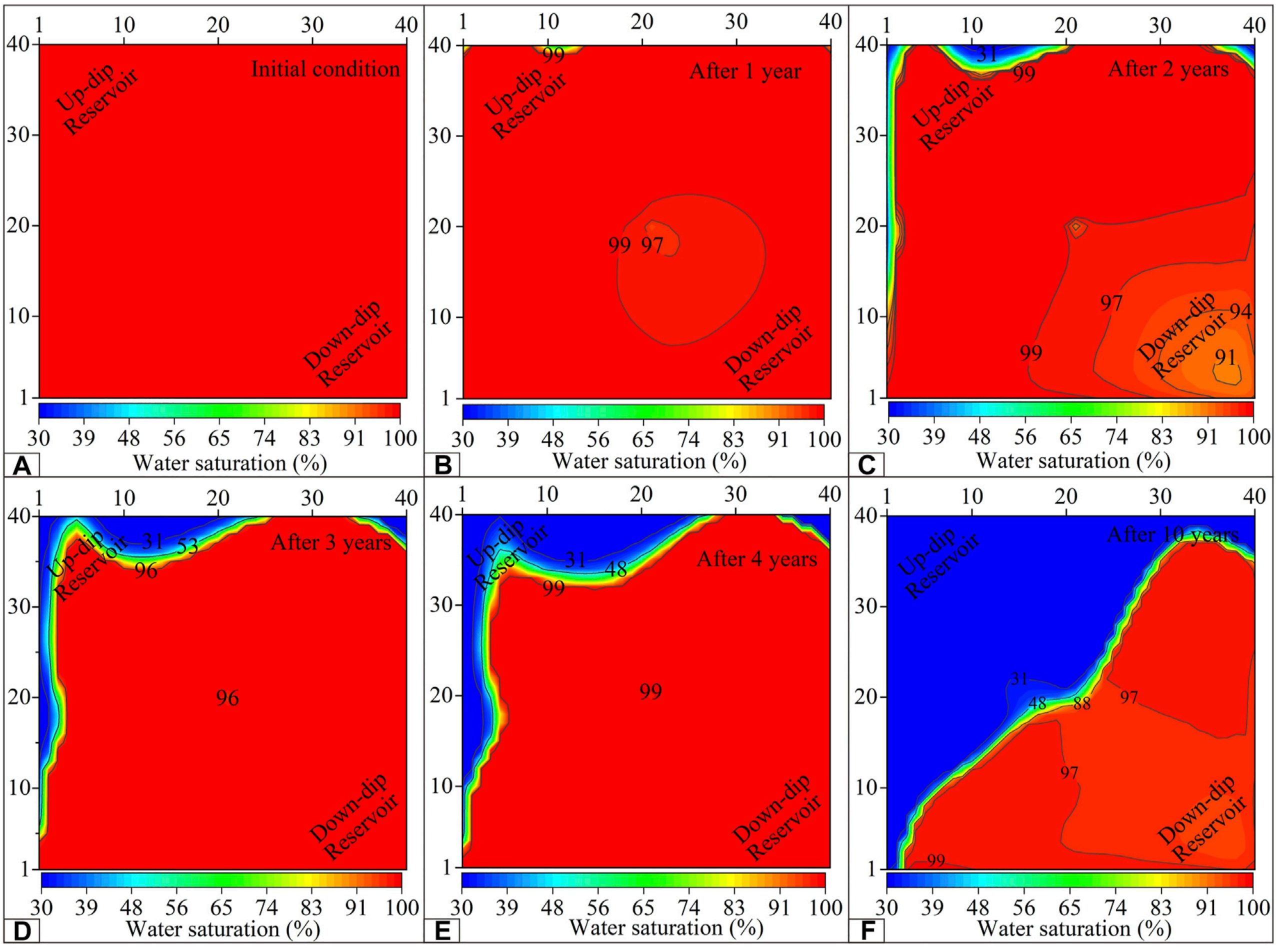

FIGURE 9
(A) Initial water saturation distribution of ASIM. **(B)** Water saturation distribution after 1 year of drainage in ASIM. **(C)** Water saturation distribution after 2 years of drainage in ASIM. **(D)** Water saturation distribution after 3 years of drainage in ASIM. **(E)** Water saturation distribution after 4 years of drainage in ASIM. **(F)** Water saturation distribution after 10 years of drainage in ASIM.

5.3.2 Reservoir pressure dynamics

For ASIM, the initial reservoir pressure ranged from 8.14 MPa to 17.25 MPa (Figure 11A). With the development of drainage, the reservoir pressure gradually propagated outward from the wellbore. The minimum reservoir pressures of the 1st, 2nd, 3rd, 4th, and 10th years of production were 5.45 MPa, 2.44 MPa, 2.34 MPa, 2.28 MPa, and 1.86 MPa, respectively. The maximum reservoir pressures of the 1st, 2nd, 3rd, 4th, and 10th years of production were 15.13 MPa, 13.95 MPa, 12.68 MPa, 12.80 MPa, and 9.53 MPa, respectively (Figures 11B–F). For ISIM, the initial reservoir pressure ranged from 8.49 MPa to 15.20 MPa (Figure 12A). The pressure drops faster in the wellbore and up-dip direction than in the down-dip direction. The reservoir pressure decreased preferentially in the up-dip reservoir and descended symmetrically in the strike centered on the wellbore. The minimum reservoir pressures of the 1st, 2nd, 3rd, 4th, and 10th years of production were 5.54 MPa, 2.60 MPa, 2.50 MPa, 2.36 MPa and 1.97 MPa, respectively. The maximum reservoir pressures of the 1st, 2nd, 3rd, 4th, and 10th years of production were 13.41 MPa, 12.64 MPa, 10.91 MPa, 10.33 MPa and 7.84 MPa, respectively (Figures 12B–F). The reservoir pressure of the ASIM decreased by 13.88% in years 0–1, 8.38% in years 1–2, 6.31% in years 2–3, 3.76% in years 3–4, 41.75% in years 4–10, and 58.57% in years 0–10. For ISIM, the overall reservoir pressure decreased by 13.71% in 0–1 year, 8.43% in 1–2 years, 8.81% in 2–3 years, 6.21% in 3–4 years, 35.62% in 4–10 years, and 56.60% in 0–10 years (Table 3).

5.3.3 Gas content dynamics

For ASIM, the initial gas content ranged from 9.08 m^3/t to 10.79 m^3/t (Figure 13A). The minimum gas content of the 1st, 2nd, 3rd, 4th, and 10th years of production was 8.15 m^3/t, 5.50 m^3/t, 5.36 m^3/t, 5.28 m^3/t, and 4.64 m^3/t, respectively. The maximum gas content of the 1st, 2nd, 3rd, 4th, and

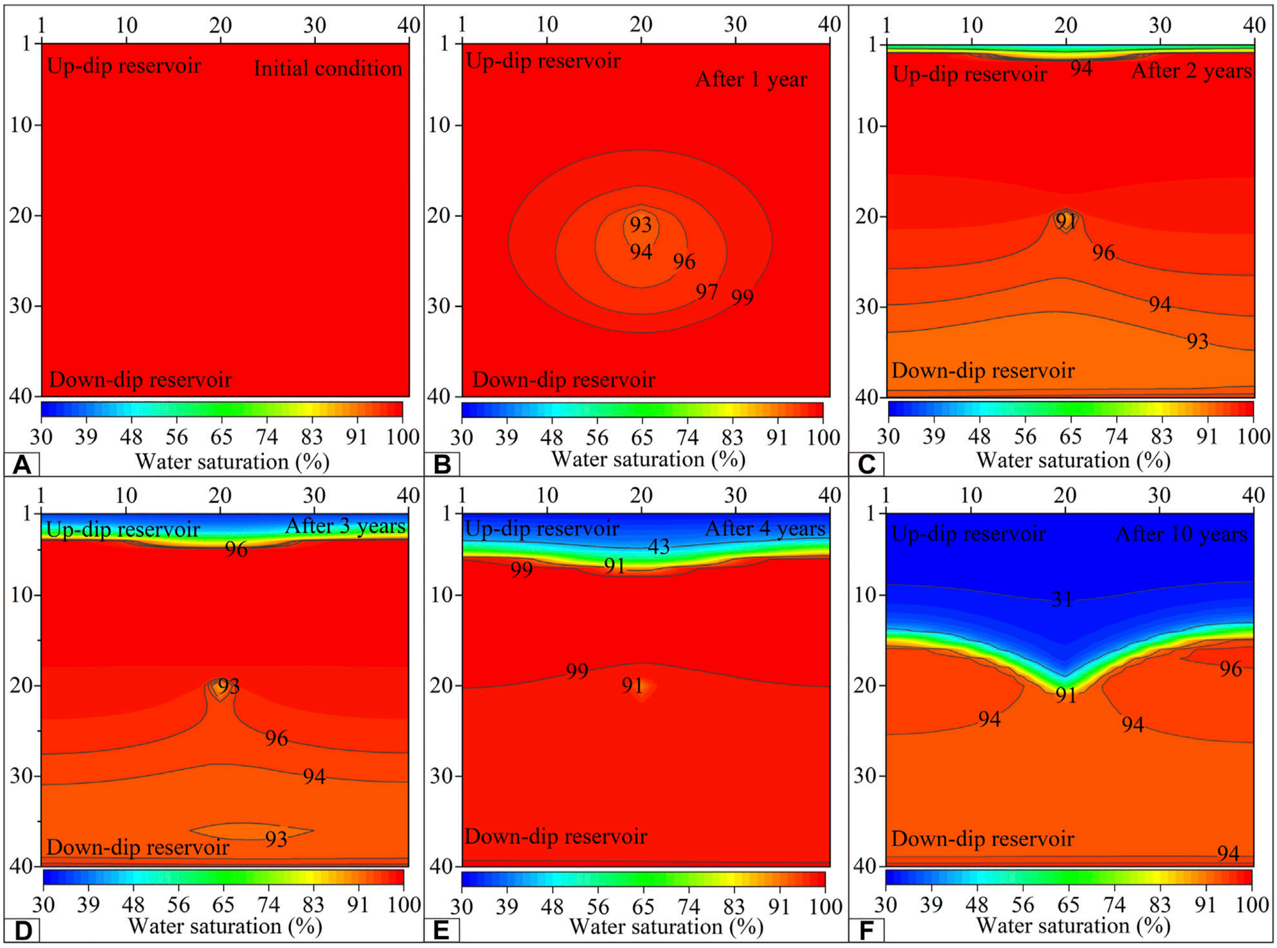

FIGURE 10
(A) Initial water saturation distribution of ISIM. **(B)** Water saturation distribution after 1 year of drainage in ISIM. **(C)** Water saturation distribution after 2 years of drainage in ISIM. **(D)** Water saturation distribution after 3 years of drainage in ISIM. **(E)** Water saturation distribution after 4 years of drainage in ISIM. **(F)** Water saturation distribution after 10 years of drainage in ISIM.

TABLE 2 Water saturation decline rate with ASIM and ISIM.

	0–1 year (%)	1–2 years (%)	2–3 years (%)	3–4 years (%)	4–10 years (%)	0–10 years (%)
ASIM	0.68	3.53	3.55	4.66	23.33	33.34
ISIM	1.08	3.99	2.92	2.47	22.73	30.22

10th years of production was 10.79 m^3/t, 10.70 m^3/t, 10.49 m^3/t, 10.48 m^3/t, and 9.79 m^3/t, respectively (Figures 13B–F). For ISIM, the initial gas content ranged from 9.19 m^3/t to 10.55 m^3/t (Figure 14A). The gas content drops faster in the wellbore and up-dip directions than in the down-dip direction. The gas content decreased preferentially in the up-dip reservoir and descended symmetrically in the strike centered on the wellbore. The minimum gas content of the 1st, 2nd, 3rd, 4th, and 10th years of production was 8.20 m^3/t, 5.71 m^3/t, 5.58 m^3/t, 5.39 m^3/t, and 4.82 m^3/t, respectively. The maximum gas content of the 1st, 2nd, 3rd, 4th, and 10th years of production was 10.55 m^3/t, 10.48 m^3/t, 10.13 m^3/t, 9.99 m^3/t, and 9.25 m^3/t, respectively (Figures 14B–F). For ASIM, the reservoir gas content decreased by 0.70% in 0–1 year, 2.25% in 1–2 years, 1.80% in 2–3 years, 1.18% in 3–4 years, 18.04% in 4–10 years, and 22.77% in

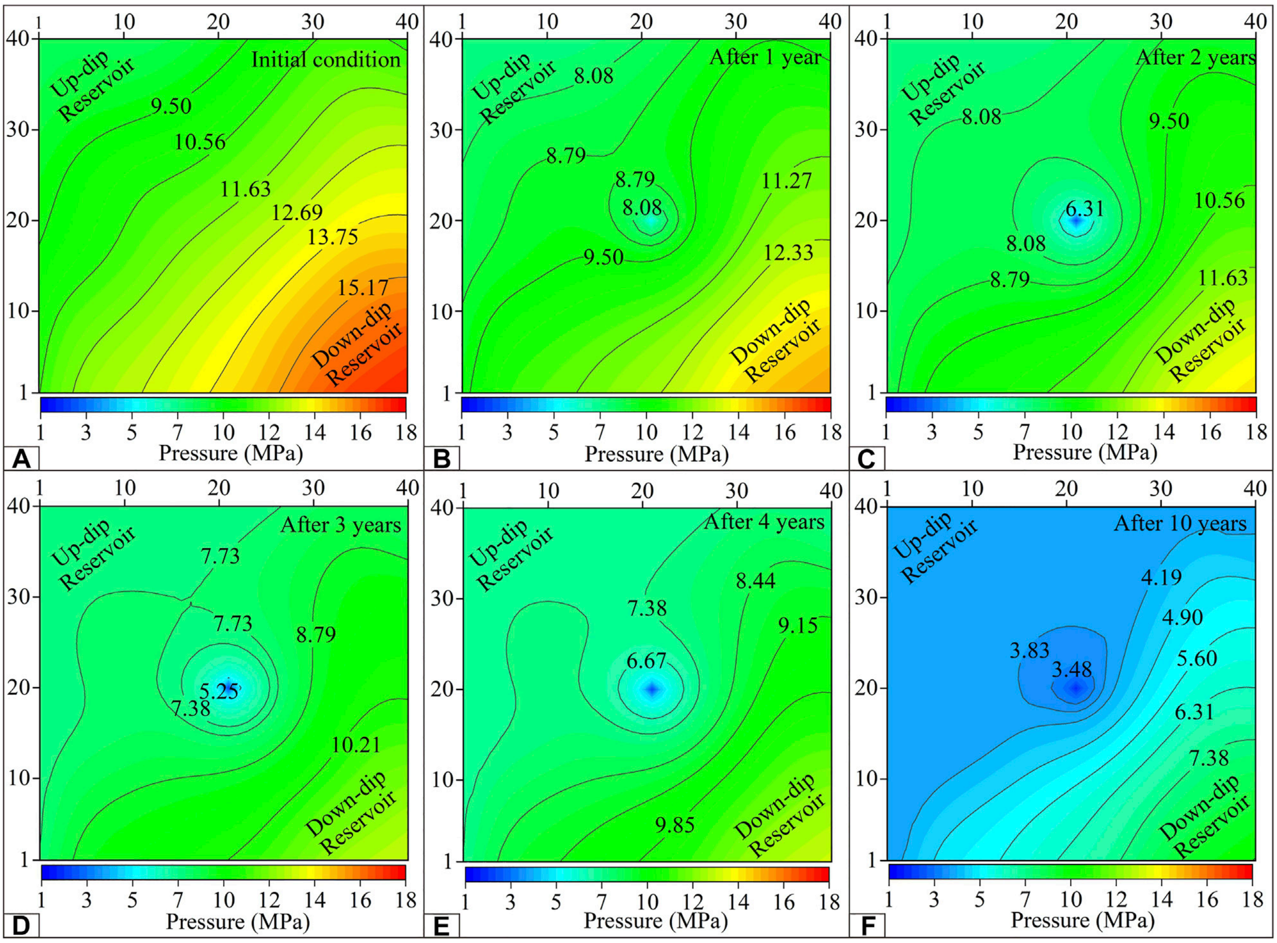

FIGURE 11
(A) Initial reservoir pressure distribution of ASIM. **(B)** Reservoir pressure distribution after 1 year of drainage in ASIM. **(C)** Reservoir pressure distribution after 2 years of drainage in ASIM. **(D)** Reservoir pressure distribution after 3 years of drainage in ASIM. **(E)** Reservoir pressure distribution after 4 years of drainage in ASIM. **(F)** Reservoir pressure distribution after 10 years of drainage in ASIM.

0–10 years. For ISIM, the reservoir gas content decreased by 0.64% in 0–1 year, 2.27% in 1–2 years, 2.53% in 2–3 years, 1.92% in 3–4 years, 14.97% in 4–10 years, and 21.05% in 0–10 years (Table 4).

6 Discussion

6.1 Reservoir physical property dynamic comparisons between the actual steeply inclined model and ideal steeply inclined model

The dynamic change in coal reservoir physical properties is becoming increasingly significant for continuous and steady CBM production (Yan et al., 2020). In recent years, some progress has been achieved in the study of CBM drainage and production dynamics (Wang et al., 2012; Kang et al., 2016; Kang et al., 2017). Based on several previous production practices, concerned scholars have monitored the physical property dynamics in the production process of CBM through passive super-low frequency (SLF) spectrum analysis, drainage analysis, and the transient electromagnetic method, providing guidance for CBM drainage (Li et al., 2009; Jiang et al., 2011; Fu et al., 2014; Wang et al., 2021). In this paper, the reservoir property dynamics of the ASIM and ISIM are manifested, and the gap between the simulation and actual situation is narrowed. According to the dynamic characteristics of drainage, the whole drainage process can be divided into three stages: 0–2 years as the first stage, 2–4 years as the second stage, and 4–10 years as the third stage.

6.1.1 Water saturation

As the medium to promote the decrease in reservoir pressure during CBM exploitation, groundwater drainage can transform

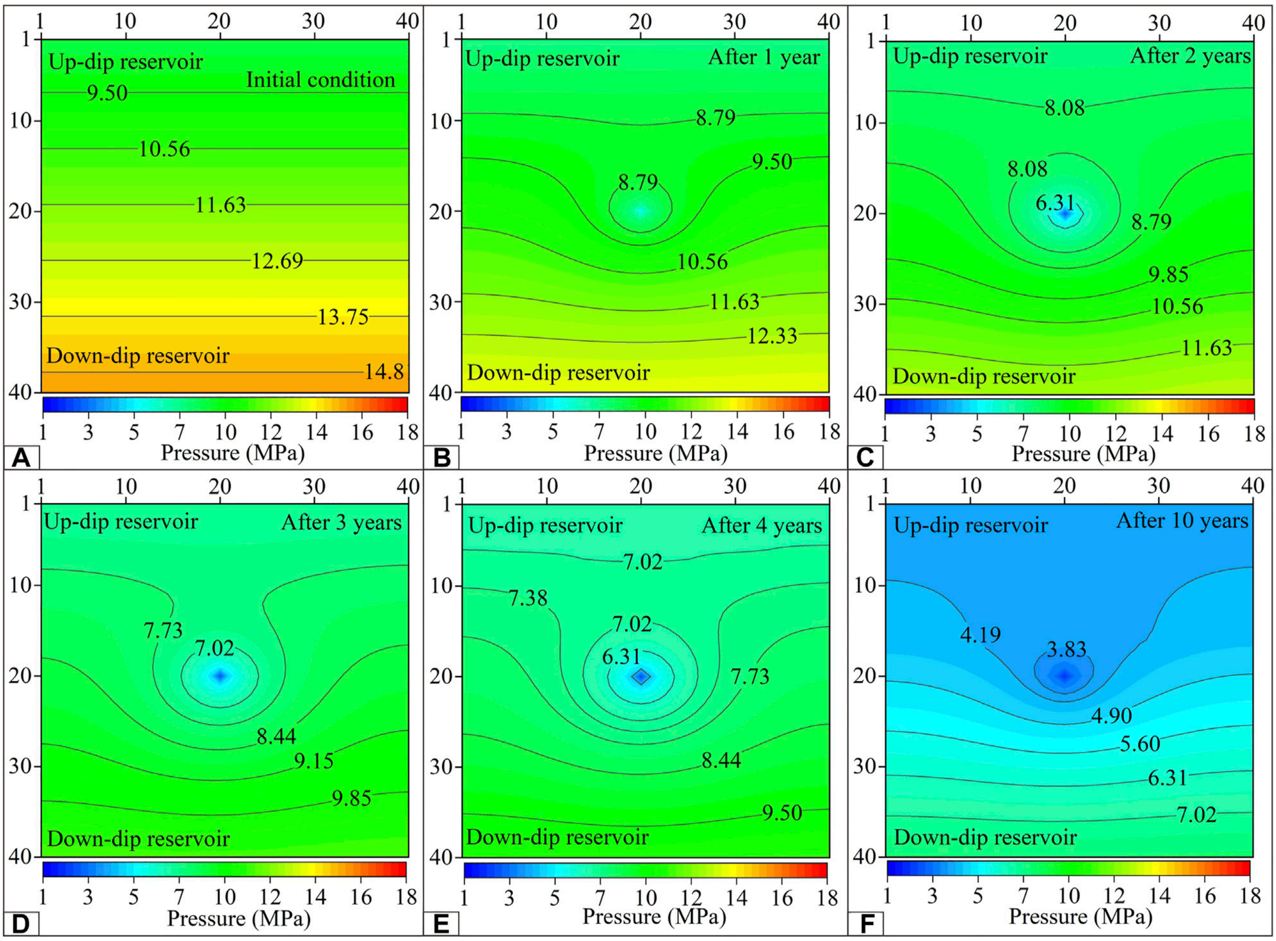

FIGURE 12
(A) Initial reservoir pressure distribution of ISIM. **(B)** Reservoir pressure distribution after 1 year of drainage in ISIM. **(C)** Reservoir pressure distribution after 2 years of drainage in ISIM. **(D)** Reservoir pressure distribution after 3 years of drainage in ISIM. **(E)** Reservoir pressure distribution after 4 years of drainage in ISIM. **(F)** Reservoir pressure distribution after 10 years of drainage in ISIM.

TABLE 3 Reservoir pressure decline rate with ASIM and ISIM.

	0–1 year (%)	1–2 years (%)	2–3 years (%)	3–4 years (%)	4–10 years (%)	0–10 years (%)
ASIM	13.88	8.38	6.31	3.76	41.75	58.57
ISIM	13.71	8.43	8.81	6.21	35.62	56.60

CBM from the adsorbed state to the free state. The differences in water drainage can affect the change in reservoir pressure propagation during CBM production, thus affecting gas production (Hu et al., 2019; Ma et al., 2021). In the initial state, the coal seam fracture was usually completely saturated with water, and the water saturation in the reservoir fracture was 100%, providing the necessary pressure for the adsorption of CBM on the coal matrix (Mohamed and Mehana, 2020).

In the ASIM and ISIM, the groundwater in the up-dip reservoir flows to the down-dip reservoir during drainage. Groundwater in the up-dip direction preferentially flows into the wellbore, providing most of the water produced by CBM wells. In the production process, the groundwater of the down-dip reservoir will be replenished from the up-dip reservoir, making the down-dip reservoir water maintain a high saturation state for a long time. In the first stage (0–2 years),

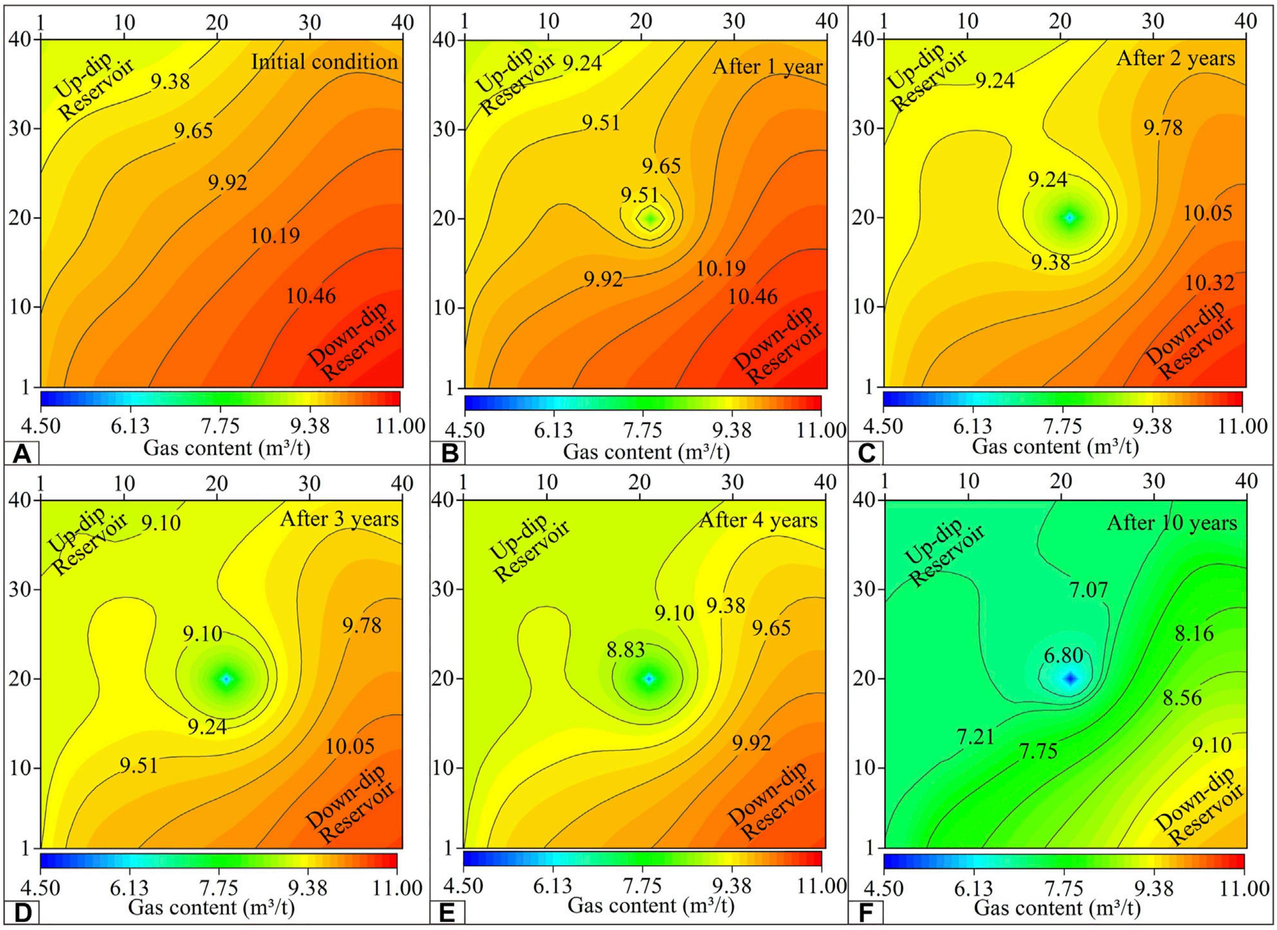

FIGURE 13
(A) Initial reservoir gas content distribution of ASIM. **(B)** Reservoir gas content distribution after 1 year of drainage in ASIM. **(C)** Reservoir gas content distribution after 2 years of drainage in ASIM. **(D)** Reservoir gas content distribution after 3 years of drainage in ASIM. **(E)** Reservoir gas content distribution after 4 years of drainage in ASIM. **(F)** Reservoir gas content distribution after 10 years of drainage in ASIM.

the water saturation decrease rate of ASIM was lower than the water saturation decrease rate of ISIM, and the drainage of the former was slower than the drainage of the latter. Due to the lower permeability and gravity hindrance, the water flow resistance is larger, and the water saturation is higher in the down-dip reservoir (Kang et al., 2019). In the second stage (2–4 years), the decrease rate of water saturation in ASIM was higher than the decrease rate of water saturation of ISIM, and the drainage effect of ASIM was better. Compared with ISIM, except for the common heterogeneity of gas content, porosity, permeability, and reservoir pressure, ASIM was characterized by the heterogeneities of reservoir distribution and dip angle, which make the water transport processes of ASIM more complex. In the third stage (4–10 years), since most of the reservoir water was reduced to the critical water saturation and stopped flowing, the ASIM and ISIM water saturation decline rates gradually slowed. In the process of drainage, the variation characteristics of water saturation in ASIM were more consistent with the actual geological conditions, but overall, groundwater migration followed the gravity effect, and the water saturation of the up-dip reservoir decreased quicker than the water saturation of the down-dip reservoir.

6.1.2 Reservoir pressure

Monitoring the pressure dynamics in the process of CBM drainage is of great significance for determining the propagation law of reservoir pressure and guiding CBM drainage (Du et al., 2011). The drainage of CBM wells causes the formation of a pressure drop funnel, but the distribution of reservoir pressure is not uniform in space, and the pressure change also shows a nonlinear curve (Wang et al., 2012). In the process of studying reservoir pressure dynamics through numerical simulation, coal

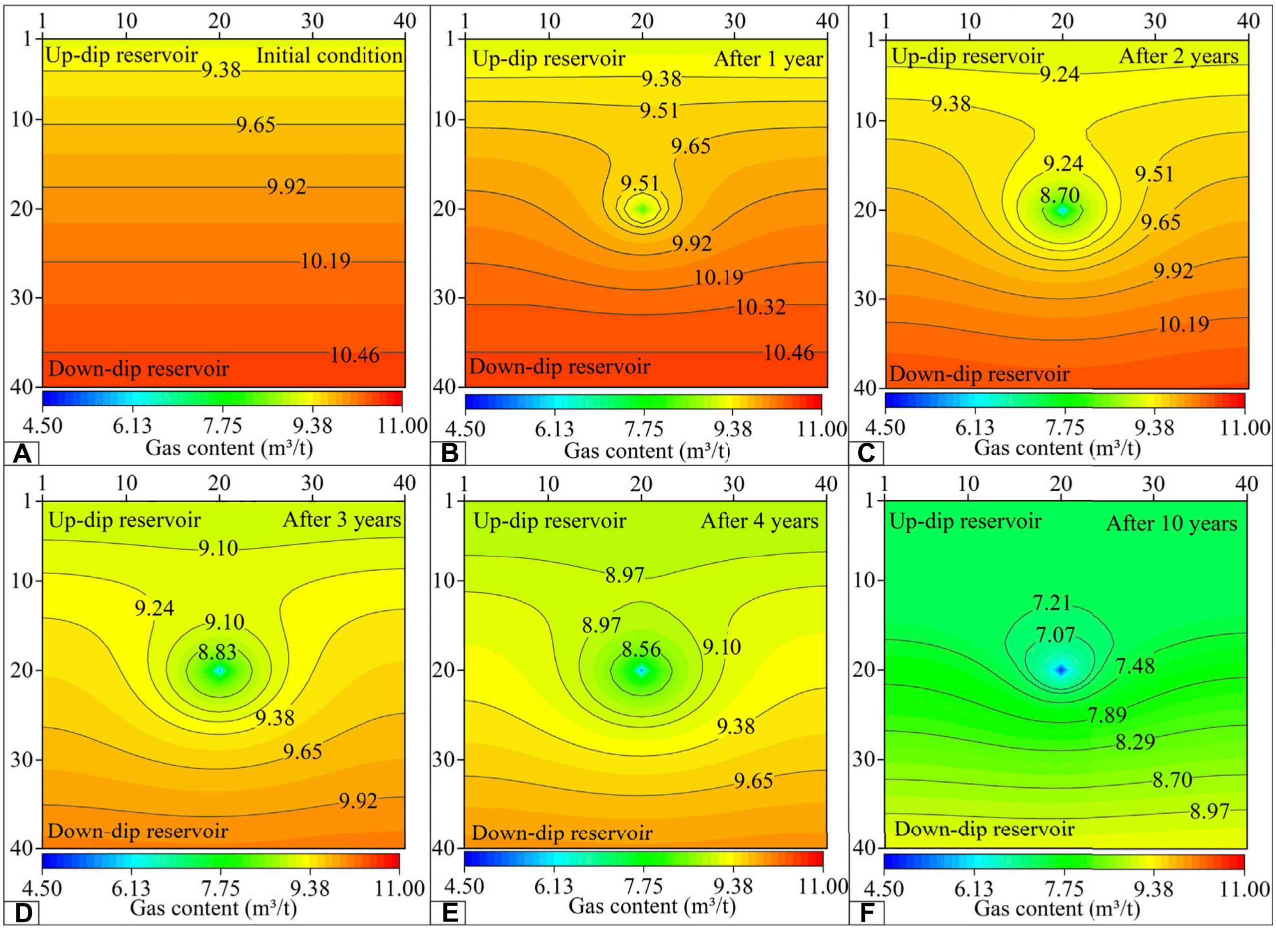

FIGURE 14
(A) Initial reservoir gas content distribution of ISIM. **(B)** Reservoir gas content distribution after 1 year of drainage in ISIM. **(C)** Reservoir gas content distribution after 2 years of drainage in ISIM. **(D)** Reservoir gas content distribution after 3 years of drainage in ISIM. **(E)** Reservoir gas content distribution after 4 years of drainage in ISIM. **(F)** Reservoir gas content distribution after 10 years of drainage in ISIM.

TABLE 4 Reservoir gas content decline rate with ASIM and ISIM.

	0–1 year (%)	1–2 years (%)	2–3 years (%)	3–4 years (%)	4–10 years (%)	0–10 years (%)
ASIM	0.70	2.25	1.80	1.18	18.04	22.77
ISIM	0.64	2.27	2.53	1.92	14.97	21.05

seams are usually assumed to be homogeneous (Yan et al., 2021). However, under special geological conditions, homogeneous coal reservoirs are no longer applicable.

The change in pressure is dominated by the production of water in the coal reservoir. With the production of groundwater, the reservoir pressure decreased gradually. Under ideal conditions, the reservoir pressure propagates radially from the wellbore center and elliptically from the fracture center after fracturing (Xu et al., 2013). Due to the production of a large amount of groundwater in the first stage (0–2 years), the reservoir pressure obviously decreases, and the reservoir pressure decreases in the ASIM and ISIM exhibit little difference. In the second stage (2–4 years) of drainage, the water production rate was relatively slower, and the reservoir pressure of the ASIM and ISIM decreased slightly compared with the first stage (0–2 years). The pressure drop of the ASIM is more difficult than the pressure drop of the ISIM in the down-dip direction. In the third stage (4–10 years), the ASIM pressure drops faster than the ISIM. In this stage, the up-dip pressure drop of ASIM was greater than that of ISIM, providing most of the pressure drop rate for the overall reservoir. The better drainage effect of ASIM (Table 3), which is more conducive to the desorption of CBM, led to a relatively larger decrease in reservoir pressure than the drainage effect of ISIM. Considering the topography distribution of the coal seam, the groundwater migrated to the down-dip reservoir due to the action of gravity and pressure difference. As a result, the up-dip reservoir pressure dropped rapidly, and it was difficult for the down-dip water to overcome its own gravity, so the pressure drop propagation speed and distance were smaller (Wang et al., 2014).

6.1.3 Gas content

For different types of coal reservoirs, the variations in gas content in the process of drainage and production were obviously different. It is of great significance to clarify the dynamic change process of gas content for revealing the dynamic process of CBM well drainage, with the purpose of guiding coal reservoir development optimization (Shao et al., 2017). The reduction rate of the gas content in a coal reservoir determines the production rate of CBM wells (Ma et al., 2021).

In the first stage (0–2 years) of drainage, the reduction rates of gas content in ASIM and ISIM were low because single water phase flow was dominant, and there was no gas-water differentiation phenomenon in ASIM and ISIM. Most of the reservoir did not reach the critical desorption pressure. The CBM near the wellbore was preferentially desorbed. In the second stage (2–4 years), the desorption range gradually expanded outward from the wellbore, and the ASIM expanded more slowly than the ISIM. The CBM reservoir had not reached the large area desorption stage. The desorption capacity of ASIM in the up-dip direction was greater than the desorption capacity of ISIM in the third stage (4–10 years). The decrease rate of gas content in ASIM was greater than the decrease rate of gas content in ISIM. Due to drainage depressurization, the CBM of the up-dip reservoir begins to desorb over a large area, and the CBM of the down-dip reservoir also gradually desorbs. In the third stage (4–10 years) of the drainage process, the gas content decline rate of ASIM was higher than the gas content decline rate of ISIM, indicating that the topography of the coal seam can improve the recovery of CBM to a certain extent. The heterogeneity of the ASIM reservoir distribution is more complex than the heterogeneity of the ISIM reservoir distribution, and the production of gas and water is more complex, thus indirectly affecting the dynamic changes in reservoir physical properties.

6.2 Prediction accuracy between actual steeply inclined model and ideal steeply inclined model

After 595 days, the ASIM was closer to the actual observed gas production data (Figure 8A), possibly because the reservoir physical properties of ISIM were more homogeneous than the reservoir physical properties of ASIM; thus, the ISIM has a period (600th day–1000th day in Figure 8A) of stable gas production stage, in which the data deviated greatly from the actual gas production data.

The distribution of real coal reservoirs is more different from the distribution of real coal reservoirs of ISIM, and the degree of heterogeneity is stronger. ASIM is more representative of the actual coal reservoir distribution than ISIM. Therefore, the variations in water saturation, pressure drop, and gas content are complicated by the heterogeneity of the actual coal seam distribution, resulting in the discontinuity of gas production. The first gas production peak occurs due to preferential desorption of the reservoir near the wellbore. The degree of reservoir heterogeneity in the vicinity of the ASIM and ISIM wells is similar, so the first peak gas production in ASIM is close to the first peak gas production in ISIM. In the later stage of drainage, the gas supply range of ASIM is larger at the same time, resulting in the daily gas production of ASIM being larger than the daily gas production of ISIM. Multiple peaks were formed in the gas production curves (Figure 8A), and different gas production peaks were contributed by different parts of the reservoir. During the horizontal reservoir drainage process, the daily gas will gradually increase to the peak and gradually decrease. With the increase of coal seam inclination angle, the double peak pattern of daily gas production gradually appeared and became more and more obvious (Alireza and Özgen, 2017; Kang et al., 2019). The variations in reservoir size, gas content, permeability, and grid dip angle under different burial depth conditions in the model promote the formation of multiple gas production peak curves. The10-year cumulative gas production of ASIM was approximately 9.94% higher than the 10-year cumulative gas production of ISIM (Figure 8B), and the peak gas production occurred relatively early.

7 Conclusion

In this study, the ASIM and ISIM of CBM drainage and production were constructed. The dynamic variation characteristics of water saturation, reservoir pressure, and gas content in ASIM and ISIM were discussed. The whole CBM extraction process was divided into three stages: the first stage (0–2 years), the second stage (2–4 years), and the third stage (4–10 years). The following conclusions were drawn.

1) The heterogeneity of the reservoir dip angle forms different gas producing regions and affects the change in the production curve. In the third stage (4–10 years) of drainage, the daily gas production and cumulative gas production of the ASIM are larger than the daily gas production and cumulative gas production of the ISIM. The drainage effect of the ASIM is considered to be better in the third stage (4–10 years);

2) In the second stage (2–4 years) and the third stage (4–10 years) of drainage, the ASIM water saturation decreased greatly due to the combination of the reservoir grid distribution and the dip angle of each reservoir grid.
3) In the first stage (0–2 years) and second stage (2–4 years) of drainage, the decrease rate of reservoir pressure in ASIM is smaller than the decrease rate of reservoir pressure in ISIM. However, in the third stage (4–10 years), the decrease rate of reservoir pressure is larger in ASIM than in ISIM because of the better drainage effect of the ASIM;
4) The variation trend of gas content was dominated by gas water differentiation. In the first stage (0–2 years) and second stage (2–4 years) of drainage, the decrease rate of gas content in the ASIM first increased and then decreased. In the third stage (4–10 years) of drainage, the ASIM has a higher recovery efficiency. Due to the heterogeneity of the ASIM reservoir distribution, the production of gas and water is more complex.

Data availability statement

The original contributions presented in the study are included in the article/supplementary material, further inquiries can be directed to the corresponding author.

Author contributions

All authors listed have made a substantial, direct, and intellectual contribution to the work and approved it for publication.

Funding

This study was funded by the National Natural Science Foundation of China (42002188), Natural Science Foundation of Xinjiang Uygur Autonomous Region (2022D01C79), and the National Innovation Training Program for College Students (202110755007).

Acknowledgments

We would like to thank Xinjiang Collingstead New Energy Co., Ltd. for providing data support and Schlumberger company for providing software technical support in this study.

Conflict of interest

The authors declare that the research was conducted in the absence of any commercial or financial relationships that could be construed as a potential conflict of interest.

Publisher's note

References

Alireza, S., and Özgen, K. C. (2017). Cross-formational flow of water into coalbed methane reservoirs: Controls on relative permeability curve shape and production profile. *Environ. Earth Sci.* 76 (5), 200. doi:10.1007/s12665-017-6505-0

Corey, A. T. (1954). The interrelation between gas and oil relative permeability. *Prod. Mon.* 38-41.

Dong, J., Cheng, Y. P., and Pan, Z. J. (2020). Comparison of transient and pseudo-steady diffusion of methane in coal and implications for coalbed methane control. *J. Petroleum Sci. Eng.* 184, 106543. doi:10.1016/j.petrol.2019.106543

Du, Y. F., Wu, C. F., Zou, M. J., Wang, C., Jiang, W., and Lei, B. (2011). Study on reservoir pressure transmission law during gas mining and drainage process of coal bed methane well. *Coal Eng.* 1 (7), 87–89. doi:10.3969/j.issn.1671-0959.2011.07.034

Duan, L. J., Qu, L. C., Xia, Z. H., Liu, L. L., and Wang, J. J. (2020). Stochastic modeling for estimating coalbed methane resources. *Energy fuels..* 34 (5), 5196–5204. doi:10.1021/acs.energyfuels.9b03549

Fu, X. H., Li, S., Yu, J. C., and Wu, Y. X. (2014). Dynamic monitor on coal reservoir water system during drainage process of coalbed methane well. *J. China Coal Soc.* 39 (1), 26–31. doi:10.13225/j.cnki.jccs.2013.0919

Fu, H. J., Tang, D. Z., Xu, H., Xu, T., Chen, B. L., Hu, P., et al. (2016). Geological characteristics and CBM exploration potential evaluation: A case study in the middle of the southern Junggar Basin, NW China. *J. Nat. Gas. Sci. Eng.* 30, 557–570. doi:10.1016/j.jngse.2016.02.024

Fu, X. H., Kang, J. Q., Liang, S., Gao, L., and Chen, X. (2018). Well type optimization and physical property in gas drainage process of steep inclined coal reservoir in Fukang Western Block. *Coal Sci. Technol.* 46 (6), 9–16. doi:10.13199/j.cnki.cst.2018.06.002

Ge, X., Liu, D. M., Cai, Y. D., and Wang, Y. J. (2018). Gas content evaluation of coalbed methane reservoir in the Fukang area of southern Junggar Basin, northwest China by multiple geophysical logging methods. *Energies* 11, 1867. doi:10.3390/en11071867

Guo, J. G., Pang, X. Q., Guo, F. T., Wang, X. L., Xiang, C. F., Jiang, F. J., et al. (2014). Petroleum generation and expulsion characteristics of lower and middle jurassic source rocks on the southern margin of Junggar Basin, northwest China: Implications for unconventional gas potential. *Can. J. Earth Sci.* 51 (6), 537–557. doi:10.1139/cjes-2013-0200

Hu, Z. P. (2019). Study on main controlling factors of coal reservoir permeability in baiyanghe mining area of Fukang. *China Coalbed Methane* 16 (2), 24–26. doi:CNKI:SUN:ZGMC.0.2019-02-008

Hu, Z. P., Wang, Q., and Wu, H. (2019). Study on water production characteristics of CBM wells in baiyanghe mining area of Fukang in Xinjiang. *China Coalbed Methane* 16 (3), 7–11. doi:CNKI:SUN:ZGMC.0.2019-03-002

Ibrahim, A. F., and Nasr-El-Din, H. A. (2015). A comprehensive model to history match and predict gas/water production from coal seams. *Int. J. Coal Geol.* 146, 79–90. doi:10.1016/j.coal.2015.05.004

Jiang, H. B., Qin, Q. M., and Li, B. S. (2011). Passive SLF spectrum analysis for tracing the mining dynamic of CBM. *Spectrosc. Spectr. Anal.* 31 (7), 1898–1901. doi:10.3964/j.issn.1000-0593(2011)07-1898-04

Kang, Y. S., Wang, J., Jiang, S. Y., Ye, J. P., Zhang, S. R., Zhang, B., et al. (2016). Analysis on controlling geological factors influencing drainage performance of coalbed methane wells. *Geol. Rev.* 62 (6), 1511–1520. doi:10.16509/j.georeview.2016.06.011

Kang, Y. S., Zhang, B., Yu, X., Yu, X., Wang, J., Jiang, S. Y., et al. (2017). Formation mechanism of well performance and CBM development strategy in Shouyang Block, Qinshui Basin. *Nat. Gas. Geosci.* 28 (1), 116–126. doi:10.11764/j.issn.1672-1926.2016.11.025

Kang, J. Q., Fu, X. H., Gao, L., and Liang, S. (2018). Production profile characteristics of large dip angle coal reservoir and its impact on coalbed methane production: A case study on the Fukang west block, southern Junggar Basin, China. *J. Pet. Sci. Eng.* 171, 99–114. doi:10.1016/j.petrol.2018.07.044

Kang, J. Q., Fu, X. H., Liang, S., Li, X., Chen, X., and Wang, Z. Z. (2019). A numerical simulation study on the characteristics of the gas production profile and its formation mechanisms for different dip angles in coal reservoirs. *J. Pet. Sci. Eng.* 181, 106198. doi:10.1016/j.petrol.2019.106198

Kang, J. Q., Fu, X. H., Elsworth, D., and Liang, S. (2020). Vertical heterogeneity of permeability and gas content of ultra-high-thickness coalbed methane reservoirs in the southern margin of the Junggar Basin and its influence on gas production. *J. Nat. Gas. Sci. Eng.* 81, 103455. doi:10.1016/j.jngse.2020.103455

Karacan, C. Ö., Drobniak, A., and Mastalerz, M. (2014). Coal bed reservoir simulation with geostatistical property realizations for simultaneous multi-well production history matching: A case study from Illinois basin, Indiana, USA. *Int. J. Coal Geol.* 131, 71–89. doi:10.1016/j.coal.2014.06.002

Karimpouli, S., Tahmasebi, P., and Ramandi, H. L. (2020). A review of experimental and numerical modeling of digital coalbed methane: Imaging, segmentation, fracture modeling and permeability prediction. *Int. J. Coal Geol.* 228, 103552. doi:10.1016/j.coal.2020.103552

Li, J. H., Su, X. B., Lin, X. Y., and Guo, H. Y. (2009). Relationship between discharge rate and productivity of coalbed methane wells. *J. China Coal Soc.* 34 (3), 376–380. doi:10.13225/j.cnki.jccs.2009.03.002

Li, X., Fu, X. H., Yang, X. S., Ge, Y. Y., and Quan, F. K. (2018). Coalbed methane accumulation and dissipation patterns: A case study of the Junggar Basin, NW China. *J. Asian Earth Sci.* 160, 13–26. doi:10.1016/j.jseaes.2018.04.003

Liang, S., Han, H., Elsworth, D., Fu, X. H., Yao, Q. L., Kang, J. Q., et al. (2020). Evolution of production and transport characteristics of steeply-dipping ultra-thick coalbed methane reservoirs. *Energies* 13, 5081. doi:10.3390/en13195081

Liu, C. L., Wang, X. H., Liu, K., Wang, J., Guo, H., and Sun, Z. Q. (2014). Occurrence features of coalbed methane in inclined coal seam of Junggar basin, Xinjiang. *Adv. Mater. Res.* 868, 696–699. doi:10.4028/www.scientific.net/AMR.868.696

Liu, N., Sun, L. L., Qin, B. T., Zhang, S. H., and Du, W. Z. (2021). Evolution of pore and fracture of coal under heating–freezing effects: An experimental study. *Fuel* 306, 121618. doi:10.1016/j.fuel.2021.121618

Ma, D. M., J, Y. S., Chen, Y., Zhen, C., Teng, J. X., Ma, Z. Y., et al. (2021). CBM well drainage data-based dynamic inversion study of reservoir gas content. *Coal Geol. Explor.* 49 (6), 67–73. doi:10.3969/j.issn.1001-1986.2021.06.007

Mohamed, T., and Mehana, M. (2020). CoalBed methane characterization and modeling: Review and outlook. *Energy Sources Part A Recovery Util. Environ. Eff.* 10, 1–23. doi:10.1080/15567036.2020.1845877

Mostaghimi, P., Armstrong, R. T., Gerami, A., Hu, Y. B., Jing, Y., Kamali, F., et al. (2017). Cleat-scale characterisation of coal: An overview. *J. Nat. Gas. Sci. Eng.* 39, 143–160. doi:10.1016/j.jngse.2017.01.025

Pu, Y. F., Tang, D. Z., Tao, S., Tang, S. L., Zhang, A. B., and Zhang, T. Y. (2021). Evaluation and optimization of development intervals under conditions of multiple coal seam combinations in Fukang area, Xinjiang Province. *J. China Coal Soc.* 46 (7), 2321–2330. doi:10.13225/j.cnki.jccs.2020.0326

Qin, Y., Moore, T. A., Shen, J., Yang, Z. B., Shen, Y. L., and Wang, G. (2018). Resources and geology of coalbed methane in China: A review. *Int. Geol. Rev.* 60 (5-6), 777–812. doi:10.1080/00206814.2017.1408034

Qin, Y. P., Xu, H., Liu, W., Liu, J., and Duan, W. P. (2020). Time- and pressure-independent gas transport behavior in a coal matrix: Model development and improvement. *Energy fuels..* 34 (8), 9355–9370. doi:10.1021/acs.energyfuels.0c01182

Qin, Y., Shen, J., and Shi, R. (2022). Strategic value and choice on construction of large CMG industry in China. *J. China Coal Soc.* 47 (1), 371–387. doi:10.13225/j.cnki.jccs.yg21.1616

Quan, F. K., Wei, C. T., Hao, S. Q., Ma, J. S., Song, Y., and Lian, Da. (2022a). Interference analysis of methane Co-production from two coal seams in southern Qinshui Basin. *Nat. Resour. Res.* 31 (3), 1475–1502. doi:10.1007/s11053-022-10043-w

Quan, F. K., Wei, C. T., Ma, J. S., Hao, S. Q., and Song, Y. (2022b). Modeling analysis of coalbed methane co-production interference: A case study in eastern yunnan basin, China. *J. Nat. Gas. Sci. Eng.* 103, 104631. doi:10.1016/j.jngse.2022.104631

Sayyafzadeh, M., Keshavarz, A., Alias, A. R. M., Dong, K. A., and Manser, M. (2015). Investigation of varying-composition gas injection for coalbed methane recovery enhancement: A simulation-based study. *J. Nat. Gas. Sci. Eng.* 27, 1205–1212. doi:10.1016/j.jngse.2015.09.071

Senthamaraikkannan, G., Budwill, K., Gates, I., Mitra, S. K., and Prasad, V. (2016). Kinetic modeling of the biogenic production of coalbed methane. *Energy fuels..* 30 (2), 871–883. doi:10.1021/acs.energyfuels.5b02450

Shao, L. Y., Hou, H. H., Tang, Y., Lu, J., Qiu, H. J., Wang, X. T., et al. (2015). Selection of strategic replacement areas for CBM exploration and development in China. *Nat. Gas. Ind. B* 2 (2-3), 211–221. doi:10.1016/j.ngib.2015.07.013

Shao, C. K., Xue, Y. Y., and Wei, C. T. (2017). Variation research of gas content of three states during coalbed methane drainage process. *Coal Technol.* 36 (8), 28–31. doi:10.13301/j.cnki.ct.2017.08.011

Shi, Y. X., Chen, X., Zhao, Y. W., Yang, X. S., and Liu, D. G. (2018). Analysis on geological influencing factors of coalbed methane productivity in Fukang Western Mining Area. *Coal Eng.* 50 (2), 133–136. doi:10.11799/ce201802035

Sun, Z., Li, X. F., Shi, J. T., Yu, P. L., Huang, L., Xia, J., et al. (2017). A semi-analytical model for drainage and desorption area expansion during coal-bed methane production. *Fuel* 204, 214–226. doi:10.1016/j.fuel.2017.05.047

Tang, Z. Q., Yang, S. Q., Xu, G., Sharifzadeh, M., and Zhai, C. (2018). Evolution law of adsorption and desorption characteristics of CH_4 in coal masses during coalbed methane extraction. *Energy fuels..* 32 (10), 10540–10548. doi:10.1021/acs.energyfuels.8b02318

Wan, Y. Z., Liu, Y. W., Ouyang, W. P., Liu, W. C., and Han, G. F. (2016). Desorption area and pressure-drop region of wells in a homogeneous coalbed. *J. Nat. Gas. Sci. Eng.* 28, 1–14. doi:10.1016/j.jngse.2015.11.026

Wang, J. L., Qin, Y., and Fu, X. H. (2012). New insight into the methanism for dynamic coalbed methane drainage. *Geol. J. China Univ.* 18 (3), 583–588. doi:10.16108/j.issn1006-7493.2012.03.012

Wang, S. W., Wang, F. M., Hou, G. J., Wu, X. M., Zhang, C., Zhang, Y. C., et al. (2014). CBM development well type for steep seam in Fukang Baiyanghe mining area, Xinjiang. *J. China Coal Soc.* 39 (9), 1914–1918. doi:10.13225/j.cnki.jccs.2014.8018

Wang, H. L., Zhang, S. A., Chen, D., Huang, H. X., and Zhao, Z. P. (2020). Dynamic distribution of remaining gas content in steep and thick coal seams in baiyanghe mining area of Fukang. *Xinjiang Pet. Geol.* 41 (5), 587–591. doi:10.7657/XJPG20200512

Wang, Z. R., Wen, Z. Y., and Chen, L. X. (2021). Productivity prediction of vertical test well for fractured coal reservoir under hydraulic fracturing. *Nat. Gas. Geosci.* 32 (4), 465–471. doi:10.11764/j.issn.1672-1926.2020.10.006

Xin, F. D., Xu, H., Tang, D. Z., Yang, J. S., Chen, Y. P., Cao, L. K., et al. (2019). Pore structure evolution of low-rank coal in China. *Int. J. Coal Geol.* 205, 126–139. doi:10.1016/j.coal.2019.02.013

Xu, B. X., Li, X. F., Haghighi, M., Ren, W. N., Du, X. Y., Chen, D., et al. (2013). Optimization of hydraulically fractured well configuration in anisotropic coal-bed methane reservoirs. *Fuel* 107, 859–865. doi:10.1016/j.fuel.2013.01.063

Yan, X. L., Zhang, S. H., Tang, S. H., Li, Z. C., Yi, Y. X., Zhang, Q., et al. (2020). A comprehensive coal reservoir classification method base on permeability dynamic change and its application. *Energies* 13 (3), 644. doi:10.3390/en13030644

Yan, X. L., Zhang, S. H., Tang, S. H., Li, Z. C., Guan, W., Zhang, Q., et al. (2021). A prediction model for pressure propagation and production boundary during coalbed methane development. *Energy fuels..* 35 (2), 1219–1233. doi:10.1021/acs.energyfuels.0c03354

Yarmohammadtooski, Z., Salmachi, A., White, A., and Rajabi, M. (2017). Fluid flow characteristics of bandanna coal formation: A case study from the fairview field, eastern Australia. *Aust. J. Earth Sci.* 64 (3), 319–333. doi:10.1080/08120099.2017.1292316

Zhang, B. X., Deng, Z., Fu, X. H., and Yin, K. (2021). A study on three-phase gas content in coal reservoirs and coalbed methane-water differential distribution in the western Fukang mining area, Xinjiang, China. *ACS omega* 6 (5), 3999–4012. doi:10.1021/acsomega.0c05930

Zhao, J. L., and Chi, J. W. (2020). Review and prospect of influencing factors and prediction methods of coal bed gas reservoir physical properties. *Prog. Geophys. (in Chinese)* 35 (1), 0272–0280. doi:10.6038/pg2020CC0542

Zou, C. N., Yang, Z., Huang, S. P., Ma, F., Sun, Q. P., Li, F. H., et al. (2019). Resource types, formation, distribution and prospects of coal-measure gas. *Petroleum Exploration and Development* 46 (3), 451–462. doi:10.1016/S1876-3804(19)60026-1

frontiers | Frontiers in Earth Science

TYPE Original Research
PUBLISHED 07 September 2022
DOI 10.3389/feart.2022.995394

OPEN ACCESS

EDITED BY
Mingjun Zou,
North China University of Water Resources and Electric Power, China

REVIEWED BY
Wang Hongjian,
North China University of Water Conservancy and Electric Power, China
Cheng Huang,
Luoyang Institute of Science and Technology, China

*CORRESPONDENCE
Zuqiang Xiong,
fccwangmh2@zzu.edu.cn

SPECIALTY SECTION
This article was submitted to Economic Geology, a section of the journal Frontiers in Earth Science

RECEIVED 15 July 2022
ACCEPTED 08 August 2022
PUBLISHED 07 September 2022

CITATION
Liu Y, Xiong Z and Zhang X (2022), Fracture network characterization of high-rank coal and its control mechanism on reservoir permeability. *Front. Earth Sci.* 10:995394.
doi: 10.3389/feart.2022.995394

Fracture network characterization of high-rank coal and its control mechanism on reservoir permeability

Yanhao Liu[1,2,3], Zuqiang Xiong[1]* and Xiaodong Zhang[1]

[1]School of Energy Science and Engineering, Henan Polytechnic University, Jiaozuo, China, [2]Henan Institute of Geology, Zhengzhou, China, [3]Key Laboratory of Coal and Coalbed Methane, Zhengzhou, China

Based on the results of previous research on the fracture systems of reservoirs of middle- and low-rank coal, we took high-rank coal in the southern Qinshui Basin as the study object in this paper and summarize the characteristics of both macro- and micro-fractures in reservoirs of different rank coals, establish a geometric model of the fracture network for different rank coals, and explore the mechanism of coal reservoir permeability change under different conditions. The study found that the structure of the fracture network of high-rank coal developed unevenly. The high-rank coal had the characteristics of rift created outside, micro-fracture development, and undeveloped endogenous fracture, which can be used to improve the permeability of the coal reservoir, to a certain extent. We concluded that given the absence of a seepage aisle in the high-rank coal, there is a rapid increase in reservoir permeability from low to high rate during the seepage process of the fracture network. However, the seepage rate in other coal rank reservoirs increases smoothly. Due to fracture compression and coal matrix shrinkage, the permeability of the coal reservoir first decreases and then increases during the drainage stage. At the same rate of pressure drop, the permeability of high-rank coal reservoir decreases at the fastest rate, followed by that of low-rank coal reservoir, and that of middle-rank coal reservoir, in that order.

KEYWORDS

high-rank coal reservoirs, fracture network, gas seepage, mechanism analysis, reservoir permeability

Introduction

Rocks form various kinds of fissures during long-term geological action, and the study of their morphological characteristics has important engineering significance, as well as coal as a kind of rock (Salmachi et al., 2016; Zhao et al., 2021). Coal reservoirs have a dual pore-fracture structure, and the connectivity and dimensions of their pore fracture system are crucial to their permeability (Yao et al., 2006; Gao et al., 2017; Shen et al., 2019; Shang et al., 2020). The permeability rate is one of the parameters affecting the effectiveness of the extraction of a coal reservoir's coalbed methane (CBM). It reflects the ease of fluid seepage within the coal reservoir and determines the transport and output of CBM. The study of characteristics of the pore and fracture development of coal seams is important for in-depth understanding of the micro-mechanism of fluid fugacity and mass transfer processes in coal seams and for the optimization of geological suitability development (Moore., 2012; Giffin S et al., 2013; Liu et al., 2021). At present, substantial progress has been made in the gas production areas of high-rank coal reservoirs represented by the Qinshui Basin, the gas production areas of middle-rank coal represented by the eastern margin of the Ordos Basin, and the gas production areas of low-rank coal represented by the Erlian Basin and the southern margin of the Junggar Basin. These results obtained are credited to the extensive basic scientific research work conducted by previous authors on the gas production mechanisms of reservoirs of different ranks of coal, as well as verification of the existence of different structural characteristics of reservoirs of different ranks of coal and corresponding differences in gas transport in the reservoirs (Liu et al., 2017; Li et al., 2018; Yu et al., 2018). The pore system controls the desorption-diffusion transport of coalbed methane, and the fracture system mainly determines the large-scale seepage output of the gas (Li et al., 2014; Fang et al., 2019; Fang et al., 2020). Due to differences in the development of connected pores, endogenous fractures, and exogenous fractures in the structure of the reservoirs, each factor will make a different contribution to the permeability values of the reservoir. In general, the seepage capacity of connected pores, endogenous fractures, and exogenous fractures decreases from exogenous fractures to endogenous fractures to connected pores in decreasing order (Zhou et al., 2018). Theoretically, the natural fracture development of the coal seam is conducive to increasing the permeability of the coal seam. Domestic and foreign scholars have shown through a large number of experimental tests that the differences in the degree of fracture network development and connectivity in coal seams have a key effect on the permeability of coal seams (Sampath et al., 2019; Wu et al., 2019; Zhang et al., 2019). For reservoirs of higher rank coal, there is a higher contribution of exogenous fractures due to the non-development of endogenous fractures and connected pore spaces. For reservoirs of middle- and low-rank coal, the contribution of endogenous fractures and connected pores to the permeability of the coal reservoir is high, and middle-rank coal is characterized by a relatively high contribution of endogenous fractures, while low-rank coal is characterized by a relatively high contribution of connected pores (Sang et al., 2009).

Previous studies on permeability in high-ranking coal reservoirs have mostly focused on the overall effect, which is limited to the overall size of permeability, while the refinement of the fracture network in high-ranking coal reservoirs and the resulting variation process of permeability size are still lacking. Research in this area will have an important impact on the drainage process in CBM development, where the variation of permeability size determines the selection of drainage parameters.

Therefore, to further illuminate the multi-stage and multi-genesis fracture network system of high-rank coal reservoirs, this paper takes high-rank coal in the southern Qinshui Basin as the research object, describes the characteristics of high-rank coal fracture network (semi-) quantitatively by means of downhole field observation, optical microscope and scanning electron microscope observation, and compared and analyzed with the previous research results of middle and low-rank coal, establishes the geometric model of fracture network of different coal rank coals, highlights the macroscopic and microscopic characteristics of high-rank coal, the macroscopic and microscopic characteristics of fractures in high-rank coal reservoirs are highlighted, their control on reservoir permeability is investigated, and the mechanism of change in permeability of high-rank coal reservoirs under different drainage stages is discussed, with a view to providing a theoretical basis for the optimization of coalbed methane extraction process in the study area.

Samples and methodology

Samples

The object of this research is the 3# coal seam in the area, the coal thickness is relatively stable, roughly between 5.0 and 7.0 m, and shows a trend of gradually increasing from south to north; the burial depth in most areas is between 500 and 1000 m, and the burial depth is relatively shallow; the coal metamorphism in the area is high and belongs to the anthracite stage, and the coal grade shows a significantly increasing trend from N to S. The macroscopic coal rock type is mainly semi-bright coal, followed by bright coal, and locally also intercalated with dull coal stratification; microscopic components are mainly mirror group, common matrix mirror body, followed by the inert group, common semi-filament body, and rare shell group. The average ash is about 12.98%, which is low ash coal, and the average volatile matter (Vdaf) is about 7.08%; the average moisture (Mad) is about 1.34%.

Methodology

In this study, a combination of field investigation and laboratory observation was adopted to conduct a comprehensive and systematic statistical analysis of the fracture network characteristics of high-order coal in the study area from macroscopic to microscopic. The macroscopic fracture characteristics of high-order coal in the study area were

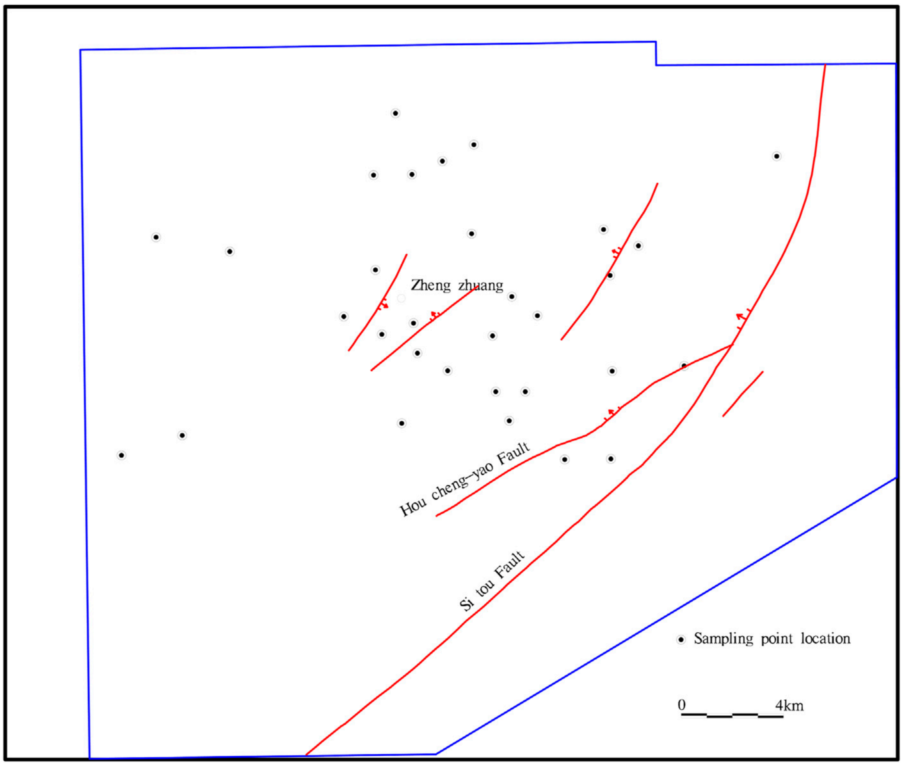

FIGURE 1
Location of the study area and distribution of sampling points.

firstly studied by using fresh coal walls from the underground of three pairs of coal mines, including Sihe, Tang'an, and Chengzhuang, combined with the sketch map of four coal rock profiles drawn and the borehole core data collected from 46 CBM parameter wells and some exploration wells; then the microscopic fractures and ultramicroscopic fractures of 40 coal samples collected were observed and counted in the laboratory by using an optical microscope and scanning electron microscope to study The microscopic fracture characteristics of high-order coal were then studied in the laboratory using an optical microscope and scanning electron microscope. See Figure 1 for details of sampling point locations.

High-Rank coal fracture network characteristics

Previous studies have distinguished the coal reservoir fracture system into visualizable exogenous fractures and endogenous fractures (cleats), and micro-fractures visible under an optical microscope (Zhong et al., 2006; Pan et al., 2016). In this paper, we take the high-rank coal of southern Qinshui Basin as the study object to reveal the multi-level and multi genesis fracture network system in high-rank coal reservoirs. This method can provide us with a way to systematically observe the reservoirs of high-rank coal and study them from macro and micro angles. Accordingly, the coal seam can be divided into two categories: macro-fractures and micro-fractures.

Macro-fractures

Based on the mechanical mechanism of fracture formation in coal, macro-fractures can be divided into exogenous fractures and endogenous fractures, among which endogenous fractures can be classified as face cleat and butt cleat. Statistical analysis of macroscopic cracks in fresh coal walls from underground coal wells and drilled coal cores in Sihe, Tangan and Chengzhuang in the study area was carried out.

Exogenous fracture

The endogenous fractures in the area are generally not developed, and the degree of their development varies at different observation sites. Tracing the direction of the fracture along the coal seam laminate, we know that the main directions of the exogenous fractures in the area are two groups of the NE direction and the NW direction, among which one group

TABLE 1 Statistical results of microscopic fracture observation.

Micro-fracture types	Lengths (μm)	Widths (μm)	Densities (pieces/cm^2)
Shrinkage micro-fracture	86.93–1636	0.53–43.65	44–640
Hydrostatic micro-fracture	567.9–1636	0.1–2	57–81
Tectonic micro-fracture	>4, 757.8–1760	2.06–8.48	49–65
Ultra-micro-fracture	<10	<0.1	

of the NE direction corresponds to the NW-SE direction extrusion in the Yanshan period and one group of the NW direction corresponds to the NE-SW direction extrusion in the Xishan period, and the two groups intersect each other and become a network. The average density of the fracture development is 1–5 fractures per meter, and the length of the extension along the laminated surface varies greatly, from several meters to hundreds of meters. The fracture generally cuts through the whole coal seam, sometimes even cutting through the top and bottom plate It is not limited to any coal rock component, and its surface is flat or serrated. It is often filled with coal dust, calcite, and other fillers, which affects the permeability of the coal reservoir in the area.

Endogenous fracture (cleat)

Endogenous fractures (cleats) mainly develop in bright coal and semi-bright coal, and their development varies from a few millimeters to a few meters. They are mainly comprised of two groups in a dominant development direction. The direction of the first group is roughly between N33°–66°E, and the cleats of this group, which are face cleats, are developed, with a density of 27–120 pieces per meter. The direction of the second group of cleats, which are butt cleats, is roughly between N42°–54°W, but the development of this group's cleats is relatively weak, with a density of 24–60 pieces per meter. As the cleat density is lower, the cleat of the second group is a butt cleat, whereas the development of the length of the cleat is controlled by the face cleat. Face and butt cleats often intersect at nearly right angles, and the inclination of the cleat surface is generally greater than 70°. Although the width of a cleat varies from a few microns to several hundred microns, most are filled by calcite in a tight state and are not conducive to the permeability of coal reservoirs, meanwhile, the development of endogenous fractures (cleats) is strictly controlled by the components and is mainly seen in the vitrinite band of bright coal, semi-bright coal, or semi-dark coal, and is not developed in dull coal. The density of the cleat development of high-rank coal is much less than that of middle-rank coal (800–1200 pieces per meter).

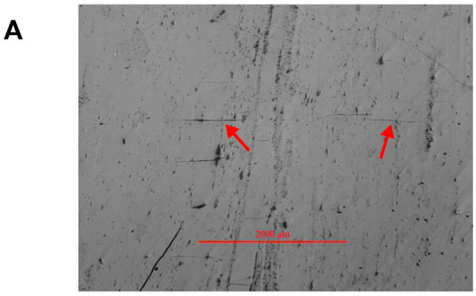

Shrinkage micro-fractures which features are short, straight and oriented

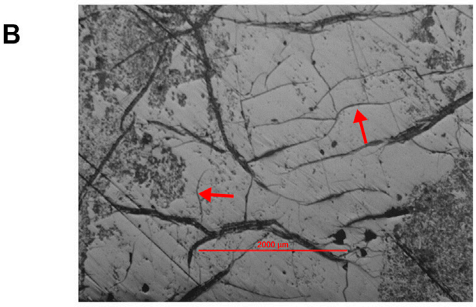

Hydrostatic micro-fractures which features are short, curved, dense and disorderly

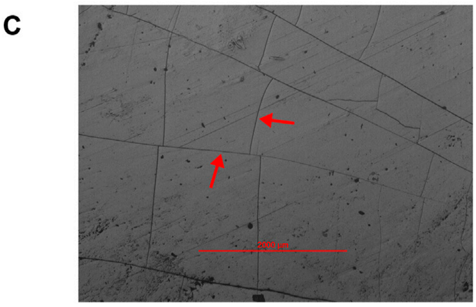

Tectonic micro-fracture which are cutting distribution by tectonic influence

FIGURE 2
Development characteristic of micro-fracture in high-rank coal reservoirs. **(A)** Shrinkage micro-fracture which features are short, straight and oriented **(B)** Hydrostatic micro-fracture which features are short, curved, dense and disorderly **(C)** Tectonic micro-fracture which are cutting distribution by tectonic influence.

Micro-fracture development characteristics

The scale of micro-fracture development, which can be further divided into two different scale levels, i.e. the micro-fracture that can be observed under an optical microscope and the ultra-micro-fracture that can be observed only under a scanning electron microscope, which mostly develop in vitrain and bright coal, is significantly lower than that of macro-fracture development. In our study, 40 coal samples were collected from coal seam No. 3 in the study area for observation and statistical analysis. The statistical results are detailed in Table 1.

Based on the study of micro-fractures under an optical microscope in high-rank coal reservoirs, we found three common micro-fracture types: shrinkage micro-fractures, hydrostatic micro-fractures, and tectonic micro-fractures. The first two are endogenous fractures. They are strictly restricted by their components which only develop in the vitrinite group. Shrinkage micro-fractures correspond to endogenous fractures (cleats) in macro-fractures. Their main morphological features are short, straight and oriented. There is no displacement on both sides of the fissures, which are largely perpendicular to the laminae and arranged at equal intervals, as in Figure 2A, with lengths ranging between 86.93 and 1636 μm, varying widely, widths ranging between 0.53 and 43.65 μm, usually greater than 1 μm, densities ranging between 44 and 640 pieces/cm^2 with average fracture numbers of 177 pieces/cm^2. Hydrostatic micro-fractures are affected by the pressure of overlying static rock during their development and are disorderly and undirected. Their main morphological features are short, curved, dense and disorderly, as in Figure 2B, with lengths ranging from 567.9 to 1636 μm, widths ranging from 0.1 to 2 μm or smaller, and densities ranging from 57 to 81 piece/cm^2, with an average value of 69 pieces/cm^2. The tectonic fissures are not restricted to specific components because their formation is subject to tectonic movements, and they are obliquely intersected by the laminae. From the cutting relationship between the two groups of fractures in the Figure 2C, it can be seen that the relatively long fissures are formed later than the relatively short ones, corresponding to two phases of tectonics. The relatively long fissures are generally 4 mm in height or even larger, while the relatively short fissures range in height from 757.8 to 1760 μm and in width from 2.057 to 8.483 μm, with a density of 49–65 pieces/cm^2 and an average of 59 pieces/cm^2. At the same time, the density of development of the three micro-fracture types is much more extensive than the endogenous fractures (cleats) and no mineral filling. Under the optical microscope, the micro-fracture of the coal reservoir in the area partially cut through the pore space or cleat with the coal seam cleat, which becomes an important channel to communicate the desorption-diffusion pore space with the cleat fracture network.

Based on the study under a scanning electron microscope of ultra-micro-fractures in high-rank coal reservoirs, we found that: ultra-micro-fractures are developed in high-rank coal reservoirs. They are caused by the directional arrangement of the coal molecules and are unique to high-rank coal and absent in middle- and low-rank coal reservoirs. The ultra-micro-fracture usually develops in a group, and the length of the fracture is generally less than 10 μm, the width is generally less than 0.1 μm or even smaller, and it is without mineral filling (Figure 3).

High-rank coal reservoir fracture network peculiarities

According to the fracture structure development characteristics of the above-mentioned high-rank coal, combined with previous research results in middle- and low-rank coal, (Fu et al., 2001a; Bi et al., 2001; Jia et al., 2015), a structural connectivity network model of coal reservoirs of different coal rank was established (Figures 4, 5). Both exogenous fractures and cleats of different ranks of coal are commonly developed in two groups, and both are roughly vertical in orientationThe coal reservoir is cut into a series of small matrix blocks, in which coalbed methane is mainly transported by seepage, flowing from cleat to exogenous fractures and then transported to the wellbore. The difference is in the different development densities of cleats in different ranks of coal. For dull type coal and semi-dull type coal, the density of the cleats in middle-rank coal and high- or low-rank coal is not very different. The cleats of bright type and semi-bright type coal are mostly developed in middle-rank coal, and are more sparsely developed in high- and low-rank coal, as shown in the left side of Figure 4 and Figure 5, as a whole, the exogenous fracture and microfracture development densities of high-rank coal and middle- and low-rank coal are comparable, and the cleats density development is smaller.

The seepage channels in coal reservoirs of different ranks of coal vary in the structure of the fracture network. The overall diffusion and transport of gas in the coal body gradually moves from the inside to the outside of the coal body through the filling pore, connecting pore, micro-fracture, endogenous fracture, and exogenous fracture. However, in the connecting pore stage, high-rank coal lacks the continuity distribution of the transition pore and the mesopore, and the gas mostly diffuses directly from the micro-pore to the micro-fracture (Zhang et al., 2011), as shown in the right side of Figure 4 and Figure 5, the pore development of the middle- and low-rank coal reservoir is balanced, the high-rank coal develops more microporous and sparse macropores, the transition pores and mesopores are not developed, but some super-microscopic fractures are developed. In the connecting stage from the endogenous fracture to the exogenous fracture, it is mostly connected from the micro-fracture to the exogenous fracture, and the connection from the secondary fracture (cleat)

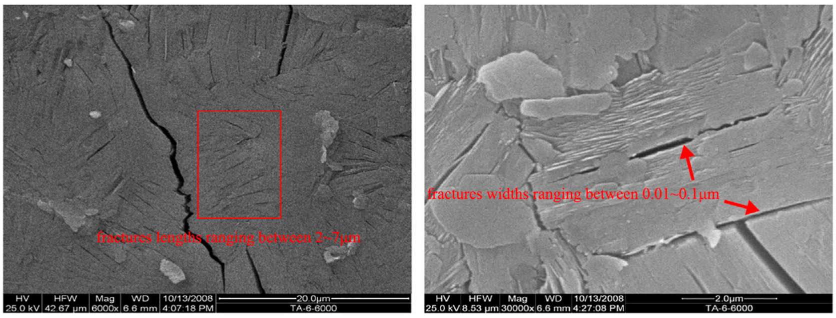

FIGURE 3
Development characteristic of ultra-micro-fracture in high-rank reservoirs.

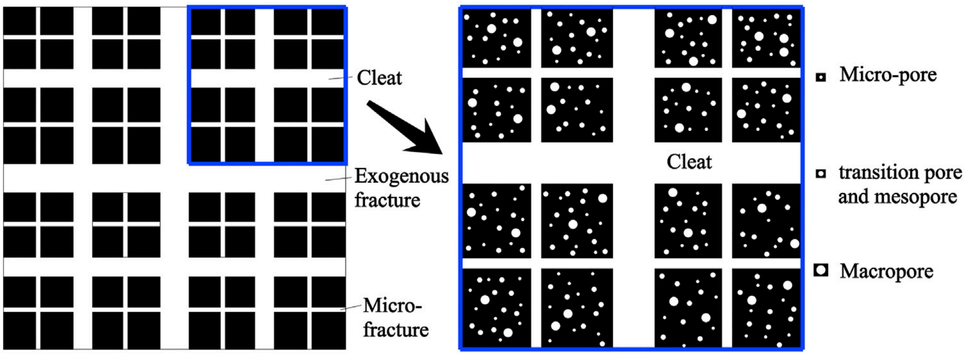

FIGURE 4
Structural connectivity network of middle- and low-rank coal reservoirs.

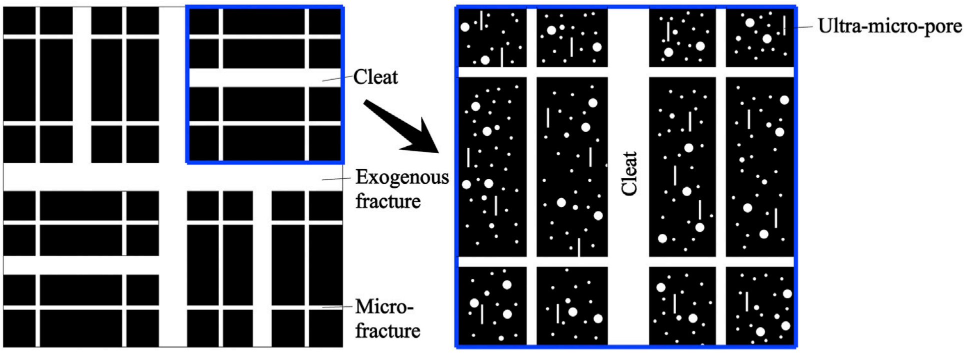

FIGURE 5
Structural connectivity network of high-rank coal reservoir.

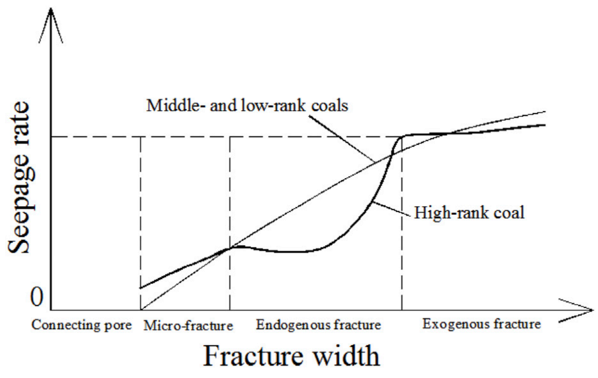

FIGURE 6
Characteristics of permeability change of different coal rank reservoirs of in original state.

to the exogenous fracture is missing in the middle, which will reduce the transport path of gas in the coal seam and cause the rapid increase of the overall gas seepage rate. High-rank coal reservoirs contain high gas content, and the difficulty of coalbed methane extraction is its unique property, but the thermal evolution and tectonic evolution characteristics of high-rank coal reservoirs have a significant impact on the reservoir structure. The development of the regional thermal metamorphic anthracite pore structure is favorable to reservoir formation, and the tectonic evolution effect is favorable to the development of exogenous fractures in coal seams, which improves the permeability of coal reservoirs.

Mechanism of permeability variation in high-rank coal reservoirs

Permeability variation under original reservoir conditions

The linear seepage permeability, K_0, within a regular fracture is related to the fracture width, w, and spacing, s, as follows (Fu et al., 2001b):

$$k_0 = \frac{1.013 \times 10^9 w^3}{12 \cdot S} \tag{1}$$

Where: w is the single fracture width (mm), S is the spacing of two adjacent fractures (mm).

The maximum fracture width of coal reservoirs under confining pressure conditions does not exceed a few tens of microns, so when considering the relationship between fracture development characteristics and permeability of different coal rank reservoirs, the fracture width with a very small variation range can be considered a constant value, and only the fracture spacing variation is considered, i.e., the numerical variation of fracture development density is used instead.

Based on the previous analysis of characteristics of fracture network development, the development density of each scale of fracture in reservoirs of different ranks of coal is substituted into Eq. 1, and the mechanism of the permeability change in reservoirs of different ranks of coal under the original state can be obtained (Figure 6). Natural coal samples in reservoirs of high-rank coal have high compressive strength and high brittleness, and are easily ruptured into blocks under the exertion of external forces, and exogenous fractures are developed under the transformation effect of latter stage tectonic movements, and tectonic fractures are developed in micro-fractures. Scanning electron microscope observations and mercury intrusion porosimetry (MIP) indicate that micro-fractures are significantly more developed than endogenous fractures in reservoirs of high-rank coal, while micro-fractures are fully developed in medium- and low-rank coals. Therefore, if the seepage field of middle- and low-rank coal is considered a kind of multi-level road network, then the seepage field of high-rank coal is a network from low rank road directly to high rank road and the transition of secondary road is missing in between. Accordingly, its seepage characteristics are significantly different from those of middle- and low-rank coals, and its seepage rate generally increases with the increase of the fracture width due to the balanced development of fractures in middle- and low-rank coals. While high-rank coal lacks the transition of secondary roads, its seepage rate has a rapid increase between the lower and higher roads.

Change in reservoir permeability during drainage

According to the model of permeability change during CBM well drainage, i.e., the Shi-Durucan (S-D) model (Shi and Durucan, 2004; Shi and Durucan, 2010):

$$K = K_0 e^{-3c_f(\sigma-\sigma_0)} \tag{2}$$

Where: C_f is the fracture compression volume factor (MPa-1), σ_0 is the effective stress at the original reservoir pressure p_0.

Where the effective stresses are as follows:

$$\sigma - \sigma_0 = -\frac{1-2\nu}{1-\nu}\left(p-p_0\right) + \frac{E}{3(1-\nu)}\varepsilon_{max}\left(\frac{p}{p+P_{50}} - \frac{p_0}{p_0+P_{50}}\right) \tag{3}$$

Assuming that the shrinkage of the substrate and the gas desorption are proportional, then Eq. 3 can be expressed as:

$$\begin{aligned}\sigma - \sigma_0 &= -\frac{1-2\nu}{1-\nu}\left(p-p_0\right) + \frac{E\alpha_s}{3(1-\nu)}\left[V(p) - V_0\right] \\ &= -\frac{1-2\nu}{1-\nu}\left(p-p_0\right) + \frac{E\alpha_s}{3(1-\nu)}\left(\frac{bp}{bp+1} - \frac{bp_0}{bp_0+1}\right)\end{aligned} \tag{4}$$

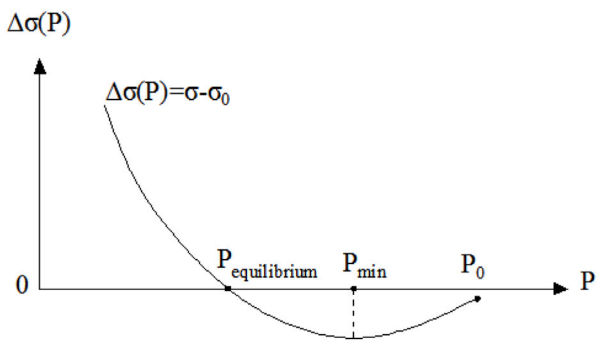

FIGURE 7
Theoretical trends in permeability rates.

Where: α_s is the matrix shrinkage expansion coefficient; V(p) is the adsorption volume at reservoir pressure; b is the Langmuir constant; V_0 is the gas adsorption volume at the initial reservoir pressure p_0.

The first and second terms in Eq. 4 represent the effects of compression of the fracture and shrinkage of the matrix, respectively. In the drainage gas extraction stage ($p< p_0$), the fracture compresses and the matrix contracts, and the amount of change in σ- s_0 depends on the relative amount of change in the interaction of the two factors.

Define $\Delta\sigma(p) = \sigma_0 - \sigma$, then:

$$\Delta\sigma = \frac{1-2\nu}{1-\nu}\left[(p-p_0) - \frac{E}{3(1-2\nu)}\frac{\alpha_s V_L b}{(bp+1)(bp_0+1)}\right] \tag{5}$$

Let $\Delta\sigma = 0$ and we can obtain:

$$p_{equilibrium} = \frac{E}{3(1-2\nu)}\frac{\alpha_s V_L b}{(bp+1)(bp_0+1)} - \frac{1}{b} \tag{6}$$

$P_{equilibrium}$ is the pressure point where the fracture compression and matrix shrinkage effects reach equilibrium, and it can be seen that $P_{equilibrium}$ is inversely proportional to the initial seam pressure, which means that the higher the original reservoir pressure is when the other properties of the coal seam are the same, the lower the pressure value at which the fracture compression and matrix shrinkage effects on coal seam permeability reach equilibrium, and the longer the time in negative effect.

Find the minimum value of pressure point P_{min} corresponding to the minimum value of Δσ:

$$p_{min} = \sqrt{\frac{E}{3(1-2\nu)b}} - \frac{1}{b} \tag{7}$$

From the above equation, we can understand that the minimum value is independent of the initial pressure.

In summary, the theoretical trend of permeability change during the drainage process can be obtained (Figure 7). We can understand that: with the minimum value of P_{min} as the dividing point, the change of permeability shows the characteristics of first decreasing and then increasing, when $P>P_{min}$, fracture compression plays a dominant role, and the permeability becomes smaller as the pressure decreases; when $P<P_{min}$, matrix contraction plays a dominant role and the permeability starts to rebound and increase.

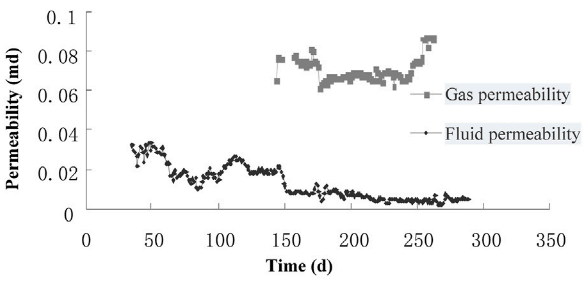

FIGURE 8
Change trend of liquid and gas permeability in well 1-1.

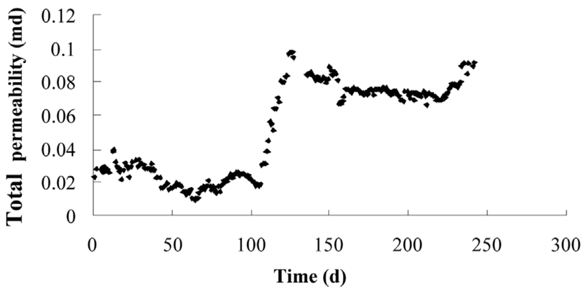

FIGURE 9
Change trend of total permeability in coal reservoir.

According to the drainage information of well 1-1 in the area, the dynamic fluid level of the well reached stability after 36 days of drainage, and the drainage data after 36 days were taken for calculation to obtain the permeability change of well 1-1, as shown in Figure 8.

As the drainage proceeds, the fluid pressure in the coal reservoir decreases and the effective stress increases, resulting in the gas permeability decreasing first and reaching a low point, and after 250 days of drainage, the gas permeability rises rapidly due to the dominant role of coal matrix contraction. The total permeability of coal reservoirs generally decreases and then increases with time. The reservoir permeability is low at the beginning of drainage and the permeability decreases, and with further drainage, the positive effect of coal matrix shrinkage increases, and the reservoir permeability increases. The course of the total permeability and the trend of the theoretical permeability are in good agreement (Figure 9).

Therefore, the permeability variation in reservoirs of different ranks of coal can be deduced from Eq. 7. Previous studies have shown that the Langmuir pressure tends to decrease gradually with increasing reflectance of the vitrinite group (Zhang et al., 2004), i.e., the Langmuir constant is greatest for high-rank coals. Young's modulus shows a trend of decreasing and then increasing and is lowest in the middle-rank coal stage (Shen and Zhang, 2000). Using the above trend in combination with Eq. 7 we can see that: the value of P_{min} in reservoirs of high-rank coal is the largest, and under the same pressure drop rate conditions, the P_{min} pressure point is reached first and the permeability drop rate is the fastest. The reservoir of middle-rank coal has the smallest value of P_{min} and reaches the minimum value the latest, with a slower rate of permeability decline, while the low-rank coal is in between. The result corresponds to the contribution of fracture network structure to reservoir permeability for different ranks of coals as described in the previous section, where the permeability of reservoirs of higher rank coal depends on exogenous fractures, which are also necessarily most influenced by fracture compression.

Conclusions

The structure of the high-rank coal fracture network is unevenly developed, and is characterized by the development of exogenous fractures and micro-fractures, but not endogenous fractures; the development of unique ultra-micro-fractures can improve the permeability of the reservoir, to a certain extent.

There is a corresponding absence of seepage channels for high-rank coals, and in the original state, with the increase of fracture width, the seepage rate of middle- and low-rank coals shows a smooth increasing trend in general, while there is a process of rapid increase from low to high seepage rate due to the lack of endogenous fractures.

Under the influence of fracture compression and the coal matrix shrinkage effect, the permeability of the coal reservoir in the drainage stage has a trend of first decreasing and then increasing. Under the same pressure drop rate condition, the permeability of the high rank coal reservoir decreases the fastest, followed by low-rank coal, and middle-rank coal, in that order.

Data availability statement

The original contributions presented in the study are included in the article/Supplementary material, further inquiries can be directed to the corresponding author.

Author contributions

YL, ZX, and XZ contributed to the conception and design of the study. YL organized the database and performed the statistical analysis, and also wrote the first draft of the manuscript. ZX and XZ wrote sections of the manuscript. All authors contributed to manuscript revision, read, and approved the submitted version.

Funding

The author(s) disclosed receipt of the following financial support for the research, authorship, and/or publication of this article: This work was supported by National Natural Science Foundation of China (Special Characterization of Tectonic Coal Structure and Its Control Mechanism on Coalbed Methane Occurrence and Migration) (No. 41072113), National Natural Science Foundation of China (Dynamic change law and control mechanism of reservoir permeability during surface mining of coalbed methane) (No. 41372162).

Conflict of interest

The authors declare that the research was conducted in the absence of any commercial or financial relationships that could be construed as a potential conflict of interest.

Publisher's note

References

Bi, J., Su, X., Han, D., et al. (2001). The relation between cleat frequency and coal rank. *J. China Coal Soc.* 26 (4), 346–349. doi:10.3321/j.issn:0253-9993.2001.04.003

Fang, H. H., Sang, S. X., and Liu, S. Q. (2020). A methodology for characterizing the multiscale pores and fractures in anthracite and semi-anthracite coals and its application in analysis of the storage and permeable capacity of coalbed methane. *SPE Reserv. Eval. Eng.* 23 (1), 177–186. doi:10.2118/195672-pa

Fang, H. H., Sang, S. X., Liu, S. Q., and Du, Y. (2019). Methodology of three-dimensional visualization and quantitative characterization of nanopores in coal by using FIB-SEM and its application with anthracite in Qinshui basin. *J. Petroleum Sci. Eng.* 182, 106285. doi:10.1016/j.petrol.2019.106285

Fu, X., Qin, Y., Jiang, B., et al. (2001b). Compress experiment of coal cleat and mathematical simulation of coal reservoir permeability. *J. China Coal Socirty* 26 (6), 573–577. doi:10.3321/j.issn:0253-9993.2001.06.003

Fu, X., Qin, Y., and Li, G. (2001a). Advance in study of coal reservoir Perme AtingAbility. *J. Liaoning Tech. Univ. Nat. Sci.* 20 (6), 739–743. doi:10.3969/j.issn.1008-0562.2001.06.002

Gao, W., Yi, T., Jin, J., et al. (2017). Pore integrated fractal characteristics of coal sample in western Guizhou and its impact to porosity and permeability. *J. China Coal Soc.* 42 (5), 1258–1265. doi:10.13225/j.cnki.jccs.2016.0869

Giffin, S., Littke, R., Klaver, J., and Urai, J. (2013). Application of BIB–SEM technology to characterize macropore morphology in coal. *Int. J. Coal Geol.* 114, 85–95. doi:10.1016/j.coal.2013.02.009

Jia, J., Zhang, H., Jia, Q., et al. (2015). Status and prospect: Study on the cleat system in coal reservoir. *Nat. Gas. Geosci.* 26 (9), 1621–1628. doi:10.11764/j.issn.1672-1926.2015.09.1621

Li, G., Meng, Z., and Wang, B. (2014). Diffusion and seepage mechanisms of high rank coal-bed methane reservoir and its numericalsimulation at early drainagerate. *J. China Coal Soc.* 39 (9), 1919–1926. doi:10.13225/j.cnki.jccs.2014.8024

Li, S., Tang, D., Pan, Z., Xu, H., Tao, S., Liu, Y., et al. (2018). Geological conditions of deep coalbed methane in the eastern margin of the Ordos Basin, China: Implications for coalbed methane development. *J. Nat. Gas Sci. Eng.* 53, 394–402. doi:10.1016/j.jngse.2018.03.016

Liu, S., Sang, S., Wang, G., Ma, J., Wang, X., Wang, W., et al. (2017). FIB-SEM and X-ray CT characterization of interconnected pores in high-rank coal formed from regional metamorphism. *J. Petroleum Sci. Eng.* 148, 21–31. doi:10.1016/j.petrol.2016.10.006

Liu, S., Wang, H., Wang, R., et al. (2021). Research advances on characteristics of pores and fractures in coal seams. *Acta Sedimentol. Sin.* 39 (01), 212–230. doi:10.14027/j.issn.1000-0550.2020.064

Moore, T. A. (2012). Coalbed methane: A review. *Int. J. Coal Geol.* 101, 36–81. doi:10.1016/j.coal.2012.05.011

Pan, J. N., Wang, K., Hou, Q. L., Niu, Q., Wang, H., and Ji, Z. (2016). Micro-pores and fractures of coals analysed by field emission scanning electron microscopy and fractal theory. *Fuel* 164, 277–285. doi:10.1016/j.fuel.2015.10.011

Salmachi, A., Rajabi, M., Reynolds, P., Yarmohammadtooski, Z., and Wainman, C. (2016). The effect of magmatic intrusions on coalbed methane reservoir characteristics: A case study from the hoskissons coalbed, gunnedah basin, Australia. *Int. J. Coal Geol.* 165, 278–289. doi:10.1016/j.coal.2016.08.025

Sampath, K. H., Perera, M. S., Ranjith, P. G., Matthai, S., and Dong-yin, L. (2019). Qualitative and quantitative evaluation of the alteration of micro-fracture characteristics of supercritical CO_2-interacted coal. *J. Supercrit. Fluids* 147, 90–101. doi:10.1016/j.supflu.2019.02.014

Sang, S., Liu, H. h., Li, Y. m., Li, M. x., and Li, L. (2009). Geological controls over coal-bed methane well production in southern Qinshui basin. *Procedia Earth Planet. Sci.* 1 (1), 917–922. doi:10.1016/j.proeps.2009.09.142

Shang, J., Liu, H., Sang, S., et al. (2020). Coupling analysis on permeability and pore fracture development in high rank coal reservoirs of southern Qinshui Basin. *Saf. Coal Mines* 51 (6), 184–190. doi:10.13347/j.cnki.mkaq.2020.06.040

Shen, W., Shao, L., Tian, W., Chen, G., Chen, F., Hou, H., et al. (2019). Study on geological controls and enrichment models of coalbed methane in the Wuwei Basin in eastern North Qilian, northwestern China. *Energy Explor. Exploitation* 37 (1), 429–452. doi:10.1177/0144598718803693

Shen, W., and Zhang, B. (2000). Testing study on mechanical parameters of coal. *Chin. J. Rock Mech. Eng.* 19, 860–862. doi:10.3321/j.issn:1000-6915.2000.z1.008

Shi, J., and Durucan, S. (2004). Drawdown induced changes in permeability of coalbeds:A new interpretation of the reservoir response to primary recovery. *Transp. Porous Media* 56, 1–16. doi:10.1023/b:tipm.0000018398.19928.5a

Shi, J., and Durucan, S. (2010). Exponential growth in San Juan Basin Fruitland Coalbed permeability with reservoir drawdown:model match and new insights. *SPE Reserv. Eval. Eng.* 6, 914–925. doi:10.2118/123206-pa

Wu, H., Zhou, Y., Yao, Y., and Wu, K. (2019). Imaged based fractal characterization of micro-fracture structure in coal. *Fuel* 239, 53–62. doi:10.1016/j.fuel.2018.10.117

Yao, Y., Liu, D., Huang, W., et al. (2006). Research on the pore-fractures system properties of coalbed methane reservoirs and recovery in Huainan and Huaibei coal-fields. *J. China Coal Socirty* 31 (2), 163–168. doi:10.3321/j.issn:0253-9993.2006.02.007

Yu, K., Qu, Z., Ju, Y., et al. (2018). Burial and thermal history of coal-bearing strata in Shengli coalfield, Erlian basin. *Acta Sedimentol. Sin.* 36 (5), 903–913. doi:10.14027/j.issn.1000-0550.2018.064

Zhang, Q., Zhang, Q., and Zhang, H. (2004). Adsorption characteristics of different rank coals in different areas China. *Coal Geol. Explor.* 32, 68–72. doi:10.3969/j.issn.1001-1986.2004.z1.015

Zhang, X., Liu, Y., Sang, S., et al. (2011). Study of the gas diffusion mechanism in high-rank coal reservoirs. *J. China Univ. Mining& Technol.* 40 (01), 43–48.

Zhang, Y., Lebedev, M., Jing, Y., Yu, H., and Iglauer, S. (2019). *In-situ* X-ray micro-computed tomography imaging of the microstructural changes in water-bearing medium rank coal by supercritical CO_2 flooding. *Int. J. Coal Geol.* 203, 28–35. doi:10.1016/j.coal.2019.01.002

Zhao, Z., Wang, H., Cui, Z., et al. (2021). Experimental study on mode-I fracture toughness using chevron straight-notched semi-circular bend (CSNSCB) method. *Theor. Appl. Fract. Mech.* 116, 103093. doi:10.1016/j.tafmec.2021.103093

Zhong, L., Zhang, Q., Xie, G., et al. (2006). *MT/T 968-2005 Description methodology of fracture in coal.* Beijing: China Coal Industry Publishing House.

Zhou, H., Zhong, J., Ren, W., Wang, X., and Yi, H. (2018). Characterization of pore-fracture networks and their evolution at various measurement scales in coal samples using X-ray μCT and a fractal method. *Int. J. Coal Geol.* 189, 35–49. doi:10.1016/j.coal.2018.02.007

frontiers | Frontiers in Earth Science

TYPE Original Research
PUBLISHED 09 September 2022
DOI 10.3389/feart.2022.1020313

EDITED BY
Mingjun Zou,
North China University of Water Resources and Electric Power, China

REVIEWED BY
Wei Jiang,
Suzhou University, China
Yu Qi,
Yanshan University, China

*CORRESPONDENCE
Keying Wang,
744491522@qq.com

SPECIALTY SECTION
This article was submitted to Economic Geology,
a section of the journal
Frontiers in Earth Science

RECEIVED 16 August 2022
ACCEPTED 22 August 2022
PUBLISHED 09 September 2022

CITATION
Wang K, Cai N, Du J, Gong S and Li Y (2022), Geological evaluation and gas bearing analysis for shale reservoir in Ziyun-Luodian typical area of southern Guizhou province, China.
Front. Earth Sci. 10:1020313.
doi: 10.3389/feart.2022.1020313

Geological evaluation and gas bearing analysis for shale reservoir in Ziyun-Luodian typical area of southern Guizhou province, China

Keying Wang[1,2]*, Ningbo Cai[1,2,3], Jiang Du[1,2], Shuhua Gong[1,2] and Yan Li[1,2]

[1]New Geological Energy Exploration and Development Engineering Technology Research Center of Hunan, Changsha, China, [2]Geophysics and Geochemistry Survey Institute of Hunan, Changsha, China, [3]Institute of Advanced Studies, China University of Geosciences, Wuhan, China

The Ziyun-Luodian area of southern Guizhou province in China is chosen as the research area and the Dawuba formation in Carboniferous system is the target stratum in this paper. Combined with laboratory experiments and mathematical analyses, geological evaluations on organic geochemistry, physical property of the reservoir, and gas bearing feature are all studied, and geological controls on gas occurrence are then analyzed. The following conclusions are achieved. The organic type is mainly II_2 or III. TOC is generally in a range of 1%–3%, and $R_{o,max}$ ranges from 1.7% to 4.4%, with an average value of 2.4%. Mineral compositions are mainly clay and quartz, with a few calcite and dolomite. The Specific surface area ranges from 6.6 to 29.8 m^2/g, with an average value of 15.2 m^2/g, and the pore volume varies from 0.012 to 0.046 cm^3/g, with an average value of about 0.02 cm^3/g. There is a strongly and positively linear relationship between specific surface area and pore volume. The porosity is mostly in the range of 1%–3%, with an average value of 1.8%. Most of permeability is below 0.01 mD, with an average value of about 0.004 mD. There is an exponential and positive relationship between porosity and permeability. The gas content is generally below 2.0 m^3/t. There are three obvious correlations for gas content versus buried depth ranges of 500–700 m, 700–1,000 m, and 2,700–3,000 m. TOC influences gas content in a linear mode, and $R_{o,max}$ influences gas content positively. The gas content has a positive relationship with clay mineral and a negative relationship with sapropelic percentage. The porosity and permeability are both positively correlated with gas content. The pore volume has a positive trend with gas content, and the specific surface area has a positively and strongly linear relationship with gas content.

KEYWORDS

geological evaluation, gas bearing analysis, shale gas, fitting analysis, southern Guizhou province

1 Introduction

Shale is a source, reservoir and trap for significant quantities of methane and minor amounts of other gases, with the coexistence of absorbed and free gas (Dow, 1977; Curtis, 2002; Jarvie et al., 2007; Ross and Bustin, 2009). This gas, referred to as shale gas, is potentially an important economic resource, and has received worldwide attentions as a clean and unconventional energy (Schmoker, 1980; Bowker, 2007; Chen et al., 2011).

Exploration and exploitation on shale gas in China are relatively late compared with that in America (Li et al., 2007). Besides, geological setting of shale gas in China is quite complex, especially in southern China. Till now, researches on shale gas in southern China usually focus on Sichuan basin, while relatively few researches have been carried out in Guizhou province (Zou C et al., 2010; Huang et al., 2012; Yang et al., 2014; Meng et al., 2016; Ma et al., 2018). As a typical area for shale gas exploration and exploitation in Guizhou province, the Ziyun-Luodian area is selected as the research area in this paper. Current researches show that multiple shale layers are developed in this area, with a vast distribution and a high organic content, among which, the Dawuba formation has been demonstrated to be the most potential stratum and is the target stratum in this study (Wang et al., 2012).

It is of great significance to study shale gas geology on reservoir geometry, organic maceral, organic type, organic abundance, organic maturity, mineral composition, pore system and gas bearing feature (Martini et al., 2003; Bowker, 2007; Martineau, 2007; Loucks et al., 2012; Zou et al., 2015a, 2015b; Qi et al., 2019; Qi et al., 2022). Combined with the physical experiments and mathematical analyses, the geological evaluation and gas bearing analysis are both conducted in this paper, which provides references for shale gas exploration in the future.

2 Samples and experiments

2.1 Sample collection and preparation

Core samples in the Dawuba formation from wells C01, D01, and Z01 were fully collected, as well as outcrop samples in cities of Ziyun, Changshun, Huishui, Qinglong, Manchang, Wangyou, Daihua, and Zhenning. Sample locations can be found in Figure 1.

Samples were immediately shipped back to the lab after collection. Three types of samples were prepared in this study. The first type was cylinder samples with a diameter of 25 mm and a height of 30–50 mm; and they were used for permeability test (PT). The second type was block samples with a maximum length of about 15 mm, which were used for mercury intrusion porosimetry (MIP), total organic carbon (TOC), and isothermal adsorption (IA). The last type was particle samples with about 3 g weight and 60 mesh in size, and they were prepared for organic maceral (OM), mineral composition (MC), vitrinite reflectance (VR), and nitrogen adsorption under low temperature (NALT).

2.2 Experimental section

All the above mentioned experiments were made on prepared samples. Besides, gas content test (GCT) was made on the field. All experiments were conducted with the guidance of

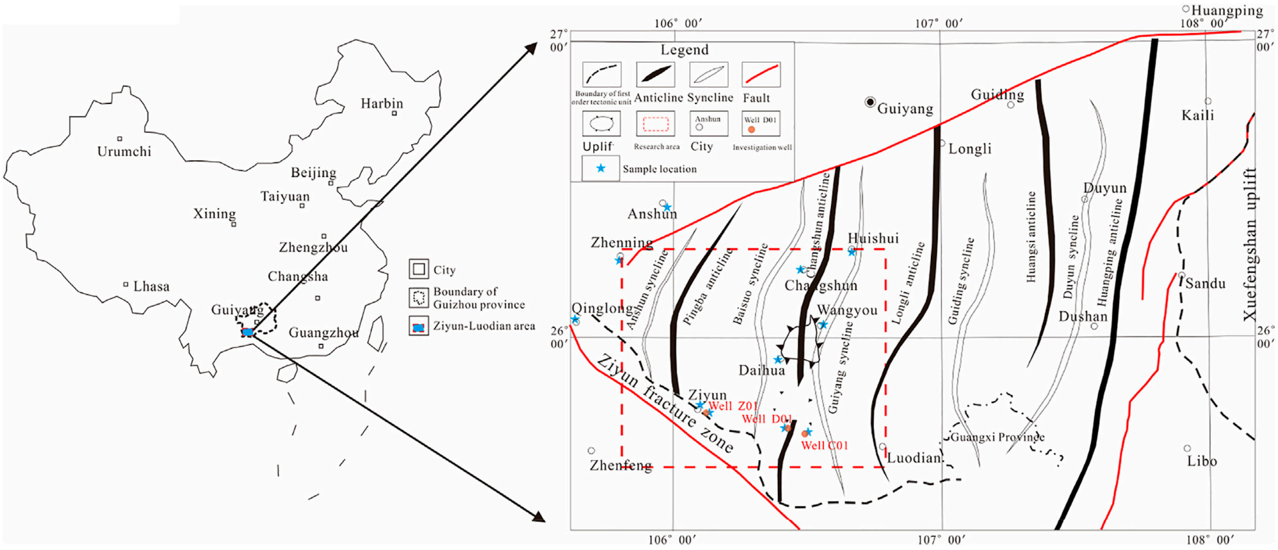

FIGURE 1
Structure outline and sample locations in the research area.

TABLE 1 Samples used in each experiment.

Experiments	Core samples			Outcrop samples							
	Well C01	Well D01	Well Z01	Ziyun	Changshun	Huishui	Qinlong	Manchang	Wangyou	Daihua	Zhenning
VR	√	√		√	√	√	√				√
OM	√	√		√	√	√				√	√
TOC	√	√		√	√	√		√	√		√
MC	√	√	√	√	√	√				√	√
MIP	√	√	√	√	√	√	√	√	√	√	
PT	√	√	√	√	√	√	√	√	√	√	
NALT	√	√	√	√	√	√					
IA								√	√	√	
GCT	√	√	√								

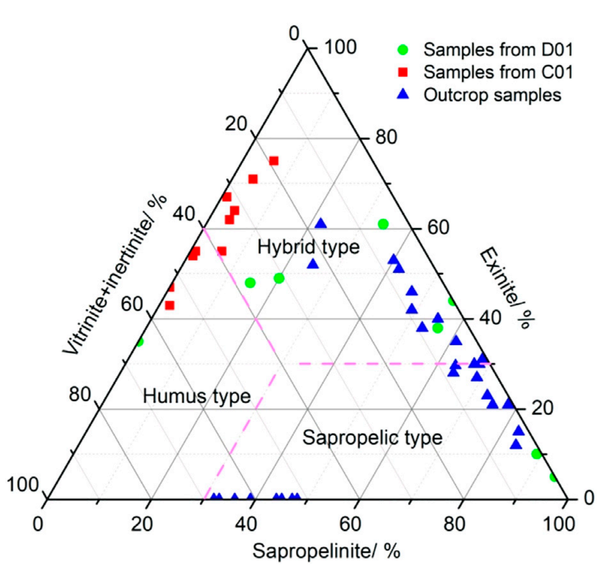

FIGURE 2
Three element diagram to distinguish organic type.

China's national standard or industry standard. Samples used in each experiment are listed in Table 1.

Some descriptions should be noted for those experiments. The MIP measurement ran up to a pressure of 6×10^4 Psia, which shows that pore diameters as small as 3 nm were penetrated. For the IA measurement, the temperature was set to 30°C, and the Langmuir equation and capacity method were adopted during the measurement. During the NALT measurement, the related parameters were set as follows: Experimental temperature, 77.37 K; degassing temperature, 120°C; degassing time, 240 min, and the BET equation was used to calculated the specific surface area and pore volume of the samples. The PT measurement was simulated under situ stress conditions using a triaxial cell with an isotropic ambient pressure of 2.5 MPa. The GCT measurement was conducted by using desorption method, and the gas content consisted of desorbed gas, residual gas and lost gas. Measurements of VR, OM, and MC are conducted following the Chinese oil and gas industry standard (SY/T) 5124-2012, 5125-2014, and 5163-2010, respectively. The TOC measurement is conducted following the China's national standard of GB/T19145-2003.

3 Geological setting

The structure outline of the research area is shown in Figure 1. The research area locates at the southern Guizhou depression of China, in which synclines and anticlines are arranged alternately. Trough-like folds are developed, with compressional north-south structures passing through the entire area. Main structures within the research area are Anshun syncline, Pingba anticline, Baisuo syncline, Changshun anticline, Guiyang syncline, and Longli anticline, et al. Major morphologies of the anticlines are box-shaped with widths of about 30–50 km, while the synclines are trough-shaped with widths of about 10–15 km. Most of the faults are thrust faults with big angles, trending north-south or northeast, and they are perpendicular with northwestern or northeastern fractures.

The Dawuba formation occurs in the lower Carboniferous system, and can be divided into two parts. The lower part mainly consists of dark gray shale, silty shale and a small amount of siltstone, while the upper part is composed of black limestone, calcareous shale and siliceous shale. The Dawuba formation is laterally stable and ranges in a thickness from 128 to 204 m for mud or shale inside, with an average value of 166 m. The thickness reaches a peak around Ziyun or Wangyou city and

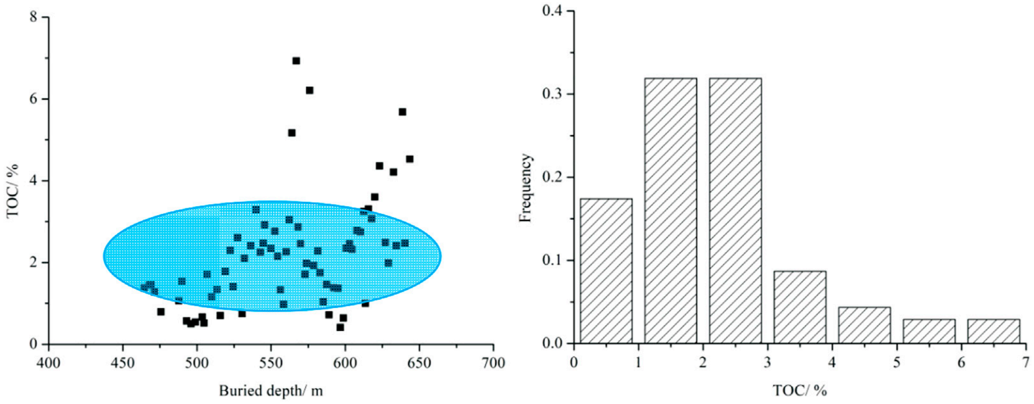

FIGURE 3
TOC variation with depth (left) and TOC frequency histogram (right) for well D01.

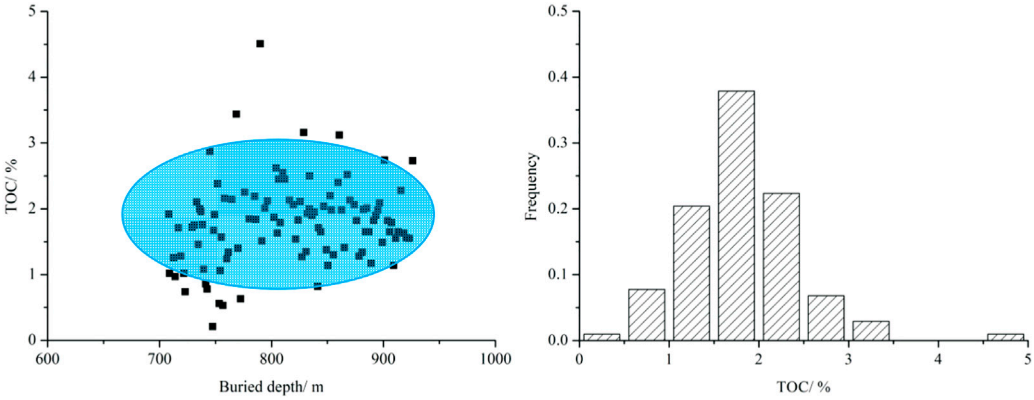

FIGURE 4
TOC variation with depth (left) and TOC frequency histogram (right) for well C01.

then reduces towards Changshun-Daihua city. The depth of the stratum shows a trend of decreasing first and then increasing from west to east. The maximum depth is about 4,500 m around Ziyuan city, and the minimum depth can reduce to less than 1,000 m in the central area.

4 Geological evaluation

4.1 Organic geochemistry

4.1.1 Organic maceral and organic type

Core samples from wells D01 and C01 and outcrop samples from cities of Ziyun, Changshun, Huishui, Daihua, and Zhenning are all collected to conduct the OM measurement. For well D01, sapropelinite varies between 15% and 95%, with an average value of 52%; and percentage ranges of exinite, vitrinite and inertinite are 5%–65%, 1%–43%, and 1%–22%, respectively, with their respective averages of 49%, 18%, and 7%. For well C01, sapropelinite is between 1 and 6%, with an average value of 3%; and percentages of exinite, vitrinite, and inertinite are 43%–75%, 13%–45%, and 3%–19%, respectively, and their respective averages are 59%, 31%, and 8%. Experiments on outcrop samples show that the sapropelinite ranges from 22% to 84%, and the average is 54%; and percentage ranges of exinite, vitrinite and inertinite are 12%–61%, 1%–30%, and 1%–43%, respectively, with their averages of 35%, 12%, and 16%, respectively.

Regarding all the samples above, a three element diagram concerning sapropelinite, vitrinite plus inertinite, and exinite is drawn as shown in Figure 2. The figure indicates that sapropelic and hybrid types are the main organic types, while the humus type is much less developed.

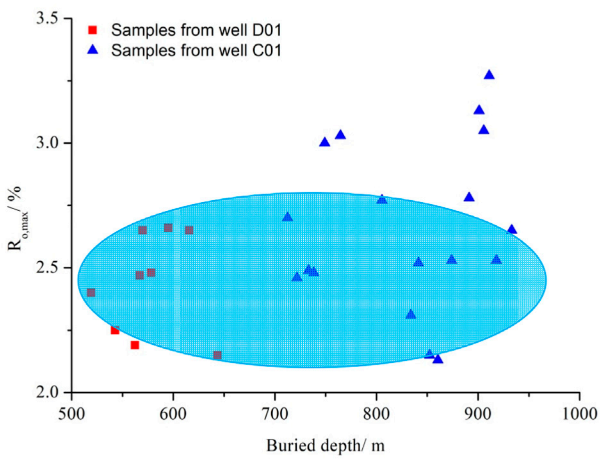

FIGURE 5
$R_{o,max}$ values for the core samples from wells D01 and C01.

As a very important parameter, TI is used here to evaluate kerogen type, which is expressed as follows,

$$TI = \frac{a \times (+100) + b \times (+50) + c \times (-75) + d \times (-100)}{100} \tag{1}$$

where, *a*, *b*, *c*, and *d* represent sapropelic, exinite, vitrinite, and inertinite, respectively.

According to Dow (1977) and Tissot and Welte (1978), four organic types are classified. They are type I with TI higher than 80, which is much beneficial for oil generation; type II_1 with TI between 80 and 40, which is quite beneficial for oil generation; type II_2 with TI between 0 and 40, which is quite beneficial for gas generation; and type III with TI lower than 0, which is much beneficial for gas generation. Then, for shale samples in well D01, TI ranges from −37 to 98, and all the four organic types can be distinguished, with type II_2 as the majority. For shale samples in well C01, TI ranges from −21 to 29, and the organic types are II_2 and III. While for outcrop samples, TI is between −30 and 89, and all the four organic types are developed. As a result, the organic types are mostly II_2 and III in this area, which is beneficial for gas generation.

4.1.2 Organic abundance

Core samples from wells D01 and C01 and outcrop samples from cities of Ziyun, Changshun, Huishui, Manchang, Wangyou, and Zhenning are all collected to conduct the TOC measurement. As can be seen from Figure 3, TOC is 0.4%–6.9% and the average value is 2.19% for samples collected from well D01. The frequency histogram in Figure 3 indicates that most of the TOC values range from 1% to 3%. As can be seen from Figure 4, TOC value varies from 0.2% to 4.5% and the average value is 1.8% for samples in well C01. The frequency histogram in Figure 4 indicates that 35% of the TOC values are higher than 2.0%, and 90% of the values are higher than 1.0%. For the outcrop samples, TOC is mainly in a range of 1.0%–3.0%. Therefore, TOC values in this area are mainly in the range of 1%–3%, and values lower than 1% or higher than 3% are relatively few. Generally, a TOC range of higher than 1% is considered to be conducive to organic matter accumulation. Therefore, most of the source rock in this area is quite beneficial for the organic accumulation.

4.1.3 Organic maturity

Core samples from wells D01 and C01 and outcrop samples from cities of Ziyun, Changshun, Huishui, Qinlong, and Zhenning are all collected to conduct the VR measurement. $R_{o,max}$ values for wells D01 and C01 are shown in Figure 5. It can be seen from the figure that the $R_{o,max}$ for well D01 ranges from 2.2% to 2.7%, with an

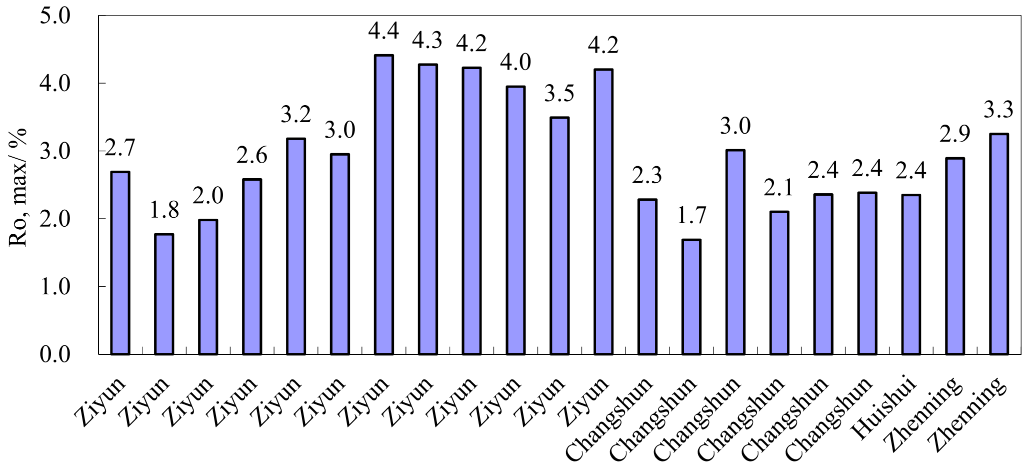

FIGURE 6
$R_{o,max}$ values for the outcrop samples.

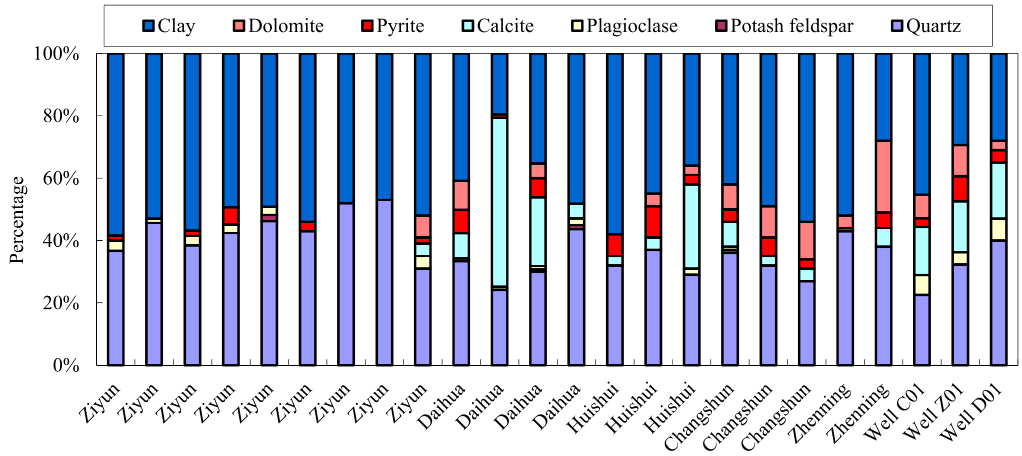

FIGURE 7
Mineral compositions for the core samples and outcrop samples.

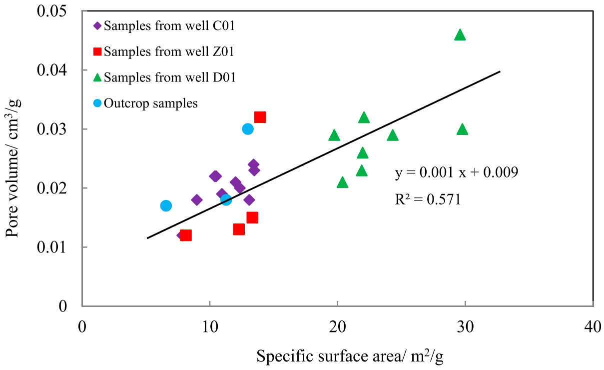

FIGURE 8
Fitting diagram between specific surface area and pore volume.

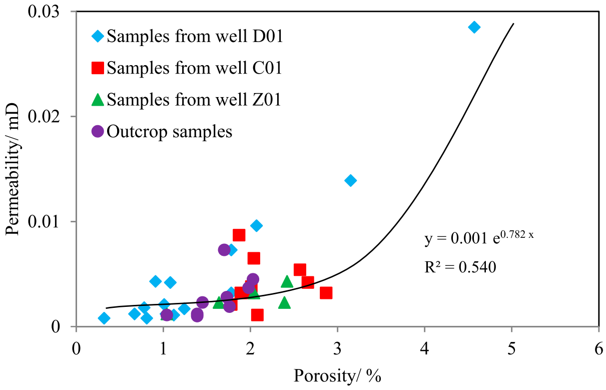

FIGURE 9
Fitting diagram between porosity and permeability.

average value of about 2.4%; and $R_{o,max}$ for well C01 varies from 2.1% to 3.3%, with an average value of about 2.7%. Generally, $R_{o,max}$ for core samples from wells D01 and C01 is from 2.2% to 2.7%. $R_{o,max}$ values for outcrop samples are shown in Figure 6. The figure shows that $R_{o,max}$ values for outcrop samples range from 1.7% to 4.4%, with an average value of about 2.4%, which is a little higher than the values from core samples. The main $R_{o,max}$ range for outcrop samples is 1.7%–3.0%, which is approximate with that for core samples. As a result, the coalification degree in this area is quite high.

4.2 Physical property of the reservoir

4.2.1 Mineral composition

Core samples from wells D01, C01, and Z01 and outcrop samples from cities of Ziyun, Changshun, Huishui, Daihua, and Zhenning are all collected to conduct the MC measurement. Mineral compositions of the Dawuba formation in the research area are mainly clay and quartz, with a few calcite and dolomite, and the contents of other minerals including plagioclase, potash feldspar, and pyrite are rarely detected, as shown in Figure 7. The percentage of clay varies from 17.6% to 58.4% and its average value is 46.3%; while the percentage of quartz ranges from 21.7% to 53.0% and its average value is 37.6%. The distribution of calcite is extremely inhomogeneous, and its percentage is between 0% and 48.6%, with an average value of about 11.9%. The dolomite also distributes inhomogeneously, and its percentage varies from 0% to 23.0%, with an average value of about 8.5%.

4.2.2 Pore system

Core samples from wells D01, C01, and Z01 and outcrop samples from cities of Ziyun, Changshun, and Huishui are all

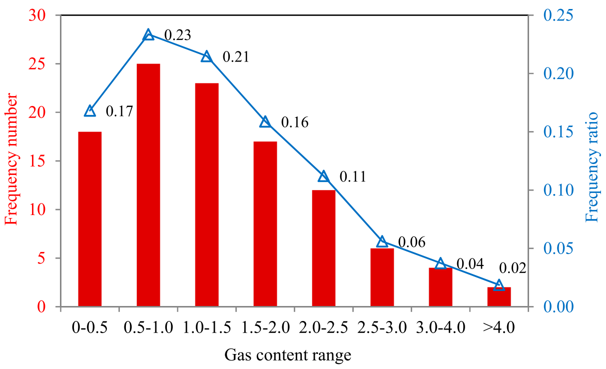

FIGURE 10
Frequency histogram of gas content for wells C01, D01 and Z01.

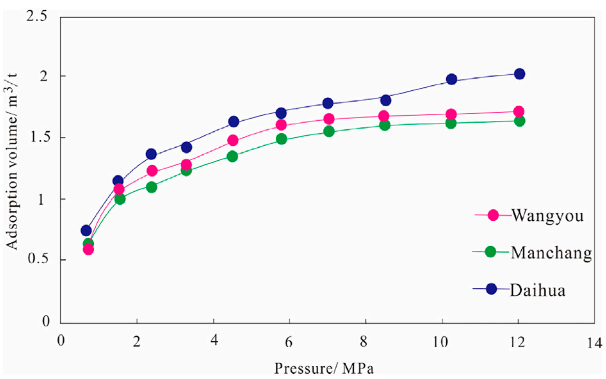

FIGURE 11
Isothermal adsorption curves for the outcrop samples.

collected to conduct the NALT measurement, and the results are shown in Figure 8. The figure shows that the specific surface area ranges from 6.6 to 29.8 m^2/g, with an average value of 15.2 m^2/g; and the pore volume varies from 0.012 to 0.046 cm^3/g, with an average value of 0.02 cm^3/g. There is a strongly and positively linear relationship between specific surface area and pore volume in this area, and the fitting degree can reach about 0.6.

Core samples from wells D01, C01, and Z01 and outcrop samples from cities of Ziyun, Changshun, Huishui, Qinlong, Manchang, Wangyou, and Daihua are all collected to conduct the MIP and PT measurements, and the results are shown in Figure 9. The figure indicates that the porosity in the research area ranges from 0.32% to 4.57%, with an average value of about 1.8% and the major range of 1%–3%; and the permeability varies from 0.001 to 0.029 mD, with an average value of about 0.004 mD, and most of the permeability is below 0.01 mD. The figure also indicates that there is an exponential and positive relationship between porosity and permeability, with a fitting degree of about 0.5.

4.3 Gas bearing feature

Thirty two core samples from well C01, 57 core samples from well D01 and 18 core samples from well Z01 are collected, and GCT measurements are then conducted on the field. The frequency histogram for gas content is therefore drawn as shown in Figure 10. The figure indicates that the gas content is mostly below 2.0 m^3/t in this area, with extremely few values higher than 4 m^3/t. Meanwhile, IA measurements for outcrop samples of Wangyou, Manchang and Daihua are conducted and shown in Figure 11. The figure indicates that adsorption volume can be higher than 2 m^3/t for the Daihua sample, and be higher than 1.5 m^3/t for the Manchang and Wangyou samples as pressure increasing, although the weathering may reduce the gas bearing property for outcrop samples. All the above indicates that the gas bearing feature is quite good, and the research area can be treated as an effective area for the shale gas exploitation in the future.

5 Geological controls on gas content

5.1 Geological evolution

After the Yanshanian movement, the strata in southern Guizhou province started to be uplifted and eroded, and Jurassic and Triassic were then failed to be deposited. As a result, the upper Paleozoic strata were exposed with fractures developed, which is much harmful for shale gas occurrence. The buried depth of the target stratum is a direct parameter to represent the geological evolution, and its influence on gas content for wells C01, D01, and Z01 are then analyzed as shown in Figure 12. Several findings can be achieved from the figure. First, there are three obvious correlations for gas content versus buried depth ranges of 500–700 m, 700–1,000 m, and 2,700–3,000 m. Second, three correlations are all linear, with fitting degrees of about 0.3. Third, as buried depth increasing, the slope of the correlation equation decreases from 0.015 to 0.003, which indicates that the gas content becomes more stable and the influence amplitude become weaker. Moreover, it is realized that the increasing gas content with buried depth is likely to be the result of the increasing reservoir pressure, which has a control on free and adsorbed gases.

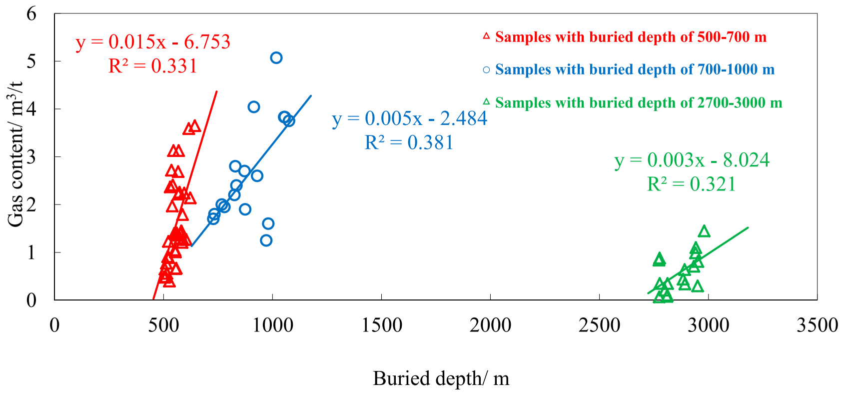

FIGURE 12
Fitting diagram for gas content and buried depth.

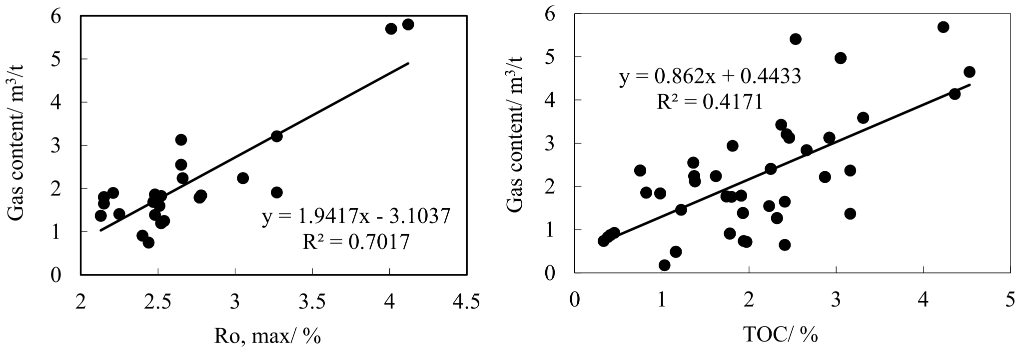

FIGURE 13
Relationships between gas content versus $R_{o,max}$ (left) and TOC (right).

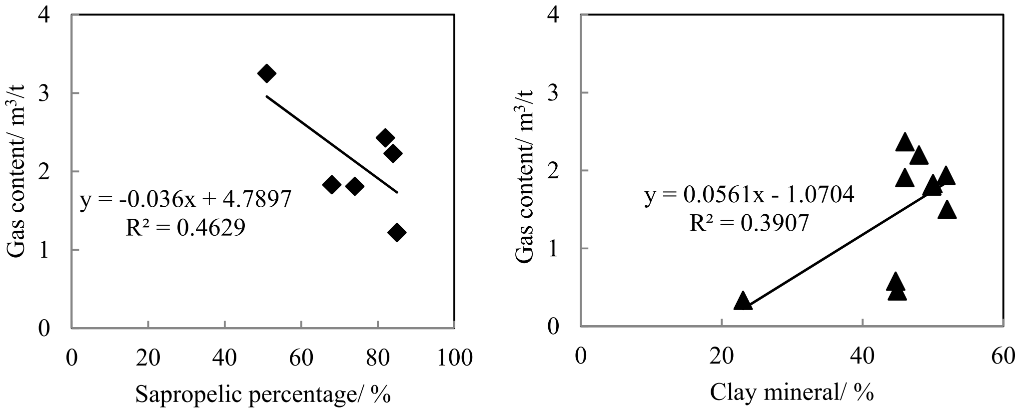

FIGURE 14
Relationships between gas content versus sapropelic percentage (left) and clay mineral (right).

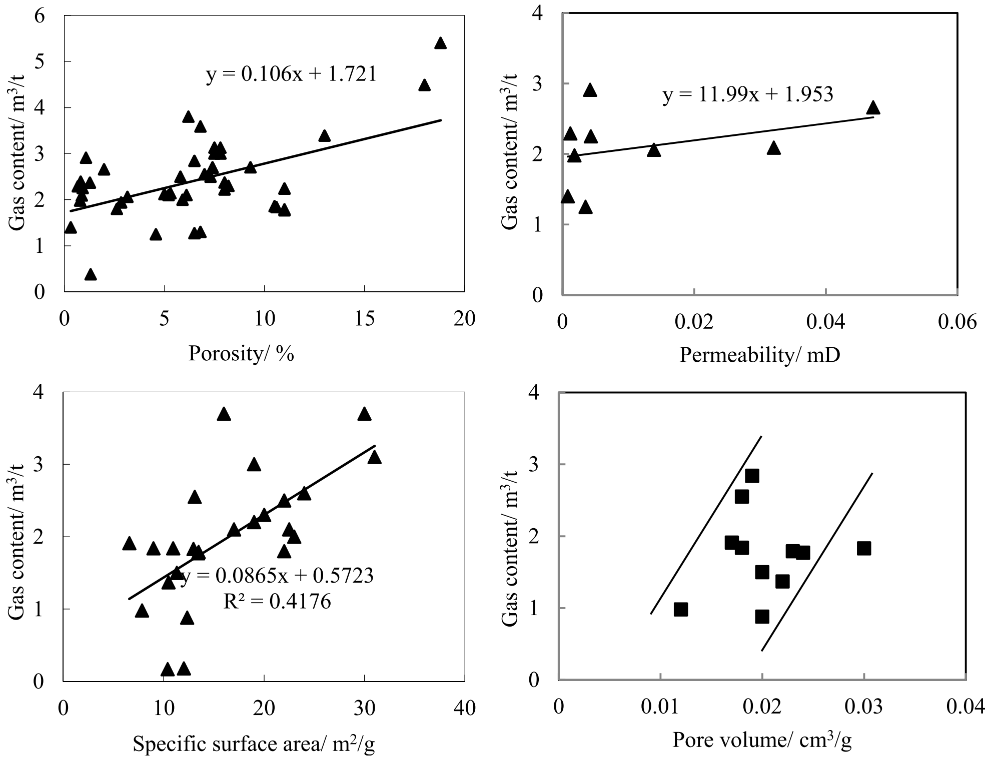

FIGURE 15
Relationships between gas content versus porosity (upper left), permeability (upper right), specific surface area (lower left) and pore volume (lower right).

5.2 Organic abundance and organic maturity

Influences of TOC and $R_{o,\ max}$ on gas content are both conducted as shown in Figure 13. As can be seen from the figure, TOC influences gas content in a linear mode with a fitting degree of about 0.4, and $R_{o,\ max}$ influences gas content linearly and positively, with a fitting degree of 0.7. TOC represents the palaeosedimentary environment and $R_{o,max}$ is an important index for coalification, both of which are related to gas source. Therefore, they two have strong relationships with gas content.

5.3 Organic maceral

As the sapropelic is a measure of organic maceral containing exinite, vitrinite, and inertinite, the sapropelic percentage is adopted here to fit with gas content as shown in Figure 14. The figure indicates that the gas content has a negative and linear relationship with sapropelic percentage, with a fitting degree of about 0.5. The sapropelic percentage is a measure of kerogen type, and type I is caused by a high sapropelic percentage, which is beneficial for oil generation but harmful for gas generation. Therefore, the sapropelic percentage has a negative relationship with gas content.

5.4 Mineral composition

Regarding to the mineral composition, the clay mineral is selected to fit with gas content as shown in Figure 14. The figure indicates that the gas content has a positive and linear relationship with clay mineral, with a fitting degree of about 0.4. There are many pores developed within clay minerals, which supports effective space for gas storage (Hill and Milburn, 1950; Aringhieri, 2004; Wang and Reed, 2009; Zou et al., 2020). Therefore, clay mineral has a positive relationship with gas content.

5.5 Pore system

Four parameters of porosity, permeability, specific surface area and pore volume are chosen to conduct fitting analyses versus gas content as shown in Figure 15. The figure indicates that porosity and permeability are both positively correlated with gas content, while the fitting degrees are quite low. The pore volume has a positive trend with gas content, and the specific surface area has a positively and strongly linear relationship with gas content, with a fitting degree of about 0.4. Gas is stored in the pores or is absorbed on the pore surface (Schafer, 1972; Zou M et al., 2010; Zou et al., 2018). Therefore, a bigger specific surface area can result in a higher gas content as shown in the figure. The other three parameters are all measures for the pore system, and they all have positive relationships and low fitting degrees with gas content.

6 Conclusion

In this paper, the Ziyun-Luodian area of southern Guizhou province in China is chosen as the research area, and the Dawuba formation in Carboniferous system is the target stratum. Core samples from wells of Z01, C01, and D01 and outcrop samples are all collected. Combined with laboratory experiments and mathematical analyses, geological evaluations on organic geochemistry, physical property of the reservoir, and gas bearing feature are all studied, and geological controls on gas occurrence are then analyzed. The following conclusions are achieved.

1) Sapropelic and hybrid types are the main organic types, while the humus type is less developed. TOC is generally in the range of 1%–3%, and the source rock in most of the research area is quite beneficial for the organic accumulation. $R_{o,max}$ ranges from 1.7% to 4.4%, with an average value of about 2.4%.

2) Mineral compositions of the Dawuba formation are mainly clay and quartz, with a few calcite and dolomite. The percentage of clay varies from 17.6% to 58.4%, with an average of 46.3%, and the percentage of quartz ranges from 21.7% to 53.0% with an average value of 37.6%.

3) Specific surface area ranges from 6.6 to 29.8 m^2/g, with an average value of 15.2 m^2/g, and the pore volume varies from 0.012 to 0.046 cm^3/g, with an average value of about 0.02 cm^3/g. There is a strongly and positively linear relationship between specific surface area and pore volume. Porosity ranges from 0.32% to 4.57% with an average value of about 1.8%, and the values are mostly in the range of 1%–3%. Permeability varies from 0.001 to 0.029 mD with an average value of about 0.004 mD, and most of the permeability is below 0.01 mD. There is an exponential and positive relationship between porosity and permeability.

4) The gas content is generally below 2.0 m^3/t, with extremely few values higher than 4 m^3/t. There are three obvious correlations for gas content versus buried depth ranges of 500–700 m, 700–1,000 m, and 2,700–3,000 m. TOC influences gas content linearly, and $R_{o,\ max}$ influences gas content positively. The sapropelic percentage and clay mineral are both fitted well with gas content. The gas content has a positive relationship with clay mineral and a negative relationship with sapropelic percentage. The porosity and permeability are both positively correlated with gas content. The pore volume has a positive trend with gas content, and the specific surface area has a positively and strongly linear relationship with gas content.

Data availability statement

The original contributions presented in the study are included in the article/Supplementary Material, further inquiries can be directed to the corresponding author.

Author contributions

KW: laboratory experiments and data analysis; NC: paper writing; JD: mathematical analysis; and SG and YL: sample collection.

Funding

The authors wish to acknowledge financial support of this study provided by the Geological survey project from Oil and Gas Resource Survey Center of China Geological Survey under Grant No. DD 20160178-02-05.

Conflict of interest

The authors declare that the research was conducted in the absence of any commercial or financial relationships that could be construed as a potential conflict of interest.

Publisher's note

References

Aringhieri, R. (2004). Nanoporosity characteristics of some natural clay minerals and soils. *Clays Clay Min.* 52 (6), 700–704. doi:10.1346/ccmn.2004.0520604

Bowker, K. A. (2007). Barnett shale gas production, fort worth basin: issues and discussion. *Am. Assoc. Pet. Geol. Bull.* 91 (4), 523–533. doi:10.1306/06190606018

Chen, S., Zhu, Y., Wang, H., Liu, H., Wei, W., and Fang, J. (2011). Shale gas reservoir characterisation: a typical case in the southern Sichuan basin of China. *Energy* 36 (11), 6609–6616. doi:10.1016/j.energy.2011.09.001

Curtis, J. B. (2002). Fractured shale gas systems. *AAPG Bull.* 86 (11), 1921–1938. doi:10.1306/61EEDDBE-173E-11D7-8645000102C1865D

Dow, W. G. (1977). Kerogen studies and geological interpretations. *J. Geochem. Explor.* 7, 79–99. doi:10.1016/0375-6742(77)90078-4

Hill, H. J., and Milburn, J. D. (1950). Effect of clay and water salinity on electrochemical behavior of reservoir rocks. *Trans. AIME* 207, 65–72. doi:10.2118/532-g

Huang, J., Zou, C., Li, J., Dong, D., Wang, S., Wang, S., et al. (2012). Shale gas generation and potential of the lower cambrian qiongzhusi formation in the southern Sichuan basin, China. *Petroleum Explor. Dev.* 39 (1), 75–81. doi:10.1016/s1876-3804(12)60017-2

Jarvie, D. M., Hill, R. J., Ruble, T. E., and Pollastro, R. M. (2007). Unconventional shale-gas systems: the Mississippian Barnett shale of north-central Texas as one model for thermogenic shale-gas assessment. *Am. Assoc. Pet. Geol. Bull.* 91 (1), 475–499. doi:10.1306/12190606068

Li, X., Hu, S., and Cheng, K. (2007). Suggestions from the development of fractured shale gas in North America. *Pet. explor. dev+.* 34 (4), 392–400. doi:10.1242/dev.01970

Loucks, R. G., Reed, R. M., Ruppel, S. C., and Hammes, U. (2012). Spectrum of pore types and networks in mudrocks and a descriptive classification for matrix-related mudrock pores. *Am. Assoc. Pet. Geol. Bull.* 96 (6), 1071–1098. doi:10.1306/08171111061

Ma, Y., Cai, X., and Zhao, P. (2018). China's shale gas exploration and development: understanding and practice. *Petroleum Explor. Dev.* 45 (4), 589–603. doi:10.1016/s1876-3804(18)30065-x

Martineau, D. F. (2007). History of the Newark East field and the Barnett shale as a gas reservoir. *Am. Assoc. Pet. Geol. Bull.* 91 (4), 399–403. doi:10.1306/intro910407

Martini, A. M., Walter, L. M., Ku, T. C., Budai, J. M., McIntosh, J. C., and Schoell, M. (2003). Microbial production and modification of gases in sedimentary basins: a geochemical case study from a devonian shale gas play, Michigan basin. *Am. Assoc. Pet. Geol. Bull.* 87 (8), 1355–1375. doi:10.1306/031903200184

Meng, J., Pan, R., Chen, H., and Tang, X. (2016). Shale gas accumulation condition and resource potential analysis of Devonian in Dian-Qian-Gui Basin. *Geoscience* 30 (1), 181–191. (in Chinese with an English abstract). doi:10.3969/j.issn.1000-8527.2016.01.020

Qi, Y., Ju, Y., Cai, J., Gao, Y., Zhu, H., Hunag, C., et al. (2019). The effects of solvent extraction on nanoporosity of marine-continental coal and mudstone. *Fuel* 235, 72–84. doi:10.1016/j.fuel.2018.07.083

Qi, Y., Ju, Y., Yu, K., Meng, S., and Qiao, P. (2022). The effect of grain size, porosity and mineralogy on the compressive strength of tight sandstones: a case study from the eastern ordos basin, China. *J. Pet. Sci. Eng.* 208, 109461. doi:10.1016/j.petrol.2021.109461

Ross, D. J. K., and Bustin, R. M. (2009). The importance of shale composition and pore structure upon gas storage potential of shale gas reservoirs. *Mar. Pet. Geol.* 26 (6), 916–927. doi:10.1016/j.marpetgeo.2008.06.004

Schafer, H. N. S. (1972). Factors affecting the equilibrium moisture contents of low-rank coals. *Fuel* 51, 4–9. doi:10.1016/0016-2361(72)90029-4

Schmoker, J. W. (1980). Organic content of Devonian shale in Western Appalachian basin. *AAPG Bull.* 64, 2156–2165.

Tissot, B. P., and Welte, D. H. (1978). *Petroleum formation and distribution- a new oil and gas exploration way*. Berlin: Organic Geochemistry Press.

Wang, F. P., and Reed, R. M. (2009). "Pore networks and fluid flow in gas shales," in Paper SPE 124253, presented at SPE Annual Technical Conference and Exhibition, New Orleans, Louisiana, America, October 4–7, 2009.

Wang, P., Chen, Z., He, X., Dong, L., Xu, Z., Ma, L., et al. (2012). Shale gas accumulation conditions and play evaluation of the Devonian in Guizhong Depression. *Oil Gas. Geol.* 33 (3), 353–363. (in Chinese with an English abstract). doi:10.11743/ogg20120304

Yang, F., Ning, Z., and Liu, H. (2014). Fractal characteristics of shales from a shale gas reservoir in the Sichuan Basin, China. *Fuel* 115, 378–384. doi:10.1016/j.fuel.2013.07.040

Zou, C., Dong, D., Wang, S., Li, J., Li, X., Wang, Y., et al. (2010). Geological characteristics and resource potential of shale gas in China. *Petroleum Explor. Dev.* 37 (6), 641–653. doi:10.1016/s1876-3804(11)60001-3

Zou, M., Wei, C., Huang, Z., and Wei, S. (2015a). Porosity type analysis and permeability model for micro-trans-pores, meso-macro-pores and cleats of coal samples. *J. Nat. Gas. Sci. Eng.* 27, 776–784. doi:10.1016/j.jngse.2015.09.025

Zou, M., Wei, C., Yu, H., and Song, L. (2015b). Modeling and application of coalbed methane recovery performance based on a triple porosity/dual permeability model. *J. Nat. Gas. Sci. Eng.* 22, 679–688. doi:10.1016/j.jngse.2015.01.019

Zou, M., Wei, S., Huang, Z., Lv, X., and Guo, B. (2018). Simulations on recoverability performances for a coalbed methane field in SE edge of Ordos basin, China. *Fuel* 233, 354–360. doi:10.1016/j.fuel.2018.06.071

Zou, M., Liu, Y., Huang, Z., Zhang, M., and Zhang, P. (2020). Geological control of irreducible water within the coal matrix and its quantified evaluation model. *ACS Omega* 5, 9540–9549. doi:10.1021/acsomega.0c00782

Zou, M., Wei, C., Pan, H., Sesay, K. S., and Cao, J. (2010). Productivity of coalbed methane wells in southern of Qinshui Basin. *Min. Sci. Technol.* 20, 0765–0777. doi:10.1016/s1674-5264(09)60278-7

frontiers | Frontiers in Earth Science

TYPE Original Research
PUBLISHED 12 September 2022
DOI 10.3389/feart.2022.999979

Migration law of different top coal thicknesses in top coal caving

Hua Nan[1,2] and Shuai Wang[1]*

[1]School of Energy Science and Engineering, Henan Polytechnic University, Jiaozuo, Henan, China,
[2]Hami Yu Xin Energy Industry Research Institute, Hami, Xinjiang, China

OPEN ACCESS

EDITED BY
Junjian Zhang,
Shandong University of Science and Technology, China

REVIEWED BY
Xuelong Li,
Shandong University of Science and Technology, China
Yuliang Zhou,
China University of Mining and Technology, China

*CORRESPONDENCE
Shuai Wang,
ws15036512947@163.com

SPECIALTY SECTION
This article was submitted to Economic Geology,
a section of the journal
Frontiers in Earth Science

RECEIVED 21 July 2022
ACCEPTED 08 August 2022
PUBLISHED 12 September 2022

CITATION
Nan H and Wang S (2022), Migration law of different top coal thicknesses in top coal caving.
Front. Earth Sci. 10:999979.
doi: 10.3389/feart.2022.999979

Top coal caving has become one of the main mining methods for thick and extrathick coal seams. Because of coal seam conditions, the top coal thickness is not constant. It is necessary to study the influence of top coal thickness changes on the top-coal-caving mining process. To explore the migration law of top coal failure, the experimental means of similar simulation experiment, numerical simulation experiment and field monitoring data were used. Through a similar simulation test of three different top coal thicknesses, the change rule of top coal migration was analyzed. Moreover, the stress and displacement changes of a 14 m coal seam over a thick top coal caving face were monitored and analyzed comprehensively with the simulation results. The results show that when the top coal thickness is unchanged, the top coal vertical displacement in the upper part is larger than that in the middle part due to the top plate rotation in front of the working face, and the stress change follows an opposite trend. The simulation results were the same as the field test results. When the top coal thickness is changed, whether it is upper top coal or middle top coal, the top coal displacement and stress changes will increase. The top coal migration will be more obvious, and thus the crushing will be more serious.

KEYWORDS

top coal caving, migration, stress, displacement, top coal thickness, similar simulation test, field test

1 Introduction

Coal has always been a solid backing for the steady and rapid development of China's economy. China's annual coal consumption has reached approximately 70%. Therefore, coal has made important contributions to China's economic development (Si et al., 2015; Wang et al., 2018; Liu et al., 2019). With the adjustment of the national energy structure, it is estimated that by 2050, the consumption ratio of coal as a one-time energy source will not be lower than 50%. In the past two decades, China's coal industry has developed rapidly. Moreover, thick coal seams are the main coal seams for high yield and high efficiency in China's coal industry. In China, thick coal seams are commonly found in Shanxi, Xinjiang, and Inner Mongolia. With the rapid application of mechanized mining techniques, thick coal seam mining currently mainly relies on top coal caving. However, thick coal seams tend to induce wide-reaching strata movements, complex stress distributions, and intensive strata behaviors in working faces because of their high efficiencies and rich production during the mining process. This is particularly true when coal seams are covered by overlying thick coal seams during mining. The long breakages, long weighting steps, and their far-reaching effects intensify the strata behaviors in working faces (Yu et al., 2020a; Yu et al., 2020b). Production practices have resulted in frequent strong strata behaviors of working faces after thick coal seam mining (Tan et al., 2010; Zheng et al., 2015; Zhang et al., 2016; Bai et al., 2017; Lan et al., 2018; Liu et al., 2020).

Research on fully mechanized coal mining technology mainly focuses on France, the Soviet Union, Russia and other countries. Around the late 1940s and early 1950s, some countries represented by France gradually adopted caving coal mining methods. However, due to the influences of both social and technological factors, some European countries represented by France did not use this method and achieved good technical and economic results (Liu, 2018). In the 1970s, the Soviet Union conducted the mechanized mining of a large-dip-angle coal seam and developed mining applications for large dip angles and all kinds of steep-seam fully mechanized stents and coal winning machines, and on the basis of an especially large angle 45° above the coal seam mining process, basically laid the foundation of science and technology in the mining of deeply inclined coal seams (Schgal and Coalfields Kumar, 1992; Bondarenko et al., 1993). A. Vakili et al. and B. Unver. also conducted relevant studies (Unver and Yasitli, 2006; Habib and Brett, 2010; Vakili and Hebblewhite, 2010; Mahdi and Charlie, 2012). Similarly, China has made many top coal mining research achievements. Other researchers have also studied in this field in different ways (S Bai and H Tu, 2020; Zhou et al., 2022; Zhang et al., 2020; Zhang and Zhang, 2019; Xie and Zhou, 2008) · In general, the research and application of thick coal seam mining technology in China is at the world's leading level.

According to China Coal seam thickness classification standard, coal seam thickness more than 8 m is called extra thick coal seam. Thick coal seam mining methods in China mainly include layered mining, full mining, and top coal mining (Xia et al., 2017; Duan et al., 2018; Szurgacz and Brodny, 2018; Zou and Lin, 2018; Lv et al., 2019; Zhai et al., 2019). In China, top coal mining technology has been extensively promoted due to its wide adaptability, and it has become one of the main thick coal seam mining methods in China. The basic principle of the caving mining method is to arrange a long wall working face with a normal mining height along the bottom of a thick coal seam (or section) at the beginning of the mining process. Conventional mining methods are used to stope the working face. By means of the action of mine pressure (top coal forms many penetrating fractures in the range of the leading stress peak area, and roof rotation simultaneously accelerates top coal crushing) and the mechanical characteristics of the coal and rock mass, the top coal above the support is broken and dispersed. It is then released from the coal discharge port behind (or above) the support and finally transported out of the working surface by a scraper conveyor. According to the working face layout, top coal mining is divided into one-time full-thickness caving coal mining, premining top-layered caving coal mining, multilayer top coal mining, and steeply inclined horizontal-section caving coal mining (Ma et al., 2016; Guo et al., 2017; Wu, 2017; Zhu, 2017; Wang, 2018). The success of the fully mechanized thick coal seam caving method is positively correlated to top coal fracturing. During fully mechanized thick coal seam caving mining, a series of mining processes, such as the stressing, deformation, migration, and crushing of top coal, have certain specialties (Wang, 2006; Mao and Yao, 2010; Huang et al., 2015; Li, 2015; Jiang et al., 2016; Wang, 2016; Li et al., 2021b). There are many factors affecting top coal movement, and the most important is geological conditions. The geological conditions mainly include the coal seam strength, pinch condition, development and distribution of geologically weak surfaces (fractures, joints, etc.), top coal thickness, mining depth, and roof lithology. We can see from initial research results that the largest factor affecting top coal output is the unique structure that it produces during the entire extrathick coal seam caving process. Therefore, top coal quality is also the result of a combination of factors (Nan et al., 2005; Wang, 2008; Nan et al., 2010; Li, 2013; Feng, 2014; Wang et al., 2015; Zhong, 2015; Ma, 2016; Cheng et al., 2017; Kong et al., 2018; Wang et al., 2019; Li et al., 2021a). However, researchers have studied the relationships between different coal seam heights and roof collapse displacement and working face coal wall distance by means of field measurements and similar simulations, etc., and obtained the top coal starting point location and top coal migration law in the front and rear of fully mechanized caving working faces (Meng et al., 2003; Zhai et al., 2009; Qian et al., 2010; Yang et al., 2011; Zhu and Yan, 2011; Liu et al., 2022).

But in the process of coal seam mining, the change of coal seam is irregular, and the thickness of top coal changes with the irregular change of coal seam, which has a very important influence on the migration law and stress change characteristics of top coal in working face. Therefore, based on this problem, in this paper, using the experimental means of similar simulation experiment, numerical simulation experiment and field monitoring data, the caving and crushing characteristics and migration law of top coal in the mining stage are systematically analyzed and studied. The mechanism of top coal crushing is revealed and the influence law of sudden change of coal thickness on top coal migration and stress in the process of super thick fully mechanized caving mining is clarified. It is of great scientific significance and application value to provide theoretical support for the

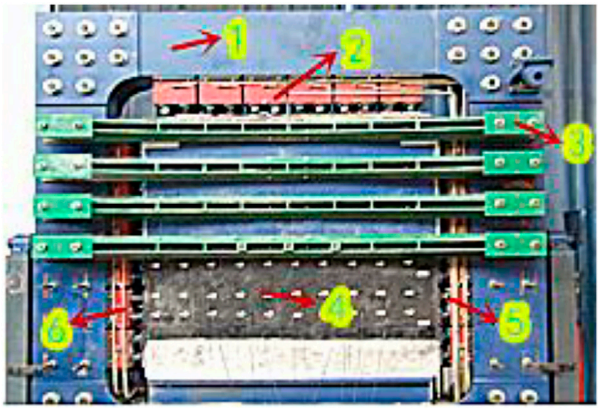

FIGURE 1
Similar simulation test model.

successful application of fully mechanized extrathick coal seam caving mining technology.

2 Similar simulation test of top coal with different thicknesses

This study takes 21121 fully mechanized caving face of Qianqiu Coal Mine in Yima Coal Industry as the background. 21121 face strike length 1386–1442 m; Inclination length 132 m; Coal seam inclination 13o55’; The thickness of coal seam is 12.55–17.16 m, with an average thickness of 13.81 m. The working face adopts comprehensive mechanized caving mining, and the cutting height of the shearer is 3.2 m.

2.1 Parameter acquisition of the model

After sample analysis and research, the corresponding conclusions are drawn: the immediate roof is composed of dark gray–black dense mudstone interbedded with very thin and fine sandstone and siltstone; the basic tops are composed of Middle Jurassic variously layered conglomerate, sandstone and siltstone. The bottom plate is composed of conglomerate. Therefore, the objects of this experiment are siltstone, mudstone, coal seam, conglomerate and sand-bearing conglomerate.

2.1.1 Density

Density refers to the mass in a unit volume of matter, which is calculated according to formula 1 (Ma, 2016):

$$\rho = \frac{M}{V} \tag{1}$$

ρ -- density of sample, kg/m^3;

M -- quality of sample, kg;

V -- volume of sample, m^3.

2.1.2 Compressive strength

Compressive strength refers to the maximum compressive stress per unit area of a material under the condition of no lateral constraints. It is calculated according to formula 2 (Yang et al., 2011):

$$\sigma_c = \frac{P}{A} \tag{2}$$

σ_c -- compressive strength of a specimen, MPa;

P -- force on the specimen when it is damaged, KN;

A -- cross-sectional area of the specimen, m^2.

The compressive strength, Young’s modulus and Poisson’s ratio mechanical parameters of the samples can be obtained by sorting and averaging the data obtained in the experiment.

Through formulas 3, 4 (Yang et al., 2011), the bulk modulus K and shear modulus G of a specimen can be obtained from the Young’s modulus E and Poisson’s ratio v of the specimen.

$$K = \frac{E}{3(1-2v)} \tag{3}$$

$$G = \frac{E}{2(1+v)} \tag{4}$$

2.1.3 Tensile strength

Tensile strength is the maximum stress that a sample can bear before it breaks. The tensile strength is measured by the splitting method in this experiment and calculated according to formula 5 (Ma, 2016):

$$\sigma_t = \frac{2P}{\pi dt} \tag{5}$$

σ_t -- tensile strength of a specimen, MPa;

P -- force on the specimen when it is damaged, KN;

d -- height of cubic specimen, m;

t -- width of cubic specimen, m.

2.1.4 Shear strength

Shear strength refers to the ratio of shear force and shear section area when a specimen is subjected to shear force on a shear plane under the condition of normal stress. The indexes used to measure the shear strength are the internal friction angle and cohesion force. The calculation formulas are shown in formulas 6 and 7 (Yang et al., 2011).

$$\sigma = \frac{P}{F} \times \cos\alpha \tag{6}$$

$$\tau = \frac{P}{F} \times \sin\alpha \tag{7}$$

σ -- average normal stress on the shear section of a specimen, MPa;

τ -- average shear stress on the shear section of the specimen, MPa;

TABLE 1 Comparison list of entity and model parameters.

	Prototype	Model
Physical range	The working face direction is 48 m, the middle mining is 42 m (more than 3 m at both ends), the working face length is 12 m, and the vertical direction is 48 m	Considering the boundary effect, the simulated mining range is 100–1500 mm
Load	Vertical 18 MPa, direction 16 MPa, working face direction 13 MPa (considering the prototype coal body impact tendency, the value is slightly smaller than the field test value)	Vertical 0.6 MPa, 0.5 MPa, working face direction 0.4 MPa (considering the influence of the dead weight of the model, the actual vertical hydraulic load of the model is 0.58 MPa, and the working face direction is 0.4 MPa)
Time	(42/3.6)×24=280 h	280/5.5 = 50.9 h

TABLE 2 List of parameters selected for the different frame simulation tests.

Rock	Layer	Lithologic thickness (m)	Compressive strength (MPa)	Model thickness (cm)	Model compressive strength (MPa)	Material similarity ratio (sand: cement: gypsum)
The first frame simulation test						
Main roof	Siltstone	4.1	83.9	13.6	2.8	6:3:7
Immediate roof	Mudstone	25.5	39.6	85	1.32	9:3:7
Coal seam	Coal seam	11.8	11.2	39.4	0.37	3:3($CaCO_3$):8
Floor	Conglomerate	1.9	52.1	6.3	1.74	8:5:5
Floor	Sand conglomerate	4.7	65.7	15.7	2.19	7:3:7
The second frame simulation test						
Main roof	Siltstone	2.1	83.9	7	2.8	6:3:7
Immediate roof	Mudstone	25.5	39.6	85	1.32	9:3:7
Coal seam	Coal seam	13.8	11.2	46	0.37	3:3($CaCO_3$):8
Floor	Conglomerate	1.9	52.1	6.3	1.74	8:5:5
Floor	Sand conglomerate	4.7	65.7	15.7	2.19	7:3:7
The third frame simulation test						
Main roof	Siltstone	0.1	83.9	0.4	2.8	6:3:7
Immediate roof	Mudstone	25.5	39.6	85	1.32	9:3:7
Coal seam	Coal seam	15.8	11.2	52.6	0.37	3:3($CaCO_3$):8
Floor	Conglomerate	1.9	52.1	6.3	1.74	8:5:5
Floor	Sand conglomerate	4.7	65.7	15.7	2.19	7:3:7

P -- force on the specimen during failure, KN;
F -- shear plane area, m^2;
α -- angle of shear fixture.

2.2 Similar simulation test

A total of three simulation tests were performed for comparative study. The second one took the original condition of the caving coal face as the simulation condition. The coal thickness of the first aircraft decreased from 2 to 11.8 m, and the other parameters were the same as those of the second aircraft. The coal thickness of the third aircraft increased by 2–15.8 m, and the other parameters were the same as those of the second aircraft.

The model block size was 160 x 160 x 40 cm^3. The loading system adopted a JSF300T-VIII2.5–31.5A2 high-precision static servo hydraulic console, which realized active loading on three

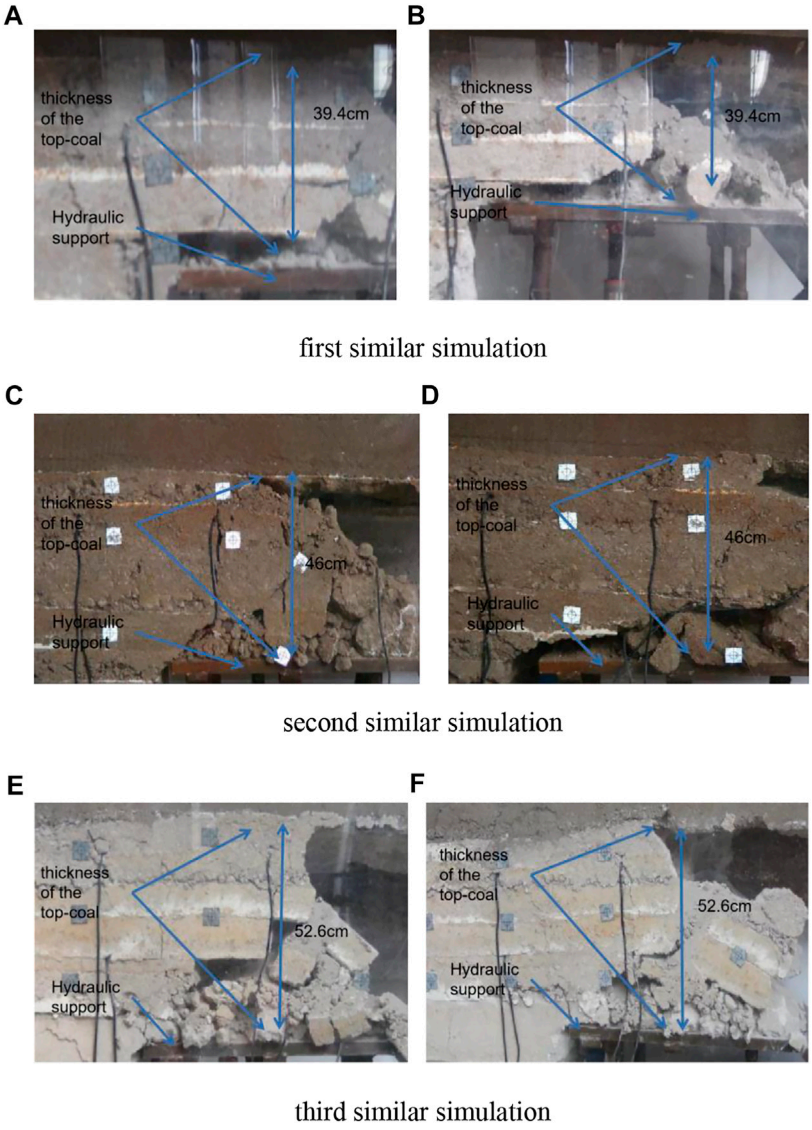

FIGURE 2
Different similar simulation diagrams of top coal migration and fragmentation. **(A,B)** respectively represent the crushing condition of top coal during and after stabilization of the first similar simulation excavation. **(C,D)** respectively represent the crushing condition of top coal during excavation and after stabilization of the second similar simulation. **(E,F)** respectively represent the crushing condition of top coal during and after stabilization of the third similar simulation excavation

sides above the left and right boundaries of the model. The maximum load concentration at the boundary of the model was 5 MPa. At both ends of the frame, the lateral center position was equipped with a plane rotating support shaft. The support shaft could flip the plane through the bearing seat fixed on the ground, which realized the simulation test of the inclination angle of different coal (rock) strata. The test instrument is shown in Figure 1. The basic structural elements of this section are (Figure 1): The framework of the mining engineering physical model test equipment (1), axial hydraulic jack (2), help plates (3), similar simulated strata (4), right-side hydraulic jack (5), and left-side hydraulic jack (6).

Similar simulation test design: River sand was used as the aggregate, and gypsum, calcium carbonate and cement were used as the cementing materials. The layered material was talcum powder. Frame contact with polyethylene friction material was made with oil to reduce friction.

Test calculation: During the test, similarity criteria, such as geometric similarity, bulk density similarity, strength similarity and time similarity, were strictly observed between the model and

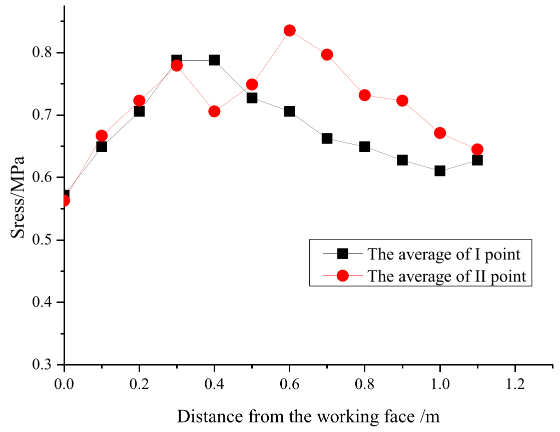

first similar simulation

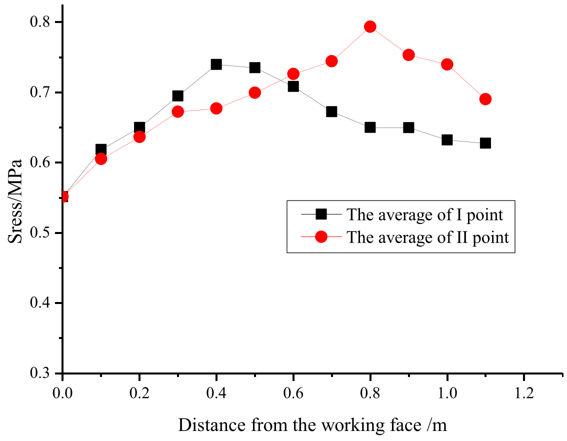

second similar simulation

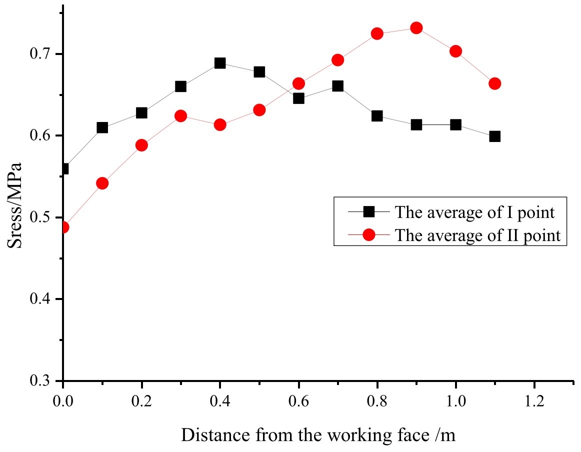

third similar simulation

FIGURE 3
Different similar simulation relationship between the mean stress and the distance from the working face.

prototype. Each similarity constant satisfied the following relationship:

$$C_\sigma = C_l + C_\gamma \tag{8}$$

$$C_t = \sqrt{C_l} \tag{9}$$

C_l -- geometric similarity constant;C_γ -- bulk density similarity constant; C_t -- time similarity constant;C_σ -- strength similarity constant;

Take the geometric similarity constant C_l =30. (If the geometric similarity constant is too large, the model thickness of top coal is too small, which will make it difficult to achieve the purpose of this simulation test. If it is too small, due to the limitation of the model frame size, it is difficult to measure the pressure, displacement and corresponding top coal crushing state of normal mining.) Coal seam bulk density similarity constant: C_γ =1.0, C_σ =30, C_σ =5.5. The parameters of the three similar simulation tests are shown in Tables 1, 2.

Arrangement of measurement points: A stress test method with an embedded pressure gauge was used. The pressure gauge was a dyb-1 miniature resistance strain soil pressure gauge with a specification of 1.0 MPa and an appearance of 7/35 H/Φ (mm); a Model YJZ digital static resistance strain gauge.

Arrangement of stress observation points: The model coal seam was directly buried, and group II was arranged. The group I distance model coal seam had a roof of 277 mm (the second frame was 310 mm; the third frame was 343 mm); group II was 60 mm away from the coal seam roof of the model (all three of them had the same value). Each group was evenly equipped with six pieces (and one piece for every 200 mm) along the 1000 mm length in the middle, with a total of 12 measuring points for each piece.

Displacement: The total station instrument was used to test the placement points. In the simulation test of similar materials, a gts-602a digital electronic total station instrument was used for observation with an observation accuracy of m<±0.1 mm.

3 Similar simulation results

3.1 Top coal migration and crushing results

The top coal migration and fragmentation in the mining processes of the three models are shown in Figure 2.

The top coal thickness in the first simulation test was 394 mm. Before the support was repeatedly raised and lowered, the thin upper top coal in the coal and rock joint was crushed more fully. Due to the stress state of the coal body and the forward movement of the support, the thin upper top coal of the support was crushed more fully. However, the top coal in the middle had a short beam structure. The brachiform short beam structure was destroyed after the support was raised and lowered repeatedly. Only the front half of the top beam of the support showed a brachiform short beam structure. After the destruction, large blocks of coal were neatly arranged. The top coal in the back half of the top beam of the support was completely broken and flowed toward the cover beam.

The top coal thickness in the second simulated test was 460 mm. Under the joint action of leading abutment pressure, roof rotation and support, the top coal under this condition was fully broken near the cover beam, and the roof presented a more regular collapse. In this test, it was more obvious that the thin upper top coal at the coal and rock junction was compressed in the range of 0.2–0.4 m in front of the working face to the coal wall of the working face.

The top coal thickness in the third simulated test was 526 mm. Under the joint action of leading abutment pressure, roof rotation and support, the top coal was broken near the shield beam under this condition, but the lumpiness was obviously higher than that of the second simulated test. In the range from 0.3 to 0.6 m in front of the working face to the coal wall of the working face, the thin upper top coal of the coal and rock joint showed the phenomenon of compaction, and the compaction of the top coal was thicker than that of the second frame. The initial collapse of the overburdened rock was more severe, and the pressure box was crushed instantly. Due to the large top coal thickness and insufficient top coal crushing, the broken top coal at the middle and lower parts and the top coal above the support experienced obvious separation, and there was a structural layer of the short top coal beam with good integrity at the end of the support.

In general, the top coal crushing degree in front of the working face gradually weakened from top to bottom, and the upper coal body above the support and near the top of the coal wall was dominated by a wedge crack at approximately 60° in the advancing direction of the working face. However, the middle and lower top coal was dominated by cracks at approximately 45° in the advancing direction of the working face. The top coal failure process of the extrathick coal seam under the action of abutment pressure mainly involved fracturing and shearing. The upper top coal failure mainly involved the formation of tiny cracks by abutment pressure and shear failure, and under the action of the roof rotation moment, the pushing direction of the working face was approximately 60° with respect to the wedge penetrating cracks formed due to tensile stress, which greatly increased the upper top coal crushing degree.

3.2 Pressure results

The pressure test results of the three comparative similar simulation tests are shown in Figure 3.

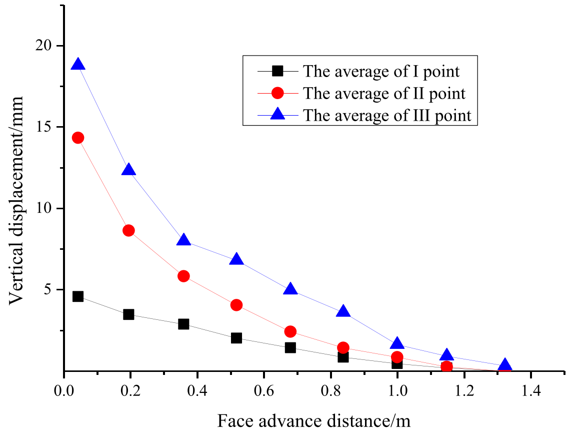

first similar simulation

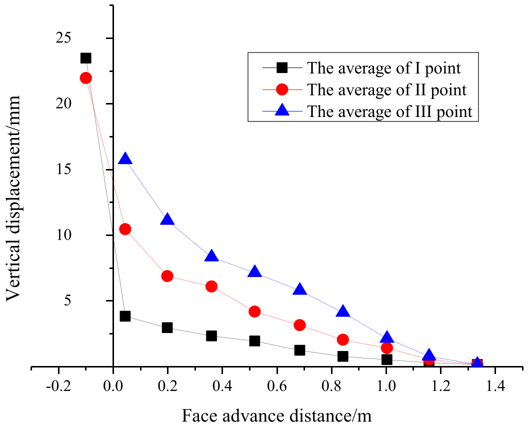

second similar simulation

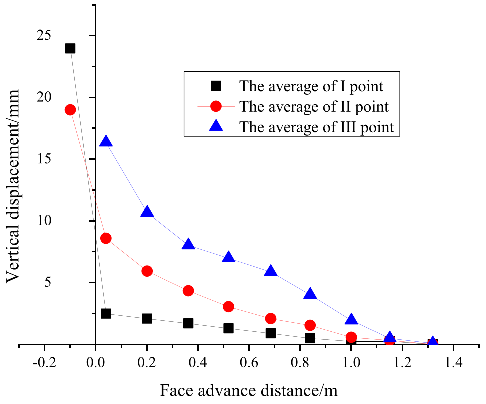

third similar simulation

FIGURE 4
Different similar simulation relationship between the mean vertical displacement and the face propulsion.

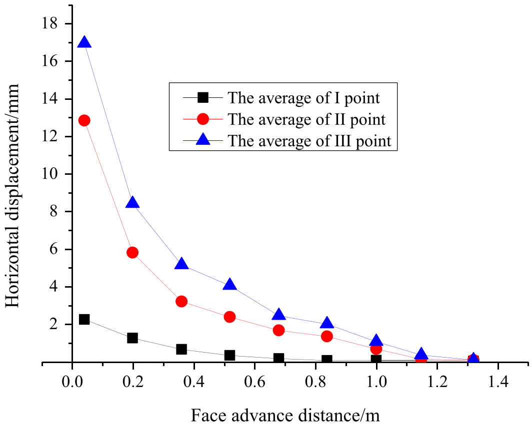

first similar simulation

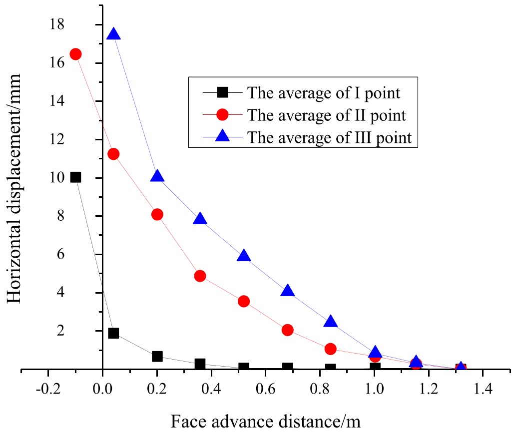

second similar simulation

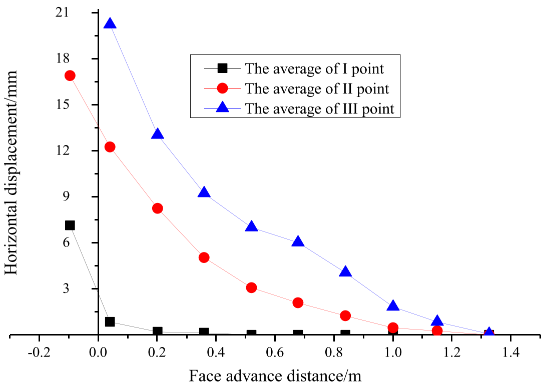

third similar simulation

FIGURE 5
Different similar simulation relationship between the mean of horizontal displacement and the face propulsion.

In the first similar simulation test (top coal thickness of 394 mm), the lower top coal (I observation line) reached a maximum abutment pressure of 0.80 MPa at 0.35 m away from the coal wall, and the upper top coal (II observation line) reached a maximum abutment pressure of 0.83 MPa at 0.60 m away from the coal wall.

In the second similar simulation test (top coal thickness of 460 mm), the lower top coal (I observation line) reached a maximum supporting pressure value of 0.74 MPa at 0.40 m away from the coal wall, and the upper top coal (II observation line) reached a maximum supporting pressure value of 0.78 MPa at 0.80 m away from the coal wall.

In the third similar simulation test (top coal thickness of 526 mm), the lower top coal (I observation line) reached a maximum abutment pressure of 0.69 MPa at 0.40 m away from the coal wall, and the upper top coal (II observation line) reached a maximum abutment pressure of 0.73 MPa at 0.90 m away from the coal wall.

With increasing top coal thickness, the extreme value of the leading supporting pressure decreases gradually, which is directly shown in the above three figures where the pressure distribution line becomes flat. The abutment pressure distribution in the top coal mining of extrathick coal seams has a great influence on the destruction of top coal. The larger the top coal thickness is, the smaller the overall coal breaking effect of the leading abutment pressure. This stress failure feature is the fundamental reason why the top coal crushing degree in the front of the coal face decreases with increasing height from the top plate.

3.3 Vertical displacement results

The vertical displacement test results of the three comparative of similar simulation tests are shown in Figure 4.

In the first similar simulation test (top coal thickness of 394 mm), the vertical displacement of the lower top coal (observation line I) was different from that of the middle top coal (observation line II) and the upper top coal (observation line III). The closer the top coal was to the roof, the greater the vertical displacement. Under 0.50 m away from the coal wall, the vertical displacement change trend was basically the same. Over 0.40 m away from the coal wall, the vertical displacement change trend of the lower top coal was obviously different from that of the middle and upper top coal. The vertical displacement increase rate of the lower top coal was not obviously different from that of the former, while the increase rates of the middle and upper top coal were obviously increased. At 0.10 m after mining, the measuring points were destroyed with the destruction of the top coal.

The vertical displacement of the lower top coal (observation line I) was different from that of the middle top coal (observation line II) and upper top coal (observation line III) in the second similar simulation test (top coal thickness of 460 mm). The closer the top coal was to the roof, the greater the vertical displacement. Under 0.40 m away from the coal wall, the vertical displacement change trend was basically the same. Over 0.20 m away from the coal wall, the vertical displacement of the lower top coal was obviously different from that of the middle and upper top coal. The vertical displacement increase rate of the lower top coal was not obviously different from that of the former, but the increase rates of the middle and upper top coal were obviously increased. At 0.10 m after the mining of the working face, the upper top coal measuring point was destroyed with the destruction of top coal. However, the vertical displacement of the lower top coal (23.1 mm) was higher than that of the middle top coal (21.5 mm), indicating that there was a slight separation between the middle and lower top coal.

The vertical displacement of the lower top coal (I observation line) was different from that of the middle top coal (II observation line) and upper top coal (III observation line) in the third similar simulation test (top coal thickness of 526 mm). The closer the top coal was to the roof, the greater the vertical displacement. Under 1.00 m away from the coal wall, the vertical displacement of the top coal was small, with a maximum value of only 1.5 mm. The vertical displacement change trend was basically consistent in the range of 1.00 m–0.40 m away from the coal wall. In the range of 0.20 m–0.04 m away from the coal wall, the vertical displacement of the lower top coal was obviously different from that of the middle and upper top coal. The vertical displacement increase rate of the lower top coal was not obviously different from that of the former, but the increase rates of the middle and upper top coal were obviously increased. At 0.10 m after the mining of the working face, the upper top coal measuring point was destroyed with the destruction of top coal. However, the vertical displacement of the lower top coal increased sharply to 23.6 mm, exceeding that of the middle top coal (the extreme value was 18.5 mm), indicating that there was stratification between the middle and lower top coal.

3.4 Horizontal displacement test results

The horizontal displacement test results of the three comparative similar simulation tests are shown in Figure 5.

In the first similar simulation test (top coal thickness of 394 mm), the horizontal displacement of the lower top coal (observation line I) was different from that of the middle top coal (observation line II) and the upper top coal (observation line III). The closer the top coal was to the roof, the larger the horizontal displacement. Under 0.40 m away from the coal wall, the vertical displacement change trend was basically the same. Over 0.20 m away from the coal wall, the horizontal displacement of the lower top coal was obviously different from that of the middle and upper top coal. The horizontal displacement increase rate of the lower top coal was small, that of the middle top coal was large, and that of the upper top coal was the largest. Near the coal wall line, the horizontal displacement of the lower top coal increased at a rate similar to that of the upper top coal. At 0.10 m after mining, the measuring points were destroyed with the destruction of the top coal.

The horizontal displacement of the lower top coal (I observation line) was different from that of the middle top coal (II observation line) and upper top coal (III observation line) in the second similar simulation test (top coal thickness of 460 mm). The closer the top coal was to the roof, the larger the horizontal displacement. In general, the vertical displacement of the lower top coal was obviously different from that of the middle and upper top coal. The horizontal displacement of the lower top coal did not change significantly outside 0.20 m in front of the coal wall (the maximum value was 0.5 mm, and the minimum value was -0.1 mm), while the horizontal displacements of the middle and upper top coal were relatively large and changed immediately within 0.80 m in front of the coal wall. At the point where the working face had been mined for nearly 0.10 m, the upper top coal measuring point was destroyed with the destruction of the top coal.

The horizontal displacement of the lower top coal (I observation line) was different from that of the middle top coal (II observation line) and upper top coal (III observation line) in the third similar simulation test (top coal thickness of 526 mm). The closer the top coal was to the roof, the larger the horizontal displacement. In general, the vertical displacement change trend of the lower top coal was obviously different from that of the middle and upper top coal. The horizontal displacement of the lower top coal had no obvious change outside 0.10 m in front of the coal wall (the maximum value was 0.5 mm, and the minimum value was -0.1 mm). However, the horizontal displacement of the top coal in the middle and upper parts was relatively large and changed at 0.90 m in front of the coal wall. At the point where the working face had been mined for nearly 0.10 m, the upper top coal measuring point was destroyed with the destruction of top coal.

4 Numerical simulation of extrathick top coal migration

4.1 Model establishment

Based on the hydrogeological conditions of the working face of the extrathick coal seam and the purpose of the numerical simulation, the rock strata were divided into five geological formations according to their basic properties and parameters, such as siltstone, mudstone, coal seam, conglomerate, and sand-bearing conglomerate. The volume of the numerical model was set at 280 × 216 × 270. The coal seam thicknesses were set at 12, 14, and 16 m. The immediate

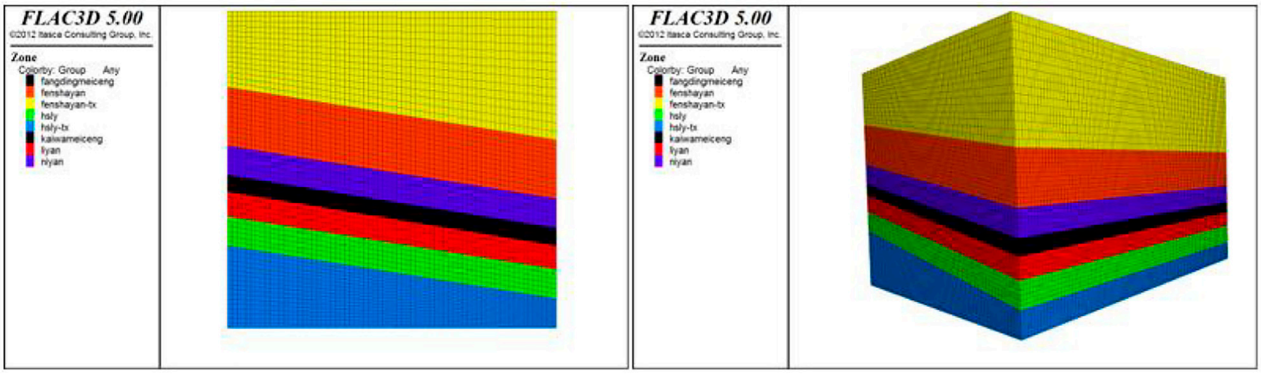

FIGURE 6
Fast-Lagrangian-analysis-of-continua (FLAC) model grid diagram.

TABLE 3 Coal and rock mechanics parameters.

Rock formation	Lithology	Density (g/cm3)	Bulk (GPa)	Shear (GPa)	Internal Friction angle (°)	Cohesion (MPa)	Tensile strength (MPa)
Main roof	Siltstone	2665	62.7	51.9	44.5	11.5	1.84
Immediate roof	Mudstone	2461	43.4	32.5	30	12	0.605
Coal seam	Coal seam	1380	5.3	2.2	32	1.25	0.15
Floor	Conglomerate	1860	38.3	17.7	37	16	1.24
Floor	Sand-bearing conglomerate	2580	33	25.2	39	4	1.54

roof thickness was set at 25 m. The basic roof thickness was set at 115 m, and the floor thickness was set at 70 m. The inclination direction of the working face was set in the Y direction, the strike direction was set in the X direction, the vertical direction of the coal seam was set in the Z direction, and the inclination angle of the coal seam was 14°. The model is shown in Figure 6.

The boundary of the numerical model in the x and y directions was given a horizontal constraint, and the boundary strike displacement was set to zero. The bottom boundary of the fixed model, given that the bottom boundary was vertical and the strike displacement was zero, and the lower part of the model Z direction was also given the same constraint. No constraints were imposed on the upper part of the model Z direction, but a certain force was applied, namely, the dead weight stress.

The physical and mechanical parameters of each coal rock layer in the simulation model are shown in Table 3.

4.2 Numerical simulation results analysis

To better monitor the extrathick top coal movement, 24 monitoring points were arranged to monitor and record the stress, horizontal displacement, and vertical displacement of the extrathick top coal with coal seam mining, as shown in Figure 7.

4.2.1 Top coal stress variation results analysis

In the process of fully mechanized caving mining, the advanced support pressure produced by stoping operation has a certain influence on the top coal release. Therefore, the variation characteristics of the advanced support pressure of the top coal with different layers in the mining process are simulated. To clarify the change rule of top coal advance support pressure in different strata and different directions, and lay the foundation for studying the influence of top coal breakage in different strata on pressure.

The propulsion distance of the working face and the stress of the upper top coal was obtained. A graph of the stress variation with the top coal in the middle is shown in Figure 8.

From Figure 8, it can see that the top coal stress in the upper part of the fully mechanized caving face of the thick coal seam was approximately 20.1 MPa, and the stress in the middle top coal at the same distance in front of the working face was basically the same, approximately 22.5 MPa. Under the influence of the leading support pressure, the stress change in front of the working face increased first and then decreased.

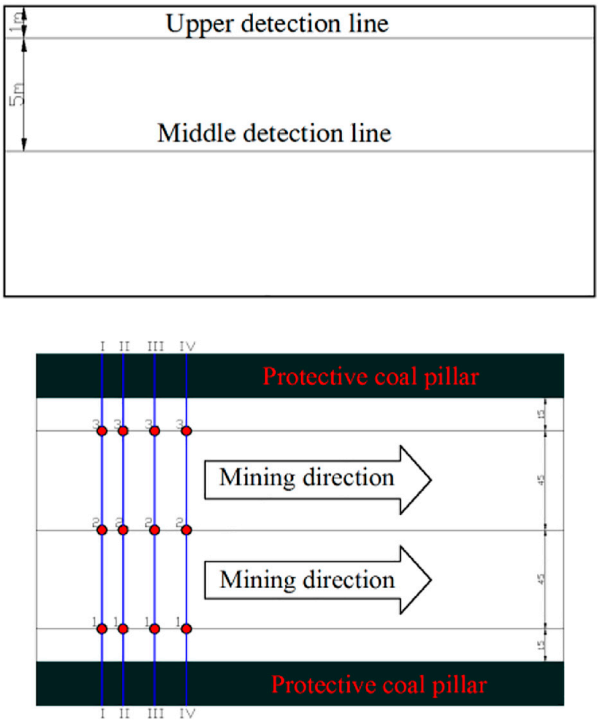

FIGURE 7
Schematic diagram of the monitoring point layout.

Therefore, the working face stress change curve reached a maximum value at the inflexion point in advance and then decreased. The stress in the middle top coal was basically the same at the same distance in front of the working face.

4.2.2 Top coal X-direction displacement results analysis

The stress changes of the upper top coal and the middle top coal in the X direction were recorded, as shown in Figure 9.

The top coal displacement in the front face of the fully mechanized caving face in the thick coal seam changed with the same amount of propulsion displacement from the working face, and monitoring point 2 was the most obvious. After analysis and judgment, the top coal in front of the working face undergoes migration and may even break. The top coal displacement is basically consistent with the working face displacement.

Comparing the X-direction displacement of the upper top coal and the middle top coal, we found that the displacements were different. When the distance from the working face was far, the displacement of the middle top coal was higher. With the advancement of the working face, the upper top coal displacement was gradually greater than that of the middle top coal. There were many cracks inside the coal seam. When the coal seam was not affected by mining, it was in the original equilibrium state. With the advancement of the working face, the cantilever top coal was gradually affected by the stress due to the friction between the top coal, the roof, and the upper top. The tensile force of the coal was greater than the tensile force of the middle top coal, which caused the top coal to migrate. When the middle top coal was closer to the working face, the strike displacement became negative, indicating that the middle coal seam changed from the previous three-direction compression to two-direction compression, which caused the middle coal seam to migrate and break.

4.2.3 Top coal Z-direction displacement results analysis

The stress changes of the upper top coal and the middle top coal in the Z direction were recorded, as shown in Figure 10.

The vertical displacement of the upper top coal in front of the fully mechanized caving face of the thick coal seam was basically the same as the advancing displacement of the working face. When the advancing distance of the working face increased, the increasing displacement rate of monitoring point 2 was continuous, and the increasing range also increased because the top coal collapsed due to damage. Moreover, the vertical displacement of the top coal in the front middle of the fully mechanized caving face of the thick coal seam was basically the same as the advancing displacement of the working face. It can be found that there were some differences between the upper top coal displacement and the middle top coal displacement. The vertical displacement of middle top coal was different from that of the upper top coal. The main reason for this was that the roof rotation caused the middle top coal to migrate; that is, the roof rotation was the main influencing factor of the middle top coal migration.

5 Comparative analysis of the numerical simulation for different top coal thicknesses

In the numerical simulation, comparative experimental analysis was also performed. Compared with the original model, the other two models had an increase or decrease in coal seam thickness by 2 m, i.e., the coal seam thickness was 16 m and 12 m, respectively. The other conditions remained unchanged.

5.1 Numerical simulation of the stress variation for the top coal in different top coal thicknesses

For the corresponding monitoring points of coal seams with different thicknesses, the maximum supporting pressure

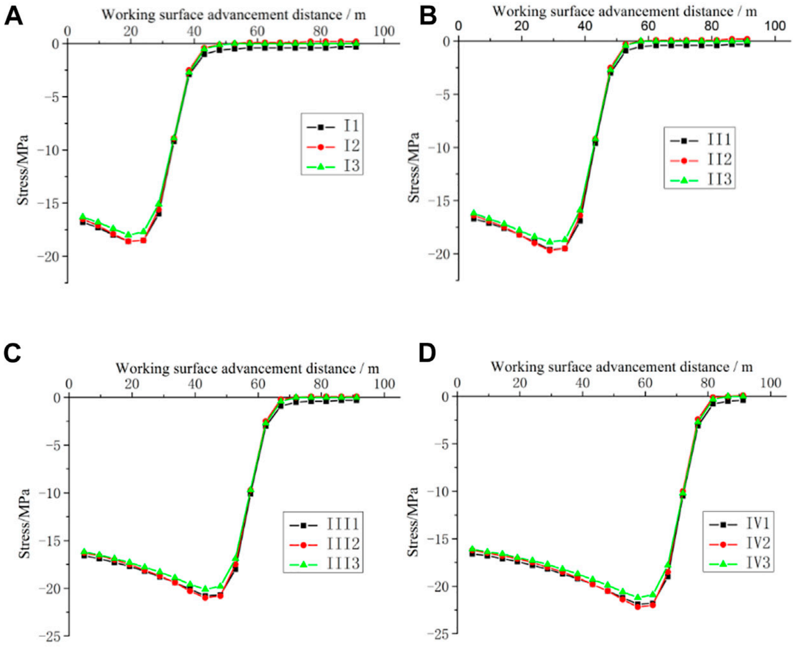

the upper top coal seams

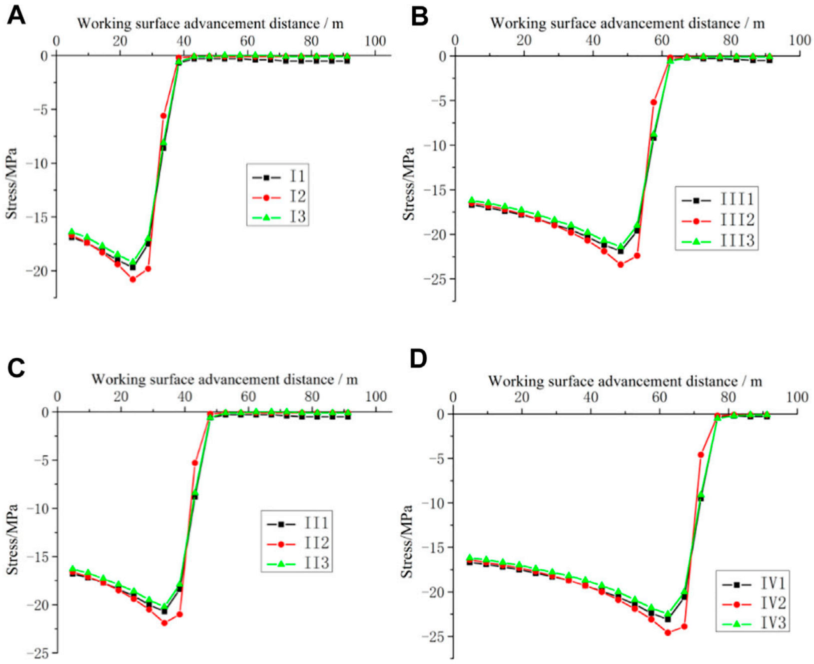

the middle of top coal seams

FIGURE 8
Stress change of monitoring points I, II, III, and IV. **(A–D)** represent the Top coal stress variation on the four detection lines I, II, III and IV.

of the thickened coal seam model in the numerical simulation was the smallest, and the maximum supporting pressure of the thinned coal seam model was the largest. From this, we can conclude that as the top coal thickness increased, the absolute value of the lead support pressure increased gradually. The stress trends of the three thicknesses were basically the same

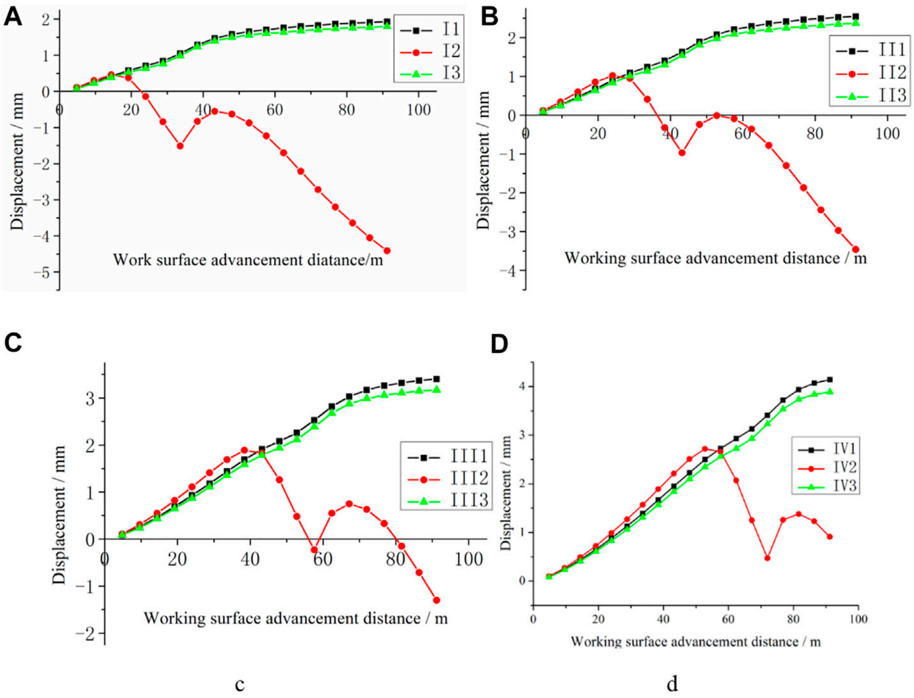

the upper top coal seams

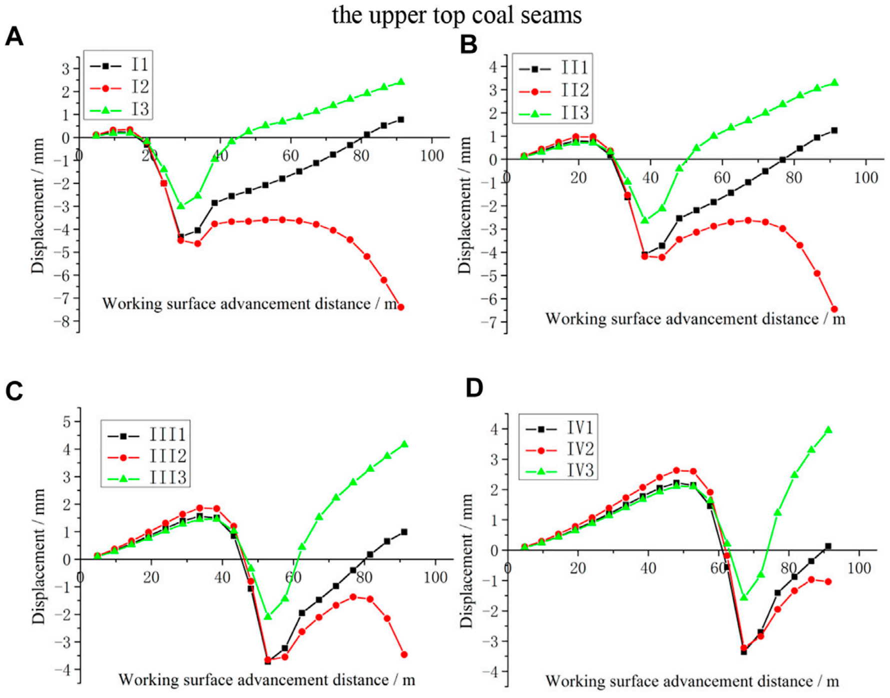

the middle of top coal seams

FIGURE 9
Displacement variation in the X direction of the monitoring points I, II, III, and IV. **(A–D)** represent the Top coal x-direction displacement on the four inspection lines I, II, III and IV, respectively

before the working surface advancement of 40 m, and the difference occurred after the propulsion distance was greater than 40 m. The change rate in the stress of the thickened coal seam increased relative to the initial coal seam, while the

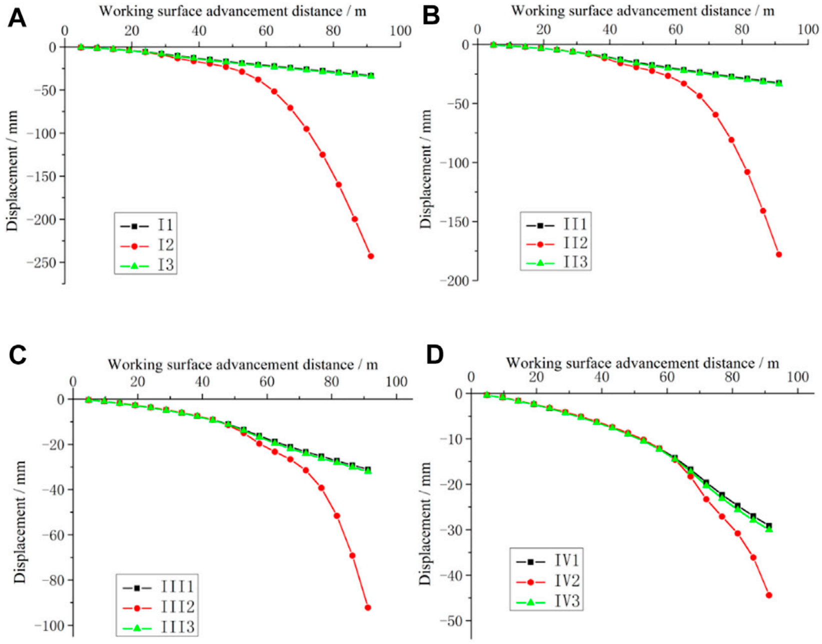

the upper top coal seams

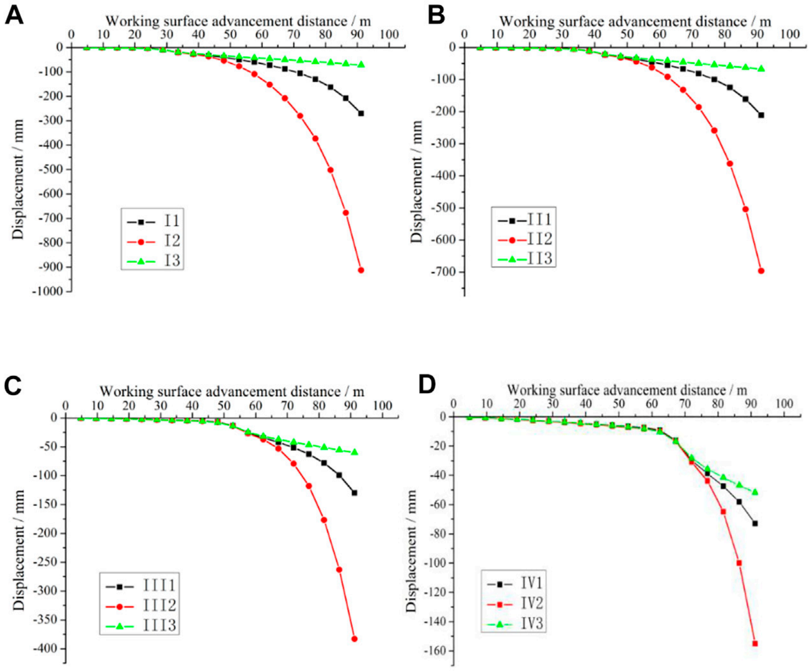

the middle of top coal seams

FIGURE 10
Displacement changes in the Z direction of the monitoring points I, II, III, and IV. **(A–D)** represent the Top coal z-direction displacement on the four inspection lines I, II, III and IV, respectively.

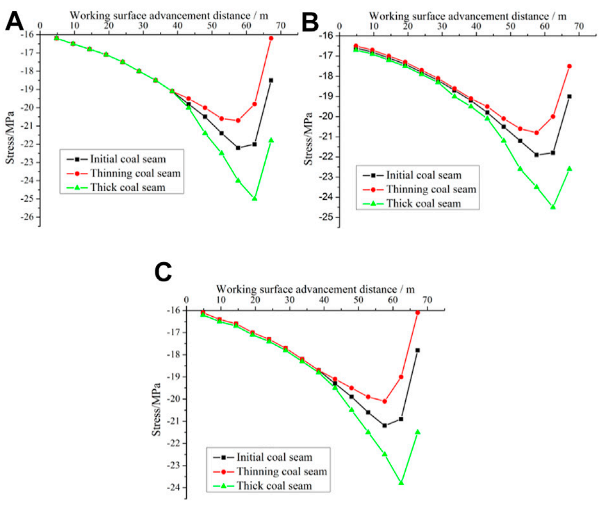

the upper top coal seams

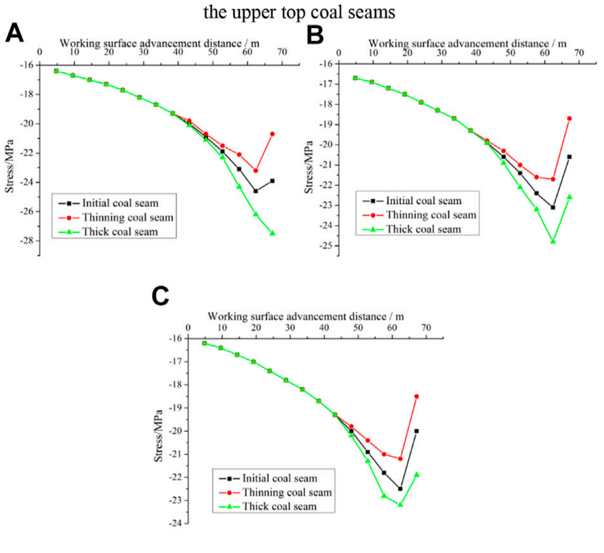

the middle of top coal seams

FIGURE 11
Stress change results of the IV1, IV2, and IV3 points of the middle coal. **(A–C)** respectively represent the Stress variation of top coal at different layers at monitoring points 1, 2 and 3 on No. IV detection line.

opposite was true for the thinned coal seam. The three layers of the coal seam stress had a maximum value and an inflection point at a propulsion distance of 50–60 m. The reason for this was that the stress in front of the working face formed a change in the leading support stress. As the working surface advanced, the stress of monitoring point IV gradually increased, reached an initial stress peak, and then gradually decreased to the initial stress. The results are shown in Figure 11.

5.2 Numerical simulation of the top coal displacement trends with different top coal thicknesses

For different coal thicknesses, the displacement of the upper top coal increased with the advancement of the working face, and the increasing rate was basically the same from 0 to 45 m. This change in the middle top coal was similar to that in the upper top coal. However, above 45 m, the thinner the coal seam thickness at the 1st monitoring point and the 3 monitoring points in the upper top coal was, the faster the displacement rate. For the monitoring point displacement, as the working face advanced, the larger the thickness of the coal seam was, and the earlier the displacement reduced, which indicated that the top coal was more affected by the tensile stress, making it more likely to migrate. The results of monitoring points 1, 2, and 3 in the middle top coal were different from those in the upper top coal. The middle top coal began to change after the working face was pushed for 40 m, and the result of the change was not only reduced but also increased in the opposite direction, and the increase rate was greater than the initial rate. This is because after the bottom coal seam was excavated, the upper part of the upper coal seam was suspended at the other end to form a simply supported beam structure. This mechanical action caused the middle top coal to move downward, and the simple supported beam structure caused the central coal seam to form an arch structure in the opposite direction. The results are shown in Figure 12.

5.3 Numerical simulation of the top coal vertical displacement results with different top coal thicknesses

For different coal thicknesses, whether it was the upper or middle top coal, the vertical displacement became increasingly larger as the working surface advanced. In the early stage of advancement, the vertical displacement increase rates for the three coal seams were similar. That is, as the coal seam thickness increased, the vertical displacement change rate gradually increased at the position corresponding to the monitoring point in front of the working surface. Moreover, the vertical displacement of the middle coal seam suddenly increased after the working face advanced 60 m, and the change rate suddenly increased. Because the coal seam of the middle top coal was excavated as the working surface advanced, the lower part of the middle top coal became a goaf, drastically changing the vertical displacement of the middle top coal. This trend also occurred for the vertical displacement of the upper coal seam but occurred later than for the middle coal seam. The results are shown in Figure 13.

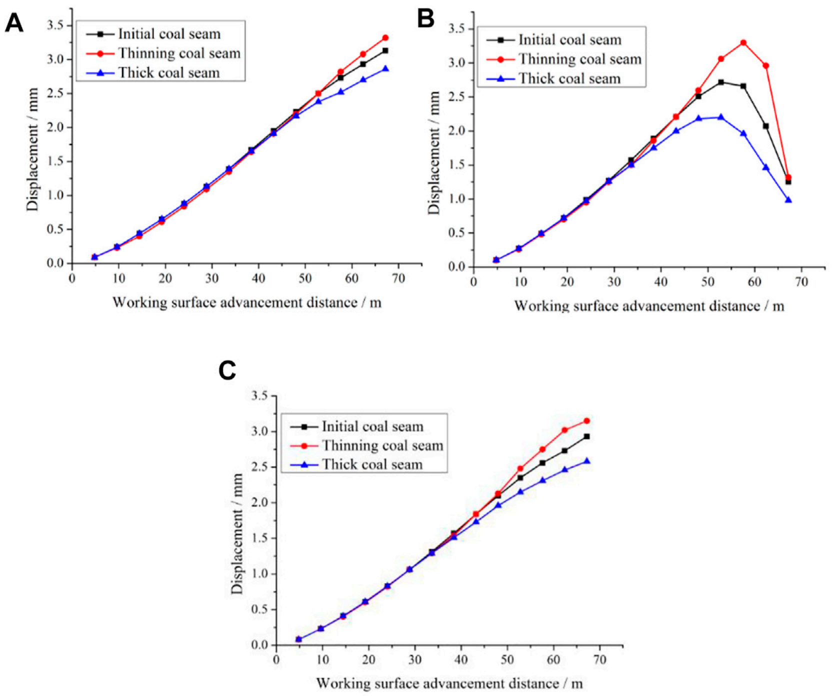

the upper top coal seams

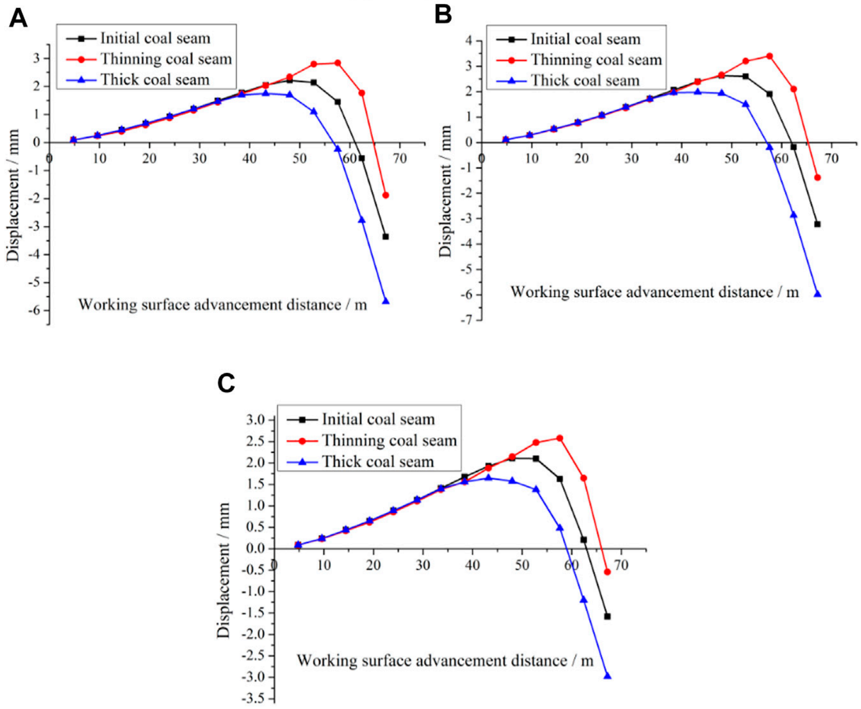

FIGURE 12
Comparison of the displacement for the IV1, IV2, and IV3 points. **(A–C)** represent the top coal displacement trends of different layers at monitoring points 1, 2 and 3 on test line IV, respectively

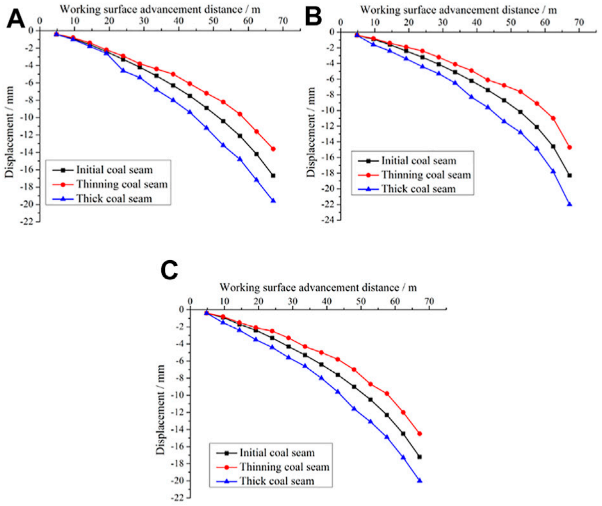

The upper top coal seams

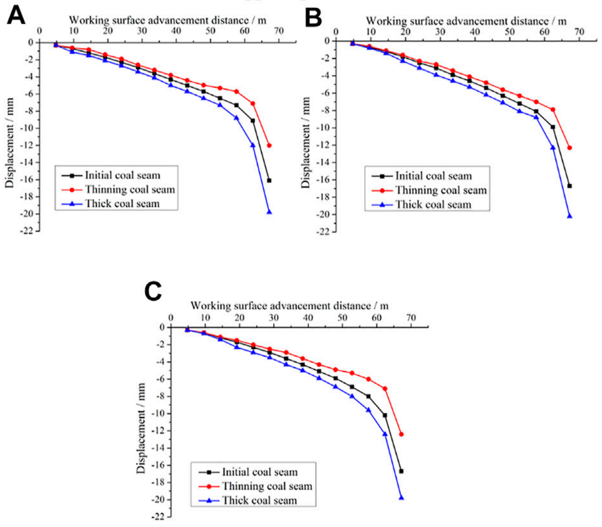

The middle of top coal seams

FIGURE 13
Comparison of the vertical displacement for the IV1, IV2, and IV3 points. **(A–C)** represent the top coal vertical displacement results of different layers of top coal at monitoring points 1, 2 and 3 on test line IV, respectively.

6 Field test

The field test mainly focused on the presupporting pressure monitoring of the full-height comprehensive mechanized top coal caving face system in the ultrathick coal seam, the deep coal point displacement observation of the top coal, and the roadway deformation observation and studied the extrathick top coal crushing and migration.

6.1 Test content, method, and device

6.1.1 Top coal stress field test

KBSII is a name for measuring borehole stress instruments. The top coal stress field test was observed using a KBSII-type borehole stress meter. Four observation lines were arranged from the bottom to the top of the working face and the gas discharge lane. Observation lines I and II had a depth of 25 m, and observation lines III and IV had a depth of 12 m. The observation lines were arranged with a spacing of 5 m. Figure 14 is schematic views showing the layout of the embedded KBS II-type borehole stress gauge.

6.1.2 Top coal displacement field test

The top coal displacement field test was observed by the deep base (drilling) hole base point tracking method, and the observation instrument was a self-designed deep-hole multipoint displacement meter. A schematic diagram of the deep base point arrangement is shown in Figure 15.

To facilitate the displacement and observation of the top coal in front of large-scale control work, three stations were arranged in the upper plane along the propulsion direction of the working plane, with one drill hole per station, and the parameters were all the same. Four anchored deep foundation points were installed in each borehole. The first base point was 0.7 m deep into the roof rock stratum of the coal seam. The second base point was located in the top coal 6 m above the top of the roadway. The third base point was located in the top coal 3 m above the top of the roadway. The fourth base point was located in the top coal 1 m above the top of the roadway, as shown in Figure 14. The deep base drilling parameters are shown that Hole depth is 28 m.Advancement direction angle is 135°. Elevation angle is 45°.Floor level to orifice height is 18 m.

6.2 Field test results

6.2.1 Stress results

To facilitate further analysis and research of the content reflected by the data, the interpolation curve method was used to obtain the relationship between the stress reading of each measuring point and the coal wall of the measuring point from the working face. The results are shown in Figure 16.

Figure 16 show that the frontal stress of the fully mechanized caving face for the extrathick coal seam was approximately 19.6 MPa, and the stress of the top coal pressure of the working face was approximately 90 m in front of the working face. It increased rapidly within 40–50 m, reaching a maximum value of approximately 26 MPa 10–40 m in front of the working surface, and the dynamic pressure coefficient of the working surface was approximately 1.3. Figure 17 indicates that the stress in the top coal at the same distance from the working face differed: the upper top coal stress was larger, and the

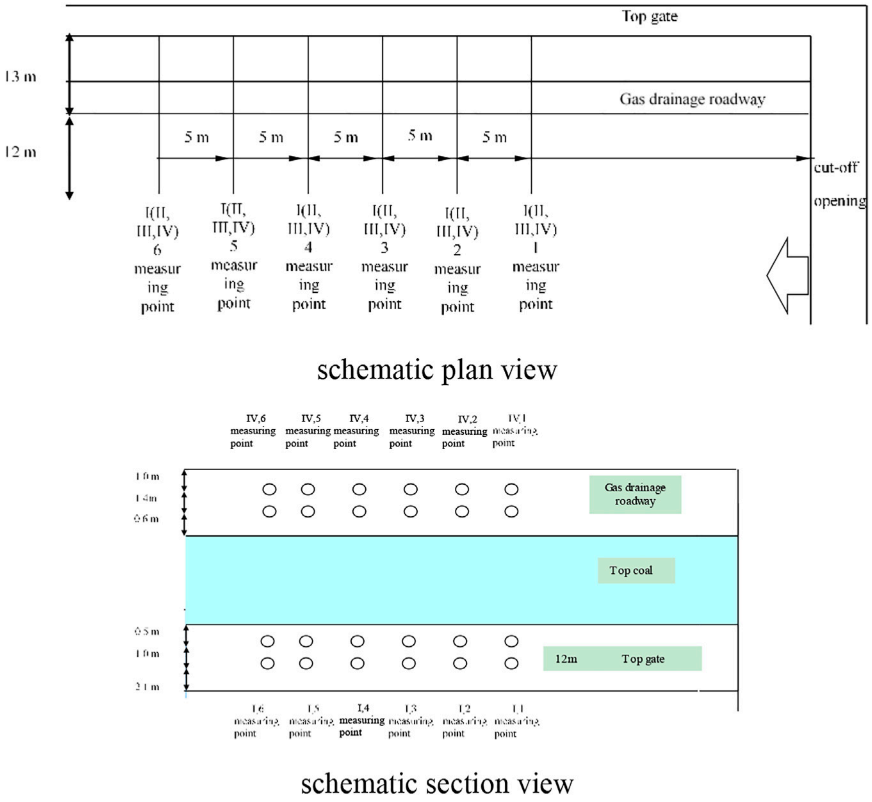

FIGURE 14
Schematic views showing the layout of the embedded KBS II-type borehole stress gauge.

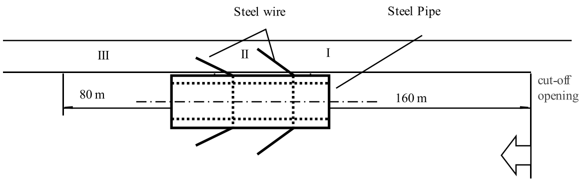

FIGURE 15
Arrangement of sublevel coal deep-hole base stations.

lower top coal stress was smaller, such as 35 m in front of the working face, where the average of the No. I line was 25.2. The mean value of lines I and II was 22.2 MPa, the average value of line III was 23.8 MPa, and the mean value of line IV was 22.6 MPa.

According to Figure 17, both the field measurement and the traditional theoretical calculation of the peak stress were greater than the uniaxial compressive strength of the coal body, which means that the top coal at the peak point was not in a uniaxial compression state but in a two- or three-axis force state. Therefore, the top coal stress environment is crucial for the destruction of top coal. Through the stress environment analysis, we can conclude that, in the vertical direction, the top coal is above the coal body to be cut by the lower coal mining machine, which is followed by the direct top and the old top, and the longitudinal mechanical system is the top plate (Direct top, old top) - top coal - bottom coal to be cut - bottom plate.

6.2.2 Displacement results

We can see from Figure 18 that the starting points of the top coal displacement in the extrathick coal seam measured by stations I, II, and III were approximately 73, 70, and 77 m in front of the working surface, respectively. The arithmetic average of the similar measuring points of the station were obtained. The starting point of the average top coal displacement was approximately 74 m in front of the working face, as shown in Figure 18. In the range of approximately 74 m–55 m, the base point displacement of the lower top coal at a depth of 1 m was basically 0 mm, while the base point displacement at 3 and 6 m depths gradually increased, and the base point of the deep top rock began to move from approximately 85 m in front of the working surface. At 55 m in front of the working face, the cumulative

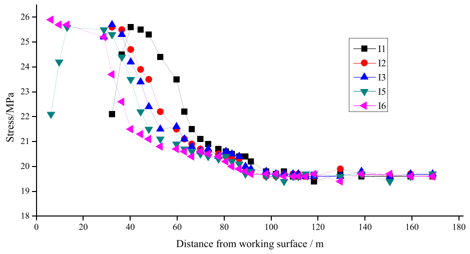

the No. I stress measuring line

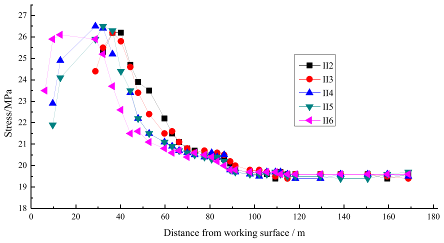

the No. II stress measuring line

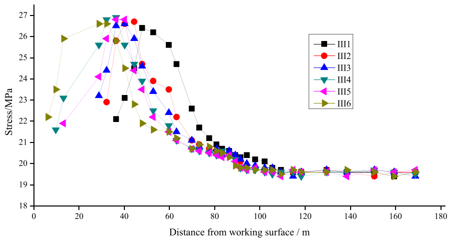

the No. III stress measuring line

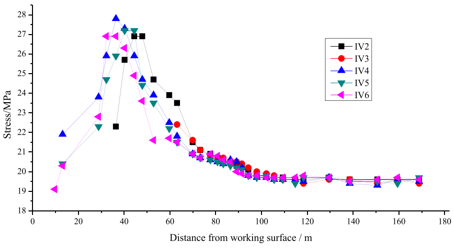

the No. IV stress measuring line

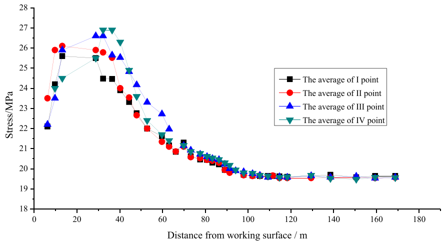

The average of all stress measuring lines

FIGURE 16
Relationship between the stress and the distance of the different stress measuring lines.

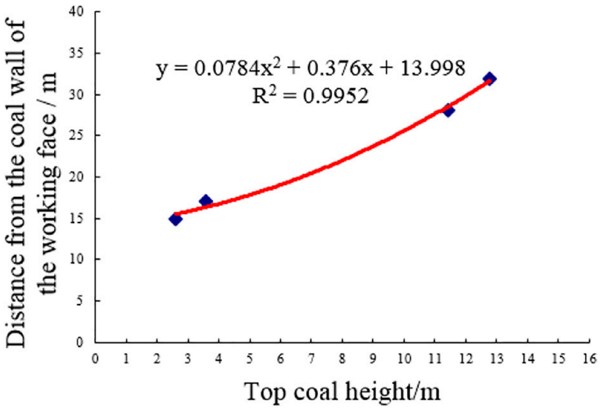

FIGURE 17
Relationship between the maximum abutment pressure and distance to face.

displacement reached 13 mm. With the advancement of the working surface, the deep base point displacement increased sharply, but the difference in the base points of different layers was larger, as shown in Figure 18. At the coal wall, the top coal in the lower base of Classes 3 and 4 was also fully compacted. The deep base point of the deep rock in the top rock was 10 m adjacent to the top of the working face, the top coal was gradually separated from the top rock, and the top rock was broken in the front 4 m. Because the coal was soft and the thickness was large, the top coal caving angle was approximately 112.6°, and the top coal was stepped and broken.

Thus, the following deformation characteristics can be obtained: The initial movement point of the top coal is approximately 74 m in front of the working face. The higher the horizon is, the farther the distance between the initial movement point and the coal wall is.

With decreasing relative distance of the working face, the top coal deformation increases gradually. According to the measured

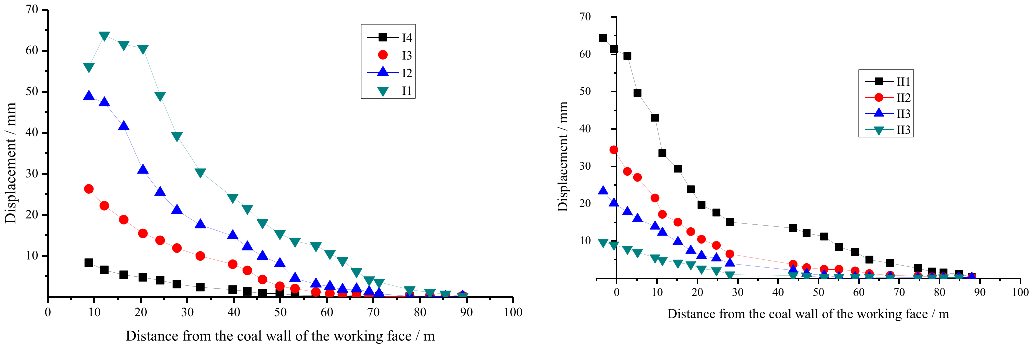

the No. I measuring line

the No. II measuring line

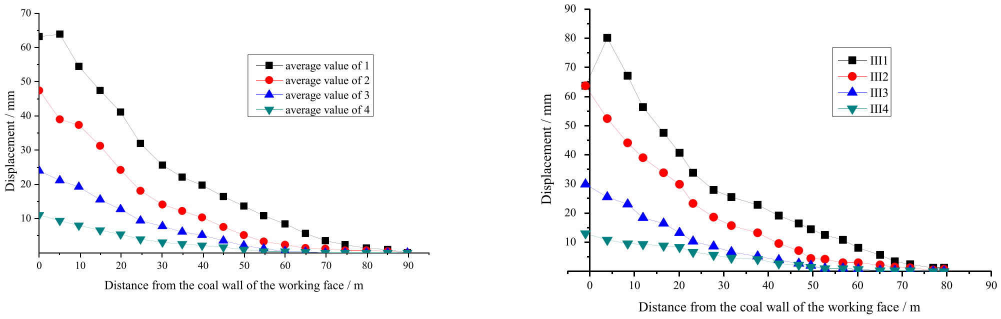

The average of all stress measuring lines

the No. III measuring line

FIGURE 18
Relationship between the sublevel coal displacement and the distance of the different measuring lines.

deformation data, the top coal deformation in front of the working face can be divided into three areas: the initial deformation area, stable deformation area and sharp deformation area.

From the initial movement point of the top coal to the area 25 m in front of the coal wall, the average top coal deformation velocity was 1 mm/d, and the total deformation was 5–25 mm. The deformation in this area was mainly due to the vertical displacement formed by the compression and closure of near-horizontal primary fractures. This area was called the initial top coal deformation zone. In the area of 10–25 m in front of the working face, the top coal deformation increased rapidly, the average deformation velocity was 7 mm/d, the deformation was relatively stable, and the maximum deformation reached 48 mm. The deformation in this area was mainly due to the vertical displacement of coal, which was similar to the linear elastic compression deformation. This area was called the stable top coal deformation area. In the working face in front of the 10 m area, the upper level of top coal deformation increased sharply, the maximum deformation rate was 13 mm/d, and the maximum deformation was reached. The main characteristic was due to upper top coal deformation caused by peak pressure after fracturing, slippage in the goaf below the direction, the displacement caused by a sharp change, and a sharp area called the top coal deformation area.

6.2.3 Roadway deformation results

During the test, station III was damaged, and the remaining results are shown in Table 4.

It can be seen from the Origin fitting in Figure 19 that the displacements of the top and bottom plates of the two stations were significantly larger than those of the two gangs; the roadway 90 m in front of the working surface began to deform; and the top and bottom plates were moved within 30–90 m of the working surface. The near speed and the two-way approaching speed were basically constant (the top and bottom plates moved closer to the average speed and stabilized at 0.6 mm/d, and the average speed of the two gangs was stable at 0.1 mm/d), while at 25–30 m, the two shifted. The near speed increased, and the approaching speed was basically constant in the range of 15–25 m (the top and bottom plates moved closer to the average speed and stabilized at 3 mm/d, and the average speed of the two gangs was stable at 1 mm/d) within 15 m of the working face.

TABLE 4 *In situ* displacement measurement results in the roadway.

Station I				**Station II**			
Distance from the working surface (m)	A1 Approaching amount (mm)	A2 Approaching amount (mm)	B Approaching amount (mm)	Distance from the working surface (m)	A1 Approaching amount (mm)	A2 Approaching amount (mm)	B Approaching amount (mm)
98.3	0	0.6	0	106.4	0	0	0
94.7	0	0.6	0	104.1	0	0	0
91.6	0	0.5	0	101.4	0	0	0
89.3	0	1.1	0	98.3	0	0	0
85.5	0	1.4	0	95.8	0	0	0
82.1	0	1.7	0	92.6	0	0.4	0
77.9	0.5	1.6	0	88.2	0.3	1.2	0
74.2				84.9	0.5	1.6	0
71.4	1.2	2.1	0	81.2	0.9	1.9	0
69.1	1.9	2.9	0	78.1	1.5	2.6	0
66.4	2.3	3.6	0	74.7	1.7	3.6	0
63.3	3.2	4.3	0.3	67.8	2.2	4.1	0
60.8	4.1	4.3	0.6	62.9	3.9	5.9	0
57.6	5.1	5.4	0.7	59.4	4.3	6.7	0
53.2	6.2	6.6	1.1	55.2	5.2	6.3	0.4
49.9	7.5	7.8	1.3	51.4	6.3	7.1	0.7
46.2	8.7	9.3	1.5	47.2	7.1	8.5	0.9
43.1	10.2	11.3	1.8	43.8	7.6	8.9	1.3
39.7	11.9	13.7	2.3	28.1	9.1	10.1	2.3
32.8	13.6	19.3	2.8	24.7	9.7	11.9	2.5
27.9	17.5	28.1	3.8	21.2	10.8	12.3	3.8
24.4	23.8	43.8	5.2	18.5	12.7	13.7	3.3
20.2	29.4	54.7	8.9	15.2	14.3	15.3	4.8
16.4	38.5	65.3	12.3	11.5	16.6	17.1	5.9
12.2	46.8	76.6	16.6	9.7	22.9	23.4	7.2
8.8	59.4	97.9	18.9	5.4	33.5	37.8	9.6

6.3 Summary results of the field test

Based on the above observation results of the working face leading support pressure, top coal stress, displacement, and roadway deformation in the extrathick coal seam, we conclude that, due to the large thickness of the primary mining, the original rock stress at 90 m in front of the working face was destroyed, and the leading support pressure gradually increased. The top coal was completely in a three-direction stress state, and the advance bearing pressure increased slightly. The obvious top coal deformation appeared at approximately 74 m in front of the working face, which reflects the "hysteresis effect" of the top coal deformation. With the shortening of the distance from the working face, the advance bearing pressure gradually increased and rapidly increased within 40–50 m of the working face. However, the top coal deformation from the initial movement point to the region 25 m from the front of the coal wall had a small average deformation velocity. The displacement was mainly caused by the compression and closure of the near-horizontal primary fractures, which also reflects the "hysteresis effect" of top coal deformation. In the area 10–25 m in front of the working face, the top coal was close to or affected by the peak of the leading supporting pressure, but due to the "hysteresis effect" of top coal deformation, the deformation still reflected the top coal movement caused by the rapid pressure growth in the peak area of the supporting pressure. The main performance was that the displacement increased rapidly, and the deformation was relatively stable and mainly due to the vertical displacement formed by the approximate linear elastic compression deformation of the coal mass. Finally, the leading bearing pressure of the working face reached a maximum value within the range of 10–40 m from the working face, resulting in the fracturing and shearing of the upper top coal and the beginning of fracturing. Therefore, in the area 10 m ahead of the working face, the horizontal deformation of the upper top coal increased sharply, and the total deformation reached a maximum value. The

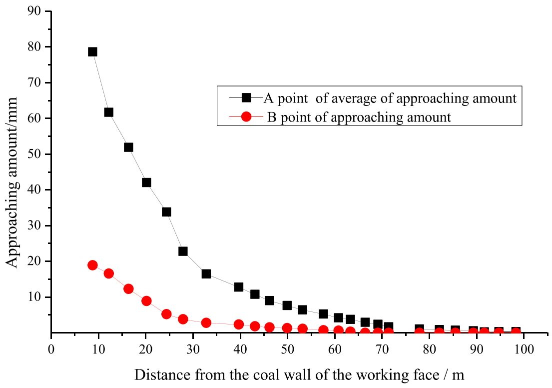

the No. I measuring line

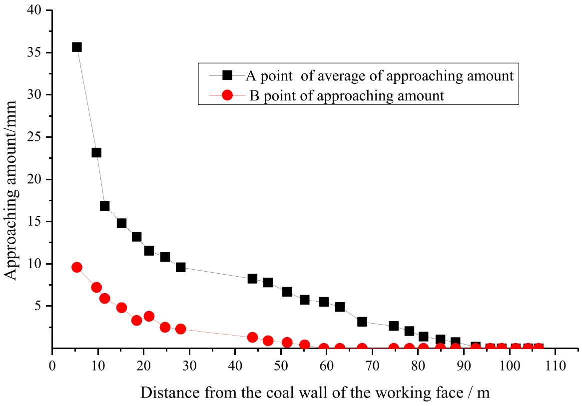

the No. II measuring line

FIGURE 19
Relationship between the displacement and the distance of the different measuring lines.

deformation in this area was mainly characterized by the upper top coal sliding to the lower direction of the goaf due to upper top coal fracturing under peak pressure, resulting in a change in the overall displacement of the deep base point and thus a sharp change in displacement. In general, because the top coal thickness of this working face was large, the dynamic pressure coefficient (approximately 1.3) was smaller than that of the general thick coal seam, and the top coal displacement increased relatively gently in the region of 10–25 m in front of the working face.

Moreover, both the extrathick coal seam stress and displacement showed obvious horizon characteristics. The top coal seam stress and displacement were large, while the bottom coal seam stress and displacement were small. Compared with the top coal displacement, the “hysteresis effect” of roadway deformation was not obvious and was basically synchronous with the change in stress. We think that the reason for this is mainly because the stresses of the lane edge and deep coal caving are different: deep top coal is completely in the three-way stress state, the lane edge coal behaves according to its interval distance on the surface of the roadway and the support form, and the support quality can be in three different stress states, including two-way and one-way, causing full space deformation.

7 Conclusion

From what has been discussed above, according to the characteristics of migration and failure of top coal in extra-thick coal seam, the damage, failure and deformation process of top coal can be divided into initial compression and plastic deformation zone, intense compression and failure zone, short beam rotation and support action zone. In the vertical direction of the coal seam in the range of roof control, according to the characteristics of deformation and crushing of the top coal in the extra-thick fully mechanized caving face, it can be successively divided into roof failure layer, short beam structure layer and support failure layer from top to bottom.

When the coal seam thickness is constant, the coal bodies at different distances in front of the working face are different in the coal seam due to the influence of the leading bearing pressure. The upper top coal stress is small, and the middle top coal stress is large. When the coal seam thickness is constant, in front of the working face, the upper top coal vertical displacement is greater than the middle top coal vertical displacement due to the top plate rotation.

For different coal thicknesses, whether it is the upper top coal or the middle top coal, in front of the advancing working face, the top coal displacement has an increasing trend. However, with the advancement of the working face, the top coal is subjected to tensile stress, and it changes from the original three-direction force to the two-direction force, causing the top coal to undergo large migration or even fracture.

The failure of the middle and lower top coal is the key to the full failure of the whole top coal. The key to the failure of lower top coal is the function of support back and forth. The complete discharge of the upper top depends on the integrity of the simply supported beam formed locally by the middle top coal. Before the failure of simply supported beam, the upper top coal is affected by the support force, and its displacement, deformation and failure degree are very small. When the simply-supported beam formed by the middle top coal is damaged by stress, the maximum displacement and failure degree of the upper top coal are larger than those of the other layers.

Data availability statement

Author contributions

Author HN is responsible for funding and improvement of the paper. Author SW is responsible for writing the first draft of the paper.

Funding

This work was financially supported by Experimental study on the performance and instability mechanism of GFRP anchor in coal roadway with back-filling by bottom expanding (51974106); The model and method for coordinated intelligent coal caving process in ultrathick coal seam mining (2018YFC0604502); Xinjiang collaborative innovation project (2017E0292); Dynamic load impact effect and mechanism of fully mechanized top coal caving face with shallow and thick coal seams based on different mining and drawing ratios (182300410120); Research fund for the doctoral program of higher education of HPU (RFDP) (660207/018); Scientific and technological research projects of Henan Province (182102310020), the research fund of the State Key Laboratory For Geomechanics And Deep Underground Engineering, China University of Mining & Technology (SKLGDUEK 2004), the research fund of the Key Laboratory Of Western Mine Exploitation And Hazard Prevention, Ministry of education (SKLCRKF 1902), the research fund of Henan Key Laboratory For Green And Efficient Mining & Comprehensive Utilization Of Mineral Resources (Henan Polytechnic University) (KCF201801).

Conflict of interest

Publisher's note

References

Bai, Q. S., Tu, S. H., Wang, F. T., and Zhang, C. (2017). Field and numerical investigations of gateroad system failure induced by hard roofs in a longwall top coal caving face. *Int. J. Coal Geol.* 173, 176–199. doi:10.1016/j.coal.2017.02.015

Bondarenko, Yu.V., Makecv, A. Yu, Zhurek, P., and Klega, L. (1993). Technology of coal extraction from steep seam in the Ostrava-Karvina basin. *Ugol Ukralny* 4 (3), 45–48.

Cheng, G., Ma, T., Tang, C., Liu, H., and Wang, S. (2017). A zoning model for coal mining-induced strata movement based on microseismic monitoring. *Int. J. Rock Mech. Min. Sci.* 94, 123–138. doi:10.1016/j.ijrmms.2017.03.001

Duan, L. Q., Dong, L., and Ma, L. J. (2018). Experimental study of acoustic emission characteristics of foamed concrete under uniaxial compression. *J. China Univ. Min. Technol.* 47 (4), 742–747.

Feng, Y. F. (2014). *Research on key technologies of fully mechanized caving mining with special thick coal seam*. China: University of Mining and Technology.

Guo, W., Tan, Y., and Bai, E. (2017). Top coal caving mining technique in thick coal seam beneath the Earth dam. *Int. J. Min. Sci. Technol.* 27 (1), 165–170. doi:10.1016/j.ijmst.2016.11.005

Habib, A., and Brett, A. P. (2010). Stress analysis of longwall top-coal caving. *Int. J. Rock Mech. Min. Sci.* 47 (1), 30–41. doi:10.1016/j.ijrmms.2009.07.004

Huang, Z. Z., Mao, D. B., and Liu, Q. J. (2015). Study on the characteristics of ultra-thick top coal migration in large mining height fully mechanized caving. *China coal.* 41 (11), 41–43+63.

Jiang, J. B., Chen, D. Y., and Li, Z. (2016). Numerical simulation study on the surrounding rock migration law of fully mechanized top coal caving face. *Inn. Mong. Coal Econ.* 10, 115–116.

Kong, B., Li, Z., Wang, E., Lu, W., Chen, L., and Qi, G. (2018). An experimental study for characterization the process of coal oxidation and spontaneous combustion by electromagnetic radiation technique. *Process Saf. Environ. Prot.* 119, 285–294. doi:10.1016/j.psep.2018.08.002

Lan, Y. W., Gao, R., Yu, B., and Meng, X. (2018). *In situ* studies on the characteristics of strata structures and behaviors in mining of a thick coal seam with hard roofs. *Energies* 11 (9), 2470. doi:10.3390/en11092470

Li, C. (2013). *Study on top coal fracture mechanism and recovery rate of fully mechanized caving face in Gongwusu Mine*. Hohhot: Inner Mongolia University of Science and Technology.

Li, P. (2015). *Study on top coal migration and ore pressure behavior in fully mechanized caving face of thick coal seam*. China: University of Mining and Technology.

Li, X. L., Chen, S. J., Liu, S. M., and Li, Z. h. (2021a). AE waveform characteristics of rock mass under uniaxial loading based on Hilbert-Huang transform. *J. Cent. South Univ.* 28 (6), 1843–1856. doi:10.1007/s11771-021-4734-6

Li, X. L., Chen, S. J., Wang, S., Zhao, M., and Liu, H. (2021b). Study on *in situ* stress distribution law of the deep mine taking Linyi Mining area as an example. *Adv. Mater. Sci. Eng.* 9 (4), 5594181–5594211. doi:10.1155/2021/5594181

Liu, H. Y., Zhang, B. Y., Li, X. L., Liu, C., Wang, C., Wang, F., et al. (2022). Research on roof damage mechanism and control technology of gob-side entry retaining under close distance gob. *Eng. Fail. Anal.* 138 (5), 106331–112022. doi:10.1016/j.engfailanal.2022.106331

Liu, S. M., Li, X. L., Wang, D. K., and Zhang, D. (2020). Investigations on the mechanism of the microstructural evolution of different coal ranks under liquid nitrogen cold soaking. *Energy Sources Part A Recovery Util. Environ. Eff.* 2020, 1–17. doi:10.1080/15567036.2020.1841856

Liu, S. M. (2018). *Study on the movement law of top coal and its overlying strata in the first mining face Of west block of zhao Zhuang two well*. Taiyuan: Taiyuan University of Technology.

Liu, X., Song, D., He, X., Wang, Z., Zeng, M., and Deng, K. (2019). Nanopore structure of deep-burial coals explored by AFM. *Fuel* 246, 9–17. doi:10.1016/j.fuel.2019.02.090

Lv, H. Y., Wang, Z. H., and Tang, Y. S. (2019). Experimental study on the law of top coal fracture and migration in fully mechanized caving mining under special thick coal seams. *Chin. J. Rock Mech. Eng.* 38 (03), 476–486.

Ma, F. (2016). *Study on the law of top coal activity and optimization of process parameters in the fully mechanized top coal caving face of Shenghua Coal Industry*. Taiyuan: University of Technology.

Ma, J. H., Hou, C., and Chen, Y. B. (2016). Numerical simulation of top coal movement law in fully mechanized caving face. *Coal Mine Saf.* 47 (08), 216–218.

Mahdi, S., and Charlie, C. L. (2012). Numerical modelling of longwall mining and stability analysis of the gates in a coal mine. *Int. J. Rock Mech. Min. Sci.* 51 (1), 24–34. doi:10.1016/j.ijrmms.2012.02.002

Mao, D. B., and Yao, J. G. (2010). Study on the adaptability of large mining height fully mechanized caving mining. *J. China Coal Soc.* 35 (11), 1837–1841.

Meng, X. R., Chen, H. B., and Hu, B. B. (2003). Top-coal move-ment theory of top-coal mining and establishment of its mathemati-cal model. *Coal Eng.* 10, 32–34.

Nan, H., Wang, Q. H., and Zhao, X. W. (2010). *Study on failure mechanism of fully mechanized top coal caving*. Beijing: Coal Industry Press.

Nan, H., Zhang, G. Y., and Chen, L. W. (2005). *Study on fully mechanized caving technology in extra-thick coal seams*. Beijing: Development and innovation of fully mechanized top coal caving, 202–208.

Qian, M. G., Shi, P. W., and Xu, J. L. (2010). *Pressure and rock formation control on mine*. Beijing: China university of mining and technology press.

S Bai, Q., and H Tu, S. (2020). Numerical observations of the failure of a laminated and jointed roof and the effective of different support schemes a case study. *Environ. Earth Sci.* 2020 (79), 202. doi:10.1007/s12665-020-08935-2

Schgal, V. K., and Coalfields Kumar, A. (1992). *Thick and steep seam mining in North EastrenInternational symposium on thick seam mining:problem and issues(ISTS'92)*. New Delhi: Oxford IBH Publishing Co, 457–469.

Si, G., Jamnikar, S., Lazar, J., Shi, J. Q., Durucan, S., Korre, A., et al. (2015). Monitoring and modelling of gas dynamics in multi-level longwall top coal caving of ultra-thick coal seams, part I: Borehole measurements and a conceptual model for gas emission zones. *Int. J. Coal Geol.* 144-145, 98–110. doi:10.1016/j.coal.2015.04.008

Szurgacz, D., and Brodny, J. (2018). Analysis of rock mass dynamic impact influence on the operation of a powered roof support control system. *E3S Web Conf.* 29, 00006. doi:10.1051/e3sconf/20182900006

Tan, Y. L., Zhao, T. B., and Xiao, Y. X. (2010). Quantitative prop support estimation and remote monitor early warning for hard roof weighting at the Muchengjian Mine in China. *Can. Geotech. J.* 47, 947–954. doi:10.1139/t10-009

Unver, B., and Yasitli, N. E. (2006). Modelling of strata movement with a special reference to caving mechanism in thick seam coal mining. *Int. J. Coal Geol.* 2006 (66), 227–252. doi:10.1016/j.coal.2005.05.008

Vakili, A., and Hebblewhite, B. (2010). A new cavability assessment criterion for longwall top-coal caving. *Int. J. Rock Mech. Min. Sci.* 47 (8), 1 317–321 329. doi:10.1016/j.ijrmms.2010.08.010

Wang, E. Y., Liu, X. F., and He, X. Q. (2018). Acoustic emission and electromagnetic radiation synchronized monitoring technology and early-warning application for coal and rock dynamic disaster. *J. China Univ. Min. Technol.* 47 (5), 953–959.

Wang, H. S. (2016). *Study on gas migration law and application of control technology in fully mechanized top coal caving*. Beijing: University of Science and Technology.

Wang, J. C. (2018). Engineering practice and theoretical progress of top-coal caving mining technology in China. *J. China Coal Soc.* 43 (1), 43–51.

Wang, J. H. (2006). Current status and development trend of fully mechanized mining technology and equipment in China. *Coal Sci. Technol.* 34 (1), 4–7.

Wang, J. (2008). *Study on the law of coal and rock caving and the parameters of coal caving in fully mechanized caving mining in thick seam*. China: University of Mining and Technology.

Wang, J., Yu, B., Kang, H., Wang, G., Mao, D., Liang, Y., et al. (2015). Key technologies and equipment for a fully mechanized top-coal caving operation with a large mining height at ultra-thick coal seams. *Int. J. Coal Sci. Technol.* 2 (2), 97–161. doi:10.1007/s40789-015-0071-4

Wang, W., Zhao, G., Lou, G., and Wang, S. (2019). Height of fractured zone inside overlying strata under high-intensity mining in China. *Int. J. Min. Sci. Technol.* 29 (1), 45–49. doi:10.1016/j.ijmst.2018.11.012

Wu, W. H. (2017). Research on overburden migration law of pillar-type caving mining in steep inclined thick coal seam. *Inn. Mong. Coal Econ.* Z1, 124–126.

Xia, H. C., Yu, B., and Li, W. (2017). Study on the coal migration law of fully mechanized top coal caving in extra-thick medium-hard coal seam in Datong mining area. *Coal Technol.* 36 (03), 35–38.

Xie, H., and Zhou, H. W. (2008). Application of fractal theory to top-coal caving. *Chaos Solit. Fractals* 36 (4), 797–807. doi:10.1016/j.chaos.2006.07.024

Yang, R. S., Zhu, Y. L., Zhu, X. L., Dongming, G., and Guihe, L. (2011). Discussions on some security mining problems of fully-mechanized top coal mining in "three soft" large inclined angle working face. *Procedia Eng.* 26, 1144–1149. doi:10.1016/j.proeng.2011.11.2284

Yu, J., Yao, W., Duan, K., Liu, X., and Zhu, Y. (2020). Experimental study and discrete element method modeling of compression and permeability behaviors of weakly anisotropic sandstones. *Int. J. Rock Mech. Min. Sci.* 104, 104437. doi:10.1016/j.ijrmms.2020.104437

Yu, J., Liu, G. Y., Cai, Y. Y., Zhou, J., Liu, S., and Tu, B. (2020). Time-dependent deformation mechanism for swelling soft-rock tunnels in coal mines and its mathematical deduction. *Int. J. Geomech.* 20 (3), 04019186. doi:10.1061/(asce)gm.1943-5622.0001594

Zhai, X. X., Li, S. M., and Du, J. P. (2009). Movement rule of top-coal with sublevel caving in bottom-slice. *J. Min-ing Saf. Eng.* 26 (3), 82–86.

Zhai, X. X., Zhao, X. F., and Tu, X. Z. (2019). Study on deformation and movement law of overlying thick conglomerate layer in top coal caving. *J. henan Polytech. Univ. Nat. Sci. Ed.* 38 (03), 16–23.

Zhang, C., Liu, J. B., X Zhao, Y., Han, P., and Zhang, L. (2020). Numerical simulation of broken coal strength influence on compaction characteristics in goaf. *Nat. Resour. Res.* 29 (4), 2495–2511. doi:10.1007/s11053-019-09613-2

Zhang, C., and Zhang, L. (2019). Permeability characteristics of broken coal and rock under cyclic loading and unloading. *Nat. Resour. Res.* 28 (3), 1055–1069. doi:10.1007/s11053-018-9436-x

Zhang, J. X., Li, B. Y., Zhou, N., and Zhang, Q. (2016). Application of solid backfilling to reduce hard-roof caving and longwall coal face burst potential. *Int. J. Rock Mech. Min. Sci. (1997).* 88, 197–205. doi:10.1016/j.ijrmms.2016.07.025

Zheng, Z. T., Xu, Y., Li, D. S., and Dong, J. H. (2015). Numerical analysis and experimental study of hard roofs in fully mechanized mining faces under sleeve fracturing. *Minerals* 5, 758–777. doi:10.3390/min5040523

Zhong, T. (2015). *Structural characteristics of coal raft flow field and top coal loss law in fully mechanized top coal caving mining in special thick seam*. China: University of Mining and Technology.

Zhou, X. M., Wang, S., Li, X. L., Meng, J., Li, Z., Zhang, L., et al. (2022). Research on theory and technology of floor heave control in semicoal rock roadway: Taking longhu coal mine in Qitaihe mining area as an Example. *Lithosphere* 2022 (11), 3810988. doi:10.2113/2022/3810988

Zhu, L. P., and Yan, S. H. (2011). Numerical simulation of top-coal move-ment rule in fully-mechanized caving mining with large mining height. *Coal Min. Technol.* 16 (1), 11–14.

Zhu, X. Y. (2017). *Study on the law of top coal and roof movement in fully mechanized caving mining in "three softs" extra-thick coal seams*. Henan Polytechnic University.

Zou, Q., and Lin, B. (2018). Fluid-solid coupling characteristics of gas-bearing coal subjected to hydraulic slotting: An experimental investigation. *Energy fuels.* 32 (2), 1047–1060. doi:10.1021/acs.energyfuels.7b02358

frontiers | Frontiers in Earth Science

TYPE Original Research
PUBLISHED 15 September 2022
DOI 10.3389/feart.2022.1018465

OPEN ACCESS

EDITED BY
Mingjun Zou,
North China University of Water
Resources and Electric Power, China

REVIEWED BY
Gaoyuan Yan,
China University of Mining and
Technology, China
Yu Qi,
Yanshan University, China

*CORRESPONDENCE
Keying Wang,
744491522@qq.com

SPECIALTY SECTION
This article was submitted to Economic Geology,
a section of the journal
Frontiers in Earth Science

RECEIVED 13 August 2022
ACCEPTED 26 August 2022
PUBLISHED 15 September 2022

CITATION
Cai N, Wang K and Du J (2022), Geological occurrence and productivity prediction for coalbed methane of central Hunan depression, China. *Front. Earth Sci.* 10:1018465.
doi: 10.3389/feart.2022.1018465

Geological occurrence and productivity prediction for coalbed methane of central Hunan depression, China

Ningbo Cai[1,2,3], Keying Wang[2,3]* and Jiang Du[2,3]

[1]Institute of Advanced Studies, China University of Geosciences, Wuhan, China, [2]New Geological Energy Exploration and Development Engineering Technology Research Center of Hunan, Changsha, China, [3]Geophysics and Geochemistry Survey Institute of Hunan, Changsha, China

To analyze the geological occurrence and predict the drainage performance of coalbed methane in the central Hunan depression of China, coal samples were collected to conduct physical experiments and numerical simulations. The following conclusions were reached. The vitrinite ranges from 54.37 to 87.80%, the inertinite is between 11.14–25.89%, and exinite is less than 1%. The inorganic components are mainly clay minerals and vary from 0.71 to 5.66%. The major porosity ranges from 7 to 9%, and it is influenced by organic/inorganic components and maturity. Both the vertical and horizontal permeabilities are at a relatively low level, mostly below 0.05 mD, indicating the reservoir is low permeable or non-permeable. The reservoir pressure ranges from 3.74 to 11.58 MPa, which has significant and positive linear correlations with closure pressure and burial depth. Gas content varies from 5 m^3/t to 20 m^3/t. The theoretical recovery ratio in the Hongshandian mining area is about 61.7%, while the values of the two spots in the Duanpiqiao mining area are 49.1 and 54.5%. Production predictions show that under the permeability of 0.01 mD, 0.05 mD, and 0.10 mD, cumulative gas productions in 10 years for a single well range from 1.7×10^6 m^3 to 3.2×10^6 m^3, and those for a well group consisting of five wells vary from 10.5×10^6 m^3 to 19.2×10^6 m^3. Thus, this area will have a high value for coalbed methane exploitation after stimulating the reservoir to increase permeability successfully.

KEYWORDS

coalbed methane, geological occurrence, productivity prediction, longtan formation, central hunan depression

1 Introduction

Since the 1990s, unconventional gas explorations have made breakthroughs in America, Canada, and other countries (Schmoker, 1980; Law, 2002a; Law, 2002b; Curtis, 2002). Foreseeing its importance, Chinese geologists (Huang, 1990) proposed using coal measure gas. As one type of coal measure gases, coalbed methane (CBM) is potentially an important and abundant economic resource that has received worldwide

TABLE 1 Basic information of coal mines and samples.

Mining area	Mining area abbreviation	Location	Geological time	Coal type	$R_{o,max}$/%
Zhadu	ZD	Central of Hunan Depression	P_3l	Anthracite	2.80
Lengshuijiang	LSJ		P_3l	Anthracite	2.78
Lumaojiang	LMJ		P_3l	Anthracite	2.68
Hongshandian	HSD		P_3l	Meager coal	2.05
Duanpoqiao	DPQ		P_3l	Lean coal	1.64
Doulishan	DLS		P_3l	Coking coal	1.23
Gujiaodi	GJD		P_3l	Lean coal	1.68
Meitanba	MTB		P_3l	Fat coal	1.05
Yonglei	YL	Southeastern Hunan Depression	P_3l	Anthracite	2.87
Taoshui	TS		P_3l	Anthracite	2.80
Matian	MaT		P_3l	Anthracite	2.29
Baisha	BS		P_3l	Anthracite	2.87
Meitian	MeiT		P_3l	Anthracite	2.89
Yuanjia	YJ		P_3l	Anthracite	2.91

Geological time: P_3l= Longtan formation of upper series Permian System

attention in recent years (Bustin and Clarkson, 1998; Wei and Zhang, 2010; Liu et al., 2013; Sun et al., 2016; Liu and Wu, 2017).

The geological and geochemical characteristics of unconventional gas-bearing systems, including CBM reservoirs, were discussed in Martini et al. (2003). With further research on unconventional gas, scholars made in-depth studies on accumulation mechanism, occurrence conditions, and exploration, development, and utilization models of unconventional gas resources in sedimentary basins, especially for CBM resources (Laubach and Gale, 2006; Liu et al., 2013; Zou et al., 2013; Liu and Wu, 2017; Qin, 2018; Zou et al., 2018; Tao et al., 2019). A consensus has been reached that it is crucial to further understand the coal reservoir features and predict recoverability performance (Wang et al., 2009; Wei et al., 2010; Zhang, 2014; Zhang and Bian, 2015). This understanding can be the basis for both delineating a target exploitation area and designing a reasonable drainage system (Wei et al., 2007).

CBM exploration and exploitation in the Hunan province has been carried out for nearly six decades. Although industrial levels of CBM flow have yet to be found, there are multiple sets of high-quality hydrocarbon source rocks in various types, multiple combinations of gas generative stratum, reservoir and cap strata, and diverse types of hydrocarbon-bearing basins in the central Hunan depression. In addition, the developed and widespread distributed coal seams of the Longtan formation in the Permian system provide a physical basis for forming unconventional gas reservoirs. The geological setting for CBM formation is extensively studied in this area (Zou et al., 2015; Zou et al., 2019; Li et al., 2020). Thus, it is of great theoretical significance to investigate the geological occurrence and production prediction of CBM resources of the Longtan formation in the central Hunan depression to guide CBM exploitation.

2 Samples and experiments

2.1 Sample collection and preparation

Coal samples were collected from the Longtan formation in different mining areas of the central Hunan depression, with a size of 30 cm × 30 cm × 15 cm. For comparison purposes, coal samples from some mining areas in the southeast Hunan depression were also collected. The samples were shipped back to the laboratory immediately after collection. Following China's national standard of GB/T 16773-2008, small pieces of samples were selected, ground to 30 mesh, and formed into pulverized coal light sheets. Then, following China's national standard of GB/T6948-1998, the reflectance of oil-impregnated vitrinite of each sample was measured with a ZEISS Imager.M1m microscopic spectrophotometer. A series of coal samples were prepared based on the maximum reflectance data, which are shown in Table 1, and the perspective locations of mining areas can be found in Figure 1.

Three types of samples were prepared for this study. The first type was cylinder samples with a diameter of 25 mm and a height of 30–50 mm; they were used for the permeability test. The second type was block samples with a maximum length of about 15 mm, which were used for the mercury intrusion porosimetry and the isothermal adsorption measurement. The last type was particle samples of about 3 g weight and 60 mesh in size, and they

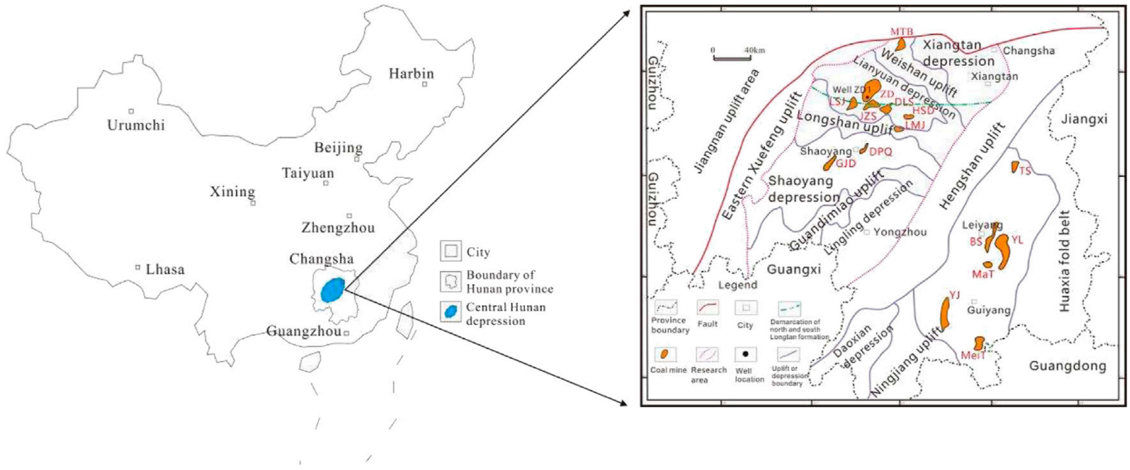

FIGURE 1
Structure outline map of central Hunan depression and distribution of mining areas.

were prepared for the scanning electron microscope analysis and the maceral component measurement.

2.2 Experimental method

The above-mentioned experiments were performed on the prepared coal samples, and gas component analysis was conducted on the gas sample collected from the CBM well. Well-testing analysis and gas content measurement were also made on the mine site.

Maceral component measurement was used to analyze the organic/inorganic compositions following the Chinese oil and gas industry standard (SY/T) 5125-2014 and 5163-2010. Scanning electron microscope analysis was used to analyze pore type and microfracture development following China's national standard of GB/T 25189-2010. Mercury intrusion porosimetry and permeability test were used to measure porosity and permeability, respectively. The mercury intrusion porosimetry measurement ran to a pressure of 6×10^4 Psia and showed that pore diameters as small as 3 nm were penetrated. The permeability test was simulated under situ stress conditions using a triaxial cell with an isotropic ambient pressure of 2.5 MPa. The isothermal adsorption measurement was used to analyze the isothermal adsorption characteristics of the samples to obtain Langmuir volume and pressure. The Langmuir equation and capacity method were adopted during the measurement with a temperature of 30 °C. The gas component analysis measured gas components, including heavy hydrocarbon content. The gas chromatography method was used in this analysis, following China's national standard of GB/T 13610-92. The gas content was measured using the desorption method, and the gas content consisted of desorbed gas, residual gas, and lost gas. The well testing analysis measured reservoir pressure and closure pressure using a common pressure build-up test.

3 Geological setting

The central Hunan depression of China is the area of research addressed in this paper. The Zhadu, Lengshuijiang, Doulishan, Hongshandian, Duanpoqiao, and Gujiaodi mining areas are located inside this depression. The Baisha, Taoshui, and Matian mining areas are distributed in the surrounding areas. The Lianyuan coal-bearing area is in the northern research area, and the main structure inside is the Lianyuan depression, in which a series of broad and gentle short synclines are distributed from west to east. In addition, the Weishan uplift and Xiangtan depression exist in the northern part of the Lianyuan depression. The Shaoyang coal-bearing area is in the center of the research area, in which the main structure is the Shaoyang depression, where there is a series of synclines of closed type or spreading type from west to east. The Lingling depression is in the south of the research area with a complex structure. It consists of a series of closed folds trending northwest and thrust faults trending northeast, which often form imbricate structures and are associated with lateral faults. The structure distribution is shown in Figure 1.

There are three coal-bearing strata in the research area: the Ceshui formation of the lower series Carboniferous system (C_1c), the Longtan formation of the upper series Permian system (P_3l) (south type and north type), and the Lower Jurassic (J_1). The Longtan formation of the upper series Permian system (P_3l) is the main coal-bearing stratum in the area, and it is the target stratum in this study. According to the contact relationship between

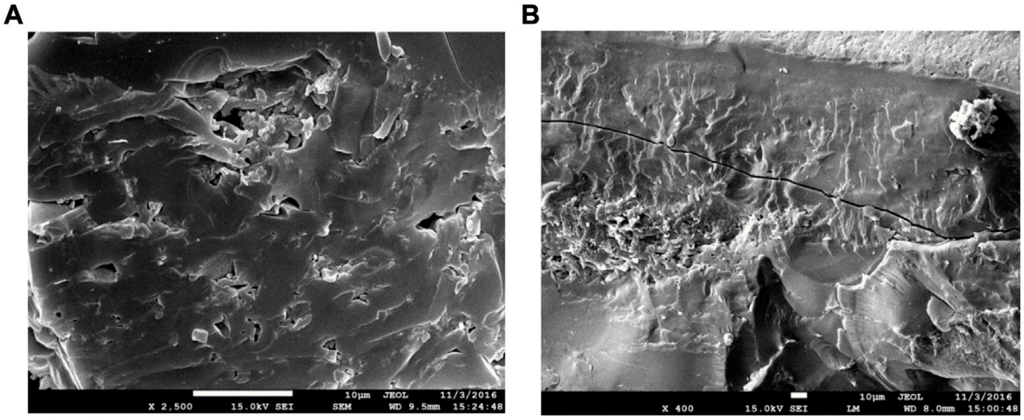

residual cellular pores

fractures

FIGURE 2
Microscopic characteristics of pores and fractures.

upper and lower strata, roughly bounded by 27°40′ N latitude, the Longtan formation in the research area is divided into northern and southern subtypes. The Longtan northern type has a thin thickness and a small quantity of coal seam layers. It is composed of sandstone, siltstone, sandy mudstone, carbonaceous mudstone, and coal seam. The thickness of the minable coal seam is 0.7–3.2 m. The Longtan south type is fully developed and has a large thickness, which can be divided into upper and lower sections. There is no coal seam in its lower section. Its upper section always contains 5–10 layers of coal seams, among which there are two extractable coal seams with a cumulative thickness of 0–12.50 m.

4 Reservoir property and recoverability evaluation

4.1 Coal petrography

Coal seams are generally light black to black or steel gray in color and possess a glassy, strong glassy, and semi-metallic to metallic luster. They have uniform block, granulose, striped, and scaly structures. Most have fractures inside. The fractures present a jagged shape or ladder pattern, graininess, and are partially conchoid. The coal type in the north type of the Longtan formation is usually semi-bright to semi-dark coal, and the bright coal is scant. In the south type of Longtan formation, most of the coal is semi-bright to bright, and the semi-dark and dark coal is scant. Maceral component measurement indicates that the vitrinite is 54.37–87.80%, the inertinite is 11.14–25.89%, the exinite is 0.35–14.08% with mostly lower than 1%, and the inorganic component is 0.71–5.66% of the total. The inorganic component is mainly clay mineral.

4.2 Pore and fracture systems

4.2.1 Pore type and porosity

Coal in the study area develops residual cellular pores and stomas, and fractures can also be detected. The primary structure of the coal body is mainly complete, as shown in Figures 2A,B.

Mercury intrusion porosimetry was conducted to obtain the porosity of coal samples in Table 1. Note that more than one sample was collected and tested in some coal areas, such as the Taoshui (TS) and Baisha (BS) coal areas. The number of tested coal samples is 17, and the results are shown in Figure 3.

The porosity ranges from 6.59 to 15.94%, mostly between 7–9%, placing it in the medium to high porosity reservoir. Scatter diagrams of vitrinite content, inertinite content, inorganic content and maximum vitrinite reflectance versus porosity are presented in Figure 4. Porosity is negatively correlated with vitrinite content and positively correlated with inertinite content. Vitrinite mainly develops micropores that result in a porosity reduction, and inertinite usually develops macropores that result in a porosity increase. Porosity is negatively correlated with the inorganic component. The porosity decreases as the inorganic component increases because the clay minerals fill the coal pores. Porosity is positively correlated with maximum vitrinite reflectance.

4.2.2 Fracture features

Scanning electron microscope analysis of the samples from the Hongshandian mining area shows that microfractures in this area are well developed. The fracture density is 19–35 strip/5 cm, as shown in Figure 5. The microfracture characteristics of the samples from other mining areas in the study area are shown in Figure 6. There is a significant correlation between microfracture density and coal type. The microfracture density decreases from

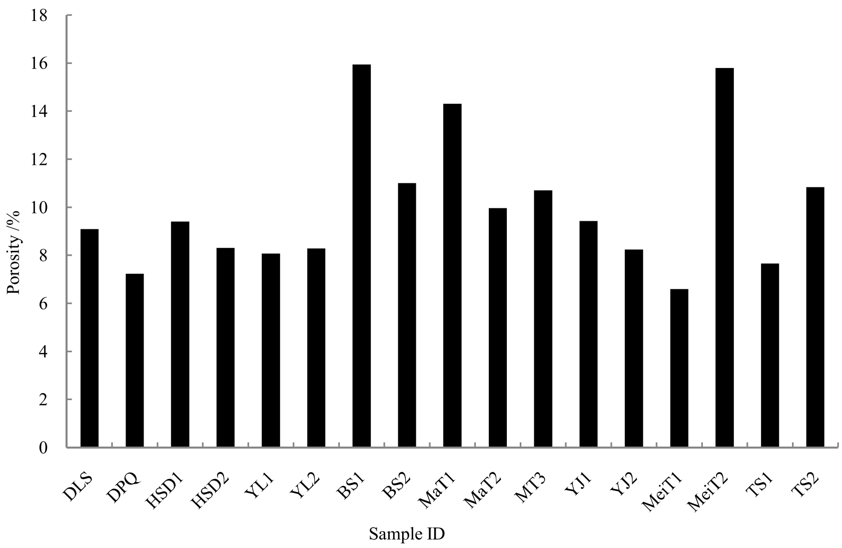

FIGURE 3
Porosity distribution of 17 samples.

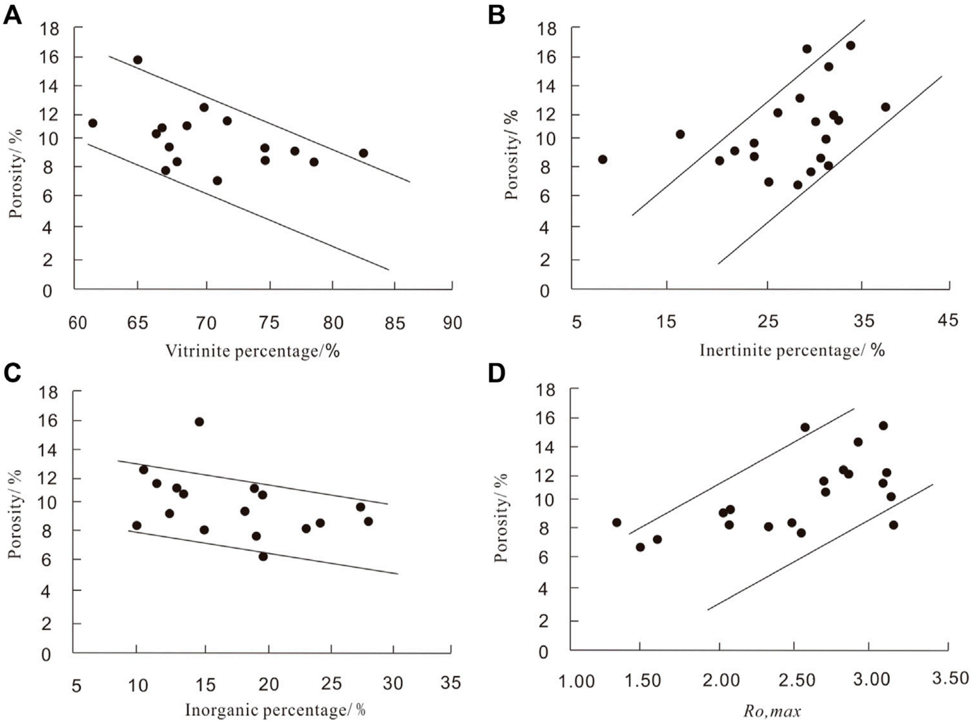

FIGURE 4
Relationships between porosity versus vitrinite **(A)**, inertinite **(B)**, inorganic **(C)**, and maximum vitrinite reflectance **(D)**.

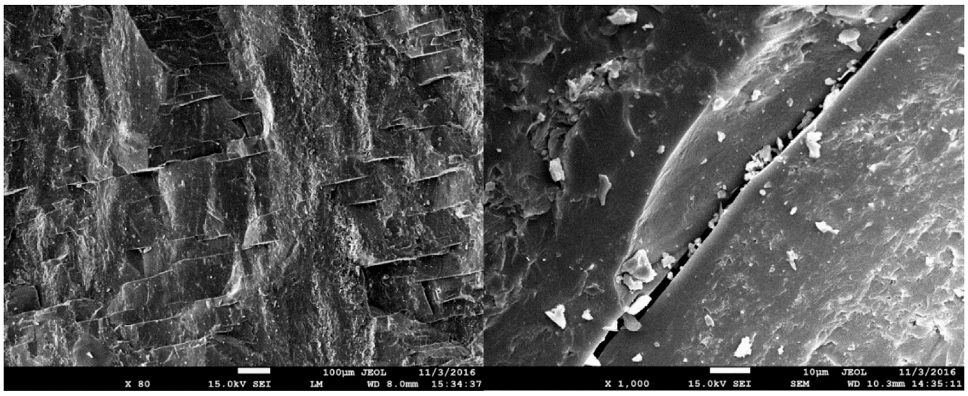

FIGURE 5
Microfractures in the Hongshandian mining area.

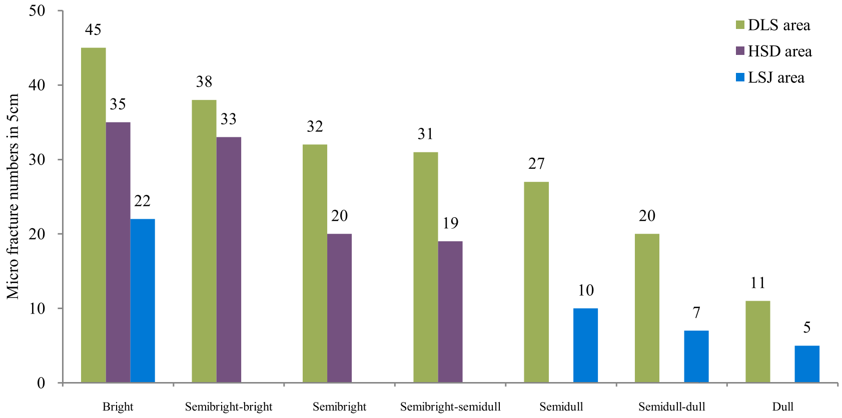

FIGURE 6
Histogram of microfracture density with coal type.

bright coal to dark coal in the same coalification. For example, in the samples from the Doulishan mining area, the microfracture density in xylovitrain is 45 strip/5 cm and decreases to only 11 strip/5 cm in dull coal. The microfracture density in the samples from the Lengshuijiang mining area also significantly decreases from 22 strip/5 cm in bright coal to 5 strip/5 cm in dull coal.

4.2.3 Permeability

Permeability test results are shown in Figure 7. With the deep burial depth and high crustal stress, the vertical permeability is relatively low, in the 0.001–0.025 mD range. Compared with vertical permeability, the horizontal permeability varies between 0.013 mD and 0.082 mD, most of which is lower than 0.05 mD. Thus, the research area is mainly low permeable or non-permeable.

4.3 Reservoir pressure

Reservoir pressure refers to the fluid pressure in coal seam pores, which represents the formation energy. It plays an important role in gas occurrence and CBM drainage. Based on the well testing, reservoir pressure, closure pressure, and corresponding burial depth data were collected in all the mining areas. A scatter diagram and a fitting analysis are shown in Figure 8. The reservoir pressure ranges from 3.74 to 11.58 MPa, which is relatively high. The fitting analysis shows that the reservoir pressure is influenced in linear and positive correlations by closure pressure and burial depth. These results show that the coal seam has higher formation energy, which is beneficial for CBM adsorption and desorption. On the other hand, the higher reservoir pressure might be caused by high

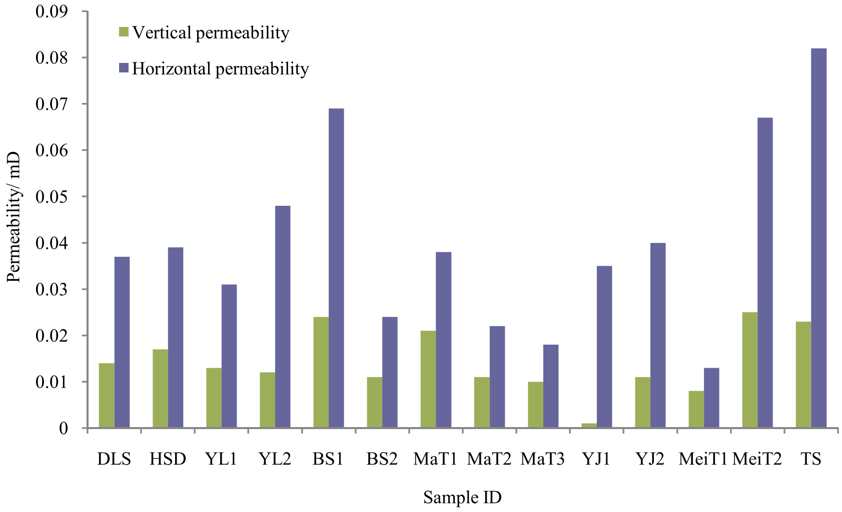

FIGURE 7
Histogram of vertical and horizontal permeability.

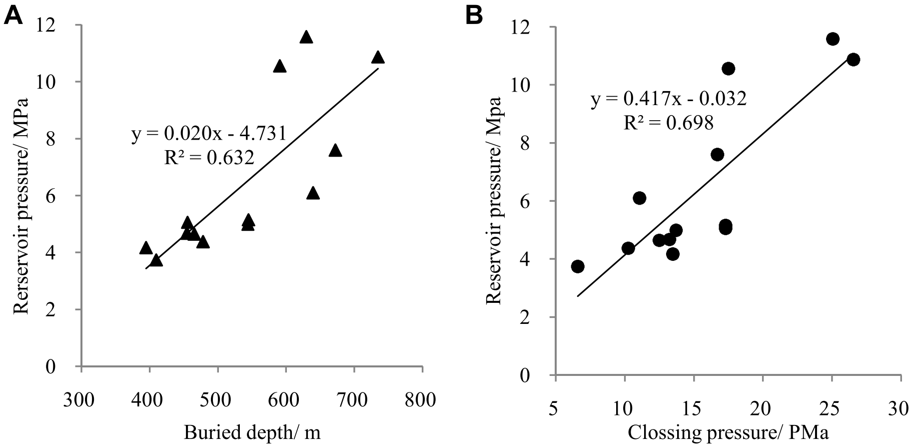

FIGURE 8
Fitting diagram of reservoir pressure versus burial depth **(A)** and crustal stress **(B)**.

crustal stress, often associated with tectonic coal and low permeability, which is unfavorable for CBM exploitation.

4.4 Adsorption characteristics

The isothermal adsorption measurement was conducted, and data pairs of Langmuir volume and pressure were both collected. The Langmuir volume is from 12.43 m^3/t to 33.27 m^3/t and is generally higher than 25 m^3/t. The Langmuir pressure varies from 1.05 to 3.63 Mpa and is mostly higher than 2 MPa. Thus, the overall Langmuir volume is large, indicating that the coal has a strong adsorption capacity. The fitting analyses between Langmuir volume/Langmuir pressure and maximum vitrinite reflectance are shown in Figure 9. This figure shows that a quadratic polynomial relation exists between Langmuir volume and maximum vitrinite reflectance, with a fitting degree of about 0.71. A weak and negative correlation exists between Langmuir pressure and maximum vitrinite reflectance.

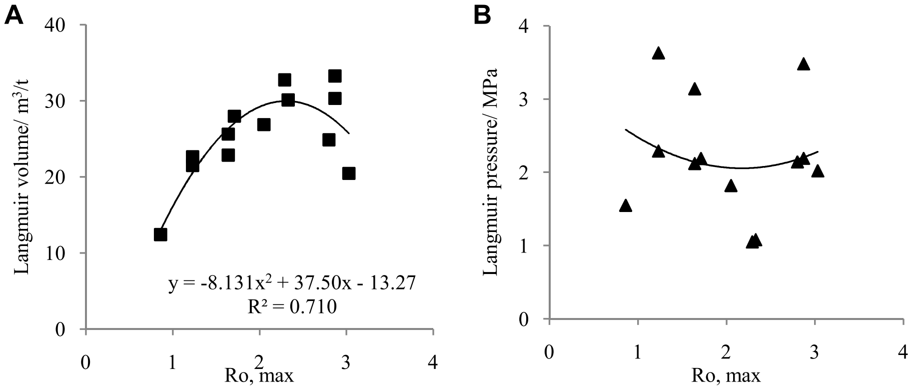

FIGURE 9
Fitting diagram between maximum vitrinite reflectance versus Langmuir volume **(A)** and Langmuir pressure **(B)**.

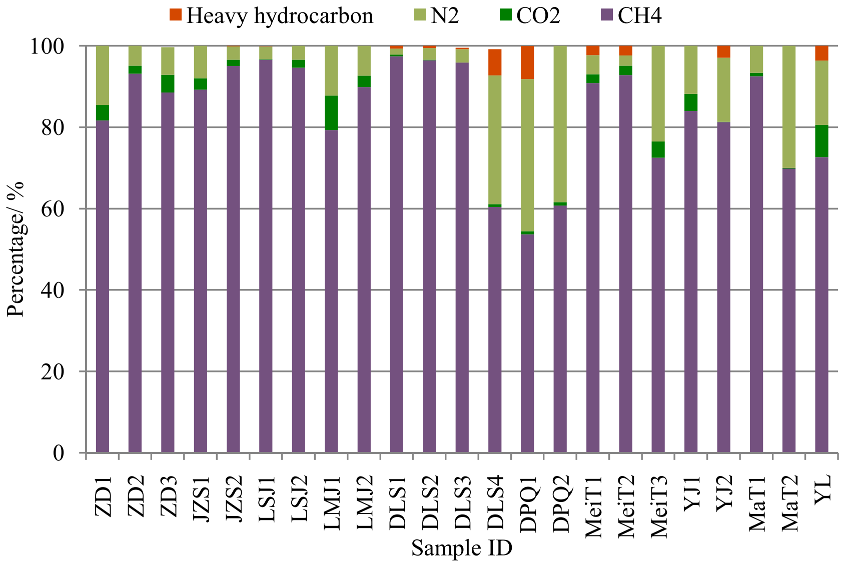

FIGURE 10
Histogram of gas components.

4.5 Gas-bearing characteristics

4.5.1 Gas component analysis

Gas component analysis was conducted for the gas samples, and the results are shown in Figure 10. Methane is the main component, and its percentage ranges from 53.7 to 97.68%, generally higher than 80%. The CO_2 percentage varies between 0.04 and 8.42%, generally higher than 2%. The N_2 percentage is between 1.5–38.4%, and the average is 12.5%. The heavy hydrocarbon percentage is between 0.067–8.11%, with an average of 2.6%.

4.5.2 Gas content

The gas content of 42 points of mining areas in the research area was collected, as shown in Figure 11. The gas content ranges between 2.0 m^3/t and 30.3 m^3/t, and most values are between 5–20 m^3/t. Therefore, CBM is relatively abundant in this area, according to China's national standard of GB/T 29119-2012.

4.6 Recoverability evaluation

Based on isothermal adsorption measurements, the recoverability can be calculated as follows. The gas content under

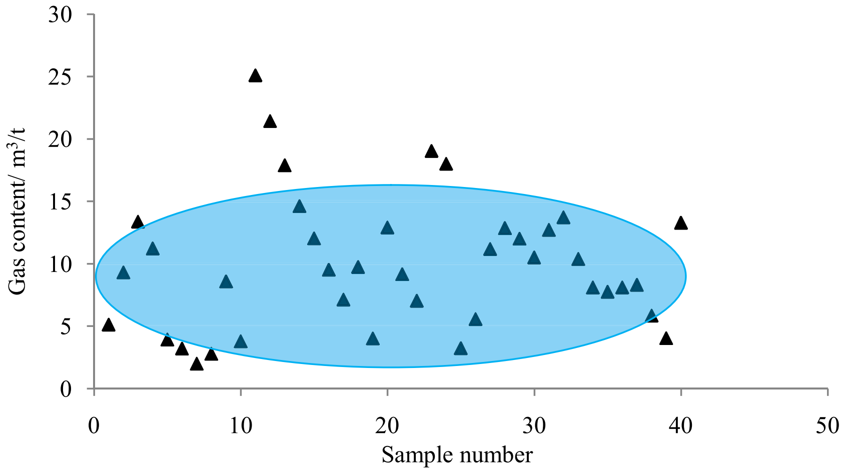

FIGURE 11
Scatter diagram of gas content.

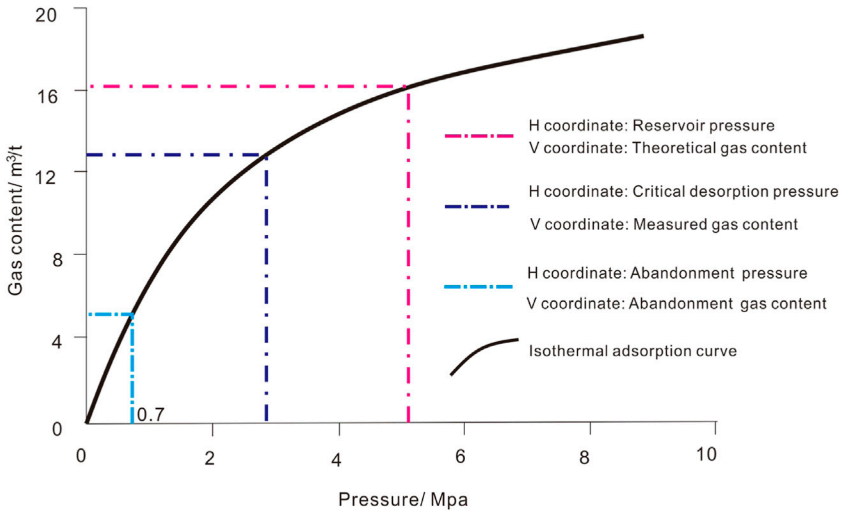

FIGURE 12
Isothermal adsorption curve and its major parameters (H: horizontal; V: vertical).

abandonment pressure (usually 0.7 MPa) can be distinguished by projecting 0.7 MPa to the isothermal adsorption curve, and the recoverability is then calculated using this gas content divided by the measured gas content. The major parameters are shown in Figure 12. Data on three points in Hongshandian and Duanpoqiao mining areas are taken as examples, and calculation results are listed in Table 2. The theoretical recoverability in the Hongshandian mining area is as high as 61.7%, while the values of the two points in the Duanpoqiao mining area are 49.1 and 54.5%. Therefore, the theoretical recoverability is relatively high in this area, indicating a high CBM exploitation value.

5 CBM productivity prediction

A typical CBM well, named well ZD01, in the Zhadu mining area is used as an example. With an assumption of a reasonable drainage system, the CBM productivities of a single well and well

TABLE 2 Recoverability evaluations for mining areas of Hongshandian and Duanpoqiao.

Coal area	HSD	DPQ1	DPQ2
Measured gas content/m^3/t	18.46	11.2	12.87
Reservoir pressure/MPa	4.65	4.43	5.10
Langmuir volume/m^3/t	27.97	22.66	23.05
Langmuir pressure/MPa	2.188	2.15	2.16
Calculated gas saturation/%	66.0	49.3	55.84
Measured gas saturation/%	97.1	73.4	79.5
Critical desorption pressure/MPa	4.25	2.10	2.70
Ratio of critical desorption pressure and reservoir pressure	0.92	0.48	0.54
Calculated recoverability/%	61.7	49.1	54.5

TABLE 3 Reservoir parameters for well ZD01.

Parameter	Value	Source
Buried depth	600 m	Tested
Permeability	0.01; 0.05; 0.1 mD	Set
Porosity	9%	Tested
Thickness	4.2 m	Tested
Gas content	22.4 m^3/t	Tested
Fracture length	140 m	Experience
Langmuir volume	30 m^3/t	Tested
Langmuir pressure	2.15 MPa	Tested
Reservoir pressure	6.0 MPa	Tested

net group in the study area are predicted using the COMET3 numerical simulation software.

5.1 Reservoir parameters

Reservoir parameters required in the simulation are shown in Table 3. It should be noted that before CBM drainage, the reservoir should be stimulated to improve the reservoir permeability. Based on actual permeability, permeability values of 0.01 mD, 0.05 mD, and 0.10 mD were set in this study.

5.2 Productivity prediction for a single well

Productivity prediction in 10 years for well ZD01 is shown in Figure 13. Under the three permeability values, the largest daily gas production is about 1,500–1,600 m^3/d. On day 250, the gas production reaches its peak value. The daily gas production is about 900–1,400 m^3/d on day 500, while it is about 600–1,000 m^3/d on day 1,000. The cumulative gas production is 1.7–3.2 × 10^6 m^3, with an average value of 2.4 × 10^6 m^3.

5.3 Productivity prediction for well net group

The well distance was set as 300 m. Production prediction in 10 years for a 5-well group was made using COMET3 software, and the results are shown in Figure 14. The maximum daily gas production of the well group is about 9,200–10,000 m^3/d. The

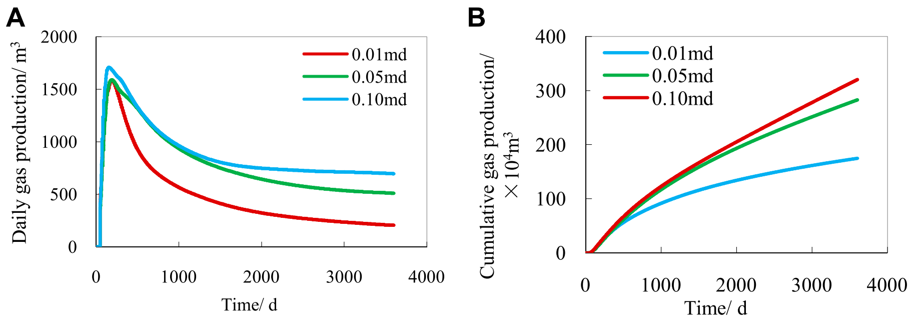

FIGURE 13
Daily **(A)** and cumulative **(B)** gas production for well ZD01.

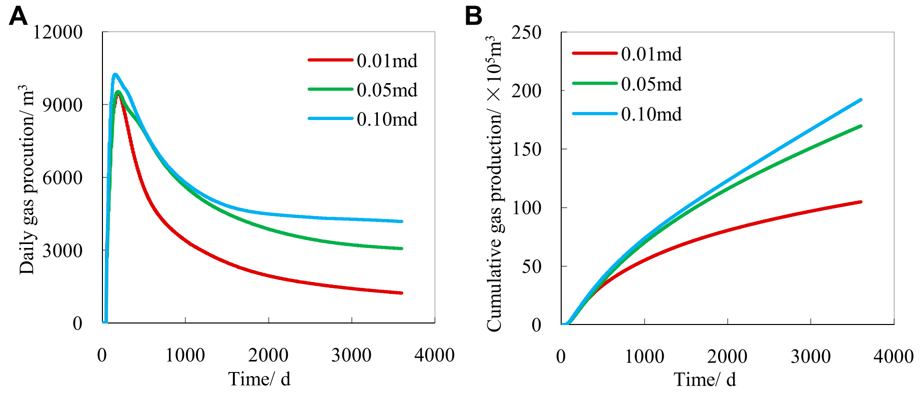

FIGURE 14
Daily **(A)** and cumulative **(B)** gas productions for a five-well group.

cumulative gas production in the first year is about 2.64 × 10^6 m^3, while it is 10.5–19.2 × 10^6 m^3 in 10 years, with an average of 14.5 × 10^6 m^3. Thus, it can be seen that there will be a high gas production in the study area after reservoir stimulation to obtain a good permeability.

6 Conclusion

The CBM geological occurrences of representative mining areas in the central Hunan depression were studied in this paper by measuring the maceral component, scanning electron microscope analysis, mercury intrusion porosimetry, permeability tests, isothermal adsorption measurements, well testing analysis, and gas content measurements. The drainage performance of a single well and a well group in the studied area were predicted using the numerical simulation method.

It was found that the vitrinite ranges from 54.37 to 87.80%, the inertinite is between 11.14 and 25.89%, and the exinite is less than 1%. The remaining 0.71–5.66% is an inorganic component, mainly clay mineral.

Most porosity is between 7 and 9%. The fitting analysis shows that the porosity negatively correlates with vitrinite content and positively correlates with inertinite content. Also, the porosity is negatively correlated with inorganic components and positively correlated with maximum vitrinite reflectance. Both the vertical and horizontal permeability are relatively low, with most values lower than 0.05 mD, indicating that the reservoir has low or no permeability.

Reservoir pressure ranges from 3.74 to 11.58 Mpa. The pressure has significant positive linear correlations with closure pressure and burial depth. Gas content varies mainly from 5 m^3/t to 20 m^3/t. The theoretical recoverability in the Hongshandian mining area is up to 61.7%, and the theoretical recovery in the two points of the Duanpoqiao mining area is 49.1 and 54.5%.

Numerical simulation results show that the cumulative gas production in 10 years for a single well is 1.7–3.2 × 10^6 m^3, and the productivity of a well net group consisting of five wells is 10.5–19.2 × 10^6 m^3 under permeabilities of 0.01 mD, 0.05 mD, and 0.10 mD.

Data availability statement

The original contributions presented in the study are included in the article/Supplementary Material; further inquiries can be directed to the corresponding author.

Author contributions

NC: laboratory experiments and data analysis; KW: paper writing; and JD: production perdition.

Acknowledgments

The authors wish to acknowledge the financial support for this study provided by the Scientific Research Project of the Natural Resource Department of Hunan Province under grant no. 2015-01.

Conflict of interest

The authors declare that the research was conducted in the absence of any commercial or financial relationships that could be construed as a potential conflict of interest.

Publisher's note

References

Bustin, R. M., and Clarkson, C. R. (1998). Geological controls on coalbed methane reservoir capacity and gas content. *Int. J. Coal Geol.* 38 (1-2), 3–26. doi:10.1016/s0166-5162(98)00030-5

Curtis, J. B. (2002). Fractured shale gas systems. *AAPG Bull.* 86 (11), 1921–1938. doi:10.1306/61EEDDBE-173E-11D7-8645000102C1865D

Huang, J. (1990). A further discussion of geochemical characteristics of natural gases in the Sichuan basin. *Geochimica* 3 (1), 307–321 [in Chinese with an English abstract]. doi:10.19700/j.0379-1726.1990.01.004

Laubach, S. E., and Gale, J. F. W. (2006). Obtaining fracture information for low permeability (tight) gas sandstones from sidewall cores. *J. Pet. Geol.* 29 (2), 147–158. doi:10.1111/j.1747-5457.2006.00147.x

Law, B. E. (2002). Basin-centered gas systems. *AAPG Bull.* 86 (11), 189–191. doi:10.1306/61EEDDB4-173E-11D7-8645000102C1865D

Law, B. E. (2002). Introduction to unconventional petroleum systems. *AAPG Bull.* 86 (11), 1851–1852. doi:10.1306/61EEDDA0-173E-11D7-8645000102C1865D

Li, Y., Wang, Y., Meng, S., Wu, X., Tao, C., and Xu, W. (2020). Theoretical basis and prospect of coal measure unconventional natural gas co-production. *J. China Coal Soc.* 45 (4), 1406–1418 [in Chinese with an English abstract]. doi:10.13225/j.cnki.jccs.2019.1305

Liu, X., and Wu, C. (2017). Simulation of dynamic changes of methane state based on NMR during coalbed methane output. *Fuel* 194, 188–194. doi:10.1016/j.fuel.2017.01.011

Liu, A., Fu, X., Wang, K., An, H., and Wang, G. (2013). Investigation of coalbed methane potential in low-rank coal reservoirs – free and soluble gas contents. *Fuel* 112, 14–22. doi:10.1016/j.fuel.2013.05.032

Martini, A. M., Walter, L. M., Ku, T. C., Budai, J. M., McIntosh, J. C., and Schoell, M. (2003). Microbial production and modification of gases in sedimentary basins: A geochemical case study from a devonian shale gas play, Michigan basin. *Am. Assoc. Pet. Geol. Bull.* 87 (8), 1355–1375. doi:10.1306/031903200184

Qin, Y. (2018). Research progress of symbiotic accumulation of coal measure gas in China. *Nat. Gas. Ind.* 38 (4), 26–36. doi:10.1016/j.ngib.2018.04.013

Schmoker, J. W. (1980). Organic content of Devonian shale in Western Appalachian basin. *AAPG Bull.* 64, 2156–2165. doi:10.1306/2F919756-16CE-11D7-8645000102C1865D

Sun, X., Zhang, Y., Li, K., and Gai, Z. (2016). A new mathematical simulation model for gas injection enhanced coalbed methane recovery. *Fuel* 183, 478–488. doi:10.1016/j.fuel.2016.06.082

Tao, S., Pan, Z., Tang, S., and Chen, S. (2019). Current status and geological conditions for the applicability of CBM drilling technologies in China: A review. *Int. J. Coal Geol.* 202, 95–108. doi:10.1016/j.coal.2018.11.020

Wang, B., Jiang, B., Liu, L., Zheng, G., Qin, Y., Wang, H., et al. (2009). Physical simulation of hydrodynamic conditions in high rank coalbed methane reservoir formation. *Min. Sci. Technol.* 19 (4), 435–440. doi:10.1016/s1674-5264(09)60081-8

Wei, Z. J., and Zhang, D. X. (2010). Coupled fluid flow and geomechanics for triple-porosity/dual permeability modeling of coalbed methane recovery. *Int. J. Rock Mech. Min. Sci.* 47 (8), 1242–1253. doi:10.1016/j.ijrmms.2010.08.020

Wei, C., Qin, Y., Wang, G. X., Fu, X., Jiang, B., and Zhang, Z. (2007). Simulation study on evolution of coalbed methane reservoir in Qinshui Basin, China. *Int. J. Coal Geol.* 72 (1), 53–69. doi:10.1016/j.coal.2006.12.001

Wei, C., Qin, Y., Wang, G., Fu, X., and Zhang, Z. (2010). Numerical simulation of coalbed methane generation, dissipation and retention in SE edge of Ordos Basin, China. *Int. J. Coal Geol.* 82 (3-4), 147–159. doi:10.1016/j.coal.2009.12.005

Zhang, J., and Bian, X. (2015). Numerical simulation of hydraulic fracturing coalbed methane reservoir with independent fracture grid. *Fuel* 143 (10), 543–546. doi:10.1016/j.fuel.2014.11.070

Zhang, J. (2014). Numerical simulation of hydraulic fracturing coalbed methane reservoir. *Fuel* 136, 57–61. doi:10.1016/j.fuel.2014.07.013

Zou, M., Wei, C., Fu, X., Bao, Y., and Cai, Z. (2013). Investigating reservoir pressure transmission for three types of coalbed methane reservoirs in the Qinshui Basin in Shan'xi Province, China. *Pet. Geosci.* 19, 375–383. doi:10.1144/petgeo2011-083

Zou, M., Wei, C., Yu, H., and Song, L. (2015). Modeling and application of coalbed methane recovery performance based on a triple porosity/dual permeability model. *J. Nat. Gas. Sci. Eng.* 22, 679–688. doi:10.1016/j.jngse.2015.01.019

Zou, M., Wei, S., Huang, Z., Lv, X., and Guo, B. (2018). Simulations on recoverability performances for a coalbed methane field in SE edge of Ordos basin, China. *Fuel* 233, 354–360. doi:10.1016/j.fuel.2018.06.071

Zou, C., Yang, Z., Huang, S., Ma, F., Sun, Q., Li, F., et al. (2019). Resource types, formation, distribution and prospects of coal-measure gas. *Petroleum Explor. Dev.* 46 (3), 451–462. doi:10.1016/s1876-3804(19)60026-1

frontiers | Frontiers in Earth Science

TYPE Original Research
PUBLISHED 21 September 2022
DOI 10.3389/feart.2022.1019716

OPEN ACCESS

EDITED BY
Junjian Zhang,
Shandong University of Science and Technology, China

REVIEWED BY
Yu Wang,
University of Science and Technology Beijing, China
Huang Zhihuai,
Pearl River Hydraulic Research Institute, China

*CORRESPONDENCE
Huaichang Yu,
yuhuaichanghb@126.com

SPECIALTY SECTION
This article was submitted to Economic Geology,
a section of the journal
Frontiers in Earth Science

RECEIVED 15 August 2022
ACCEPTED 05 September 2022
PUBLISHED 21 September 2022

CITATION
Yu H, Wang G, Zhang Z, Niu R and Cheng G (2022), Experimental study on the effect of prefabricated fissures on the creep mechanical properties and acoustic emission characteristics of sandstone under uniaxial compression. *Front. Earth Sci.* 10:1019716.
doi: 10.3389/feart.2022.1019716

Experimental study on the effect of prefabricated fissures on the creep mechanical properties and acoustic emission characteristics of sandstone under uniaxial compression

Huaichang Yu[1,2]*, Guanqiang Wang[1], Zhongyu Zhang[3], Rui Niu[1] and Guangli Cheng[4]

[1]College of Geosciences and Engineering, North China University of Water Resources and Electric Power, Zhengzhou, China, [2]Henan Province Key Laboratory of Rock and Soil Mechanics and Structural Engineering, Zhengzhou, China, [3]School of Mechanics and Civil Engineering, China University of Mining and Technology, Beijing, China, [4]Beijing Engineering Corporation Limited, Beijing, China

This study investigates the effect of prefabricated fissures on the creep mechanical strength and acoustic emission (AE) characteristics of sandstone. Under the same test conditions, indoor uniaxial compression creep AE tests were performed on intact and artificially fissured sandstone specimens using a rock rheometer and a PCI-II AE tester controlled with an RLJW-2000 microcomputer. The variation characteristics of strain, long-term strength, number of AE events, AE ringing count, AE energy, and RA value of the two specimens were then analyzed to determine the effect of prefabricated fissures on the creep mechanical properties and AE characteristics of sandstone. The results show that under the same stress level, the instantaneous strain, creep strain, and total strain of the prefabricated fissures specimen was larger than the corresponding values of the intact specimen. The prefabricated fissures exhibited the most significant influence on the creep strain of the specimen, followed by the total strain. The fissures showed the least influence on the instantaneous strain of the specimen. Furthermore, the long-term strength of the prefabricated fissures specimen was only 37.5% of that of the intact specimen. Owing to the influence of the prefabricated fissures, the long-term strength of the sandstone was significantly reduced. In engineering practice, fissures should be noted and analyzed for the potential failure of a formation. Moreover, as the stress level increases, the number of AE events of the specimen also increases. The number of AE events and cumulative AE events generated by the prefabricated fissures specimen at various stress levels is significantly higher than the corresponding values of the intact specimen. The maximum ringing count of the prefabricated fissures specimen was 7.3 times that of the intact specimen, and the maximum AE energy was 3.8 times that of the intact specimen. The cumulative AE ringing count was 1.5 times that of the intact specimen, and the cumulative energy was 4.5 times that of the intact specimen. The prefabricated fissures significantly affect the maximum AE ringing count, maximum AE energy, cumulative AE ringing count, and cumulative AE energy of the specimen. Finally, tensile fissures were the main microcracks generated inside the intact specimen during creep, and shear cracks were secondary. The microcracks generated inside the prefabricated fissures specimen consisted of mixed tension-shear cracks, but mainly consisted of shear cracks with fewer tension cracks. The RA value correlates well with the observed internal microcracks, indicating that the RA value can be used to characterize fractures in sandstone specimens. The RA value has a guiding significance for characterizing the type of internal microcracks in the process of rock creep.

KEYWORDS

sandstone, prefabricated fissures, creep, acoustic emission, uniaxial compression

Introduction

A fissured rock mass is one of the most common and essential geological media in water conservancy, mining, transportation, energy, national defense, and other industries (Vásárhelyi and Bobet, 2000; Haeri et al., 2014). Owing to the rock formation and tectonic movement, joints, and fissures with different scales are present inside the rock mass. The deformation and failure characteristics of a fissured rock mass directly affect the safety and stability of large-scale underground powerhouses, ultra-long hydraulic tunnels, underground energy storage, and underground nuclear waste isolation. It is one of the critical factors that should be considered in engineering design, construction, and long-term operation. Numerous engineering practices show that the fracture and instability of engineering rock mass are mostly caused by the initiation, expansion, and penetration of cracks of various scales in the rock mass under the action of environmental forces. In engineering, processes occurring in a fissured rock mass from the initial deformation to the final rupture and instability constitute a time-dependent and complex non-linear progressive process, and in this process, the rock mass undergoes creep failure. For example, the marble of Jinping I Hydropower Station in China, the gneiss of Xiaowan Hydropower Station, and the granite of the Three Gorges Hydropower Station all show substantial creep deformation and failure characteristics, along with well-developed fissures (Yang et al., 2018). Therefore, investigation of the effect of fissures on the creep characteristics of rock mass is significantly essential research and has very important engineering practical significance for revealing the fracture mechanism of rock mass, evaluating the long-term stability of rock mass engineering, and taking reasonable preventive measures.

Scholars have performed conventional mechanical tests on fissured rock masses to study the effect of fissures on the mechanical characteristics of rock masses. Some researchers used similar materials such as gypsum and cement mortar to fabricate fissured rock masses and conducted laboratory experiments on the mechanics. Feng et al. (2018) conducted uniaxial compression tests on rock-like specimens with two different fissures inclination angles and studied the effect of strain rate on the mechanical behavior of the specimens. Li et al. (2020) conducted uniaxial compression tests on double-fissure-like sandstone specimens and analyzed the fracture failure characteristics and strength loss laws of the specimens under different rock bridge inclination angles. Yi et al. (2021) conducted uniaxial compression tests on rock-like materials with different inclination angles and different numbers of fissures. They analyzed the influence of these variables on the strength and deformation characteristics of the specimen. Chen et al. (2012) systematically studied the influence of fracture connectivity on the uniaxial compression strength, deformation, and fracture characteristics of the rock mass. These studies have enriched the research on the conventional mechanical properties of fractured rock masses in rock-like materials. However, these studies did not take into account fissures in natural specimens.

Furthermore, studies have also been conducted on natural rock specimens with prefabricated fissures via laboratory mechanical test experiments. For instance, Yang and Jing, 2011 conducted uniaxial compression tests on single-fracture brittle sandstone specimens and studied the effects of the length and inclination of the fissures on the strength, deformation, and failure behavior of sandstone materials. Huang and Huang, 2010 conducted uniaxial compression tests on marble with prefabricated fissures and analyzed the influence of the fissures on mechanical characteristics. Lu et al. (2015) conducted a uniaxial compression test on sandstone with a single three-dimensional (3D) surface crack and studied the influence of the geometric parameters of the crack on the strength of the sandstone. These studies have enriched the effect of cracks on mechanical properties of real rock under uniaxial compression. Although effective, these techniques did not include acoustic emissions (AE), which can significantly enhance their findings and application in the field.

Researchers have also combined AE technology to further study the mechanics and AE characteristics of fissured rock masses (Zhu et al., 2019; Song, 2021). Wang et al. (2019)

conducted AE tests on the whole and prefabricated fissured sandstone specimens under uniaxial compression. They analyzed the influence of the prefabricated fissures on the mechanical properties and AE characteristics. Yang et al. (2013) conducted a uniaxial compression test on red sandstone with two non-parallel fissures and used AE monitoring technology to analyze the influence of the fracture inclination on the strength, deformation, and failure characteristics of red sandstone. These studies used AE technology to further explain the mechanical properties of fractured rock masses but have not addressed creep failure in the specimens. They focused on brittle failure rather than plastic and elastic deformation.

Overall, most rocks under stress undergo creep failure due to the constant load for an extended period, leading to a project's instability and eventual catastrophe. This has been shown by various studies on creep AE tests of intact rock specimens. Xu et al. (2014) conducted creep AE tests on marble and analyzed the influence of different stress levels on internal damage. The AE number and energy release rate suddenly increased when the specimen was subjected to the creep process. Ma et al. (2018) conducted AE tests on coal samples with different moisture contents and studied the influence of moisture content on the creep characteristics of coal. The results showed that the AE characteristics of coal well reflected the evolution process of its creep damage. Zhao et al. (2020) studied the changes in axial stress-strain and AE signal time-frequency parameters of red sandstone specimens under uniaxial compression through the AE event rate, average frequency centroid, peak frequency, and amplitude, and revealed the failure mechanism of red sandstone. Chen et al. (2015) studied the effects of temperature and stress conditions on the creep failure process of granite based on granite creep tests under different temperature and stress states combined with real-time monitoring information of three-dimensional AE. Wu et al. (2016) conducted triaxial creep tests on rock salt and studied the AE characteristics during the first two stages of creep. Jiang et al. (2017) performed long-term and step-loading creep tests of sandstone and collected AE signals throughout the test. The statistical characteristics of the AE energy of the specimen were analyzed by using histogram statistics and maximum likelihood estimation. Shkuratnik et al. (2019) performed simultaneous AE and strain measurements on rock salt specimens and analyzed the changes in the parameters of the salt rock stability and progressive creep stages. Yao et al. (2019) conducted a triaxial creep AE test on sandstones with different water contents and studied the change in the AE RA value at each creep stage.

Overall, the above-mentioned studies have enriched the research results in rock AE experiments. However, the use of AE to understand the creep process of rock masses with prefabricated fissures has rarely been reported till date. The fissures have a significant impact on the creep damage of the rock mass and are one of the critical factors affecting the long-term stability of any engineering project. Therefore, it is necessary to further quantitatively study the effect of fissures on the AE characteristics of rock mass creep.

Therefore, in this study, the effects of prefabricated fissures on the stability and creep process of Triassic sandstone from the Xiaolangdi reservoir area were systematically studied. Under the same test conditions, indoor uniaxial compression creep AE tests were performed on intact sandstone specimens and prefabricated double-fissures sandstone specimens for comparative analysis. The variation characteristics of strain, long-term strength, number of AE events, AE ringing count, AE energy, and RA value of the two specimens were analyzed. The effects of prefabricated fissures on the creep mechanical properties and AE characteristics of sandstone were further obtained. The research results provide a scientific reference for the long-term stability and safety evaluation in rock engineering.

Specimen preparation and test methods

Specimen preparation

The rock blocks used in the test were obtained from the Triassic sandstone in the Dongmiaojia landslide of the Xiaolangdi Reservoir. The sampling site is shown in Figure 1. After arriving in the laboratory, the rock blocks were cut using CNC machine tools. Rectangular parallelepiped specimens with a size of 70 mm × 70 mm × 140 mm (length × width × height) were cut. The uneven deviation of the end surface of the specimen was controlled within the range of ±0.05 mm, and the deviation of the verticality of the end face to the axis was controlled within ±0.25° (Ulusay and Hudson, 2007).

The prefabricated fissures specimen consisted of double-fissures that spanned at an angle through the specimen. The geometric characteristics of the fissures are shown in Figure 2. The length of the fissures was $2a = 30$ mm, and the distance between the top ends of the fissures was $2b = 25$ mm. The inclination angle of the fissure was $\alpha = 45°$, where a is the angle formed by the fissure and the horizontal direction. The inclination angle of the rock bridge was $\beta = 135°$, where β is the angle formed between the top line inside the fissure and the horizontal direction.

The prepared intact specimen and the specimen with prefabricated fissures are shown in Figure 3.

Test method

A microcomputer (RLJW-2000) was used to control the rock rheometer and AE tester (PCI-II). Indoor uniaxial compression

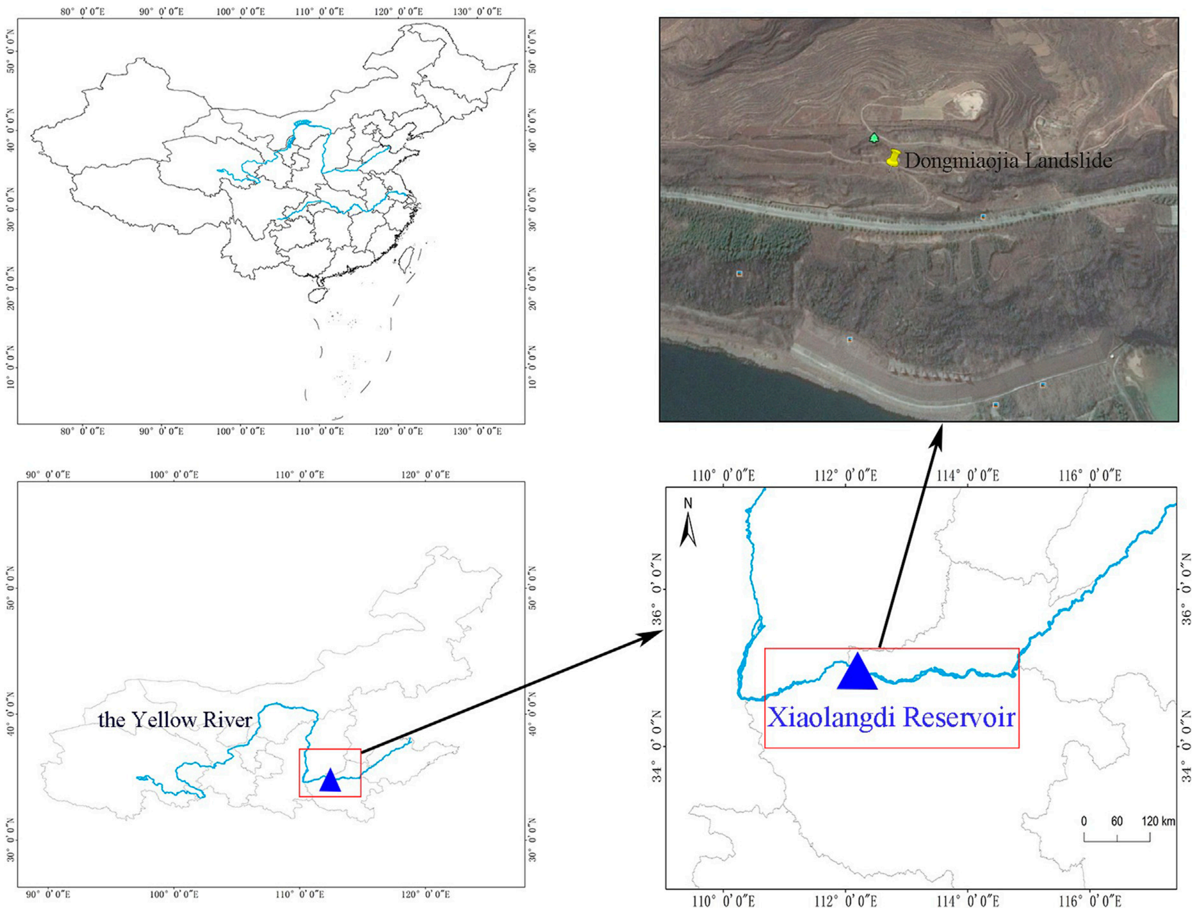

FIGURE 1
Sampling site in the Xiaolangdi Reservoir.

creep AE tests were carried out on the intact and prefabricated double-fissures specimens under the same test conditions.

Axial stress was applied in 15 MPa increments *via* the stepped loading method to compare the creep mechanical properties of the two specimens under the same stress level. Before the failure of the specimen, the axial stress increments were appropriately reduced according to the AE characteristics of the specimen to avoid specimen failure during the loading process. After loading to the first stress level value, the load was kept constant for 2 h and then reloaded to the next stress level value until the specimen underwent creep failure. The stress loading rate was 0.40 $kN \cdot s^{-1}$. In the test, the deceleration creep stage of the specimen usually lasted about 0.1 h, and the constant creep stage lasted for about 1.0 h after the specimen reached the steady-state creep stage.

Eight R6A AE probes for signal acquisition were used. The probes were arranged in four layers along the side of the specimen to avoid the coplanarity of adjacent probes affecting the acquisition of AE signals. The probe layout is shown in Figure 4. Petroleum jelly was applied to the surface of the AE probe, which was then bonded to the surface of the specimen. The AE threshold was 45 dB, the preamp gain was 40 dB, the specimen rate was one million times s^{-1}, and the filter frequency was in the range of 1 kHz–1 MHz.

The YR-1 rock deformation testing system was used to measure the deformation of the test specimen. The AE and deformation test system used in the experiment is shown in Figure 5.

The stress loading was strictly maintained throughout the experiment. The deformation and AE monitoring were performed simultaneously during the test. The stress, strain, and AE parameters of the two specimens were studied throughout the whole process of change in rock creep change with time. Two sets of parallel tests were performed on the prefabricated fissures specimen, and two sets of parallel comparative tests were also performed on the intact specimens to reduce the dispersion of the test results.

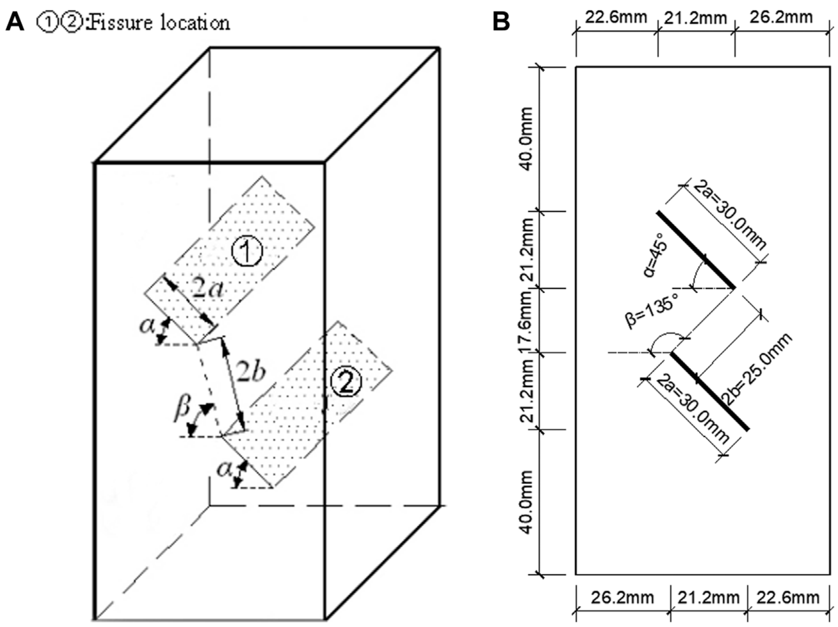

FIGURE 2
The geometric characteristics of the fissures. **(A)** Fissure stereogram. **(B)** Fissure size arrangement.

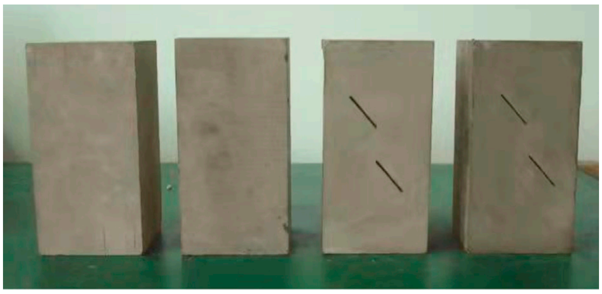

FIGURE 3
Typical sandstone rock specimens without and with fabricated fissures.

Results

Conventional physical and mechanical tests were performed on sandstone specimens. The measured density of the sandstone specimen was 2.64 g·cm^{-3}, the uniaxial compressive strength of the intact specimen was 170.5 MPa, and the uniaxial compressive strength of the prefabricated fissures specimen was 104.9 MPa.

The parallel test results were similar, therefore, representative test results were selected from the intact specimen and the prefabricated fissures specimen for analysis. The graded loading creep curves of the two specimens are shown in Figure 6.

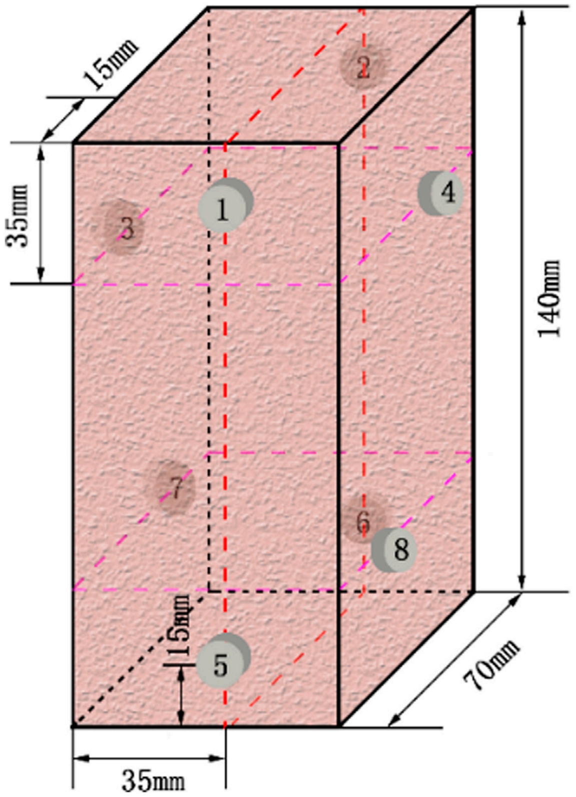

FIGURE 4
Layout of AE sensor probes.

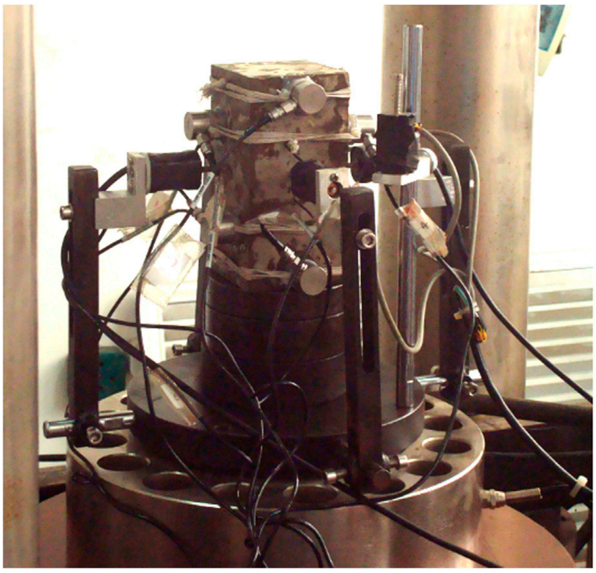

FIGURE 5
AE and deformation test system.

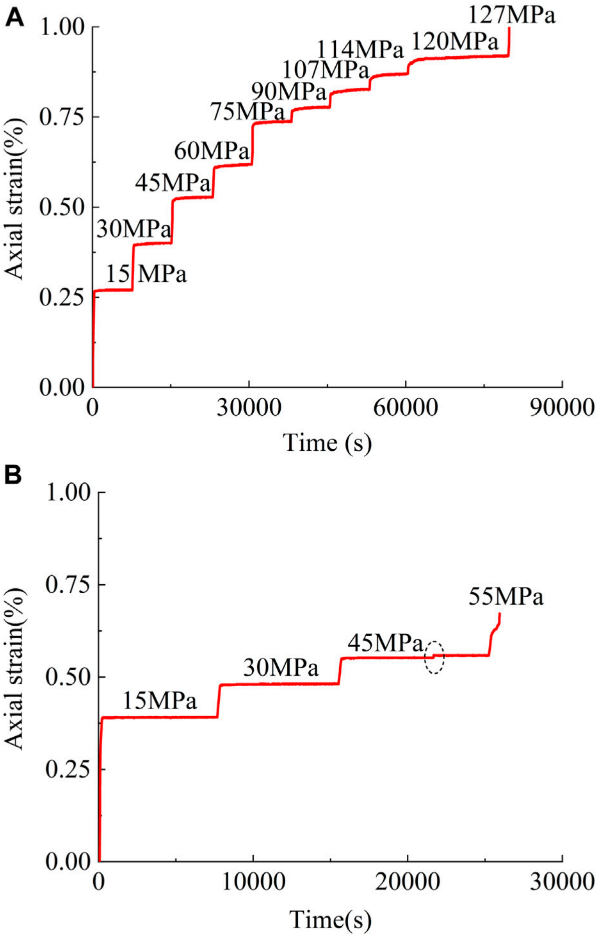

FIGURE 6
Creep curves of sandstone specimen under multi-step loading.**(A)** Intact specimen, and **(B)** prefabricated fissures specimen.

The number on the curve in Figure 6 represents the value of the applied stress level. In the test, 10 and 4 stress levels were applied to the intact specimen and the prefabricated fissures specimen, respectively. The first three stress levels were 15, 30, and 45 MPa for both specimens. Both specimens underwent accelerated creep failure under the action of the last stress level.

Specimen creep mechanical properties

Strain characteristics

According to the hierarchical loading curve shown in Figure 6, Chen's loading method (Tan and Kang, 1980) was used to transform it into a separate loading creep curve, as shown in Figure 7. The creep curves of the two specimens under the first several stress levels can be divided into two stages, namely, deceleration creep and constant velocity creep. Under the last stress level, the creep curve of the specimens can be divided into three stages, namely, decelerating creep, constant velocity creep, and accelerated creep. Noteworthy, the strain curve of the intact rock specimen at the last stress level undergoes the above-mentioned three stages, and the creep time lasts only 91 s. Therefore, the three stages of the strain curve of the intact specimen at the last stress level are not visually displayed in Figure 6A. The creep curves of the intact specimen at all stress levels are relatively straight and smooth, while the creep curves of the prefabricated fissures specimen exhibit a significant step-like sudden increase at a stress level of 45 MPa. Overall, the intact specimen does not undergo the same creep process as the specimen with prefabricated fissures. Under constant stress, the internal cracks in the specimen gradually initiated and expanded over time, and the deformation of the specimen was continuous without a sudden increase. Owing to the influence of prefabricated fissures, stress concentration was likely to occur at the ends of the prefabricated fissure. The secondary microcracks along the ends of prefabricated fissures continued to sprout, expand, overlap, and partially penetrate each other, resulting in a sudden increase in the creep curve.

Under various stress levels, the axial strain of the intact specimen and the prefabricated fissures specimen can be divided into instantaneous strain and creep strain. When the stress is applied at each level, the specimen deforms instantaneously, and then under constant stress, the deformation of the specimen

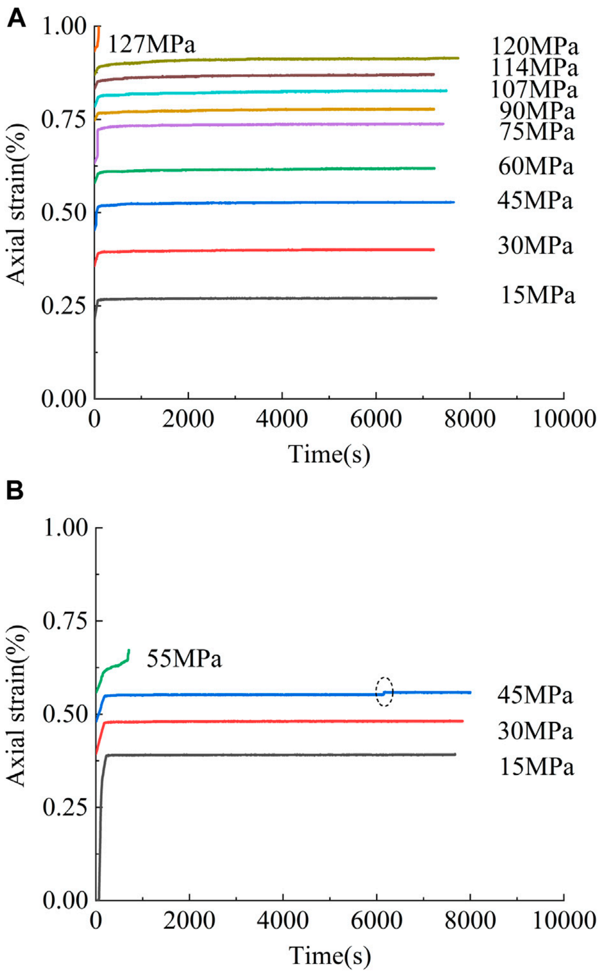

FIGURE 7
Creep Curves of sandstone specimen under respective loading. **(A)** Intact specimen. **(B)** Prefabricated fissures specimen.

increases with time (Yu et al., 2012, Yu et al., 2017). The axial instantaneous strain, creep strain, and total strain of the two specimens under the same first three stress levels are shown in Table 1. Table 1 shows the ratios of the strain of the intact specimen to the strain of the prefabricated fissures specimen.

With the increase in the stress level, the instantaneous strain, creep strain, and total strain of the two specimens gradually increase. Under the same stress level, the instantaneous strain, creep strain, and total strain of the prefabricated fissures specimen are greater than the corresponding values of the intact specimen. The instantaneous strain of the intact specimen is 69.2%–94.4% of the prefabricated fissures specimen, and the creep strain is 57.1%–71.4%, and the total strain is 69.0%–93.8%. Under the same stress level, the creep strain difference between the intact and prefabricated fissures specimen is the largest, followed by the total strain and the instantaneous strain. This indicates that prefabricated fissures have the most significant influence on the creep strain of the specimen.

Long-term strength

Long-term strength is one of the critical parameters for evaluating long-term stability and safety of any engineering project. Researchers have realized the importance of long-term rock strength to long-term stability and safety of some major projects. However, the current research results mainly focus on the long-term strength of macroscopically intact rock specimens, and the long-term strength of rock masses with prefabricated fissures has rarely been investigated. It is necessary to quantitatively study the effect of fissures on the long-term strength of the specimen.

The long-term strength is the maximum axial deviator stress corresponding to the load acting for a long enough time before the creep rupture of a rock specimen occurs (Wan et al., 2021; Zhang et al., 2011). The test results show the comparison between the conventional uniaxial compressive strength and the long-term strength of the two specimens as presented in Table 2. Compared with conventional uniaxial compressive strength, the long-term strengths of the two specimens are reduced to various degrees. The long-term strength of the intact specimen is 70.4% of the conventional uniaxial compressive strength, and the long-term strength of the prefabricated fissures specimen is 42.9% of the conventional uniaxial compressive strength. After considering the time effect, the long-term strength of the

TABLE 1 The instantaneous strain, creep strain, and total strain of specimens under the same stress level.

Stress level value (MPa)	Instantaneous strain (%)			Creep strain (%)			Total strain (%)		
	Intact specimen	Prefabricated fissures specimen	Ratio	Intact specimen	Prefabricated fissures specimen	Ratio	Intact specimen	Prefabricated fissures specimen	Ratio
15	0.267	0.386	0.692	0.004	0.007	0.571	0.271	0.393	0.690
30	0.394	0.475	0.829	0.006	0.009	0.667	0.400	0.484	0.826
45	0.519	0.550	0.944	0.010	0.014	0.714	0.529	0.564	0.938

TABLE 2 Comparison of conventional uniaxial compressive strength and long-term strength of specimens.

Specimen type	Conventional uniaxial compressive strength (MPa)	Long-term strength (MPa)
Intact specimen	170.5	120.0
Prefabricated fissures specimen	104.9	45.0

TABLE 3 Long-term strength of specimens.

Specimen type	Intact specimen (MPa)	Prefabricated fissures specimen (MPa)	Ratio (%)
Long-term strength	120.0	45.0	37.5

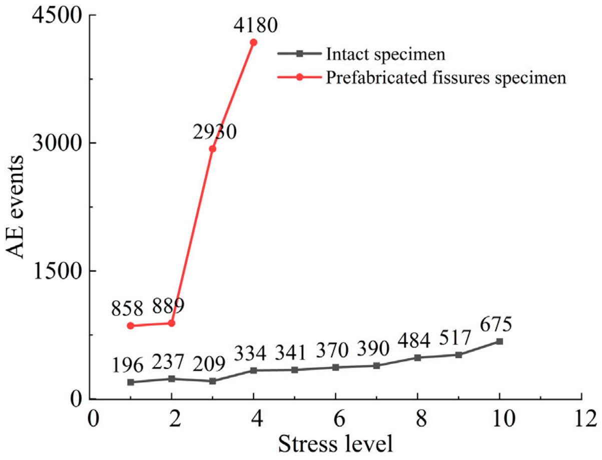

FIGURE 8
AE events of specimens under various stress levels.

specimen is significantly lower than its uniaxial compressive strength. Therefore, compared with the conventional uniaxial compressive strength commonly used in engineering, the long-term strength index of the specimen is more scientific and reasonable for the long-term stability and evaluation of operational safety of a project.

The comparative analysis of long-term strength of the two specimens is presented in Table 3.

Compared with the intact specimen, the long-term strength of the prefabricated fissures specimen is significantly reduced, only 37.5% of the long-term strength of the intact specimen. Long-term strength directly affects the long-term stability and safety of rock engineering. Therefore, the long-term rock strength drop caused by fissures should be addressed in engineering practice.

Acoustic emission characteristics of the specimen

Number of acoustic emission events

The number of AE events and cumulative AE events are parameters that reflect the degree of micro-fracture activity in the rock. Figure 8 shows the number of AE events of the specimen under various stress levels. With an increase in stress level, the number of AE events of the two specimens showed an overall increasing trend, indicating that the higher the stress level results in a greater number of AE events generated by the specimen. The number of AE events of the intact specimen under various stress levels is relatively small, and the curve shows a gentle upward trend with the increase in stress level. However, the number of AE events of the prefabricated fissures specimens under all stress levels is greater than those of the intact specimen.

When the stress levels of the first two levels are relatively small, the difference in the number of AE events between the two specimens is slight, and the curve rises gently. Under the third and fourth stress levels, the curve of the intact specimen still rises gently, while the curve of the prefabricated fissures specimen increases sharply. The number of AE events of the prefabricated fissures specimen increased sharply from 889 to 2,930 under the third stress level. This indicates that the internal fissures rapidly initiate, expand, overlap, and penetrate. Nonetheless, the number of AE events of the intact specimen under this stress level changes slightly. The number of AE events in the prefabricated fissures specimen increased from 2,930 to 4,180 under the fourth stress level, while the number of AE events in the intact specimen only increased from 209 to 334. At the last stress level, the number of AE events of the two specimens reached the maximum values. The number of AE events of the prefabricated fissures specimen was 4,180, which is 6.2 times the number of AE events of the intact specimen of 675. Consequently, the existence of

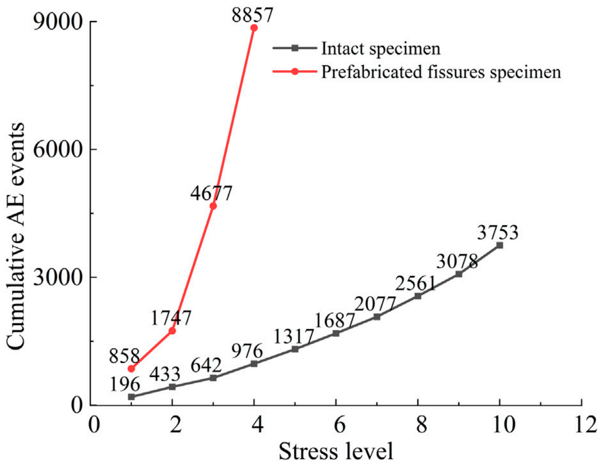

FIGURE 9
Cumulative AE events of specimens under various stress levels.

prefabricated fissures caused more AE events during the creep process of the specimen.

The number of accumulated AE events generated by the specimen under various stress levels is shown in Figure 9. Under various stress levels, the cumulative number of AE events of the intact specimen increases smoothly without sudden increase, with an almost linear slope. In contrast, the number of cumulative AE events of the prefabricated fissures specimen suddenly increases after the second stress level, and the slope of the curve changes significantly. The total number of cumulative AE events generated by the prefabricated fissures specimen reached 8,857, which is 2.4 times the total number of cumulative AE events of the intact specimen of 3,753. As a result, the existence of prefabricated fissures causes more accumulative AE events during the creep process.

In summary, due to the influence of prefabricated fissures, the number of AE events and cumulative AE events generated by prefabricated fissures specimen at various stress levels is significantly higher than the corresponding values of the intact specimen. Prefabricated fissures significantly impact the number of AE events and the number of cumulative AE events. This is attributed to the fact that under constant stress, microcracks easier to initiate, expand, overlap, and penetrate each other at the ends of the prefabricated fissures. In particular, before the final stress level accelerates the creep failure, the number of AE events and the number of cumulative AE events of the prefabricated fissures specimen increase sharply. Therefore, the existence of prefabricated fissures leads to more violent micro-fracture activities inside the specimen and more AE events.

Ringing count and energy

During the creep process, the AE ringing count, AE energy, accumulated AE ringing count, and accumulated AE energy exhibit certain regularities. The axial strain-AE ringing count-cumulative AE ringing count-time curves of the two specimens are shown in Figure 10, and the axial strain-AE energy-cumulative AE energy-time curves of the two specimens are shown in Figure 11. The AE ringing count and AE energy change characteristics are similar during the entire creep process of the two specimens. At each stage of stress loading, the AE ringing count and AE energy of the specimens increase continuously with the increase of time. In contrast, at each stage of constant stress, the AE ringing count and AE energy of the specimens continuously reduce with the increase of time. Therefore, the AE ringing count and AE energy of the specimens exhibit an increase–decrease trend with the increase of time. The AE ringing count and AE energy increase over time under constant stress and show a constant decreasing trend. In the accelerated creep stage during the last stress level, the AE ringing count and the AE energy of the two specimens reach their maximum values. Compared with the intact specimen, the concentration of the AE signal of the prefabricated fissures specimen at this stage is more prominent. AE ringing count and AE energy of the two specimens are presented in Table 4.

The maximum AE ringing count and maximum AE energy of the prefabricated fissures specimen are significantly higher than the corresponding values of the intact specimen. The maximum AE ringing count of the prefabricated fissures specimen is 7.3 times that of the intact specimen, and the maximum AE energy is 3.8 times that of the intact specimen. The prefabricated fissures significantly affect the maximum AE ringing count and maximum AE energy of the specimen.

Furthermore, the change in the cumulative AE ringing count and cumulative AE energy of the two specimens are similar to the change in the specimen strain curve. During the loading stage, the rapid linear rise indicates that the internal cracks of the specimen are constantly initiating and expanding at this stage. As the time prolongs, the curve rises slowly in the constant loading stage, indicating the slowing down of the growth and penetration rate of the internal cracks in the specimen at this stage. The accumulative AE ringing count and accumulative AE energy rise of the prefabricated fissures specimen under the last stress level are significantly larger than the corresponding values of the intact specimen.

The cumulative AE ringing count and cumulative AE energy of the two specimens before the final stress level accelerate the creep failure as presented in Table 4. The

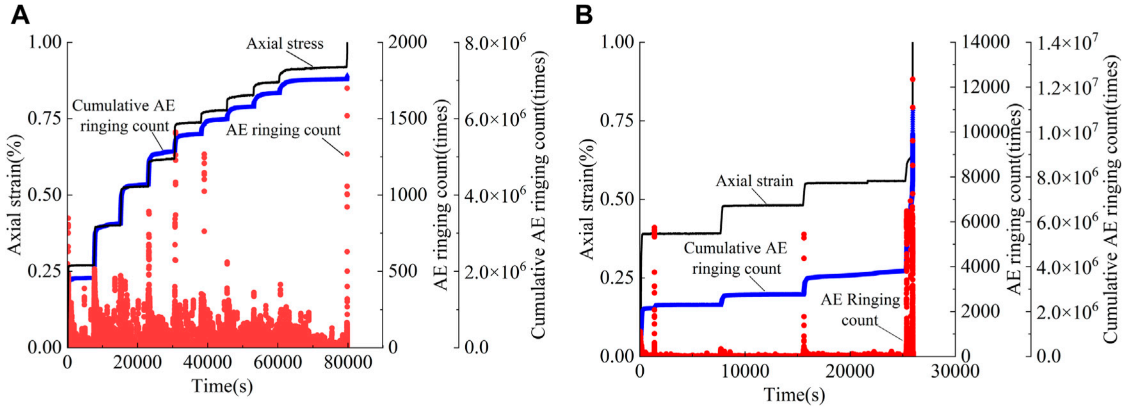

FIGURE 10
Axial strain-AE ringing count-cumulative AE ringing count-time curves of specimens. **(A)**Intact specimen. **(B)** Prefabricated fissures specimen.

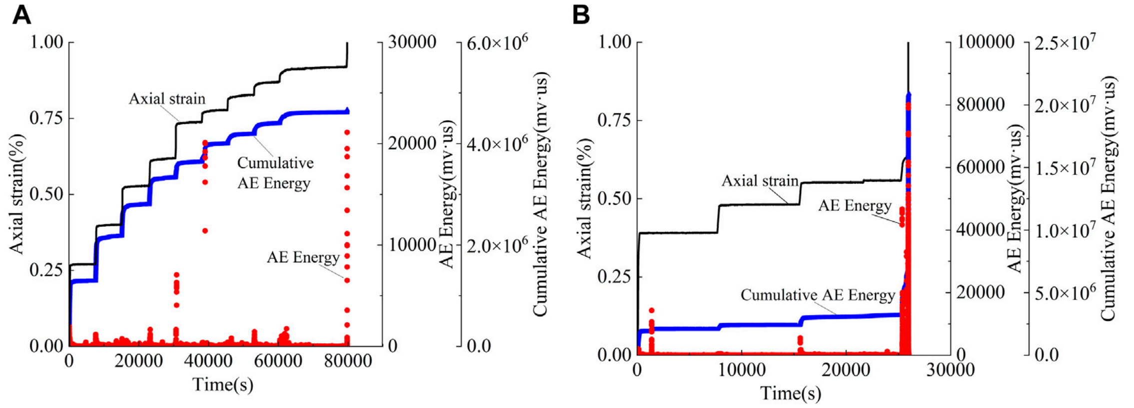

FIGURE 11
Axial strain-AE energy-cumulative AE energy-time curves of specimens. **(A)** Intact specimen. **(B)** Prefabricated fissures specimen.

TABLE 4 AE ringing count and AE energy of specimens under the last stress level.

Specimen type	Maximum AE ringing count (times)	Maximum AE energy (mv·us)	Cumulative AE ringing count (times)	Cumulative AE energy (mv·us)
Intact specimen	1,700	21,112	7.14×10^6	4.67×10^6
Prefabricated fissures specimen	12,348	80,027	1.10×10^7	2.09×10^7

cumulative AE ringing count and cumulative AE energy of the prefabricated fissures specimen are significantly higher than those of the intact specimen. The cumulative AE ringing count of the prefabricated fissures specimen is 1.5 times that of the intact specimen, and the cumulative AE energy is 4.5 times greater. Owing to the effect of prefabricated fissures, stress concentrations are more likely to occur at the fissure ends, and microcracks along the prefabricated fissures ends continue to initiate, expand, overlap, and penetrate, resulting in significantly higher AE ringing count and AE energy for

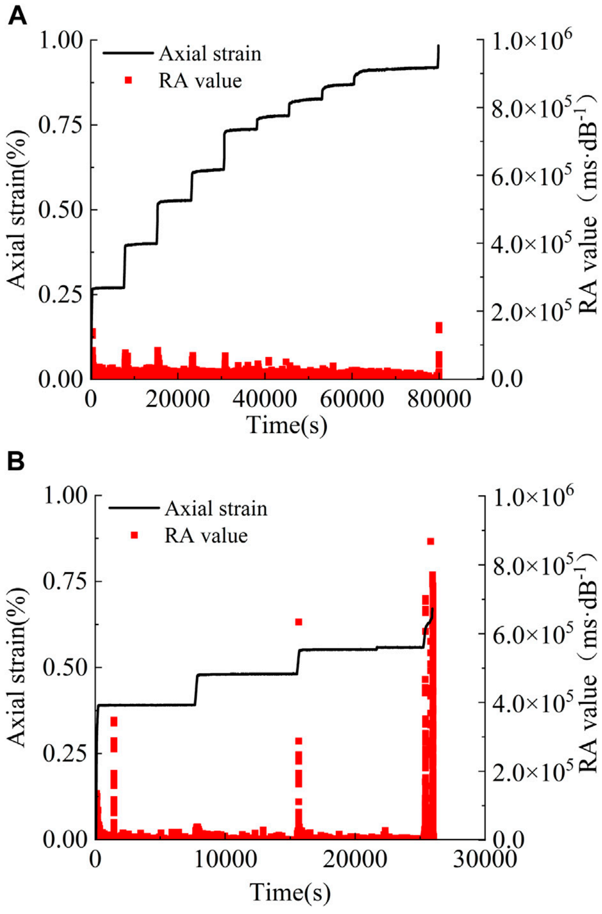

FIGURE 12
Axial strain-RA value-time curve of specimens. **(A)** RA value of Intact specimen. **(B)** RA value of prefabricated fissures specimen.

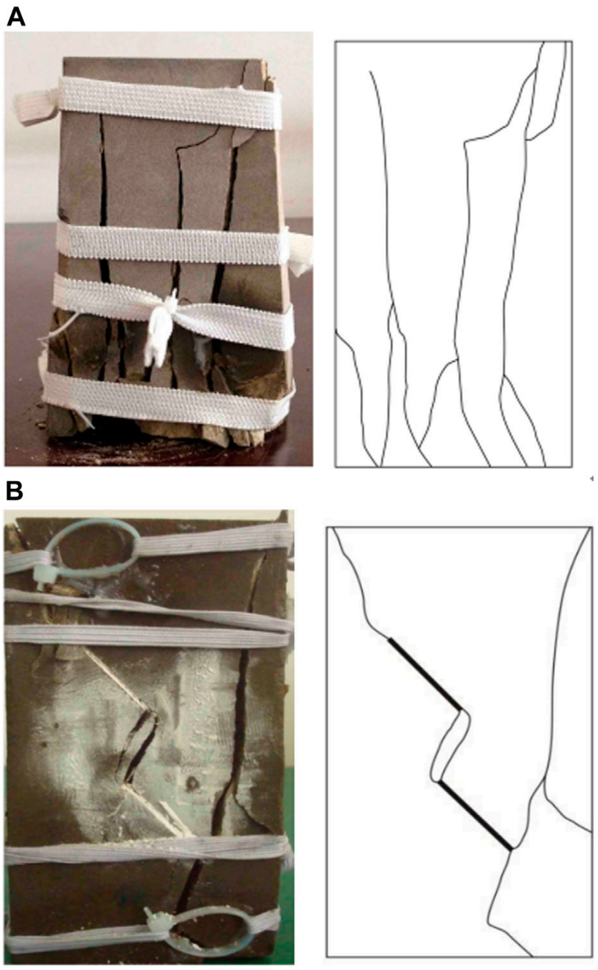

FIGURE 13
Photographs of specimens after creep failure. **(A)** Intact specimen. **(B)**Prefabricated fissures specimen.

the prefabricated fissures specimen than the corresponding values for the intact specimen.

AE RA value

The AE RA-value can characterize the type of cracks inside a material. The parameter RA is defined by Masayasu (2016):

$$RA = \frac{RiseTime\,(RT)}{Amplitude\,(dB)} \tag{1}$$

The unit of RA is ms·dB^{-1}. From a probabilistic statistical perspective, the corresponding relationship between rock AE parameters and crack properties is as follows: an AE signal with a high RA value usually represents the occurrence or development of shear cracks, and an AE signal with a low RA value corresponds to tension cracks.

The axial strain-AE RA-value-time curves of the two specimens under various stress levels are shown in Figure 12. A high RA value and low RA value of the two specimens coexist during the stress loading stage. In the constant stress stage, the RA values of the two specimens are mainly low. Figure 12 exhibits the existence of mutation points in the RA values of the two specimens, which is caused by the continuous initiation, expansion, overlapping, and penetration of microcracks to form a large number of shear microcracks. Figure 12A exhibits that the AE RA-value of the intact specimen is relatively small, all below 157,661.765 (ms·dB^{-1}). The RA value of the specimen significantly increases only during the accelerated creep stage of the final stress level. During the creep process, the cracks generated inside the intact specimen are mainly tensile, and shear cracks are secondary.

Figure 12B demonstrates that the low RA value of the prefabricated fissures specimen is usually less than the low RA value of the intact specimen. However, the number and values of the high RA value of the prefabricated fissures specimen significantly increase compared to those of the intact specimen. The high RA value of the prefabricated fissures specimen increases sharply compared with that of the intact specimen during the last loading stage. The maximum AE RA-value of the prefabricated fissures specimen is 868,213.333 (ms·dB^{-1}), which is 5.5 times the RA value maximum of the intact specimen of 157,661.765 (ms·dB^{-1}). There are 552 RA values for the prefabricated fissures specimen that exceed the maximum RA value of the intact specimen. Analysis of the relationship between the RA value and the type of crack indicates that the type of crack generated inside the prefabricated fissures specimen during the creep process is an obvious mixed tension–shear crack; however, the shear crack is the main one, and the tension crack is the supplement.

Photographs of the two specimens after creep failure are shown in Figure 13. There are more macroscopic tensile cracks (cracks approximately parallel to the axial loading direction) after the creep failure of the intact specimen. Shear cracks appear in the upper and lower parts of the specimen (cracks oblique to the axial loading direction). This is consistent with the observed changes in the internal microcracks of the specimen characterized by the AE RA-value of the specimen. The continuous expansion, overlap, and gradual penetration of the internal microcracks of the specimen eventually lead to the macroscopic cracks of the specimen and the formation of visible damage.

In contrast, the creep damage of the prefabricated fissures specimen mainly occurs around the ends of the prefabricated fissures, and shear cracks are generated at the outer ends of the prefabricated fissures extend to the top and bottom surfaces of the specimens (Wang et al., 2022a; Wang et al., 2022b) (Figure 13B). The shear cracks merge and penetrate with the tensile cracks generated on one side of the specimen. The cracks generated at the inner end of the prefabricated fissures merge to form a tensile–shear composite penetration in the rock bridge area. This is consistent with the change in microcracks characterized by the AE RA-value of the specimen.

In summary, the existence of prefabricated fissures changes the type and number of microcracks inside a specimen, resulting in more shear microcracks. When the macroscopic failure characteristics change, the specimen is more prone to macroscopic shear failure. Identification of the characteristics of internal microcracks in the creep process of the specimen by the RA value is consistent with the macroscopic rupture characteristics of the specimen. Therefore, the RA value, as an essential parameter of AE, shows an excellent guiding significance for characterizing the type of internal microcracks in the process of rock creep.

Conclusion

In this study, uniaxial compression creep acoustic emission (AE) tests were performed on intact sandstone specimens and prefabricated fissures sandstone specimens. The effect of prefabricated fissures on mechanical properties and AE characteristics of sandstone was obtained.

1. Under the same stress level, the instantaneous strain, creep strain, and total strain of the prefabricated fissures specimen were more significant than the corresponding values of the intact specimen. The difference in creep strain between the two specimens was the largest, followed by the total strain and instantaneous strain. This indicates that the prefabricated fissures exhibit the most significant influence on the creep strain of the specimen, followed by the total strain, and the least on the instantaneous strain.
2. Compared with the conventional uniaxial compressive strength, the long-term strength of the two specimens was reduced to various degrees. It is more scientific and reasonable to use the rock's long-term strength to evaluate the long-term stability and safety of an engineering project. The long-term strength of the prefabricated fissures specimen was only 37.5% of the long-term strength of the intact specimen. Owing to the influence of prefabricated fissures, the long-term strength of sandstone was significantly reduced. Notably, in engineering applications, the long-term rock strength drop caused by fissures should be critically evaluated.
3. With the increase in the stress level, the number of AE events of the specimen increases. Under the last stress level, the number of AE events of the specimen reaches its maximum. Furthermore, the number of AE events of the prefabricated fissures specimen was 6.2 times that of the intact specimen at their failure stages. The total number of accumulative AE events of the prefabricated fissures specimen was 2.4 times that of the intact specimen. The number of AE events and cumulative AE events generated by the prefabricated fissures specimen at various stress levels was significantly higher than the corresponding values of the intact specimen. The existence of prefabricated fissures significantly impacts the number of AE events and the number of cumulative AE events in the specimen.
4. The maximum AE ringing count of the prefabricated fissures specimen was 7.3 times that of the intact specimen, the maximum AE energy was 3.8 times that of the intact specimen, the cumulative AE ringing count was 1.5 times that of the intact specimen, and the cumulative AE energy was 4.5 times that of the intact specimen. The prefabricated fissures significantly affect the maximum AE ringing count, maximum AE energy, cumulative AE ringing count, and cumulative AE energy of specimen.

(5) The intact specimen was dominated by a low RA value, indicating that the microcracks generated by the specimen were mainly tensile cracks, and shear cracks were secondary. Compared with the intact specimen, the number and value of the high RA values of the prefabricated fissures specimen were significantly higher. This indicates that the type of microcracks generated inside the prefabricated fissures specimen was a mixed tension-shear crack dominated by shear cracks. The characteristics of microcracks inside the specimen shown by the RA value were consistent with the macro-fracture characteristics of the specimen. The RA value shows an excellent guiding significance for characterizing the type of internal microcracks in the process of rock creep.

Data availability statement

The original contributions presented in the study are included in the article/Supplementary Material, further inquiries can be directed to the corresponding author.

Author contributions

Conceptualization, HY; conceived and designed the experiments, HY; software, ZZ; validation, GW and ZZ; RN and GC contributed materials and theoretical foundations; writing—original draft preparation, GW; writing—review and editing, HY; All authors have read and agreed to the published version of the manuscript.

Funding

This study was supported by the National Natural Science Foundation of China (Grant No. 51309100), the Opening fund of State Key Laboratory of Geohazard Prevention and Geoenvironment Protection (Chengdu University of Technology) (Grant No. SKLGP 2019K025), the Henan Province Key R&D and Promotion Special (Technology Tackling Key) Project (Grant No. 192102310007), Fund of Innovative Education Program for Graduate Students at North China University of Water Resources and Electric Power, China (Grant No. YK-2021-70).

Conflict of interest

GC was employed by Beijing Engineering Corparation Limited.

The remaining authors declare that the research was conducted in the absence of any commercial or financial relationships that could be construed as a potential conflict of interest.

Publisher's note

References

Chen, X., Wang, S. Z., and Li, L. (2012). Characteristics of fragments of jointed rock mass model under uniaxial compression. *Chin. J. Rock Mech. Eng.* 31 (5), 898–907. (in Chinese). doi:10.1001/2013.jamainternmed.272

Chen, L., Liu, J. F., Wang, C. P., Liu, J., and Wang, J. (2015). Experimental investigation on the creep behaviour of Beishan granite under different temperature and stress conditions. *Eur. J. Environ. Civ. Eng.* 19 (S1), 43–53. doi:10.1080/19648189.2015.1064619

Feng, P., Dai, F., Liu, Y., Xu, N. W., and Du, H. B. (2018). Coupled effects of static-dynamic strain rates on the mechanical and fracturing behaviors of rock-like specimens containing two unparallel fissures. *Eng. Fract. Mech.* 207, 237–253. doi:10.1016/j.engfracmech.2018.12.033

Haeri, H., Shahriar, K., Marji, M. F., and Moarefvand, P. (2014). Experimental and numerical study of crack propagation and coalescence in pre-cracked rock-like disks. *Int. J. Rock Mech. Min. Sci.* 67 (4), 20–28. doi:10.1016/j.ijrmms.2014.01.008

Huang, D., and Huang, R. Q. (2010). Physical model test on deformation failure and crack propagation evolution of fissured rocks under unloading. *Chin. J. Rock Mech. Eng.* 29 (03), 502–512. (in Chinese).

Jiang, D. Y., He, Y., Ouyang, Z. H., Pan, P. Z., Wang, X. S., Xie, K. N., et al. (2017). Acoustic emission energy statistical properties of sandstone during uniaxial creep and its fracture surfaces morphology. *J. China Coal Soc.* 42 (6), 1436–1442. (in Chinese). doi:10.13225/j.cnki.jccs.2016.1101

Li, P., Tang, X. H., Liu, Q. S., and Luo, P. D. (2020). Experimental study on fracture characteristics and strength loss of intermittent fractured quasi-sandstone under freezing and thawing. *Chin. J. Rock Mech. Eng.* 39 (01), 115–125. (in Chinese). doi:10.13722/j.cnki.jrme.2019.0679

Lu, Y. L., Wang, J. G., and Derek, E (2015). Uniaxial strength and failure in sandstone containing a pre-existing 3-D surface flaw. *Int. J. Fract.* 194 (1), 59–79. doi:10.1007/s10704-015-0032-3

Ma, D. P., Zhou, Y., and Liu, C. X. (2018). Creep behavior and acoustic emission characteristics of coal samples with different moisture content. *Acta Geodyn. Geomaterialia* 15 (4), 405–412. doi:10.13168/AGG.2018.0030

Masayasu, O (2016). *Innovative AE and NDT techniques for on-site measurement of concrete and masonry structures*. Springer Netherlands. doi:10.1007/978-94-017-7606-6

Shkuratnik, V. L., Kravchenko, O. S., and Filimonov, Y. L. (2019). Stresses and temperature affecting acoustic emission and rheological characteristics of rock salt. *J. Min. Sci.* 55 (4), 531–537. doi:10.1134/S1062739119045879

Song, Z. Y. (2021). Experimental study on the characteristics of acoustic emission source of rock under uniaxial compression. *IOP Conf. Ser. Earth Environ. Sci.* 791 (1), 012003. doi:10.1088/1755-1315/791/1/012003

Tan, T. K., and Kang, W. F. (1980). Locked in stresses, creep and dilatancy of rocks, and constitutive equations. *Rock Mech.* 13 (1), 5–22. doi:10.1007/BF01257895

Ulusay, R., and Hudson, J. A. (2007). *The complete ISRM suggested methods for rock characterization, testing and monitoring: 1974- 2006*. Compilation arranged by the ISRM Turkish national group: Ankara, Turkey. doi:10.1007/s10064-009-0213-2

Vásárhelyi, B., and Bobet, A. (2000). Modeling of crack initiation, propagation and coalescence in uniaxial compression. *Rock Mech. Rock Eng.* 33 (2), 119–139. doi:10.1007/s006030050038

Wan, Y., Chen, G. Q., Sun, X., and Zhang, G. Z. (2021). Triaxial creep characteristics and damage model for red sandstone subjected to freeze-thaw cycles under different water contents. *Chin. J. Geotechnical Eng.* 43 (08), 1463–1472. (in Chinese). doi:10.11779/CJGE202108011

Wang, G. L., Zhang, L., Wang, Z., Zhang, J. Z., Sun, F., and Qiu, P. Y. (2019). Acoustic-mechanical responses of intact and flaw-contained rock deformation under uniaxial compression: A comparison. *Adv. Civ. Eng.* 2019, 1–12. doi:10.1155/2019/7940923

Wang, Y., Li, J. Z., Zhu, C., and Mao, T. Q. (2022a). Fatigue failure identification using deformation and energy rate for hole-fissure contained granite under freeze–thaw and variable-frequency–variable-amplitude cyclic loads. *Fatigue Fract. Eng. Mat. Struct.* 45 (3), 834–851. doi:10.1111/ffe.13639

Wang, Y., Song, Z. Y., Mao, T. Q., and Zhu, C. (2022b). Macro–meso fracture and instability behaviors of hollow-cylinder granite containing fissures subjected to freeze–thaw–fatigue loads. *Rock Mech. Rock Eng.* 55, 4051–4071. doi:10.1007/s00603-022-02860-5

Wu, C., Liu, J. F., Zhou, Z. W., and Zhuo, Y. (2016). Creep acoustic emission of rock salt under triaxial compression. *Chin. J. Geotechnical Eng.* 38 (S2), 319–323. (in Chinese). doi:10.11779/CJGE2016S2052

Xu, Z. J., Qi, Q. X., Li, H. Y., Zhang, N. B., and Su, R. H. (2014). Acoustic emission characteristics of marble creep damage under different stress levels. *J. China Coal Soc.* 39 (S1), 70–74. (in Chinese). doi:10.13225/j.cnki.jccs.2013.0199

Yang, S. Q., and Jing, H. W. (2011). Strength failure and crack coalescence behavior of brittle sandstone samples containing a single fissure under uniaxial compression. *Int. J. Fract.* 168 (2), 227–250. doi:10.1007/s10704-010-9576-4

Yang, S. Q., Liu, X. R., and Jing, H. W. (2013). Experimental investigation on fracture coalescence behavior of red sandstone containing two unparallel fissures under uniaxial compression. *Int. J. Rock Mech. Min. Sci.* 63, 82–92. doi:10.1016/j.ijrmms.2013.06.008

Yang, C., Huang, D., Cai, R., and Huang, R. Q. (2018). Triaxial unloading creep tests on rock mass with an open and penetrating flaw. *Rock Soil Mech.* 39 (1), 53–62. (in Chinese). doi:10.16285/j.rsm.2015.2821

Yao, Q. L., Zhu, L., Huang, Q. X., Yang, P., and Xu, Z. (2019). Experimental study on the effect of moisture content on creep characteristics of fine-grained feldspar lithic sandstone. *J. Min. Saf. Eng.* 36 (5), 1034–1042. (in Chinese). doi:10.13545/j.cnki.jmse.2019.05.022

Yi, T., Tang, J. X., and Wang, Y. L. (2021). Effect of fracture dip angle and number on mechanical properties and failure modes of rock mass. *Chin. J. Undergr. Space Eng.* 17 (01), 98–106.

Yu, H. C., Li, Y. L., and Liu, H. D. (2012). Comparative study of conventional mechanical, creep and stress relaxation properties of silty mudstone under triaxial compression. *Chin. J. Rock Mech. Eng.* 31 (01), 60–70. (in Chinese). doi:10.3969/j.issn.1000-6915.2012.01.008

Yu, H. C., LiuHuang, H. D. Z. Q., and Shi, G. C. (2017). Experimental study on time-dependent behavior of silty mudstone from the Three Gorges Reservoir Area, China. *KSCE J. Civ. Eng.* 21 (3), 715–724. doi:10.1007/s12205-016-3645-9

Zhang, Q. Y., Yang, W. D., Chen, F., Li, W. G., and Wang, J. H. (2011). Long-term strength and microscopic failure mechanism of hard brittle rocks. *Chin. J. Geotechnical Eng.* 33 (12), 1910–1918. (in Chinese).

Zhao, K., Yang, D. X., Gong, C., Zhuo, Y. L., Wang, X. J., and Zhong, W. (2020). Evaluation of internal microcrack evolution in red sandstone based on time-frequency domain characteristics of acoustic emission signals. *Constr. Build. Mater.* 260, 120435. doi:10.1016/j.conbuildmat.2020.120435

Zhu, L., Zhang, Y., Dong, L., Wu, J. W., Duan, L. Q., and Zhang, L. (2019). Experimental study on acoustic emission characteristics of intermittent jointed rock mass under uniaxial compression. *IOP Conf. Ser. Earth Environ. Sci.* 283 (1), 012015. doi:10.1088/1755-1315/283/1/012015

frontiers | Frontiers in Earth Science

TYPE Original Research
PUBLISHED 23 September 2022
DOI 10.3389/feart.2022.1017429

Pore structure characterization for coal measure shales of the Xiashihezi Formation in the Sunan Syncline block, southern North China basin

Qian Wang[1,2], Xianbo Su[1,3,4,5]*, Yi Jin[1,4], Peihong Chen[6]*, Weizhong Zhao[1,7] and Shiyao Yu[1]

[1]School of Resources and Environment, Henan Polytechnic University, Jiaozuo, China, [2]State Key Laboratory Cultivation Base for Gas Geology and Gas Control, Henan Polytechnic University, Jiaozuo, China, [3]Unconventional Gas Research Institute, Henan Polytechnic University, Jiaozuo, China, [4]Collaborative Innovation Center of Coalbed Methane and Shale Gas for Central Plains Economic Region, Jiaozuo, Henan, China, [5]School of Energy Resources, China University of Geosciences, Wuhan, China, [6]School of Emergency Management and Safety Engineering, China University of Mining and Technology, Beijing, China, [7]Department of Environmental Engineering, Technical University of Denmark, Lyngby, Denmark

OPEN ACCESS

EDITED BY
Junjian Zhang,
Shandong University of Science and Technology, China

REVIEWED BY
Xuguang Dai,
China University of Mining and Technology, China
Fuhua Shang,
Inner Mongolia University of Technology, China
Yunbing Hu,
China University of Mining and Technology, China

*CORRESPONDENCE
Xianbo Su,
suxianbo@hpu.edu.cn
Peihong Chen,
916269755@qq.com

SPECIALTY SECTION
This article was submitted to Economic Geology,
a section of the journal
Frontiers in Earth Science

RECEIVED 12 August 2022
ACCEPTED 07 September 2022
PUBLISHED 23 September 2022

CITATION
Wang Q, Su X, Jin Y, Chen P, Zhao W and Yu S (2022), Pore structure characterization for coal measure shales of the Xiashihezi Formation in the Sunan Syncline block, southern North China basin.
Front. Earth Sci. 10:1017429.
doi: 10.3389/feart.2022.1017429

To characterize the coal measure shale pore structure of the Xiashihezi Formation in the Sunan Syncline block, a series of experiments were conducted. Results show that the main components of the shales are clay minerals and quartz, and organic matter, fluid escaping, interlayer, intercrystalline and interparticle pores are well-developed. The shale pore specific surface area (SSA) is concentrated in the pores with the size of <50 nm and is significantly higher in the pores with the size of < 5 nm, indicating that these pores have an important effect on gas adsorption. The shale pore volume is mainly concentrated near the pore size of 10 nm, followed by 10,000–100,000 nm, indicating that in addition to the fractures, the matrix pores with a size of about 10 nm contribute the most to pore volume and free gas accumulation. The volume and SSA of the micropore, small pore, and mesopore increase with the TOC content when it is lower than 6%, leading to higher porosity and total pore SSA of the shales. However, this positive correlation disappears under the compaction effect when the TOC content is higher than 6%. The clay mineral content has negative correlations with the volume and SSA of the mesopore and macropore under the compaction and pore blockage effects, but it correlates poorly with those of the micropore and small pore, causing a decrease in the shale porosity as it increases, while the brittle mineral can promote mesopore and macropore development and is conducive to micropore and small pore maintenance when its content is higher than 45%. As a result, the shale porosity tends to increase with the brittle mineral content. This study is helpful in clarifying the coal measure shale gas enrichment law in the block and in providing fundamental support for coal measure gas efficient development.

KEYWORDS

Sunan Syncline Block, Xiashihezi formation, coal measure shale, pore structure, coal measure gas development

1 Introduction

Coal measure shales are fine-grained sedimentary rocks that have genetic relationships with coal seams in coal-bearing formation and are characterized by lamellae or laminated structures, as well as complicated composition and pore structure (Cao et al., 2014; Cao et al., 2015; Zuo et al., 2017). Based on the color and mixture composition, it can be divided into siltstone, silty mudstone, and mudstone that include carbonaceous, calcareous, siliceous, ferruginous mudstones etc. Previous studies show that coal measure shales generally possess low porosity, permeability, and gas content but high resource abundance because of high thickness, and its pore structure characteristics have a significant effect on gas enrichment and development conditions (Wang et al., 2016a).

Shales have a pore–fracture system, and the matrix pores determine the shale gas occurrence, desorption, and diffusion, while the fractures determine the conduit for fluid seepage flow. Related research studies have been focused on the pore volume and specific surface area (SSA) distributions, genetic types, and influencing factors of the pore structure (Schmitt et al., 2013; Zhang et al., 2017a; Middleton et al., 2017; Wang et al., 2021). There are two types of methods that have been widely adopted to analyze pore structure. One is morphological observations, including optical microscopy (Wang et al., 2017), scanning electron microscopy (SEM) (Wang et al., 2016b), transmission electron microscopy (TEM) (Wei et al., 2018), and atomic force microscopy (AFM) (Zhao et al., 2019), and the other is physical measurements, including mercury injection (Li et al., 2018a), low-temperature N_2 and CO_2 adsorption (Liu et al., 2017; Song et al., 2017), nuclear magnetic resonance (NMR) (Zhang et al., 2019a), computed tomography (micro- and nano-CT) (Josh et al., 2012) and small-angle neutron scattering/ultra-small-angle scattering (SANS/USAS) (Clarkson et al., 2013). In addition, two methods have been widely adopted for pore classification according to the pore size distribution. One is the method that was proposed by the International Union of Pure and Applied Chemistry (IUPAC), who classified the pores into micropore (<2 nm), mesopore (2–50 nm), and macropore (>50 nm). The other was proposed by B. B. ХОДОТ, and the pores are classified into micropores, small pores, mesopores, and macropores by the boundaries of 10, 100, and 1,000 nm (Cao and Guo, 2020).

In terms of the genetic types and major composition, shale pores can be classified as OM pores, interparticle pores, intercrystalline pores, dissolved pores, fluid escaping pores etc. Among them, the OM pores and the intercrystalline and interparticle pores in clay minerals are the main types (Li et al., 2018b; Chen et al., 2016; Slatt and O'Brien, 2011; Ko et al., 2018). Most shale pores are slit-shaped with a pore size of less than 100 nm. The pore volume and SSA are mainly provided by the pores with the size of < 50 nm, and the pores with the size of < 10 nm contribute well to the total SSA (Fishman et al., 2012; Zhang et al., 2016a; Zhang et al., 2016b; Chen et al., 2017; Zuo et al., 2017). Previous studies show that the coal measure shale pore structure is affected by multiple factors. Pan et al. studied the coal measure shale pore structure of the Taiyuan Formation in Huainan Coalfield and found that the OM and clay mineral can promote nanoscale pore development, while the quartz content correlates poorly with the pore structure (Pan et al., 2017; Ge et al., 2020). Zhang et al. (2019b) and Yuan et al. (2021) studied the shale pore structure of Shanxi and Taiyuan formations in the central Qinshui basin. They found that the OM has a significant promotion effect on the development of pores with a size of < 50 nm, followed by the clay mineral content; however, quartz is not conducive to pore development (Zhang et al., 2019b; Yuan et al., 2021). Zhang et al. (2017b) demonstrated that all the contents of OM, clay, and brittle minerals correlate poorly with the porosity and total pore SSA when they studied the coal measure shales of the Yan'an and Taiyuan formations in the northeastern margin of the Ordos Basin and thought that the effect of a single factor on the pore structure is not significant. Some other researchers found that both the OM and brittle mineral have a promotion effect on shale pore development, and the support effect provided by the brittle mineral is important for pore maintenance, especially for the transitional shale that possesses relatively higher clay mineral content. Also, the increase of clay mineral content may aggravate pore collapse, leading to the decrease in pore volume and SSA (Pan et al., 2017; Zhao et al., 2017). According to the abovementioned research studies, there are certain differences in the coal measure shale pore structure and its control effect in different regions. To date, most shale pore studies have focused on marine and terrestrial shales, while the research of coal measure shale pore structure is still lacking comparatively and needs to be further performed.

The coal seams of the Xiashihezi Formation, Middle Permian, in the Sunan Syncline block are the main target for coalbed methane (CBM) development in the area. However, affected by geological and technical factors, the CBM wells generally face the problem of low gas production. Previous tests and theoretical analyses show that the coal measure shales in the Xiashihezi Formation have abundant gas resources, and engineering tests indicate that the combined development of CBM and the shale gas (i.e., coal measure gas development) can effectively increase the gas production of the low-yield CBM wells, indicating that gas resources in the coal measure shales possess important development value (Su et al., 2018a). However, previous studies of the Permian coal-bearing formation are mainly focused on coal seams, while there is still a lack of research on the coal measure shales in the formation, which hinders efficient development of coal measure gas in the block (Wei et al., 2007; Gui and Chen, 2016; Liu et al., 2016). Therefore, this study aims to study the pore structure characteristics of these coal measure shales and to provide fundamental supports for clarifying the shale gas enrichment

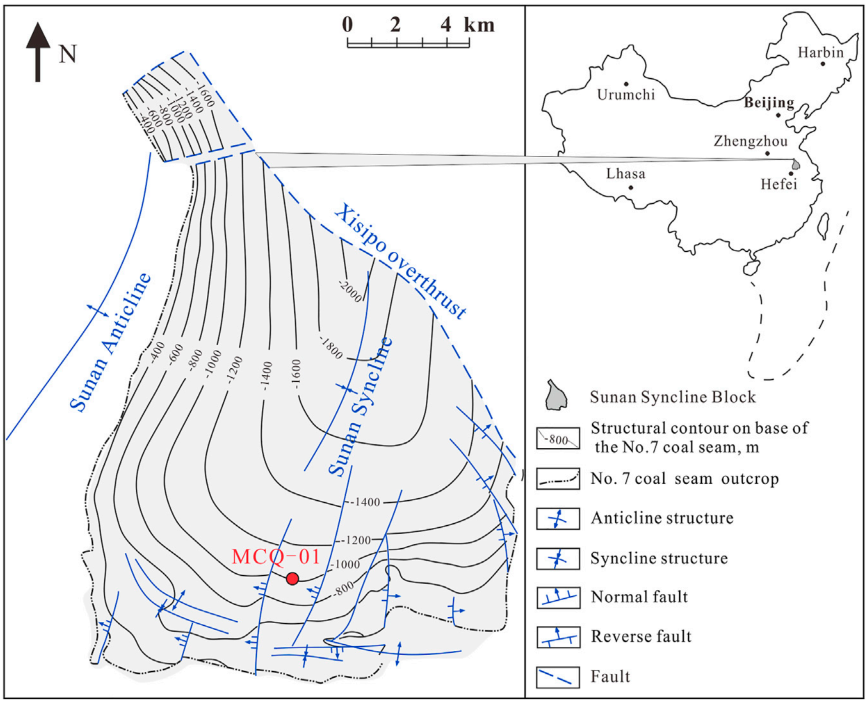

FIGURE 1
Location of the Sunan Syncline block and the structural contour map of the No. 7_1 coal seam floor.

law and the efficient development of coal measure gas in the block.

2 Geological setting and methodology

2.1 Geological settings

Sunan Syncline block is located in the southern part of the North China basin, and the Sunan Syncline is a south–north distributed open-branched syncline. The formations in the southern block are continuous, while some formations in the northeast are interrupted by a northwest-trending overthrust fault (Figure 1). The syncline was infilled with sediments of the Xiashihezi Formation that were deposited under a regression delta plain environment during the late Paleozoic and with a burial depth of 447–2,000 m. The Xiashihezi Formation is about 127–386 m thick and is generally thicker in the north and center than in the south and two flanks of the block (Wang et al., 2020). The lithology of this formation includes a series of shallow gray fine sandstones, siltstones, gray to dark, and gray to grayish black silty mudstones, carbonaceous mudstones, and No. 4–No. 9 coal seams. Also, the Xiashihezi Formation can be divided into two parts separated by a sandstone on the top of the No. 6 coal seam. The lithologies of the lower part are mainly gray, dark gray, and grayish black mudstone that contains some oolitic structures and siderite, sandy mudstones, and gray and grayish black fine sandstones that are interbedded with a gray and greyish white fine sandstone. The lower part also contains No. 6–No. 9 coal seams that are the main target of CBM development (Figure 2) and is the study section of this article.

2.2 Methodology

A total of 18 coal measure shale samples were collected from the Xiashihezi Formation of the Well MCQ-01 (see Figure 2 for the locations). X-ray diffraction (XRD) analysis was conducted on the shale powder samples with a D/max2500 type diffractometer according to the Chinese standard SY/T 5163-2010 to obtain the mineral composition (The Chinese Standard of Petroleum and Natural Gas Industry, 2010). An FE-SEM test was conducted on the shale samples using a QUANTA-FEG 250 ESEM following the standard SY/T 5162–2014 to observe the micromorphology of the pore and fractures, as well as the mineral composition (The Chinese Standard of Petroleum and Natural Gas Industry, 2014). Also, the total organic carbon (TOC) content of the samples was measured

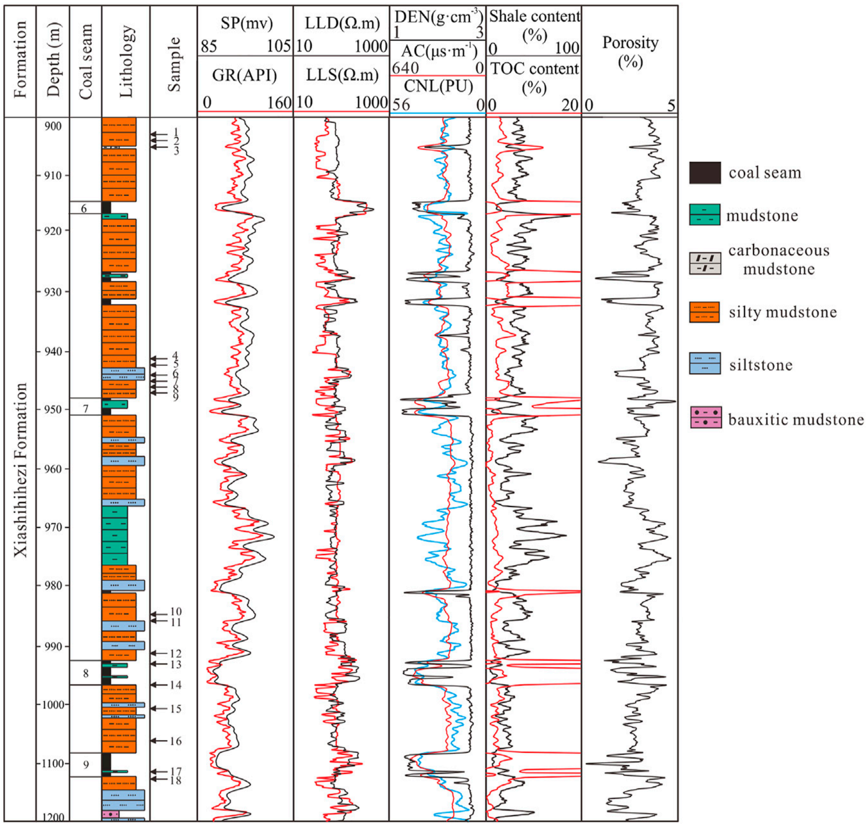

FIGURE 2
Lithology, logging, and sample acquisition at the Well MCQ-01.

by a LECOCS-200 carbon and sulfur analyzer in accordance with the Chinese standard GB/T 19145-2003 (The National Standard of the People's Republic of China, 2003).

To characterize the shale pore structure at the micrometer scale to the nanometer scale, mercury injection and low-temperature N_2 and CO_2 adsorption tests were adopted. The mercury injection test employed a PoreMaster-33 mercury porosimetry apparatus and follows the Chinese standard GB/T 21650.1-2008 (The National Standard of the People's Republic of China, 2008a). The low-temperature N_2 and CO_2 adsorption tests employed a V-Sorb 2800TP pore surface analyzer and follow the Chinese standards GB/T 21650.2-2008 and GB/T 21650.3-2011 (The National Standard of the People's Republic of China, 2008b; The National Standard of the People's Republic of China, 2011; Zhang et al., 2020).

In addition, considering that the main object of coal measure gas development in this area is the CBM, the pore classification method proposed by B. B. ХОДОТ that has been widely used for coal pore characterization was adopted to classify the shale pores for facilitating the comprehensive evaluation of coal and shale reservoirs.

3 Results and discussion

3.1 Coal measure shale types

The coal measure shales are mainly composed of quartz with a content of 22.78%–55.87%, clay minerals with a content of 28.90%–76.27%, and little plagioclase and siderite. Also, calcite and pyrite were observed in individual samples. The clay minerals are mainly composed of illite–smectite mixed-layer (I/S) and kaolinite, which account for more than 95% of the mineral content, as well as little illite and chlorite. In addition, the TOC content of the shales ranges from 0.18% to 14.30% (Table 1). Based on the mineral composition, structural, and logging characteristics, the coal measure shales of the Xiashihezi Formation are classified into four types (Figure 3).

3.1.1 Mudstones

The mudstones in the formation are mainly dark gray and grayish black in color with mostly horizontal beddings and slab and schistose structures (Figure 3A). Some mudstones are interbedded with light-colored siltstones and silty mudstones,

TABLE 1 TOC content and mineral composition of the coal measure shale samples of the Xiashihezi Formation.

Sample	Lithology	TOC (%)	Quartz (%)	Calcite (%)	Plagioclase (%)	Siderite (%)	Pyrite (%)	Smectite (%)	I/S (%)	Illite (%)	Kaolinite (%)	Chlorite (%)
1	Silty mudstone	3.82	55.78	4.81	4.81	1.92	0	0	2.6	0.87	25.39	0
2	Silty mudstone	0.18	41.92	0	2.99	2.99	0	0	7.79	1.04	43.08	0
3	Silty mudstone	0.39	40.84	0	4.98	3.98	0	0	8.96	1	39.84	0
4	Silty mudstone	1.72	43.24	0	0	0	0	0	14.31	1.10	39.63	0
5	Silty mudstone	1.29	39.48	0	0	0	0	0.59	13.03	0	45.6	0
6	Siltstone	1.65	43.27	0	0	0	0	0	31.39	1.10	22.58	0
7	Silty mudstone	0.7	32.77	0	0	1.99	2.98	0	17.24	2.46	41.86	0
8	Mudstone	0.96	22.78	0	0	0	0	0	6.1	0.76	69.4	0
9	Carbonaceous mudstone	14.3	29.14	0	0	0	0	0	6.79	1.13	48.64	0
10	Silty mudstone	1.85	50.06	0	0	2.94	0	0	20.32	1.35	23.48	0
11	Siltstone	1.22	36.55	0	0	0	0	0	16.18	1.24	44.81	0
12	Carbonaceous mudstone	13.3	40.75	0	6.94	2.6	0	0	29.86	1.09	5.46	0
13	Carbonaceous mudstone	6.5	46.94	0	4.49	3.18	0	0	33.84	0	3.5	1.56
14	Silty mudstone	4.26	37.82	0	2.11	0	0	0	30.7	2.79	13.95	8.37
15	Mudstone	1.75	25.55	0	0	0	0	0	21.81	1.45	49.44	0
16	Silty mudstone	2.4	32.21	0	0	1.95	0	0	30.45	1.90	31.09	0
17	Carbonaceous mudstone	13	33.93	0	0	0.87	0	0	26.62	1.04	24.53	0
18	Silty mudstone	0.55	42.76	0	13.92	2.98	0	0	34.61	1.99	3.18	0

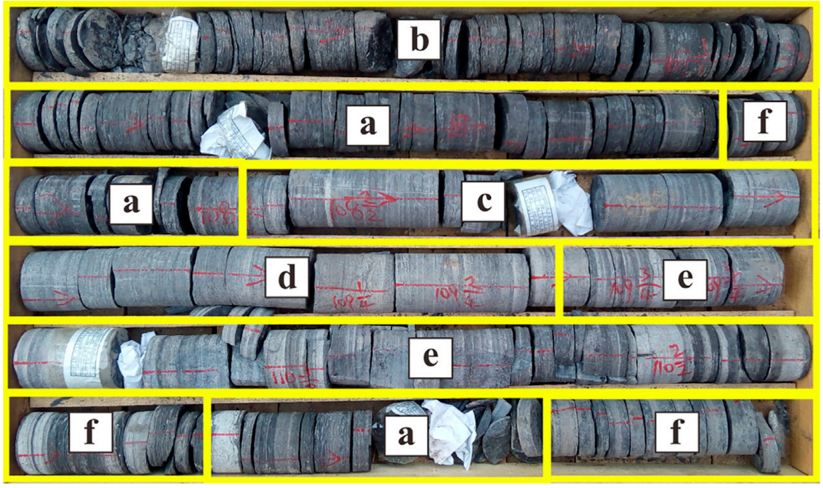

FIGURE 3
Core image of different coal measure shales from the Well MCQ-01. **(A)** Mudstones; **(B)** carbonaceous sediments; **(C)** silty mudstone; **(D)** siltstone; **(E)** mudstone and siltstone alternating layers; and **(F)** mudstone and silty mudstone alternating layers.

and both directionally aligned muscovite and plant detritus on bedding planes (Figures 3E,F). The mudstones mainly comprise clay minerals (accounting for more than 70%), clastic quartz (accounting for 20%–25%), and little OM, calcite, plagioclase, siderite, and mica (accounting for lower than 5% in total). The clay minerals are mainly composed of kaolinite and I/S, of which the kaolinite content accounts for more than 50% (Table 1). Compared with other shales, the mudstones possess relatively high clay mineral content and are characterized by the logging responses of high natural gamma ray (GR), high spontaneous potential (SP), high bulk density (DEN), high compensated neutron log (CNL), low sonic slowness (AC), and low resistivity (R_t). Data from the Well MCQ-01 indicate that the GR values of the mudstones are greater than 100 API, while the SP values are greater than 97 mV. The logging interpretations indicate that the mudstones generally possess high shale content (V_{sh}) and porosity and low TOC content (Figure 2).

3.1.2 Carbonaceous mudstone

The carbonaceous mudstones are mainly grayish black and black in color and contain textures that include both slab and schistose structures caused by the horizontal beddings (Figure 3B). The rock composition is complicated and includes clay minerals, quartz, siderite, and plagioclase. The content of clay minerals and quartz is generally higher than 80%. Also, this shale is mainly distributed adjacent to coal seams or developed independently as thin beds and contains lots of fossil fragments. The TOC contents of the carbonaceous mudstone samples are 6.5%–14.3% (avg. 11.27%), which are obviously higher than those of other shales (0.18%–4.26%, avg. 2.4%), indicating that these shales may possess better gas accumulation condition and high development value (Table 1), while its logging responses are basically similar to the mudstones (Figure 2).

3.1.3 Silty mudstone

The silty mudstones in the formation are mainly gray and dark gray in color and developed with horizontal and wavy beddings. Also, it generally presents as thin beds and is interbedded with other rocks (Figures 3C,F). The minerals in this shale are mainly clay minerals with a content of 30%–70%, as well as silt clasts composed of quartz, calcite, plagioclase, and siderite (Table 1). The clay mineral and TOC contents of the silty mudstones are relatively lower than those of the mudstones and carbonaceous mudstones, respectively, while its brittle mineral content is relatively higher, indicating that it may possess higher fracability and is more favorable for hydrofracturing (Su et al., 2018b). Also, compared with the mudstones and siltstones, the GR, DEN, CNL, AC, and RT of the silty mudstones show a "median value". In particular, the GR, SP, and CNL values of the silty mudstones are 70–100 API, 93–97 mV, and 18–28 PU, respectively, and the logging interpretations show that it generally possesses medium V_{sh} and TOC and low porosity (Figure 2).

3.1.4 Siltstone

The siltstones in the formation are generally gray or grayish white in color and contain well-developed horizontal and wavy beddings and also present the form of thin bed interbedded with other rocks (Figures 3D,E). The thickness of this shale can be up to 3–5 m, and it is mainly composed of fine and pulverous sand clasts with the content of more than 70% in total, as well as few

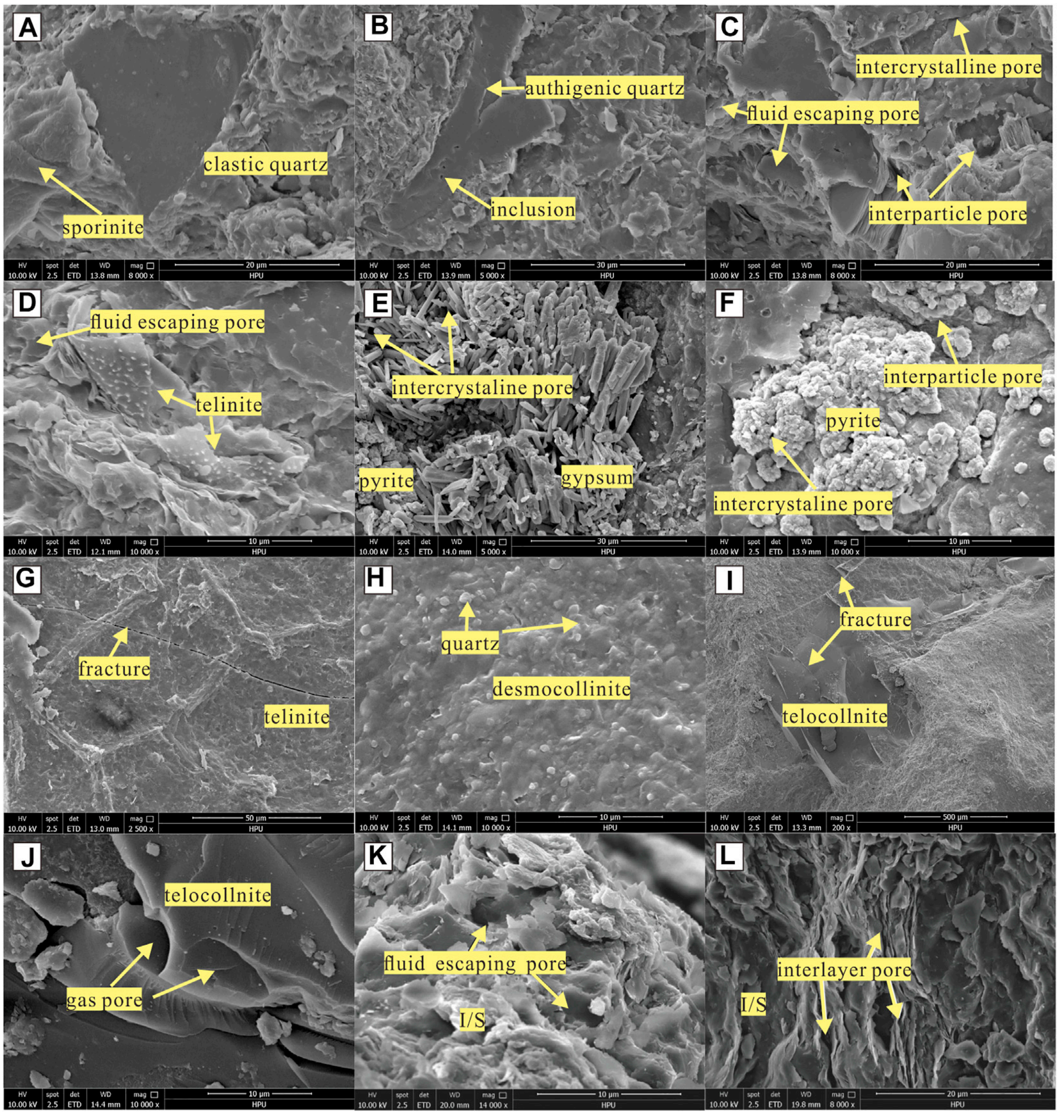

FIGURE 4
Field emission scanning electron microscope (FE-SEM) images of the coal measure shale samples.

clay minerals. The mineral composition of this shale is generally similar with that of the silty mudstone (Table 1), and it is characterized by low GR, low SP, low CNL, low AC, high DEN, and high RT values, and the logging interpretations indicate that it has low V_{sh} and TOC but high porosity.

3.2 FS-SEM observations and pore types

The results of the FS-SEM test show that the coal measure shales are not only mainly composed of quartz and clay minerals but also contain small amounts of feldspar, gypsum, pyrite, and OM clasts. In particular, quartz can be subdivided into clastic and authigenic forms according to the genesis (Figures 4A–C), of which authigenic quartz is shown as secondary enlargements and contains inclusions (Figure 4B). Also, the feldspar cleavage is present in the samples (Figure 4C), and the gypsum presents typical columnar crystals and characteristics of hydrothermal genesis (Figure 4E). The strawberry-shaped pyrite crystals are developed inside the desmocollinite of the samples, indicating it was formed under a strongly reducing environment (Figure 4F). The kaolinite and I/S are the dominant clay minerals (Figures 4K,L), and the kaolinite can be classified into feldspar alternation and depositional types according to the differences in genesis. The feldspar alternation type retains the cleavage texture of feldspar (Figure 4D), while the depositional type has a wormy texture (Figure 4C). The maceral of OM includes telinite (Figures 4D,G), desmocollinite (Figure 4H), telocollinite (Figures 4I,J),

TABLE 2 Results of the porosity and pore volume distribution of the coal measure shale samples by the mercury injection test.

Sample	Porosity (%)	Pore volume (cm^3/g)					Pore volumetric ratio (%)			
		Micropore	Small pore	Mesopore	Macropore	Total	Micropore	Small pore	Mesopore	Macropore
2	2.04	0.0008	0.0033	0.0002	0.0037	0.0080	10.20	41.04	2.94	45.8
3	3.36	0.0022	0.0046	0	0.0066	0.0134	16.44	34.30	0	49.26
4	3.18	0.0014	0.0034	0.0008	0.0073	0.0129	10.85	26.36	5.82	56.97
5	2.38	0.0015	0.0033	0.0006	0.0040	0.0094	15.59	35.37	6.82	42.21
6	2.25	0.0009	0.0027	0.0004	0.0050	0.0090	10.34	29.66	4.83	55.17
8	2.57	0.0024	0.0051	0.0002	0.0033	0.0110	21.37	46.81	1.65	30.17
9	3.71	0.0022	0.0052	0.0004	0.0072	0.0150	14.34	35.00	2.64	48.03
11	2.68	0.0015	0.0048	0.0007	0.0038	0.0108	13.89	44.44	6.83	34.84
12	4.89	0.0022	0.0032	0.0010	0.0153	0.0218	10.04	14.87	4.59	70.50
13	5.49	0.0034	0.0061	0.0011	0.0114	0.0220	15.47	27.69	5.00	51.83
14	6.31	0.0058	0.0148	0.0018	0.0026	0.0249	23.17	59.28	7.14	10.41
15	2.73	0.0016	0.0021	0	0.0074	0.0111	14.81	18.52	0	66.66
16	3.63	0.0027	0.0092	0.0012	0.006	0.0191	14.15	48.38	6.07	31.40
17	2.30	0.0018	0.0028	0.0002	0.0046	0.0093	19.00	29.97	1.65	49.38
18	3.18	0.0019	0.0040	0.0003	0.0066	0.0129	14.56	31.18	2.41	51.85

and sporinite (Figure 4A), of which the desmocollinite contains quartz grains at the nanometer-scale (Figure 4H), while cleats are developed in the telocollinite (Figure 4I).

Different types of pores were observed in the samples at the nanometer-scale to micrometer-scale, which are well-developed in the OM and clay minerals. The observations show that the OM pore is mostly globose, ellipsoid, and honeycomb-shaped between 5 and 2,000 nm in size (Figure 4I), and the natural fractures in the samples act as channels connecting the matrix pores (Figures 4G,I). Numerous fluid escaping, interlayer, intercrystalline, and interparticle pores are also developed in the clay minerals, and these pores, presenting mostly ellipsoid, band, and triangular shapes, are between about 5 and 1,000 nm in size and possess good connectivity. Fluid escaping, intercrystalline, and interparticle pores were observed in the kaolinite (Figures 4C,D), while fluid escaping and interlayer pores also commonly exist in the I/S (Figures 4K,L). Interparticle pores are well-developed between the clastic mineral grains, including quartz and feldspar, and have the size between 0.2 and 3 μm (Figure 4C). Meanwhile, the observations also show that the pyrite and gypsum contain intercrystalline pores (Figures 4E,F).

3.3 Mercury injection test

Mercury injection can measure the pores ranging from nanometer- to millimeter-scales which is conducive to explore the overall distribution characteristics of pores. The results show that the porosity of the coal measure shale samples ranges from 2.04% to 6.31% (avg. 3.38%), while the total pore volume ranges from 0.008 to 0.0249 cm^3/g (avg. 0.0140 cm^3/g), and the total SSA ranges from 0.9531 to 6.2959 m^2/g (avg. 2.1897 m^2/g) (Tables 2, 3).

The volumetric ratios of the micropores, small pores, mesopores, and macropores are 10.04%–21.37% (avg. 14.95%), 14.87%–59.28% (avg. 34.86%), 0%–7.14% (avg. 3.98%), and 10.41%–70.50% (avg. 46.30%), respectively, indicating that the macropores and small pores are the main contributors to the pore volume and provide the main spaces for the free gas (Table 2). Additionally, the SSA ratios of the micropores, small pores, mesopores, and macropores are 34.30%–61.63% (avg. 49.29%), 38.32%–65.28% (avg. 50.15%), 0%–1.12% (avg. 0.48%), and 0.02%–1.16% (avg. 0.08%), respectively, showing that the micropores and small pores are the main contributors of the SSA and impose more impact on shale gas adsorption (Table 3).

Also, the pore volume distributions can be classified into unimodal, bimodal, and multimodal types. In particular, the unimodal type only exists in individual silty mudstones, and the pore volume is mainly provided by the micropores and small pores. The mercury injection curve of the unimodal type increases quickly in the micropore and small pore regions, and the pore volume peak appears at about 10 nm diameter (Figure 5A). The bimodal type is observed in mudstones and partial silty mudstones and is mainly characterized by two peaks of pore volume, i.e., one at about 10 nm diameter and the other at the region of 10,000–100,000 nm diameter. Moreover, fewer

TABLE 3 Results of the specific surface area distribution of the coal measure shale samples by the mercury injection test.

Sample	Specific surface area ($m^2 \cdot g^{-1}$)					Specific surface area ratio (%)			
	Micropore	Small pore	Mesopore	Macropore	Total	Micropore	Small pore	Mesopore	Macropore
2	0.3769	0.7175	0.0028	0.0018	1.099	34.30	65.28	0.26	0.16
3	1.0968	1.2326	0	0.0006	2.3300	47.07	52.90	0	0.03
4	0.6955	0.6481	0.0152	0.0023	1.3611	51.1	47.62	1.12	0.16
5	0.7362	0.8246	0.0121	0.0012	1.5741	46.77	52.39	0.77	0.08
6	0.4496	0.496	0.0062	0.0013	0.9531	47.18	52.04	0.65	0.13
8	1.1759	1.1912	0.0043	0.0006	2.3720	49.57	50.22	0.18	0.02
9	1.0840	1.1175	0.0068	0.0017	2.1100	49.05	50.57	0.31	0.08
11	0.7180	1.0073	0.0140	0.0017	1.7410	41.24	57.86	0.81	0.09
12	1.0872	0.7044	0.0185	0.0029	1.8130	59.97	38.85	1.02	0.16
13	1.6729	1.2690	0.0222	0.0027	2.9670	56.38	42.78	0.75	0.09
14	2.7994	3.4620	0.0325	0.002	6.2959	44.46	54.99	0.52	0.03
15	0.8253	0.5131	0	0.0006	1.3390	61.63	38.32	0	0.05
16	1.3466	2.0956	0.0221	0.0018	3.4661	38.85	60.46	0.64	0.05
17	0.9288	0.6200	0.0012	0.001	1.5510	59.88	39.98	0.08	0.06
18	0.9709	0.8983	0.0026	0.0012	1.8730	51.83	47.96	0.14	0.06

pores exist within the 100–10,000 nm diameter range, where the mercury injection curve presents an increasing segment, and the pore volumetric ratio is lower than 5% (Figure 5B). The multimodal type is only observed in individual silty mudstones and shares similar features with the bimodal type, although the mesopore volume increases slightly in this type (Figure 5C). In addition, the SSA of the samples is mainly concentrated within the micropores and the small pores with the size of < 50 nm and presents unimodal characteristics (Figure 5).

3.4 Low-temperature N_2 adsorption test

The low-temperature N_2 adsorption test can quantitatively determine pore structural characteristics between 2 and 50 nm. It should be noted that the pores with the size of < 50 nm are the main contributor to the SSA according to the mercury injection test, and it would be helpful for clarifying the gas occurrence characteristics by conducting a more detailed study on these pores separately.

The Barrett–Joyner–Halenda (BJH) and Brunauer–Emmett–Teller (BET) methods were adopted to obtain the pore volume and SSA parameters, respectively (Gregg and Sing, 1982; Ross and Bustin, 2008). The results show that there are significant differences in the pore volume and SSA distributions of the pores with the size of lower or higher than 5 nm. Particularly, for pores with the size of 2–5 nm, the total pore volume is 0.0004–0.0061 cm^3/g (avg. 0.0029 cm^3/g), and the pore volumetric ratio is relatively low, i.e., 14.29%–36.22% (avg. 21.72%). Also, the total SSA of these pores is 0.5653–7.9056 m^2/g (avg. 3.7765 m^2/g), and the SSA ratio is 46.10%–67.63% (avg. 57.04%). For the pores with the size of 5–50 nm, the total pore volume and volumetric ratio are 0.0027–0.0131 cm^3/g (avg. 0.0099 cm^3/g) and 63.78%–85.71% (avg. 78.28%), respectively. The total SSA and SSA ratio of these pores are 0.6609–3.9798 m^2/g (avg. 2.6612 m^2/g) and 32.37%–53.90% (avg. 42.97%), respectively (Table 4). The aforementioned results indicate that as the pore size decreases, the complexity of the shale pore surface increases, resulting in more spaces for shale gas adsorption.

In addition, the pore structure characteristics of the coal measure shale exhibit universal regularity. Particularly, the pore volume increases slowly between the sizes of 2 and 5 nm and then rapidly increases between 5 and 50 nm (Figure 6A). A peak of the SSA appears at the pore size of about 3 nm, and the SSA decreases between the sizes of 3 and 5 nm and then slowly increases as the pore size increase until it reaches a peak at about 30 nm. After that, the SSA slowly decreases (Figure 6B).

The N_2 adsorption test can also provide a reference for characterization of the micropores with the size of < 2 nm, and the Saito–Foley (SF) theory is generally adopted to obtain the pore volume distributions. The results show that the lower limit of the pore size that can be detected is 0.7 nm, and the pore volume increases with the decrease of pore size in the range of 0.7–2 nm (Figure 7A). Given that the pore surface complexity tends to increase with the decrease of pore size, the SSA ratio of the pores might be higher as the pore size decreases.

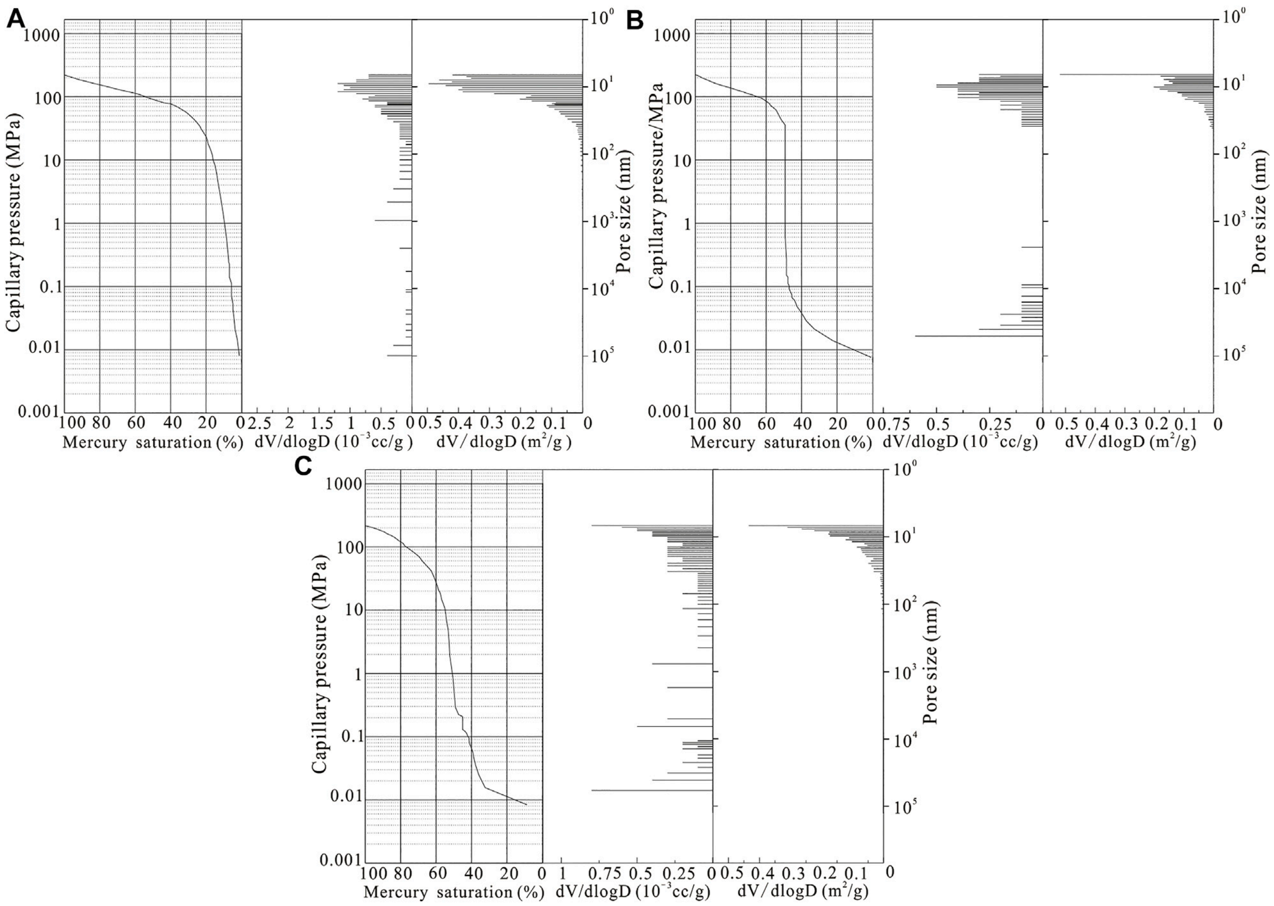

FIGURE 5
Mercury injection curves of the coal measure shale samples. **(A)** sample 14; **(B)** sample 3; **(C)** sample 13. V, pore volume; S, specific surface area; and D, pore size.

In addition, the International Union of Pure and Applied Chemistry (IUPAC) classified the gas adsorption isotherms into six types (i.e., Ⅰ–Ⅵ) and the hysteresis loop into four types (i.e., H1–H4) (Ji et al., 2014). Accordingly, the adsorption and desorption isotherms of the coal measure shales can be classified as type II and H3, indicating that the slit-shaped pores are well-developed in the shales (Figure 7B). This is consistent with the observations by FE-SEM, of which the clay minerals in the shale samples develop numerous intercrystalline pores that belong to the slit-shaped pores.

3.5 Low-temperature CO_2 adsorption test

The low-temperature CO_2 adsorption test has been widely applied to evaluate the micropore structure characteristics when the pore size is lower than 2 nm. The Horvath–Kawazoe (HK) theory was employed to calculate the volume of micropores, and the Dubinin–Radushkevich (DR) and Dubinin–Astakhov (DA) equations were employed to calculate the SSA of micropores. The results show that under the test range of lower than 2 nm, the median value of the pore size is 0.8180–1.7216 nm (avg. 1.3558 nm), and the total pore volume is 0.0021–0.0079 cm^3/g (avg. 0.0055 cm^3/g), and the total SSAs calculated by the DR and DA equations are 5.1167–19.6384 m^2/g (avg. 13.6109 m^2/g) and 6.5152–25.9762 m^2/g (avg. 17.3002 m^2/g), respectively (Table 5). Thus, the total SSA of the pores with the size of < 2 nm is higher than that of the other pores, indicating they are important places for shale gas adsorption. In addition, the results show that there are significant differences in the pore volume distribution among the samples under the pore size of lower than 2 nm. For example, the pore volume of some samples is concentrated at the pores with the size of 0.5–1 nm, and the total pore volume is relatively low (e.g., samples 3 and 5 in Figure 8), while that of some other samples is mainly distributed in the pores with the size of 0.7–1.7 nm (e.g., samples 2 and 8 in Figure 8). However, the pore volume of all samples shows a general trend of decrease with the increase of pore size, and given the pore surface complexity change, it is speculated that the pore SSA also tends to decrease as the pore size increases.

TABLE 4 Results of the pore volume, specific surface area, and their ratios of the coal measure shale samples by the low-temperature N_2 adsorption test.

Sample	V_{BJH} ($cm^3 \cdot g^{-1}$)		V_{BJH} ratio (%)		S_{BET} ($m^2 \cdot g^{-1}$)		S_{BET} ratio (%)	
	2–5 nm	5–50 nm	2–5 nm	5–50 nm	2–5 nm	5–50 nm	2–5 nm	5–50 nm
1	0.0028	0.0104	21.46	78.54	3.7433	2.6982	58.11	41.89
2	0.0021	0.0080	21.07	78.93	2.8199	2.0696	57.67	42.33
3	0.0024	0.0108	18.38	81.62	3.2003	2.6741	54.48	45.52
4	0.0016	0.0075	17.90	82.10	2.1605	1.9104	53.07	46.93
5	0.0004	0.0027	14.29	85.71	0.5653	0.6609	46.10	53.90
6	0.0018	0.0082	18.29	81.71	2.3585	2.1653	52.13	47.87
7	0.0023	0.0116	16.75	83.25	3.0719	2.4747	55.38	44.62
8	0.0043	0.0112	27.53	72.47	5.6286	3.3662	62.58	37.42
9	0.0028	0.0111	20.38	79.62	3.6910	2.7767	57.07	42.93
10	0.0027	0.0095	22.37	77.63	3.6309	2.5125	59.10	40.90
11	0.0019	0.0084	18.72	81.28	3.5027	2.0807	54.89	45.11
12	0.0027	0.0088	23.23	76.77	3.5027	2.0807	62.73	37.27
13	0.0036	0.0131	21.50	78.50	4.5389	3.6021	55.75	44.25
14	0.0036	0.0150	19.15	80.85	4.4847	3.9798	52.98	47.02
15	0.0033	0.0117	22.10	77.90	4.2898	3.2749	56.71	43.29
16	0.0028	0.0090	23.49	76.51	3.5697	2.6432	57.46	42.54
17	0.0061	0.0107	36.22	63.78	7.9056	3.7834	67.63	32.37
18	0.0041	0.0104	28.05	71.95	5.3119	3.1478	62.79	37.21

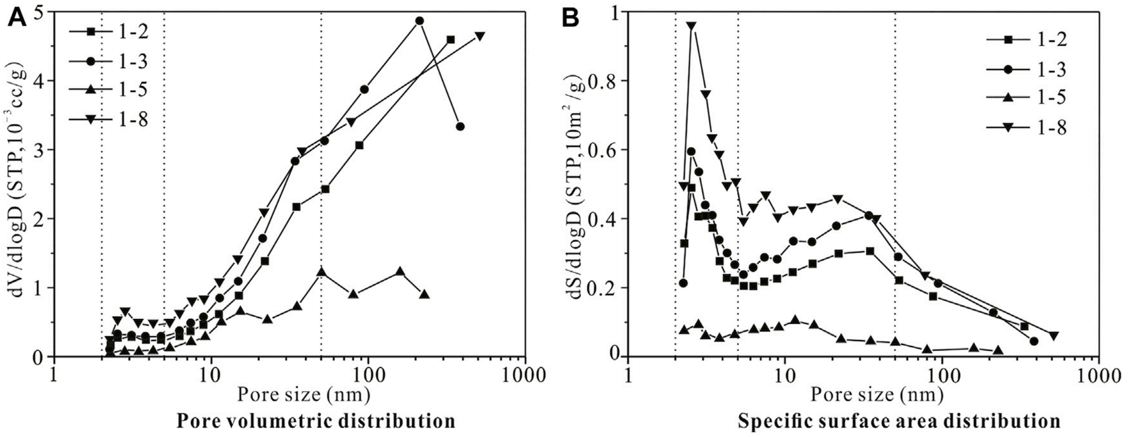

FIGURE 6
Pore volume and SSA distributions of the coal measure shale samples by the BJH and BET methods. **(A)** pore volumetric distribution; **(B)** pore SSA distribution. V—pore volume; S—SSA; D—pore size; and STP—standard temperature and pressure.

3.6 Controlling factors of the shale pore structure

Combining the aforementioned test results, the controlling factors of the shale pore structure are analyzed in this part. According to data statistics, the pore structure characteristics of different types of shales show certain differences. Among them, the porosity of carbonaceous mudstone is higher than that of others, while the volume and SSA of the mudstone and carbonaceous mudstone pores with the size of < 5 nm are higher than those of the siltstone and silty mudstone. This indicates that the shale composition has an important

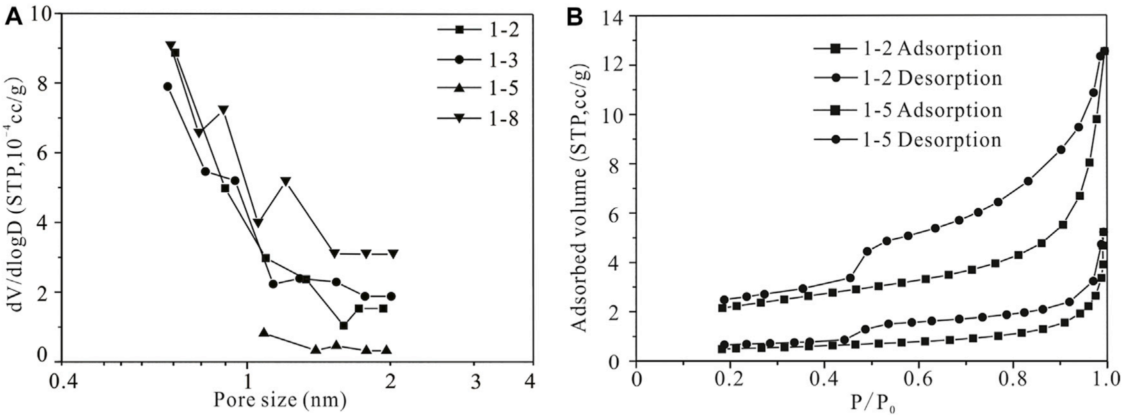

FIGURE 7
Pore volume distributions of micropore volume by N_2 adsorption **(A)** and the N_2 adsorption and desorption isotherm **(B)** of the shales. V—pore volume; D—pore size; and STP—standard temperature and pressure.

TABLE 5 Results of the pore volume and specific surface area of the coal measure shale samples by the low-temperature CO_2 adsorption test.

Sample	Median value of the pore size (nm)	V_{HK} ($cm^3 \cdot g^{-1}$)	SSA ($m^2 \cdot g^{-1}$)	
			DR	DA
2	1.1675	0.0032	7.9981	10.9166
3	0.8180	0.0053	13.1013	16.8235
5	0.9402	0.0021	5.1167	6.5152
6	0.9579	0.0050	12.5519	15.8866
7	1.6799	0.0050	12.5521	15.4677
8	1.1653	0.0079	19.6384	25.9762
9	0.9063	0.0064	15.8580	19.6429
10	1.6611	0.0070	17.5555	20.8681
11	1.3008	0.0053	13.1621	16.8577
12	1.6311	0.0077	19.3174	25.2236
15	1.7126	0.0060	15.0602	19.2182
16	1.7216	0.0046	11.3771	14.0189
17	1.6481	0.0064	16.0227	20.3640
18	1.6712	0.0045	11.2415	14.4241

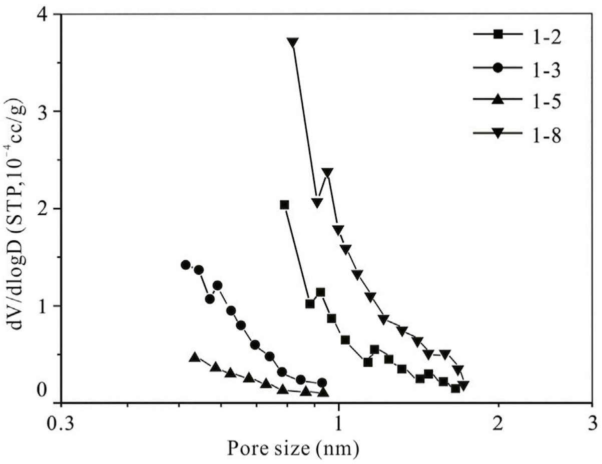

FIGURE 8
Pore volume distributions of the coal measure shale samples by the HF method. V—pore volume; D—pore size; STP—standard temperature and pressure.

influence on pore structure characteristics, including organic matter, brittle, and clay minerals.

The results of correlation analysis between shale components and porosity and total SSA show that the TOC content is closely related to the porosity and total SSA. Particularly, when the TOC content is lower than 6%, both the porosity and total SSA possess a strong positive correlation with the TOC content, indicating that organic matter in shale plays an important role in shale pore development. However, when the TOC content is higher than 6%, this positive correlation disappears, and the porosity and total SSA show a decreasing trend with the increase of the TOC content. The reason is that the shale organic matter has plastic characteristics, and as the TOC content increases, the shale plasticity is enhanced, making the shale pores more susceptible to the compaction effect and more difficult to preserve. This has also been verified by Milliken et al. (2013), and the critical TOC content they found is 5.6%. In addition, the brittle and clay mineral contents have negative and positive correlations with the porosity, respectively, but poor correlation with the total SSA. The reason is that the brittle

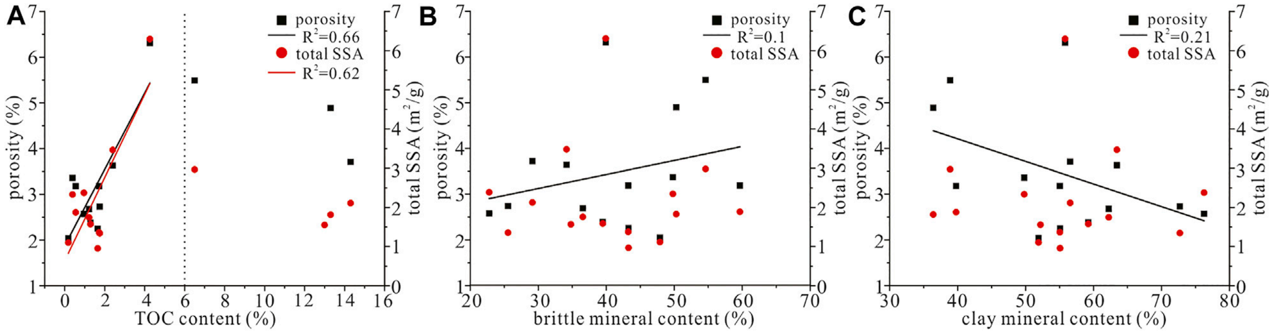

FIGURE 9
Plots showing the correlations of porosity and total SSA with TOC **(A)**, brittle mineral, **(B)** and clay mineral **(C)** contents.

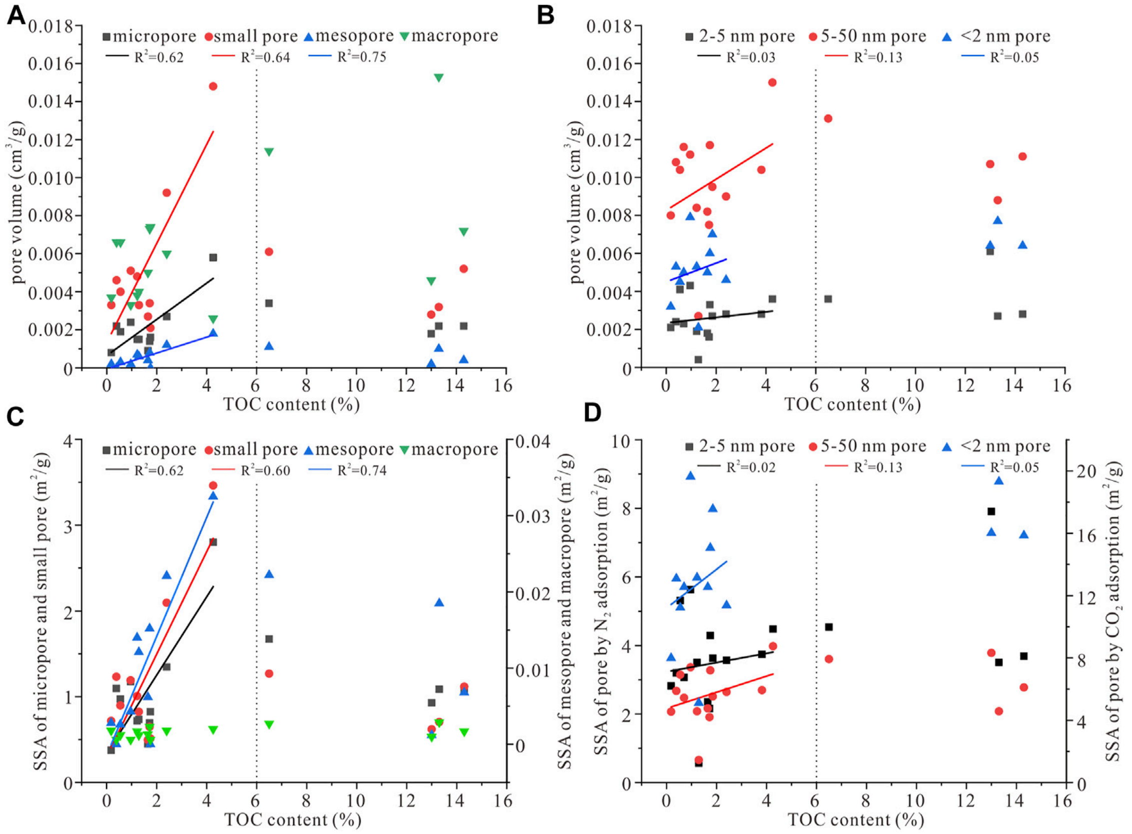

FIGURE 10
Plots showing the correlations of TOC content with pore volume and SSA by mercury injection **(A,C)** and N_2 and CO_2 adsorption **(B,D)**.

mineral, generally quartz in this area, constitutes the main rigid framework of shales, which can resist compaction stress and protect the pores (Zhao et al., 2017; Xi et al., 2019). However, the clay mineral has the characteristics of high plasticity and easy deformation and is easily squeezed into pores under the action of external force and reduces pore space. Also, when there is not enough brittle mineral to provide support, the increase of clay mineral content can lead to collapse of organic matter pores and interlayer pores of clay minerals, making the shale pores difficult to preserve (Figure 9) (Slatt and O'Brien, 2011).

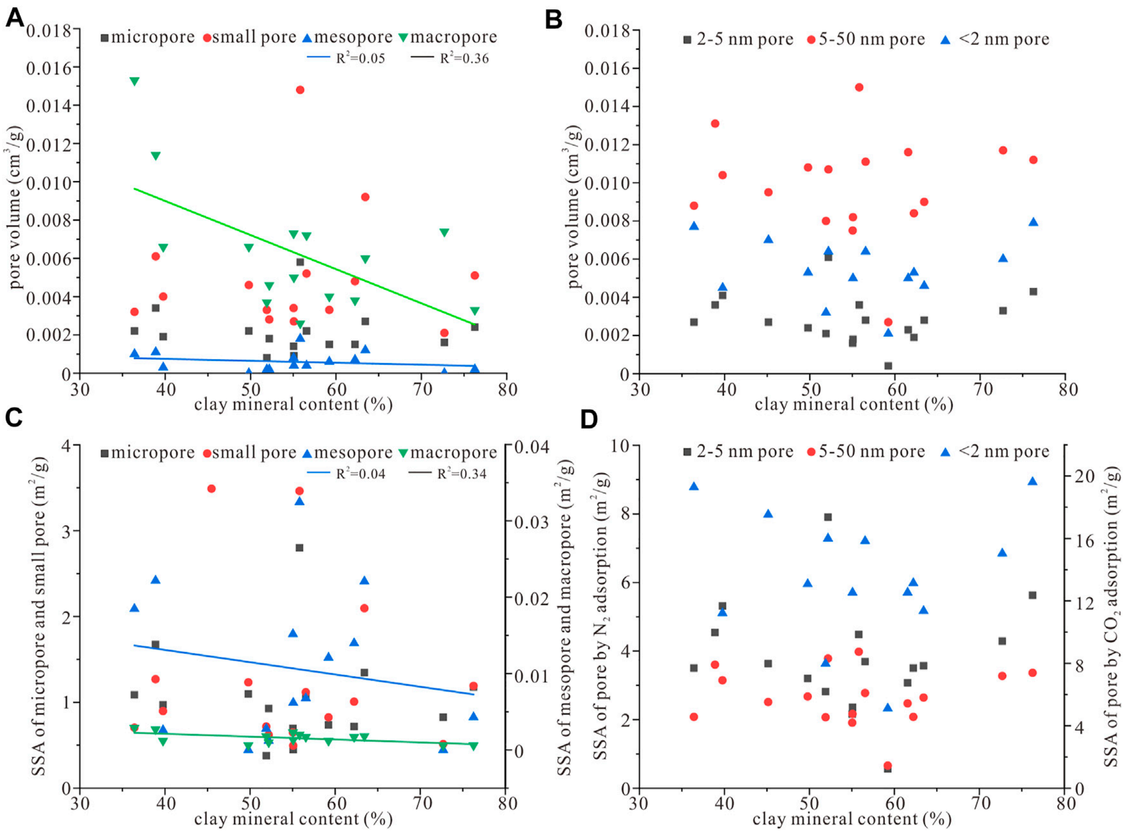

FIGURE 11
Plots showing the correlations of clay mineral content with pore volume and SSA by mercury injection **(A,C)** and N_2 and CO_2 adsorption **(B,D)**.

Furthermore, the relationships between the shale components and the pore structure at all levels are analyzed. The results show that when the TOC content is less than 6%, it has a positive correlation with the pore volume and SSA of the micropore, small pore, and mesopore measured by the mercury intrusion and the pores measured by the N_2 and CO_2 adsorptions, especially the pores of < 50 nm, indicating that the organic matter has a control effect on these pores, which is consistent with the previous research results (Pan et al., 2017; Zhang et al., 2019b; Ge et al., 2020; Yuan et al., 2021). However, under the influence of the compaction effect, the development of pores at all levels is limited when the TOC content is higher than 6%, and this effect tends to weaken as the pore size decreases (Figure 10).

The clay mineral content has a negative correlation with the pore volume and SSA of the mesopore and macropore, but it correlates poorly with those of the micropore and small pore. The reason is that the mesopore and macropore generally possess large apertures, and the clay mineral is more likely to enter and block these pores under the compaction effect, resulting in decrease of these pore spaces as there is an increase of clay mineral content. Also, the increase of clay mineral content can lead to a decrease of brittle mineral content, aggravating the compaction and pore blockage effects. However, the micropore and small pore are well-developed in clay minerals, and the volume and SSA of these pores tend to increase with the clay mineral content, which offsets some of the pore blockage effects. Additionally, the SSA of the micropore in organic matter is generally higher than that of the clay mineral (Xiong et al., 2017), weakening the correlations between the clay mineral content and the micropore SSA and the total SSA of the shale pore (Figure 11).

In addition, the brittle mineral has a significant control effect on mesopore and macropore development, and the volume and SSA of these pores tend to increase with its content. For the micropore and small pore, when the brittle mineral content is lower than 45%, the pore volume and SSA tend to decrease with the increase of brittle mineral content. This is because an increase in the brittle mineral content will lead to a decrease in the total content of organic matter and clay minerals, which are the main providers of these pores. However, when the brittle mineral content is higher than 45%, the volume and SSA of the micropore and small pore tend to increase. The reason is that the support effect on the shale pores provided by the brittle

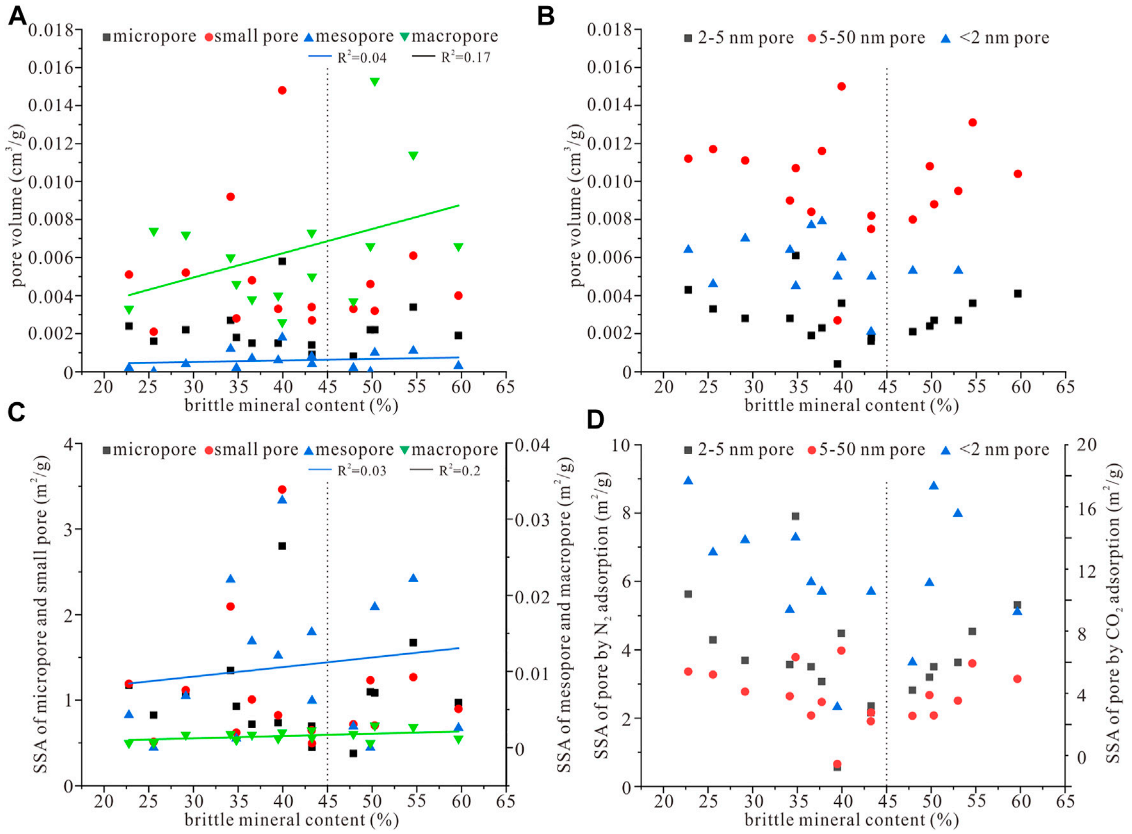

FIGURE 12
Plots showing the correlations of brittle mineral content with pore volume and SSA by mercury injection **(A,C)** and N_2 and CO_2 adsorption **(B,D)**.

mineral becomes significant for these pores, which is conducive to the maintenance of the pores in organic matter and clay minerals (Figure 12).

4 Conclusion

In this study, the coal measure shales of the Xiashihezi Formation in the Sunan Syncline block are taken as a research object, and its pore structure characteristics are systematically studied through experiments such as XRD, FE-SEM, mercury intrusion, and low-temperature N_2 and CO_2 adsorption. The main conclusions are as follows:

1. Four types of coal measure shales have been observed in the Xiashihezi Formation. Among them, the carbonaceous mudstone, characterized by high TOC content, has the highest porosity, and the pore volume and SSA of the mudstone and carbonaceous mudstone with the pore size of less than 5 nm are higher than those of the siltstone and silty mudstone.
2. The pore SSA of the coal measure shale is mainly concentrated in the micropores and small pores with the size of < 50 nm, and that of the micropores with the size of < 5 nm is significantly higher, indicating these pores have an important effect on gas adsorption. The matrix pores with the size of about 10 nm make significant contributions to pore volume and provide great spaces for free gas.
3. When the TOC content is lower than 6%, it has a strong positive correlation with the pore volume and total SSA of the shales. However, this positive correlation disappears when it is higher than 6% under the enhancement of the compaction effect, while the brittle and clay mineral contents have negative and positive correlations with the porosity, respectively, but poor correlation with the total SSA.
4. The organic matter has a control effect on the micropore, small pore, and mesopore of the shales and the volume as well as SSA of these pores increase with the TOC content (<6%). The clay mineral content has negative correlations with the volume and SSA of the mesopore and macropore under the compaction and pore blockage effects but correlates poorly with those of the micropore and small pore. In addition, the brittle mineral promotes the development of mesopore and macropore and is conducive to the micropore and small pore maintenance when the content is higher than 45%.

Data availability statement

The original contributions presented in the study are included in the article/Supplementary Material; further inquiries can be directed to the corresponding authors.

Author contributions

QW: methodology, investigation, writing—original draft, and writing—review and editing. XS: conceptualization, project administration, funding acquisition, and supervision. YJ: data curation and writing—review and editing. PC: methodology and writing—original draft. WZ: methodology and investigation. SY: writing—review and editing.

Funding

This work was supported by the Science and Technology Major Project of Shanxi Province (20191102001), the National Natural Science Foundation of China (42202209), the Natural Science Foundation for Young Scientists of Henan Province, China (222300420173), the China Postdoctoral Science Foundation (2022M711055), and the State Key Laboratory Cultivation Base for Gas Geology and Gas Control (Henan Polytechnic University) (WS2021B13).

Conflict of interest

The authors declare that the research was conducted in the absence of any commercial or financial relationships that could be construed as a potential conflict of interest.

Publisher's note

References

Cao, L., and Guo, Y. (2020). Study on pore structure characteristics of mud shale in Wuxiang Block of eastern Qinshui Basin. *Coal Sci. Technol.* 48 (4), 230–236. doi:10.13199/j.cnki.cst.2020.04.027

Cao, D., Yao, Z., and Li, J. (2014). Evaluation status and development trend of unconventional gas in coal measure. *Coal Sci. Technol.* 42, 89–92. doi:10.13199/j.cnki.cst.2014.01.021

Cao, Q., Zhou, W., Deng, H., and Chen, W. (2015). Classification and controlling factors of organic pores in continental shale gas reservoirs based on laboratory experimental results. *J. Nat. Gas Sci. Eng.* 27, 1381–1388. doi:10.1016/j.jngse.2015.10.001

Chen, Q., Zhang, J., Tang, X., Li, W., and Li, Z. (2016). Relationship between pore type and pore size of marine shale: An example from the Sinian–Cambrian formation, upper Yangtze region, South China. *Int. J. Coal Geol.* 158, 13–28. doi:10.1016/j.coal.2016.03.001

Chen, L., Jiang, Z., Liu, K., Tan, J., Gao, F., and Wang, P. (2017). Pore structure characterization for organic-rich lower silurian shale in the upper yangtze platform, south China: A possible mechanism for pore development. *J. Nat. Gas Sci. Eng.* 46, 1–15. doi:10.1016/j.jngse.2017.07.009

Clarkson, C. R., Solano, N., Bustin, R. M., Bustin, A., Chalmers, G., He, L., et al. (2013). Pore structure characterization of North American shale gas reservoirs using USANS/SANS, gas adsorption, and mercury intrusion. *Fuel* 103, 606–616. doi:10.1016/j.fuel.2012.06.119

Fishman, N. S., Hackley, P. C., Lowers, H. A., Hill, R. J., Egenhoff, S. O., Eberl, D. D., et al. (2012). The nature of porosity in organic-rich mudstones of the upper jurassic kimmeridge clay formation, north sea, offshore United Kingdom. *Int. J. Coal Geol.* 103, 32–50. doi:10.1016/j.coal.2012.07.012

Ge, T., Pan, J., Wang, K., Liu, W., Mou, P., and Wang, X. (2020). Heterogeneity of pore structure of late Paleozoic transitional facies coal-bearing shale in the Southern North China and its main controlling factors. *Mar. Petroleum Geol.* 122, 104710. doi:10.1016/j.marpetgeo.2020.104710

Gregg, S. J., and Sing, K. S. W. (1982). *Adsorption, surface area and porosity*. New York: American Academic Press.

Gui, H., and Chen, S. (2016). Isotopic geochemical characteristics of groundwater and its geological significance in Sunan mining area. *Earth Sci. Front.* 3, 133–139. doi:10.13745/j.esf.2016.03.017

Ji, W., Song, Y., Jiang, Z., Wang, X., Bai, Y., and Xing, J. (2014). Geological controls and estimation algorithms of lacustrine shale gas adsorption capacity: A case study of the triassic strata in the southeastern Ordos Basin, China. *Int. J. Coal Geol.* 134–135 (1), 61–73. doi:10.1016/j.coal.2014.09.005

Josh, M., Esteban, L., Delle Piane, C., Sarout, J., Dewhurst, D., and Clennell, M. (2012). Laboratory characterisation of shale properties. *J. Petroleum Sci. Eng.* 88, 107–124. doi:10.1016/j.petrol.2012.01.023

Ko, L. T., Ruppel, S. C., Loucks, R. G., Hackley, P. C., Zhang, T., and Shao, D. (2018). Pore-types and pore-network evolution in Upper Devonian-Lower Mississippian Woodford and Mississippian Barnett mudstones: Insights from laboratory thermal maturation and organic petrology. *Int. J. Coal Geol.* 190, 3–28. doi:10.1016/j.coal.2017.10.001

Li, X., Kang, Y., and Haghighi, M. (2018). Investigation of pore size distributions of coals with different structures by nuclear magnetic resonance (NMR) and mercury intrusion porosimetry (MIP). *Measurement* 116, 122–128. doi:10.1016/j.measurement.2017.10.059

Li, X., Zhang, J., Wang, Y., Guo, M., Wang, Z., and Wang, F. (2018). Accumulation condition and favorable area evaluation of shale gas from the Niutitang Formation in northern Guizhou, South China. *J. Nat. Gas Geoscience* 3, 1–10. doi:10.1016/j.jnggs.2018.03.001

Liu, H., Tong, L., and Yan, J., (2016). Controlling effect of geological structure on the thickness variation of 72 coal seam in Sunan mining area. *Coal Geol. Explor.* 44, 24–28. doi:10.3969/j.issn.1001-1986.2016.02.005

Liu, K., Ostadhassan, M., Zhou, J., Gentzis, T., and Rezaee, R. (2017). Nanoscale pore structure characterization of the Bakken shale in the USA. *Fuel* 209, 567–578. doi:10.1016/j.fuel.2017.08.034

Middleton, R. S., Gupta, R., Hyman, J. D., and Viswanathan, H. S. (2017). The shale gas revolution: Barriers, sustainability, and emerging opportunities. *Appl. energy* 199, 88–95. doi:10.1016/j.apenergy.2017.04.034

Milliken, K. L., Rudnicki, M., Awwiller, D. N., and Zhang, T. (2013). Organic matter-hosted pore system, marcellus formation (devonian), Pennsylvania. *Am. Assoc. Pet. Geol. Bull.* 97 (2), 177–200. doi:10.1306/07231212048

Pan, J., Peng, C., Wan, X., Zheng, D., Lv, R., and Wang, K. (2017). Pore structure characteristics of coal-bearing organic shale in Yuzhou coalfield, China using low pressure N_2, adsorption and FESEM methods. *J. Petroleum Sci. Eng.* 153, 234–243. doi:10.1016/j.petrol.2017.03.043

Ross, D. J. K., and Bustin, R. M. (2008). Characterizing the shale gas resource potential of Devonian–Mississippian strata in the Western Canada sedimentary basin: Application of an integrated formation evaluation. *Am. Assoc. Pet. Geol. Bull.* 92 (1), 87–125. doi:10.1306/09040707048

Schmitt, M., Fernandes, C. P., da Cunha Neto, J. A. B., Wolf, F. G., and dos Santos, V. S. (2013). Characterization of pore systems in seal rocks using nitrogen gas adsorption combined with mercury injection capillary pressure techniques. *Mar. Petroleum Geol.* 39 (1), 138–149. doi:10.1016/j.marpetgeo.2012.09.001

Slatt, R. M., and O'Brien, N. R. (2011). Pore types in the Barnett and Woodford gas shales: Contribution to understanding gas storage and migration pathways in fine-grained rocks. *Am. Assoc. Pet. Geol. Bull.* 95 (12), 2017–2030. doi:10.1306/03301110145

Song, Y., Jiang, B., Li, F., and Jiegang, L. (2017). Structure and fractal characteristic of micro-and meso-pores in low, middle-rank tectonic deformed coals by CO_2 and N_2 adsorption. *Microporous Mesoporous Mater.* 253, 191–202. doi:10.1016/j.micromeso.2017.07.009

Su, X., Wang, Q., Lin, H., Song, J., and Guo, H. (2018). A combined stimulation technology for coalbed methane wells: Part 2. Application. *Fuel* 233, 539–551. doi:10.1016/j.fuel.2018.06.086

Su, X., Wang, Q., Lin, H., Song, J., and Guo, H. (2018). A combined stimulation technology for coalbed methane wells: Part 1. Theory and technology. *Fuel* 233, 592–603. doi:10.1016/j.fuel.2018.06.087

The Chinese Standard of Petroleum and Natural Gas Industry (2010). *Analysis method for clay minerals*. Beijing: The Chinese Standard of Petroleum and Natural Gas Industry. SY/T 5163-2010.

The Chinese Standard of Petroleum and Natural Gas Industry (2014). *Analytical method of rock sample by scanning electron microscope*. Beijing: The Chinese Standard of Petroleum and Natural Gas Industry. SY/T 5162–2014.

The National Standard of the People's Republic of China (2003). *Determination of total organic carbon in sedimentary rock*. Beijing: The National Standard of the People's Republic of China. GB/T 19145-2003.

The National Standard of the People's Republic of China (2008a). *Pore size distribution and porosity of solid materials by mercury porosimetry and gas adsorption—Part 1: Mercury porosimetry*. Beijing: The National Standard of the People's Republic of China. GB/T 21650.1-2008.

The National Standard of the People's Republic of China (2008b). *Pore size distribution and porosity of solid materials by mercury porosimetry and gas adsorption—Part 2: Analysis of mesopores and macropores by gas adsorption*. Beijing: The National Standard of the People's Republic of China. GB/T 21650.2-2008.

The National Standard of the People's Republic of China (2011). *Pore size distribution and porosity of solid materials by mercury porosimetry and gas adsorption—Part 3: Analysis of micropores by gas adsorption*. Beijing: The National Standard of the People's Republic of China. GB/T 21650.3-2011.

Wang, D., Shao, L., Li, Z., Li, M. p., Lv, D., and Liu, H. (2016). Hydrocarbon generation characteristics, reserving performance and preservation conditions of continental coal measure shale gas: A case study of mid-jurassic shale gas in the yan'an Formation, Ordos Basin. *J. Petroleum Sci. Eng.* 145, 609–628. doi:10.1016/j.petrol.2016.06.031

Wang, Y., Pu, J., Wang, L., Jiang, Z., Song, Y. F., Wang, C. C., et al. (2016). Characterization of typical 3D pore networks of Jiulaodong formation shale using nano-transmission X-ray microscopy. *Fuel* 170, 84–91. doi:10.1016/j.fuel.2015.11.086

Wang, Z., Wagner, J., Ghosal, S., Bedi, G., and Wall, S. (2017). SEM/EDS and optical microscopy analyses of microplastics in ocean trawl and fish guts. *Sci. Total Environ.* 603, 616–626. doi:10.1016/j.scitotenv.2017.06.047

Wang, Q., Su, X., Su, L., and Zhou, F. (2020). CBM geological characteristics and exploration potential in the Sunan Syncline block, southern north China basin. *J. Petroleum Sci. Eng.* 186, 106713. doi:10.1016/j.petrol.2019.106713

Wang, Y., Liu, L., and Cheng, H. (2021). Gas adsorption characterization of pore structure of organic-rich shale: Insights into contribution of organic matter to shale pore network. *Nat. Resour. Res.* 30 (3), 2377–2395. doi:10.1007/s11053-021-09817-5

Wei, C., Jiang, B., and Fu, X., (2007). Numerical simulation on geological evolution history of coalbed methane in Sunan Syncline area. *Acta Pet. Sin.* 28 (1), 54–57. doi:10.7623/syxb200701010

Wei, Z., Wang, Y., Wang, G., Sun, Z., and Xu, L. (2018). Pore characterization of organic-rich late permian da-long formation shale in the sichuan basin, southwestern China. *Fuel* 211, 507–516. doi:10.1016/j.fuel.2017.09.068

Xi, Z., Tang, S., Li, J., Zhang, Z., and Xiao, H. (2019). Pore characterization and the controls of organic matter and quartz on pore structure: Case study of the Niutitang Formation of northern Guizhou Province, South China. *J. Nat. Gas Sci. Eng.* 61, 18–31. doi:10.1016/j.jngse.2018.11.001

Xiong, F., Jiang, Z., Li, P., Wang, X., Bi, H., Li, Y., et al. (2017). Pore structure of transitional shales in the Ordos Basin, NW China: Effects of composition on gas storage capacity. *Fuel* 206, 504–515. doi:10.1016/j.fuel.2017.05.083

Yuan, Y., Li, Z., and Zhong, M., (2021). Pore structure characteristics of Taiyuan formation coal measures shale in south central Qinshui Basin. *Coal Sci. Technol.* 49 (9), 184–192. doi:10.13199/j.cnki.cst.2021.09.026

Zhang, Y., Shao, D., Yan, J., Jia, X., Li, Y., Yu, P., et al. (2016). The pore size distribution and its relationship with shale gas capacity in organic-rich mudstone of Wufeng-Longmaxi Formations, Sichuan Basin, China. *J. Nat. Gas Geoscience* 1 (3), 213–220. doi:10.1016/j.jnggs.2016.08.002

Zhang, X., Si, Q., and Zuo, Z., (2016). Characteristics and the main controlling factors of pore structure in the continental coal-shale gas reservoirs. *Acta Geol. Sin.* 90 (10), 2930–2938. doi:10.3969/j.issn.0001-5717.2016.10.028

Zhang, J., Li, X., Wei, Q., Gao, W., Liang, W., Wang, Z., et al. (2017). Quantitative characterization of pore-fracture system of organic-rich marine-continental shale reservoirs: A case study of the upper permian longtan formation, southern sichuan basin, China. *Fuel (Lond).* 200, 272–281. doi:10.1016/j.fuel.2017.03.080

Zhang, Y., Liu, J., and Xu, H., (2017). Comparison between pore structure and fractal characteristics of continental and transitional coal measures shale: A case study of yan'an and taiyuan formations at the northeastern margin of Ordos Basin. *Acta Pet. Sin.* 38 (9), 1036–1046. doi:10.7623/syxb201709005

Zhang, J., Wei, C., Ju, W., Yan, G., Lu, G., Hou, X., et al. (2019). Stress sensitivity characterization and heterogeneous variation of the pore-fracture system in middle-high rank coals reservoir based on NMR experiments. *Fuel* 238, 331–344. doi:10.1016/j.fuel.2018.10.127

Zhang, M., Fu, X., Zhang, Q., and Cheng, W. (2019). Research on the organic geochemical and mineral composition properties and its influence on pore structure of coal-measure shales in Yushe-Wuxiang Block, South Central Qinshui Basin, China. *J. Petroleum Sci. Eng.* 173, 1065–1079. doi:10.1016/j.petrol.2018.10.079

Zhang, J., Tang, Y., He, D., Sun, P., and Zou, X. (2020). Full-scale nanopore system and fractal characteristics of clay-rich lacustrine shale combining FE-SEM, nano-CT, gas adsorption and mercury intrusion porosimetry. *Appl. Clay Sci.* 196, 105758. doi:10.1016/j.clay.2020.105758

Zhao, J., Jin, Z., Jin, Z., Hu, Q., Hu, Z., Du, W., et al. (2017). Mineral types and organic matters of the Ordovician-Silurian Wufeng and Longmaxi Shale in the Sichuan Basin, China: Implications for pore systems, diagenetic pathways, and reservoir quality in fine-grained sedimentary rocks. *Mar. Petroleum Geol.* 86, 655–674. doi:10.1016/j.marpetgeo.2017.06.031

Zhao, S., Li, Y., Wang, Y., Ma, Z., and Huang, X. (2019). Quantitative study on coal and shale pore structure and surface roughness based on atomic force microscopy and image processing. *Fuel* 244, 78–90. doi:10.1016/j.fuel.2019.02.001

Zuo, Z., Zhang, X., and Chen, S. (2017). Heterogeneity of shale gas reservoirs in coal measures: A case study of the taiyuan and Shanxi format. *Acta Geol. Sin.* 91 (5), 1130–1140. doi:10.3969/j.issn.0001-5717.2017.05.013

frontiers | Frontiers in Earth Science

TYPE Original Research
PUBLISHED 27 September 2022
DOI 10.3389/feart.2022.1024483

True triaxial experimental study on the influence of axial pressure on coal permeability

Jianbao Liu[1,2], Zhimin Song[1,2,3], Chengtao Yang[4]*, Bing Li[1], Jiangang Ren[1] and Ming Xiao[1]

[1]Henan University of Engineering, Zhengzhou, China, [2]Henan Polytechnic University, Jiaozuo, China, [3]North China University of Water Resources and Electric Power, Zhengzhou, China, [4]Henan Energy and Chemical Industry Group Research Institute Co., Ltd, Zhengzhou, China

Check for updates

OPEN ACCESS

EDITED BY
Junjian Zhang,
Shandong University of Science and Technology, China

REVIEWED BY
Run Chen,
China University of Mining and Technology, China
Gaofeng Liu,
Henan Polytechnic University, China

*CORRESPONDENCE
Chengtao Yang,
byctat@163.com

SPECIALTY SECTION
This article was submitted to Economic Geology,
a section of the journal
Frontiers in Earth Science

RECEIVED 21 August 2022
ACCEPTED 07 September 2022
PUBLISHED 27 September 2022

CITATION
Liu J, Song Z, Yang C, Li B, Ren J and Xiao M (2022), True triaxial experimental study on the influence of axial pressure on coal permeability.
Front. Earth Sci. 10:1024483.
doi: 10.3389/feart.2022.1024483

The permeability of coal is a key parameter affecting coal and gas outbursts and coal seam gas drainage. The permeability is clearly affected by geo-stress. In this study, the influence of the axial pressure on the permeability of the coal seam was studied using a self-developed true triaxial stress permeability experimental device to set fixed gas and confining pressures, and to change the magnitude of the axial pressure. The experimental results show a polynomial relationship between the axial pressure and the permeability of the coal seam. With an increase in axial pressure, the permeability initially decreased slightly and then increased gradually. When the axial pressure exceeded 30 MPa, the permeability of the coal seam sharply increased. This may be due to plastic deformation of the coal seam under a large axial pressure, resulting in new fractures and significantly improving the permeability of the coal seam. Using the COMSOL numerical simulation software, the effect of *in situ* stress on the coal seam gas drainage efficiency was calculated by comprehensively considering the adsorption/desorption, diffusion, and seepage of gas. The calculation results show that with an increase in the axial pressure, the gas drainage efficiency of the coal seam increases continuously. As the axial pressure increased from 5 to 30 MPa, the gas drainage efficiency increased to 2–3 times that of the original value.

KEYWORDS

true triaxial seepage experiment, anthracite, permeability, numerical simulation, drainage efficiency

Introduction

The risk of coal and gas outbursts in high-gas mines, and coal and gas outburst mines, increases with an increase in coal mining depth. Simultaneously, different structural phenomena such as folds and small faults are encountered in the coal mining process. These structures form stress concentration areas, which are the ideal areas for gas occurrence and coal and gas outbursts (Meng and Li, 2017; Shi et al., 2018; Yan et al., 2019; Lv et al., 2022; Tatyana et al., 2022; Wang et al., 2018). This phenomenon is caused by the distribution of *in situ* stress having an impact on the permeability of coal seams, which reduces the permeability of local coal seams and forms gas accumulation zones (Guo et al., 2019; Lin et al., 2022; Liu et al., 2022). By studying permeability change laws in Permian coal reservoirs, it was found that the link between the development characteristics of natural fractures and the current *in situ* stress state has an important control effect on the permeability of Permian coal reservoirs in eastern Yunnan and western Guizhou (Ju et al., 2022). Therefore, studying the change law of coal and rock permeability under stress can reduce the occurrence of gas accidents in coal mining and improve the efficiency of gas drainage.

Previous studies investigated the relationship between axial pressure and permeability, albeit with different interpretations (Chao et al., 2019; Cheng et al., 2022; Luo et al., 2022). There are three main viewpoints regarding coal permeability as it relates to increased axial pressure: decrease permeability, increased permeability, and an initial decrease in permeability followed by an increase. A variety of fitting structures have also been proposed for the relationship model between axial pressure and coal permeability (Connell et al., 2010; Rong et al., 2018; Zhou et al., 2019; Liu and Yu, 2022; Wang et al., 2022). The first point of view is that when gas and confining pressures are constant, the permeability of coal samples decrease exponentially with an increase in axial pressure (Xue et al., 2020; Li B. B et al., 2020). A study on the permeability of hard and soft coal by Sun et al. (2016) found that the change in axial pressure and permeability of hard coal conforms to the change law of linear decrease, and the influence of axial pressure on the permeability of soft coal is greater than that of hard coal. The second point of view is that the permeability of coal and rock mass in the pre- and post-peak stages show an exponential growth trend with stress; however, there are obvious differences in the growth amount between the two (Xue et al., 2017). The third point of view is that the permeability decreases first and then increases with the type of coal sample. This means that the permeability of gas bearing coal shows a “V" shape change pattern (Zhao, 2018; Li H. G et al., 2020). At the initial stage of loading where pore compression and elastic deformation occurs, the pores and fractures in the coal were gradually compacted, decreasing the permeability of the coal sample. In the plastic deformation stage, owing to an increase in axial stress, the fractures in the coal expand, the permeability of the coal sample increases, and the acoustic emission activity intensity increases and reaches its peak (Xie et al., 2016; Meng et al., 2020; Bai et al., 2021; Zhu et al., 2021). Through the triaxial compression of compacted clay, Wang et al. (2020) found that when the sample’s confining pressure was greater than the pre-consolidation pressure, the sample always showed volume shrinkage and became denser during triaxial compression. Therefore, the permeability coefficient decreased with an increase in the axial strain and subsequently stabilized. When the sample’s confining pressure is much less than the pre-consolidation pressure, a concentrated shear band is produced, which is unfavorable for seepage. The concentrated shear band became the seepage channel, and the axial permeability coefficient of the sample increased significantly with increasing axial strain.

There is also previous knowledge on the causes of permeability change (Li J. Q et al., 2020; Xue et al., 2021). Through an unloading experimental study on coal permeability, it is believed that the expansion of the original fracture and the generation of a new fracture causes the sudden increase in the permeability of the unloaded coal body (Cheng et al., 2014; Wang et al., 2021). The development law of coal sample fractures is related to loading and unloading rates (Jiang et al., 2020). The coal gradually develops from multiple macrofractures to a single macrofracture surface with an increase in the loading and unloading rate ratio, resulting in structural failure.

In this study, the change law of coal seam permeability with axial pressure was studied through the triaxial stress permeability test device under the context of fixed gas and confining pressures, and the influence of vertical formation stress on gas drainage efficiency was calculated using the COMSOL numerical analysis software.

Sample and experimental devices

Sample

The experimental sample was obtained from the Xiyang mining area in Shanxi Province. Large original coal samples with a relatively good integrity were collected from the coal mining face. The coal samples were packed, sealed, and transported to the laboratory. After cutting and grinding, the samples were processed into 100 × 100 × 100 mm cubes. The industrial analysis of coal is the main index used to understand the characteristics of coal quality and the basis for evaluating coal quality. The industrial analysis data of the coal samples measured according to GB/T212-2008 are shown in Table 1. The coal sample was anthracite, with a fixed carbon content of 72.15%.

A microscope with transmission light and reflection fluorescence functions was used to obtain quantitative statistics on the percentage content of each maceral in coal using the number point method. To determine the type of organic matter, a type index was calculated according to the different weighting coefficients of each maceral. The macerals of the coal mainly included exinite, vitrinite, and inertinite. The maceral data of the coal samples, measured according to GB/T8899-2013, are listed in Table 1. The vitrinite content of the coal sample was 82.81%.

Experimental devices

Experiments were performed using a self-developed true triaxial stress permeability test device (Figures 1, 2). The experimental equipment can complete the experimental research on gas permeability in an underground reservoir environment (triaxial pressure and temperature), and provide necessary technical support and basic scientific research data for gas disaster prevention and gas drainage in

TABLE 1 Industrial analysis and microstructure of the coal sample.

Coal types	Industrial analysis				Microstructure		
	M_{ad}/%	A_d/%	V_{daf}/%	*FCad*/%	Exinite/%	Vitrinite/%	Inertinite/%
WY	2.43	16.67	8.75	72.15	0.96	82.81	16.23

Note: M_{ad} is moisture on an air-dry basis, A_d is ash on a dry basis, V_{daf} is volatile matter on a dry ash-free basis, *and* FC_{ad}, is carbon on an air-dry basis.

FIGURE 1
Overall diagram of experimental device.

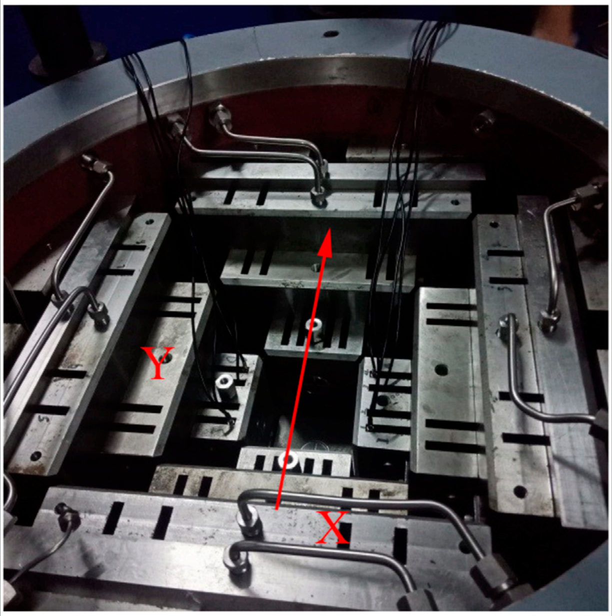

FIGURE 2
Core part of gripper. Note: The arrow stands for the gas seepage direction.

coal mines. The technical parameters of the equipment were as follows: 1) core size of 100 × 100 × 100 mm (optional sample size included 200 × 200 × 200 mm and 300 × 300 × 300 mm), a 100 × 100 × 100 mm sample was selected; 2) the maximum hydraulic pressure in the X-, Y-, and *Z*-axes of the three-axis hydraulic pressure is 40 MPa, and the control accuracy is ±0.1 MPa; 3) the gas permeability measurement range is 0.001–1,000 mD.

At home and abroad, silicone sleeves are mainly used to seal the edges of samples to prevent gas leakage during seepage. However, during the experiment, it was found that when the axial pressure was high, the silicone sleeve was more likely to be cut off. The experiment proves that the copper sleeve can not only ensure the sealing effect but also has a specific strength, strong pressure resistance and shear resistance, and that its sealing effect is better than that of the silicone sleeve. To further ensure the sealing effect, the copper sleeve was coated with epoxy resin.

Experimental results and discussions

Fracture development characteristics

The bedding plane of the experimental coal sample was placed horizontally. The two sides of the coal sample were marked as the X and Y planes, respectively, and the top surface was marked as the Z plane. The X planes are the planes through which the gas passes, and the Z planes are parallel to the bedding plane. The inlet gas pressure was set as 1.8 MPa. When the *x*-axis stress was set to 30 MPa, the *y*-axis stress was 20 MPa, and the x- and *y*-axis stresses remained unchanged. The *z*-axis stress was set to 5 MPa, 10 MPa, 15 MPa, 20 MPa, 25 MPa, 30 MPa, and 35 MPa (Figure 3) to study the influence of axial pressure change on permeability. After the experiment, the coal sample was taken out, and photographs were taken to observe the damage to the coal sample (Figure 4–6).

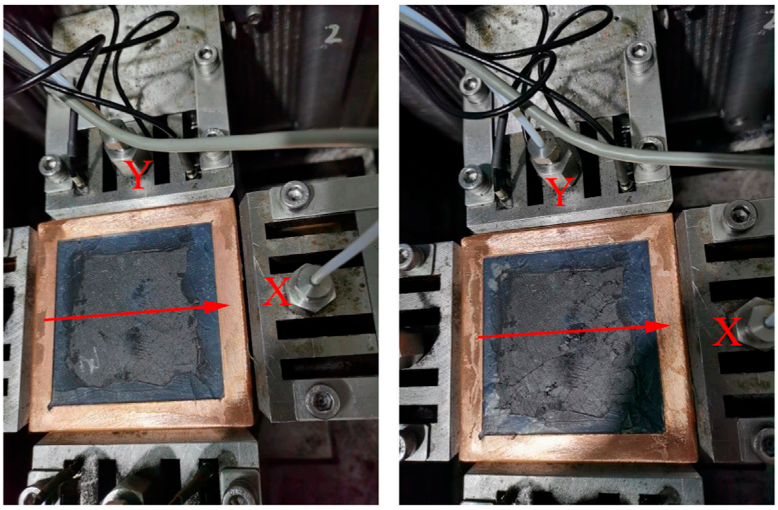

FIGURE 3
Coal sample before (left) and after (right) an axial compression permeability experiment. Note: The arrow stands for the gas seepage direction.

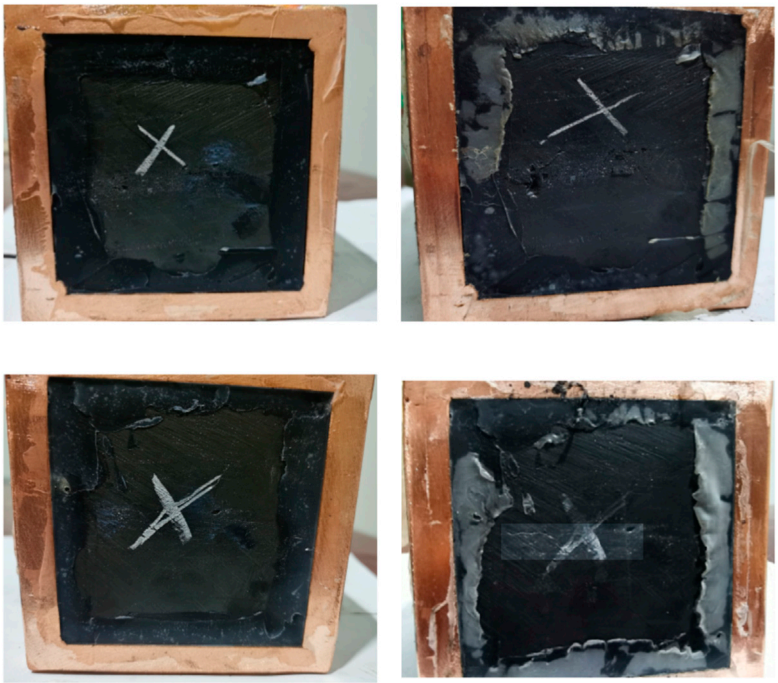

FIGURE 4
Comparison of the X plane before (left) and after (right) the experiment. Note: The fractures are highlighted with transparent frames. Fractures parallel to the bedding plane were formed.

The *in situ* stress has strong directionality, including mainly two horizontal stresses (σ_x and σ_y) and vertical stress (σ_z). In a formation where the natural fracture is not developed, the fracture shape depends on the three-dimensional stress state. According to the principle of minimum principal stress, fracture always occurs in the direction with the weakest strength and

FIGURE 5
Comparison of the Y plane before (left) and after (right) the experiment. Note: The fractures are highlighted with transparent frames. Fracture system perpendicular to the bedding plane and parallel to the bedding plane were formed.

smallest resistance. In other words, the rock fracture surface is perpendicular to the direction of the minimum principal stress (Barnett et al., 2015). Horizontal fractures tend to occur when the horizontal stress is greater than the vertical stress. On the same vein, vertical fractures are easily generated when the vertical stress is greater than the horizontal stress. The relationship between the stress and fractures is shown in Figure 7.

Therefore, in the process of σ_z change, the coal samples formed fractures in different directions. When σ_z was 5–20 MPa, the minimum principal stress was σ_z, and fractures perpendicular to the *z*-axis were formed, parallel to the bedding plane. The difference between the maximum and minimum principal stresses at this stage was 10–25 MPa. The formed fracture was evident on the Y plane of the sample. When σ_z is between 20 and 30 MPa and 30 and 35 MPa, the minimum principal stress is still σ_y. However, the maximum principal stress changes from σ_x to σ_z, and the intermediate principal stress changes from σ_z to σ_x. The stress difference increases from 10 MPa to 10–15 MPa, and fractures are formed on the Y and Z planes of the coal sample. However, the fractures are not well-developed on the X plane. This may be related to the heterogeneity of the coal samples and local development of microcracks. Under the action of triaxial stress, fractures develop along the direction of the microcracks, which are associated with macroscopic fractures. These provide channels for methane seepage and increase the permeability of the coal seams.

Variation characteristics of permeability

When the *z*-axis stress was low (less than 30 MPa), the permeability changed slightly with the change in axial pressure. However, when the axial pressure was high (more than 30 MPa), the permeability increased significantly. To further study the relationship between the axial pressure and initial permeability, as well as the permeability change, exponential function fitting, power function fitting, and polynomial fitting were performed on the experimental data using MATLAB. The fitting results are shown in Figure 8, Figure 9, and Figure 10 and Table 2. The best fitting model was the polynomial fitting, and the sum of the residual squares is one order of magnitude lower than the exponential and power functions. By analyzing the fitting curve, it can be found that with an increase in axial pressure,

FIGURE 6
Comparison of the Z plane before (left) and after (right) the experiment. Note: The fractures are highlighted with transparent frames. Fractures develop along the direction of the microcracks.

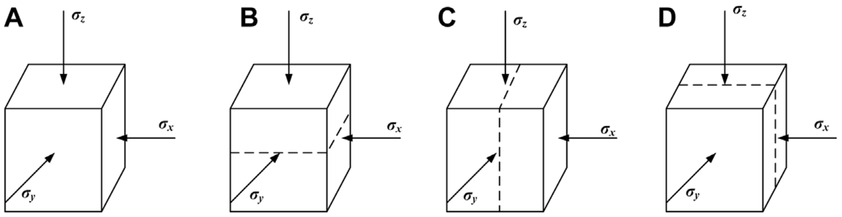

FIGURE 7
Relationship between stress and fracture morphology.**(A)** Three-dimensional stress state. **(B)** When σ_z is the minimum principal stress, horizontal fractures are formed. **(C)** When σ_x is the minimum principal stress, fractures perpendicular to σ_x are formed. **(D)** When σ_y is the minimum principal stress, fractures perpendicular to σ_y are formed.

the permeability shows a slight decrease at the stage of low axial pressure and then increases slowly. When the axial pressure exceeded 30 MPa, permeability increased sharply. This may be because the increase in the axial pressure condenses the pores and fractures of the coal sample in the initial stage; however, when the axial pressure exceeds the elastic deformation stage of the coal sample, plastic deformation begins to occur, forming new fractures, improving the permeability of the coal seam, and increasing permeability significantly.

Numerical simulation

To evaluate the influence of *in situ* stress on coal seam gas drainage efficiency, COMSOL was used to fully consider the overall process of gas adsorption/desorption, diffusion, and seepage through fluid–solid coupling analysis; a model was established for numerical analysis and calculation. Drawing from previous research results (Wang et al., 2016), the parameter settings for each module are listed in Table 3. The length and width of the model were set to 100 m, height

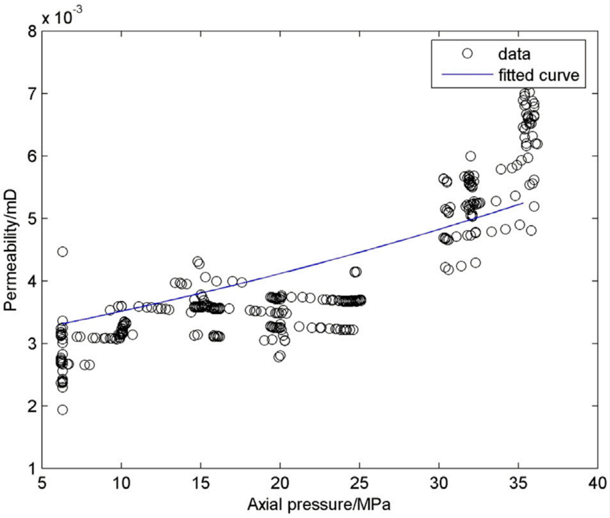

FIGURE 8
Exponential function fitting between axial pressure and permeability.

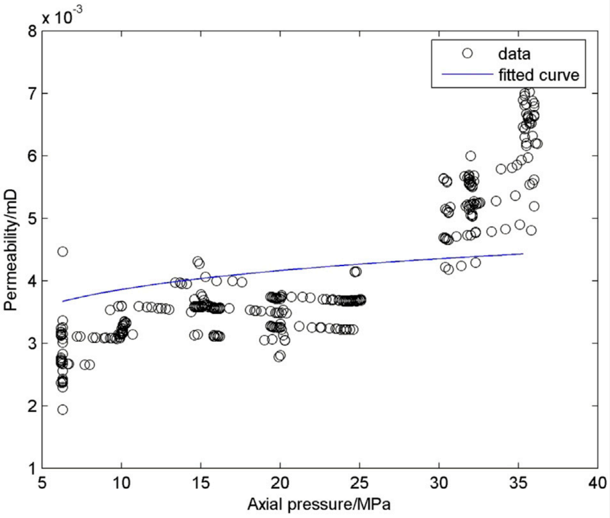

FIGURE 9
Power function fitting between axial pressure and permeability.

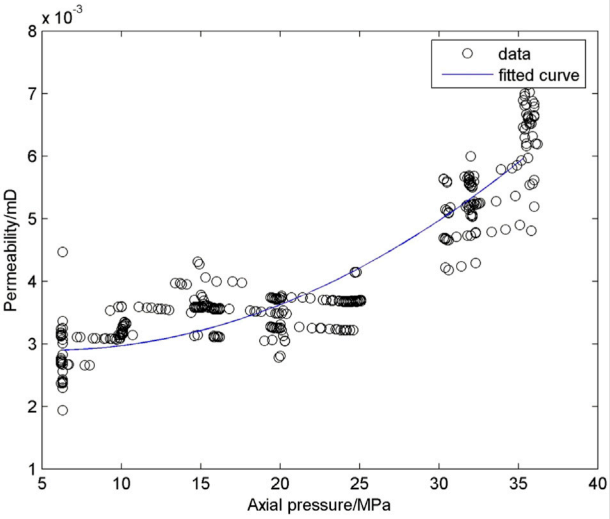

FIGURE 10
Polynomial fitting between axial pressure and permeability.

was set to 6 m, and drilling radius was set to 0.1 m. The established geometric model is shown in Figure 11.

The solid mechanics module adopts the linear elastic model and sets the left interface, front interface, and lower interface as the sliding boundary; in other words, the displacement in the normal direction is 0. The right interface was set as the pressure boundary, with a pressure of 30 MPa, simulating the *x*-axis stress in the true triaxial stress seepage experiment. The rear interface was set as the pressure interface with a pressure of 20 MPa, simulating the *y*-axis stress in the experiment. The upper boundary was set as the pressure boundary, and its stress was set to 5, 10, 15, 20, 25, and 30 MPa, simulating the stress in the *z*-axis direction perpendicular to the bedding plane of the coal seam.

The diffusion process was simulated using a general partial differential equation. In the process of gas extraction, the adsorbed gas in the coal matrix is desorbed as a mass source, so that diffusion and seepage continue. The mass exchange between the coal matrix and the fracture system can be expressed as:

$$Q = \frac{M}{tRT}(u - p). \tag{1}$$

There are both adsorbed gas and free gas in the pores of coal matrix. The total gas storage quality can be expressed as:

$$m = \frac{V_L u}{u + P_L}\rho_m \rho_g + \varphi_0 \frac{M}{RT} u. \tag{2}$$

The partial derivative of formula 2 to time is the mass exchange between coal matrix and fracture system. Therefore, the following formula can be obtained:

$$\frac{\partial m}{\partial t} = -\frac{M}{tRT}(u - p). \tag{3}$$

Then the diffusion source term *f* is expressed as:

TABLE 2 Comparison of fitting results of different methods.

Fitting formula	Fitting results	Sum of squares of residuals
$y = k_0 e^{ax}$	$y = 0.003e^{0.0158x}$	2.0835e-004
$y = k_0 x^a$	$y = 0.003x^{0.1093}$	4.1057e-004
$y = ax^2 + bx + k_0$	$y = 0.0001 \times (0.0343x^2 - 0.3737x) + 0.003$	9.5060e-005

Note: k_0 is the initial permeability, which was taken as 0.003 mD according to the results of the true triaxial stress seepage experiment.

TABLE 3 Numerical simulation parameters.

Parameters	Value [unit]	Descriptions
E	2,713 [MPa]	Elastic modulus of coal
ν	0.339	Poisson's ratio of coal
ρ_m	1,250 [kg/m³]	Coal seam density
ρ_g	0.717 [kg/m³]	Methane density under standard conditions
k_0	0.00315 [mD]	Initial permeability
φ_0	0.06	Initial porosity
μ	1.08E-5 [Pa·s]	Dynamic viscosity of methane
V_L	0.02 [m³/kg]	Langmuir constant (limit adsorption capacity)
P_L	1 [MPa]	Langmuir pressure
V_M	22.4 [L/mol]	Molar volume of methane under standard conditions
R	8.413,510 [J/mol/K]	Gas state constant
T	293 [K]	Sample temperature
M	16 [g/mol]	Gas molecular mass of methane
F_x	30 [MPa]	Confining pressure in X direction
F_y	20 [MPa]	Confining pressure in Y direction
F_z	5, 10, 15, 20, 25, 30 [MPa]	Axial pressure in Z direction
r	0.1 [m]	Drilling radius
p_0	1.8 [MPa]	Initial pressure
p_b	0.087 [MPa]	Pumping negative pressure
t	9.2 [d]	Adsorption time

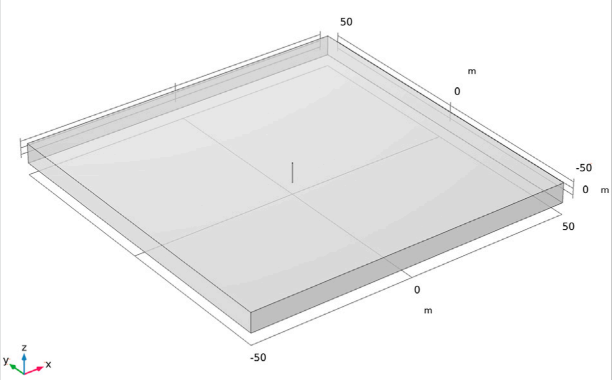

FIGURE 11
Geometric model of gas drainage numerical simulation.

$$f = \frac{\partial u}{\partial t} = -\frac{V_M (u - p)(u + P_L)^2}{tV_L RTP_L \rho_m + t\varphi_0 V_M (u + P_L)^2}, \tag{4}$$

where u represents the gas pressure in the pore and p represents the gas pressure in the fracture.

Darcy's law was adopted for the seepage model. The initial pressure of the model was set as 1.8 MPa, the conditions of four boundaries perpendicular to the bedding plane were set as the pressure boundary, the gas pressure was set as 1.8 MPa, and the pumping negative pressure of the pumping hole was set to 0.087 MPa. The permeability was taken as the fixed permeability k_0 (the axial pressure was set to 5 MPa) and the permeability k (the axial pressure was set to 10 MPa, 15 MPa, 20 MPa, 25 MPa, and 30 MPa) that changed with the axial stress.

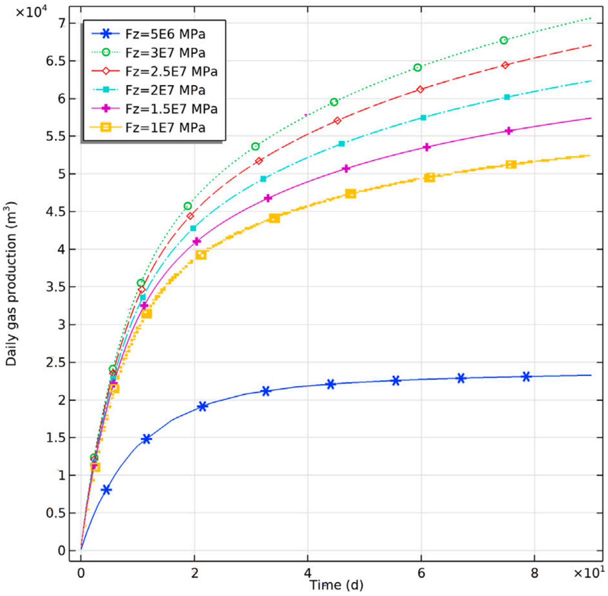

FIGURE 12
Comparison of drainage performance under different axial pressures.

The expression is as follows according to the results of the true triaxial stress seepage experiment in Table 2:

$$k = 0.0001 \times \left(0.0343\sigma_z^2 - 0.3737\sigma_z\right) + 0.003. \tag{5}$$

σ_Z is the stress in Z direction. It should be noted that here we use σ_Z replaces F_Z, because we think that on an infinitesimal element, stress can better express the influence of *in-situ* stress on permeability.

The results of the numerical simulation show that under the condition of fixed permeability, the daily gas production of boreholes maintains a high rising rate within 20 days, and the rising rate slows down in 20–40 days (Figure 12). After 40 days, the daily gas production reached equilibrium and was stable at 23,000 m^3. When the permeability varies with stress, the daily gas production of boreholes increases gradually with an increase in axial stress, and the number of days to reach equilibrium increases significantly. The daily gas production reached 52,000–70 000 m^3, which is 2–3 times that under the condition of fixed permeability. With an increase in the axial pressure, the amplification of the daily gas production decreased.

Conclusion

The results of the true triaxial stress seepage experiment with fixed confining pressure, fixed gas pressure, and axial pressure change show that with the change in axial pressure, the largest principal stress and minimum principal stress continuously change, forming fractures in different directions. The fracture surface perpendicular to the direction of the minimum principal stress was relatively developed, forming a fracture system perpendicular to the bedding plane and parallel to the bedding plane, which significantly improved the permeability of the coal sample.

Polynomial fitting was found to be the best method to fit the relationship between permeability and axial pressure through statistical processing of the experimental data with MATLAB. With an increase in axial pressure, the permeability first decreases and reaches a minimum value at approximately 5.5 MPa, which may be related to the compression of pores and fractures in the elastic deformation stage. Subsequently, it increased slowly. When the axial pressure was greater than 30 MPa, permeability increased significantly. This may be because a fracture system with vertical and parallel bedding planes was formed during the plastic deformation stage.

With an increase in axial pressure, the permeability of coal increased, and the drainage efficiency of coalbed methane increased. The daily gas production of variable permeability is 2–3 times that of fixed permeability, and the time required to reach the equilibrium drainage volume is extended.

Data availability statement

The original contributions presented in the study are included in the article/supplementary material, further inquiries can be directed to the corresponding author.

Author contributions

JL and ZS write the manuscript. CY does the experimental design. BL and JR make the sample. MX draw the figures.

Funding

We would like to express appreciation to the following financial support. The National Natural Science Foundation of China, grant number 41972177, 41872169, 42172189; the Postdoctoral Science Foundation China, grant number 2018M642747; tackling key scientific and technological problems in Henan Province, grant number, 222102320346; the National Natural Science Foundation of Henan province, grant number 202300410099.

Conflict of interest

Author CY was employed by Henan Energy and Chemical Industry Group Research Institute Co., Ltd.

The remaining authors declare that the research was conducted in the absence of any commercial or financial relationships that could be construed as a potential conflict of interest.

Publisher's note

References

Bai, X., Wang, D. K., and Tian, F. C. (2021). Permeability model of damaged coal under triaxial stress loading-unloading. *Chin. J. Rock Mech. Eng.* 40 (08), 1536. doi:10.13722/j.cnki.jrme.2021.0053

Barnett, S. B., Flottmann, T., and Paul, P. K. (2015). Influence of basement structures on *in-situ* stresses over the Surat Basin, southeast Queensland. *J. Geophys. Res. Solid Earth* 120, 1. doi:10.1002/2015JB011964

Chao, J. K., Yu, M. G., Chu, T. X., Han, X., Teng, F., and Li, P. (2019). Evolution of broken coal permeability under the condition of stress, temperature, moisture content, and pore pressure. *Rock Mech. Rock Eng.* 52 (8), 2803–2814. doi:10.1007/s00603-019-01873-x

Cheng, X. Z., Chen, L. J., Luan, H. J., Zhang, J., and Jiang, Y. (2022). Why coal permeability changes under unconstrained displacement boundary conditions: Considering damage effects. *J. Nat. Gas Sci. Eng.* 105, 104702. doi:10.1016/j.jngse.2022.104702

Cheng, Y. P., Liu, H. Y., Guo, P. K., et al. (2014). A theoretical model and evolution characteristic of mining-enhanced permeability in deeper gassy coal seam. *J. China Coal Soc.* 39 (08), 1650. doi:10.13225/j.cnki.jccs.2014.9028

Connell, L. D., Lu, M., and Pan, Z. J. (2010). An analytical coal permeability model for tri-axial strain and stress conditions. *Int. J. Coal Geol.* 84 (2), 103–114. doi:10.1016/j.coal.2010.08.011

Guo, J. N., Liu, J. F., Li, Q., Xu, C., Chen, Z., and Huang, B. (2019). Variation law of coal permeability under cyclic loading and unloading. *Therm. Sci.* 23 (3), 1487–1494. doi:10.2298/tsci180907215g

Jiang, C. B., Wei, A. D., and Chen, Y. F. (2020). Experimental study of mechanical and permeability characteristics of raw coal under loading stress condition. *Saf. Coal Mines* 51 (02), 5. doi:10.13347/j.cnki.mkaq.2020.02.003

Ju, W., Wang, S. Y., and Jiang, B. (2022). Characteristics of present-day *in-situ* stress field and the Permian coal reservoir permeability in the eastern Yunnan and Western Guizhou regions. *Coal Sci. Technol.* 50 (2), 179. doi:10.13199/j.cnki.cst.2021-0169

Li, B. B, B. B., Wang, B., and Yang, K. (2020). Coal seepage mechanism effeeted by stress and temperature. *J. China Univ. Min. Technol.* 49 (05), 844. doi:10.13247/j.cnki.jcumt.001183

Li, H. G, H. G., Gao, B. B., and Wang, H. L. (2020). Numerical simulation on change of equivalent permeability of coal rock under different stress ratios. *Saf. Coal Mines* 51 (1), 195. doi:10.13347/j.cnki.mkaq.2020.11.041

Li, J. Q, J. Q., Zhou, J. H., and Huang, H. X. (2020). Study on coal rock permeability characteristics under pore pressure-stress coupling. *Coal Technol.* 39 (11), 27. doi:10.13301/j.cnki.ct.2020.11.008

Lin, F. J., Huang, G. L., Jiang, D. Y., He, Y., and Fan, J. (2022). Experimental study on coal permeability and damage evolution under the seepage-stress coupling. *Front. Earth Sci. (Lausanne).* 10, 847392. doi:10.3389/feart.2022.847392

Liu, H. H., Yu, B., Lin, B. Q., Li, Q., Mou, J., and Wang, X. (2022). Coupled effective stress and internal stress for modeling coal permeability. *Fuel* 323, 124411. doi:10.1016/j.fuel.2022.124411

Liu, Z. D., Lin, X. S., Wang, Z. Y., Zhang, Z., Chen, R., and Wang, L. (2022). Modeling and experimental study on methane diffusivity in coal mass under *in-situ* high stress conditions: A better understanding of gas extraction. *Fuel* 321, 124078. doi:10.1016/j.fuel.2022.124078

Luo, N., Suo, Y. C., Fan, X. R., Yuan, Y., Zhai, C., and Sun, W. (2022). Research on confining pressure effect of pore structure of coal-rich in coalbed methane under cyclic impact. *Energy Rep.* 8, 7336–7348. doi:10.1016/j.egyr.2022.05.238

Lv, R. S., Xue, J., Zhang, Z., Ma, X., Li, B., and Zhu, Y. (2022). Experimental study on permeability and stress sensitivity of different lithological surrounding rock combinations. *Front. Earth Sci. (Lausanne).* 9, 762106. doi:10.3389/feart.2021.762106

Meng, Y., and Li, Z. P. (2017). Triaxial experiments on adsorption deformation and permeability of different sorbing gases in anthracite coal. *J. Nat. Gas Sci. Eng.* 46, 59–70. doi:10.1016/j.jngse.2017.07.016

Meng, Z. P., Zhang, P., and Tian, Y. D. (2020). Experimental analysis of stress-strain, permeability and acoustic emission of coal reservoir under different confining pressures. *J. China Coal Soc.* 45 (7), 2544. doi:10.13225/j.cnki.jccs.DZ20.0479

Rong, T. L., Zhou, H. W., and Wang, L. J. (2018). A damage-based permeability models of deep coal under mining disturbance. *Rock Soil Mech.* 39 (11), 3983. doi:10.16285/j.rsm.2018.0787

Shi, X. H., Pan, J. N., and Hou, Q. L. (2018). Micrometer-scale fractures in coal related to coal rank based on micro-CT scanning and fractal theory. *Fuel* 212, 162–172. doi:10.1016/j.fuel.2017.09.115

Sun, G. Z., Guo, B. B., and Wang, G. Z. (2016). Experimental study on permeability to variable axial pressure and confining pressure of two kinds of coal sample. *Sci. Technol. Eng.* 16 (14), 132. doi:10.13718/j.cnki.xdzk.2019.12.016

Tatyana, V., Andrey, K., Akhmed, I., Doroshkevich, A., Ludzik, K., and Chudoba, D. M. (2022). Permeability of a coal seam with respect to fractal features of pore space of fossil coals. *Fuel* 329, 125113. doi:10.1016/j.fuel.2022.125113

Wang, D. K., Peng, M., and Fu, Q. C. (2016). Evolution and numerical simulation of coal permeability during gas drainage in coal seams. *Chin. J. Rock Mech. Eng.* 35 (04), 704. doi:10.13722/j.cnki.jrme.2015.0931

Wang, G., Wei, L. Y., and Wei, X. (2020). Permeability evolution of compacted clay during triaxial compression. *Rock Soil Mech.* 41 (01), 32. doi:10.16285/j.rsm.2018.2135

Wang, K., Guo, Y. Y., and Xu, H. (2021). Deformation and permeability evolution of coal during axial stress cyclic loading and unloading: An experimental study. *Geomechanics Eng.* 24 (6), 519. doi:10.12989/gae.2021.24.6.519

Wang, Z. W., Qin, Y., Shen, J., Li, T., Zhang, X., and Cai, Y. (2022). A novel permeability prediction model for coal based on dynamic transformation of pores in multiple scales. *Energy* 257, 124710. doi:10.1016/j.energy.2022.124710

Wang, Z. Z., Pan, J. N., and Hou, Q. L. (2018). Anisotropic characteristics of low-rank coal fractures in the Fukang mining area, China. *Fuel* 211, 182–193. doi:10.1016/j.fuel.2017.09.067

Xie, H. P., Zhang, Z. T., and Gao, F. (2016). Stress-fracture-seepage field behavior of coal under different mining layouts. *J. China Coal Soc.* 41 (10), 2405. doi:10.13225/j.cnki.jccs.2016.1393

Xue, J. H., Li, Y. H., and Li, H. B. (2021). Experimental study on change mechanism of coal and rock permeability under total stress and strain condition. *Saf. Coal Mines* 52 (02), 33. doi:10.13347/j.cnki.mkaq.2021.02.008

Xue, Y., Gao, F., and Gao, Y. N. (2017). Research on mining-induced permeability evolution model of damaged coal in post-peak stage. *J. China Univ. Min. Technol.* 46 (03), 521. doi:10.13247/j.cnki.jcumt.000681

Xue, Y. G., Zhang, D. M., and Yang, Y. S. (2020). Permeability analysis of gassy raw coal under three stresses. *Min. Saf. Environ. Prot.* 47 (03), 22. doi:10.19835/j.issn.1008-4495.2020.03.005

Yan, Z. M., Wang, K., Zang, J., Wang, C., and Liu, A. (2019). Anisotropic coal permeability and its stress sensitivity. *Int. J. Min. Sci. Technol.* 29 (3), 507–511. doi:10.1016/j.ijmst.2018.10.005

Zhao, Y. X., Cao, B., and Zhang, T. (2018). Experimental study on influences of permeability of axial pressures and penetrative pressures on broken rocks. *J. Min. Sci. Technol.* 3 (05), 434. doi:10.19606/j.cnki.jmst.2018.05.003

Zhou, H. W., Rong, T. L., and Mou, R. Y. (2019). Development in modeling approaches to mining-induced permeability of coals. *J. China Coal Soc.* 44 (01), 221. doi:10.13225/j.cnki.jccs.2018.5029

Zhu, J., Wang, Q., and Tang, J. (2021). Evolution characteristics of strain and permeability of coal samples under loading and unloading conditions. *J. China Coal Soc.* 46 (04), 1203. doi:10.13225/j.cnki.jccs.dy20.0280

frontiers | Frontiers in Earth Science

TYPE Original Research
PUBLISHED 04 January 2023
DOI 10.3389/feart.2022.1037658

EDITED BY
Junjian Zhang,
Shandong University of Science and Technology, China

REVIEWED BY
Hong Pang,
China University of Petroleum, Beijing, China
Yuehan Yan,
Henan Polytechnic University, China

*CORRESPONDENCE
Jingyi Chen,
Chenjingyi@ncwu.edu.cn

SPECIALTY SECTION
This article was submitted to Economic Geology, a section of the journal Frontiers in Earth Science

RECEIVED 06 September 2022
ACCEPTED 29 September 2022
PUBLISHED 04 January 2023

CITATION
Chen J, Zhang H, Chang H and Wang Q (2023), Research on main controlling factors of tight sandstone gas accumulation in coal-bearing strata in the southern North China Basin: Comparison with the Ordos Basin. *Front. Earth Sci.* 10:1037658. doi: 10.3389/feart.2022.1037658

Research on main controlling factors of tight sandstone gas accumulation in coal-bearing strata in the southern North China Basin: Comparison with the Ordos Basin

Jingyi Chen[1]*, Hongwei Zhang[2], Hailiang Chang[2] and Qingwei Wang[1]

[1]College of Geosciences and Engineering, North China University of Water Resources and Electric Power, Zhengzhou, China, [2]Institute of Natural Resource Investigation and Evaluation, Henan Academy of Land and Resources Sciences, Zhengzhou, China

Tight sandstone gas (TSG) reservoirs develop extensively in the upper Paleozoic coal bearing strata in both the southern North China Basin and the Ordos Basin. The former has not achieved important advances in TSG exploration, while the latter has built the largest TSG production facility in China. By comparing the TSG accumulation conditions in the Tongxu area of the southern North China Basin and the Fuxian area of the Ordos Basin, the main controlling factors of TSG accumulation in the southern North China Basin were analyzed in this article. The results indicate that the organic matter type of the upper Paleozoic source rocks are mainly type III kerogen, vitrinite reflectance values (Ro) are greater than 3.1%, source rocks are over mature, and the reservoir strata are characterized by low porosity and extra low permeability; therefore reservoir forming conditions are similar to those of the Ordos Basin. During the Late Jurassic-Early Cretaceous period, after a large-scale generation of hydrocarbons from source rocks in the two basins, the tectonic movements in the Yanshan period controlled the differential accumulation of TSG. The Ordos Basin has been uplifted as a whole by tectonic processes since the Triassic, which allowed a continuous deposition of Triassic strata, thus providing good sealing conditions for the upper Paleozoic TSG reservoirs. The southern North China Basin has experienced multi-stage compressive and extensive tectonic actions, so the original unified Paleozoic basin was divided into several residual blocks. However, the residual thickness of Triassic strata in slopes and sags is higher. The source rocks, reservoir strata, caprocks, and overlying strata continuously deposited in time, and the time allocation of reservoir forming elements is favorable. Therefore, this is conducive to the preservation of TSG reservoirs in the upper Paleozoic. Such reservoirs are defined by high gas saturation and enriched sandstone gas.

KEYWORDS

tight sandstone, resource rock, reservoir, accumulation, southern North China Basin, Ordos Basin

Introduction

The Late Paleozoic sequences from the southern North China Basin and the Ordos Basin belong to the North China sedimentary system, which is characterized by a good horizontal comparison of strata and deposition conditions (Yang et al., 2010). The coal-bearing source rocks widely develop in the Late Carboniferous Taiyuan Formation and the Early Permian Shanxi Formation, which provide a resource basis for tight sandstone gas (TSG) reservoirs in the Shihezi Formation and Shanxi Formation. The complete theoretical systems of TSG accumulation have been established in the Ordos Basin, which effectively guide the exploration and development of TSG reservoirs (Fu et al., 2005; Yang et al., 2008; Li et al., 2009a; Zou et al., 2009; Xu et al., 2011; Yang et al., 2012; Zhao et al., 2014; Li et al., 2016; Meng et al., 2016; Wang et al., 2017; Wu et al., 2022). Sandstone gas came from coal bearing strata of the Upper Paleozoic (Wang et al., 2014; Chen et al., 2016; Hao et al., 2016; Dai et al., 2019; Fu et al., 2019; Zou et al., 2019). TSG accumulation mainly occurred in Jurassic Period and Cretaceous Period (Ren et al., 2006; Xie and Zhou, 2006; Yang et al., 2015; Wang et al., 2018). Pressure sealing created efficient storage conditions (Li et al., 2009b; Zhao et al., 2012; Yang et al., 2015). At present, the largest TSG production facility in China has been built in the Ordos Basin. TSG production of the Changqing oilfield reached $323\ m^3 \times 10^8\ m^3$ in 2020 (He et al., 2021). After more than 60 years of TSG exploration in the upper Paleozoic formations of the southern North China Basin, no substantial breakthrough has been achieved, although some wells have successively obtained gas shows or low-yield gas flow (Zhou, 2010; Zhang et al., 2017).

TSG accumulation conditions in the Tongxu area of the southern North China Basin and the Fuxian area of the Ordos Basin are similar. There are few differences in the development characteristics, types and maturity of source rocks and composition and physical properties of reservoir rocks. In this study, based on the theories of TSG accumulation in the Ordos Basin, main controlling factors of TSG accumulation in the upper Paleozoic of the southern North China basin have been defined through a comprehensive comparative study of the geological conditions in combination with the analysis of oil and gas accumulation processes. Additionally, we suggest favorable exploration directions to provide theoretical supports for the breakthrough of TSG exploration in the southern North China Basin.

Formation conditions of tight sandstone gas reservoir

Tectonic characteristics

The Ordos Basin has experienced multiple episodes of tectonic movements since the Triassic. The strata in the interior of the basin did not suffer obvious fold deformations.

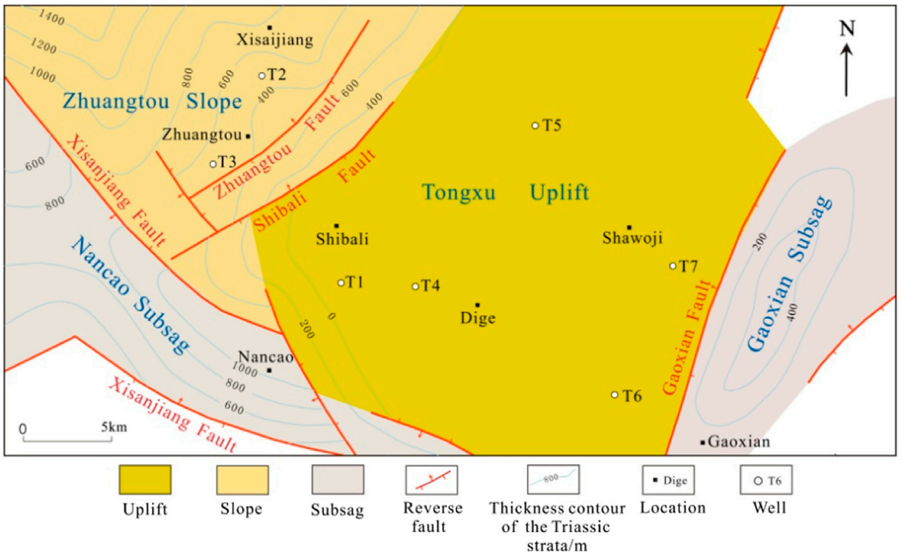

FIGURE 1
Tectonic units and the stratum distribution characteristic of the Triassic strata in the Tongxu area.

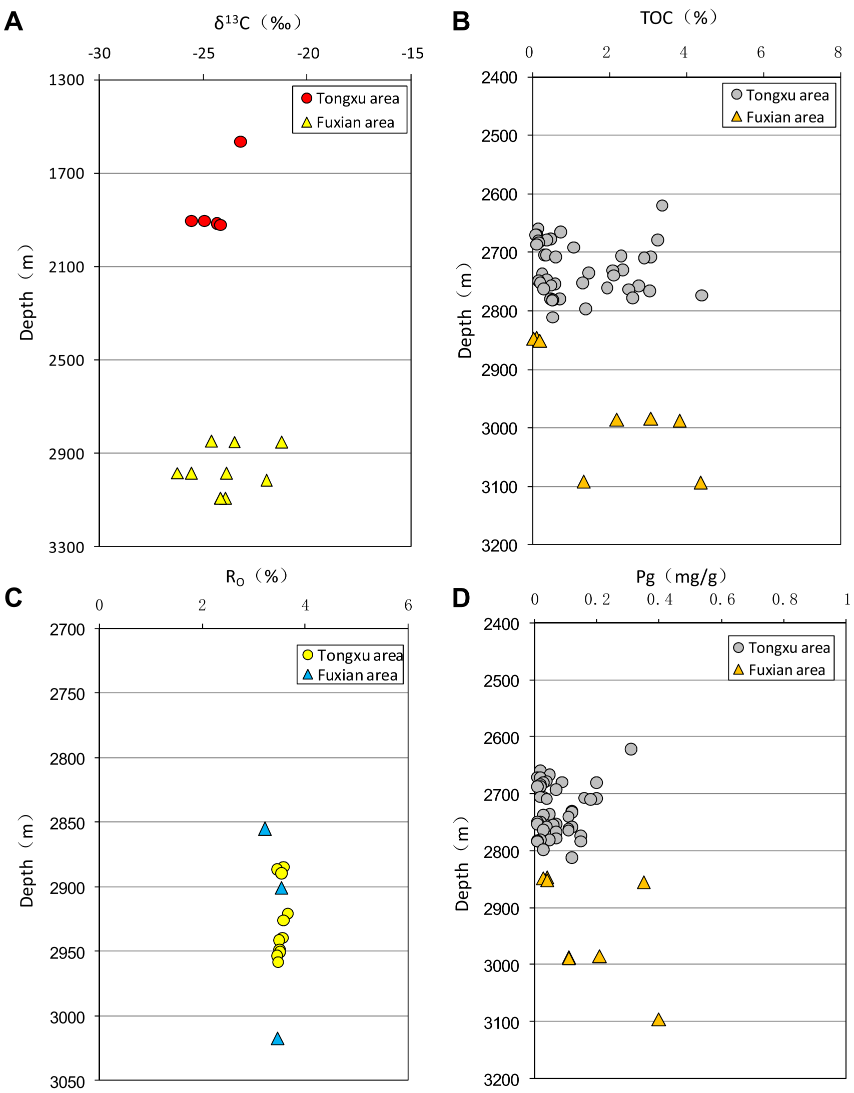

FIGURE 2
Source rocks geochemical characteristics in both the Tongxu area and the Fuxian area, **(A)** Theδ^{13}C values are greater than −26‰, **(B)** TOC contents are less than 4.5%, **(C)** Ro values that are greater than 3.1%, **(D)** Pg values are less than 0.4 mg/g.

The overall structure is stable, and the original configuration of the Paleozoic strata is well preserved. The structural changes in the terminal stage mainly show the general pattern of “Uplift in the eastern part and depression in the western part” (Zhao et al., 2010). The Fuxian area is located in the southern part of the Yishan Slope in the interior of the basin. The tectonic characteristics show the same tectonic pattern and persist in this part of the basin. The main body is a west-dipping slope with an average gradient of about 5 m/km. No significant faults were identified, and the nose-shaped uplift developed with low tectonic amplitude in the Yishan slope.

Initially, the structures of the southern North China Basin had a NW-NWW direction and were primarily controlled by the Qinling-Dabie orogenic belt. Afterwards, they were affected by the Tanlu strike-slip fault system on the east side, superimposing the structures in a NE-NNE direction (Xu et al., 2003). The current structures of the basin are mostly established as a block uplift and block depression tectonic pattern. The Tongxu area is located in the central and northern parts of the southern North China Basin. The main body is an uplift distributed in the NW direction, superimposing with NE broad and gentle anticlines and synclines, and is cut by NWW and NE faults. According to the tectonic characteristics, it can be divided into four tectonic units, including the Tongxu Uplift, the Zhuangtou Slope, the Nancao subsag, and the Gaoxian Subsag (Figure 1). The Paleozoic strata in the western part of the area are widely

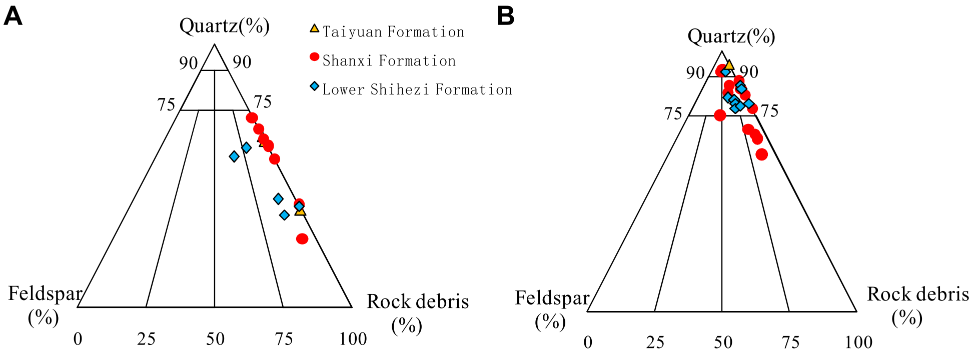

FIGURE 3
The sandstone component comparison in the triangular diagram, **(A)** The main reservoirs from the Tongxu area are predominantly lithic sandstones, **(B)** The quartz content in the Fuxian area is significantly higher.

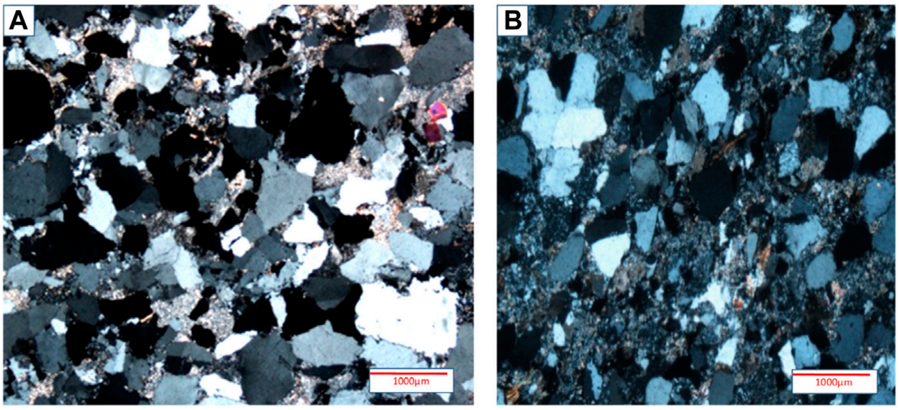

FIGURE 4
Identification characteristics of sandstone slice image [×2 (+)], **(A)** In Fuxian area, the sandstone of the Lower Shihezi Formation contains 83% quartz, intragranular pores and microcracks are visible, **(B)** In Tongxu area, the sandstone of the Lower Shihezi Formation contains only 65% quartz, intragranular dissolved pores are visible.

distributed, while the Triassic strata are predominantly residual in slopes and subsags.

Source rocks geochemical characteristics

During the Late Carboniferous—Early Permian, a succession of dark coal-bearing strata characterized by marine—continental transitional facies deposited in North China (Wu et al., 2015), which provided an important source of gas for TSG reservoirs in the upper Paleozoic formations.

The source rocks in the Tongxu area and the Fuxian area consist of coal and dark mudstone, with little difference in quality, thickness, and maturity of the source rocks. By analyzing the kerogen stable carbon isotopes ratio ($\delta^{13}C$) of the source rocks, the$\delta^{13}C$ values in both regions are greater than −26‰ (Figure 2A), indicating that the organic matter originates from terrestrial higher plants (Huang et al., 1984). The petrographic analysis of kerogen under transmitted light reveals that 75% of the kerogen micro-components of the mud shale are represented by vitrinite, followed by the sapropelic group, with little content of exinite and no inertinite, while kerogen type is mainly humic. The total organic carbon (TOC) contents of the mudstone from the Tongxu area vary between 0.3% and 4.5% with an average value of 1.5% (Figure 2B), and the cumulative thickness of mudstone strata is 40–60 m. The TOC content of coal varies between 50% and 55%, and the cumulative thickness is between 0 and 5 m. However, the thickness distribution is irregular, which is thick in the northern and western parts, and thin in the southern and

TABLE 1 Comparing the TSG accumulation conditions in the Tongxu area of the Southern North China basin and the Fuxian area of the Ordos basin.

Accumulation conditions	Basic parameters	Basin (area)	
		The Southern North China (Tongxu)	The Ordos Basin (Fuxian)
Structural features	Fracture	Development	Undevelopment
	Structural amplitude/m	Gentle slope	Uplift or sag
	Fault dip/°	20–30	—
	Fault displacement/m	100–1,200	—
	Fault extension length/m	20–30	—
	Depth at the bottom of Upper Paleozoic strata/m	1900–3,000	2,750–3,100
Source rocks	Cumulative thickness of coal seam/m	0–8	4–6
	TOC content of coal/%	50–55	45–55
	Mudstone thickness/m	30–60	35–50
	TOC content of mudstone/%	0.3–4.5	0.5–4.2
	Ro/%	3.1~3.6	3.2~3.5
	Gas generation intensity/(average value)/ 10^8 $m^3 \cdot km^{-2}$	10~50 (25)	15~25 (20)
	Scope of hydrocarbon generation area	Large area	Large area
Reservoir rocks	Sedimentary microfacies	Underwater distributary channel	Underwater distributary channel
	Sand-stratum ratio/%	5–10	6–12
	Composition types of sandstone	Lithic sandstone and feldspar lithic sandstone	Lithic quartz sandstone and quartz sandstone
	Quartz content/%	60–70	65–95
	Reservoir pore types	Intergranular pore and intragranular pore	Intergranular pore and intragranular pore
	Porosity (average value)/%	0.4–5.6 (4.6)	0.8–7.8 (5.2)
	Permeability (average value)/$10^{-3}\mu m^2$	0.01–0.58 (0.19)	0.01–0.76 (0.22)
Cap rocks	Lithologic character	Mudstone and coal	Mudstone and coal
	Cumulative thickness/m	80–150	70–130
	Single layer thickness of mudstone/m	20–50	15–40
	Single layer thickness of mudstone/m	2–6	0–4
	Storage mechanism	Capillary pore and gas concentration	Capillary pore and gas concentration
	Thickness of Triassic strata/m	0–1,200	2,200–2,500
	Distribution characteristics of Triassic strata	Local area	Large area

eastern parts. The TOC contents of the mudstone from the Fuxian area range between 0.5% and 4.2% with an average value of 1.8% (Figure 2B). The cumulative thickness is 35–50 m.The TOC content of coal is 45%–55%, the cumulative thickness is between 4 and 6 m, and the distribution is relatively stable. Both regions experienced late Triassic tectonic thermal events (Ren et al., 2006; Xie and Zhou, 2006; Wang et al., 2018). The abnormally high geothermal field caused the source rocks to enter the over mature stage. This has been confirmed by the high vitrinite reflectance values (Ro) that are greater than 3.1% (Figure 2C). The Rock-Eval pyrolysis data show that the hydrogen index values in the two areas are generally less than 20 mg/g, and the hydrocarbon generation potential (Pg) is less than 0.4 mg/g (Figure 2D), which indicates that the liquid hydrocarbons in the source rocks have been completely cracked by heating under pressure.

Reservoir properties

The sedimentary environment of the Carboniferous-Permian strata in North China is characterized by marine-continental transitional facies, and distributary channel sand bodies are the most favorable reservoirs. The Fuxian area and the Tongxu area are defined by strong compaction, the sandstones are generally densely cemented, and the thickness of a single layer is usually 3–10 m. The reservoir spaces are dominated by intergranular pores and intragranular dissolved pores, which are characterized by low porosity and extra-low permeability.

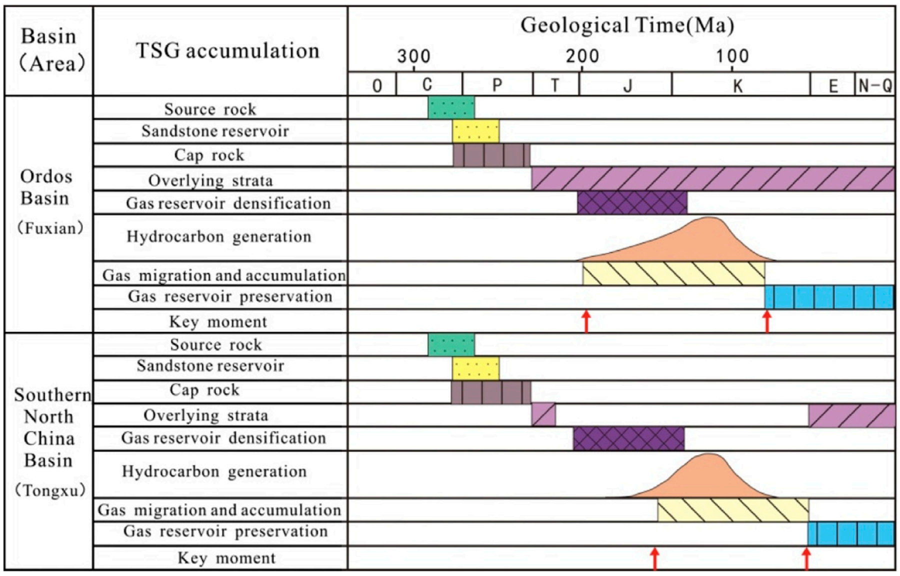

FIGURE 5
The comparison of TSG accumulation events. The southern North China Basin has distinct differences in the underlying Carboniferous-Permian TSG reservoirs due to the thicknesses of the Triassic strata.

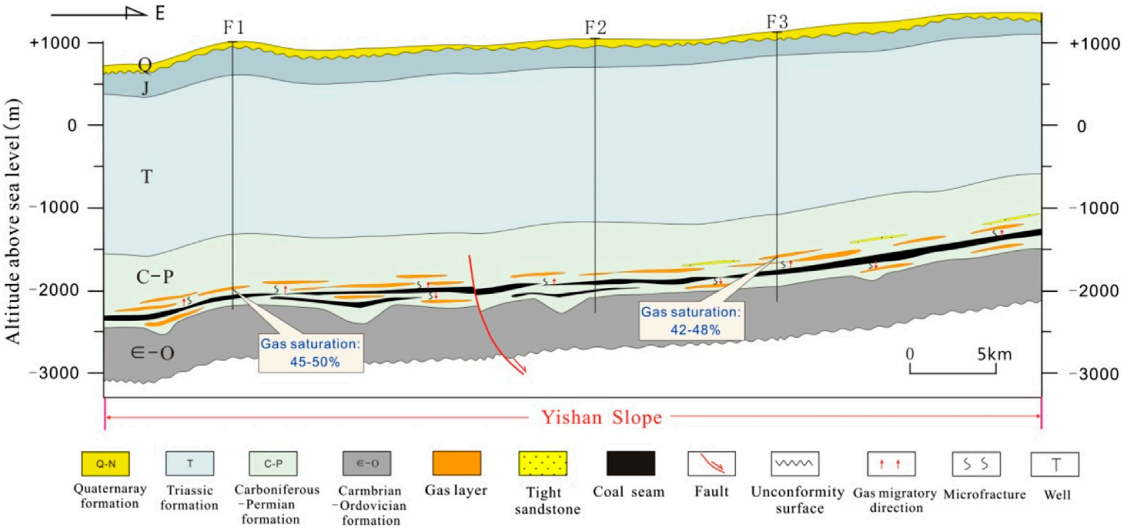

FIGURE 6
The TSG reservoir section in the Fuxian area of the Ordos Basin. Due to the stable thickness of the overlying strata and less faults, the gas saturation of the gas reservoirs is high.

The sandstone component comparison in the triangular diagram illustrates that the main reservoirs in the upper Paleozoic strata from the Tongxu area are predominantly medium to fine-grained lithic sandstones (Figure 3A), while the Lower Shihezi Formation contains feldspar lithic sandstones. The quartz content of each section is less than 75%, which generally varies between 61% and 72% with an average value of 64%, while the feldspar content is usually between 0% and 5% with an average value of 2%. The rock debris content ranges between 12% and 43% with an average

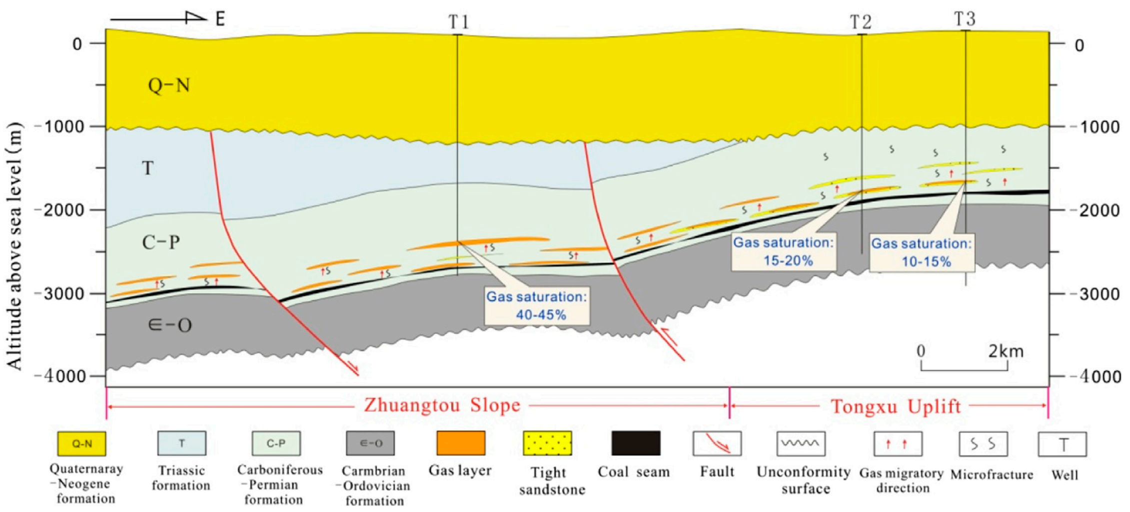

FIGURE 7
The TSG reservoir section in the southern North China Basin. The gas saturation values of the TSG reservoirs varied with the thickness of the Triassic strata.

of 33.5%. The sandstones are poorly to moderately sorted, and the grains are sub-angular with pore-type cementation. Some quartz particles develop secondary enlarged edges, and the particles are in point-line contact. The primary reservoirs in the Fuxian area are medium to fine-grained lithic quartz sandstones, followed by quartz sandstones, and some sections of the Shanxi Formation also consist of lithic sandstone reservoirs (Figure 3B). The quartz content of the Lower Shihezi Formation and Taiyuan Formation is generally higher. It is greater than 75% with an average value of 85%. The contents of feldspar and rock debris are lower, which range between 10% and 25% with an average value of 13%. The sandstone reservoirs of the Shanxi Formation are enriched in rock debris, which can reach up to 30%. Sandstones have medium to good sorting properties. Sandstone particles are sub-angular and sub-rounded, porous cementation, and in point-line contact. The quartz content of the upper Paleozoic sandstones in the Fuxian area is significantly higher in comparison with the sandstones from the Tongxu area. Figure 4 shows that the sandstones of the Lower Shihezi Formation in Fuxian area contain 83% quartzs, the Surface porosity is 1.7%, and intragranular pores and microcracks are visible (Figure 4A); In Tongxu area, the sandstones of the Lower Shihezi Formation contain only 65% quartzs, the Surface porosity is 0.8%, and intragranular dissolved pores are visible (Figure 4B).

The pore permeability of the upper Paleozoic sandstone reservoir in the Fuxian area is slightly better than in the Tongxu area. The average reservoir porosity and permeability of the former are 5.2% and 0.19 mD, respectively, and those of the latter are 4.6% and 0.19 mD, respectively. It might be an important argument for the difference in the physical properties of the upper Paleozoic reservoirs in these two areas (Zheng and Hu, 2006).

Caprock properties

The original structure of the Paleozoic strata in the Ordos Basin is well preserved. Thus, several sets of lacustrine and swamp facies argillaceous cap rocks are developed, as well as multiple sets of caprocks are vertically superimposed. The Triassic Triassic, Jurassic, and Cretaceous strata in the interior of the basin are characterized by continuous deposition and large thicknesses. They cover the Paleozoic formations parallel to the bedding surfaces, which provide exceptional sealing conditions for the Paleozoic gas reservoirs.

The characteristics of the upper Paleozoic caprocks in the southern North China Basin are similar to those in the Ordos Basin, and multiple sets of mudstone and coal-bearing caprocks overlie the upper Paleozoic strata. The cumulative thickness in the Tongxu area is 80–150 m, of which the thicknesses of the mudstone and coal layers are 20–50 m and 2–6 m, respectively. A set of thick mudstones developed in the upper Shihezi Formation, which can be considered a regional caprock. These characteristics are slightly better in comparison with the Fuxian area. Consequently, it is beneficial to the preservation of gas reservoirs during stable tectonic periods. Due to the multi-stage tectonic actions of Triassic and Cenozoic extrusion-strike-slip-extension, this region has been strongly reorganized tectonically. The overlying Triassic and even

Permian strata have been denuded to varying degrees, therefore forming, or damaging the previous gas sealing system, and some or all gas reservoirs have been destroyed. In the Tongxu uplift area, the Triassic strata are completely denuded, while in the subsag and slope zones, the Triassic strata are relatively thick. In Nancao subsag, the thickness of the Triassic strata is the highest, with the maximum thickness exceeding 1,000 m, which is conducive to the preservation of TSG reservoirs in the Upper Paleozoic (Figure 1).

Controlling factors of gas accumulation

By comparing the TSG accumulation conditions (Table 1) and events (Figure 5) in the Tongxu area of the southern North China Basin and the Fuxian area of the Ordos Basin, the main controlling factors of TSG accumulation in the southern North China Basin have been analyzed.

In the Ordos Basin, the upper Paleozoic source rocks experienced early gas generation in the early Triassic. The gas gradually migrated into the adjacent sandstone reservoirs, which was extremely favorable for the preservation of pores before the reservoirs increased (Zheng and Hu, 2006). Due to the tectonic thermal events in the Early Jurassic-Late Cretaceous, the source rocks entered the over mature window (Ren et al., 2006; Xie and Zhou, 2006; Wang et al., 2018), and enormous quantities of gases were generated. Although the interior structure of the basin was affected by the Yanshan tectonic movement and experienced tectonic uplift, the lateral adjustments were not powerful. They were characterized only by an overall monoclinic rise and fall, and the faults did not develop. Additionally, the upper Triassic strata were missing locally, while the upper Paleozoic strata were not affected by denudation. The temporal continuity of deposition in reservoirs, caprocks, and overlying strata was consistent without obvious damage to the upper Paleozoic gas reservoirs. Due to the stable thickness of the overlying strata and good preservation conditions in the Carboniferous-Permian TSG reservoir, the gas saturation of the gas reservoirs is high, with values between 40% and 50% (Figure 6).

The large-scale gas generation in the Tongxu area of the southern North China Basin also occurred during the Early Jurassic-Late Cretaceous when the porosity of the upper Paleozoic sandstone reservoirs decreased (Zhou, 2010). With the occurrence of the Yanshan Movement, this area was continuously squeezed and stretched, the strata were significantly uplifted, and the local differential rises and falls were substantial. In the uplift zones, the Triassic strata were denuded to varying degrees, and even the upper Permian strata were partially eroded, resulting in discontinuities between the source rocks, the reservoirs, the caprocks and the overlying strata. Therefore, the generated gas partially or completely migrated to the surface, and the gas saturation of the underlying Carboniferous-Permian TSG reservoir is low, with values ranging between 10% and 20%. In the subsags and slope zones, the Triassic strata remained relatively intact, and the depositional continuity of the source rocks, the reservoirs, the caprocks and the overlying strata was good, which was favorable for gas accumulation. Thus, the gas saturation of the TSG reservoirs in the underlying Carboniferous-Permian strata is high, ranging between 40% and 45% (Figure 7).

In conclusion, the southern North China Basin has distinct differences in the underlying Carboniferous-Permian TSG reservoirs due to the influence of the Yanshan tectonic movement. The main factors controlling the enrichment of gas reservoirs are the distribution characteristics of the overlying Triassic strata. Specifically, the areas with greater thicknesses of the Triassic strata were favorable for TSG reservoirs.

Conclusion

The geochemical characteristics, distribution of the source rocks and composition, porosity, and permeability of the sandstone reservoirs in the upper Paleozoic strata of the southern North China Basin are similar to those of the Ordos Basin, which have the basic conditions for TSG accumulation.

The comparative analysis of the gas accumulation process indicates that the main controlling factor for upper Paleozoic TSG accumulation in the Tongxu area of the southern North China Basin is the preservation condition. The Triassic strata in slopes and subsags are relatively thick and well preserved. Additionally, the time allocation for TSG accumulation is good because the source rocks, the reservoirs, the caprocks and the overlying strata have continuity in slopes and subsags.

Data availability statement

The original contributions presented in the study are included in the article/supplementary material, further inquiries can be directed to the corresponding author.

Author contributions

JC designed the study and wrote the manuscript. HZ and HC analyzed the data. QW reviewed the manuscript. All authors contributed to the article and approved the submitted version.

Funding

This study was jointly supported by Natural Science Foundation of Henan Province (Grant No. 202300410278), the Start Project of High Level Researchers of North China University of Water Resources and Electric Power (No. 40758) and Henan Geologica Survey (Projects YZRZ201922 and YGTZ201646).

Acknowledgments

Prof. Wang Feiyu from State Key Laboratory of Petroleum Resources and Prospecting, China University of Petroleum (Beijing), is thanked for helping us to improve this manuscript with his insightful suggestions.

Conflict of interest

The authors declare that the research was conducted in the absence of any commercial or financial relationships that could be construed as a potential conflict of interest.

Publisher's note

References

Chen, J. Y., Jia, H. C., Li, Y. J., An, C., Li, W., and Liu, S. H. (2016). Origin and source of natural gas in the upper paleozoic of the yimeng uplift, Ordos basin. *Oil Gas Geol.* 37, 205–209. doi:10.11743/ogg20160208

Dai, J. X., Qin, S. F., Hu, G. Y., Ni, Y. Y., Gan, L. D., Huang, S. P., et al. (2019). Major progress in the natural gas exploration and development in the past seven decades in China. *Petroleum Explor. Dev.* 46, 1100–1110. doi:10.1016/s1876-3804(19)60266-1

Fu, J. H., Wei, X. S., and Huang, D. J. (2005). Law of reservoir formulation and exploration techniques of natural gas lithologic reservoir in Ordos Basin. *J. Oil Gas Technol.* 27, 137–141. CNKI:SUN:JHSX.0.2005-S1-001.

Fu, J. H., Wei, X. S., Luo, S. S., Zuo, Z. F., Zhou, H., Liu, B. X., et al. (2019). Discovery and geological knowledge of the large deep coal-formed qingyang gas field, Ordos basin, NW China. *Petroleum Explor. Dev.* 46, 1111–1126. doi:10.1016/s1876-3804(19)60267-3

Hao, S. M., Li, L., Zhang, W., Qi, Rong., Ma, C., and Chen, J. Y. (2016). Forming conditions of large-scale gas fields in Permo-Carboniferous in the northern Ordos Basin. *Oil Gas Geol.* 37, 149–154. doi:10.11743/ogg20160201

He, J. C., Yu, H. J., He, G. H., Zhang, J., and Li, Y. (2021). Natural gas development prospect in Changqing gas rovince of the Ordos Basin. *Nat. Gas. Ind.* 41, 23–32. doi:10.3787/j.issn.1000-0976.2021.08.003

Huang, D. F., Li, J. C., and Zhang, D. J. (1984). Kerogen types and study on effectiveness, limitation and interrelation of their identification parameters. *Acta Sedimentol. Sin.* 3, 18–33. CNKI: SUN: CJXB.0.1984-03-001.

Li, Y., Tang, D. Z., Wu, P., Niu, X. L., Wang, K., Qiao, P., et al. (2016). Continuous unconventional natural gas accumulations of Carboniferous-Permian coal-bearing strata in the Linxing area, northeastern Ordos basin, China. *J. Nat. Gas Sci. Eng.* 36, 314–327. doi:10.1016/j.jngse.2016.10.037

Li, Z. D., Hao, S. M., Li, L., Xi, K. Y., and Guo, M. (2009b). Comparison between the Upper Paleozoic gas reservoirs in Ordos Basin and deep basin gas reservoirs. *Oil Gas Geol.* 30, 149–155. doi:10.11743/ogg20090204

Li, Z. D., Hao, S. M., Xi, K. Y., Li, L., and Guo, M. (2009a). Discussion on relation of gas accumulation mechanism between deep basin and Upper Paleozoic in the Ordos Basin. *Mineralogy Petrology* 29, 86–92. doi:10.19719/j.cnki.1001-6872.2009.01.014

Meng, D. W., Jia, A. L., Ji, G., and He, D. B. (2016). Water and gas distribution and its controlling factors of large scale tight sand gas fields: A case study of Western sulige gas field, Ordos basin, NW China. *Petroleum Explor. Dev.* 43, 663–671. doi:10.1016/s1876-3804(16)30077-5

Ren, Z. L., Zhang, S., Gao, S. L., Cui, J. P., and Liu, X. S. (2006). Research on region of maturation anomaly and formation time in Ordos basin. *Acta Geol. Sin.* 80, 675–684. doi:10.3321/j.issn:0001-5717.2006.05.006

Wang, L. Z., Wang, L. Y., Peng, P. A., Dai, T. M., and Liu, D. Y. (2018). A thermal event in the Ordos basin: Insights from illite 40Ar-39Ar dating with regression analysis. *J. Earth Sci.* 29, 629–638. doi:10.1007/s12583-017-0903-7

Wang, M., Tang, H. M., Zhao, F., Liu, S., Yang, Y., Zhang, L. H., et al. (2017). Controlling factor analysis and prediction of the quality of tight sandstone reservoirs: A case study of the He8 member in the eastern sulige gas field, Ordos basin, China. *J. Nat. Gas Sci. Eng.* 46, 680–698. doi:10.1016/j.jngse.2017.08.033

Wang, T. B., Dong, L., and Zhang, Y. W. (2014). Distribution of large and giant coal-related gas fields in China and its significance. *Oil Gas Geol.* 35, 167–182. doi:10.11743/ogg20140201

Wu, W. T., Zhao, J. Z., Wang, Y. Z., Guo, M. Q., Wu, H. Y., Li, J., et al. (2022). Main controlling factors and enrichment model of a multi layer tight sandstone gas reservoir: Case study from the linxing gas field, eastern Ordos basin, northern China. *Arab. J. Geosci.* 15, 1313. doi:10.1007/s12517-022-10596-3

Wu, W., W, Y. H., Cao, G. S., Huang, X. F., and Liu, W. Q. (2015). The geochemical characteristics of the carboniferous and permian source rocks in the western henan, southern North China basin. *Nat. Gas. Geosci.* 26, 128–136. doi:10.11764/j.issn.1672-1926.2015.01.0128

Xie, D. N., and Zhou, L. F. (2006). Discussion on hydrocarbon generation potential and secondary hydrocarbon generation of organic matter from Permo-Carboniferous coal measures in the southern North China. *Coal Geol. Explor.* 34, 20–33. doi:10.3969/j.issn.1001-1986.2006.01.009

Xu, H. L., Zhao, Z. J., Yang, Y. N., and Tang, Z. W. (2003). Structural pattern and structural style of the southern North China basin. *Acta Geosci. Sin.* 24, 27–33. doi:10.3321/j.issn:1006-3021.2003.01.005

Xu, H., Tang, D. Z., Zhang, J. F., Yin, W., Zhang, W. Z., and Lin, W. J. (2011). Factors affecting the development of the pressure differential in Upper Paleozoic gas reservoirs in the Sulige and Yulin areas of the Ordos Basin, China. *Int. J. Coal Geol.* 85, 103–111. doi:10.1016/j.coal.2010.10.005

Yang, F., Zhou, X. J., and Ni, C. H. (2010). Analysis paleozoic reservoir preservation in the north China. *Petroleum Geol. Exp.* 32, 527–531. doi:10.11781/sysydz201006527

Yang, H., Fu, J. H., Liu, X. S., and Meng, P. L. (2012). Accumulation conditions and exploration and development of tight gas in the Upper Paleozoic of the Ordos Basin. *Petroleum Explor. Dev.* 39, 315–324. doi:10.1016/S1876-3804(12)60047-0

Yang, H., Fu, J. H., Wei, X. S., and Liu, X. S. (2008). Sulige field in the Ordos Basin: Geological setting, field discovery and tight gas reservoirs. *Mar. Petroleum Geol.* 25, 387–400. doi:10.1016/j.marpetgeo.2008.01.007

Yang, H., Liu, X. S., Yan, X. X., and Zhang, H. (2015). The shenmu gas field in the Ordos basin: Its discovery and reservoir-forming geological characteristics. *Nat. Gas. Ind.* 35, 1–13. doi:10.3787/j.issn.1000-0976.2015.06.001

Zhang, J. D., Zeng, Q. N., Zhou, X. G., Liu, X. F., Zhang, H. D., Wang, Y. F., et al. (2017). Drilling achievements and gas accumulation in the upper paleozoic in Western new area of taikang uplift, southern North China basin. *Nat. Gas. Geosci.* 28, 1637–1649. doi:10.11764/j.issn.1672-1926.2017.09.004

Zhao, J. Z., Bai, Y. B., Cao, Q., and Er, C. (2012). Quasi-continuous hydrocarbon accumulation: A new pattern for large tight sand oilfields in the Ordos basin. *Oil Gas Geol.* 33, 811–827. doi:10.11743/ogg20120601

Zhao, J. Z., Wang, L., Sun, B. H., Bai, Y. B., and Wu, W. T. (2010). Effect of structural evolution on formation and distribution of Upper Paleozoic giant gas fields in the East Ordos Basin. *Nat. Gas. Geosci.* 21, 875–881. doi:10.11764/j.issn.1672-1926.2010.06.875

Zhao, J. Z., Zhang, W. Z., Li, J., Cao, Q., and Fan, Y. F. (2014). Genesis of tight sand gas in the Ordos Basin, China. *Org. Geochem.* 74, 76–84. doi:10.1016/j.orggeochem.2014.03.006

Zheng, H. R., and Hu, Z. Q. (2006). Gas pool forming conditions for bohai bay basin and Ordos basin in the upper paleozoic. *Acta Pet. Sin.* 27, 1–5. CNKI:SUN:SYXB.0.2006-03-000.

Zhou, X. J. (2010). Analysis of hydrocarbon accumulation conditions of the Upper Palaeozoic sequence of the southern North China basin. *Petroleum Geol. Exp.* 32, 420–427. doi:10.11781/sysydz201005420

Zou, C. N., Tao, S. Z., Yuan, X. J., Zhu, R. K., Hou, L. H., Wang, L., et al. (2009). The formation conditions and distribution characteristics of continuous petroleum accumulations. *Acta Pet. Sin.* 30, 324–331. doi:10.7623/syxb2009002

Zou, C. N., Yang, Z., Huang, S. P., Ma, F., Sun, Q. P., Li, F. H., et al. (2019). Resource types, formation, distribution and prospects of coal-measure gas. *Petroleum Explor. Dev.* 46, 451–462. doi:10.1016/s1876-3804(19)60026-1

frontiers | Frontiers in Earth Science

TYPE Original Research
PUBLISHED 06 January 2023
DOI 10.3389/feart.2022.1031218

Quantitative interpretation of coal industrial components using a gray system and geophysical logging data: A case study from the Qinshui Basin, China

Jianhong Guo[1], Zhansong Zhang[1]*, Hang Xiao[2], Chaomo Zhang[1], Linqi Zhu[3] and Can Wang[4]

[1]Key Laboratory of Exploration Technologies for Oil and Gas Resources, Ministry of Education, Yangtze University, Wuhan, China, [2]Research Institute of Exploration & Development, Sinopec Jianghan Oilfeld Company, Wuhan, China, [3]Institute of Deep-Sea Science and Engineering, Chinese Academy of Sciences, Sanya, China, [4]Hubei Institute of Hydrogeology and Engineering Geology, Jingzhou, China

OPEN ACCESS

EDITED BY
Mingjun Zou,
North China University of Water Resources and Electric Power, China

REVIEWED BY
Biao Guo,
North China University of Water Conservancy and Electric Power, China
Haihai Hou,
Liaoning Technical University, China

*CORRESPONDENCE
Zhansong Zhang,
Zhangzhs@yangtzeu.edu.cn

SPECIALTY SECTION
This article was submitted to Economic Geology,
a section of the journal
Frontiers in Earth Science

RECEIVED 29 August 2022
ACCEPTED 26 September 2022
PUBLISHED 06 January 2023

CITATION
Guo J, Zhang Z, Xiao H, Zhang C, Zhu L and Wang C (2023), Quantitative interpretation of coal industrial components using a gray system and geophysical logging data: A case study from the Qinshui Basin, China.
Front. Earth Sci. 10:1031218.
doi: 10.3389/feart.2022.1031218

The content of industrial components of coalbeds, one of the main parameters of coalbed methane (CBM) reservoirs, is crucial in the entire coal mine resource exploration and exploitation process. Currently, using geophysical logging data to determine the content of industrial components is the most widely implemented method. In this study, the PZ block in the Qinshui Basin was employed as a target block to evaluate ash (A_{ad}), fixed carbon (FC_{ad}), volatile matter (V_{daf}), and moisture (M_{ad}) under the air-dry (AD) base condition based on the autocorrelation between the geophysical logging curves and industrial component contents combined with the OBGM (1, N) model. The results indicate that 1) the geophysical logging curves combined with the OBGM (1, N) model can accurately predict the A_{ad} and FC_{ad} contents and an increase in geophysical logging curve types can effectively improve the model performance, compared to using a single geophysical logging curve for prediction. 2) When predicting the V_{daf} content, using the geophysical logging curves combined with A_{ad} and FC_{ad} contents had the highest prediction accuracy. Further, prediction bias does not exist, compared to using only the geophysical logging curve or the autocorrelation between the industrial component contents. The entire evaluation process begins with an assessment of the A_{ad} and FC_{ad} contents. Then, the V_{daf} content was assessed using the content of these two industrial components combined with geophysical logging data. Finally, the M_{ad} content was calculated using the volumetric model. Accurate application results were obtained for the verification of new wells, demonstrating the efficacy of the method and procedure described in this study. 3) The OBGM (1, N) model has the

---

Abbreviations: CBM, Coalbed methane; RBF, Gaussian radial basis function; AD, Air-dry basis; A_{ad}, Ash on an air-dry basis; FC_{ad}, Fixed carbon on an air-dry basis; V_{daf}, Volatile matter on air-dry basis; M_{ad}, Moisture on an air-dry basis; RD_{ad}, Relative density on an air-dry basis; AC, Acoustic time difference log; DEN, Compensation density log; CNL, Compensated neutron log; CAL, Caliper log; SP, Spontaneous potential log; GR, Nature gamma log; RD, Deep lateral resistivity log; RS, Shallow lateral resistivity log; RXO, Flushed-zone resistivity log; R^2, Fitting coefficient.

highest prediction accuracy compared with the multiple regression and GM (0, N) models, which have the same computational cost. The geophysical logging interpretation model of the proposed coalbed industrial component contents is simple to calculate and suitable for small samples, providing a new method for the evaluation process of industrial component contents.

KEYWORDS

coal quality analysis, industrial components, ash content, geophysical logging data, Qinshui Basin, OBGM (1, N)

1 Introduction

Currently, China is responsible for a significant proportion of coal production and consumption (Ward, 2016; Yang et al., 2018; He et al., 2020), in addition to having the highest coal sales worldwide (Gao et al., 2019). The Chinese government has made significant improvements toward the use of green coal resources (Jiang et al., 2010; Cai et al., 2011; Feng et al., 2020). With the current decline in conventional oil resources, the exploration and exploitation of unconventional oil and gas resources have become a research hotspot (Hamawand et al., 2013). Among them, coalbed methane (CBM) is a clean energy source (Palmer, 2010), and its exploration and exploitation is safer than conventional coal mining, in addition to producing less greenhouse gases (Karacan et al., 2011; Moore, 2012). Among coal quality parameters, the industrial components of coalbeds are crucial throughout the entire process of coal exploration and exploitation, mining, design, and processing (Feng et al., 2020). The industrial components of coalbeds can effectively evaluate the CBM content, whether they play a corrective role in the KIM or Langmuir coal order equations (Ahmed et al., 1991; Hawkins et al., 1992), or they directly use the industrial components of the coalbeds to predict the CBM content (Zhou and Guan, 2016; Zhou et al., 2015). Therefore, an accurate evaluation of the industrial components of coal quality is an important parameter that may lead to considerable economic benefits.

In an air-dry (AD) base state, coal industrial components contain ash (A_{ad}), fixed carbon (FC_{ad}), volatile matter (V_{daf}), and moisture (M_{ad}). The simplest method of obtaining the content of each industrial component is to send coal samples from core boreholes to a laboratory for geochemical analysis (Shao et al., 2013; Roslin and Esterle, 2015), which is time-consuming and expensive, and the fragility of the CBM reservoirs during drilling limits the number of samples (Fu et al., 2009b; Wang et al., 2018). To solve this problem, several studies have proposed solutions; an example is using geophysical logging data, which has been widely employed worldwide, to evaluate the industrial component contents of coalbeds (Yegireddi and Bhaskar, 2009). Geophysical logging techniques have the advantage of being continuous and cost-effective as a reliable method for characterizing the variations in the physical properties of rocks at high resolution (Morin, 2005; Ghosh et al., 2014). By constructing a relationship between the geophysical logging data and industrial components, the variation curve of the industrial components in the CBM reservoirs can be predicted. Furthermore, this method can be extended to boreholes without coring samples but with the geophysical logging data, laying the foundation for subsequent mapping of the 2D contour distribution of industrial components and 3D refinement model (Zhou et al., 2015).

The evaluation of the coal industrial components quality has been promising. Initially, volumetric models and statistical analysis methods for the determination of coal quality were proposed by Bond and Mullen, respectively (Bond et al., 1971; Mullen, 1988); however, they could not be combined with geophysical logging data. Subsequently, Pan et al. analyzed the density logging response with a strong correlation to the A_{ad} content and used this relationship to evaluate the industrial components of CBM reservoirs (Pan and Huang, 1998). It was then determined that the geophysical logging data are subject to multiple factors, the evaluation results of a single curve are not necessarily accurate, and multiple series of geophysical logging curves are more reliable in constructing a predictive model (Daniels et al., 1983; Chatterjee and Paul, 2013; Ghosh et al., 2014). With the development of mathematical methods, multiple regression (Zhang, 2013), machine learning (Zhou et al., 2016), and other methods have been gradually introduced to construct linear and nonlinear relationships between industrial components and geophysical logging curves. For example, (Liu et al., 2021) constructed linear relationships between the geophysical logging curves and industrial components and obtained promising results in the Qaidam Basin, whereas (Zhou and O'Brien, 2016) constructed relationships between the geophysical logging curves and multiple parameters, such as industrial components, using the Gaussian radial basis function (RBF) method, exhibiting the feasibility of a machine learning approach, and validated it in several studies. Similarly, methods such as fuzzy mathematics (Huang et al., 2020) have been applied to predict the contents of industrial components. However, it should be noted that these mathematical–statistical methods are based on a large sample size, and it is difficult to simplify them for small-sample datasets. The applicability of random forest and support vector machine methods, which are applicable to small-sample datasets, are also limited by the determination of hyperparameters and the uncertainty of the method.

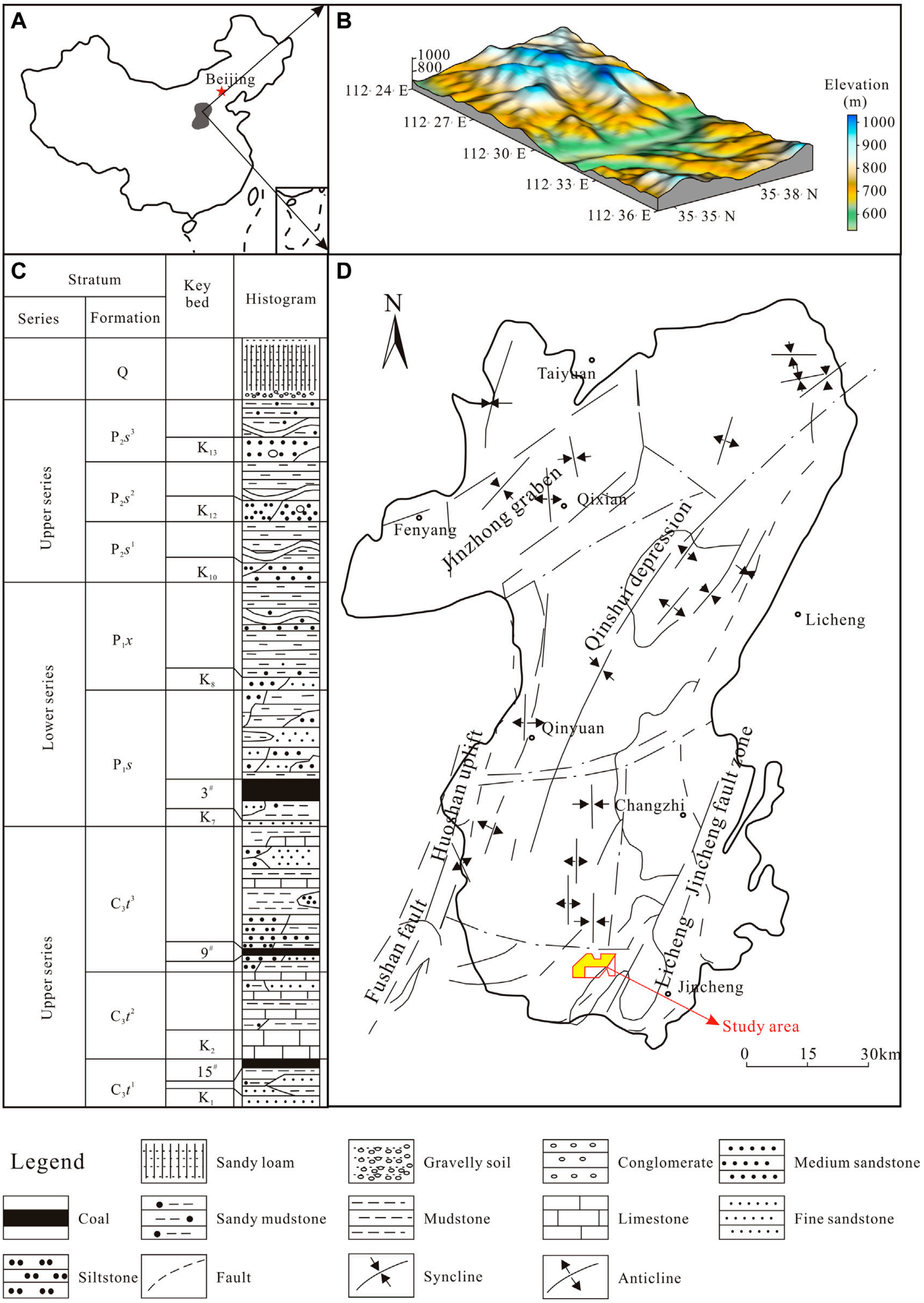

FIGURE 1
Schematic diagram of the PZ block in Qinshui Basin. **(A)** The location of the Qinshui Basin in China. **(B)** Geological schematic diagram of the PZ block. **(C)** Lithological column profile of the PZ block. **(D)** Schematic diagram of the location and geological structure of the study area.

Hence, this study applies the gray system OBGM (1, N) model, which is applicable to small-sample data, for predicting the industrial components of coal quality and evaluating the content of each industrial component in the PZ block based on geophysical logging data. The results indicate that using geophysical logging data combined with the OBGM (1, N) model can effectively predict the A_{ad} and FC_{ad} contents. Further, using multiple logging curves can effectively improve the accuracy of industrial component predictions compared to using a single logging curve. This paper proposes a set of evaluation processes for industrial components applicable to the PZ block, considering the autocorrelation between the industrial component contents, and tests the model of this study using new wells, exhibiting the effectiveness of the proposed method.

2 Geological background

2.1 Overview of the study area

The PZ block is in the Qinshui Basin, Shanxi Province, China (Figure 1A), and started commercial production in 2016. The tectonics within the PZ block are dominated by near-north-south folds (Figures 1B,D), which occur in the form of backward-sloping intervals (small dip angles; mainly 5–15°; averaging <10°) (Xu et al., 2014). The No.3 and No.15 coal seams are the main coal seams for CBM exploration and exploitation (Figure 1C) (Lv et al., 2012). The No.3 coal seam is in the Shanxi Formation and is a shallow water deltaic sedimentary system with a stable thickness of 3.45–7.02 m and an average thickness of 5.74 m. The No.15 coal seam is in the Taiyuan Formation, which is a set of composite deposition systems of barrier wall lagoons and carbonate terraces. The swampy deposits developed on the barrier wall coast of the No.15 coal seam are stable, are 0.85–6.25 m thick, and have an average thickness of 2.62 m. From the analysis of the coal samples collected in the boreholes, the average vitrinite, inertinite, and exinite group contents of the coal samples from the No.3 coal seam were 75.14%, 20.61%, and 4.25%, respectively; the contents of the three microscopic components of the No.15 coal seam are 77.46%, 13.02%, and 9.53%, respectively, all of which are dominated by the specular group. The vitrinite reflectivity ranges within 3.18%–4.36% and 3.97%–4.25% for the No.3 and 15 coal seams, respectively, and are both anthracites in terms of thermal evolution.

2.2 Difficulties in the evaluation

As one of the oldest exploration and mining works in the PZ block, the number of boreholes with coring information is small. Seven parameter wells from the same batch were collected, and 59 sets of core coal samples, that met the experimental specifications and requirements, were collected. The bare-hole logging data only contained conventional logging curves; in the lithology logging series, caliper (CAL), natural gamma (GR), and spontaneous potential (SP) log curves were collected; in the resistivity logging series, there were deep lateral resistivity (RD) and shallow lateral resistivity (RS) log curves, and a few boreholes contained the flushed-zone resistivity (RXO) log curve; in the three-porosity logging series, compensation density (DEN), compensated neutron (CNL) and acoustic time difference (AC) log curves correlated, and there was no array acoustic or nuclear magnetic resonance (NMR) logging data. Compared to the later developed study blocks, the PZ block did not have a porosity logging curve with multiple source distances in the conventional series and no electric imaging logging series. Owing to the technological development at that time, the restricted core coal sampling, coupled with the lack of logging series, was difficult to upscale using data-driven machine learning methods. Therefore, this study used a gray system method applicable to small-sample datasets combined with geophysical logging data, to construct a coal quality industrial component prediction model.

3 Method principle

3.1 Gray static model GM (0, N)

The GM (0, N) model is a static model without derivatives, which is fundamentally different from the multiple linear regression model. The typical multiple linear regression model is based on the original data, whereas the GM (0, N) model is based on the new data series accumulated from the original data. The modeling form of the GM (0, N) model weakens the randomness among the original data (Zhang and Jiang, 2005; Zhu et al., 2012), increases data regularity, and requires a small amount of statistical data, which is more suitable for use in practical production.

Specifying $x_1^{(0)} = \{x_1^{(0)}(1), x_1^{(0)}(2), \cdots, x_1^{(0)}(n)\}$ as the sequence of system characteristics, the sequence of correlated factors of interest is specified as

$$\begin{aligned} x_2^{(0)} &= \left\{x_2^{(0)}(1), x_2^{(0)}(2), \cdots, x_2^{(0)}(n)\right\} \\ x_3^{(0)} &= \left\{x_3^{(0)}(1), x_3^{(0)}(2), \cdots, x_3^{(0)}(n)\right\} \\ &\vdots \\ x_N^{(0)} &= \left\{x_N^{(0)}(1), x_N^{(0)}(2), \cdots, x_N^{(0)}(n)\right\} \end{aligned}$$

where $x_i^{(1)}$ denotes a cumulative generating sequence of $x_i^{(0)}$; that is, a 1-AGO sequence. The GM (0, N) model can be written as

$$x_1^{(1)}(k) = a + b_2 x_2^{(1)}(k) + b_3 x_3^{(1)}(k) + \cdots + b_N x_N^{(1)}(k) \quad (1)$$

The static GM (0, N) model can construct the corresponding prediction model by least-squares fitting with the target

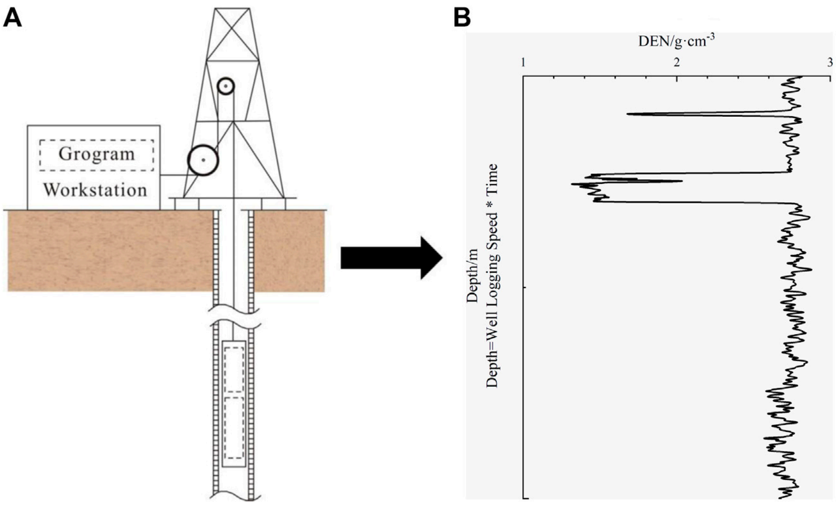

FIGURE 2
Geophysical logging data acquisition diagram. **(A)** Data collection process. **(B)** Schematic diagram of logging curves.

accumulation sequence after completing the accumulation of the feature sequence. The predicted target sequence is then reduced (cumulative subtraction) to obtain the predictions.

3.2 OBGM (1, N) prediction model

Compared to the GM (0, N) model, the OBGM (1, N) model consists of first-order ordinary differential equations (Zeng et al., 2016; Zeng and Li, 2018). Here, assumptions must be made regarding the actual geophysical logging information, and it is clear from Figure 2 that the geophysical logging curve is a characterization of the physical properties of the formation rocks. During the geophysical logging data acquisition, the logging instrument is gradually lifted from the bottom to the wellhead, a process that can be viewed as a time series; that is, the actual response of the geophysical logging data reflects the physical properties of the measured rock, whereas the measurement time is another influencing factor. The response of each logging curve can then be affected by the coupling of rock physical property and time changes, and the response of the logging data is written as shown in Eq. 2:

$$\begin{cases} \dfrac{dx_{DEN1}^{(1)}}{dt} = a_{11}x_{DEN1}^{(1)} + a_{12}x_{DEN2}^{(1)} + \cdots + a_{1N}x_{DENN}^{(1)} + b_1 \\ \dfrac{dx_{GR1}^{(1)}}{dt} = a_{21}x_{GR1}^{(1)} + a_{22}x_{GR2}^{(1)} + \cdots + a_{2N}x_{GRN}^{(1)} + b_2 \\ \vdots \\ \dfrac{dx_{CAL1}^{(1)}}{dt} = a_{N1}x_{CAL1}^{(1)} + a_{N2}x_{CAL2}^{(1)} + \cdots + a_{NN}x_{CALN}^{(1)} + b_N \end{cases} \tag{2}$$

The OBGM (1, N) model is a simplified and improved model of the GM (1, 1) model in the case of N variables (geophysical logging curves), consisting of a system of N first-order ordinary differential equations, with each variable considered as a database of modeled system characteristics, and the system of equations for each variable forming the OBGM (1, N) model. The matrix transformation of Eq. 2 can be expressed as Eq. 3.

$$\frac{dX^{(1)}}{dt} = AX^{(1)} + B \tag{3}$$

Adding the corresponding settable parameter column $\hat{a} = [A, B]^T$, the form of Y becomes

$$Y = \begin{bmatrix} x_1^{(0)}(2) & x_2^{(0)}(2) & \cdots & x_N^{(0)}(2) \\ x_1^{(0)}(3) & x_2^{(0)}(3) & \cdots & x_3^{(0)}(3) \\ \vdots & \vdots & \vdots & \vdots \\ x_1^{(0)}(n) & x_2^{(0)}(n) & \cdots & x_N^{(0)}(n) \end{bmatrix} \tag{4}$$

The least-squares estimated parameter column of the OBGM (1, N) model can then be written as

$$\hat{a} = \left(M^T M\right)^{-1} M^T Y \tag{5}$$

where M can be expressed as

$$M = \begin{bmatrix} z_1^{(1)}(2) & \cdots & z_N^{(1)}(2) & 1 \\ z_1^{(1)}(3) & \cdots & z_1^{(1)}(3) & 1 \\ \vdots & \vdots & \vdots & \vdots \\ z_1^{(1)}(n) & \cdots & z_N^{(1)}(n) & 1 \end{bmatrix} \tag{6}$$

The approximate time response equation corresponding to the OBGM (1, N) model is

$$\hat{X}^{(1)}(k) = e^{A(k-1)}X^{(1)}(1) + A^{-1}\left(e^{A(k-1)} - I\right) \cdot B \tag{7}$$

In Eq. 7, $k = 1, 2, \ldots$, and the cumulative reduction values are

$$\begin{cases} \hat{X}^{(0)}(1) = X^{(0)}(1) \\ \hat{X}^{(0)}(k) = \hat{X}^{(1)}(k) - \hat{X}^{(1)}(k-1) \end{cases} \tag{8}$$

In this theory, there is a background value coefficient, ξ, which has a significant impact on the prediction performance of the OBGM (1, N) model. In practice, ξ is typically used as a constant value of 0.5 (Tan et al., 2015). In addition, the time response function of the OBGM (1, N) model and its reduced form were expanded. The sequences, $X_i^{(0)}$ and $X_j^{(1)}$ ($i = 1, 2, \ldots; j = 1, 2, \ldots$), are defined as

$$\begin{aligned} & x_1^{(0)}(k) + a\xi x_1^{(1)}(k) + a(1-\xi)x_1^{(1)}(k-1) \\ & = \sum_{i=2}^{N} b_i x_i^{(1)}(k) + kc + d, k = 2, 3, \ldots, \end{aligned} \tag{9}$$

The parameters in Eq. 9 are expressed in a matrix as

$$\hat{p} = [b_2, b_3, \ldots, b_N, a, c, d]^T \tag{10}$$

In Eq. 10, b_N is the column of parameters obtained by least squares estimation, and depends on the number of logging curve bars involved in the model construction.

The OBGM (1, N) model is inexpensive to construct and does not require a significant number of calculations. Therefore, this study used geophysical logging curves as the basis for model construction, explored the effects of different curve numbers on the model, and recorded model performance for subsequent analysis.

4 Data preprocessing and quality checking

In this study, 59 sets of experimental samples were collected from wells PZ1–PZ7. The thickness of the CBM reservoirs was stable, and the industrial component determination method implemented industry standards: A_{ad}, M_{ad}, and V_{daf} were determined by laboratory heating, and FC_{ad} was determined using the differential subtraction method.

During geophysical logging data processing, the depth of the core sample is normalized to avoid the effects of misalignment caused by the stretching of the drill pipe (Fu et al., 2009b), and the geophysical logging response values were normalized through dense layers on the coal seam to eliminate effects caused by the borehole environment and instrumentation. Simultaneously, this study investigated the dilation of the core drill hole in the PZ block and performed a dilation correction of the geophysical logging curve for the dilation section.

To verify the reliability of the experiments and pretreatment, correlation tests were performed on the samples. A significant correlation was observed when comparing the laboratory relative density on an air-dry basis (RD_{ad}) of the coal samples with the A_{ad} contents (Figure 3A). The autocorrelation between the FC_{ad} and A_{ad} contents was significant (Figure 3B), indicating the reliability of the sample experiment. As shown in Figure 3C, the PZ block dilation is not clear, and the box plot shows the CAL curve response values of each cored coal sample in the seven cored boreholes, by comparing the bit diameters (21.59 cm). The dilation rate of each borehole was determined to be within 15%; that is, the dilation correction was completed by fitting the logging response values of the undilated section to the dilated section by regression. After preprocessing was completed, the DEN curve response values also exhibited a significant correlation with the RD_{ad} content (Figure 3D) when comparing them (Zhou and O'Brien, 2016), indicating the reliability of the logging data in this study with the validity of the preprocessing. It should be noted that the actual corrected density logging response values differ from the laboratory apparent density, which is related to the actual formation envelope pressure, fracture conditions, and the effects of human correction.

5 Results

Pearson index analysis was performed using the geophysical logging data with the coalbed industrial component contents to identify geophysical logging curves that are sensitive to the industrial component contents (Table 1). The feasibility of using geophysical logging data to predict the industrial component contents has been confirmed in previous studies (Shao et al., 2013; Ghosh et al., 2016). Multiple logging curves are more reliable to predict the contents of the industrial components than using only the DEN curve (Zhou and O'Brien, 2016). Correlation analysis revealed significant correlations between the industrial component contents, the A_{ad} content correlated significantly with the FC_{ad} content, and both correlated with the V_{daf} content. The A_{ad} content, as an industrial component, correlated significantly with other industrial component contents, and is typically the first to be evaluated (Liu et al., 2021).

5.1 Evaluation prediction of A_{ad}

Ash yield is vital, and the effect of the A_{ad} content on the porosity and CBM content has been proven previously (Li et al., 2007; Zhou and Guan, 2016). The experimental A_{ad} content in the study block ranged from 4.05% to 32.78%, with an average value of 11.8%. The correlation between each logging series and A_{ad} content was plotted in this study (Figure 4). The correlation between the A_{ad} content and the response values of the four curves (DEN, GR, AC, and RD) was outstanding, in which the A_{ad} content correlated significantly with the response values of DEN and GR (Figures 4A,B). The coalbeds are not radioactive;

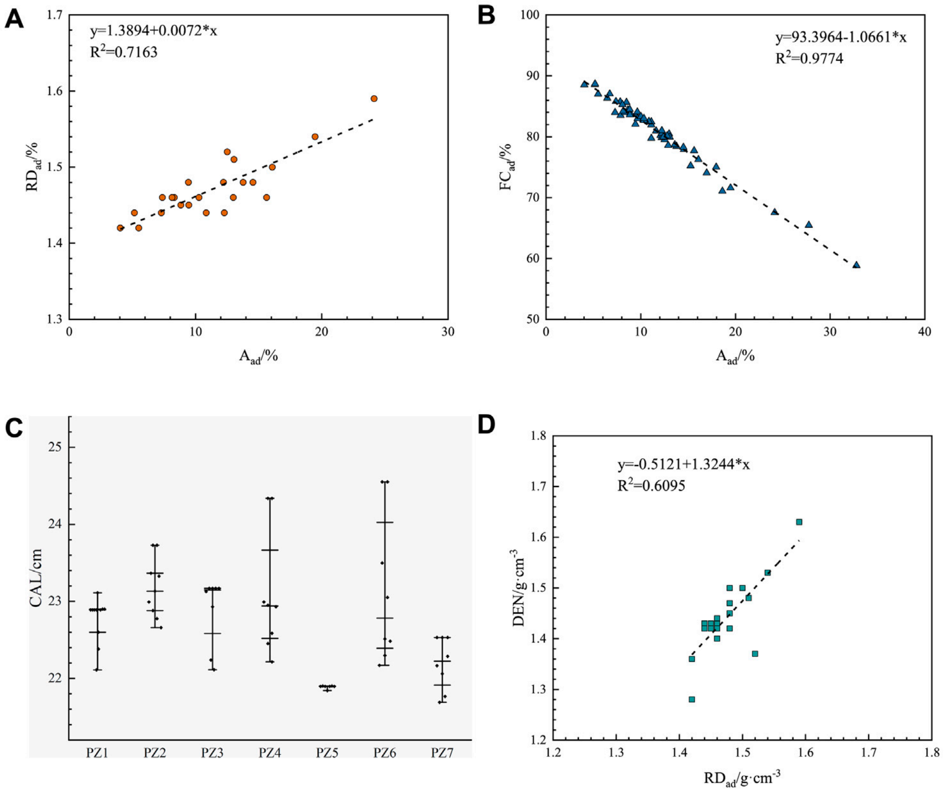

FIGURE 3
Pre-processing and quality checking of experimental data and geophysical logging processing of coal samples. **(A)** Correlation analysis plot of the A_{ad} content and RD_{ad}. **(B)** Correlation analysis plot of the A_{ad} content and the FC_{ad} content. **(C)** Dilation of core drilling. **(D)** Correlation analysis of the pre-processed DEN curve response values with the RD_{ad} of the laboratory coal samples.

TABLE 1 The Pearson index analysis of the response values of the industrial components and the geophysical logging curves of coalbeds in the PZ block.

	Mad	A_{ad}	Vd_{af}	FC_{ad}	AC	CNL	DEN	GR	RD	CAL
	(%)	(%)	(%)	(%)	(μs/m)	(V/V)	(g/cm³)	(API)	(Ω·m)	(cm)
Mad (%)	1.00									
A_{ad} (%)	−0.03	1.00								
Vd_{af} (%)	−0.20	0.51	1.00							
FC_{ad} (%)	−0.08	−0.99	−0.58	1.00						
AC (μs/m)	0.49	−0.61	−0.44	0.56	1.00					
CNL (V/V)	−0.04	0.00	0.20	−0.01	−0.10	1.00				
DEN (g/cm³)	0.05	0.89	0.47	−0.89	−0.50	−0.02	1.00			
GR (API)	0.00	0.85	0.39	−0.84	−0.51	−0.09	0.69	1.00		
RD (Ω·m)	−0.12	−0.53	−0.08	0.52	0.25	0.26	−0.36	−0.67	1.00	
CAL(cm)	0.21	−0.23	−0.01	0.19	0.32	0.18	−0.23	−0.32	0.39	1.00

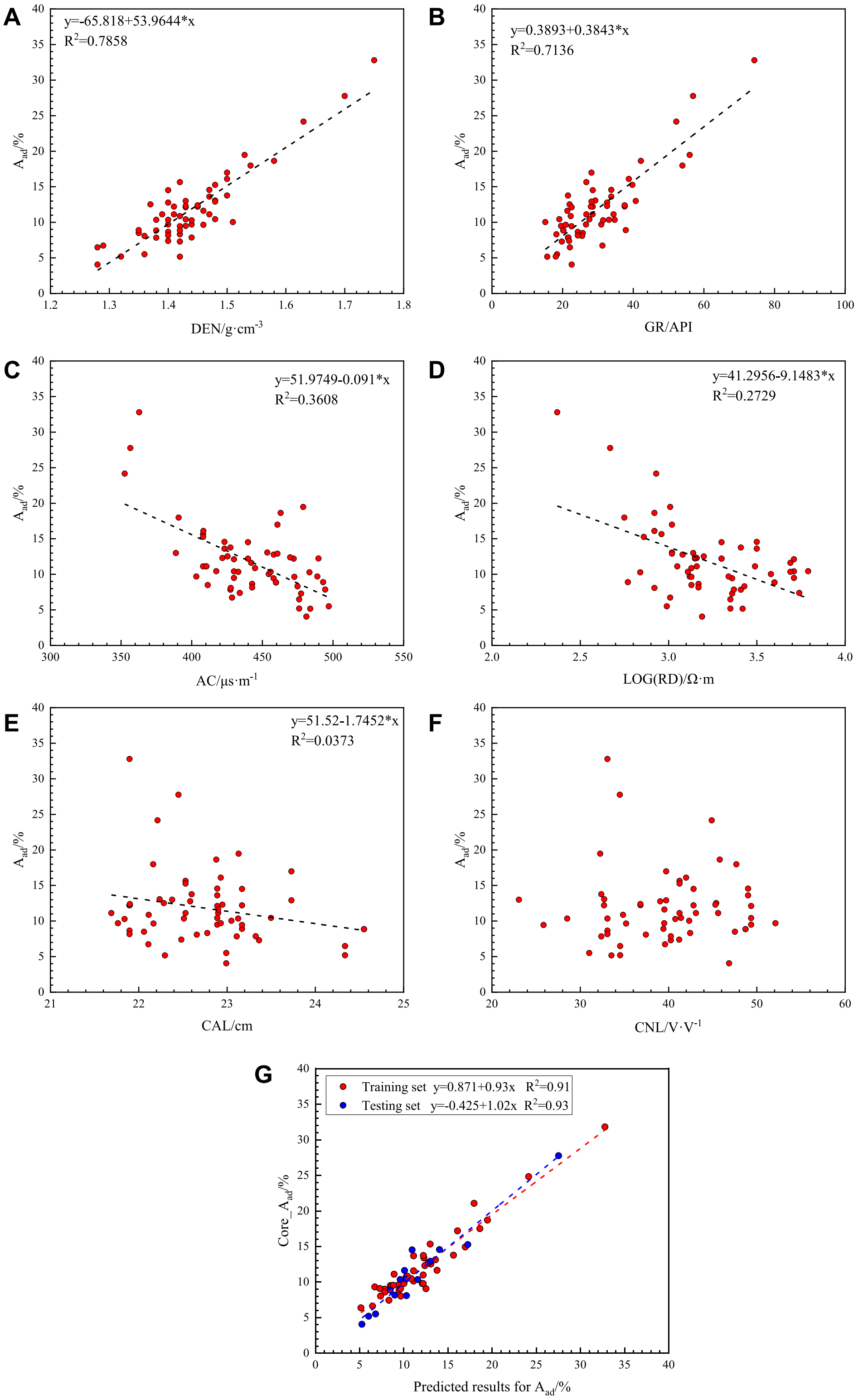

FIGURE 4
Correlation analysis of the A_{ad} content and the geophysical logging data response with the predicted results of the A_{ad} content. **(A)** Relationship between the A_{ad} content and DEN. **(B)** Relationship between the A_{ad} content and GR. **(C)** Relationship between the A_{ad} content and AC. **(D)** Relationship between the A_{ad} content and RD. **(E)** Relationship between the A_{ad} content and CAL. **(F)** Relationship between the A_{ad} content and CNL. **(G)** Performance of the OBGM (1, 5) prediction model on the training and test sets for the A_{ad} content.

thus, the response values of the GR curves are low, and their radioactivity mainly originates from clay minerals during coal formation (Shao et al., 2013; Liu et al., 2021), indicating that in addition to the DEN curve, the GR curve can also be an important curve for predicting A_{ad} content. In addition, the response values of the AC curve and the logarithmically processed RD also exhibit slight correlation with the A_{ad} content (Figures 4C,D); however, the correlation was weaker than that of GR and DEN, the correlation between the CAL curve and A_{ad} content was insignificant, and the response of the CNL curve exhibited almost no correlation with the A_{ad} content (Figures 4E,F). The A_{ad} content exhibited a negative correlation with the FC_{ad} content. Shi et al. (2020) showed that in high-rank coals, for different coal structures, the vitrinite content of tectonic coals is significantly higher than that of undeformed coals, subjecting the different brittle coal rocks to different destructive effects. Different coal structures provide different adsorption areas for CBM, which slightly increases the gas content of tectonic coals overall; this has been verified by the analysis of deep coal in the Jiaozuo Coalfield (Hou et al., 2017). Similarly, Hou H. H et al. (2021), Hou et al. (2019) showed that coal seams with high vitrinite content and low ash yield contain higher gas contents. These combined factors led to an increase in the response values of the AC curve corresponding to the coalbed sections with respect to the RD curve (Fu et al., 2009a; Ren et al., 2018). Although the response of the RD curve is controlled by various factors (Hou H. H et al., 2021; Zhu et al., 2021, 2022), there is some correlation with the data. The analysis of this correlation was confirmed in the SZB block adjacent to the PZ block, indicating that the content of A_{ad} correlates with the response values of the AC and RD curves.

Analyzing Figure 4 and Table 1, the geophysical logging curves sensitive to the A_{ad} content were determined, and the OBGM (1, N) model was used to predict the A_{ad} content. A total of 59 groups of coal seam industrial components were collected, and 15 groups of A_{ad} contents were randomly selected as the test dataset to verify the effect of the model.

While constructing the prediction model for the A_{ad} content, the effect of the number of geophysical logging curves on the model was analyzed by increasing the number of geophysical logging curves. Table 2 presents the results and lists the training dataset and prediction effects of the test dataset involved in the construction of the model. The first column in Tables 2–4 show the combination of the cumulative curves, which gradually increased from 1. The second column shows the average relative error results of the back-judgments of the datasets involved in the construction of the prediction model, and the third to fifth columns show the test results of the randomly selected datasets, which were not involved in the model construction, showing the average relative, minimum relative, and maximum relative errors, respectively; the sixth to ninth columns show the parameters. That is, the parameter matrix demonstrated in Eq. 10 (b_N, a, c, and d), correspond to the parameters in Eq. 9. Table 2 shows the prediction and evaluation results of the A_{ad} content. With an increase in the number of geophysical logging curves, the relative error of both the training and test datasets decreased and stabilized when there were five geophysical logging curves. Because the response value of the CNL curve has almost no correlation with the content of A_{ad}, the A_{ad} content can be effectively predicted by using five logging curves (i.e., DEN, GR, AC, RD, and CAL). Currently, the average relative error of the test dataset of the A_{ad} content was 12.42%, and the minimum relative error was 0.76%. The maximum relative error was 30.11%, which is the lowest value in each combination curve. Figure 4G shows the rendezvous diagram of the training and test datasets corresponding to the A_{ad} content. It was determined that the model in this study effectively predicted A_{ad} content, and the model had no deviation. The high correlation between the prediction and experimental results in the training and test data also proves the effectiveness of the model.

5.2 Evaluation prediction of FC_{ad}

The FC_{ad} content, similar to the A_{ad} content, is an important geological parameter that plays a key role in the evaluation of CBM content (Ghosh et al., 2016; Zhou and Guan, 2016). The experimental FC_{ad} content in the study block ranged from 58.84% to 88.68%, with an average value of 80.82%. Because of the strong correlation between the FC_{ad} and A_{ad} contents, the correlation between the FC_{ad} content and the response values of the geophysical logging curves was consistent with that of the A_{ad} content, with an opposite trend (Figures 5A-D). For example, in the study block, the burial depths of different coal seams differ significantly, and the seam numbers are not distinguished in the autocorrelations of the industrial component contents. Based on the data, the effect of burial depth does not have a significant impact on the autocorrelation between the industrial component contents, the M_{ad} content is lower in all cases, and the M_{ad} content of the No.3 coal seam is slightly higher than that of the No.15 coal seam. The total sulfur content exhibits a significant difference, the total sulfur content of the No.15 coal seam is 7–10 times higher than that of the No.3 coal seam, the total sulfur content of the No.3 coal seam is approximately 0.5%, and that of the No.15 coal seam is approximately 2.7%. Considering the semi-industrial analysis of this study and the small amount of data in this block and the predominance of the No.3 coal seam, the data are processed in general. For coal seams with different burial depths, the discussion should be divided into layers if the amount of data meets the requirements (Hou H et al., 2021), particularly for coal rock sections with significant differences in coal structures (Hou et al., 2017).

FC_{ad} and A_{ad} used the same data samples in the study, and the process and results in the exploration of logging curves are listed in Table 3. The same results were obtained for the prediction of the A_{ad} content, and the FC_{ad} content was

TABLE 2 Performance and parameters of the A_{ad} content prediction models under different logging curves.

	Average relative error/%	Average relative error/%	Min. Error/ %	Max. Error/ %	Parameter columns			
A_{ad}	**Training set**	**Test set**	**Test set**	**Test set**	**b_N**	**a**	**c**	**d**
DEN	27.67	30.29	0.04	86.25	19.31	0.35	−23.68	11.91
DEN, GR	17.19	25.91	0.56	115.67	7.58, 0.29	0.97	−7.97	1.15
DEN, GR, AC	11.77	12.66	0.48	42.86	22.35, 0.25, −0.03	0.95	−16.45	−3.37
DEN, GR, AC, RD	11.70	13.73	0.55	41.29	25.25, 0.20, −0.03, −2.13	0.99	−8.91	−6.08
DEN, GR, AC, RD, CAL	10.68	12.62	0.76	30.11	28.34, 0.19, −0.04, −3.21, 0.99	0.97	−30.23	−3.49
DEN, GR, AC, RD, CAL, CNL	10.61	12.27	0.35	38.25	28.50, 0.18, −0.04, −3.49, 0.84, 0.04	0.97	−28.02	−4.59

TABLE 3 Performance and parameters of the FC_{ad} content prediction models under different logging curves.

	Average relative error/%	Average relative error/%	Min. Error/ %	Max. Error/ %	Parameter columns			
FC_{ad}	**Training set**	**Test set**	**Test set**	**Test set**	**b_N**	**a**	**c**	**d**
DEN	4.68	4.59	0.29	20.78	−17.63	0.29	48.75	57.17
DEN, GR	3.16	3.02	0.03	11.96	−9.18, −0.21	0.65	72.12	34.82
DEN, GR, AC	2.78	2.49	0.19	6.59	−23.99, −0.16, 0.03	0.58	73.96	44.43
DEN, GR, AC, RD	2.79	2.53	0.19	6.54	−23.30, −0.17, 0.03, −0.50	0.58	75.39	44.14
DEN, GR, AC, RD, CAL	2.02	1.42	0.01	3.63	−30.62, −0.21, 0.04, 2.57, −2.47	0.84	150.19	21.25
DEN, GR, AC, RD, CAL, CNL	2.04	1.43	0.43	3.73	−30.76, −0.21, 0.03, 2.81, −2.33, −0.04	0.84	148.00	22.36

TABLE 4 Performance and parameters of the Vd_{af} content prediction models under different logging curves.

	Average relative error/%	Average relative error/%	Min. Error/ %	Max. Error/ %	Parameter columns			
V_{daf}	**Training set**	**Test set**	**Test set**	**Test set**	**b_N**	**a**	**c**	**d**
DEN	8.09	13.91	2.06	41.08	−0.41	0.02	0.70	5.74
DEN, GR	8.01	15.31	0.23	43.25	−0.25, −0.002	0.02	0.52	5.77
DEN, GR, AC	7.90	9.09	2.14	28.82	1.01, −0.006, −0.004	0.10	0.82	4.79
DEN, GR, AC, RD	7.89	9.08	2.06	28.84	1.02, −0.006, −0.004, −0.007	0.10	0.83	4.78
DEN, GR, AC, RD, CAL	7.91	8.54	0.49	30.06	1.07, −0.006, −0.004, −0.01, 0.06	0.13	−0.11	4.73
DEN, GR, AC, RD, CAL, CNL	7.89	8.51	1.52	30.44	1.06, −0.005, −0.005, 0.01, 0.07, −0.002	0.14	−0.25	4.78
DEN, GR, AC, Aad, FCad	8.04	8.23	0.58	31.16	1.16, −0.004, −0.01, −0.22, −0.19	0.42	22.82	2.86

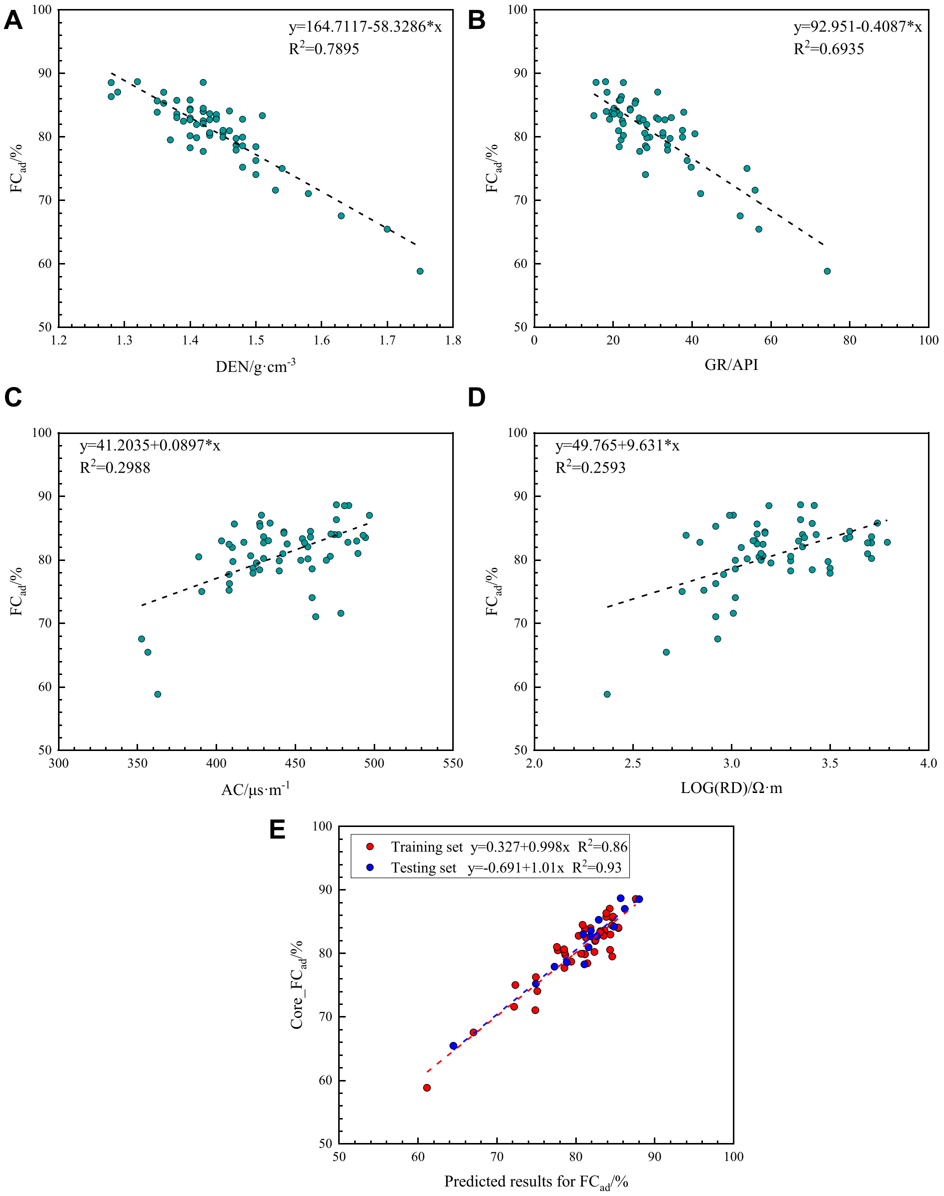

FIGURE 5
Correlation analysis of the FC_{ad} content and the geophysical logging data response with the predicted results of the FC_{ad} content. **(A)** Relationship between the FC_{ad} content and DEN. **(B)** Relationship between the FC_{ad} content and GR. **(C)** Relationship between the FC_{ad} content and AC. **(D)** Relationship between the FC_{ad} content and RD. **(E)** Performance of the OBGM (1, 5) prediction model on the training and test sets for the FC_{ad} content.

accurately predicted when five curves were generated. The analysis determined that the model in this study effectively predicted the FC_{ad} content. The average relative error of the data in the test set was 1.42%, and the maximum relative error was 3.63%, with high prediction accuracy. Furthermore, Figure 5E shows that bias does not occur in the prediction results, and the fitting coefficient (R^2) between the prediction and experimental results in the test data was 0.93, exhibiting the effectiveness of the prediction method.

5.3 Evaluation prediction of V_{daf}

The V_{daf} content is dependent on several factors, such as the degree of coalification and sedimentary environment (J. Hou et al., 2014; Liu et al., 2021). It is also an important factor in determining the degree of coalification of coal rocks. It tends to increase and then decrease with increasing coalification, reaching maximum and minimum values in brown and anthracite coals, respectively. The V_{daf} content of the coal samples from the PZ

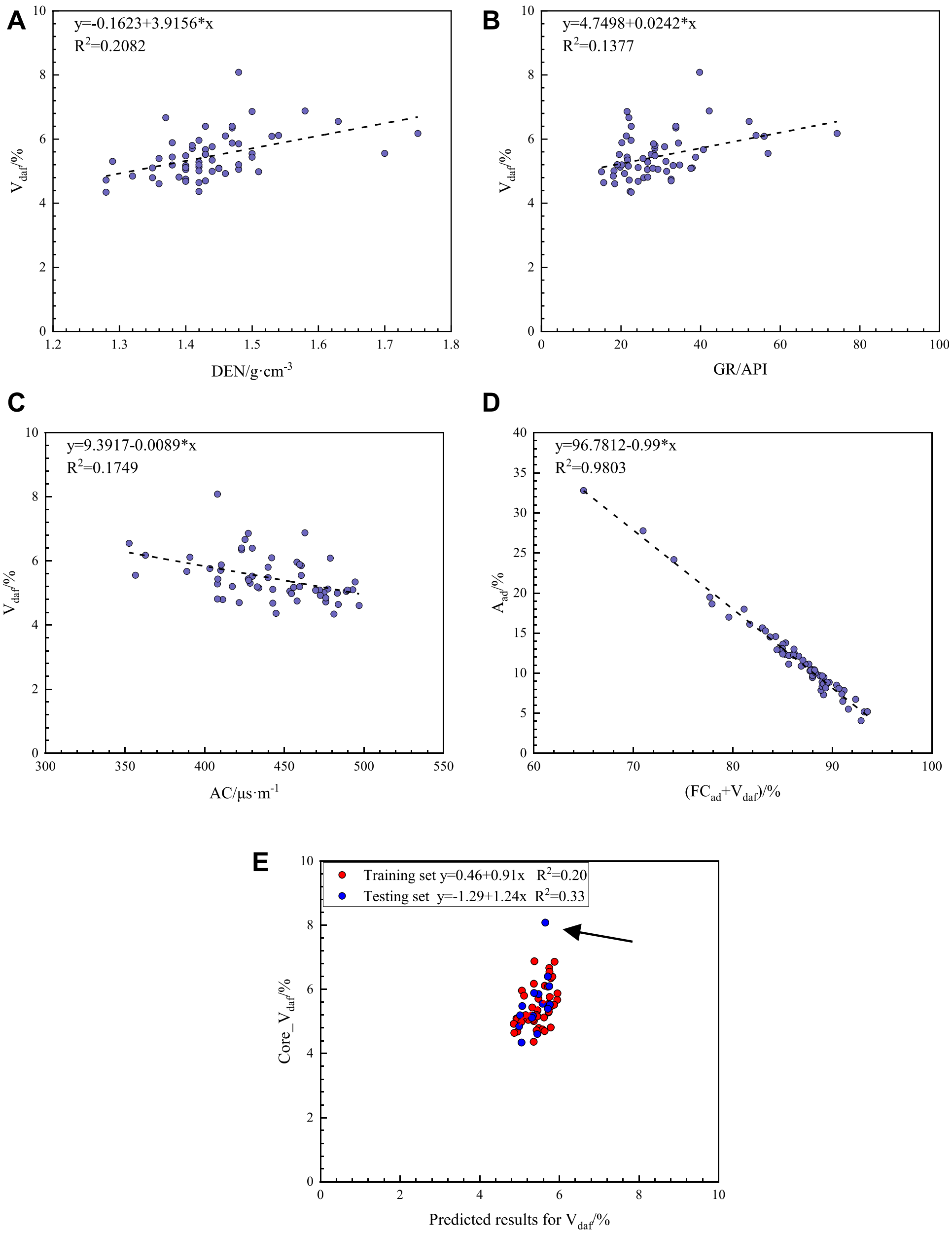

FIGURE 6
Correlation analysis of the Vd_{af} content and the geophysical logging data response with the predicted results of the Vd_{af} content. **(A)** Relationship between the Vd_{af} content and DEN. **(B)** Relationship between the Vd_{af} content and GR. **(C)** Relationship between the Vd_{af} content and AC. **(D)** Autocorrelation between industrial component contents. **(E)** Performance of the OBGM (1, 6) prediction model on the training and test sets for the Vd_{af} content.

block measured in the laboratory ranged from 4.34% to 8.08%, with an average value of 5.47%. The V_{daf} content was extremely low, and the block was a typical anthracite coal. The Pearson index and rendezvous plots (Figure 6) indicate that the correlation between the V_{daf} content and the response values of the geophysical logging data was weak, and only the response values of DEN, GR, and AC are correlated (Figures 6A–C). Furthermore, the autocorrelation between the contents of industrial components indicated that the A_{ad} content had a strong correlation with the numerical sum of the FC_{ad} and V_{daf} contents (Figure 6D). Hence, two methods are proposed in this paper for the prediction of the V_{daf} content. The first method is to compare the error using the same exploration, as in Sections 5.1, 5.2, by increasing the logging curves to construct a

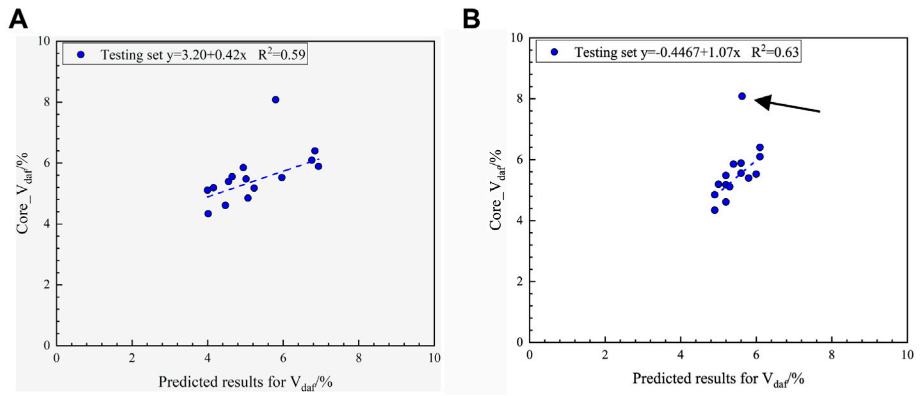

FIGURE 7
(A) Application effect of the Vd_{af} content prediction model constructed using industrial component content autocorrelation. **(B)** Application effect of the Vd_{af} content prediction model constructed using the geophysical logging curves and the industrial component contents combined with OBGM (1, 5) model.

model. As presented in Table 4, the best results were achieved with six geophysical logging curves, and the average and maximum relative errors of the test dataset reached minimums. Thus, the prediction results of the training and test datasets were plotted (Figure 6E). The overall model was biased, with high predictions for low values of the core experiments and low predictions for high values of the experimental results, forming a significantly biased phenomenon (Figure 6E), although the error value of the V_{daf} content predicted using the geophysical logging curves was low. This prediction effect does not have a simplified value despite the low error levels. Note that there was an abnormally high value in the test data of the V_{daf} content; that is, the test result of the V_{daf} content in the laboratory was 8.08% (shown in black arrows). To prevent the comparison of the abnormal point (shown in black arrows) to the subsequent models, this point is ignored when the correlation between the predicted and experimental data is discussed in subsequent multiple methods.

Owing to the poor results of using only the logging curves directly, a second method was used in this study; that is, a calculation using the autocorrelation between industrial component contents according to the autocorrelation regression equation:

$$A_{ad} = 96.7812 - 0.99\left(FC_{ad} + V_{daf}\right) \tag{11}$$

$$V_{daf} = \frac{96.7812 - A_{ad}}{0.99} - FC_{ad} \tag{12}$$

Calculations were performed according to the regression equation (Eq. 12), and to test the simplification of this method, the A_{ad} and V_{daf} contents in the test datasets are the results of the predictions in Sections 5.1, 5.2, rather than the core experimental results. The V_{daf} content predicted from the autocorrelation of the industrial component content is shown in Figure 7A. Compared with the OBGM (1, 6) prediction model using only the geophysical logging curves directly, the correlation between the predicted and experimental results of the test dataset using autocorrelation Eq. 12 increased from 0.33 to 0.59. This phenomenon indicates that using the autocorrelation of industrial component contents is an effective prediction method.

This paper also proposes a new prediction model for predicting the V_{daf} content, which is created by combining the geophysical logging curves sensitive to the V_{daf} content and the A_{ad} and FC_{ad} contents in the industrial components with the OBGM (1, N) while maintaining the test dataset. The values of the A_{ad} and FC_{ad} contents in the test datasets also use the prediction results in Sections 5.1, 5.2, rather than the core experimental results (Figure 7B). By comparing the content prediction model of the V_{daf} content constructed by three different combination modes, combined with the actual error data and correlation, it is considered that the prediction model using the geophysical logging curves combined with industrial component contents has the best effect, average relative error, and R^2, and there is no significant prediction deviation. The construction method of comprehensive geophysical logging data and component relationships not only allows the original logging curve to participate but also considers the autocorrelation and cumulative error between industrial component contents. The prominent application effect also demonstrated the effectiveness of the model construction method. Note that there is no local magmatic intrusion. The change in the degree of coal metamorphism needs to meet Hilt's law, which is a precondition (Hou H. H. et al., 2021). The corresponding model parameters are listed in the last row of Table 4.

5.4 Evaluation prediction of M_{ad}

The current calculation of the M_{ad} content in industrial components can be divided into two types: volumetric models (Liu et al., 2021) and geophysical logging curves combined with mathematical models (Zhou and O'Brien, 2016; Zhou et al., 2016). The correlation analysis of the Pearson index shows that the M_{ad} content does not exhibit a significant correlation with the contents of various industrial components and the response values of the geophysical logging curves, and the PZ block does not collect sufficient data to use the data-driven method for model construction; therefore, the volumetric model was used for calculations in this study. The volumetric model treats coal rock as consisting of four industrial components, and because the CBM in this area is mainly in the adsorbed state rather than the free state, without considering the volume of CBM, it is determined by Eq. 13.

$$A_{ad} + FC_{ad} + V_{daf} + M_{ad} = 1 \tag{13}$$

The corresponding M_{ad} can then be expressed as

$$M_{ad} = 1 - A_{ad} - FC_{ad} - V_{daf} \tag{14}$$

In Eqs 13, 14, M_{ad} denotes the moisture on an air-dry basis (%), FC_{ad} the fixed carbon on an air-dry basis (%), A_{ad} the ash on an air-dry basis (%), and V_{daf} the volatile matter on an air-dry basis (%).

Through seven core boreholes in the PZ block, a complete procedure for evaluating the industrial component contents of coalbeds was obtained in this study. That is, the A_{ad} and FC_{ad} contents are predicted using the geophysical logging curves, and the predicted components are then combined with the geophysical logging curves to predict the V_{daf} content. Finally, the M_{ad} content is calculated using the volumetric model, that is, the differential subtraction method.

5.5 Application of new wells

To ensure the validity and generalization of the model in this study, the model constructed by the industrial component content evaluation process, combined with the training dataset, was applied using two new wells in the block, PZ8 and PZ9. Figures 8A,B show the results and graphs of the two new wells. The first track in the figure is the log depth track; the second is the lithology logging track, containing CAL, GR, and SP curves; the third is the resistivity logging track, showing the RD curve; the fourth is the porosity logging series, containing CNL, AC, and DEN curves; the fifth to eighth tracks are the laboratory analysis values of each industrial component content and the model prediction curves in this study, A_{ad}, FD_{ad}, V_{daf}, and M_{ad}, respectively; and the ninth track is the lithology channel, which contains the top and bottom plates of coal and mudstone lithologies. Figure 8C and Table 5 show a rendezvous diagram and listed data of the new wells, respectively. The prediction results of the A_{ad} and FC_{ad} contents are uniformly distributed on both sides of the zero-error line in Figure 8C, and the prediction errors of each industrial component content are given in Table 5. The prediction effects of the A_{ad}, FC_{ad}, and V_{daf} contents in the new wells are consistent with the performance of the model on the test datasets, indicating the effectiveness and generalization of the method in this study. The prediction curves for the contents of FC_{ad} and A_{ad} correlate with the experimental analysis of the changing trend, and the overall error of the prediction results for the V_{daf} content is slightly higher than for the previous two, according to a thorough analysis that includes the actual geophysical logging plots and data table. Because the M_{ad} content is calculated using the differential subtraction method, the accuracy of the evaluation of the contents of the first three components limits the prediction results of the M_{ad} content, and the error is the cumulative error of the prediction of the three industrial component contents. Because the M_{ad} content typically does not exceed 3% in this block, the small error accumulating continuously has an amplifying effect on M_{ad}, giving a corresponding maximum relative error of 64.1%. Given that the prediction errors of the other three industrial component contents are consistent with the performance of the test data, this typically demonstrates the validity and generalization of the model in this study, which can provide a reliable method for industrial component content prediction in the field.

6 Discussion and analysis

6.1 Problem with determining the background value

In the method principle, the background value, ξ, is typically used as 0.5, which is verified in this study. Using the A_{ad} content as an example, the background value was constantly changed, the model was constructed from a defined training dataset, and an error test was performed using the same set of test data, using the average relative error as the standard. Figure 9A shows that the average relative error of the training dataset increased slightly with an increase in the background value and then increased rapidly when ξ exceeded 0.8. The error of the test data shows a decreasing and then increasing trend, that is, an excessively large x has a greater impact on the accuracy of the model. It is also shown that ξ (taken as 0.5), can satisfy the conditions of model construction and obtain sufficient accuracy; if the background value needs to be optimized, grid search or other optimization methods can be introduced, however this will inevitably decrease the speed of model construction, particularly when cross-validation is introduced to reduce the chance (Mahmood and

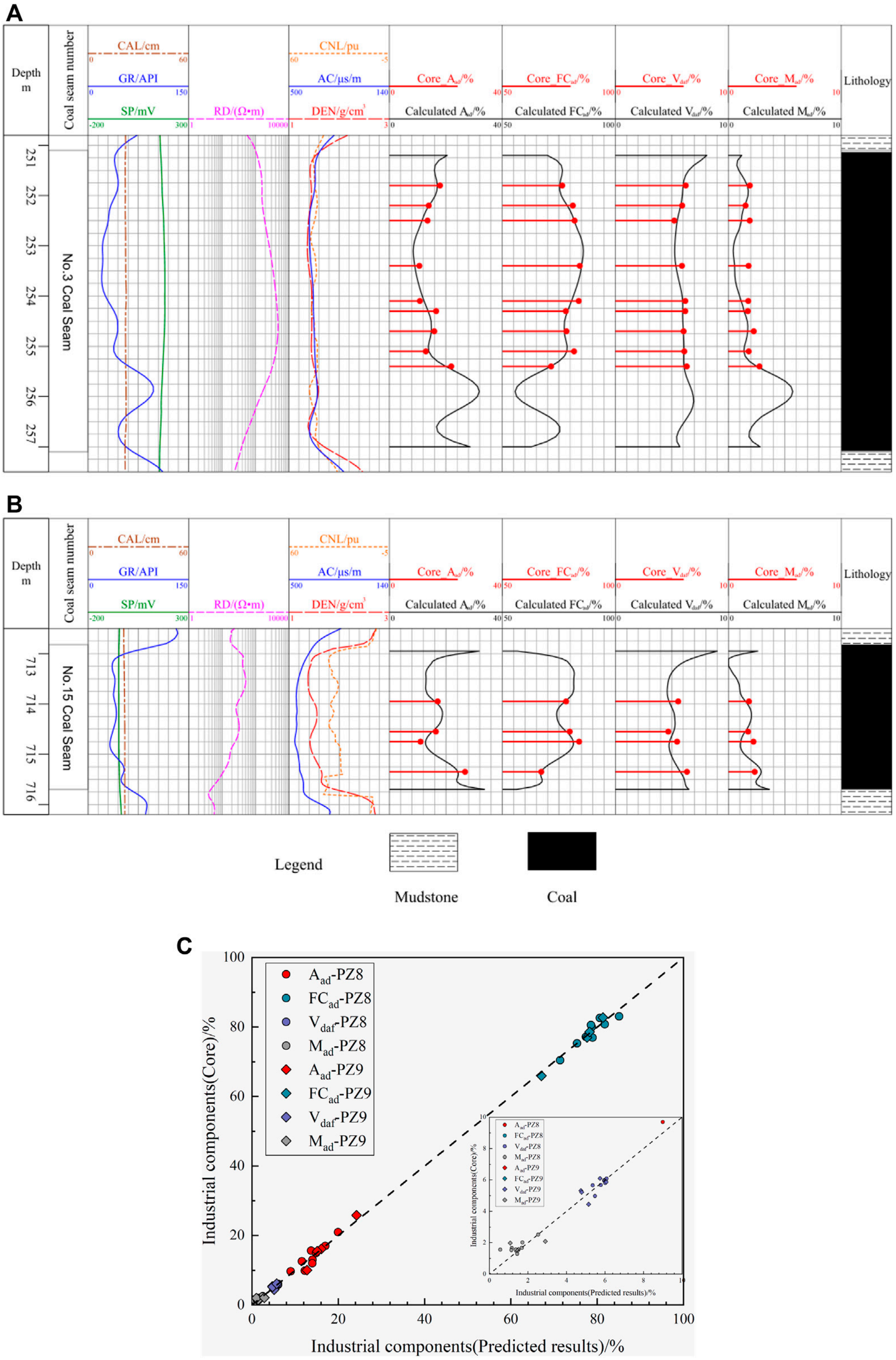

FIGURE 8
(A) Predicted industrial component contents of the new well PZ8 in the PZ block. (B) Predicted industrial component contents of the new well PZ9 in the PZ block. **(C)** Correlation between the predicted results and the experimental results for each industrial component in the new wells.

TABLE 5 Calculated and experimental values from wells of PZ8 and PZ9.

		Ash content/%			Fixed carbon content/%			Volatile matter content/%			Moisture content/%		
		Core	Predicted	Relative	Core	Predicted	Relative	Core	Predicted	Relative	Core	Predicted	Relative
Well	Depth	Value	Value	Error	Value	Value	Error	Value	Value	Error	Value	Value	Error
PZ8	251.82	17.00	16.99	0.06	75.33	75.34	0.01	6.00	5.99	0.17	1.67	1.68	0.60
	252.23	13.01	14.04	7.92	80.02	78.74	1.60	5.68	5.78	1.76	1.29	1.44	11.63
	252.51	11.58	11.58	7.95	80.78	81.78	1.24	4.98	5.48	10.04	1.66	1.16	30.12
	253.37	9.70	9.00	7.22	83.08	85.08	2.41	5.66	5.36	5.30	1.56	0.56	64.10
	254.12	9.88	12.28	24.29	82.63	80.63	2.42	5.96	5.95	0.17	1.53	1.14	25.49
	254.31	15.72	13.72	12.16	76.94	78.94	2.60	5.95	5.96	0.17	1.49	1.39	6.71
	254.68	14.77	14.87	0.67	77.20	77.40	0.26	5.81	6.01	3.44	2.02	1.71	15.35
	255.11	11.99	13.99	16.68	80.57	78.57	2.48	5.87	6.07	3.41	1.57	1.37	12.74
	255.45	20.98	19.98	4.77	70.41	71.41	1.42	6.09	6.08	0.16	2.52	2.53	0.40
PZ9	713.92	16.12	16.08	0.25	76.98	77.66	0.88	5.32	4.75	10.71	1.58	1.51	4.43
	714.54	15.48	15.13	2.26	78.57	78.25	0.41	4.45	5.15	15.73	1.50	1.47	2.00
	714.75	10.06	12.77	26.94	82.74	81.36	1.67	5.22	4.79	8.24	1.98	1.08	45.45
	715.37	25.82	24.26	6.04	65.99	67.10	1.68	6.10	5.74	5.90	2.09	2.90	38.76

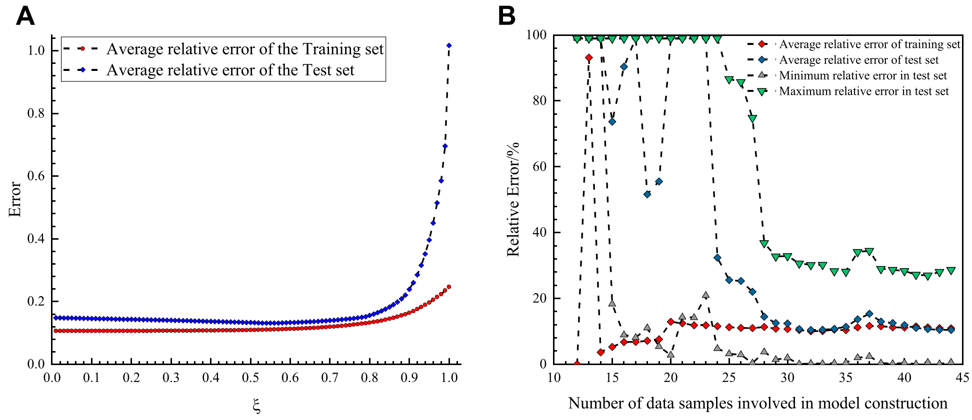

FIGURE 9
(A) The effect of changes in background value coefficients on the model performance (using the A_{ad} content as an example). **(B)** The effect of data sample size on the prediction model performance (using the A_{ad} content as an example).

Khan, 2009); thus, this study only discusses the determination, which can be further investigated in future studies.

6.2 Effect of the number of training datasets on the model

Gray systems are suitable for constructing evaluation models with small sample sizes. In contrast, data-driven methods, such as machine-learning methods, tend to have higher requirements for the amount of data in the sample. Although there are vector machine type methods for small-sample datasets, when applying these methods to build models, the determination of the hyperparameters must be combined with optimization modes, such as cross-validation or grid search, a process that is computationally expensive and difficult to avoid when the sample is small. In the OBGM (1, N) model, the magnitude of the background value, ξ, was determined in Section 6.1, on which the number of samples involved in the model construction was based and tested in this study. The A_{ad} content prediction was explored with a basis of 11 sets of data, and the number of training datasets was continuously increased. The average relative error was calculated by back-judging the training dataset, and the average, maximum, and minimum relative errors in 15 sets of test data were calculated. The error was given as 100% when it exceeded 100%; that is, it could not be predicted. The results are shown in Figure 9B. When the training dataset had <30 groups, the prediction effect is unstable, and the average relative error of the test dataset exhibits a decreasing trend, which should currently be underfitted. When the training dataset exceeded 30 groups, the average relative errors of the training and test datasets tended to be stable, only minor fluctuations occur, and the average relative errors of the training and test datasets were similar. Thus, it can be determined that the constructed model can be used, and the overfitting phenomenon does not occur. During this exploration, the A_{ad} content covered the low and high value levels, and a certain random factor may appear in the accumulation process. However, this model has some effect when the training dataset reaches 28 groups and is highly applicable for >30 groups, proving that the method is applicable to small-sample datasets.

6.3 Comparison of the methods

To further illustrate the advantages of the model in this study, the method used here was compared with the multiple regression method and static gray model (GM) (0, N). The same multiple regression and GM (0, N) models were constructed for the same data, using A_{ad} content as an example. To compare the variability between the methods, consistent with the data explored previously for the OBGM model, 44 sets of data were used for the model construction, and 15 sets of the same data were used for the test data to show the performance of the model on the test data.

$$A_{ad} = -37.53 + 33.66DEN + 0.12GR - 0.02AC - 3.64\,Ln(RD) + 0.9CAL \tag{15}$$

$$A_{ad}^{(1)} = -7.31 + 15.92DEN^{(1)} + 0.19GR^{(1)} - 0.03AC^{(1)} - 3.29\,Ln(RD)^{(1)} + 0.27CAL^{(1)} \tag{16}$$

Eqs 15, 16 are the fitted equations of the multiple regression and static GM (0, N) models, respectively. A_{ad} denotes the ash on

TABLE 6 Comparison of the application effect between different methods.

Method	OBGM (1, N)	GM (0, N)	Multiple regression
Average relative error/%	12.62	18.85	17.96
Minimum relative error/%	0.76	1.81	0.73
Maximum relative error/%	30.11	46.82	46.53
R^2	0.93	0.85	0.9

an air-dried basis, $A_{ad}^{(1)}$ the cumulative equation (1-AGO) of A_{ad}, and $DEN^{(1)}$ the cumulative terms of DEN.

Table 6 shows the application effect of the three models for the prediction of the A_{ad} content in the test dataset, and the analysis by the mean relative error indicates that the OBGM (1, N) model is better than the multiple regression and GM (0, N) models. The correlation between the prediction and actual coring results in the test dataset indicated that the model used in this study had the highest correlation and lowest maximum relative error. The OBGM (1, N) model had the most stable relative error and the highest correlation between the prediction and experimental results among the methods with the same computational cost.

6.4 Error discussion

The prediction errors for the contents of the four industrial components were analyzed in this study. The prediction errors for the A_{ad} and FC_{ad} contents can be grouped into the following categories:

1) The process of geophysical logging data acquisition is inevitably subject to interference, and the logging curve is a comprehensive characterization of the physical properties of the rock and contains noise information as well as disturbances during experiments, such as coal sample coring from the delivery to the laboratory. These types of errors are mainly systematic errors. The study as much as possible corrects errors caused by the instrumentation, borehole, and other environmental factors during the logging process by standardizing the preprocessing. Although there is a certain degree of human interference, the results after preprocessing demonstrates the feasibility of the method; for the experimental problem, this study shows the correlation between component contents and between the A_{ad} and RD_{ad} contents, indicating that such errors are within acceptable limits.
2) In the process of matching logging response data, such as core depth homing and dilation correction, it is difficult to avoid the interference caused by human factors. However, such operations can significantly decrease the impact of instruments and construction, reducing the overall error.

It is not possible to construct a separate model to reject these two types of errors, and such errors can be ignored during the construction of the prediction model for industrial component contents; however, they will be added to the results. The predictions of the A_{ad} and FC_{ad} contents indicated that the errors of both were within acceptable limits, and the model used in this study was advantageous.

In contrast, the prediction errors of the V_{daf} and M_{ad} contents are somewhat different from these errors. In addition to these two types of errors, there are cumulative errors in the prediction of the A_{ad} and FC_{ad} contents. Because the V_{daf} content is autocorrelated with the contents of other industrial components, two industrial component contents are used in the model construction, in addition to the geophysical logging data. The results of this study indicate that the use of both geophysical logs and industrial component contents to predict the V_{daf} content yields better prediction results. Even after accounting for the cumulative error, it achieves more satisfactory practical use than when only geophysical logs or industrial component contents are used for autocorrelation.

The correlation between the M_{ad} content and response of the geophysical logging data and the industrial component content was not significant, and the prediction model could not be constructed using machine learning methods when the sample size was small. Therefore, the prediction errors of the M_{ad} content are all derived from the laboratory and cumulative errors of the first three component contents, which is why the prediction of the M_{ad} content has the largest relative errors in the actual application of new wells.

This study provides a set of prediction models for the industrial component contents of coal seams in the PZ block, which is not processed by stratification owing to the limitation of sample quantity. In the case of coal seams with different geological backgrounds, burial depths, and coal seams, statistics and analyses must be performed in conjunction with specific data, particularly when there are significant differences in M_{ad} content and the presence of magma intrusion (Hou et al., 2017; Hou H et al., 2021). Other factors must be considered before the evaluation process is determined using the OBGM model in conjunction with the actual data. Simultaneously, it should be noted that the gray system model involves the accumulation and reduction of sequences, and the change in data order has a minor impact on the prediction results but does not affect the conclusion.

6.5 Future trends

With the development of experiments, the progress and diversification of logging instruments can provide more accurate experimental data and geophysical logging information in the future (Zhou and O'Brien, 2016). Meanwhile, with an increase in the number of core samples, the sample data limitation is alleviated, and machine learning or deep learning methods can be used to construct industrial component prediction models, particularly for the prediction of M_{ad} content, which can be further improved.

In the short term, the effective prediction of the industrial component contents, which can provide the variation curve of industrial component contents in the vertical direction of a single well, is conducive for the evaluation and prediction of the CBM content and helps in the identification of CBM resource dessert zones. For long-term benefits, there is guidance for the subsequent mining of high-quality coal.

7 Conclusion

In this study, the geophysical logging data were combined with the OBGM (1, N) model to construct a prediction model for the contents of coalbed industrial components, which plays a guiding role in the subsequent exploration of coalbed methane and coal mine resources. The following conclusions were made:

1) In this study, a set of prediction models was proposed for the industrial component contents applicable to the PZ block by combining the geophysical logging data with the OBGM (1, N) model based on the actual industrial component content data of the PZ block. For predicting the contents of A_{ad} and FC_{ad}, the DEN, GR, AC, RD, and CAL curves were selected to obtain the best prediction effect. An increase in the geophysical logging curve types can effectively enhance the model performance, unlike when a single logging curve is used for the evaluation.
2) The modeling approach differs in the prediction of V_{daf} and M_{ad} contents, wherein the combination of geophysical logging curves with A_{ad} and FC_{ad} contents provides the best prediction accuracy, compared to the autocorrelation of geophysical logging curves or industrial component contents. In this study, an evaluation procedure was achieved for the PZ block; that is, the A_{ad} and FC_{ad} contents were first predicted using the geophysical logging data, the V_{daf} content was then predicted, and finally the M_{ad} content was calculated. This model was applied to new wells in the same block, and the validity of this process was demonstrated through error analysis.
3) Regarding model prediction accuracy, compared with the multiple regression and GM (0, N) models having the same computational cost, the OBGM (1, N) model has the best effect.

Therefore, the proposed geophysical logging interpretation model can cost effectively satisfy the effective evaluation of the industrial component contents of coalbeds in the PZ block and can provide a new method for evaluating the system of industrial component contents in this block.

Data availability statement

The original contributions presented in the study are included in the article/Supplementary Material, further inquiries can be directed to the corresponding author.

Author contributions

JG designed the study and wrote the manuscript. ZZ provided funding. HX and CZ developed the ideas. LZ contributed to revising the manuscript. CW added the geological understanding and mapping. All coauthors actively contributed to the manuscript with their comments, ideas, and suggestions.

Funding

This study was conducted in the Southern Shizhuang block of the Qinshui Basin and was financially sponsored by the Open Fund of the Key Laboratory of Exploration Technologies for Oil and Gas Resources, Ministry of Education (Nos. K2021–03 and K2021-08), National Natural Science Foundation of China (No. 42106213), and Hainan Provincial Natural Science Foundation of China (No. 421QN281).

Acknowledgments

The authors wish to express their gratitude to the staff of the Qinshui Coalfield in the Shanxi Province.

Conflict of interest

Author HX was employed by Sinopec Jianghan Oilfeld Company.

Publisher's note

Supplementary material

The Supplementary Material for this article can be found online at: https://www.frontiersin.org/articles/10.3389/feart.2022.1031218/full#supplementary-material

References

Ahmed, U., Johnston, D., and Colson, L. (1991). An advanced and integrated approach to coal formation evaluation. Paper presented at the SPE Annual Technical Conference and Exhibition.

Bond, L. O., Alger, R. P., and Schmidt, A. W. (1971). *Well log applications in coal mining and rock mechanics*.

Cai, Y., Liu, D., Yao, Y., Li, J., and Qiu, Y. (2011). Geological controls on prediction of coalbed methane of No. 3 coal seam in Southern Qinshui Basin, North China. *Int. J. Coal Geol.* 88 (2-3), 101–112. doi:10.1016/j.coal.2011.08.009

Chatterjee, R., and Paul, S. (2013). Classification of coal seams for coal bed methane exploitation in central part of Jharia coalfield, India - a statistical approach. *Fuel* 111, 20–29. doi:10.1016/j.fuel.2013.04.007

Daniels, J. J., Scott, J. H., and Liu, J. (1983). "Estimation of coal quality parameters from Geophysical well logs," in *Transactions of the SPWLA 24th Annual logging Symposium* 2, 1-19.

Feng, Y., Lu, J., Wang, J., Mi, J., Zhang, M., Ge, M., et al. (2020). Desulfurization sorbents for green and clean coal utilization and downstream toxics reduction: A review and perspectives. *J. Clean. Prod.* 273, 123080. doi:10.1016/j.jclepro.2020.123080

Fu, X., Qin, Y., Wang, G. G. X., and Rudolph, V. (2009a). Evaluation of coal structure and permeability with the aid of geophysical logging technology. *Fuel* 88 (11), 2278–2285. doi:10.1016/j.fuel.2009.05.018

Fu, X., Qin, Y., Wang, G. G. X., and Rudolph, V. (2009b). Evaluation of gas content of coalbed methane reservoirs with the aid of geophysical logging technology. *Fuel* 88 (11), 2269–2277. doi:10.1016/j.fuel.2009.06.003

Gao, M., Zhang, S., Li, J., and Wang, H. (2019). The dynamic failure mechanism of coal and gas outbursts and response mechanism of support structure. *Therm. Sci.* 23, S867–S875. doi:10.2298/tsci180610122g

Ghosh, S., Chatterjee, R., Paul, S., and Shanker, P. (2014). Designing of plug-in for estimation of coal proximate parameters using statistical analysis and coal seam correlation. *Fuel* 134, 63–73. doi:10.1016/j.fuel.2014.05.023

Ghosh, S., Chatterjee, R., and Shanker, P. (2016). Estimation of ash, moisture content and detection of coal lithofacies from well logs using regression and artificial neural network modelling. *Fuel* 177, 279–287. doi:10.1016/j.fuel.2016.03.001

Hamawand, I., Yusaf, T., and Hamawand, S. G. (2013). Coal seam gas and associated water: A review paper. *Renew. Sustain. Energy Rev.* 22, 550–560. doi:10.1016/j.rser.2013.02.030

Hawkins, J. M., Schraufnagel, R. A., and Olszewski, A. J. (1992). Estimating coalbed gas content and sorption isotherm using well log data." in Paper presented at the SPE Annual Technical Conference and Exhibition.

He, Z., Xie, H., Gao, M., Deng, G., Peng, G., and Li, C. (2020). The fracturing models of hard roofs and spatiotemporal law of mining-induced stress in a top coal caving face with an extra-thick coal seam. *Geomech. Geophys. Geo. Energy. Ge. Resour.* 7 (1), 2. doi:10.1007/s40948-020-00202-9

Hou, H., Shao, L., Guo, S., Li, Z., Zhang, Z., Yao, M., et al. (2017). Evaluation and genetic analysis of coal structures in deep Jiaozuo Coalfield, northern China: Investigation by geophysical logging data. *Fuel* 209, 552–566. doi:10.1016/j.fuel.2017.08.020

Hou, H., Shao, L., Wang, S., Xiao, Z., Wang, X., Li, Z., et al. (2019). Influence of depositional environment on coalbed methane accumulation in the carboniferous-permian coal of the qinshui Basin, northern China. *Front. Earth Sci.* 13 (3), 535–550. doi:10.1007/s11707-018-0742-8

Hou, J., Zou, C., Huang, Z., Xiao, L., Yang, Y., Zhang, G., et al. (2014). Log evaluation of a coalbed methane (CBM) reservoir: A case study in the southern Qinshui Basin, China. *J. Geophys. Eng.* 11 (1), 5009. doi:10.1088/1742-2132/11/1/015009

Hou, H. H, H. H., Zhang, H. J., Shao, L. Y., Guo, S. Q., Zhao, M. E., and Wang, S. (2021). Coal macrolithotype distribution and its genetic analyses in the deep Jiaozuo coalfield using geophysical logging data. *Acs Omega* 6 (51), 35523–35537. doi:10.1021/acsomega.1c05012

Hou, H., H., Liang, G., Shao, L., Tang, Y., and Mu, G. (2021). Coalbed methane enrichment model of low-rank coals in multi-coals superimposed regions: A case study in the middle section of southern junggar basin. *Front. Earth Sci.* 15 (2), 256–271. doi:10.1007/s11707-021-0917-6

Huang, B., Qin, Y., Zhang, W., Zheng, Q., Shi, S., and Wang, G. (2020). Prediction of high-quality coalbed methane reservoirs based on the fuzzy gray model: An investigation into coal seam No. 8 in Gujiao, Xishan, North China. *Energy Explor. Exploitation* 38 (4), 1054–1081. doi:10.1177/0144598720901444

Jiang, B., Qu, Z., Wang, G. G. X., and Li, M. (2010). Effects of structural deformation on formation of coalbed methane reservoirs in Huaibei coalfield, China. *Int. J. Coal Geol.* 82 (3-4), 175–183. doi:10.1016/j.coal.2009.12.011

Karacan, C. O., Ruiz, F. A., Cote, M., and Phipps, S. (2011). Coal mine methane: A review of capture and utilization practices with benefits to mining safety and to greenhouse gas reduction. *Int. J. Coal Geol.* 86 (2-3), 121–156. doi:10.1016/j.coal.2011.02.009

Li, S., Zhang, C., Hu, A., Chen, D., and Yan, S. (2007). Building porosity model of coalbed using collocated cokriging. *J. China Coal Soc.* 32 (9), 980–983. doi:10.3321/j.issn:0253-9993.2007.09.019

Liu, S., Liu, R., Tang, S., Zhao, C., Liu, B., Diao, J., et al. (2021). Quantitative measurement on coal components through the interpretation model of geophysical log: A case study from the Qaidam Basin, NW China. *Energy Explor. Exploitation* 39 (6), 2027–2044. doi:10.1177/01445987211020450

Lv, Y., Tang, D., Xu, H., and Luo, H. (2012). Production characteristics and the key factors in high-rank coalbed methane fields: A case study on the fanzhuang block, southern Qinshui Basin, China. *Int. J. Coal Geol.* 96-97, 93–108. doi:10.1016/j.coal.2012.03.009

Mahmood, Z., and Khan, S. (2009). On the use of K-fold cross-validation to choose cutoff values and assess the performance of predictive models in stepwise regression. *Int. J. Biostat.* 5 (1). doi:10.2202/1557-4679.1105

Moore, T. A. (2012). Coalbed methane: A review. *Int. J. Coal Geol.* 101, 36–81. doi:10.1016/j.coal.2012.05.011

Morin, R. H. (2005). Hydrologic properties of coal beds in the powder river basin, montana. I. Geophysical log analysis. *J. Hydrology* 308 (1-4), 227–241. doi:10.1016/j.jhydrol.2004.11.006

Mullen, M. J. (1988). "Log evaluation in wells drilled for coal-bed methane," in *Geology and coalbed methane resources of the northern San Juan Basin, Colorado and New Mexico. Rocky Mountain Association of Geologists*. Denver. Rocky Mountain Association of Geologists, 113–124.

Palmer, I. (2010). Coalbed methane completions: A world view. *Int. J. Coal Geol.* 82 (3-4), 184–195. doi:10.1016/j.coal.2009.12.010

Pan, H., and Huang, Z. (1998). Log interpretation model of determining coalbed coal quality parameters. *Geoscience* 12 (3), 154

Ren, P., Xu, H., Tang, D., Li, Y., Sun, C., Tao, S., et al. (2018). The identification of coal texture in different rank coal reservoirs by using geophysical logging data in northwest Guizhou, China: Investigation by principal component analysis. *Fuel* 230, 258–265. doi:10.1016/j.fuel.2018.05.019

Roslin, A., and Esterle, J. S. (2015). Electrofacies analysis using high-resolution wireline geophysical data as a proxy for inertinite-rich coal distribution in late permian coal Seams, bowen Basin. *Int. J. Coal Geol.* 152, 10–18. doi:10.1016/j.coal.2015.08.003

Shao, X., Sun, Y., Sun, J., Tang, D., Xu, H., Dong, X., et al. (2013). Log interpretation for coal petrologic parameters: A case study of hancheng mining area, central China. *Petroleum Explor. Dev.* 40 (5), 599–605. doi:10.1016/s1876-3804(13)60078-6

Shi, J. X., Zeng, L. B., Dong, S. Q., Wang, J. P., and Zhang, Y. Z. (2020). Identification of coal structures using geophysical logging data in qinshui basin, china: investigation by kernel fisher discriminant analysis. *Int. J. Coal Geol.* 217, 103314. doi:10.1016/j.coal.2019.103314

Tan, L.-Z., Ouyang, A. J., Peng, X.-Y., Li, E.-X., Tung Khac, T., and Hao, L. (2015). A fast and stable forecasting model to forecast power load. *Intern. J. Pattern Recognit. Artif. Intell.* 29 (3), 1559005. doi:10.1142/s0218001415590053

Wang, Y., Liu, D., Cai, Y., Yao, Y., and Zhou, Y. (2018). Evaluation of structured coal evolution and distribution by geophysical logging methods in the Gujiao Block, northwest Qinshui basin, China. *J. Nat. Gas Sci. Eng.* 51, 210–222. doi:10.1016/j.jngse.2018.01.022

Ward, C. R. (2016). Analysis, origin and significance of mineral matter in coal: An updated review. *Int. J. Coal Geol.* 165, 1–27. doi:10.1016/j.coal.2016.07.014

Xu, H., Tang, D. Z., Tang, S. H., Zhao, J. L., Meng, Y. J., and Tao, S. (2014). A dynamic prediction model for gas-water effective permeability based on coalbed methane production data. *Int. J. Coal Geol.* 121, 44–52. doi:10.1016/j.coal.2013.11.008

Yang, N., Tang, S.-h., Zhang, S.-h., Xi, Z.-d., Li, J., Yuan, Y., et al. (2018). In seam variation of element-oxides and trace elements in coal from the eastern Ordos Basin, China. *Int. J. Coal Geol.* 197, 31–41. doi:10.1016/j.coal.2018.08.002

Yegireddi, S., and Bhaskar, G. U. (2009). Identification of coal seam strata from geophysical logs of borehole using Adaptive Neuro-Fuzzy Inference System. *J. Appl. Geophys.* 67 (1), 9–13. doi:10.1016/j.jappgeo.2008.08.009

Zeng, B., and Li, C. (2018). Improved multi-variable grey forecasting model with a dynamic background-value coefficient and its application. *Comput. Industrial Eng.* 118, 278–290. doi:10.1016/j.cie.2018.02.042

Zeng, B., Luo, C., Liu, S., Bai, Y., and Li, C. (2016). Development of an optimization method for the GM(1, N) model. *Eng. Appl. Artif. Intell.* 55, 353–362. doi:10.1016/j.engappai.2016.08.007

Zhang, C., and Jiang, Q. (2005). The prediction of small sample time-displacement data based on GM(0, N) and RBF. *Comput. Eng. Appl.* 5, 62. doi:10.3321/j.issn:1002-8331.2005.05.022

Zhang, Z. (2013). On coalbed methane industrial components and gas content calculation model in heshun area. *Well Logging Technol.*, 37(1), 99. doi:10.16489/j.issn.1004-1338.2013.01.021

Zhou, B., and O'Brien, G. (2016). Improving coal quality estimation through multiple geophysical log analysis. *Int. J. Coal Geol.* 167, 75–92. doi:10.1016/j.coal.2016.09.013

Zhou, D., Wang, Z., and Li, X. (2016). The application of GRNN and LS-SVM to coal properties calculation. *Geophys. Geochem. Explor.* 40 (1), 88. doi:10.1016/S0375-9601(01)00735-6

Zhou, F., and Guan, Z. (2016). Uncertainty in estimation of coalbed methane resources by geological modelling. *J. Nat. Gas Sci. Eng.* 33, 988–1001. doi:10.1016/j.jngse.2016.04.017

Zhou, F., Yao, G., and Tyson, S. (2015). Impact of geological modeling processes on spatial coalbed methane resource estimation. *Int. J. Coal Geol.* 146, 14–27. doi:10.1016/j.coal.2015.04.010

Zhu, J., Fu, T., Mao, D., Li, H., Huang, Z., and Wang, J. (2012). Static calibration and decoupling of multi-dimensional force sensor based on GM(0, N) model. *J. Grey Syst.* 24 (3), 225. doi:10.1155/2012/490810

Zhu, L., Ma, Y., Cai, J., Zhang, C., Wu, S., and Zhou, X. (2021). Key factors of marine shale conductivity in southern china-part I: The influence factors other than porosity. *J. Petroleum Sci. Eng.* 205, 108698. doi:10.1016/j.petrol.2021.108698

Zhu, L., Ma, Y., Cai, J., Zhang, C., Wu, S., and Zhou, X. (2022). Key factors of marine shale conductivity in southern china-Part II: The influence of pore system and the development direction of shale gas saturation models. *J. Petroleum Sci. Eng.* 209, 109516. doi:10.1016/j.petrol.2021.109516

frontiers | Frontiers in Earth Science

TYPE Original Research
PUBLISHED 06 January 2023
DOI 10.3389/feart.2022.1030501

OPEN ACCESS

EDITED BY
Reza Rezaee,
Curtin University, Australia

REVIEWED BY
Junjian Zhang,
Shandong University of Science and Technology, China
Yanhui Yang,
Henan University of Urban Construction, China

*CORRESPONDENCE
Hewu Liu,
hwliu65@163.com

SPECIALTY SECTION
This article was submitted to Economic Geology,
a section of the journal
Frontiers in Earth Science

RECEIVED 29 August 2022
ACCEPTED 20 September 2022
PUBLISHED 06 January 2023

CITATION
Liu H, Song Y and Du Z (2023), Molecular dynamics simulation of shear friction process in tectonically deformed coal.
Front. Earth Sci. 10:1030501.
doi: 10.3389/feart.2022.1030501

Molecular dynamics simulation of shear friction process in tectonically deformed coal

Hewu Liu[1,2]*, Yu Song[3] and Zhigang Du[4]

[1]State Key Laboratory of Mining Response and Disaster Prevention and Control in Deep Coal Mines, Anhui University of Science and Technology, Huainan, China, [2]School of Earth and Environment, Anhui University of Science and Technology, Huainan, China, [3]School of Resources and Earth Science, China University of Mining and Technology, Xuzhou, China, [4]School of Civil Engineering, Luoyang Institute of Science and Technology, Luoyang, Henan, China

Shear friction is an important deformation process in tectonically deformed coals (TDCs) and is closely related to the dynamic metamorphism of coal. In the current study, we perform a molecular dynamics (MD) simulation of the shear friction process on primary structure coal. The simulation results show that coal friction is a process of energy transformation. The mechanical energy of shear friction work can lead to temperature increases and chain motion. Chain diffusion and reorientation are the two main chain motion modes during friction. Chain diffusion behavior is regular in the initial friction stage and becomes irregular in the later friction stage. The orientation change is different for various fused aromatic chains. The orientation changes of pentacenes and naphthacenes are more significant than those of the other fused aromatic chains, indicating that fused aromatic chains with a higher aspect ratio are preferentially reorientated by shear friction. It is also demonstrated that the C-O and C-N bonds in coal are more easily disassociated by shear friction. The research results directly confirm the molecular evolution during coal friction caused by shear stress.

KEYWORDS

shear friction, tectonically deformed coal, dynamic metamorphism, molecular structure, molecular dynamics simulation

1 Introduction

Tectonically deformed coals (TDCs) formed under the action of tectonic stress have significantly altered structures, including physical, optical, and even chemical structures (Hou et al., 2012; Niu et al., 2017; Zhang et al., 2019; Pan et al., 2022; Yu et al., 2022). The structural variation of TDCs directly affects the gas occurrence state (Ju and Li, 2009; Jiang et al., 2010; Zhang et al., 2022). Therefore, the development and structural deformation characteristics of TDCs must be considered when performing coal mining and coalbed methane (CBM) exploitation (Jiang et al., 2010; Fan et al., 2017; Cheng and Pan, 2020; Fan et al., 2020; Zhang et al., 2021; Fan et al., 2022). More recently, the chemical structural evolution of TDCs has become one of the hottest topics in coal research. According to the coal mechanochemistry, tectonic stress can cause coals that are mainly composed of organic compounds to undergo dynamic metamorphism (Hou et al., 2017). Furthermore, molecular evolution, gas generation, and the formation of ultramicropores caused by dynamic metamorphism can lead to a change in the occurrence state and content of coalbed methane, which affects coal mining safety and CBM exploitation efficiency (Hou et al., 2017; Li et al., 2020; Zhang et al., 2021).

The effects of tectonic stress on TDC molecules have been discovered by many researchers. Different changes take place in various parts of TDC molecules under the influence of tectonic stress. The side chains or bridge bonds in coal molecules are preferentially disassociated into gases such as CO_x gases and even hydrocarbons when subject to tectonic stress (Xu et al., 2014; Hou et al., 2017; Liu et al., 2018). The changes in the fused aromatic structures of TDCs caused by tectonic stress are complicated; the structures can be reorientated, condensed, deformed, and even ruptured (Cao et al., 2007; Han et al., 2017; Song et al., 2019; Song et al., 2020). The condensation of aromatic structures promotes the evolution of coal molecules (Cao et al., 2007; Song et al., 2019), while the deformation and rupture of aromatic structures lead to the generation of secondary structural defects (Han et al., 2017). In addition, noncovalent bonds, which are less stable structures in coal, can be effortlessly cleaved by tectonic stress, which significantly increases the mobility of molecular segments (Liu and Jiang, 2019).

The mechanism of tectonic stress action is the key to revealing the molecular evolution process of TDCs. Many coal geology researchers have explored the molecular evolution theory of TDCs, and their work has promoted the development of coal mechanochemistry. Two mainstream hypotheses about TDC evolution mechanism have been proposed by coal researchers. Some researchers have shown that the molecular structures of coal can be altered under the influence of thermal or strain energies that are generated and transformed from the mechanical energy created by tectonic stress (Cao et al., 2007; Xu et al., 2014). More recently, based on new mechanochemistry findings, some researchers believe that tectonic stress might even directly act on chemical bonds and lead to their rotation or cleavage (Hou et al., 2017). However, these hypotheses have not been proven and need further investigation.

When TDC researchers clarify the mechanism of tectonic stress action, shear stress is the most cited type of tectonic stress (Ju and Li, 2009; Han et al., 2016; Wang et al., 2021a; Yang et al., 2021). This is because shear friction is an important deformation process in TDCs (Li et al., 2003) and can significantly alter TDC's molecular structure (Han et al., 2017; Wang et al., 2021a; Yang et al., 2021). From the perspective of geotribology, shear friction behavior can be universally found in geological bodies under relative motion (Boneh and Reches, 2018). Coal seams sandwiched between hard rock strata are preferentially dislocated along the bedding planes under the influence of regional tectonic movements (Li et al., 2003; Ju and Li, 2009). Macroscopically, the shearing dislocation of coal seams leads to the formation of low-angle faults with large-scale friction fault planes; microscopically, shear dislocation also occurs among the shattered fragments, which also leads to the formation of friction surfaces (Frodsham and Gayer, 1999; Li, 2001; Ju et al., 2004). Our previous studies have shown that shear friction is common in TDCs, and friction surfaces are well developed in different types of TDCs (Figure 1) (Liu, 2020). Furthermore, Fourier transform infrared spectrometry (FTIR) detection results indicate that the molecular structure of coal friction films in TDCs is changed under the action of shearing dislocation (Li, 2013). It is easy to appreciate that coal friction caused by shear stress plays an important role in the dynamic metamorphism of coal (Cao et al., 2007; Ju and Li, 2009). Therefore, the molecular evolution of coal induced by shear friction is explored further in this study.

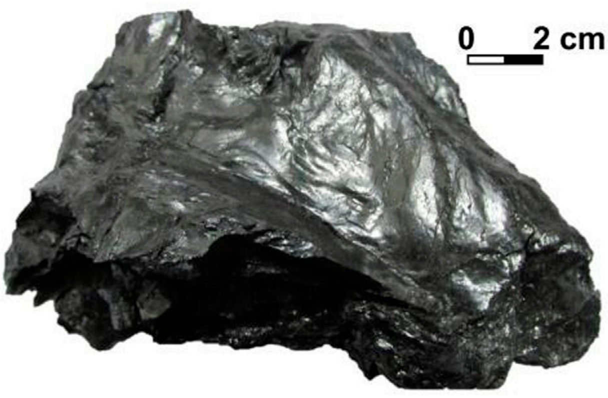

FIGURE 1
Friction surface morphologies in a TDC.

Molecular dynamics (MD) simulations have proven to be a very effective research method to reveal the molecular evolution process of coal caused by stress (Wang et al., 2021b; Yang et al., 2021). Wang et al. (2017), Wang et al. (2021a), and Wang et al. (2021b) successfully applied the MD simulation method to study the gas generation mechanism in coal under shear stress. They showed that the aromatic structure and functional groups of the molecular structure of coal could be attacked and transformed into gases (including CO_x, hydrocarbons, H_2O, and H_2) by shear stress. Yang et al. (2020) and Yang et al. (2021) used and MD simulation to investigate the influence of tensile and shear stresses on the chemical bonds in coal molecular structures. According to their simulation results, both tensile and shear stress can break the chemical bonds in coal to form free radicals. Meng et al. (2021) and Liu et al. (2022) also showed that external force could change the molecular structures of the coal matrix when they performed an MD simulation on coal nanoindentation. To the best of our knowledge, there is still a lack of studies involving the MD simulation of coal shear friction.

Therefore, an MD simulation of coal shear friction was performed in this study. A sandwich friction system was

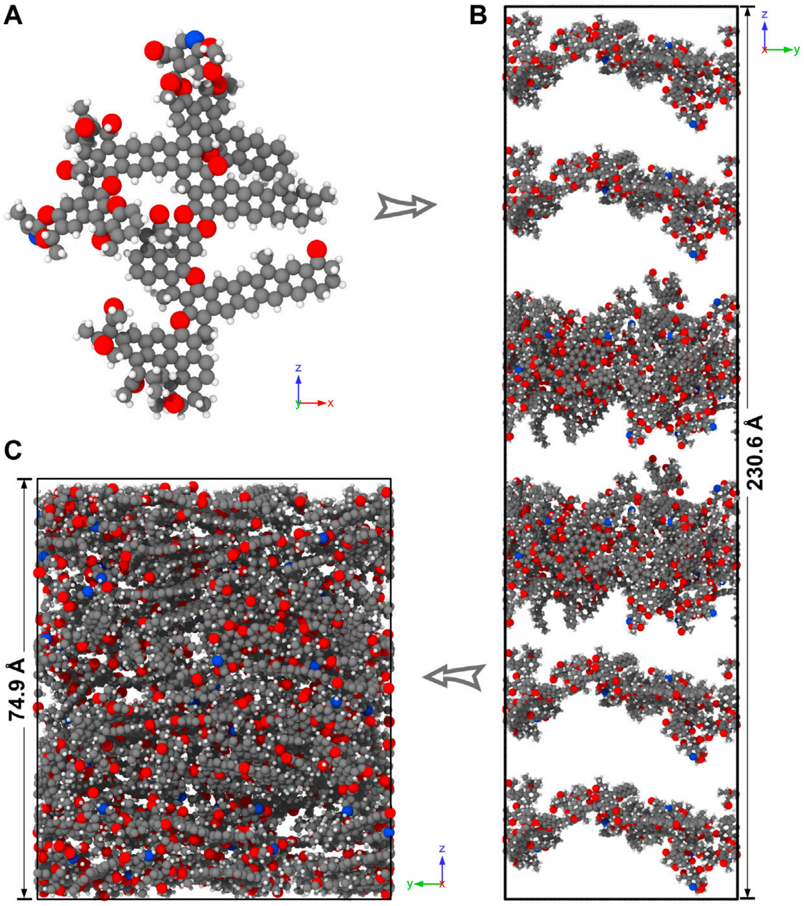

FIGURE 2
Construction procedure of the sandwich system for the shear friction simulation. (The gray refers to carbon atoms, the red refers to oxygen atoms, the blue refers to nitrogen atoms, and the white refers to hydrogen atoms.) **(A)** Conformation of the primary structure coal, **(B)** initial sandwich coal friction system, and **(C)** optimized coal friction system.

constructed and optimized based on the molecular conformation of primary structure coal. The shear friction process in a TDC was simulated by applying a constant velocity to the slider along the positive Y-axis. By clarifying the variation of temperature, energies, mean square displacement, friction force, and configuration during the friction process, the evolution of the coal's molecular structures is revealed in detail.

2 Experiment and simulation methodology

2.1 Model construction and optimization

To avoid the interference of tectonic stress in geological time, a primary structure coal from our previous research was chosen for analysis. The primary structure coal is a low-medium bituminous coal with a carbon content of 80.61% (Liu et al., 2019). Material Studio software was used to construct the conformation of the primary structure coal according to the composition and structure information obtained from elemental analysis and spectral detection results (Figure 2A). The comparison between experimental ^{13}C nuclear magnetic resonance (^{13}C NMR) spectra and simulated spectra demonstrates that the constructed conformation is very close to real coal molecules (Liu et al., 2019). The chemical formula of the built conformation is $C_{206}H_{166}N_2O_{26}$.

The sandwich coal friction system comprises two types of layers, including four thin layers and two thick layers. The thin layer consists of four conformations with a chemical formula of $C_{824}H_{664}N_8O_{104}$, and the thick layer consists of ten conformations with a chemical formula of $C_{2060}H_{1660}N_{20}O_{260}$. First, the two types of layers were constructed using the Amorphous Cell (AC) module in Material Studio. The density of the layers was set to 0.8 g/cm^3, and the

COMPASS forcefield was chosen when performing the AC calculation. Then, the atom-based summation method was used to calculate the electrostatic and van der Waals interactions between particles. Second, the initially constructed layers were optimized using the Forcite module. The geometrical structure of the layers was refined utilizing a smart method in the geometry optimization task. After the geometrical optimization, the layer structures were periodically heated and cooled in the Anneal task, and the initial and mid-cycle temperatures during the Anneal process were 298.0 K and 500.0 K, respectively. Third, the optimized layers were inserted into a simulation box to form the initial sandwich friction system ($C_{7416}H_{5976}N_{72}O_{936}$) using the Build Layers command (Figure 2B).

The initially constructed sandwich friction system did not meet all the requirements of friction simulation. Therefore, the initial system was exported from Material Studio and imported into the large-scale atomic/molecular massively parallel simulator (LAMMPS) (Plimpton, 1995) to perform the next optimization steps. First, each layer in the friction system was compressed by moving the reflecting walls along the negative Y-axis to the specified positions, and the final density of each of the layers was set to 1.0 g/cm^3, which is equal to our previous research results (Liu et al., 2019). The compression procedure was accomplished in a canonical ensemble (nvt), and the temperature of the entire system was controlled at 298.0 K through Nosé–Hoover thermostatting. Furthermore, to maintain the flat layered structure, each layer was compressed separately using the reflecting walls. The compressing procedure of each layer lasted for 2000 fs. After the layers were compressed, the redundant vacuum space above the uppermost layer was eliminated by directly changing the box size.

The compressed friction system required additional optimization to acquire a more reasonable structure. The optimization procedure follows. First, the system was heated from 298.0 K to 500.0 K with a heating rate of 0.101 K/fs in an nvt ensemble. Second, the temperature of the friction system was maintained at 500.0 K in the nvt ensemble using a Nosé–Hoover thermostat. The constant temperature heating process lasted for 200,000 fs Third, the temperature was reduced to 298.0 K, again in an isothermal-isobaric (npt) ensemble. To release the internal pressure of the friction system, 1 atm pressure was applied to the X and Y dimensions, and the "couple" keyword was used to allow the box to change in both the X and Y dimensions. The thermostatting and barostatting during the cooling process were achieved using the Nosé–Hoover method. The temperature and pressure change processes continued for 200,000 fs. Finally, the sandwich friction system was relaxed for 1,100,000 fs in an nvt ensemble, and the relaxation temperature was maintained at 298.0 K. Then, the fully optimized sandwich friction system was ready for the following shear friction simulation (Figure 2C).

2.2 Implementation of shear friction

2.2.1 Initial settings

The ReaxFF potential developed by van Duin et al. (2001) was selected to describe the pair interactions of particles, and the parameters of the C, O, N, and H particles have been previously proposed by Mattsson et al. (2010). A periodic boundary condition was applied to the X and Y dimensions, and a non-periodic and fixed boundary condition was applied to the Z dimension. The ReaxFF, which is based on the bond-order concept, is accurate enough to describe a coal's molecular evolution caused by stress (van Duin et al., 2001; Wang et al., 2021a). The six layers in the sandwich friction system play different roles during the shear friction simulation (Figure 3A). The top and bottom layers in grey were set as independent rigid bodies. The temperature of the thermal-quenched layers in blue was maintained by thermostatting at 298.0 K utilizing the Nosé–Hoover method in an nvt ensemble, which allows for the diffusion of thermal energy caused by friction. Meanwhile, the slider and free layer in purple and yellow were both set into a microcanonical (nve) ensemble, which is beneficial for the free motion of particles in these two layers during the friction process.

2.2.2 Shear friction simulation

The coal shear friction simulation can be divided into two stages. First, along the negative Z-axis, a constant normal force (0.625 MPa) was applied to each particle in the uppermost rigid layer before friction. The resultant force of the forces applied on all the particles in the rigid layer is equal to 2 GPa (number of particles (1,600) × 0.625 MPa), which significantly compresses the friction system (Figure 3B). Because of the area contact difference between nano and macro scales, the normal force in MD simulation can be several orders of magnitude larger than the actual situation (Qiang et al., 2020). The compression process continued for 400 ps to obtain a more stable friction system with almost constant total energy (Figure 4). Second, the slider was linearly moved along the positive Y-axis with a velocity of 0.005 Å/fs (500 m/s) (Figure 3B), and the shear friction of the slider lasted for 1,000 ps. The selected friction velocity in the MD simulation is much higher than the geological conditions, which can significantly accelerate the mechanolysis reaction processes of shear friction.

3 Results and discussion

3.1 The friction mode of coal

According to previous research, the interfacial contact mode of a friction system is important to determine the

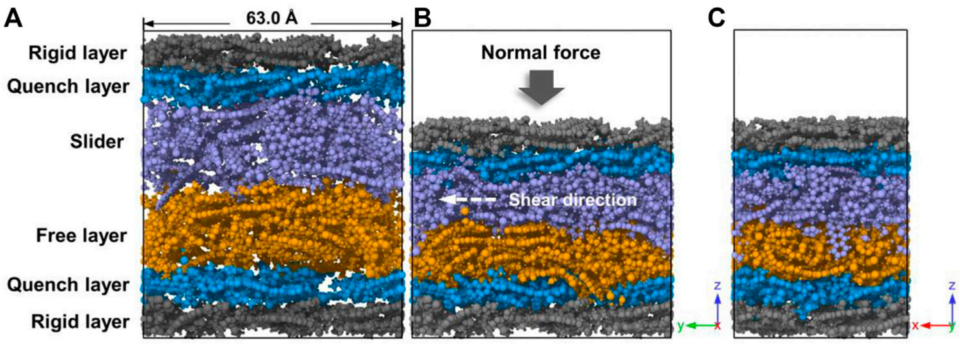

FIGURE 3
The sandwich structures of the friction system and the configuration of the friction system after compression. **(A)** The sandwich structure of the coal friction system, **(B)** the left view of the friction system after compression, and **(C)** the back view of the friction system after compression.

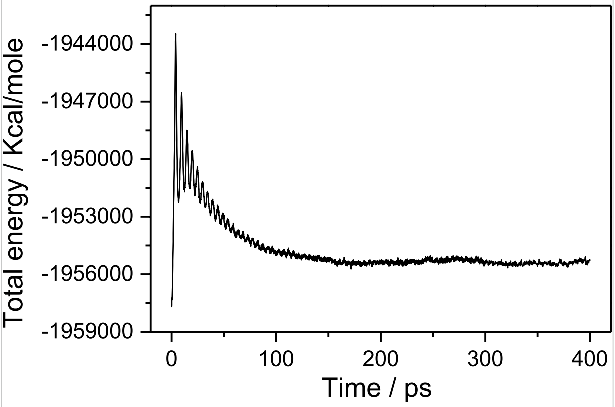

FIGURE 4
Variation of the total energy of the friction system during the compression stage.

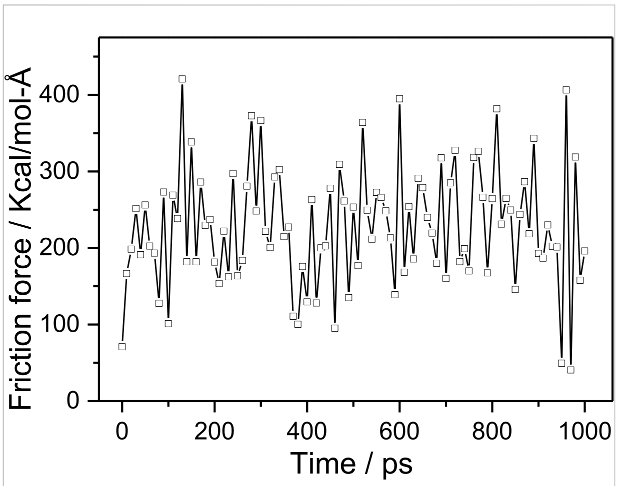

FIGURE 5
Variation of the friction force between the slider and the free layer with simulation time.

friction mode. The configuration of the friction system shows that the chains at the slider and free layer surfaces are intertwined, indicating that the interface between them is rough and robustly locked (Figures 3B,C). Generally, a rougher interface is more likely to generate a stick-slip friction mode because of the interactions of the chains at the interface (Dai et al., 2011). In this study, the friction force between the slider and the free layer steadily fluctuated between 40.5 and 420.7 Kcal/mol-Å without any regular variation (Figure 5). Therefore, the coal friction mode in the current simulation belongs to the dynamic friction type (Dai et al., 2011). The main reason for this is that the sliding velocity of 500 m/s is higher than the maximum velocity of the surface atoms in a free layer, which means that the chains in these two layer surfaces cannot adhere to each other during friction.

3.2 The frictional heating of coal

Before the friction simulation, the temperature of the entire system was maintained at 298.0 K. The temperature significantly rose to the maximum value (844.4 K) at the initial stage of friction and then decreased slightly (around 700 K) to form a plateau (Figure 6A). Studies on natural fault planes and friction experiments indicate that frictional heat can be generated during the friction between coal and other types of rocks (Bustin, 1983; Kitamura et al., 2012). Furthermore, the temperature increase caused by friction can even reach several hundred degrees (Bustin, 1983; Kitamura et al., 2012). Thus, the temperature increase in the molecular simulation is in line with actual situations.

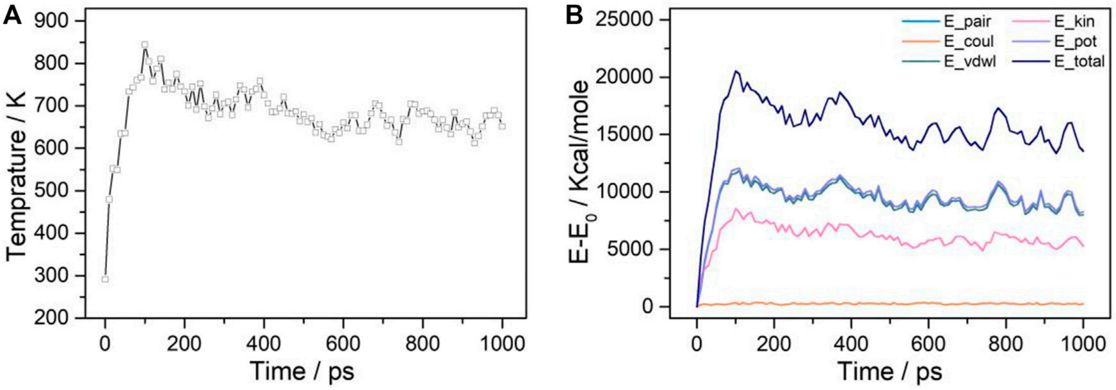

FIGURE 6
Temperature **(A)** and energy variation **(B)** of the slider during the friction process.

The shear friction work is an energy transformation process; the increasing temperature in the simulation indicates that the mechanical energy caused by shear stress is transformed into thermal energy (Hu et al., 2013). The temperature increase in the initial friction stage indicates the accumulation of thermal energy, which is closely related to the adhesive forces between interfacial atoms (Qiang et al., 2020). To start the friction process, the adhesive force between the interfacial atoms must first be overcome, which can lead to instantaneous heat generation (Qiang et al., 2020). The plateau of the temperature–time curve illustrates that less mechanical energy is dissipated in the later friction process (Rittel, 2000).

During friction, most of the mechanical energy is released through the motion of atoms and heat generation (Qiang et al., 2020). The energy difference between the energy at 0 ps(E_0) and the energy at different friction times (E) was applied to characterize the energy variation. The variation of the total energy (E_total) is basically the same as the variation in the temperature, indicating the transformation of energy into temperature (Figure 6). The total energy is the sum of other energies; therefore, the variation of the total energy is ascribed to the variation of other energies. It can be illustrated that the variation of the other types of energies also demonstrates the energy transformation process.

3.3 Chain motion during the friction process

3.3.1 Chain diffusion

Under the action of shear friction, chain motion, including chain diffusion and chain reorientation, will occur in the free layer, which can change the configuration of molecules. Mean square displacement (MSD) is commonly used to characterize chain diffusion mobility (Harmandaris et al., 1998). The slope of the MSD-time curve is positively correlated with chain diffusion mobility (Qiang et al., 2020). During the coal friction process, the MSD of the free layer increases slowly within 200 ps and then increases more significantly in the later friction stage (Figure 7).

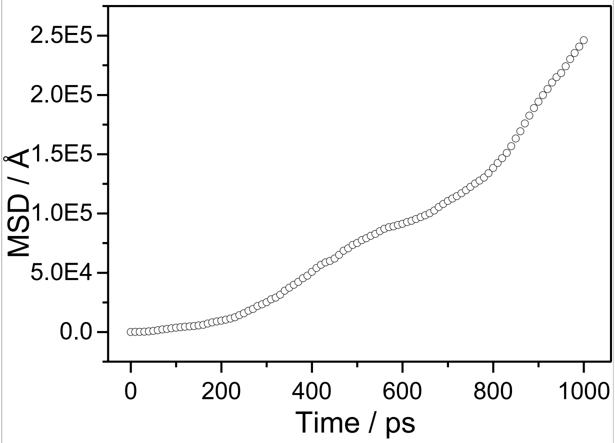

FIGURE 7
MSD variation of the slider during the friction process.

Atom trajectory analysis was performed to further reveal the chain diffusion behavior during the coal friction process. A 6 Å-thick atomic slice along the Z-axis was marked in green to analyze the chain diffusion in the free and quenched layers. Figures 8A–C depict that the shear track within 30 ps is very regular, and the track becomes very irregular after 30 ps (Figure 8D), indicating that the chain diffusion mobility increases significantly after 30 ps.

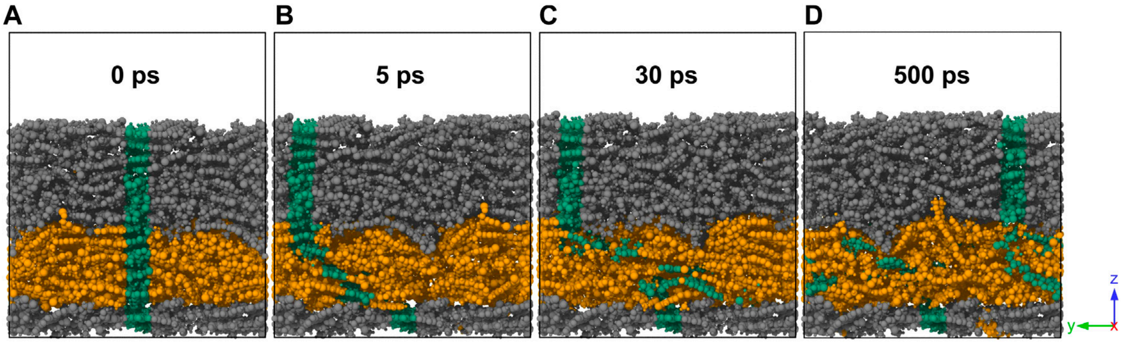

FIGURE 8
Configuration change at different shear friction times.

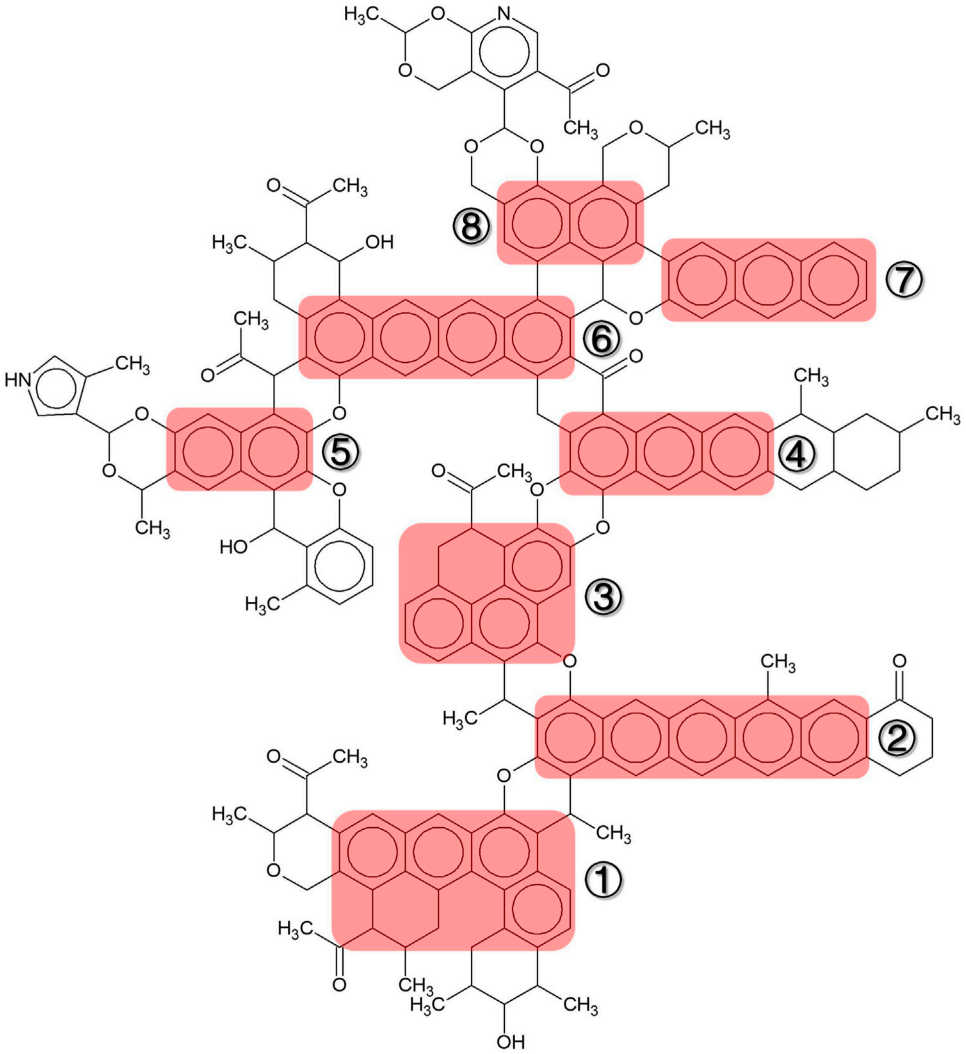

FIGURE 9
Selected fused aromatic chains in the plane model of the primary structure coal conformation. 1—Benz(a)anthracene; 2—pentacene; 3—phenanthrene; 4—anthracene A; 5—naphthalene A; 6—naphthacene; 7—anthracene B; 8—naphthalene B.

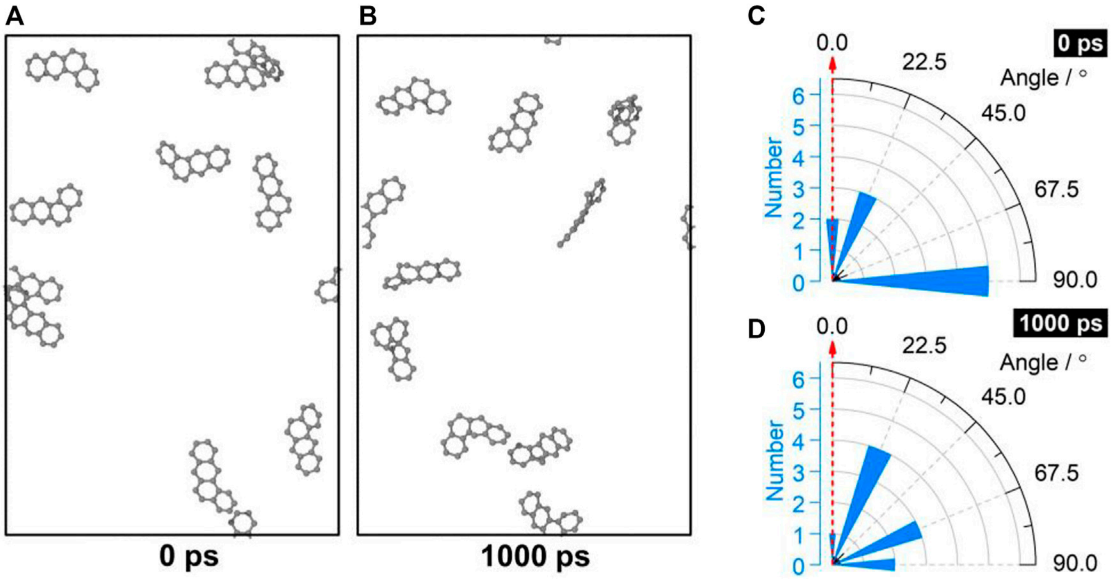

FIGURE 10
Orientation distribution of benz(a)anthracene. **(A)** and **(B)** The distribution of benz(a)anthracene at 0 ps, **(C)** and **(D)** rose diagram of the orientation of the benz(a)anthracene at 0 ps and 1,000 ps.

3.3.2 Chain reorientation

To reveal the orientation change in the friction process, the orientation of eight types of fused aromatic chains in the free layer were counted at 0 ps and 1,000 ps, respectively (Figure 9). The acute angle between the strike of fused aromatic chains (the connection between the proximal and distal C atoms) and the shear direction (the positive direction of the Y-axis) is defined as the orientation of the fused aromatic chains. The free layer is composed of ten conformations; therefore, ten acute angles can be counted for each frame (Figures 10A,B). Then, a rose diagram (0–90°) of the orientation of the fused aromatic chains can be drawn according to the statistical data (Figures 10C,D).

Among the eight types of fused aromatic chains, the benzene rings of the benz(a)anthracenes and the phenanthrenes are not in a linear arrangement, while the other six types of aromatic structures are linearly arranged. By comparing the orientation of the benz(a)anthracenes at 0 ps and 1000 ps, it can be found that five benz(a)anthracenes are in the range of 78.75–90° at 0 ps, while the number decreases to two at 1,000 ps, and more benz(a) anthracenes are rotated into the 11.25–33.75° range (Figures 10C,D). For the phenanthrenes, the orientation is mainly concentrated at 33.75–56.25°, and the number of phenanthrenes in the range of 0–33.75° increases from one to three under the action of shear friction (Figures 11C,D). Therefore, the orientation of the nonlinearly arranged aromatic chains is more parallel to the shear direction, especially for the benz(a)anthracenes.

The linearly arranged pentacenes are of the maximum length in all the aromatic chains. The orientation of the pentacenes is mainly in the range of 56.25–78.75° at 0 ps, while at 1,000 ps, the dominant orientation is within 11.25–33.75° (Figures 11A,B). The orientation angles of seven pentacenes are larger than 56.25° at 0 ps, and only two angles are in this range at 1,000 ps. Similarly, the orientations of the naphthacenes that are linear arrangements of four benzene rings are also significantly altered by shear friction. Before friction, the orientation angles of the naphthacenes mainly fall in the range of 56.25–90°, and eight angles fall into this range (Figure 11I). At the end of friction, six naphthacenes are turned parallel to the shear direction, and the orientation angles of those naphthacenes are all within the range of 0–33.75° at 1,000 ps (Figure 11J). It can be easily seen that the orientation distribution modes of the pentacenes and naphthacenes are significantly altered before and after shear fiction.

Anthracenes A and B are composed of three linearly arranged benzene rings. For anthracene A, only one orientation angle is lower than 33.75° at 0 ps, while the number increases to three at 1,000 ps by shear modification (Figures 11E,F). The orientation change of anthracene B is similar to anthracene A. Compared with the orientations at 0 ps, two more anthracene orientation angles are rotated and fall into the range of 0–33.75° at 1,000 ps (Figures 11K,L). Apart from the above change, the orientation distribution modes of anthracenes A and B remain similar at 0 ps and 1,000 ps.

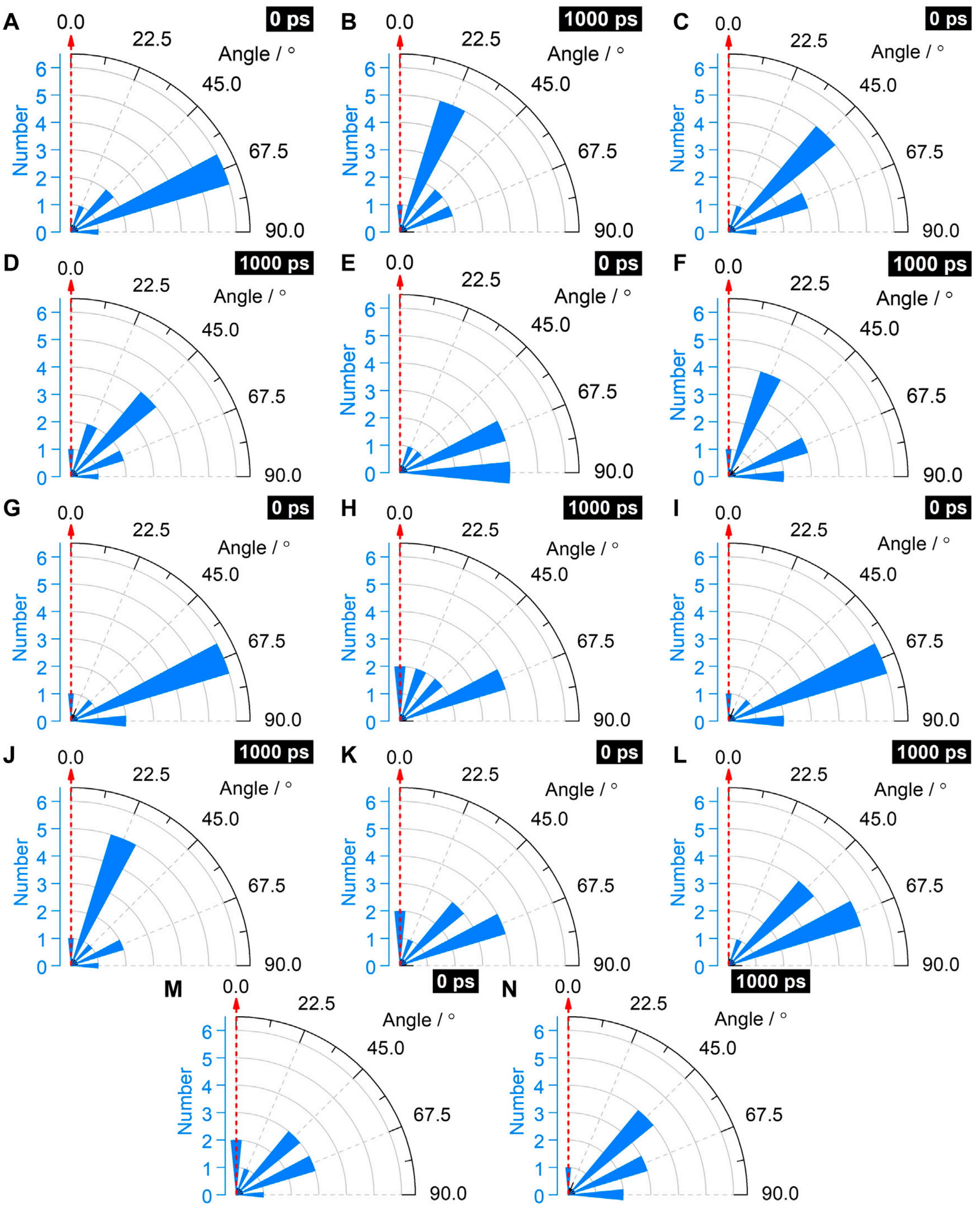

FIGURE 11
Rose diagram of the orientation of the fused aromatic chains. **(A)** and **(B)** Pentacene, **(C)** and **(D)** phenanthrene, **(E)** and **(F)** anthracene A, **(G)** and **(H)** naphthalene A, **(I)** and **(J)** naphthacene, **(K)** and (L) anthracene B, **(M)** and **(N)** naphthalene B.

Naphthalenes A and B, which are composed of two benzene rings, are the shortest among the fused aromatic chains. At 0 ps, the orientation angles of naphthalene A are mainly in the range of 56.25–90°. However, at 1,000 ps, the number of naphthalenes A with orientation angle in the range of 56.25–90° is reduced by four, and the number of naphthalenes A with orientation angle in the range of 0–33.75 is increased by four (Figures 11G,H). Compared to naphthalene A, the orientation of naphthalene B

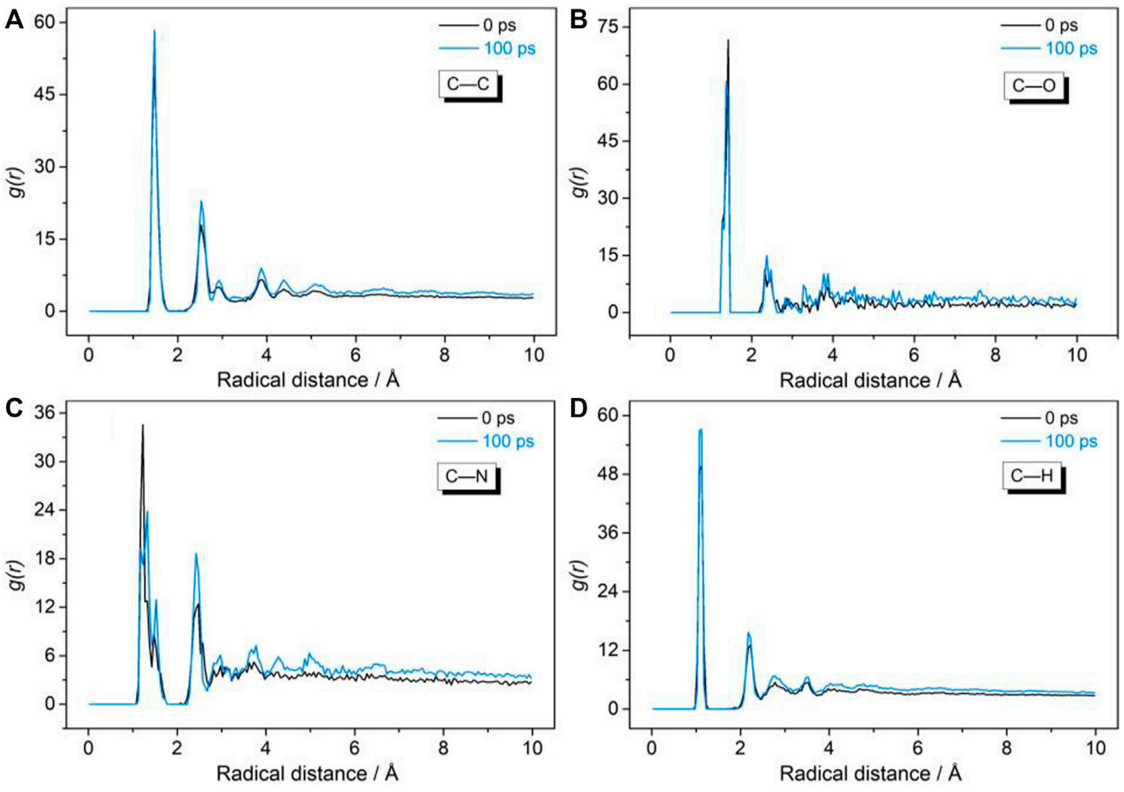

FIGURE 12
The **(A)** C-C, **(B)** C-O, **(C)** C-N, and **(D)** C-H radical distribution functions of the friction system before and after shear friction.

is less affected by shear friction. The number of orientation angles of naphthalene B within 0–33.75 is reduced from three to only one (Figure 11M,N).

In summary, under the action of shear friction, the orientation of eight types of fused aromatic chains is changed to a greater or lesser extent. The orientation change is consistent with the detection results of natural TDCs using a high-resolution transmission electron microscope (HRTEM). Order degree of the aromatic fringe of schistose and scaly coals (two types of TDCs formed in shear stress environments) observed by HRTEM is higher than that of unaltered coals, which indicates that shear stress can promote the order degree of aromatic structures (Song et al., 2020). The MD simulation results also demonstrate the orientation change behavior caused by shear friction. Furthermore, under the same shear friction conditions, the orientation change degree is different for various types of fused aromatic chains. The orientation of linearly arranged pentacenes and naphthacenes is more parallel to the shear direction at 1,000 ps than is the orientation of other types of fused aromatic chains. This is mainly because the orientation change of the fused aromatic chains is closely correlated with the aspect ratio of fused aromatic chains. Fused aromatic chains with larger aspect ratios are more prone to be reoriented by shear friction.

3.4 Atomic separation characteristics

The radical distribution function (RDF) *g(r)* is usually applied to reveal the interatomic separations and structure of molecular systems (Hua et al., 2020). The *g(r)* before and after friction is calculated to investigate the atomic interaction variation, including the interactions of C-C, C-O, C-N, and C-H atoms. The first peaks all appear within the radical distance range of 1.0–2.0 Å, which reflects the basic structural characteristic of coal molecules well (Figure 12). This is because the average nearest-neighbor distances of C-C (1.54 Å), C-O (1.43 Å), C-N (1.32 Å), and C-H (1.09 Å) are all in this range.

The intensity of the first *g(r)* peak of C-O decreases after shear friction, which may indicate that the C-O bonds have a high likelihood of being disassociated or deviated from the equilibrium position by shear stress (Hong et al., 2011) (Figure 12B). The first *g(r)* peak of C-N shifts to a higher radical distance after shear friction, which means that the neighbor distance between the carbon and nitrogen atoms becomes larger (Figure 12C). Thus, the C-N bonds of coal are also more prone to be cleaved by shear stress. In contrast, the intensities of the first peak of C-C and C-H at 1,000 ps are higher than that at 0 ps(Figures 12C,D), which may be caused by the increasing density under the action of normal force. Normal force constantly compresses the friction system and decreases the free volume, which makes the carbon and hydrogen atoms become closer. Therefore, it can be concluded that C-O and C-N bonds are more easily disassociated by shear friction. The simulation results are consistent with the experimental results that the functional groups with heteroatoms are preferentially cleaved by tectonic stress into gases (Xu et al., 2014).

4 Conclusion

In this study, a sandwich friction system is constructed utilizing the conformation of primary structure coal. A normal force and constant shear velocity are applied to the molecular friction system to simulate the shear friction behavior. The MD simulation results are consistent with the experimental results of natural TDCs in other studies. First, coal friction is actually an energy transformation process. The shear friction work can both transform into thermal energy and lead to an increase in temperature and can also transform into kinetic energy, leading to atomic motion. Chain diffusion and reorientation are two important atomic motion types during coal friction. Atom trajectory analysis demonstrates that chain diffusion is regular within 30 ps friction, following which the diffusion behavior becomes irregular. The orientation before and after shear friction is revealed for eight types of fused aromatic chains. The fused aromatic chains are more or less reorientated by the shear friction. However, compared with the other fused aromatic chains, the orientation of pentacenes and naphthacenes are more parallel to the shear direction, indicating that the higher aspect ratio is beneficial to the reorientation caused by shear friction. Furthermore, the decreasing intensity of the first C-O peak and the radical distance shift of the first C-N peaks both indicate that the C-O and C-N bonds are preferentially cleaved by shear friction.

Data availability statement

The raw data supporting the conclusion of this article will be made available by the authors without undue reservation.

Author contributions

HL undertook the experiments, prepared the manuscript and analyzed the data; YS and ZD commented on the manuscript.

Funding

This work was supported by the National Natural Science Foundation of China (grant number 42102221), the Anhui Provincial Natural Science Foundation (grant number 2108085QD167), the Natural Science Foundation of Henan Province (grant number 222300420242), the Independent Research Fund of the State Key Laboratory of Mining Response and Disaster Prevention and Control in Deep Coal Mines (grant number SKLMRDPC20ZZ10), the Natural Science Foundation of Henan Province (grant number 222300420242), the Science and Technology Development Project of Luoyang (grant number 2101025A), the Heluo Young Talent Lifting Project of the Society and Technology Association of Luoyang (grant number 2022HLTJ06), and the Scientific Research Starting Foundation for the Introduced Talents of Anhui University of Science and Technology.

Conflict of interest

The authors declare that the research was conducted in the absence of any commercial or financial relationships that could be construed as a potential conflict of interest.

Publisher's note

References

Boneh, Y., and Reches, Z. E. (2018). Geotribology - friction, wear, and lubrication of faults. *Tectonophysics* 733, 171–181. doi:10.1016/j.tecto.2017.11.022

Bustin, R. M. (1983). Heating during thrust faulting in the rocky mountains: Friction or fiction? *Tectonophysics* 95 (3), 309–328. doi:10.1016/0040-1951(83)90075-6

Cao, D., Li, X., and Zhang, S. (2007). Influence of tectonic stress on coalification: Stress degradation mechanism and stress polycondensation mechanism. *Sci. China Ser. D.* 50 (1), 43–54. doi:10.1007/s11430-007-2023-3

Cheng, Y., and Pan, Z. (2020). Reservoir properties of Chinese tectonic coal: A review. *Fuel* 260, 116350. doi:10.1016/j.fuel.2019.116350

Dai, L., Minn, M., Satyanarayana, N., Sinha, S. K., and Tan, V. B. C. (2011). Identifying the mechanisms of polymer friction through molecular dynamics simulation. *Langmuir* 27 (24), 14861–14867. doi:10.1021/la202763r

Fan, C., Li, S., Elsworth, D., Han, J., and Yang, Z. (2020). Experimental investigation on dynamic strength and energy dissipation characteristics of gas outburst-prone coal. *Energy Sci. Eng.* 8 (4), 1015–1028. doi:10.1002/ese3.565

Fan, C., Li, S., Luo, M., Du, W., and Yang, Z. (2017). Coal and gas outburst dynamic system. *Int. J. Min. Sci. Technol.* 27 (1), 49–55. doi:10.1016/j.ijmst.2016.11.003

Fan, C., Wen, H., Li, S., Bai, G., and Zhou, L. (2022). Coal seam gas extraction by integrated drillings and punchings from the floor roadway considering hydraulic-mechanical coupling effect. *Geofluids* 2022, 1–10. doi:10.1155/2022/5198227

Frodsham, K., and Gayer, R. A. (1999). The impact of tectonic deformation upon coal seams in the South Wales coalfield, UK. *Int. J. Coal Geol.* 38 (3), 297–332. doi:10.1016/S0166-5162(98)00028-7

Han, Y., Wang, J., Dong, Y., Hou, Q., and Pan, J. (2017). The role of structure defects in the deformation of anthracite and their influence on the macromolecular structure. *Fuel* 206, 1–9. doi:10.1016/j.fuel.2017.05.085

Han, Y., Xu, R., Hou, Q., Wang, J., and Pan, J. (2016). Deformation mechanisms and macromolecular structure response of anthracite under different stress. *Energy fuels.* 30 (2), 975–983. doi:10.1021/acs.energyfuels.5b02837

Harmandaris, V. A., Mavrantzas, V. G., and Theodorou, D. N. (1998). Atomistic molecular dynamics simulation of polydisperse linear polyethylene melts. *Macromolecules* 31 (22), 7934–7943. doi:10.1021/ma980698p

Hong, Z., Hwang, S., and Fang, T. (2011). The deposition of Fe or Co clusters on Cu substrate by molecular dynamic simulation. *Surf. Sci.* 605 (1-2), 46–53. doi:10.1016/j.susc.2010.09.020

Hou, Q., Han, Y., Wang, J., Dong, Y., and Pan, J. (2017). The impacts of stress on the chemical structure of coals: A mini-review based on the recent development of mechanochemistry. *Sci. Bull.* 62 (13), 965–970. doi:10.1016/j.scib.2017.06.004

Hou, Q., Li, H., Fan, J., Ju, Y., Wang, T., Li, X., et al. (2012). Structure and coalbed methane occurrence in tectonically deformed coals. *Sci. China Earth Sci.* 55 (11), 1755–1763. doi:10.1007/s11430-012-4493-1

Hu, Y., Ma, T., and Wang, H. (2013). Energy dissipation in atomic-scale friction. *Friction* 1 (1), 24–40. doi:10.1007/s40544-013-0002-6

Hua, D., Ye, W., Jia, Q., Zhou, Q., Xia, Q., and Shi, J. (2020). Molecular dynamics simulation of nanoindentation on amorphous/amorphous nanolaminates. *Appl. Surf. Sci.* 511, 145545. doi:10.1016/j.apsusc.2020.145545

Jiang, B., Qu, Z., Wang, G. G. X., and Li, M. (2010). Effects of structural deformation on formation of coalbed methane reservoirs in Huaibei coalfield, China. *Int. J. Coal Geol.* 82 (3-4), 175–183. doi:10.1016/j.coal.2009.12.011

Ju, Y., and Li, X. (2009). New research progress on the ultrastructure of tectonically deformed coals. *Prog. Nat. Sci.* 19 (11), 1455–1466. doi:10.1016/j.pnsc.2009.03.013

Ju, Y. W., Wang, G. L., Jiang, B., and Hou, Q. L. (2004). Microcosmic analysis of ductile shearing zones of coal seams of brittle deformation domain in superficial lithosphere. *Sci. China Ser. D.* 47 (5), 393–404. doi:10.1360/02yd0291

Kitamura, M., Mukoyoshi, H., Fulton, P. M., and Hirose, T. (2012). Coal maturation by frictional heat during rapid fault slip. *Geophys. Res. Lett.* 39 (16), a–n. doi:10.1029/2012GL052316

Li, H., Ogawa, Y., and Shimada, S. (2003). Mechanism of methane flow through sheared coals and its role on methane recovery☆. *Fuel* 82 (10), 1271–1279. doi:10.1016/S0016-2361(03)00020-6

Li, H. Y. (2001). Major and minor structural features of a bedding shear zone along a coal seam and related gas outburst, Pingdingshan coalfield, northern China. *Int. J. Coal Geol.* 47 (2), 101–113. doi:10.1016/S0166-5162(01)00031-3

Li, M. (2013). *Structure evolution and deformation mechanism of tectonically deformed coal*. Xuzhou: China University of Mining and Technology. (In Chinese with English Abstract).

Li, Y., Song, D., Liu, S., and Pan, J. (2020). Characterization of ultramicropores and analysis of their evolution in tectonically deformed coals by Low-Pressure CO2 adsorption, XRD, and HRTEM techniques. *Energy fuels.* 34 (8), 9436–9449. doi:10.1021/acs.energyfuels.0c01403

Liu, H., Hou, C., and Song, Y. (2022). Molecular dynamics simulation of the nanoindentation of coal vitrinite. *Front. Earth Sci.* 10. doi:10.3389/feart.2022.856290

Liu, H., Jiang, B., Liu, J., and Song, Y. (2018). The evolutionary characteristics and mechanisms of coal chemical structure in micro deformed domains under sub-high temperatures and high pressures. *Fuel* 222, 258–268. doi:10.1016/j.fuel.2018.02.117

Liu, H., Jiang, B., Song, Y., and Hou, C. (2019). The tectonic stress-driving alteration and evolution of chemical structure for low- to medium-rank coals-by molecular simulation method. *Arab. J. Geosci.* 12 (23), 1–16. doi:10.1007/s12517-019-4909-8

Liu, H., and Jiang, B. (2019). Stress response of noncovalent bonds in molecular networks of tectonically deformed coals. *Fuel* 255, 115785. doi:10.1016/j.fuel.2019.115785

Liu, H. (2020). *The dynamic differentiation characteristics and mechanisms of stress-sensitive elements and minerals in tectonically deformed coals*. Xuzhou: China University of Mining and Technology. (In Chinese with English Abstract).

Mattsson, T. R., Lane, J. M. D., Cochrane, K. R., Desjarlais, M. P., Thompson, A. P., Pierce, F., et al. (2010). First-principles and classical molecular dynamics simulation of shocked polymers. *Phys. Rev. B* 81 (5). doi:10.1103/PhysRevB.81.054103

Meng, J., Cao, Z., Zhang, S., Wang, C., and Nie, B. (2021). Micro-mechanical properties and damage mechanisms of coal under cyclic loading: A nanoindentation experiment and molecular dynamics simulation. *Mol. Simul.* 48, 354–365. doi:10.1080/08927022.2021.2015070

Niu, Q., Pan, J., Cao, L., Ji, Z., Wang, H., Wang, K., et al. (2017). The evolution and formation mechanisms of closed pores in coal. *Fuel* 200, 555–563. doi:10.1016/j.fuel.2017.03.084

Pan, J., Mou, P., Ju, Y., Wang, K., Zhu, Q., Ge, T., et al. (2022). Micro-nano-scale pore stimulation of coalbed methane reservoirs caused by hydraulic fracturing experiments. *J. Petroleum Sci. Eng.* 214, 110512. doi:10.1016/j.petrol.2022.110512

Plimpton, S. (1995). Fast parallel algorithms for short-range molecular dynamics. *J. Comput. Phys.* 117, 1–19. doi:10.1006/jcph.1995.1039

Qiang, Y., Wu, W., Lu, J., Jiang, B., and Ziegmann, G. (2020). Progressive molecular rearrangement and heat generation of amorphous polyethene under sliding friction: Insight from the United-Atom molecular dynamics simulations. *Langmuir* 36 (38), 11303–11315. doi:10.1021/acs.langmuir.0c01949

Rittel, D. (2000). An investigation of the heat generated during cyclic loading of two glassy polymers. Part I: Experimental. *Mech. Mater.* 32 (3), 131–147. doi:10.1016/S0167-6636(99)00051-4

Song, Y., Jiang, B., Li, M., Hou, C., and Mathews, J. P. (2020). Macromolecular transformations for tectonically-deformed high volatile bituminous via HRTEM and XRD analyses. *Fuel* 263, 116756. doi:10.1016/j.fuel.2019.116756

Song, Y., Jiang, B., and Qu, M. (2019). Macromolecular evolution and structural defects in tectonically deformed coals. *Fuel* 236, 1432–1445. doi:10.1016/j.fuel.2018.09.080

van Duin, A. C. T., Dasgupta, S., Lorant, F., and Goddard, W. A. (2001). ReaxFF: A reactive force field for hydrocarbons. *J. Phys. Chem. A* 105 (41), 9396–9409. doi:10.1021/jp004368u

Wang, J., Han, Y., Chen, B., Guo, G., Hou, Q., and Zhang, Z. (2017). Mechanisms of methane generation from anthracite at low temperatures: Insights from quantum chemistry calculations. *Int. J. Hydrogen Energy* 42 (30), 18922–18929. doi:10.1016/j.ijhydene.2017.06.090

Wang, J., Hou, Q., Zeng, F., and Guo, G. (2021). Gas generation mechanisms of bituminous coal under shear stress based on ReaxFF molecular dynamics simulation. *Fuel* 298, 120240. doi:10.1016/j.fuel.2021.120240

Wang, J., Hou, Q., Zeng, F., and Guo, G. (2021). Stress sensitivity for the occurrence of coalbed gas outbursts: A reactive force field molecular dynamics study. *Energy fuels.* 35, 5801–5807. doi:10.1021/acs.energyfuels.0c04201

Xu, R., Li, H., Guo, C., and Hou, Q. (2014). The mechanisms of gas generation during coal deformation: Preliminary observations. *Fuel* 117, 326–330. doi:10.1016/j.fuel.2013.09.035

Yang, Y., Pan, J., Hou, Q., Wang, K., and Wang, X. (2021). Stress degradation mechanism of coal macromolecular structure: Insights from molecular dynamics simulation and quantum chemistry calculations. *Fuel* 303, 121258. doi:10.1016/j.fuel.2021.121258

Yang, Y., Pan, J., Wang, K., and Hou, Q. (2020). Macromolecular structural response of Wender coal under tensile stress via molecular dynamics. *Fuel* 265, 116938. doi:10.1016/j.fuel.2019.116938

Yu, S., Bo, J., Vandeginste, V., and Mathews, J. P. (2022). Deformation-related coalification: Significance for deformation within shallow crust. *Int. J. Coal Geol.* 256, 103999. doi:10.1016/j.coal.2022.103999

Zhang, J., Chu, X., Wei, C., Zhang, P., Zou, M., Wang, B., et al. (2022). Review on the application of Low-Field nuclear magnetic resonance technology in coalbed methane production simulation. *ACS Omega* 7, 26298–26307. doi:10.1021/acsomega.2c02112

Zhang, J., Wei, C., Ju, W., Yan, G., Lu, G., Hou, X., et al. (2019). Stress sensitivity characterization and heterogeneous variation of the pore-fracture system in middle-high rank coals reservoir based on NMR experiments. *Fuel* 238, 331–344. doi:10.1016/j.fuel.2018.10.127

Zhang, J., Wei, C., Zhao, C., Zhang, T., Lu, G., and Zou, M. (2021). Effects of nano-pore and macromolecule structure of coal samples on energy parameters variation during methane adsorption under different temperature and pressure. *Fuel* 289, 119804. doi:10.1016/j.fuel.2020.119804

frontiers | Frontiers in Earth Science

TYPE Review
PUBLISHED 09 January 2023
DOI 10.3389/feart.2022.1034341

OPEN ACCESS

EDITED BY
Junjian Zhang,
Shandong University of Science and Technology, China

REVIEWED BY
Xiaoqi Wang,
Suzhou University, China
Yu Song,
China University of Mining and Technology, China

*CORRESPONDENCE
Xiaobing Zhang,
xiaobingzhang@hpu.edu.cn
Yugui Zhang,
zyg@hpu.edu.cn

SPECIALTY SECTION
This article was submitted to Economic Geology,
a section of the journal
Frontiers in Earth Science

RECEIVED 01 September 2022
ACCEPTED 27 September 2022
PUBLISHED 09 January 2023

CITATION
Zhang H, Zhang X, Zhang Y and Wang Z (2023), The characteristics of methane adsorption capacity and behavior of tectonic coal.
Front. Earth Sci. 10:1034341.
doi: 10.3389/feart.2022.1034341

The characteristics of methane adsorption capacity and behavior of tectonic coal

Hang Zhang[1], Xiaobing Zhang[2,3]*, Yugui Zhang[1,2]* and Zhenzhi Wang[4]

[1]School of Safety Science and Engineering, Henan Polytechnic University, Jiaozuo, Henan, China, [2]State Key Laboratory Cultivation Base for Gas Geology and Gas Control, Jiaozuo, Henan, China, [3]School of Emergency Management, Henan Polytechnic University, Jiaozuo, Henan, China, [4]School of Resources and Geoscience, China University of Mining and Technology, Xuzhou, Jiangsu, China

The research of methane adsorption on tectonic coal is an important content to gas disaster prevention and coalbed methane (CBM) exploration in outburst coal seams. Many projects of methane adsorption capacity and behavior of tectonic coal, such as adsorption difference between tectonic coal and its untectonic coal, adsorption evaluation of tectonic coal, factors for adsorption capacity of tectonic coal, gas-solid coupling feature in tectonic coal and supercritical adsorption phenomena of tectonic coal, were carried out by scientists. Combined with a long-term study on organic matter structure and methane adsorption of tectonic coal, the author summarized recent-years' researches on adsorption capacity and behavior of tectonic coal-methane at home and abroad from the dispute of adsorption ability determination, the thermodynamic characterization of methane adsorption capacity, and the methane adsorption behavior of quantum chemical calculation of the adsorption and the gas content calculation based on loss compensation, respectively. It is believed that the coal structure controls the methane adsorption capacity and behavior characteristics of different tectonic coals, and from the perspective of thermodynamics, the adsorption capacity of different types of coals can be better distinguished. In the future, a more scientific and complete quantum chemical calculation of methane adsorption by tectonic coal and a compensation method based on instantaneous emission loss should be established, so as to better reveal the methane adsorption behavior of tectonic coal and the mechanism of coal and gas outburst. The research has a reference to fine research of coal adsorption and CBM exploration practices.

KEYWORDS

tectonic coal, methane adsorption, adsorption capacity, adsorption behavior, structure-property relationship, gas content

Introduction

The theoretical research and engineering practice of gas geology attach great importance to the research on tectonic coal (Aguado and Nicieza, 2007; Wold et al., 2007; Jiang et al., 2009; Yan et al., 2013; Zhang et al., 2021; Lin et al., 2022; Tu et al., 2022): On the one hand, coal and gas outburst is the result of the combination of tectonic coal, gas and tectonic actio. The "Regulations on Prevention and Control of Coal and Gas Outbursts" formulated by the State Administration of Work Safety of China even has listed tectonic coal as the first index for predicting the risk of coal seam outbursts; on the other hand, the low strength, low permeability and complex gas-solid coupling relationship of tectonic coal make coalbed methane (CBM) extraction more difficult. For example, the gas geology community often takes the prediction of tectonic coal as the basis for predicting coal and gas outburst, and discusses why tectonic coal has the risk of outburst from the aspects of coal structure and mechanical properties (Cao et al., 2003); when drilling a seam with developing tectonic coal, the instantaneous gas emission is large, making it difficult to accurately measure the gas content, which in turn affects the accuracy of gas emission prediction seriously. Perhaps it was because of the existence of tectonic coal, an associated "product" that shared the same parent material with normal coal (in this paper, the "untectonic coal" which is not affected by structural deformation is used to represent "normal coal"), when predecessors studied the characteristics of gas adsorption of coal, they paid special attention to the gas adsorption of different types of destruction coals (different types of tectonic coals). Ju et al. (2004) divided tectonic coal into three deformation sequences: brittle deformation, brittle-ductile and ductile deformation according to the tectonic deformation mechanism system. Jiang et al. (2016) considered that the brittle series of tectonic coal, cataclastic coal, mortar coal, granulitic coal and schistose coal were favorable target layers for CBM development, while Mylonitic coal of ductile deformation was considered to be a high-incidence area of coal and gas outbursts. The special pore and fissure structure of tectonic coal determined the coalbed methane (gas) adsorption capacity and behavior characteristics different from that of untectonic coal, and generally believed that the characteristics of structural fragmentation, large specific surface area and large molecular gap made tectonic coals have stronger adsorption capacity for methane (Qu et al., 2015). However, there are also reports that there is no significant difference in methane adsorption capacity between tectonic coal and co-existing untectonic coal, or the increase in the degree of damage does not improve the methane adsorption capacity of coal (Wang et al., 1993; Dong., 2019).

At present, researchers mostly use experimental methods to study the gas adsorption capacity and behavior characteristics of coal. The experimental method is to reflect the adsorption characteristics of coal samples from a macro perspective, the control variates method is often used to study the influence of a certain factor (such as temperature, pressure, etc.) on the gas adsorption capacity of coal, and the single-layer adsorption model (Langmuir adsorption model) and the multi-layer adsorption model (BET model) are mainly used for calculation. Scholars have done a lot of experimental research on the methane adsorption characteristics of tectonic coal. Zhang et al. (2007) and Jiang et al. (2009) believed that in the process of tectonic coal deformation, in addition to the evolution of chemical structure and coal macromolecular structure to order and high aromatization, many low molecular compounds and gaseous hydrocarbons (gas) were produced, which further improved the gas-bearing performance of the tectonic coal distribution area. Ju et al. (2008) carried out isothermal adsorption and desorption experiments on untectonic coal and tectonic coal under equilibrium water conditions, and found that due to differences in pore structure and chemical structure, the adsorption and desorption mechanism of tectonic coal was different from that of untectonic structural coal. Pan et al. (2012) believed that the adsorption of coalbed methane was related to the deformation structure of tectonic coal at different temperatures and pressures, and the methane adsorption of coal decreased with the increase of temperature. At a certain temperature, the adsorption of methane by different structural deformed coals was also different. For example, at a constant temperature of 30°C, the adsorption capacity of strong brittle-ductile deformed coal was significantly higher than that of weakly brittle deformed coal and strong brittle deformed coal; under low pressure conditions, the adsorption capacity of strong brittle deformed coal was significantly higher than that of weakly brittle deformed coal; however, with the increase of pressure, the adsorption capacities of the two coals tended to be the same. Cheng and Pan, 2020 found that the Langmuir volume and Langmuir pressure of tectonic and untectonic coals showed a "U" shape relationship with the degree of metamorphism. It was believed that the affinity between methane and tectonic coal was stronger than that of untectonic coal, so tectonic coal had stronger methane adsorption capacity.

The most fundamental factor affecting the macroscopic experimental results of the gas adsorption capacity and behavior of tectonic coal is the change of its microstructure. Therefore, it is difficult to explore the adsorption characteristics of gas in tectonic coal from the mechanism only by means of experimental methods, and molecular simulation can be used to analyze the adsorption mechanism of gas molecules in coal reservoirs from the molecular level at the microscopic scale. Thus, in recent years, molecular dynamics simulation has gradually become an important way to solve the complex adsorption behavior of coal. At present, the molecular simulation methods of coal are mainly based on molecular dynamics and molecular mechanics theory, and use molecular dynamics (MD), molecular mechanics (MM), finite element simulation and other molecular simulation and statistical methods to model the molecular structure and pore structure of coal. This allows people to more comprehensively and intuitively understand the structural characteristics of coal, and helps to study the physical and chemical properties of coal through computer means. Wang et al. (2016) used the Monte Carlo simulation method to study the relationship between the surface structure of coal and the amount of methane adsorption based on the advanced evolution structure characteristics of tectonic coal, believing that the methane adsorption capacity of coal per unit mass decreased with the increase of the number of stacking layers of aromatic units, and the existence of defects and oxygen-containing functional groups was not conducive to the adsorption of methane. Han et al. (2017) used quantum chemical calculations and discussed the role of structural defects in anthracite-grade tectonic coals and their effects on macromolecular structure. The results showed that stress could promote the evolution of chemical structure of coal. Song. (2019) constructed a macromolecular structure model of mylonite coal, and a grand canonical monte carlo (GCMC) simulation of methane adsorption was performed. By comparing with the interaction between untectonic coal and methane, the gas adsorption characteristics and microscopic interaction mechanism of mylonitic coal were explained.

A large number of studies have shown that the research on the complex and exclusive characteristics of tectonic coal not only establishes the basic theory of geological body structure and tectonic changes under the action of geotectonic movement, but also plays an important guiding role in engineering practice such as coal seam outburst risk prediction and underground gas drainage in CBM low-permeability enrichment areas (Pan et al., 2012; Li et al., 2019; Zhang et al., 2022). Based on the long-term research and knowledge in structural composition of organic matter in tectonic coal and coal-methane adsorption through the author's research group (Huan et al., 2015; Zhang et al., 2018; Wang et al., 2021a; Yang et al., 2021), this paper summarizes and prospects the progress made in the study of methane adsorption capacity and behavior of tectonic coal in recent years, hoping to share and communicate, and promote further research on the adsorption of tectonic coal, so as to provide a reference for the prediction and prevention of gas disasters in outburst coal seam and to improve the recovery ratio of coal seam methane.

Methane adsorption capacity of tectonic coal

Determination of the methane adsorption capacity of tectonic coal

On the research of methane adsorption capacity of tectonic coal, there are many reports at home and abroad, but the understanding is different. Early research results show that there is no significant difference in the methane adsorption capacity of tectonic coal and untectonic coal (Wang et al., 1993), and the volume of methane adsorption does not increase with the increase of the degree of coal damage; In recent years, relevant research results also show that there is indifference in gas adsorption volume compare with tectonic coal and untectonic coal, while the gas adsorption rate of tectonic coal is higher than that of untectonic coal (Dong, 2018). However, Zhang et al. (2006) pointed out that the methane adsorption capacity of tectonic coal is significantly higher than that of untectonic coal when discussing the controlling factors of coal adsorption capacity; Wang et al. (2012) and Hu et al. (2016) conducted a comparative study on tectonic coal and untectonic coal in Jincheng, Jiaozuo, WuYi, Pingdingshan and other mining areas, concluding that the adsorption limit of tectonic coal is greater than that of untectonic coal on the whole.

In the experimental study of high pressure isothermal adsorption of methane on coal (Figure 1), it has been found that: the supercritical adsorption phenomenon occuring in the high pressure section, in which the adsorption pressure increases and the adsorption capacity decreases (Figure 1A), is quite different from the Ⅰ~Ⅴ adsorption isotherms that are generally believed to conform to the Langmuir equation (Figure 1), and the adsorption mechanism is different from that of gases below the critical temperature (Gao. 2011). The experimental results of Ju and Li, 2009 show that the methane adsorption capacity of weakly deformed coal increases with the increase of adsorption pressure, which conforms to the Langmuir equation, while the adsorption isotherms of strong and ductile deformed coal show different types (Figure 2). According to its analysis, desorption occurs when the adsorption pressure reaches a certain level, and the tectonic coal is compressed and deformed during the process, causing the deformation of its macromolecules and pore structure, and forming thin bottleneck pores; with the increase of adsorption pressure, the pores gradually closes, resulting in the decrease of adsorption heat and the desorption behavior, which leads to the decrease of methane adsorption capacity.

In view of the different understandings of the adsorption capacity of different types of tectonic coals and untectonic coal, and the factors affecting the capacity of methane adsorbed by coal are vast and complex, it is obviously meaningless to find out the strong and weak relationship between the methane adsorption capacity of different types of tectonic coals and co-existing untectonic coal only by discussing the difference in adsorption amount. Under normal formation conditions, CH_4 and N_2 in coal with extremely low critical temperature are supercritical gas, and CO_2 in coal will also be in supercritical state with the increase of burial depth. Apparently, the author suggests it is necessary to start from the perspective of studying the difference in methane adsorption energy between different types of tectonic coals and symbiotic untectonic coal, combine with the research idea of gas supercritical adsorption, and determine which coal of different

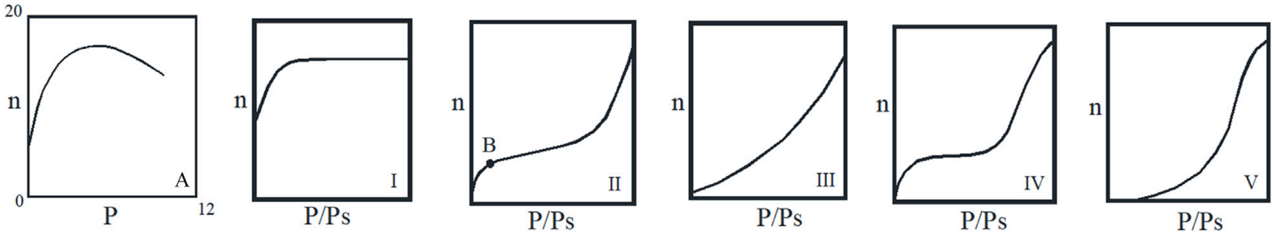

FIGURE 1
Type of adsorption isotherm: (A) Adsorption isotherm of methane and coal under critical temperature, (I~V) Adsorption isotherms of the Langmuir equation under critical temperature (modified from Gao., 2011).

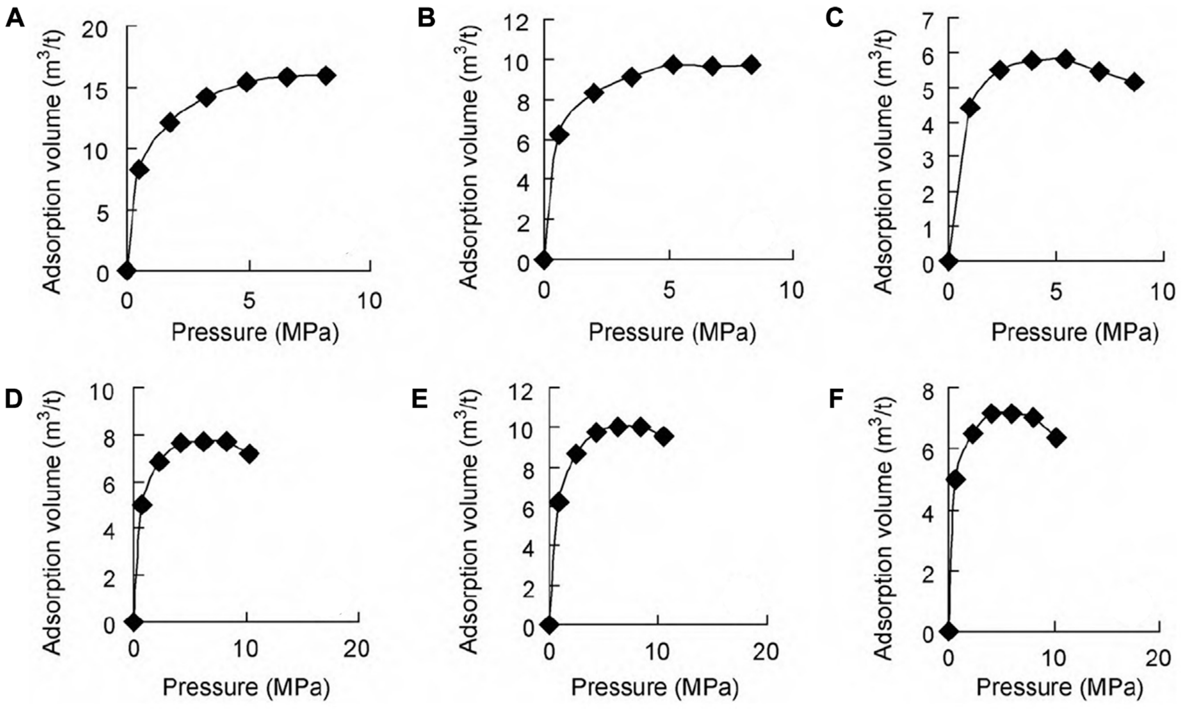

FIGURE 2
Isothermal adsorption curves of tectonic coals and untectonic coal. **(A)** Untectonic coal; **(B)** cataclastic structure coal; **(C)** schistose structure coal in brittle deformation coals; **(D)** schistose-wrinkle structure coal in brittle-ductile superimposed coals; **(E)** scaled structure coal in brittle-ductile deformation coals; **(F)** mylonitic structure coal in ductile deformation coals. (Ju and Li, 2009, reprinted with permission of the copyright holders).

structure types has a stronger or weaker adsorption capacity for methane through experimental analysis and theoretical estimation, the coal seam gas content is also calibrated accordingly. Jian et al. (2014), Wang et al. (2016) and Song et al. (2017), have carried out a lot of research in this area, and the progress is slow at present, but it does not affect the theoretical value of the problem exploration and the engineering application value of the development of high-performance coal-based methane storage materials with tectonic coal as precursor (Zhang et al., 2017).

Thermodynamic characterization of methane adsorption of tectonic coal

As mentioned above, people have different opinions on whether the methane adsorption capacity of different types of tectonic coals must be greater than that of symbiotic untectonic coal. It is a new idea to use adsorption energy to examine the adsorption capacity of coal of different damage types. Since there is no method to directly test the adsorption energy of coal-methane, the adsorption heat can be used instead of the

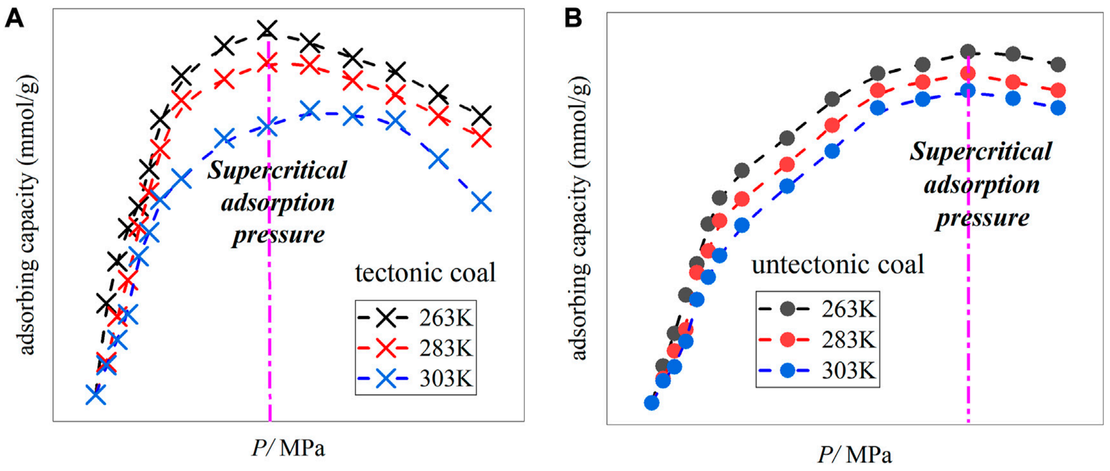

FIGURE 3
Diagram of supercritical adsorption isotherm at 263–303 K fat coal rank tectonic/untectonic coal. **(A)** tectonic coal; **(B)** untectonic coal (modified from Wei., 2012).

adsorption energy. The basic process of adsorption heat index characterization is: based on the adsorption isotherm experiment, the real adsorption capacity, that is, the absolute adsorption capacity, is calculated with the help of the adsorption model, and the adsorption heat index and the thermodynamic effect of coal-methane adsorption are combined to calibrate the adsorption capacity of tectonic coal for methane. Two common adsorption heats, limit adsorption heat and isosteric adsorption heat, can be calculated from adsorption isotherms. Among them, limit adsorption heat is the effect of adsorption heat when the adsorption amount tends to zero, and is often used as a representative value of heat of adsorption; isosteric adsorption heat is a fractional amount, that is, the thermal effect generated by the increase in the amount of adsorption during the adsorption process.

This research group has carried out the isotherm adsorption experiment of methane on fat coal rank tectonic coal and co-existing untectonic coal from low temperature to room temperature, and has obtained a series of supercritical adsorption isotherms of methane on tectonic coal at 263–303 K, showing supercritical adsorption characteristics, namely: the methane adsorption capacity of both tectonic coal and untectonic coal increases with the increase of equilibrium pressure (Figure 3), and the adsorption curve decreases when the equilibrium pressure reaches a certain value, indicating that the adsorption capacity has a maximum value; the adsorption curve is type I before the maximum appears (Figure 1), and the pressure point at which the maximum appears lags with increasing temperature (Wei., 2012). The adsorption capacity measured by the volumetric method above is the excess adsorption capacity, not the real adsorption capacity of coal to methane, that is, the absolute adsorption capacity, and cannot objectively describe the adsorption of coal reservoirs. Therefore, before calculating the heat of adsorption, in order to explore the methane adsorption characteristics of tectonic coal, it is necessary to establish an absolute adsorption capacity calculation model and obtain the absolute adsorption capacity curve of methane adsorption of tectonic coal according to the experimental data (Zhou and Zhou, 1998; Wei., 2012). As shown in (Figure 4), the absolute adsorption curve no longer has a maximum point, before reaching the adsorption equilibrium, the adsorption amount increases with the increase of pressure. It belongs to the I-type isotherm adsorption curve and obeys the Langmuir equation. The absolute adsorption amount is the real value of coal seam adsorption of methane, which has important guiding significance for accurately predicting coal and gas outburst.

The coal surface is the main place for the adsorption/desorption of coalbed methane. When the adsorption of methane and coal occurs, the coal surface tension will decrease (surface thermodynamics), so the change of coal surface tension in the process of coal-methane adsorption can be calculated by the Gibbs formula. Different from the aforementioned adsorption heat studies, in order to further investigate "whether the methane adsorption capacity of tectonic coal is stronger than that of symbiotic untectonic coal" from the perspective of the surface energy drop of coal adsorbing methane, we used the IS-100 isothermal adsorption/desorption instrument from Terra Tek, United States. The isothermal adsorption experiment of methane with tectonic/untectonic coal with 293, 303, and 313 K coal ranks being coking coal was carried out (Figure 5), and the maximum adsorption equilibrium pressure was 8 MPa (Jian et al., 2014). The results show that: the process of coal adsorption of methane

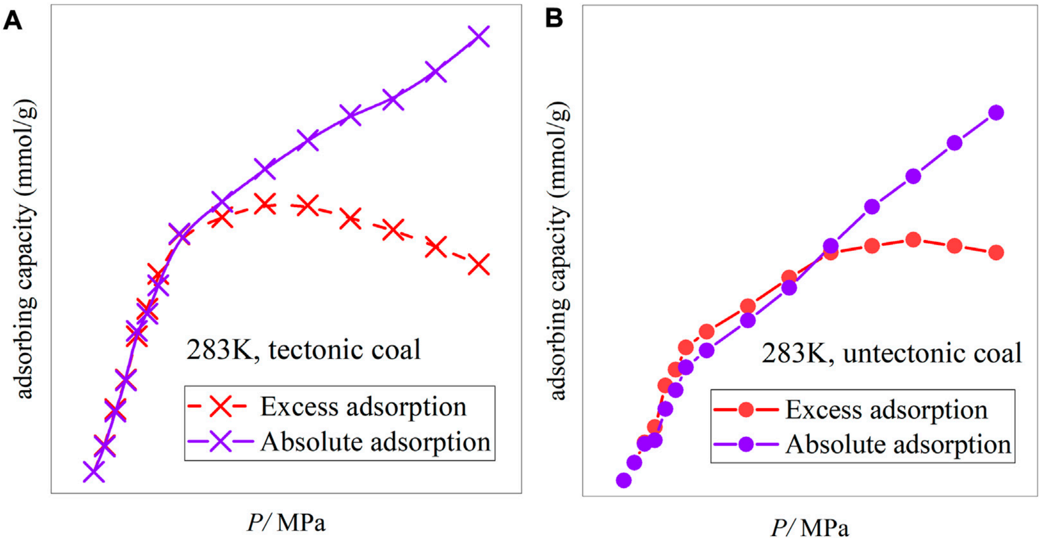

FIGURE 4
Diagram of excess methane adsorption and absolute adsorption isotherms of fat coal rank tectonic/untectonic coal. **(A)** tectonic coal; **(B)** untectonic coal (modified from Wei., 2012).

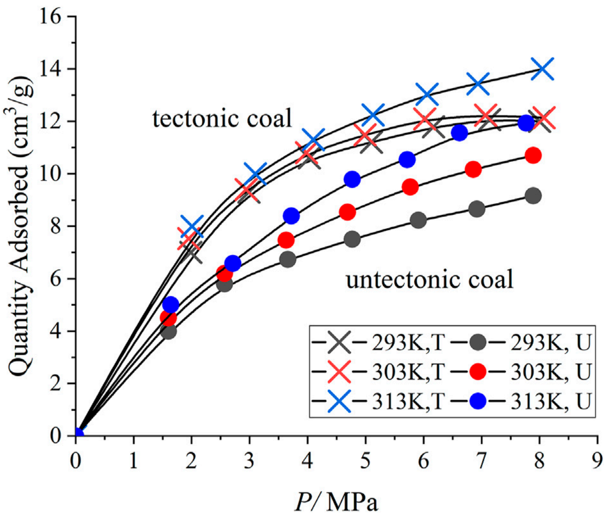

FIGURE 5
Methane adsorption curves of tectonic/untectonic coal under different temperatur conditions (modified from Jian et al., 2014)

is a process of coal surface energy reduction (Table 1), the overall performance of the experimental coal samples is that the surface energy reduction of tectonic coal adsorbing methane is greater than that of co-existing untectonic coal, both the increase in temperature and the increase in equilibrium pressure make the surface energy drop value of the tectonic coal larger than that of the co-produced untectonic coal (Figure 6). Berkheim has pointed out that "the expansion deformation of solid is proportional to its surface energy drop," and combined with the surface energy drop of coal adsorbing methane and theoretical calculations, it is believed that adsorption deformation can promote layer slip and dislocation of coal. Obviously, the surface energy reduction of tectonic coal adsorbing methane is greater than that of co-existing untectonic coal, but its coal strength is lower, and it is prone to adsorption expansion, deformation and damage, which may be one of the important reasons why tectonic coal is closely related to coal and gas outburst.

Methane adsorption behavior of tectonic coal

Quantum chemical calculation of methane adsorption of tectonic coal

The high complexity and heterogeneity of coal structure make its adsorption behavior more complicated than that of conventional solid adsorbents (Crawford and Mainwaring, 2001; Wang et al., 2021a; Wang et al., 2021b). Theoretical and experimental studies show that the structure and composition of coal are closely related to the coal organic polymer network structure and the low molecular compounds dispersed in it, which are the intrinsic factors affecting the adsorption/desorption of coalbed methane (Ji et al., 2015; Yang et al., 2021). The quantum chemical calculation of the coal surface

TABLE 1 Statistics of surface energy drop of tectonic/untectonic coal adsorbed methane at different temperatures (modified from Jian et al., 2014).

Untectonic coal	293 K	P	1.6	2.57	3.66	4.77	5.91	6.92	7.89
		△γ	6729.69	10001.32	131183.73	16017.10	18595.63	20655.44	22469.66
	303 K	P	1.6	2.57	3.63	4.69	5.77	6.86	7.89
		△γ	7274.68	10779.02	14084.47	16975.93	19591.49	21961.69	23998.70
	313 K	P	1.64	2.71	3.72	4.77	5.72	6.62	7.77
		△γ	7870.48	11887.58	15145.09	18117.88	20521.76	22595.56	25007.63
Tectonic coal	293 K	P	1.99	2.99	4.03	5.1	6.17	7.14	8.28
		△γ	11284.40	15345.04	18907.35	22061.95	24825.99	27066.88	29442.06
	303 K	P	1.95	2.94	3.98	4.99	6.02	7.07	8.08
		△γ	11539.22	15744.6142	19467.4509	22586.6485	25385.8766	27928.4180	30135.6364
	313 K	P	2.01	3.1	4.1	5.13	6.06	6.94	8.05
		△γ	12341.84	17068.34	20710.154	23958.04	26553.65	28774.43	31309.89

Note: P- adsorption equilibrium pressure, MPa; △γ-surface energy drop, J/m^2.

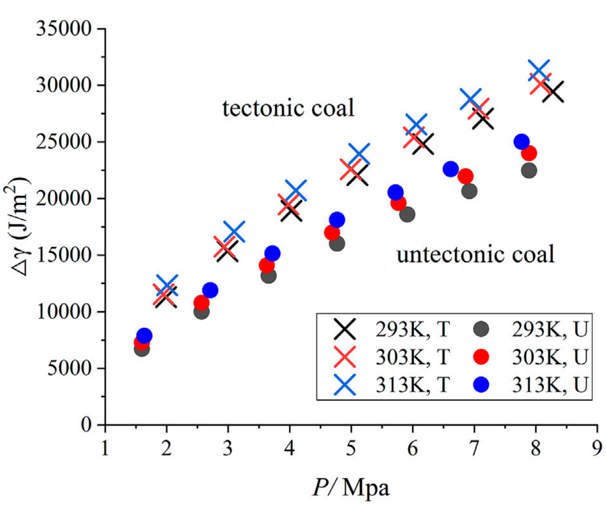

FIGURE 6
The surface energy changed of tectonic/untectonic coal adsorbed methane under different temperatur conditions (modified from Jian et al., 2014)

can reflect the coal surface properties, and the adsorption and interaction studies of methane molecules on solid surfaces are multi-faceted, so the theoretical calculation of methane adsorption on coal surfaces by quantum chemical methods is more rigorous.

Chen et al. (2000) has modeled atomic clusters on the coal surface and has carried out quantum chemical *ab initio* calculations with base set (STO-4-31G). The results show that the interaction between methane and the coal surface is anisotropic. When methane overlaps with a regular triangular pyramid on the coal surface, the energy is the lowest, and the maximum adsorption potential is 2.65 kJmo1^{-1}, which belongs to the category of physical adsorption and is manifested as surface condensation. Wang et al. (2008) has proceeded DFT calculation on the mechanism of coal and gas outburst, showing that the adsorption of coal and methane is physical adsorption, and the adsorption energy is 1.16 kJ mo1^{-1}, when the coal-methane adsorption system absorbs electromagnetic waves in the 23–61 cm^{-1} frequency range, the methane molecules can be desorbed, that is, coal and gas outburst occurs. In this paper, according to the XRD analysis data of co-existing tectonic coal and untectonic coal in the same layer (Table 2), and corresponding to each index in the anthractie coal aromatic ring structure, the untectonic coal and tectonic coal are constructed combined with the unit cell parameters of graphite in the inorganic crystal structure database (ICSD), the models are denoted as M_1 and M_2 (Jing et al., 2010), respectively (Figure 7). Using the adsorption isotherm calculation task in the sorption module of Materials Studio software, at 298 K and 303 K, the isotherm adsorption curves of untectonic coal (M_1), tectonic coal (M_2) and methane are calculated respectively (Jing et al., 2010) (Figure 8), shows that the methane adsorption curves of the two models are consistent with Langmuir adsorption characteristics. At 298 K, the saturated adsorption capacity of untectonic coal (M_1) is about 28 methane molecules, and that of tectonic coal (M_2) is about 50 methane molecules, and the methane adsorption capacity of the tectonic coal is about twice that of the untectonic coal (Figure 8A). At 303 K, the methane adsorption behavior of the tectonic/untectonic coal has the same characteristics as that at 298 K (Figure 8B). Theoretical calculation studies combining quantum chemistry and model intermolecular interactions suggest that: during the formation of tectonic coal, the coal deformation increases, the structure of the side chain on the aromatic core of the coal changes, and the steric hindrance weakens, reducing the rate of methane passing through the coal body. In addition, the side groups and even the polymer main chain are partially broken to form a high free

TABLE 2 $R_{o,max}$ and XRD analysis data of different types of anthractie coal (modified from Jing et al., 2010).

Coal sample number	Structure type of coal body	Ro,max/%	d002/Å	Lc/Å	La/Å
M1	untectonic coal	3.99	3.463	22.908	16.201
M2	tectonic coal	4.78	3.446	25.798	19.937

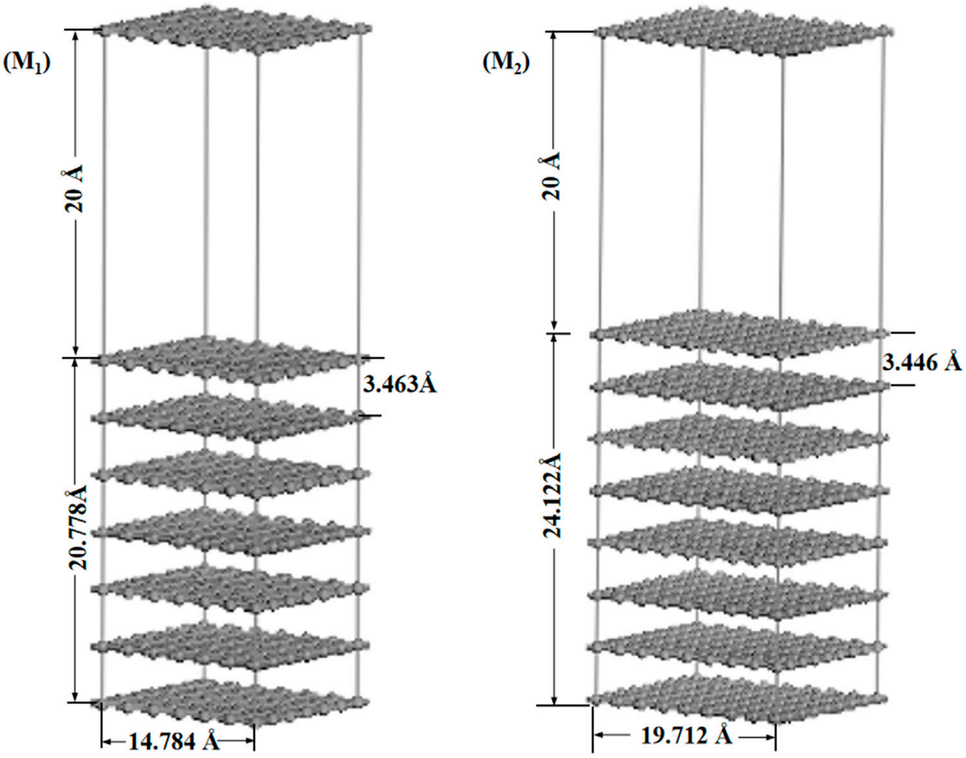

FIGURE 7
Models of untectonic anthractie coal (M_1) and anthractie tectonic coal (M_2) (modified from Jing et al., 2010).

energy center, which is conducive to the diffusion of methane, when the energy of free methane is equal to or higher than the binding energy of the side groups on the aromatic core of coal, methane can naturally penetrate into the side groups of the coal structure, and occupy vacancies (adsorption sites) there, which adsorption behavior reduces the free energy of coal. The adsorption energy of methane on the surface of tectonic coal is greater than that of untectonic coal (Table 3), indicating that tectonic coal can store a larger amount of methane than co-existing untectonic coal (Wang et al., 2009). The study of methane activation and adsorption by coal surface structure is helpful to deeply understand the methane adsorption behavior on coal surface, and reveal the mechanism of coal and gas outburst from the molecular level.

Determination of gas content in tectonic coal based on compensation for instantaneous emission loss quantity

A large number of on-site tests and survey statistics show that the two tentative indicators for predicting the risk of coal seam outbursts tentatively set in the "Regulations on Prevention and Control of Coal and Gas Outbursts," the initial velocity of gas emission (ΔP, the critical value is 10 ml s^{-1}) and coal seam gas content (W, the critical value is 8 m^3 t^{-1}), almost become insensitive indicators (or the critical value is inappropriate) in the coal seam developed in tectonic coal, which lacks scientificity and reliability, and should attract the attention of researchers. However, in the current engineering practice, the risk of coal seam outburst is still judged accordingly. Most of predecessors

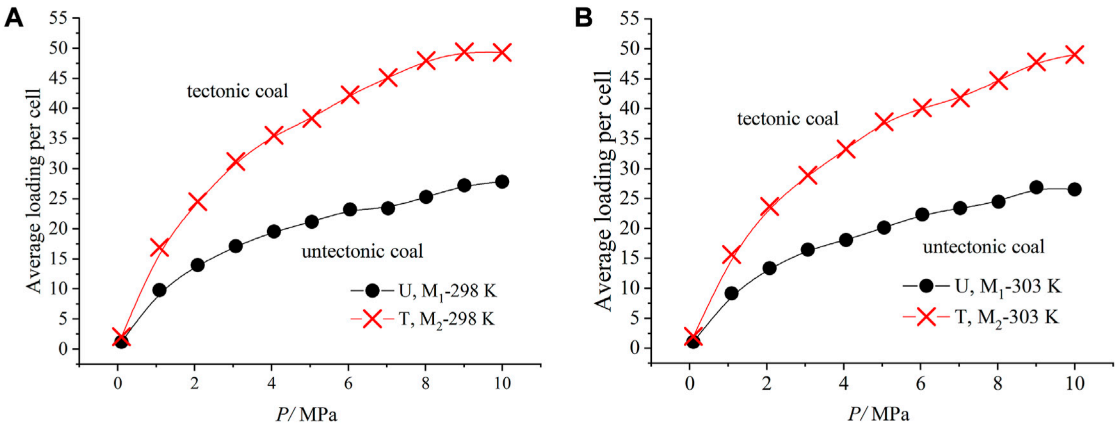

FIGURE 8
CH_4 adsorption isotherms of anthractie untectonic coal (M_1) and tectonic anthractie coal (M_2) at 298 K and 303 K. **(A)** 298 K; **(B)** 303 K (modified from Jing et al., 2010).

TABLE 3 Gas and different types of coal adsorption distance, adsorption energy and bond order (modified from Wang et al., 2009).

Adsorbed gas	Structure type of coal body	Adsorption distance/Å	Adsorption energy/(kJ/mol)	Bond order
CH_4	untectonic coal	2.11	−12.34	0.01
	tectonic coal	1.94	−15.75	0.02

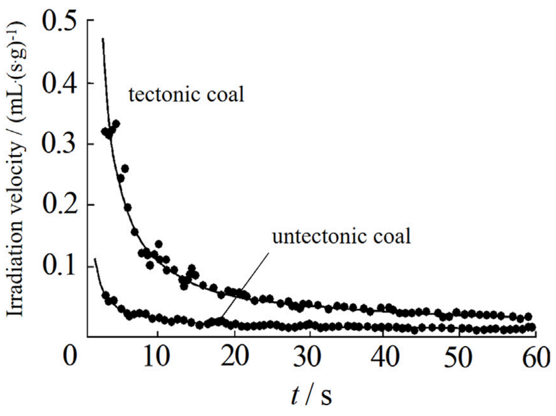

FIGURE 9
Coal sample irradiation velocity curve (modified from Fu et al., 2008).

have used isothermal adsorption/desorption experiments to explore the gas properties of coal, but the research on the instantaneous emission mechanism of coal and gas is weak, which is the basis for the determination of gas content in tectonic coal and the prediction of coal seam outburst risk (Zhang and Y, 2014). It can be seen that revealing the initial gas desorption law of tectonic coal, finding out the loss quantity in the determination of gas content in tectonic coal-developed coal seams, and establishing a compensation method for the loss quantity have important practical significance for mine gas disaster prediction and coalbed methane resource evaluation.

Based on coal seam gas content, the "Regulations on Prevention and Control of Coal and Gas Outbursts" sets the critical value for predicting regional outburst risk as 8 $m^3 t^{-1}$. However, when the developed coal seam of tectonic coal is drilled, the instantaneous gas emission is large (Figure 9), which makes it difficult to accurately measure the gas content (Fu et al., 2008). It is generally believed that the main reason is: coal seam gas content includes loss, on-site desorption and residual gas, among which the measurement errors of on-site desorption and residual gas are negligible, and the error mainly comes from the calculation of the loss; when drilling a developed coal seam of tectonic coal to measure the gas content, the rapid expansion of the coal micro-cracks makes the relatively closed original cracks and pores communicate and connect, resulting in that the instantaneous gas desorption rate in the coal is great, and the instantaneous amount of escape is large, so accurately calculating the gas loss of tectonic coal is a difficult point in the determination of coal seam gas content.

Domestic and foreign scholars have done a lot of research on the problem of loss compensation in the process of gas content determination (Qi et al., 2007; Liu et al., 2013; Song et al., 2021; Yi et al., 2022). The established empirical/semi-

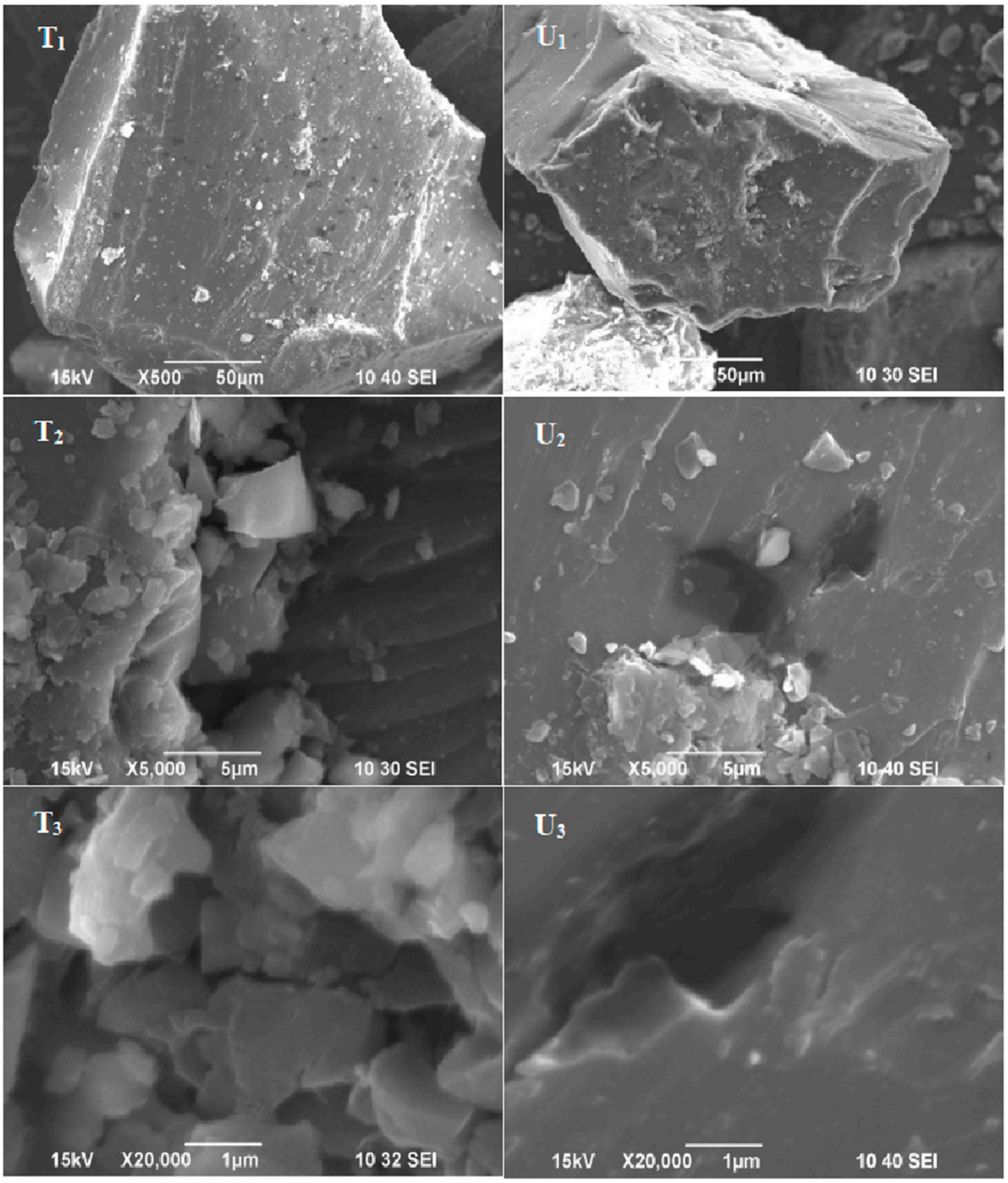

FIGURE 10
SEM images comparing morphological features of fat coal rank tectonic/untectonic coal (modified from Gao., 2011). Note: T_1, T_2, and T_3 are tectonic coal samples; U_1, U_2, and U_3 are untectonic coal samples.

empirical loss calculation formula plays an important role in revealing the gas desorption law and calculating the gas loss, but it also has certain limitations. For example, the error of Barrel's formula increases with the extension of desorption time; the Venter formula conforms to the law of initial gas desorption, but the error increases with the extension of desorption time; the Bott formula is inconsistent with the initial desorption amount of gas; the exponential formula is the basis for determining the gas content of the coal seam by the underground desorption method of coal mines in China, but when the measured coal seam is of tectonic coal, the calculated gas loss has a large deviation from the actual value. In recent years, China has reported many studies on gas desorption law and gas loss. For example, He (2010) has obtained the influence coefficient of temperature on gas desorption of tectonic coal through regression analysis of gas desorption of tectonic coal at different temperatures $\eta = \exp\,[0.012\cdot(T\text{-}10)]$, and then obtains the calculation formula $Q_T = \eta\cdot Q_{10}$ of gas loss at different temperatures; Li (2010) has investigated the effects of desorption empirical formulas, desorption time and

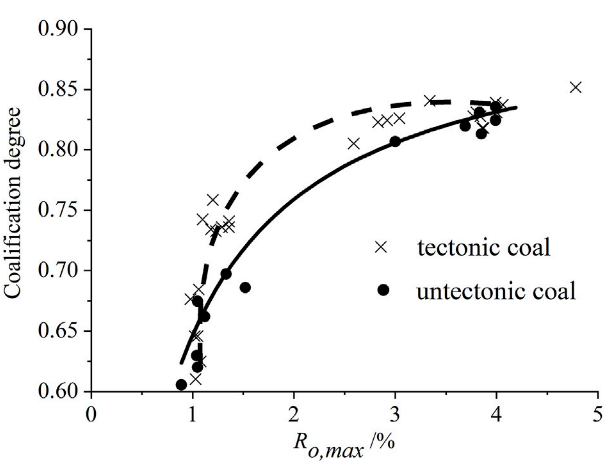

FIGURE 11
Relationship between coalification degree and average maximum reflectance of vitrinite ($R_{o,max}$) of different types coal (modified from Zhang et al., 2016).

desorption temperature on the gas desorption amount, and consideres that $Q_{T(t)}= \exp\,[0.011\cdot(T\text{-}20)]\ K\cdot\sqrt{t}$ is applicable to the calculation of gas loss when the desorption temperature changes; Li et al. (2013) have believed that the Vent method has good stability and reliability in calculating the gas loss of tectonic coal.

Based on the relationship between the residual gas volume (W_C, ml/g) and gas pressure (P, Mpa), remaining in the Changcun mine's tectonic coal and co-existing untectonic coal after being exposed for a certain period of time, the research group has established the following content-pressure calculation formula (Xie., 2014):

$$\begin{cases} \text{untectonic: } W_c = 11.483P^{0.4491},\ (R^2 = 0.9787, 0 \le t < 30\text{ min}) \\ \text{untectonic: } W_c = 4.6927\ln P + 10.949,\ (R^2 = 0.9835, 30\text{ min} \le t < 1\text{h}) \\ \text{tectonic: } W_c = 10.51P^{0.4603},\ (R^2 = 0.97710 \le t < 30\text{ min}) \\ \text{tectonic: } W_c = 4.3722\ln P + 9.7734,\ (R^2 = 0.9849, 30\text{ min} \le t < 1\text{h}) \end{cases} \tag{1}$$

After on-site inspection, it is considered that the proposed calculation method of gas loss, that is, the method of calculating gas content from residual gas, is accurate and reliable.

Understand the methane adsorption capacity and behavior characteristics of tectonic coal from the structure-property relationship

The complex structure and heterogeneity of tectonic coal make it difficult to accurately characterize the influence of various factors on its adsorption capacity and behavior, so people are more inclined to use the academic thought "structure-property" to explore its structural relationship. The adsorption properties of coal are not only related to the physical properties such as specific surface area and pore size distribution (Wang et al., 2018), its surface chemical structure/composition also has an important influence on the adsorption behavior. The essence of the difference in the methane adsorption capacity and behavior characteristics of coal with different coal structureis differences in physicochemical structure of coal, which is initiated by different degrees of brittle cracking, crushing or ductile deformation or superimposed failure of primary structure of tectonic coal under the action of one or more periods of tectonic stress.

Xu et al. (2010) observed the surface structure of briquette with different particle sizes, noticing that the smaller the particle size of briquette samples was, the higher the degree of pore development was, and the shear strength decreased with the increase of particle size; adsorption experiments showed that the briquette made of large particle size coal powder had larger porosity, better connectivity and permeability. Li et al. (2003) investigated the pore structure of tectonic coal in China's Pingdingshan mining area by Mercury intrusion and found that compared with co-existing non-tectonic coal, the porosity of tectonic coal was 3–8 times higher and the specific surface area was 2–10 times higher. Among them, brittle deformed coal had higher porosity, large specific surface area and wider cracks, while ductile deformed coal had supramaximal specific surface area and narrow cracks. The introduction of High Resolution Transmission Electron Microscopy (HRTEM) technology has facilitated the identification of nano-scale pores in coal, which is considered to be the main storage space for coalbed methane (Song et al., 2019; Song et al., 2020). HRTEM results of different types of tectonic coals show: from brittle deformed coal to ductile deformed coal, the cumulative pore volume, total specific surface area and nitrogen adsorption increase rapidly with the increase of deformation degree (Ju et al., 2005). Li et al. (2012) discussed the influence of deformation of different mechanisms on the coal macromolecules-nano-scale pore structure, and established a coupling model of tectonic coal macromolecules-nano-scale pore structure, believing that the change of the macromolecular structure of coal during the formation of tectonic coal is the main reason for the change of the nano-scale pore structure of coal. Our research group has observed the surface morphology of tectonic coal/symbiotic untectonic coal with Scanning Electronic Microscopy (SEM), finding that as shown in Figure 10, micro-pores on the inner surface of tectonic coal are prevalent, and compared with untectonic coal, it has a more complex pore structure (Gao. 2011). It is considered that the change of coal macromolecular structure caused by tectonic extrusion and shearing promotes the development of coal microporous structure, which is the main space for methane adsorption and diffusion. This is consistent with the research on the correlation between the ultrastructure of tectonic coal and chemical/physical coalification carried out by Ju and Li, 2009.

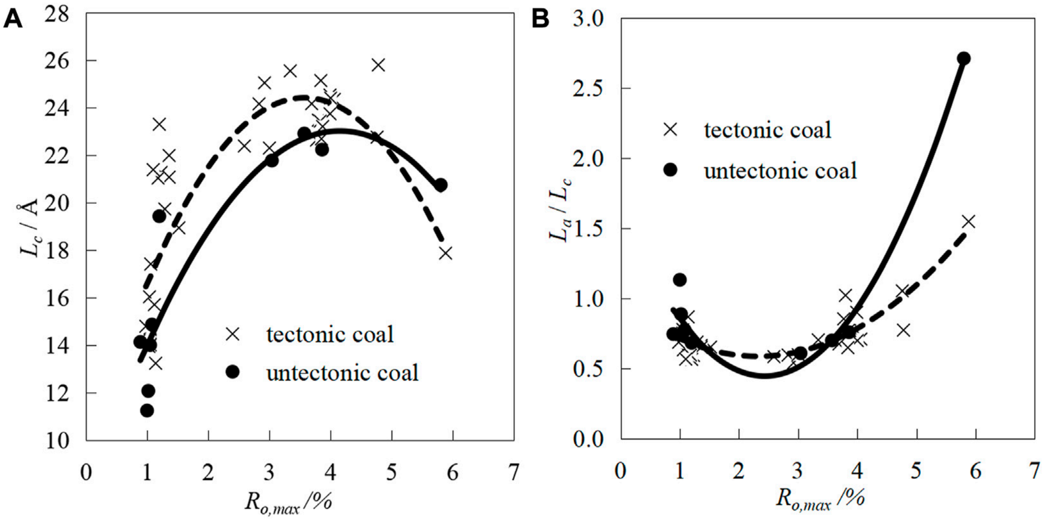

FIGURE 12
Growth characteristics of microcrystalline structure of tectonic coal and untectonic coal: **(A)** Relation between L_c and $R_{o,\max}$, **(B)** Relation between L_a/L_c and $R_{o,\max}$ (modified from Zhang et al., 2016).

Adsorption will occur on the new surface generated by the deformation and rupture of the coal, combining the genesis and physical properties of tectonic coal, our research group believes that adsorption is involved in the formation process of tectonic coal (Zhang and Y, 2014). It is expressed as: during the formation of tectonic coal, the structure of coal is broken and pulverized, increasing the pore space and inner surface area of coal, and providing more space for methane accumulation; the gas adsorption causes the expansion and deformation of the coal rock, which generates the change of the pore structure of the coal rock. Methane in coal is mainly in the adsorbed state, and compared with the symbiotic untectonic coal, the microstructure characteristics of tectonic coal show: on the one hand, the development of micro-cracks and pore structures in tectonic coal provides space for gas accumulation, which may increase the gas storage capacity of coal (Qu, 2011); on the other hand, the tectonic coal structure evolves in advance (Figure 11), and the aromatic layers of coal nuclei are stacked vertically and stretched horizontally (Figure 12), which may enhance the adsorption capacity of coal (Zhang et al., 2016), and the difference in adsorption capacity of methane should be one of the reasons for the prominent danger of tectonic coal. In addition, in terms of nature that making tectonic coal prone to trigger coal and gas outbursts, adsorption behavior aggravates the fragmentation of the coal structure, and while reducing the coal strength, new pore spaces and inner surfaces may be formed to accumulate more gas; the coal shrinkage after gas discharge can cause pressure relief. The uneven distribution of gas in the coal seam will cause uneven distribution of stress, and the release of adsorption behavior will constitute a potential driving force for starting and promoting coal and gas outbursts.

Conclusion

The research on the methane adsorption capacity and behavior characteristics of tectonic coal is of great significance to the production practice activities, such as coalbed methane resource exploration (energy development) and mine gas outburst (safety mining). Combing with the author’s long-term exploration and practice in the study of structural composition of tectonic coal and structure relationship of coal-methane adsorption, in this paper, the author summarized recent-years’ researches on adsorption capacity and behavior of tectonic coal-methane at home and abroad from the dispute of adsorption ability determination, the thermodynamic characterization of methane adsorption capacity, and the methane adsorption behavior of quantum chemical calculation of the adsorption and the gas content calculation based on loss compensation, respectively. It is believed that the coal structure controls the methane adsorption capacity and behavior characteristics of different tectonic coals, and from the perspective of thermodynamics, the adsorption capacity of different types of coals can be better distinguished. In the future, a more scientific and complete quantum chemical calculation of methane adsorption by tectonic coal and a compensation method based on instantaneous emission loss should be established, so as to better reveal the methane adsorption behavior of tectonic coal and the mechanism of coal and gas outburst. It is hoped that we can share and communicate, and promote further research on the adsorption of tectonic coal, so as to provide scientific reference for the prevention and control of outburst coal seam gas disasters and the improvement of coalbed methane recovery.

Author contributions

HZ: data curation, formal analysis, writing—original draft. XZ: conceptualization, data curation, supervision. YZ: conceptualization, funding acquisition, supervision. ZW: supervision.

Funding

This work was supported by the National Science and Technology Major Projects of China (No. 2016ZX05067006).

Conflict of interest

The authors declare that the research was conducted in the absence of any commercial or financial relationships that could be construed as a potential conflict of interest.

Publisher's note

References

Aguado, M. B. D., and Nicieza, C. G. (2007). Control and prevention of gas outbursts in coal mines, Riosa-Olloniego coalfield, Spain. *Int. J. Coal Geol.* 69, 253–266. doi:10.1016/j.coal.2006.05.004

Cao, Y. X., Davis, A., Liu, R., Liu, X. W., and Zhang, Y. G. (2003). The influence of tectonic deformation on some geochemical properties of coals—A possible indicator of outburst potential. *Int. J. Coal Geol.* 53, 69–79. doi:10.1016/S0166-5162(02)00077-0

Chen, C. G., Wei, X. W., and Xian, X. F. (2000). AB intio study on the interaction between CH_4 and the coal surface. *J. chongqing Univ. Sci. Ed.* 23, 77–80. doi:10.3969/j.issn.1000-582X.2000.03.021

Cheng, Y. P., and Pan, Z. J. (2020). Reservoir properties of Chinese tectonic coal: A review. *Fuel* 260, 116350. doi:10.1016/j.fuel.2019.116350

Crawford, R. J., and Mainwaring, D. E. (2001). The influence of surfactant adsorption on the surface characterisation of Australian coals. *Fuel* 80, 313–320. doi:10.1016/S0016-2361(00)00110-1

Dong, J. (2019). *Gas diffusion properties of coal mass based on equivalent physical structure and its application*. PHD thesis. CHINA: China University of Mining and Technology.

Fu, X., Wang, K. J., and Yang, T. H. (2008). Gas irradiation feature of tectonic coa. *J. China Coal Soc.* 33, 775–779. doi:10.3321/j.issn:0253-9993.2008.07.011

Gao, F. (2011). *Study on the microstructure and methane adsorption of deformed coal*. Master's thesis. CHINA: Henan Polytechnic University.

Han, Y. Z., Wang, J., Dong, Y. J., Hou, Q. L., and Pan, J. N. (2017). The role of structure defects in the deformation of anthracite and their influence on the macromolecular structure. *Fuel* 206, 1–9. doi:10.1016/j.fuel.2017.05.085

He, Z. G. (2010). *Study on the effect of temperature on the desorption law of tectonic coal gas*. Master's thesis. China: Henan Polytechnic University.

Hu, P. H., Shao, S. Y., Sun, Y. F., and Dong, L. H. (2016). Study on emission and adsorption characteristics of tectonic coal and original-structure coal. *China Min. Mag.* 25, 156–163. doi:10.3969/j.issn.1004-4051.2016.04.033

Huan, X., Zhang, X. B., and Wei, H. W. (2015). Research on parameters of adsorption potential via methane adsorption of different types of coal. *J. China Coal Soc.* 40, 1859–1864. doi:10.13225/j.cnki.jccs.2014.1220

Ji, H. J., Li, Z. H., Peng, Y. J., Yang, Y. L., and Zhou, Y. B. (2015). Analysis of extracts and effects of them on methane adsorption characteristics of coal. *J. China Coal Soc.* 40, 856–862. doi:10.13225/j.cnki.jccs.2014.3021

Jian, K., Zhang, Y. G., He, S. P., and Gao, C. R. (2014). The surface energy of methane adsorption of tectonic coal. *Coal Geol. Explor.* 42, 31–34. doi:10.3969/j.issn.1001-1986.2014.01.007

Jiang, B., Li, M., Qu, Z. H., Liu, J. G., and Li, W. (2016). Current research status and prospect of tectonically deformed coal. *Adv. Earth Sci.* 31, 335–346. doi:10.11867/j.issn.1001-8166.2016.04.0335

Jiang, B., Qin, Y., Ju, Y. W., Wang, J. L., and Li, M. (2009). The coupling mechanism of the evolution of chemical structure with the characteristics of gas of tectonic coals. *Earth Sci. Front.* 16, 262–271. doi:10.1016/S1003-6326(09)60084-4

Jing, W. (2010). Molecular simulation of adsorption and diffusion of methane in deformed coal. China Taiyuan Polytechnic University. Master' thesis.

Ju, Y. W., Jiang, B., Hou, Q. L., and Wang, G. L. (2004). The new structure-genetic classification system in tectonically deformed coals and its geological significance. *J. China Coal Soc.* 5, 513–517. doi:10.3325/j.cnki.Jccs.2004.05.001

Ju, Y. W., Jiang, B., Hou, Q. L., Wang, G. L., and Fang, A. (2005). Structural evolution of nano-scale pores of tectonic coals in Southern North China and its mechanism. *Acta Geol. Sin.* 79, 269–285. doi:10.3321/j.issn:0001-5717.2005.02.013

Ju, Y. W., Jiang, B., Hou, Q. L., Tan, Y. J., Wang, G. L., and Xiao, W. J. (2008). Behavior and mechanism of the adsorption/desorption of tectonically deformed coals. *Chin. Sci. Bull.* 54, 88–94. doi:10.1007/s11434-008-0412-4

Ju, Y. W., and Li, X. S. (2009). New research progress on the ultrastructure of tectonically deformed coals. *Prog. Nat. Sci.* 19, 1455–1466. doi:10.1016/j.pnsc.2009.03.013

Li, H. (2010). *Experimental study on the effect of ambient temperature on the gas desorption law of granular coal*. Master's thesis. China: Henan Polytechnic University.

Li, H. Y., Ogawa, Y., and Shimada, S. (2003). Mechanism of methane flow through sheared coals and its role on methane recovery. *Fuel* 82, 1271–1279. doi:10.1016/S0016-2361(03)00020-6

Li, X. S., Ju, Y. W., Hou, Q. L., and Lin, H. (2012). Spectra response from macromolecular structure evolution of tectonically deformed coal of different deformation mechanisms. *Sci. China Earth Sci.* 55, 1269–1279. doi:10.1007/s11430-012-4399-y

Li, Y. B., Zhang, Y. G., Zhang, Z. M., and Jiang, B. (2013). Experimental study on gas desorption of tectonic coal at initial stage. *J. China Coal Soc.* 38, 16–20. doi:10.13225/j.cnki.jccs.2013.01.017

Li, W., Jiang, B., and Zhu, Y. M. (2019). Impact of tectonic deformation on coal methane adsorption capacity. *Adsorpt. Sci. Technol.* 37, 698–708. doi:10.1177/0263617419878541

Lin, J., Cheng, Y. P., Ren, T., Liu, Q. Q., and Tu, Q. Y. (2022). New insights into failure behaviors of tectonic coal under triaxial conditions using reconstituted coal specimens. *Rock Mech. Rock Eng.* 55, 1361–1374. doi:10.1007/s00603-021-02715-5

Liu, Y. W., Wei, J. P., He, Z. G., and Liu, M. j. (2013). Influence rules and mechanisms of temperature on dynamic process of gas diffusion from coal particles. *J. China Coal Soc.* 38, 100–105. doi:10.13225/j.cnki.jccs.2013.s1.042

Pan, J. N., Hou, Q. L., Ju, Y. W., Bai, H. L., and Zhao, Y. Q. (2012). Coalbed methane sorption related to coal deformation structures at different temperatures and pressures. *Fuel* 102, 760–765. doi:10.1016/j.fuel.2012.07.023

Qi, L. M., Zhao, Y. Q., Wang, Y. B., Song, X. Y., and Liu, D. M. (2007). Analysis on the gas pressure measurement result revision on the basis of gas loss quantity before bore being sealed. *J. China Coal Soc.* 32, 60–63. doi:10.3321/j.issn:0253-9993.2007.01.013

Qu, Z. H., Jiang, B., Wang, J. L., and Li, M. (2015). Micropore properties and its origin of tectonically deformed coals. *J. China Coal Soc.* 40, 1093–1102. doi:10.13225/j.cnki.jecs.2014.0900

Qu, Z. H. (2011). Study of tectonized coal texture and its controlling mechanism on gas properties. *J. China Coal Soc.* 36, 533–534. doi:10.13225/j.cnki.jccs.2011.03.032

Song, H. R., Lin, B. Q., Zhong, Z., and Liu, T. (2021). Experimental study on methane diffusion kinetics in three typical metamorphic coals. *Fuel* 311, 122601. doi:10.1016/j.fuel.2021.122601

Song, Y. (2019). *Evolution mechanism of nano-pore and macromolecule in low, medimum-rank tectonically deformed coals*. PHD thesis. CHINA: China University of Mining and Technology.

Song, Y., Jiang, B., Li, M., Hou, C. L., and Mathews, J. P. (2019). Macromolecular transformations for tectonically-deformed high volatile bituminous via HRTEM and XRD analyses. *FUEL* 263, 116756. doi:10.1016/j.fuel.2019.116756

Song, Y., Jiang, B., Li, M., Hou, C. L., and Xu, S. C. (2020). A review on pore-fractures in tectonically deformed coals. *FUEL* 278, 118248. doi:10.1016/j.fuel.2020.118248

Song, Y., Jiang, B., Li, M., Liu, J. G., and Liu, H. W. (2017). Super critical CH_4 adsorption characteristics and applicability of adsorption models for low, middlerank tectonically deformed coals. *J. China Coal Soc.* 42, 2063–2073. doi:10.13225/j.cnki.jecs.2016.1853

Tu, Q. Y., Cheng, Y. P., Xue, S., and Ren, Ting. (2022). Effect of particle size on gas energy release for tectonic coal during outburst process. *Fuel* 307, 121888. doi:10.1016/J.FUEL.2021.121888

Wang, Y. A., Tao, Y. M., Wang, K. J., and Cai, C. G. (1993). The deformation and force based on coal/gas adsorption. *Saf. Coal Mines* 6, 19–26. doi:10.13347/j.cnki.mkaq.1993.06.005

Wang, J. R., Deng, C. B., and Deng, H. Z. (2008). Study on the microcosmic mechanism for coal-gas outburst. *J. China Coal Soc.* 33, 131–135. doi:10.3325/j.cnki.jccs.2008.02.016

Wang, B. J., Ling, L. X., Zhao, Q. Y., Zhang, R. G., and Xie, K. C. (2009). Design method of the new Chinese nation surname system. *Syst. Eng. - Theory & Pract.* 60, 188–192. doi:10.1016/S1874-8651(10)60079-8

Wang, X. H., Wang, Y. B., Gao, S. S., Hong, P. F., and Zhang, M. J. (2012). Differences in pore structures and absorptivity between tectonically deformed and undeformed coals. *Geol. J. China Univ.* 03, 528–532. doi:10.16108/j.issn1006-7493.2012.03.003

Wang, B. J., Zhang, L. N., Ling, L. X., and Zhang, R. G. (2016). Effects of coal molecular structure on adsorption and diffusion behaviors of coalbed methane. *CIESC J.* 67, 2549–2557. doi:10.11949/j.issn.0438-1157.20151780

Wang, Z. Z., Pan, J. N., Hou, Q. L., Yu, B. S., Li, M., and Niu, Q. H. (2018). Anisotropic characteristics of low-rank coal fractures in the Fukang mining area, China. *Fuel* 211, 182–193. doi:10.1016/j.fuel.2017.09.067

Wang, Z. Z., Fu, X. H., Deng, Z., and Pan, J. N. (2021a). Investigation of adsorption–desorption, induced strains and permeability evolution during N2–ECBM recovery. *Nat. Resour. Res.* 30, 3717–3734. doi:10.1007/S11053-021-09884-8

Wang, Z. Z., Fu, X. H., Hao, M., Li, G. F., Pan, J. N., Niu, Q. H., et al. (2021b). Experimental insights into the adsorption-desorption of CH_4/N_2 and induced strain for medium-rank coals. *J. Petroleum Sci. Eng.* 204, 108705. doi:10.1016/j.petrol.2021.108705

Wei, H. W. (2012). *Experimental study on gas loss quantity of tecnonic coal*. Master's thesis. CHINA: Henan Polytechnic University.

Wold, M. B., Connell, L. D., and Choi, S. K. (2007). The role of spatial variability in coal seam parameters on gas outburst behaviour during coal mining. *Int. J. Coal Geol.* 75, 1–14. doi:10.1016/j.coal.2008.01.006

Xie, X. X. (2014). *Experimental study on gas loss quantity of tecnonic coal*. Master's thesis. CHINA: Henan Polytechnic University.

Xu, J., Liu, D., Peng, S. J., Wu, X., and Lu, Q. (2010). Experimental research on influence of particle diameter on coal and gas outbursts. *Chin. J. Rock Mech. Eng.* 6, 1231–1237. doi:10.1016/S1876-3804(11)60004-9

Yan, J. W., Zhang, X. B., and Zhang, Z. M. (2013). Research on geological control mechanism of coal-gas outburst. *J. China Coal Soc.* 38, 1174–1178. doi:10.13225/j.cnki.jccs.2013.07.025

Yang, H., Bi, W. Y., Zhang, Y. G., Y, J. K., Yan, J. W., Lei, D. J., et al. (2021). Effect of tectonic coal structure on methane adsorption. *J. Environ. Chem. Eng.* 9, 106294. doi:10.1016/J.JECE.2021.106294

Yi, M. H., Wang, L., Cheng, Y. P., Wang, C. H., and Hu, B. (2022). Calculation of gas concentration-dependent diffusion coefficient in coal particles: Influencing mechanism of gas pressure and desorption time on diffusion behavior. *Fuel* 320, 123973. doi:10.1016/J.FUEL.2022.123973

Zhang, L. P., Su, X. B., and Zeng, R. S. (2006). Discussion on the controlling effects of coal properties on coal adsorption capacity. *Acta Geol. Sin.* 80, 910–915. doi:10.3321/j.issn:0001-5717.2006.06.013

Zhang, Y. G., Zhang, Z. M., and Cao, Y. X. (2007). Deformed-coal structure and control to coal-gas outburst. *J. China Coal Soc.* 03, 281–284. doi:10.3321/j.issn:0253-9993.2007.03.013

Zhang, X. B., Wang, W., Zhang, Y. G., Gao, F., and Huan, X. (2016). Oriented growth mechanism of tectonic coal microcrystal. *J. china coal Soc.* 41, 712–718. doi:10.13225/j.cnki.jccs.2015.0373

Zhang, X. B., Huan, X., Zhang, H., and Zhang, Y. G. (2017). Microstructure and methane adsorption of coal-based activated carbons with different coal body structure. *J. China Univ. Min. Technol.* 46, 155–161. doi:10.13247/j.cnki.jcumt.000628

Zhang, H., Zhang, X. B., Zhang, Y. G., and Lei, D. J. (2018). Study on acidic oxygen group and its methane adsorption inhibition of Yima lignite methane maceral composition. *J. china Univ. Min. Technol.* 47, 1149–1156. doi:10.13247/j.cnki.jcumt.000930

Zhang, H., Zhang, Y. G., Lei, D. J., and Jiao, Y. Q. (2021). Characterization of structure of kaolinite in tectonically deformed coal: Evidence of mechanochemistry. *Energy Sources Part A Recovery Util. Environ. Eff.* 5, 1–12. doi:10.1080/15567036.2021.1910751

Zhang, Q. H., Liu, X. F., Nie, B. S., Wu, W. B., and Wang, R. (2022). Methane sorption behavior on tectonic coal under the influence of moisture. *Fuel* 327, 125150. doi:10.1016/j.fuel.2022.125150

Zhang, X. B., and Y, J. W. (2014). Physical conditions and process of forming gas outburst coal. *J. Saf. Sci. Technol.* 11, 48–53. doi:10.11731/j.issn.1673-193x.2014.11.008

Zhou, L., and Zhou, Y. P. (1998). Linearization of adsorption isotherms for high pressure applications. *Chem. Eng. Sci.* 53, 2531–2536. doi:10.1016/S0009-2509(98)00065-7

frontiers | Frontiers in Earth Science

TYPE Review
PUBLISHED 09 January 2023
DOI 10.3389/feart.2022.1021983

OPEN ACCESS

EDITED BY
Zhenzhi Wang,
Henan Polytechnic University, China

REVIEWED BY
Haihai Hou,
Liaoning Technical University, China
Run Chen,
China University of Mining and Technology, China
Daping Xia,
Henan Polytechnic University, China

*CORRESPONDENCE
Xiaoying Lin,
linxiaoying@zzu.edu.cn

SPECIALTY SECTION
This article was submitted to Economic Geology,
a section of the journal
Frontiers in Earth Science

RECEIVED 18 August 2022
ACCEPTED 22 September 2022
PUBLISHED 09 January 2023

CITATION
Lin X, Liu C and Wang Z (2023), The influencing factors of gas adsorption behaviors in shale gas reservoirs.
Front. Earth Sci. 10:1021983.
doi: 10.3389/feart.2022.1021983

The influencing factors of gas adsorption behaviors in shale gas reservoirs

Xiaoying Lin*, Caijie Liu and Zhirong Wang

School of Water Conservancy Engineering, Zhengzhou University, Zhengzhou, China

The adsorption state is one of the main states for shale gas occurrence, and the gas adsorption behavior in shale directly affects shale gas content under reservoir conditions. This paper provides a comprehensive literature review on shale gas adsorption behavior and its affecting factors that have been developed in recent years. Influence factors of gas adsorption behavior are examined, including total organic carbon content (TOC), organic matter type, organic matter maturity, minerals and clay minerals, moisture content, pore characteristics and other characteristics of the shale itself. The characteristics of gas adsorption behavior under high temperature and pressure conditions showed that adsorption behaviors were difficult to describe by the Langmuir equation. This review indicates that shale contains higher organic matter content and organic matter maturity and has a higher adsorption capacity. The adsorption capacity with type III kerogen is higher than that for type II or type I. Clay minerals can provide free space for gas adsorption and promote adsorption. Normally, as the moisture content increased, adsorption capacity decreased. Micro pores provided a larger specific surface area for gas adsorption. As the temperature increased, the adsorption capacity decreased. As the pressure increased, shale adsorption characteristics showed two different behaviors as follows: one obeyed the Langmuir equation, and the other presented an inverted, U-shaped, single-peak distribution. However, there are some controversies surrounding adsorption, especially regarding the aspects of clay minerals, water content, pore characteristics, etc. The key is that the mechanism of adsorption in shale is unclear. There will be many new challenges in the field of shale gas adsorption research. Such challenges include studying the organic matter chemical structure, understanding the interaction between organic matter and clay minerals and how they affect adsorption, clarifying gas adsorption behavior changes, predicting favorable areas of adsorbed gas with the coupling of reservoir temperature and pressure, and building a better theory and model of shale gas adsorption.

KEYWORDS

shale gas, adsorption behavior, organic matter, pore characteristics, moisture content, clay minerals, temperature, pressure

1 Introduction

With the increasing worldwide demand of natural gas, shale gas, as a new and unconventional natural gas resource, has attracted more and more attention. In the United States. Energy Information Administration's International Energy Outlook 2016 and Annual Energy Outlook 2016, global shale gas is expected to account for 30% of the world's total natural gas output by the end of 2040. At present, commercial development of shale gas has been achieved in the United States, Canada, Argentina and China. The United States successfully drilled the first shale gas well in the Appalachian Basin in 1821 and shale gas production has continued to develop for the last 200 ears. In the 21st century, shale gas production has increased rapidly in the United States. That production reached $3{,}800\times10^8\ m^3$ in 2015, accounting for more than half of total natural gas production. The rapid development of shale gas production has changed the US natural gas supply pattern, leading to significant drops in natural gas and liquefied natural gas imports (Zhang, 2012). Since 2005, China has evaluated geological conditions and conducted development tests for shale gas. Now, China has made significant breakthroughs in geological theory, exploration and development techniques (Dong et al., 2012), especially in the study of marine and continental organic-rich shales in the southern Paleozoic/northern Mesozoic areas of the Sichuan Basin, the Triassic area in the Ordos Basin, as well as several other regions and ages (Zou et al., 2010; Lin et al., 2012; Ren et al., 2014; Yu et al., 2014), and has made great progress in geological characteristics with rich organic, formation, occurrence and reservoir conditions, prospective zone optimization for shale gas, etc. In the past 5 years, more than 700 shale gas wells have been drilled in China. Shale gas production surpassed $50\times10^8\ m^3$ in 2016. Shale gas is primarily a natural gas preserved in dark mud and high carbonaceous shale (Yang et al., 2014a). Zhang et al. (2008) showed that adsorbed gas and free gas are mainly states. The adsorption effect is one important mechanism of shale gas accumulation. Mavor, 2003 showed that adsorbed gas accounts for 61% of original geological reserves of shale gas in the Barnett Formation. Li et al. (2007) showed that adsorbed shale gas occupies at least 40% of the total gas content. Nie and Zhang, 2010 and Rani et al. (2015) reported that 40%–60% of gas is adsorbed. According to Barnett shale gas characteristics, shale gas is stored in matrix pores and accounts for more than 50% of the total gas content (Montgomery et al., 2005; Bowker, 2007; Kinley et al., 2008). It has been shown that shale gas occurs primarily in the adsorption state, free state or dissolved state; of these, adsorption state is the most important. Adsorbed gas accounts for 20%–85% of the total shale gas content, which mainly accounts for 40%–60% (Mavor, 2003; Li et al., 2007; Zou et al., 2011; Chareonsuppanimit et al., 2012). Therefore, adsorption capacity of shale is one of the key factors that affect shale gas content. In recent years, with the large-scale development of shale gas, shale gas exploration depths are increasing. Exploration depths have increased from 180–2000 m to 2,300–4,500 m, and have reached up to 6,000 m in individual basins in America (Nie and Zhang, 2010). In China, the Weiyuan-Changning gas field was the first to realize commercialized production, Cambrian-Ordovician shale has a depth of 1,500–4,500 m (Zou et al., 2016). The adsorption behavior in shale directly affects adsorption gas content with increasing burial depth, which becomes the key to obtaining more accurate information on the amount of shale gas resources, and has an important significance for shale gas reserve evaluation, reserve prediction and productivity predictions.

Therefore, the estimation of initial adsorbed gas in place is one of the primary concerns in shale gas reservoir studies, and it is also important for reservoir-engineering analysis, such as gas production forecasting (Wu et al., 2012; Li et al., 2016).

In this review, based on previous research results, influencing factors of adsorption capacity in shale are summarized, effects of different factors on adsorption capacity are analyzed in detail, a main adsorption theory and adsorption model is noted, and challenges and development prospects associated with the field of shale gas adsorption are put forth.

2 Change of gas adsorption behaviors on shale

In the current environment of rapid changing climate conditions and increasing human activities, meteorological and hydrological conditions may change. Bernaola Galvan proposed a heuristic segmentation algorithm (BG algorithm) in 2001 (Bernaola-Galvan et al., 2001), which can test the stationary status of the sequence, detect the mutation point, and divide the non-stationary sequence into several stationary sequences. The main ideas are as follows:

Adsorption is a phenomenon by which gas molecules remain attached or retained on the surface of a solid substance when a gas interacts with a solid. The gas molecules remain attached on the surface of a solid by molecular attraction. The attraction of gas adsorption in shale reserves is mainly Van der Waals force. Therefore, the adsorption process is reversible and is called physisorption. Adsorption depends on temperature, pressure, specific surface area and activation energy of solid. In a given system of gas-solid, the activation energy of a solid is certain, and the adsorption volume is a function related to pressure when temperature is fixed. The relationship is called adsorption isothermal, which is often used to describe a change in adsorption behaviors. The isothermal of gas adsorption in shale can be divided into two types. Type I is Langmuir pattern. With the increase of pressure, the adsorption volume first increases, eventually reaches a maximum value, which is represented by the Langmuir volume constant, and then

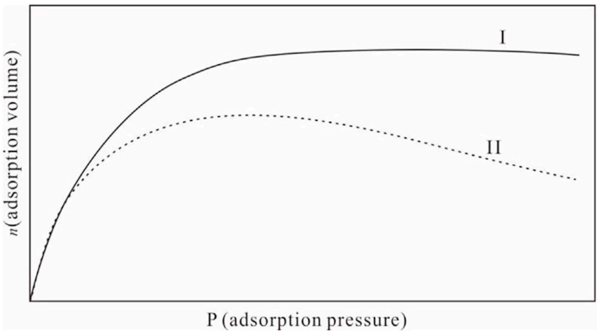

FIGURE 1
Types of adsorption isotherms on shale.

stabilizes. The relationship between adsorption volume and pressure conforms to the Langmuir equation (Figure 1) (Lu et al., 1995; Ross and Bustin, 2007; Chalmers and Bustin, 2008; Liu and Wang, 2012). Gas adsorption needs more binding energies in low pressure. With increases of pressure, necessary binding energy decreases, and the amount of adsorption increases (Raut et al., 2007). This is the most common type of adsorption isothermal that can be explained by monolayer adsorption theory.

Type II is an inverted “U” pattern. As the pressure increases, the adsorption volume first increases but then decreases. The relationship between adsorption volume and pressure does not completely follow the Langmuir equation. This adsorption phenomenon has been found by many scholars (Chalmers and Bustin, 2008; Ross and Bustin, 2008; Chareonsuppanimit et al., 2012). We studied adsorption capacity of Permian, Triassic and Jurassic shale in the Jiyuan Depression and the Carboniferous shale in Ordos Basin and showed that with a pressure increase, the adsorption isothermal showed two kinds of changes. One change is that the relationship between the adsorption volume and pressure obeys the Langmuir equation (type I); the other is that a “single peak” adsorption phenomenon is observed (type II), and the maximum adsorption value occurs between 5 MPa and 12 MPa (Figure 2). The same conclusion has been found in the study of CH_4 and CO_2 adsorption on coal, and the maximum adsorption value appears with an increase in pressure (Type II) (Nandi and Walker, 1975; Marecka and Mianowski, 1998; Tang et al., 2003; Yu et al., 2004; Day et al., 2008; Zhang et al., 2009; Gensterblum et al., 2013). Chilev et al. (2012) indicated that the maximum gas adsorption in porous media might appear at the maximum adsorption value in the range of 10 MPa and 30 MPa above the critical temperature. Many other researchers also found a similar phenomenon (Menon, 1965; Malbrunot et al., 1992; Zhou et al., 1994; Aranovich et al., 2000; Dreisbach et al., 2002; Do and Do, 2005; Siemons and Busch, 2007). Malbrunot et al. (Malbrunot et al., 1992) and Menon, 1965 noted that the adsorption capacity reached a maximum value at 10 MPa–30 MPa with a minimum value between 550 MPa and 650 MPa as the pressure increased.

In view of this phenomenon, it is generally believed that the adsorption amount follows the Gibbs definition of adsorption.

Gibbs’ definition states that the adsorbate molecules in the adsorbed phase on the surface of the adsorbent cannot all be classified as “adsorption,” in which the gas molecule distributed in adsorbed space by way of the bulk gas density is independent of the force between the gas and solid. The adsorbed gas amount

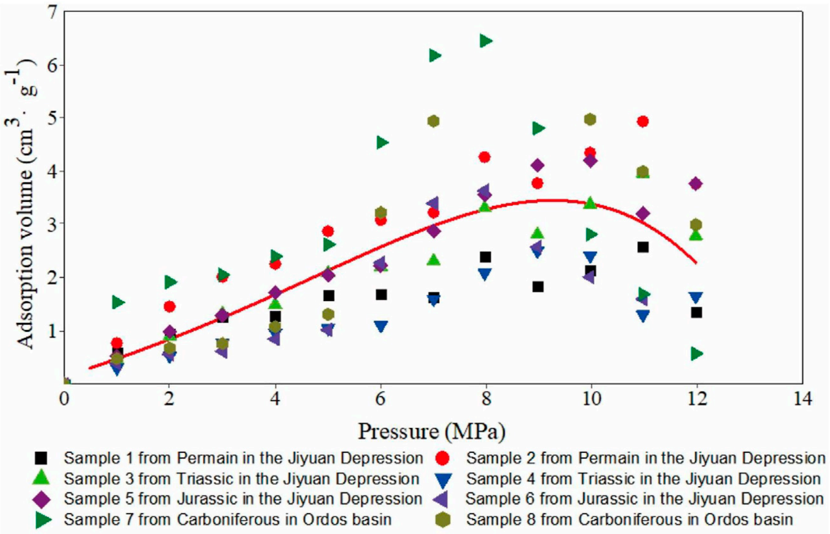

FIGURE 2
Relationship between pressure and methane adsorption volume.

is the excess amount at the interface between the two bulk phases. The absolute adsorption is a function of the bulk gas phase density and adsorbed phase density. The Gibbs adsorption is expressed as:

$$\mathbf{n} = \int (\boldsymbol{\rho}(\mathbf{z}) - \boldsymbol{\rho}_\mathbf{g})\mathbf{dV} \tag{1}$$

where $\boldsymbol{\rho}_\mathbf{g}$ is the bulk gas density in the free state; $\boldsymbol{\rho}(\mathbf{z})$ is the adsorbed phase density along the normal direction on the solid surface; and $\mathbf{n}$ is the excess adsorbed amount of substance at pressure p.

If the density function of the adsorbed phase $\boldsymbol{\rho}(\mathbf{z})$ is known, n can be obtained from Eq. 1. $\boldsymbol{\rho}(\mathbf{z})$ can be estimated by molecular simulation but cannot be determined experimentally. Another expression of $\mathbf{n}$ is

$$\mathbf{n} = \mathbf{n}_\mathbf{s} - \boldsymbol{\rho}_\mathbf{g}\mathbf{V}_\mathbf{a} = \mathbf{V}_\mathbf{a}(\boldsymbol{\rho}_\mathbf{a} - \boldsymbol{\rho}_\mathbf{g}) \tag{2}$$

where $\mathbf{n}_\mathbf{s}$ is the total amount of adsorbed gas, called the absolute amount adsorbed, and $\mathbf{V}_\mathbf{a}$ is the volume of adsorbed space (adsorbed phase volume). $\boldsymbol{\rho}_\mathbf{a}$ is the molar density of the adsorbed phase and represents the mean value of the density of the adsorbed phase.

The critical temperature of CH_4 is 190.6 K, the critical pressure is 4.54 MPa CH_4 is supercritical at room temperature and cannot be liquefied at high pressure. Therefore, the gas molecules cannot condense on the surface of solid. The force between the gas-solid is greater than the force between gas-gas. The gas adsorption is monolayer. When the gas coverage on the solid surface is low, the adsorbed gas volume increases with an increase of pressure, the gas distribution is monolayer, and the adsorption isotherm shows Type I. The distribution and amount of adsorption space determine the amount and density of the adsorbed phase, both of which are capped. The gas cannot condense, so $\boldsymbol{\rho}_\mathbf{g}$ increases with an increase in pressure. When the increasing rates of $\boldsymbol{\rho}_\mathbf{g}$ and $\boldsymbol{\rho}_\mathbf{a}$ are equivalent, the maximum adsorption value is reached. When the pressure increases further, $\boldsymbol{\rho}_\mathbf{g}$ approaches $\boldsymbol{\rho}_\mathbf{a}$, and the absolute adsorption is close to zero (Menon, 1965; Salem et al., 1998).

However, this view could not reasonably explain why a difference exists in the pressure at maximum adsorption values of different adsorbents. Some researchers explained this phenomenon based on other influencing factors. Gensterblum et al. (2013) considered that differences in the maximum values of different adsorption capacities in coal are related to coal characteristics such as temperature, moisture and adsorbed gas properties. Day et al. (2008) and Siemons and Busch, 2007 (Day et al., 2008) concluded that supercritical absorption capacities in coal are related to coal rank, porosity, moisture content and other factors; with the effect of porosity on adsorption capacity being significant. Chilev et al. (2012) believed that the appearance of an adsorption maximum value is related to the following: solid-phase deformation under high pressure, change of direction of molecular motion, filling of pores and others, but it is unknownhow these factors influence absoption maximum. Fang et al. (2010) considered that the phenomenon of an adsorption anomaly in shale is related to clay mineral content, moisture content, organic matter and supercritical adsorption characteristics. Nie and Zhang, 2010 analyzed the cause of the inverted U phenomenon for adsorption curves from the standpoint of the adsorption experiment principle, microscopic pore structures, adsorbent, etc. And concluded that the phenomenon is attributed to the difference between the experimental adsorption amount and the actual adsorption quantity. Zhang and Cao, 2003 also noted that the gas compression rate increases with increasing pressure, thereby increasing the storage capacity of free gas and resulting in a decrease in the amount of adsorption gas content.

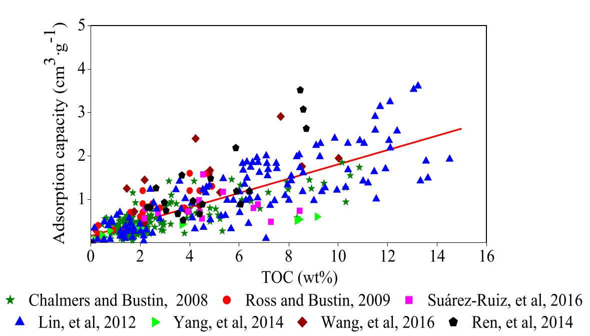

FIGURE 3
Relationship between TOC and methane adsorption capacity.

3 Influencing factors of gas adsorption behaviors

3.1 Organic matter in shale gas reservoirs

Organic matter is one of the factors that affect shale adsorption capacity. Ross and Bustin, 2009 noted that approximately 90% of methane adsorption content is related to organic matter, and approximately 10% is related to the minerals in shale. Organic matter mainly affects the adsorption capacity through organic carbon content, organic matter maturity and organic matter type.

(1) Total organic carbon content (TOC)

Current research has shown that as the TOC increases, so does the adsorption capacity of shale (Figure 3). Lu et al. (1995) demonstrated that organic matter was the primary storage media for adsorbed gas. Hill et al. (2007) showed that there is a positive

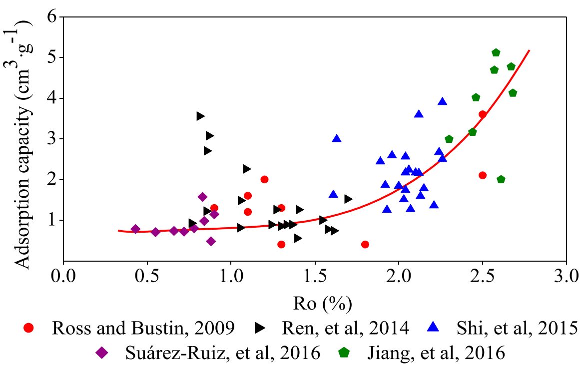

FIGURE 4
Relationship between $R_{o,max}$ and methane adsorption capacity.

linear correlation between TOC and methane adsorption capacity. Chalmers and Bustin, 2008 studied the adsorption capacity of the Lower Cretaceous shale in northeastern British Columbia and the Barnett and Barnett shale in Mitchell (T.P.Sims well); they all reached the same conclusion, that is, TOC is higher, and shale gas adsorption capacity is stronger. There are three main reasons to explain those observations. First, the TOC is higher, gas generation potential is greater, and shale gas content is higher; secondly, kerogen, with a large number of micro porosity channels and higher specific surface areas, provides more space for gas adsorption (Chalmers and Bustin, 2007; Ross and Bustin, 2009); finally, the kerogen surface is lipophilic, which favors gas adsorption. In addition, dissolution of gaseous hydrocarbons in amorphous and non-structured matrix asphalt bodies also has a significant contribution to the adsorption capacity (Wu et al., 2012; Lin et al., 2019).

(2) Organic matter maturity

In the field of shale gas adsorption, the current basic consensus is that increasing the thermal evolution degree of organic matter increases the gas adsorption capacity (Figure 4). Jiang et al. (2018) conducted isothermal adsorption tests on Barnett shale with different amounts of TOC ranging from 6.6% to 7.9% and found that adsorption capacity increased with an increase in organic maturity. This conclusion can be explained based on three properties of the TOC. The first is that thermally mature shale tends to exhibit larger micro pore volumes and larger specific surface areas than immature shale, which results in higher adsorption capacities (Chalmers and Bustin, 2007; Ross and Bustin, 2007; Chalmers and Bustin, 2008; Zhang, 2012). Second, during the stage of low-temperature evolution, a large amount of asphaltenes and colloids are generated and fill the pore space; the connectivity and porosity of pores decreases and leads to a decrease in specific surface area for gas adsorption (Franco et al., 2013). Lastly, with an increase in organic maturity, the amount of hydrogen in the organic matter decreases and enhances the aromatization of organic matter. Kerogen rich in aromatic structures has a stronger affinity for methane than kerogen with high aliphatic hydrocarbon content (Zhang, 2012). The conclusion is consistent with the gas adsorption capacity in coalbeds (Wang et al., 2018); namely, as the degree of coalification increases, the adsorption capacity of coalbed methane also increases.

(3) Organic matter type

Gas adsorption capacity in shale is complex, as shale contains a high degree of heterogeneity in its organic matter maceral composition. Maceral composition controls the organic matter type, influences the surface characteristics and the pore size distribution of shale, all of which affect the sorption capacity. Type III kerogen is mainly derived from terrestrial higher plants, and its microcosmic components are dominated by vitrinite (Hou et al., 2022). Type I kerogen is mainly derived from planktonic organisms and is mainly composed of chitin. Type III has more micro pores than type I, resulting in larger specific surface areas for gas adsorption, so adsorption capacity is stronger. The components of type II kerogen are a mixture of both types I and III. Zhang , 2012 conducted isothermal adsorption experiments with different types of kerogen and indicated that type III kerogen has the highest adsorption capacity, followed by type II and type I. Chen et al. (Chen et al., 2015) showed that the adsorption capacity of different kerogen types followed the following order: type II_2> type II_1> type I. Generally, the adsorption capacity order of different kerogen types is as follows: type II/III or type III> type I or type II (Chalmers and Bustin, 2008; Zhang, 2012; Jiang et al., 2016) (Figure 5). Chalmers and Bustin, 2007 (Chalmers and Bustin, 2008) and Wang et al. (2004) studied the adsorption capacity of the Late Cretaceous Fort St. John shale in the northeastern British Columbia and indicated that the high adsorption capacity of shale is related to the amount of vitrinite and inertinite. Vitrinite contains more micropores, i.e., more surface area, and has a positive effect on gas adsorption capacity, while liptinite contains more macropores than micropores, which has a negative effect on gas absorption (Perera et al., 2012). This means that type III kerogen has higher gas adsorption than that of type I. The kerogen types have less of an effect on adsorption compared with TOC content (Figure 5). The type I with higher TOC possibly has a larger adsorption capacity than that of type III.

3.2 Mineral and clay mineral

The mineral composition of shale is complex and includes the following: clay minerals such as illite, montmorillonite and

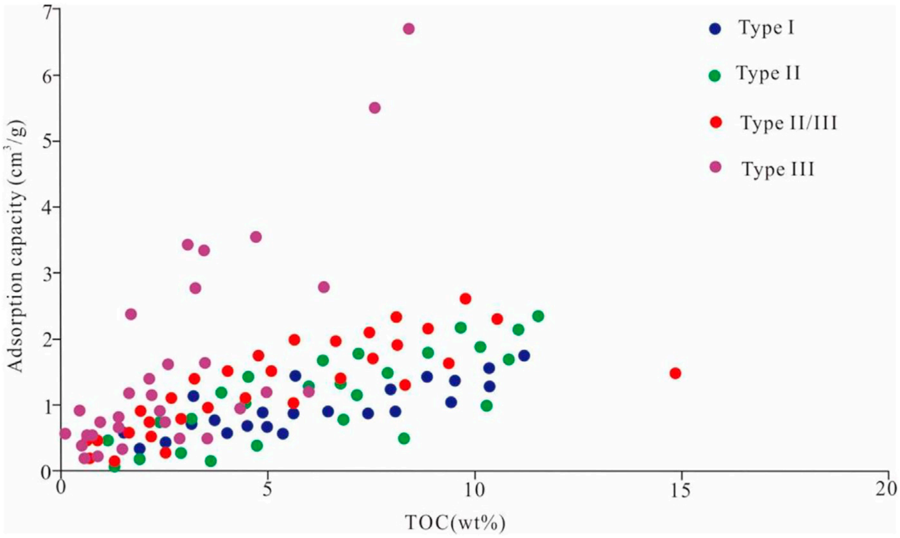

FIGURE 5
Relationship between kerogen types and methane adsorption capacity (Data from: Chalmers and Bustin, 2008; Zhang et al., 2012; Jiang et al., 2016).

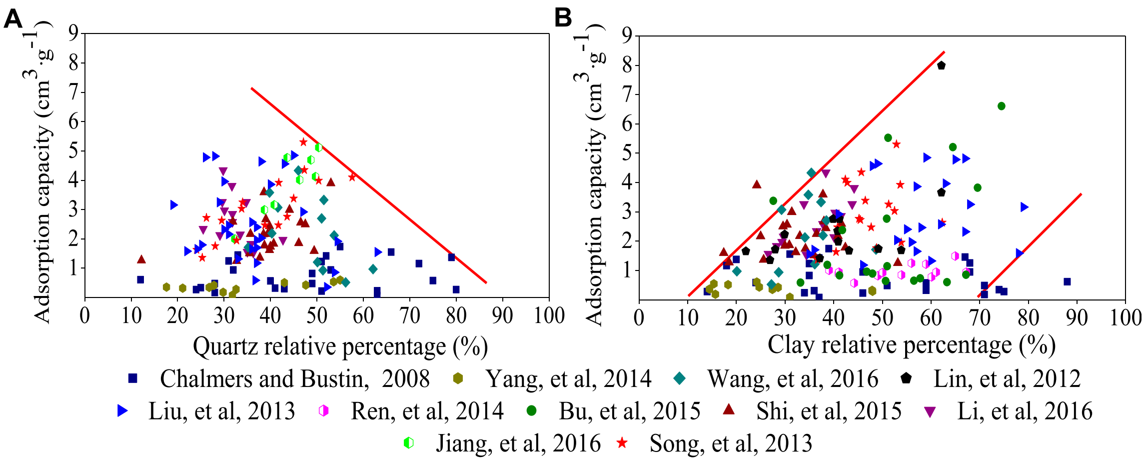

FIGURE 6
(A): Relationship between quartz and methane adsorption capacity and **(B)**: Relationship between clay minerals and methane adsorption capacity.

kaolinite; brittle minerals such as quartz, calcite, feldspar, mica and other detrital minerals and authigenic minerals. These minerals can all affect the adsorption capacity. For instance, brittle minerals can reduce porosity, which leads to a decrease of adsorption capacity and storage space of the free gas (Figure 6A) (Li et al., 2007; Loucks and Ruppel, 2007; Chalmers and Bustin, 2008). However, the presence of clay minerals is favorable for gas adsorption (Figure 6B) (Lu et al., 1995; Cheng and Huang, 2004; Wang et al., 2004; Loucks and Ruppel, 2007; Ji et al., 2012a; Ji et al., 2012b). On the one hand, micro pores with apertures of 1 nm–2 nm often exist between the crystal layers of clay minerals, which have great micro-pore volumes, large specific surface areas and are the primary sites for gas adsorption (Cheng and Huang, 2004; Wang et al., 2004; Loucks and Ruppel, 2007; Ji et al., 2012a; Ji et al., 2012b; Niu et al., 2021). On the other hand, a layer of water film can form on clay mineral surfaces due to electrochemical characteristics of the clay mineral surface, which plays an important role in methane adsorption and

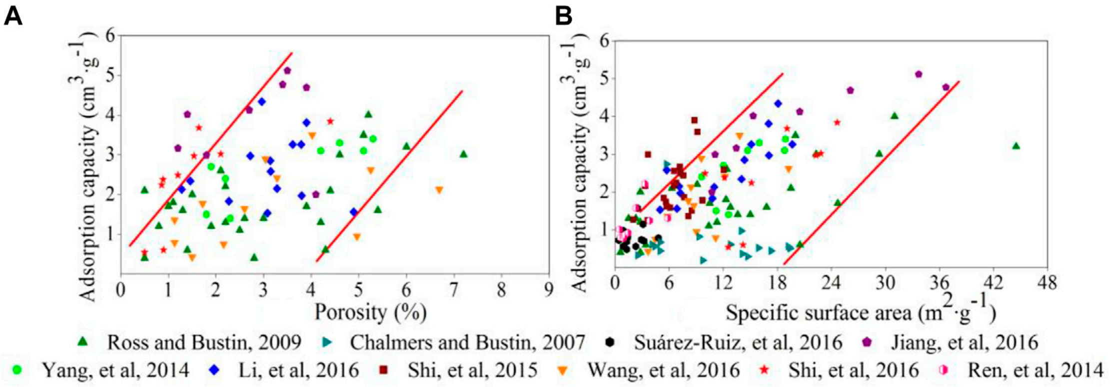

FIGURE 7
(A): Relationship between porosity and methane adsorption capacity and **(B)**: Relationship between specific surface area and methane adsorption capacity.

might combine with methane to form gas hydrates (Park and Sposito, 2003). Of course, some scholars hold different views about the relationship between adsorption capacity and clay minerals; Liu and Wang, 2012 studied the adsorption characteristics in marine shale in southern China, and concluded that the maximum adsorption capacity is not related to clay mineral composition under the conditions of similar TOC contents.

Different clay minerals have different chemical compositions, crystal structures, particle sizes and petro physical properties, in which crystal spaces, inter-layer and gap sizes between particles, shapes and surface areas are different (Lu et al., 1995). Kennedy et al., 2002 found that the inner surface area of montmorillonite is much larger than that of kaolinite, approximately 90 times higher than kaolinite, which is favorable for gas adsorption. Ji et al., (2012b) showed that the methane adsorption capacity of different clay minerals differed, and the adsorption capacity order is as follows: montmorillonite > illite/montmorillonite mixed layer > kaolinite > chlorite > illite. The influence of clay minerals on methane adsorption capacity is also affected by their own digenetic evolution and rock formation.

3.3 Pore characterization

On the one hand, pore structure controls storage and output of shale gas. Heterogeneity of pore size distribution plays an important role in the adsorption process. Pore structure is more complex, porosity and surface area are larger, and the adsorption capacity increases (Heller and Zoback, 2014; Hinai et al., 2014; Chen et al., 2015; Li et al., 2016) (Figures 7A,B). Kim et al. (2017) studied the Horn River Basin shale in northeastern British Columbia and found that even in the case of low organic carbon content, adsorption capacity is still strong, as long as the specific surface area is large. Increasing the specific surface area and the number of micro pores with a pore size <2 nm increased the adsorption capacity (Lu et al., 1995; Brandon, 2005; Raut et al., 2007; Chalmers and Bustin, 2008; Weniger et al., 2010; Yan et al., 2013). Several groups compared macro pores with micro pores and found that micro pores had larger specific surface areas and adsorption capacities and concluded that specific surface area is the key factor for adsorption capacity (Dubinin, 1975; Cheng and Huang, 2004; Chalmers and Bustin, 2007; Loucks and Ruppel, 2007; Pan et al., 2019) (Figure 7B). Kim et al. (Kim et al., 2017) indicated that the micro pores account for 56.21%–80.95% of the specific surface area. Wu et al. (Wu et al., 2012) studied gas adsorption capacity in shale and its controlling factors from Well Yuye 1 of Longmaxi Formation of Lower Silurian at the southeast of Chongqing, which indicated that a saturated adsorption capacity has a negative correlation on pore volume; this might be related to smaller pore throat sizes in micro pores that could not reach the kinetic diameter of methane molecules. In contrast, mesopores and macro pores have relatively large pore throats and pore diameters compared to micro pores, making methane molecules more likely to flow into the pores. Therefore, mesopores and macro pores have additional effects on methane adsorption capacity (Yang et al., 2014b). Methane molecules are mainly adsorbed in narrow micro pores of solid asphalt. However, these relationships are complex. In micro pores, the methane adsorption phase density in the smallest pore size is large, and the methane adsorption capacity increases with a decrease in the volume of micro pores; however, for samples with larger pore sizes (pore size >1.1 nm), the amount of methane adsorbed molecules are modest as porosity increases, since CH_4 has a lower density (Suárez-Ruiz et al., 2016). Qajar et al. (2015) considered that

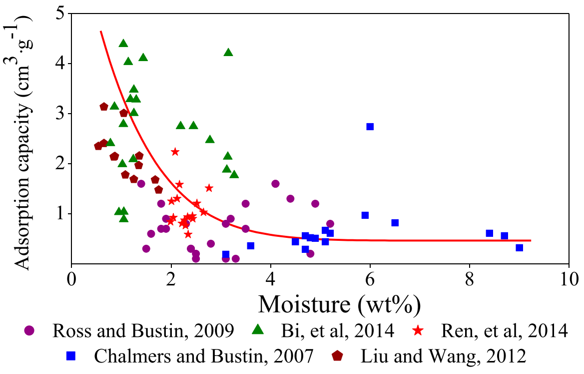

FIGURE 8
Relationship between moisture content and methane adsorption capacity.

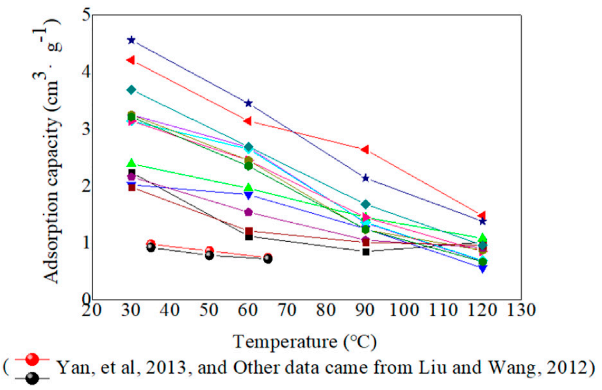

FIGURE 9
Relationship between temperature and methane adsorption capacity.

absorption gas mainly concentrates in pore sizes between 2 nm and 50 nm.

One the other hand, pore types affect the gas adsorption. Pores in shale are mainly composed of organic matter pores and mineral pores. It is considered that gas is adsorbed on organic pore surfaces and is freely distributed in spaces of clay mineral pores (He et al., 2022). It can be seen that organic matter pores play a major role in methane adsorption (Ross and Bustin, 2009; Huang et al., 2015; Suárez-Ruiz et al., 2016). Hou et al. (2014) studied the Lower Paleozoic marine shale and Mesozoic continental shale in the western Yangtze basin and concluded that clay minerals with low thermal evolution can provide more specific surface area for methane adsorption and that organic matter pores gradually became the primary controlling factor in gas adsorption capacity as the maturity increased.

3.4 Moisture content

Moisture content has an influence on the adsorption capacity of shale. Water occupies more pore space with higher moisture content and reduces the surface position of free hydrocarbon gas shelter volume and adsorption sites on mineral surfaces. Namely, the adsorption capacity is smaller with higher moisture content (Figure 8). Ross and Bustin, 2008 found that when water content is higher (moisture content >4%), adsorption capacity decreases, and the adsorption capacity of saturated water samples is 40% lower than for dried samples. However, Chalmers and Bustin, 2008 studied the adsorption of shale with water content from 1.5% to 11% and found that there is no correlation between water content and adsorption capacity, and that samples with high water content also might have high methane adsorption capacity. Research on gas adsorption abilities in coal with different water content has a certain reference value for understanding the effect of water content on shale gas adsorption capacity. Effective adsorption sites on the inner surface of coal that could be provided for residence of gaseous molecules are limited. As the moisture content in coal increases, the amount of effective absorption sites decreases, and fewer effective absorption sites remain for methane molecules, which decreases the methane adsorption capacity. However, effective adsorption points occupied by water are related to the number of oxygen-containing functional groups. The more oxygen-containing functional groups there are, the greater the water content is, which affects the adsorption capacity. The moisture content is called equilibrium moisture, and once the content exceeds the equilibrium moisture, an increase in moisture content will no longer affect the adsorption capacity (Figure 8).

3.5 Temperature, pressure and the burial depth of shale

Under reservoir conditions, the gas adsorption capacity will be influenced by not only the above factors but also temperature and pressure. Currently, most exploration depths for shale gas has exceeded 1,000 m; this means the reservoir pressure in most areas is more than 5 Mpa which is greater than the critical pressure of methane. Therefore, under the high pressure and reservoir temperature conditions, whether adsorption capacity in shale still follows the adsorption capacity curve law that changes are subject to the Langmuir equation. The gas adsorption process is exothermic. With a temperature increase, gas adsorption capacity decreases (Figure 9). Liu and Wang, 2012 analyzed factors that affected the adsorption capacity in marine mudstone in southern China and found that temperature had a significant effect on adsorption capacity; the maximum adsorption gas content decreased by 1.46 cm^3/g from 30°C to 120°C. Chalmers and Bustin, 2007 found that the gas adsorption curve shows a negative exponential state reduction with a temperature increase and has a greater influence on adsorption capacity than organic carbon. Loucks et al. (2009) thought that adsorption gas was negligible and that free gas was the primary gas at higher temperatures.

Adsorption capacity in shale does not change monotonically (monotonically increased) with the change of burial depth because of the combined effect of temperature and pressure, and it appears at the maximum value. Ji et al. (2015) studied methane adsorption capacity in marine shale from the Longmaxi Formation of the Lower Silurian in southern China and found that the maximum methane adsorption value was in the depth range of 800–1,350 m.

4 Challenges of gas adsorption on shale

In the field of shale gas adsorption, although researchers have carried out a great deal of research on many aspects, such as affecting factors of adsorption, adsorption characteristics, adsorption theory, and shale gas adsorption, research in this area still faces some challenges.

(1) Organic matter in shale has complex physical and chemical structures that play important roles in gas adsorption. In the past, the influence of organic matter on adsorption was studied mainly from the aspects of physical structures. However, chemical structures with different kerogen types or different thermal evolution degrees also have effects on gas adsorption. For example, the surface energy of organic matter with different structures is different, resulting in different gas adsorption capacities.

(2) Porosity provides space for shale gas occurrence. Adsorbed gas mainly occurs on the surface of the matrix layer. Currently, there are arguments on the influence of pore size on gas adsorption behavior. On the one hand, micro pores provide more specific surface area, but many pore diameters are smaller than the kinetic diameter of methane molecules. Can the micro pores truly become the main pore space for gas adsorption? On the other hand, clay minerals provide micro pore volumes for gas adsorption that account for 60%–80% of the total pore volumes in shale. It is unclear whether the important contribution to adsorption is *via* organic matter pore volumes or clay mineral pore volumes?

(3) Organic matter and clay minerals are the main adsorbents for shale gas adsorption. The contribution of clay minerals to gas adsorption is still controversial. Some researchers believe that clay minerals contribute little to gas adsorption; however, the contribution of organic matter and clay minerals to gas adsorption is not clear. The reason is that under actual geological conditions, 90% of organic matter and clay minerals exist in the form of organic-clay complexes; only a small fraction of organic matter is associated with mineral particles. Therefore, the interaction between organic matter and clay minerals and its effects on adsorption still need further research.

(4) Moisture content is another factor that influences shale adsorption behavior, but its impact on shale adsorption is also controversial. Whether the effect of moisture content on gas adsorption in shale is equal to that of coal is a question worth exploring, especially regarding how the presence of expansive minerals impacts adsorption.

(5) With changes in pressure, shale adsorption behavior does not entirely obey the monolayer adsorption. In the supercritical state, gas adsorption will be affected not only by adsorption phase volume but also by the shale's morphological characteristics, structural features, composition, etc. The impact of these many variables on the mechanism of shale adsorption needs additional study.

(6) Under varying temperature and pressure conditions, adsorption characteristics in shale are almost blank, making an adsorption profile difficult to establish in a geological reservoir. Research has shown that in the coalbed methane field, the adsorption capacity in coal increased with an increase in pressure and decreased with an increase in temperature. Under geological conditions, the influence of pressure on the adsorption capacity plays a dominant role when the burial depth is less than 800–1,500 m, while temperature plays a leading role when the buried depth is more than 800–1,500 m. The influence of burial depth is different in different regions because of different effective stress. In other words, when burial depth is approximately 800–1,500 m, the coal seam has the largest adsorption capacity. The relationship between gas adsorption capacity and pressure is complex. With the influence of temperature, the relationship between the maximum adsorption capacity and depth is even more complex. Research in these areas is currently lacking and needs to be examined in greater detail.

5 Conclusion

Shale adsorption behavior, in addition to its own nature, is greatly impacted by external factors such as pressure and temperature. This paper presents a review of gas adsorption behaviors that can be applied to evaluate the gas content in shale reservoirs.

The main variables of shale gas adsorption are organic matter and clay minerals; other variables include moisture content, TOC, organic matter type and organic matter maturity. It is generally believed that higher shale TOC, vitrinite content or organic matter maturity contributes to a higher gas adsorption capacity. The reason is that there are many of pores in kerogen, especially type III kerogen that provide a comparatively large area for gas occurrence, and pores in organic matter gradually increase with the increase of thermal evolution degree. Brittle minerals will lead to a lower adsorption capacity. Clay minerals are good materials for gas adsorption due to their micro pores, large specific surface area and special electrochemical properties that provide more places for adsorbed gas. There are differences in shale gas adsorption capacities due to differences in chemical composition, crystal structure, particle size and petro physical properties of different clay mineral types. However, the influence of clay minerals on adsorption properties is still controversial. Generally, there exists a negative correlation between moisture content and gas adsorption capacity, but some researchers held the opposite view.

Under reservoir conditions, in addition to the abovementioned factors, temperature and pressure both increase with the increase of burial depth that have an influence on gas adsorption behavior. Gas adsorption capacity decreased with an increase in temperature. As the pressure increases, gas adsorption characteristics mainly show two characteristics—an adsorption curve that obeyed the Langmuir equation and another where the adsorption maximum value appeared as a "single peak" adsorption phenomenon with an inverted U shape at a pressure value distribution in the range of 5–12 MPa. The latter characteristic is difficult to describe with the Langmuir equation. In addition to the influence of adsorbed volume phase, composition, structure and morphology also have influences on shale.

There are still many problems in the study of adsorption behaviors in shale that pose a great challenge for research in this field. These problems include chemical structures of organic matter in shale; pore size distribution; clay minerals; interaction between clay minerals and organic matter; and especially the factor of moisture content which is rich in clay minerals. All of these variables need to be further studied. Under reservoir temperature and pressure conditions, the adsorption characteristics are difficult to describe by the single molecular layer adsorption theory. The mechanism of adsorption behavior changes and the adsorption model involving a variety of factors are problems that urgently need to be solved, with a particular emphasis on studying the variation of temperature and pressure with the influence of other factors that directly affect the estimation of adsorption content in shale under reservoir conditions.

Author contributions

XL is responsible for the overall conception of the paper and the writing of Sections 1, 3.1, 3.2.3.3, 4 and 5, CL is responsible for the information search and writing of Section 2, and ZW is responsible for the writing of Sections 3.4 and 3.5.

Funding

We acknowledge the National Natural Science Foundation Projects of China (42272199), the Natural Science Foundation Projects of Henan Province (222300420556), the Cultivate Funds for Young Teachers of Zhenghou University (JC202042035) for providing research funding.

Conflict of interest

The authors declare that the research was conducted in the absence of any commercial or financial relationships that could be construed as a potential conflict of interest.

Publisher's note

References

Aranovich, G. L., Sangwichien, C., and Donohue, M. D. (2000). Intermolecular repulsions in adsorbed layers. *J. Colloid Interface Sci.* 227 (2), 553–560. doi:10.1006/jcis.2000.6893

Bernaola-Galvan, P., Ivanov, P. C., Nunes Amaral, L. A., and Stanley, H. E. (2001). Scale invariance in the nonstationarity of human heart rate. *Phys. Rev. Lett.* 87 (16), 168105. doi:10.1103/PhysRevLett.87.168105

Bowker, K. A. (2007). Barnett shale gas production, Fort worth basin: Issues and discussion. *Am. Assoc. Pet. Geol. Bull.* 91 (4), 523–533. doi:10.1306/06190606018

Brandon, C. N. (2005). *Analysis of devonian black shales in Kentucky for potential carbon dioxide sequestration and enhanced natural gas production quarterly report.* United States, United States. doi:10.2172/842849

Chalmers, G. R. L., and Bustin, R. M. (2008). Lower cretaceous gas shales in northeastern British Columbia, Part I: Geological controls on methane sorption capacity. *Bull. Can. Petroleum Geol.* 56 (1), 1–21. doi:10.2113/gscpgbull.56.1.1

Chalmers, G. R. L., and Bustin, R. M. (2007). The organic matter distribution and methane capacity of the lower Cretaceous strata of northeastern British Columbia, Canada. *Int. J. Coal Geol.* 70 (1-3), 223–239. doi:10.1016/j.coal.2006.05.001

Chareonsuppanimit, P., Mohammad, S. A., Robinson, R. L., and Gasem, K. A. M. (2012). High-pressure adsorption of gases on shales: Measurements and modeling. *Int. J. Coal Geol.* 95, 34–46. doi:10.1016/j.coal.2012.02.005

Chen, Y., Zou, C., Maria, M., Zhu, R., Yang, Z., et al. (2015). Porosity and fractal characteristics of shale across a maturation gradient. *Nat. Gas. Geosci.* 26 (9), 1646–1656. doi:10.11764/j.issn.1672-1926.2015.09.1646

Cheng, A. L., and Huang, W. L. (2004). Selective adsorption of hydrocarbon gases on clays and organic matter. *Org. Geochem.* 35 (4), 413–423. doi:10.1016/j.orggeochem.2004.01.007

Chilev, C., Lamari, F. D., Kirilova, E., and Pentchev, I. (2012). Comparison of gas excess adsorption models and high pressure experimental validation. *Chem. Eng. Res. Des.* 90 (11), 2002–2012. doi:10.1016/j.cherd.2012.03.012

Day, S., Duffy, G., Sakurovs, R., and Weir, S. (2008). Effect of coal properties on CO2 sorption capacity under supercritical conditions. *Int. J. Greenh. Gas Control* 2 (3), 342–352. doi:10.1016/s1750-5836(07)00120-x

Do, D. D., and Do, H. D. (2005). Adsorption of argon from sub- to supercritical conditions on graphitized thermal carbon black and in graphitic slit pores: A grand canonical Monte Carlo simulation study. *J. Chem. Phys.* 123 (8), 084701. doi:10.1063/1.1996573

Dong, D., Zou, C., Yang, H., Wang, Y., and Li, X. (2012). Progress and prospects of shale gas exploration and development in China. *Acta Pet. Sin.* 33 (S1), 107–114. doi:10.7623/syxb2012S1013

Dreisbach, F., Losch, H. W., and Harting, P. (2002). Highest pressure adsorption equilibria data: Measurement with magnetic suspension balance and analysis with a new adsorbent/adsorbate-volume. *Adsorpt. Bost.* 8 (2), 95–109. doi:10.1023/a:1020431616093

Dubinin, M. M. (1975). *Physical adsorption of gases and vapors in micropores* (Elsevier), 1–70. D.A, C., J.F, D., M.D, R. doi:10.1016/B978-0-12-571809-7.50006-1

Fang, J., Zhu, Y., Wei, W., Du, Z., and Chen, S. (2010). Preliminary study of abnormalities of shale isothermal adsorption experiment. *Tuha Oil Gas* 15 (4), 317–320.

Franco, C. A., Nassar, N. N., Ruiz, M. A., Pereira-Almao, P., and Cortes, F. B. (2013). Nanoparticles for inhibition of asphaltenes damage: Adsorption study and displacement test on porous media. *Energy fuels.* 27 (6), 2899–2907. doi:10.1021/ef4000825

Gensterblum, Y., Merkel, A., Busch, A., and Krooss, B. M. (2013). High-pressure CH4 and CO2 sorption isotherms as a function of coal maturity and the influence of moisture. *Int. J. Coal Geol.* 118, 45–57. doi:10.1016/j.coal.2013.07.024

He, J., Cai, J., Lei, T., Song, M., Liu, H., and Wang, X. (2022). Characteristics comparison and occurrence mode of different types of soluble organic matter in lacustrine shale in the Dongying Sag, eastern China. *Int. J. Coal Geol.* 254, 103971. doi:10.1016/j.coal.2022.103971

Heller, R., and Zoback, M. (2014). Adsorption of methane and carbon dioxide on gas shale and pure mineral samples. *J. Unconv. Oil Gas Resour.* 8, 14–24. doi:10.1016/j.juogr.2014.06.001

Hill, R. J., Jarvie, D. M., Zumberge, J., Henry, M., and Pollastro, R. M. (2007). Oil and gas geochemistry and petroleum systems of the Fort Worth Basin. *Am. Assoc. Pet. Geol. Bull.* 91 (4), 445–473. doi:10.1306/11030606014

Hinai, A. A., Rezaee, R., Esteban, L., and Labani, M. (2014). Comparisons of pore size distribution: A case from the western Australian gas shale formations. *J. Unconv. Oil Gas Resour.* 8, 1–13. doi:10.1016/j.juogr.2014.06.002

Hou, H., Shao, L., Li, Y., Liu, L., Liang, G., Zhang, W., et al. (2022). Effect of paleoclimate and paleoenvironment on organic matter accumulation in lacustrine shale: Constraints from lithofacies and element geochemistry in the northern Qaidam Basin, NW China. *J. Pet. Sci. Eng.* 208, 109350. doi:10.1016/j.petrol.2021.109350

Hou, Y., He, S., Yi, J., Zhang, B., Chen, X., Wang, Y., et al. (2014). Effect of pore structure on methane sorption potential of shales. *Petroleum Explor. Dev.* 41 (2), 272–281. doi:10.1016/S1876-3804(14)60033-1

Huang, X., Zhang, J., Li, X., Sun, R., Peng, J., and Long, S. (2015). Pore types and characteristics of continental shale and discussion on the process of oil and gas accumulation:A case study of the western sag of liaohe depression. *Nat. Gas. Geosci.* 26 (7), 1422–1432. doi:10.11764/j.issn.1672-1926.2015.07.1422

Ji, L., Qiu, J., and Xia, Y. (2012a). Micro-pore characteristics and methane adsorption properties of common clay minerals by electron microscope scanning. *Acta Pet. Sin.* 33 (2), 249–256. doi:10.7623/syxb201202009

Ji, L., Qiu, J., Zhang, T., and Xia, Y. (2012b). Experiments on methane adsorption of common clay minerals in shale. *Earth Sci. J. China Univ. Geosci. (China)* 37 (5), 1043–1050. doi:10.3799/dqkx.2012.111

Ji, W., Song, Y., Jiang, Z., Chen, L., Li, Z., Yang, X., et al. (2015). Estimation of marine shale methane adsorption capacity based on experimental investigations of Lower Silurian Longmaxi formation in the Upper Yangtze Platform, south China. *Mar. Pet. Geol.* 68, 94–106. doi:10.1016/j.marpetgeo.2015.08.012

Jiang, Z., Tang, X., Li, Z., Huang, H., Yang, P., Yang, X., et al. (2016). The whole-aperture pore structure characteristics and its effect on gas content of the Longmaxi Formation shale in the southeastern Sichuan basin. *Earth Sci. Front.* 23 (2), 126–134. doi:10.13745/j.esf.2016.02.013

Jiang, Z., Zhao, L., and Zhang, D. (2018). Study of adsorption behavior in shale reservoirs under high pressure. *J. Nat. Gas. Sci. Eng.* 49, 275–285. doi:10.1016/j.jngse.2017.11.009

Kennedy, M. J., Pevear, D. R., and Hill, R. J. (2002). Mineral surface control of organic carbon in black shale. *Science* 295 (5555), 657–660. doi:10.1126/science.1066611

Kim, J., Kim, D., Lee, W., Lee, Y., and Kim, H. (2017). Impact of total organic carbon and specific surface area on the adsorption capacity in Horn River shale. *J. Pet. Sci. Eng.* 149, 331–339. doi:10.1016/j.petrol.2016.10.053

Kinley, T. J., Cook, L. W., Breyer, J. A., Jarvie, D. M., and Busbey, A. B. (2008). Hydrocarbon potential of the Barnett shale (mississippian), Delaware basin, west Texas and southeastern new Mexico. *Am. Assoc. Pet. Geol. Bull.* 92 (8), 967–991. doi:10.1306/03240807121

Li, A., Ding, W., He, J., Dai, P., Yin, S., and Xie, F. (2016). Investigation of pore structure and fractal characteristics of organic-rich shale reservoirs: A case study of lower cambrian qiongzhusi formation in malong block of eastern yunnan Province, south China. *Mar. Pet. Geol.* 70, 46–57. doi:10.1016/j.marpetgeo.2015.11.004

Li, X., Suyun, H. U., and Cheng, K. (2007). Suggestions from the development of fractured shale gas in North America. *Petroleum Explor. Dev.* 34 (4), 392–400. doi:10.3321/j.issn:1000-0747.2007.04.002

Lin, L. M., Zhang, J. C., Xuan, T., and Hua, Z. (2012). Gas-bearing characteristics of paleozoic gas shale reservoir in south China. *J. Jilin Univ. Sci. Ed.* 42, 88–94.

Lin, X., Huang, M., Chen, H., Wang, J., and Wang, R. (2019). Influence of different polar solvent extraction on pore structure in shale. *Acta Pet. Sin.* 40 (12), 1485–1494. doi:10.7623/syxb201912007

Liu, H., and Wang, H. (2012). Adsorptivity and influential factors of marine shales in South China. *Nat. Gas. Ind.* 32 (9), 5–9. doi:10.3787/j.issn.1000-0976.2012.09.002

Loucks, R. G., Reed, R. M., Ruppel, S. C., and Jarvie, D. M. (2009). Morphology, Genesis, and distribution of nanometer-scale pores in siliceous mudstones of the Mississippian Barnett Shale. *J. Sediment. Res.* 79 (11-12), 848–861. doi:10.2110/jsr.2009.092

Loucks, R. G., and Ruppel, S. C. (2007). Mississippian Barnett shale: Lithofacies and depositional setting of a deep-water shale-gas succession in the Fort worth basin, Texas. *Am. Assoc. Pet. Geol. Bull.* 91 (4), 579–601. doi:10.1306/11020606059

Lu, X. C., Li, F. C., and Watson, A. T. (1995). Adsorption measurements in Devonian shales. *Fuel* 74 (4), 599–603. doi:10.1016/0016-2361(95)98364-k

Malbrunot, P., Vidal, D., Vermesse, J., Chahine, R., and Bose, T. K. (1992). Adsorption measurements of argon, neon, krypton, nitrogen, and methane on activated carbon up to 650 MPa. *Langmuir* 8 (2), 577–580. doi:10.1021/la00038a044

Marecka, A., and Mianowski, A. (1998). Kinetics of CO2 and CH4 sorption on high rank coal at ambient temperatures. *Fuel* 77 (14), 1691–1696. doi:10.1016/s0016-2361(98)00071-4

Mavor, M. (2003). *Barnett shale gas-in-place volume including sorbed and free gas volume*. Texas, USA: AAPG Southwest Section Meeting.

Menon, P. G. (1965). Adsorption of carbon monoxide on alumina at high Pressures1. *J. Am. Chem. Soc.* 87 (14), 3057–3060. doi:10.1021/ja01092a006

Montgomery, S. L., Jarvie, D. M., Bowker, K. A., and Pollastro, R. M. (2005). Mississippian Barnett Shale, Fort Worth basin, north-central Texas: Gas-shale play with multi-trillion cubic foot potential. *Am. Assoc. Pet. Geol. Bull.* 89 (2), 155–175. doi:10.1306/09170404042

Nandi, S. P., and Walker, P. L. (1975). Activated diffusion of methane from coals at elevated pressures. *Fuel* 54 (2), 81–86. doi:10.1016/0016-2361(75)90061-7

Nie, H., and Zhang, J. (2010). Shale gas reservoir distribution geological law, characteristics and suggestions. *J. Cent. South Univ. Sci. Technol. (China)* 41 (2), 700–708.

Niu, Q. H., Cao, L., Sang, S., Wang, W., Zhou, X., Yuan, W., et al. (2021). Experimental study on the softening effect and mechanism of anthracite with CO2 injection. *Int. J. Rock Mech. Min. Sci.* 138, 104614. doi:10.1016/j.ijrmms.2021.104614

Pan, J. N., Lv, M. M., Hou, Q. L., Han, Y. Z., and Wang, K. (2019). Coal microcrystalline structural changes related to methane adsorption/desorption. *Fuel* 239, 13–23. doi:10.1016/j.fuel.2018.10.155

Park, S. H., and Sposito, G. (2003). Do montmorillonite surfaces promote methane hydrate formation? Monte Carlo and molecular dynamics simulations. *J. Phys. Chem. B* 107 (10), 2281–2290. doi:10.1021/jp021427q

Perera, M. S. A., Ranjith, P. G., Choi, S. K., Airey, D., and Weniger, P. (2012). Estimation of gas adsorption capacity in coal: A review and an analytical study. *Int. J. Coal Prep. Util.* 32 (1), 25–55. doi:10.1080/19392699.2011.614298

Qajar, A., Daigle, H., and Prodanovic, M. (2015). Methane dual-site adsorption in organic-rich shale-gas and coalbed systems. *Int. J. Coal Geol.* 149, 1–8. doi:10.1016/j.coal.2015.07.006

Rani, S., Prusty, B. K., and Pal, S. K. (2015). Methane adsorption and pore characterization of Indian shale samples. *J. Unconv. Oil Gas Resour.* 11, 1–10. doi:10.1016/j.juogr.2015.03.003

Raut, U., Fama, M., Teolis, B. D., and Baragiola, R. A. (2007). Characterization of porosity in vapor-deposited amorphous solid water from methane adsorption. *J. Chem. Phys.* 127 (20), 204713. doi:10.1063/1.2796166

Ren, Z., Liu, L., Gao, X., Xiao, F., Wang, Y., Wu, K., et al. (2014). Adsorption capacity and its influence factors of the jurassic shalein the northeastern kuqa depression. *Nat. Gas. Geosci.* 25 (4), 632–640. doi:10.11764/j.issn.1672-1926.2014.04.0632

Ross, D. J. K., and Bustin, R. M. (2008). Characterizing the shale gas resource potential of Devonian-Mississippian strata in the Western Canada sedimentary basin: Application of an integrated formation evaluation. *Am. Assoc. Pet. Geol. Bull.* 92 (1), 87–125. doi:10.1306/09040707048

Ross, D. J. K., and Bustin, R. M. (2007). Impact of mass balance calculations on adsorption capacities in microporous shale gas reservoirs. *Fuel* 86 (17-18), 2696–2706. doi:10.1016/j.fuel.2007.02.036

Ross, D. J. K., and Bustin, R. M. (2009). The importance of shale composition and pore structure upon gas storage potential of shale gas reservoirs. *Mar. Pet. Geol.* 26 (6), 916–927. doi:10.1016/j.marpetgeo.2008.06.004

Salem, M. M. K., Braeuer, P., Szombathely, M. v., Heuchel, M., Harting, P., Quitzsch, K., et al. (1998). Thermodynamics of high-pressure adsorption of argon, nitrogen, and methane on microporous adsorbents. *Langmuir* 14 (12), 3376–3389. doi:10.1021/la970119u

Siemons, N., and Busch, A. (2007). Measurement and interpretation of supercritical CO2 sorption on various coals. *Int. J. Coal Geol.* 69 (4), 229–242. doi:10.1016/j.coal.2006.06.004

Suárez-Ruiz, I., Juliao, T., Suárez-García, F., Marquez, R., and Ruiz, B. (2016). Porosity development and the influence of pore size on the CH4 adsorption capacity of a shale oil reservoir (Upper Cretaceous) from Colombia. Role of solid bitumen. *Int. J. Coal Geol.* 159, 1–17. doi:10.1016/j.coal.2016.03.020

Tang, S., Yang, Q., and Tang, D. (2003). Comparison between the experimental results of isothermal adsorption of binary mixed gas and the predicted values of the extended Langmuir equation. *Geol. Sci. Technol. Inf.* 2, 68–70. doi:10.3969/j.issn.1000-7849.2003.02.014

Wang, C. C., Juang, L. C., Lee, C. K., Hsu, T. C., Lee, J. F., and Chao, H. P. (2004). Effects of exchanged surfactant cations on the pore structure and adsorption characteristics of montmorillonite. *J. Colloid Interface Sci.* 280 (1), 27–35. doi:10.1016/j.jcis.2004.07.009

Wang, Z. Z., Pan, J., Hou, Q., Yu, B., Li, M., and Niu, Q. (2018). Anisotropic characteristics of low-rank coal fractures in the Fukang mining area, China. *Fuel* 211, 182–193. doi:10.1016/j.fuel.2017.09.067

Weniger, P., Kalkreuth, W., Busch, A., and Krooss, B. M. (2010). High-pressure methane and carbon dioxide sorption on coal and shale samples from the Parana Basin, Brazil. *Int. J. Coal Geol.* 84 (3-4), 190–205. doi:10.1016/j.coal.2010.08.003

Wu, J., Yu, B., and Li, Y. (2012). Adsorption capacity of shale gas and controlling factors from the well Yuye 1 at the southeast of chongqing. *J. Southwest Petroleum Univ.* 34 (4), 40–48. doi:10.3863/j.issn.1674-5086.2012.04.005

Yan, J., Zhang, T., Li, Y., Lu, H., and Zhang, X. (2013). Effect of the organic matter characteristics on methane adsorption in shale. *J. China Coal Soc.* 38 (5), 805–811.

Yang, F., Ning, Z., Wang, Q., Liu, H., and Kong, D. (2014a). Thermodynamic analysis of methane adsorption on gas shale. *J. Central South Univ. Sci. Technol.* 45 (8), 2871–2877.

Yang, F., Ning, Z. F., and Liu, H. Q. (2014b). Fractal characteristics of shales from a shale gas reservoir in the Sichuan Basin, China. *Fuel* 115, 378–384. doi:10.1016/j.fuel.2013.07.040

Yu, H., Fan, W., Sun, M., and Ye, J. (2004). Study on fitting models for methane isotherms adsorption of coals. *J. China Coal Soc.* 29 (4), 463–467. doi:10.3321/j.issn:0253-9993.2004.04.019

Yu, C., Nie, H., Zeng, C., Cheng, L., and Shao, X. (2014). Shale reservoir space characteristics and the effect on gas content in lower palaeozoic erathem of the eastern Sichuan Basin. *Acta Geol. Sin.* 88 (7), 1311–1320. doi:10.3969/j.issn.0001-5717.2014.07.008

Zhang, Q., and Cao, L. (2003). Study of data processing in coal orption isotherm testing. *J. China Coal Soc.* 28 (2), 131–135. doi:10.1115/1.1564062

Zhang, L. (2012). The success of shale gas development in the United States. *Sinopec*, 12, 17–28.

Zhang, J., Wang, Z., Nie, H., Xu, B., Deng, F., Zhang, P., et al. (2008). Shale gas and its significance for exploration. *Geoscience* 22 (4), 640–646. doi:10.3787/j.issn.1000-0976.2008.06.040

Zhang, T., Ellis, G., Ruppel, S., Milliken, K., and Yang, R. (2012). Effect of organic-matter type and thermal maturity on methane adsorption in shale-gas systems. *Org. Geochem.* 47, 120–131. doi:10.1016/j.orggeochem.2012.03.012

Zhang, Z., Liu, G., Zhang, X., and Yang, X. (2009). Adsorption-disorption experiments of CH_4 and CO_2 with different consistency. *J. China Coal Soc.* 34 (04), 551–555.

Zhou, C., Hall, F., Gasem, K., and Robinson, R. L. (1994). Predicting gas adsorption using two-dimensional equations of state. *Ind. Eng. Chem. Res.* 33 (5), 1280–1289. doi:10.1021/ie00029a026

Zou, C., Li, J., Dong, D., and Li, X. (2010). Abundant nanoscale pores with founding in shale gas reservoirs for the first time in China. *Petroleum Explor. Dev.* 37 (05), 508–509.

Zou, C., Dong, D., Yang, H., Wang, Y., and Huang, J. (2011). Formation conditions and shale gas exploration in China. *Nat. Gas. Ind.* 31 (12), 26–39+125. doi:10.3787/j.issn.1000-0976.2011.12.005

Zou, C. N., Dong, D., Wang, Y., Li, X., Huang, J., Wang, S., et al. (2016). Shale gas in China: Characteristics, challenges and prospects (II). *Petroleum Explor. Dev.* 43 (2), 182–196. doi:10.1016/s1876-3804(16)30022-2

frontiers | Frontiers in Earth Science

TYPE Original Research
PUBLISHED 13 January 2023
DOI 10.3389/feart.2022.991304

OPEN ACCESS

EDITED BY
Junjian Zhang,
Shandong University of Science and Technology, China

REVIEWED BY
Fangkai Quan,
China University of Mining and Technology, China
Zhihui Ma,
Sichuan University of Science and Engineering, China

*CORRESPONDENCE
Minggao Yu,
13333910808@126.com

SPECIALTY SECTION
This article was submitted to Economic Geology, a section of the journal Frontiers in Earth Science

RECEIVED 11 July 2022
ACCEPTED 30 August 2022
PUBLISHED 13 January 2023

CITATION
Teng F, Yu M, Han X and Chao J (2023), Study on the mechanism of coal pillar breaking and fracture development under repeated mining in a close seam group.
Front. Earth Sci. 10:991304.
doi: 10.3389/feart.2022.991304

Study on the mechanism of coal pillar breaking and fracture development under repeated mining in a close seam group

Fei Teng[1], Minggao Yu[1,2]*, Xuefeng Han[1] and Jiangkun Chao[2]

[1]School of Safety Science and Engineering, Henan Polytechnic University, Jiaozuo, China, [2]State Key Laboratory of Coal Mine Disaster Dynamics and Control, Chongqing University, Chongqing, China

The study show the influence of coal mining on pillar under a repeated mining, in a close coal seam group, the fracture and instability process and influence mechanism of fracture development on the oxidation of coal pillars. In this paper, FLAC^{3D} numerical simulation software is used to simulate the dynamic evolution characteristics of stress, displacement of the upper coal pillar. The results show that 1) The theoretical length of the fracture along the strike of the upper coal pillar is obtained by establishing the mechanical model of the upper coal pillar, which is consistent with the numerical simulation results. 3) In this paper, according to the dynamic evolution characteristics of displacement and stress on the coal pillar, the coal pillar is divided into the "step subsidence area", "fracture compaction area" and "reverse stress area", and the high risk area of the coal spontaneous combustion is determined.

KEYWORDS

fire and explosion, coal, coal spontaneous combustibility, fracture, cracks, rock and coal system

1 Introduction

Coal spontaneous combustion is a serious problem of coal mining (Ramani, 1997; Wactawi, 1998; Wang et al., 2003; Genc and Cook, 2015). Some important coalfields in China, there are a huge number of shallow buried depth of 80–240 m coal, the mining of them will lead to a large area of land subsidence and destroy the local ecological environment. Some scholars (Ju and Xu, 2015; Bi et al., 2019; Chen et al., 2019) take a series of field monitoring and comparisons with previous studies. Some scholars introduces a new profile function method for prediction of surface subsidence due to inclined coal-seam mining and use DInSAR technology to identify and monitoring subsidence basins caused by underground coal mining activities (Asadi et al., 2005; Przylucka et al., 2015). Flac3D software were used to simulate the actual geological conditions and improve insufficiency of the classical method according to the simulate results, which confirm the Flac3D is a simple and effective way predict surface mining displacement (Xie and Zhou, 1999). The surface subsidence caused by coal mining threatens the local ecological environment seriously.

The occurrence characteristics of shallow buried and close distances of coal seams, which make the coal remaining in goaf vulnerable to the influence of the mining of adjacent coal seam, which form a leakage passage through the working face, gob and surface, some scholar measured the displacement, stress changes of strata in the process of longwall mining and monitored them, and simulated the stress and permeability changes of strata, and study the distribution and evolution of displacement, fracture and stress through similar material simulation test. (Ma et al., 2013; Guo et al., 2012; Kidybinski and Babcock, 1973; Majdi et al., 2012; Prucz et al., 1989; Li et al., 2013). The mining-induced cracks, which leads to air leakage caused by the repeated mining of shallow coal seams a, and a similar simulation experiment was carried out in the laboratory, and then the ground mining-induced cracks were observed and the crack air leakage was detected. As the source of air leakage in the goaf, these cracks through the surface greatly increase the possibility of coal spontaneous combustion disaster in the goaf (Lu and Qin, 2015; Cheng et al., 2017; Hao et al., 2019; Wang et al., 2019; Zhuo et al., 2019).

In the mining process, the stability of the pillar will be affected by mining disturbances in the next adjacent layer and will be in a state of dynamic balance or even fracture instability. (Huang and Cao, 2019; Pan et al., 2017; Liu et al., 2016; Liu, 2019; Wang et al., 2018a; Wang et al., 2018b). The key characterization parameters and functional relationship that affect the permeability change of coal bodies through experimental research and theoretical analysis, providing theoretical support for the oxidation and spontaneous combustion characteristics of coal bodies under different stress loading paths. Through the establishment of a unified mathematical model to describe the permeability of coal pores and fractures, the gas seepage in coal can be divided into three types: pore control type, fracture control type and pore fracture joint control type (Jaiswal and Shrivastva, 2009; Wattimena et al., 2013).

At present, research on spontaneous coal combustion is mainly focused on the prevention and control of remaining coal in a goaf; however, there is little mention of that the coal pillars spontaneous combustion. Obviously, coal pillar of the goaf is a core area of spontaneous combustion of shallow buried and close-distance coal seams. Therefore, studying the mechanism of the breaking and oxidation of the coal pillar in the upper goaf can guide the prevention and control of spontaneous coal combustion.

By using FLAC^{3D} numerical simulation software to simulate the dynamic excavation process and combining with the change law of the plastic area and displacement of the pillar, this paper explores the fracture development and breaking mechanism of the pillar in the repeated mining process and judges the high-risk area of spontaneous combustion of it of the upper coal seam. The prevention and control of spontaneous combustion in the goaf is of great practical significance.

2 Numerical model and parameter setting

2.1 Model establishment

The physics model was established in accordance with the working face drilling histogram of the Bulianta Coal Mine. There were three mining faces (A, B, C and D) with lengths of 300 m and a face C with a length of 400 m. Additionally, 100–200 m of coal remained on both sides of the boundary tunnel to avoid the boundary effect. The mining was conducted according to the order of the mining faces (A, B, C and D). There was a coal pillar (about 40 m) between A and B, and the coal pillar of the lower coal seam was staggered with the coal pillar of the upper coal seam by 100 m. The simulated conditions of the recovery are shown in Table 1, and the model is shown in Figure 1.

2.2 Mechanical parameter setting and simulation scheme

According to the distribution of rock strata in the working face (Li et al., 2016), the mechanical parameters of each rock mass are determined. Mohr Coulomb yield criterion is adopted for model calculation. See Table 2 for physical and mechanical parameters of coal and rock mass in each layer.

3 Results and discussion

3.1 Stress distribution at different mining stages

Figures 2, 3 show the z-direction stress distribution map of the top and bottom surfaces of the coal pillar after the mining of working faces A, B, C and D. In different mining stages, the comparative distribution of stress at the top and bottom of coal pillar along the strike of 140 and 250 m is shown in Figures 4, 5, 6, 7. FLAC^{3D} specifies that the direction of the force is negative downward and positive upward along the z-direction.

3.1.1 Completion of stope A

Stress concentration is formed along one side of the goaf of the coal body, and the maximum stress at the top of the coal pillar is 8–8.3 mpa. With the increase of the distance between the coal body and the goaf, the stress on the coal body decreases. At the left boundary, the stress slightly increased compared with the original rock stress. There is an obvious stress concentration area along the coal pillar 565–585 m dip angle, with a stress of 6–7 MPa at 590–595 m along the dip. The stress decreases to approximately 5.9 MPa; along

TABLE 1 Simulated condition of recovery.

Working face	depth/m	Strike length/m	Dip length/m	Coal thickness/m	Mining thickness/m
A	162	300	300	5.5	4.5
B	162	300	300	5.5	4.5
C	192	300	400	6.2	5
D	192	300	300	6.2	5

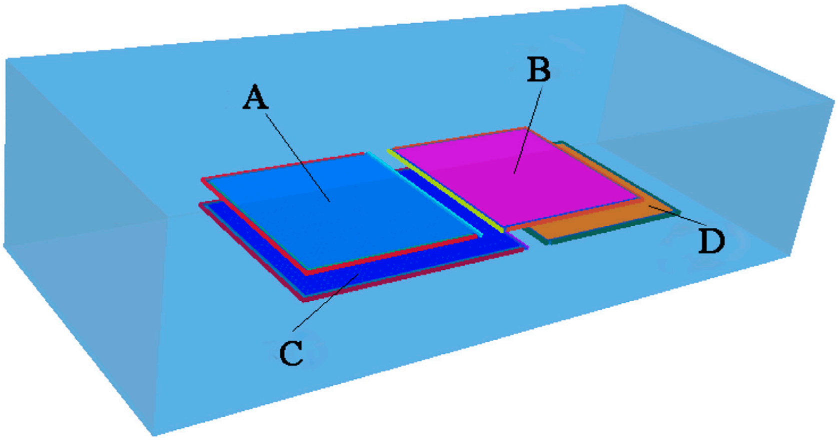

FIGURE 1
The coal mine excavation model.

the incline from 590 to 600 m, the stress concentration zone running through the strike appears again at the bottom of the coal pillar. When mining face A is completed, the variation trend of stress at the bottom of the coal pillar is quite different from that at the top of the coal pillar.

3.1.2 Completion of stope B

The *z*-direction stress on the top surface of the coal pillar is basically distributed symmetrically, and the maximum stress value along the goaf on both sides of the coal pillar is approximately 10 MPa. The minimum *z*-direction stress in the middle of the core area of the coal pillar is approximately 7.4 MPa. The stress distribution at the bottom of the coal pillar is basically the same as that at the top, but the stress concentration at the bottom appears at 100–150 and 350–400 m along the strike of the coal pillar, and the minimum *z*-direction stress in the middle of the core area of the coal pillar is approximately 7.4 MPa.

3.1.3 Completion of stope C

The coal pillar of the upper coal seam is in the disturbed fracture zone of the lower coal seam, and the mining of the lower coal seam leads to a new balance of the coal pillar of the upper coal seam. At this time, 200–300 m along the strike of the left side of the coal pillar is the place with the largest stress on the top of the whole coal pillar, and the maximum stress is approximately 4 MPa. Taking this as the centre, the absolute value of the stress decreases in an elliptical wave to the right until the stress value at the right boundary of the coal pillar reaches 1.5 MPa, and the stress direction is downward.

At 125–175 and 325–375 m along the strike of the right boundary of the coal pillar, the *z*-direction stress on the top surface of the coal pillar changes from vertical downward to vertical upward, and the stress value is approximately 0.2 MPa. The recovery of face C is a pressure relief process for the coal pillar of the upper coal seam. In this process, the stress on the top of the coal pillar drops below the stress of the primary rock, and the stress direction in some areas has changed. The stress distribution of the coal pillar bottom and top is consistent; taking the left side of the coal pillar as the centre along the strike of 200–300 m, the absolute value of stress decreases to the right, the value of stress at the right boundary of the coal pillar reaches 1–1.4 MPa, and the direction of stress is downward. At 125–175 and 325–375 m along the strike of the coal pillar, the

TABLE 2 The mechanical parameters of coal and rock.

Strata	Burying depth/m	Density/kg·m-3	Modulus of elasticity/GPa	Friction angle/°	Cohesion/ MPa	Tensile strength/MPa	Poisson's ratio/°
Aeolian sand	17	1,450		24.7	1.0	1.0	0.26
Sandy mudstone	41	2,250	1.52	28.6	1.1	0.7	0.28
Siltstone	43	2050	2.31	30.8	6.5	1.77	0.27
Mudstone	62	2,600	1.9	33.1	2.2	1.01	0.25
Fine sandstone	71	2090	1.15	23.4	2.8	0.75	0.27
Medium grain sandstone	76	2050	0.43	29.8	8.31	2.62	0.26
Fine sandstone	81	2,219	1.27	22.3	1.26	0.49	0.27
Siltstone	87	2,313	0.81	34.1	1.16	1.75	0.31
Fine sandstone	124	2,295	16.04	26.8	9.31	4.28	0.16
Sandy mudstone	134	2,334	14.34	24.7	6.28	1.78	0.29
Mudstone	139	2,326	4.08	26	10.12	2.76	0.28
Coarse-grained sandstone	155	2,204	6.71	19.5	12.4	1.33	0.23
1–2 coal seam	16	1,284	1.76	23.6	17.9	1.68	0.27
Sandy mudstone	177	2,308	7.27	26.1	18.96	5.24	0.26
Fine sandstone	181	2,226	7.39	24.5	14.68	3.38	0.24
Coarse-grained sandstone	190	2,185	3.88	14.1	27.6	2.88	0.27
2–2 coal seam	195	1,303	1.99	24.5	19.25	1.17	0.23

z-direction stress direction of the coal pillar bottom changed from downward along the z-direction to upward along the z-direction, and the stress value was 0.2 MPa.

3.1.4 Completion of stope D

The maximum stress is 7.5 MPa on the left side of the top of coal pillar along the strike of 200–300 m; it decreases to the right and reaches approximately 5 MPa at the right boundary of coal pillar, and the stress on the top of the coal pillar increases to more than 4.5 MPa at 200–300 m along the strike. The stress on the top of the coal pillar decreases from the middle to both sides along the strike; at 100–200 m and 300–400 along the strike, the stress on the top of the coal pillar is less than that of the primary rock; At 100–150 m and 350–400 m along the strike of coal pillar, the z-direction stress direction changes (from z-down to z-up) in some areas, and the maximum value of the upward stress is approximately 0.5 MPa.

3.2 Z-displacement distribution coal pillars in different mining stages

Figure 8 the z-displacement distribution map of bottom surfaces of the coal pillar after the mining of working faces A, B, C and D. FLAC^{3D} specifies that the direction of the force is negative downward and positive upward along the z-direction.

3.2.1 Completion of stope A

The z-direction displacement of the bottom of the coal pillar increases from left to right, and the overall subsidence ranges between 0.01 and 0.15 m. The subsidence at the bottom of the coal pillar is less than that at the top, the whole coal pillar is in the compression state, and the compression at the left side of the coal pillar is the largest, with a compression of 0.1 m.

3.2.2 Completion of stope B

At this time, the z-direction displacement of the bottom of the coal pillar ranges between 0.17 and 0.34 m, which is slightly less than the z-direction displacement of the top of the coal pillar at this stage. The coal pillar is in the compression state, and the z-direction displacement of the bottom of the coal pillar is less than the middle on both sides (along the trend).

3.2.3 Completion of stope C

The z-direction displacement of the bottom surface of the coal pillar in the upper coal seam changes greatly due to the mining of working face C. 1) In the middle of the coal pillar, the entire coal pillar sinks approximately 3.6 m along the strike of 150–350 m, and the sinking area accounts for nearly 2/3 of the top slice of the whole coal pillar. 2) The z-direction displacement on the bottom of the coal pillar is basically symmetrical in the strike, and it decreases on both sides along the strike. At the

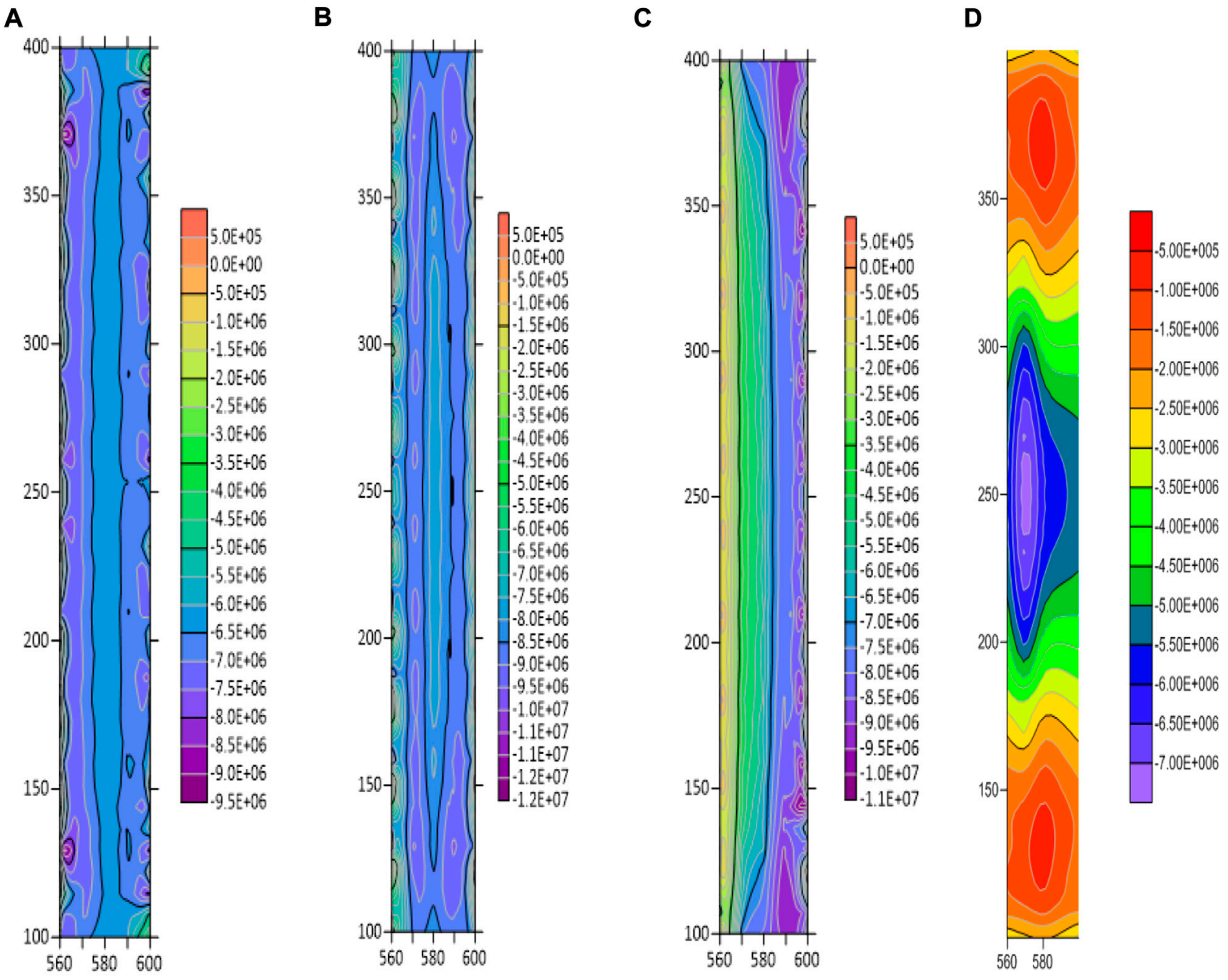

Completion of stope	Completion of stope	Completion of stope	Completion of stope

FIGURE 2
Z-Stress distribution of the top surface at different stages. Completion of stope **(A)**, **(B)**, **(C)** and **(D)** represent the mining of working face **(A)**, **(B)**, **(C)** and **(D)** respectively.

cutting hole, the minimum *z*-direction displacement on the bottom of the coal pillar is only approximately 0.4 m 3) The maximum relative z-displacement in the *Z* direction at the top of the coal pillar is 3.2 m. The recovery of face C is a process of pressure release for the coal pillar.

3.2.4 Completion of stope D

The *z*-direction displacement of the coal pillar bottom basically shows the same trend as the previous mining stage, with a large amount of decline in the middle and a small amount of decline on both sides along the strike. The mining of face D is a stress concentration process for the coal pillar, and the coal pillar is further compacted after the mining of face D is completed.

3.3 Stability analysis of the upper coal pillar

According to the calculation of A.H Wilson's empirical formula, it is considered that the coal pillar maintains good stability after the completion of mining faces A and B, the plastic failure area on the coal pillar is less than 20% of the whole coal pillar, and the coal pillar is in a stable state as a whole. Due to the particularity of repeated mining conditions of the close seam group, the A.H Wilson's empirical formula is not suitable for the stability judgement of the coal pillar after mining the adjacent layer below.

When the mining of face C is completed, the distribution diagram of the plastic area of the whole coal pillar is as follows in Figure 9:

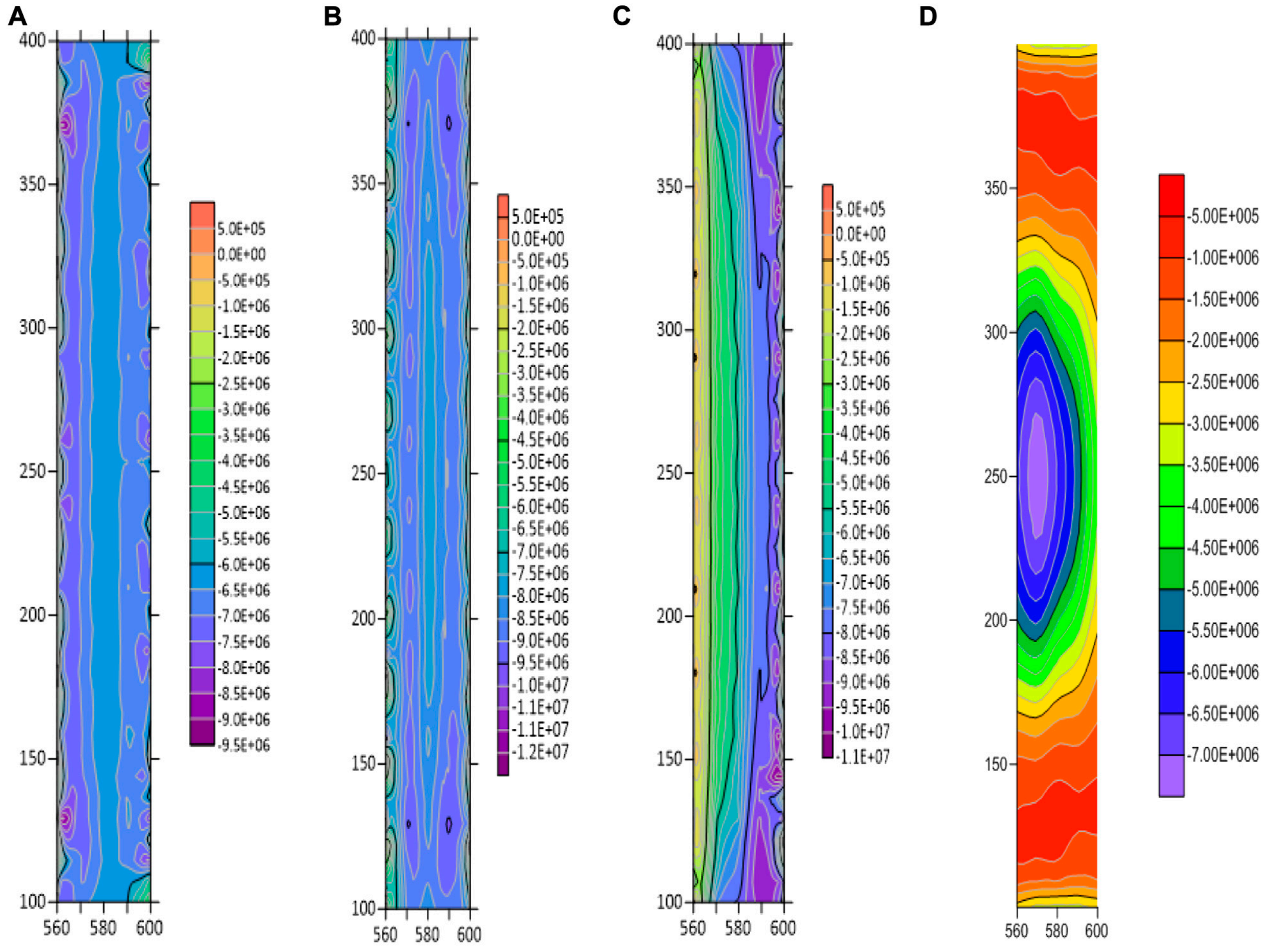

Completion of stope Completion of stope Completion of stope Completion of stope

FIGURE 3
Stress distribution of the bottom surface in different mining stages. Completion of stope **(A)**, **(B)**, **(C)** and **(D)** represent the mining of working face **(A)**, **(B)**, **(C)** and **(D)** respectively.

In Figure 9, shear indicates shear failure, tension indicates tensile failure, - p indicates that the coal body in this area has experienced plastic failure in the past, and - n indicates that the coal body in this area is still in plastic failure state; as shown in the figure, when face C is fully recovered, the coal pillar is in a plastic state as a whole. The influence of the mining of the adjacent coal seam on its disturbance is not considered. It can be seen from the figure that the coal pillar has plastic damage due to the mining of coal face C. However, according to the analysis of the load strength of the coal pillar, the recovery of face C is a pressure relief process for the coal pillar (from the above analysis, it can be seen that the stress state of the whole coal pillar is greatly reduced after the completion of recovery of face C, but the coal pillar changes from the stable state at the end of recovery of face B to the unstable state after the completion of recovery of face C).

3.4 Breaking mechanism of coal pillar along strike

Therefore, in this paper, the author analyses the instability mechanism of coal pillar under the special conditions of repeated mining and staggered arrangement of coal pillars in shallow and short-distance coal seams in combination with the abovementioned changes of z-displacement and stress of coal pillars in different stages of mining.

It can be seen from Figures 10, 11 that with the continuous mining of face C, as the overburden rock continues to collapse towards the goaf of face C, when the hanging length of the coal pillar in upper coal seam exceeds a certain distance, the coal pillar will break along the strike, thus forming block articulated blocks G and H. At this time, it is not the excessive upper load that causes the collapse and instability of the coal pillar, but the

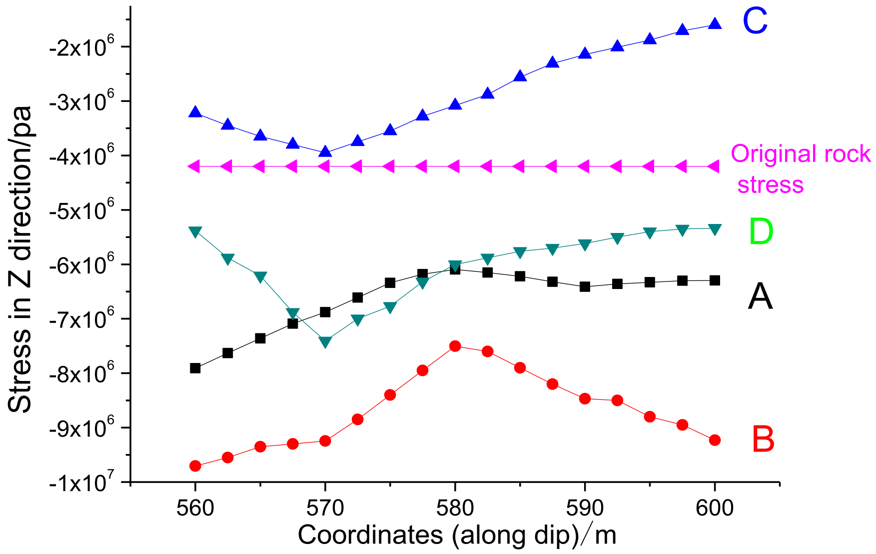

FIGURE 4
Stress variation at different mining stages (Y=250 m).

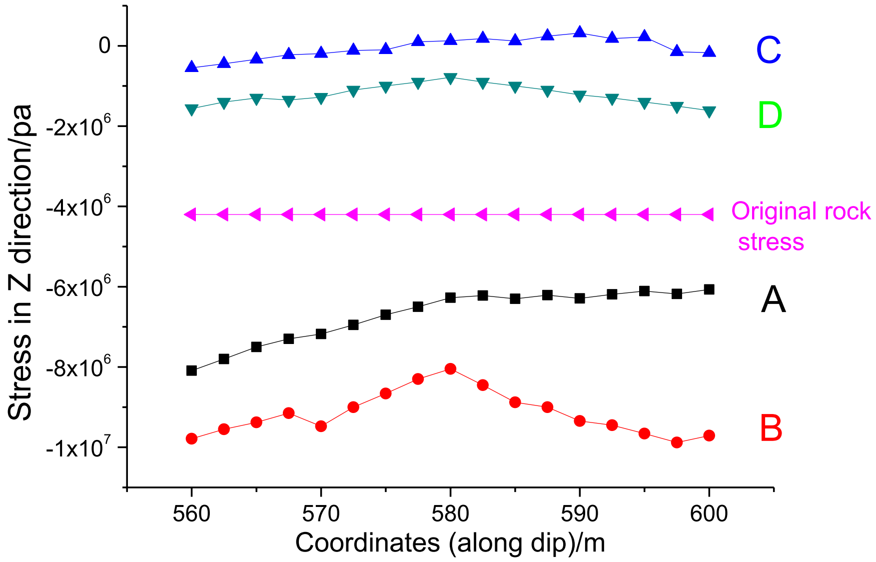

FIGURE 5
Stress variation at different mining stages (Y=140 m).

bedrock at the bottom of the coal pillar is affected by the mining of the lower coal seam, leading to the fracture and instability of the coal pillar along the strike. It can be seen from the above analysis that when the mining of face C is completed, there is a situation in which the stress direction on the coal pillar is along the *z*-axis. It is precisely because of the existence of this stress difference on the whole coal pillar that the coal pillar forms relative cutting along the strike, resulting in the fracture and instability of the coal pillar.

According to the above analysis, the "masonry beam" theory is used to analyse the coal pillar broken along the strike. At the moment when the coal pillar starts to break, the mechanical

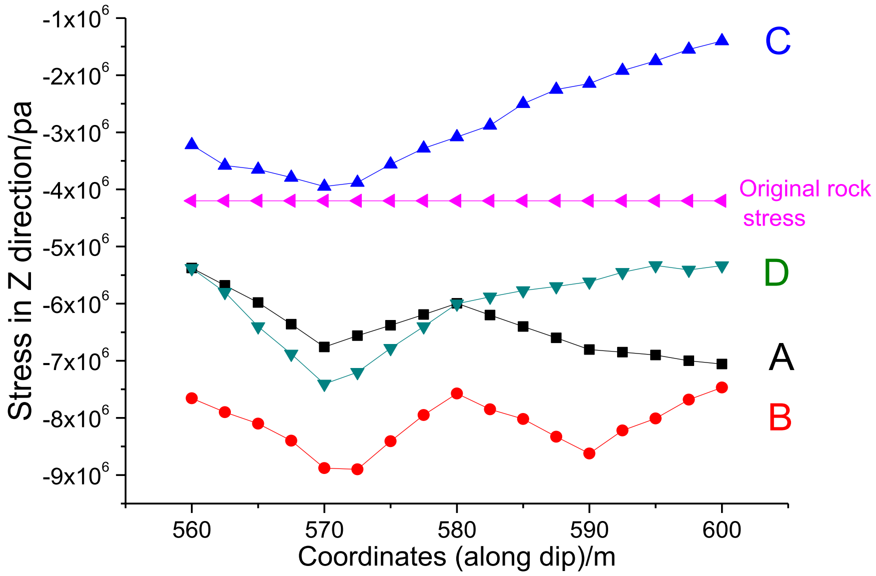

FIGURE 6
Bottom surface stress variation at different mining stages (Y=250 m).

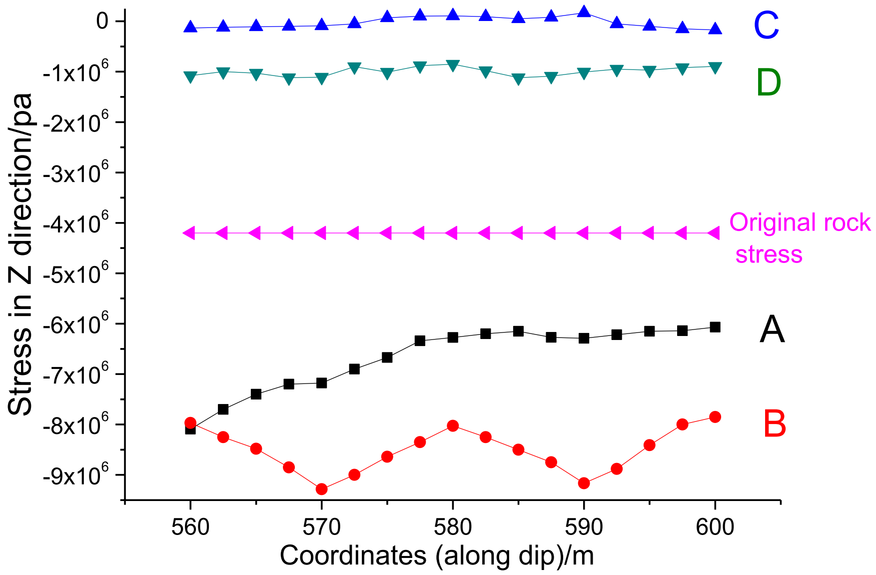

FIGURE 7
Bottom surface stress variation at different mining stages (Y=140 m).

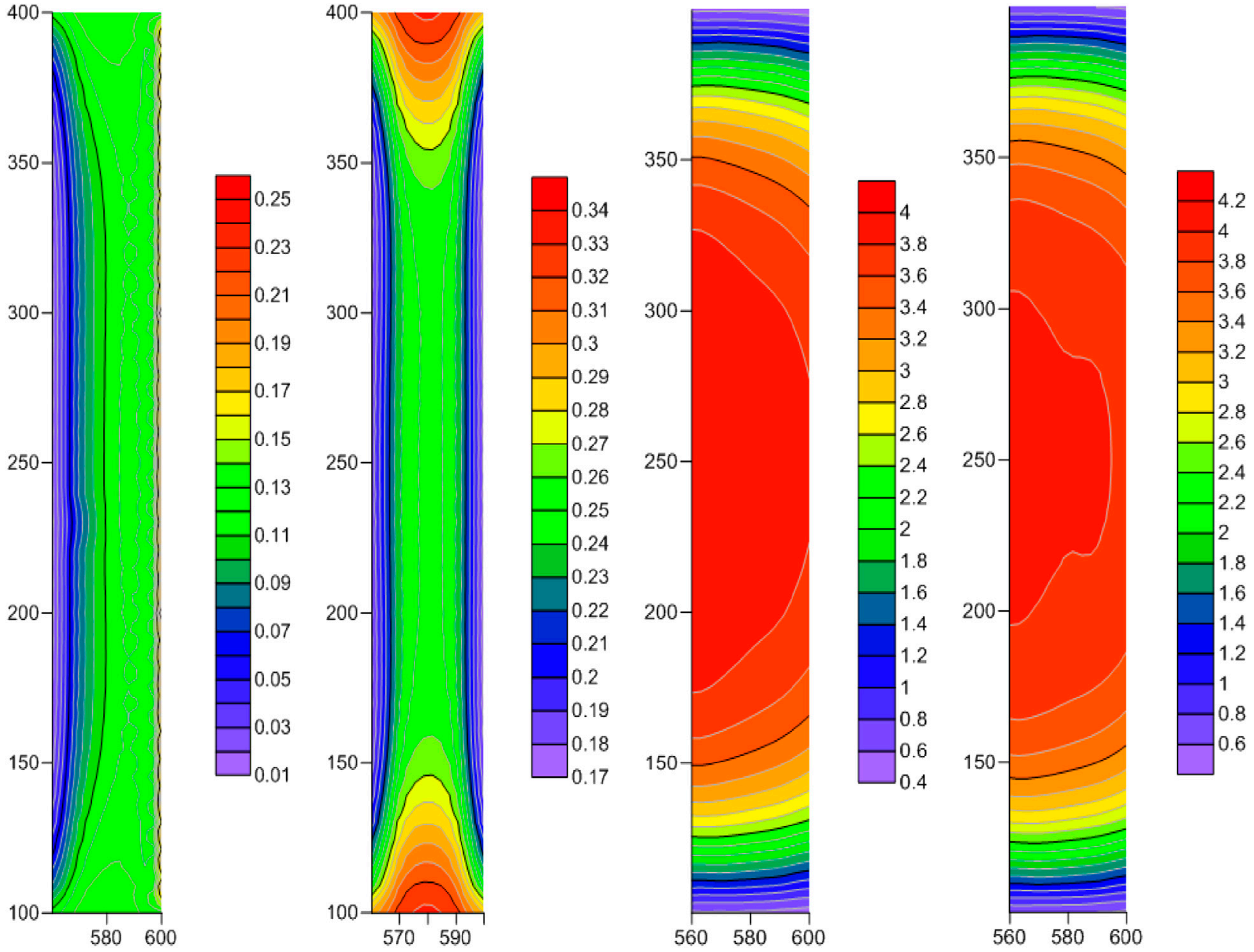

FIGURE 8
Z-displacement distribution at the bottom of the coal pillar in different mining stages.

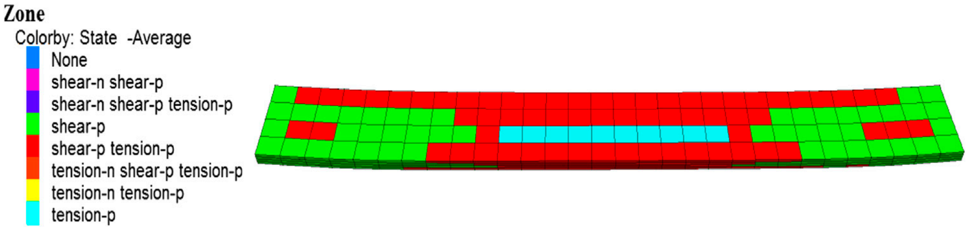

FIGURE 9
Plastic zone distribution of coal pillars after C recovery.

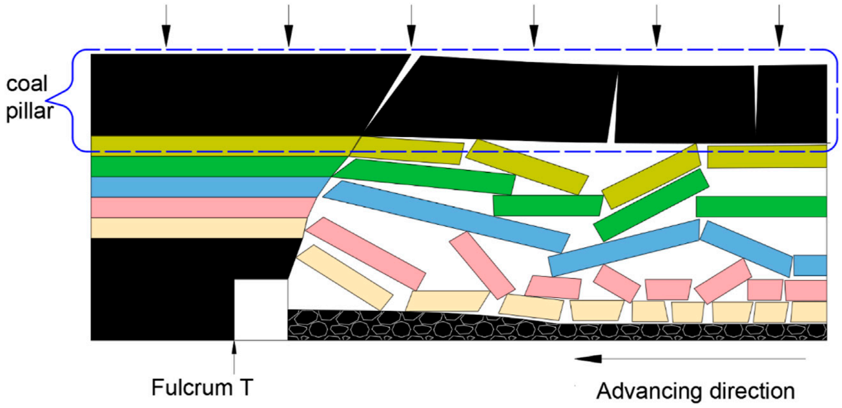

FIGURE 10
Section of the coal pillar along the trend at the stage of C recovery.

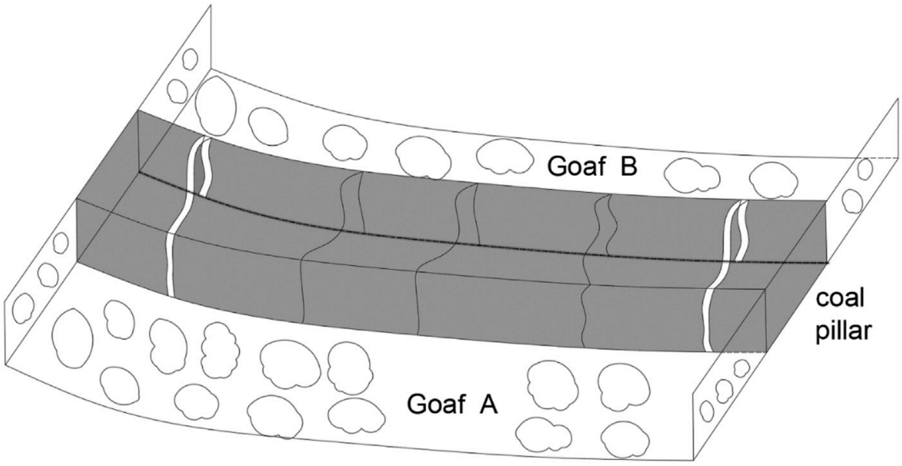

FIGURE 11
Fracture and instability diagram of coal pillar along strike.

model shown in Figure 12 is established for the key block G. Among them, F_B is the supporting force of coal pillar floor bedrock to coal pillar fracture block G. According to the moment balance relationship, it can be solved as follows:

$$F_B = \frac{1}{k_b}\left(R_H + \frac{1}{2}ql_g\right) \tag{1}$$

In the following formula: $\boldsymbol{l_g}$ is the length of the broken coal body **G**; $\boldsymbol{R_H}$ is the shear stress of the hinge between the broken coal body **G** and **H**; $\boldsymbol{q}$ is the load on the coal pillar; $\boldsymbol{k_b}$ is the coefficient, $\boldsymbol{k_b = l_b/l_g}$; and $\boldsymbol{l_b}$ is the strike distance of the supporting force $\boldsymbol{F_b}$ relative to the broken coal body boundary T.

In the above formula, $\boldsymbol{l_1}$ is the length of the broken coal pillar, $\boldsymbol{h_1}$ is the width of the broken coal pillar, and $\boldsymbol{\alpha}$ is the rotation angle of the broken coal rock mass H. Therefore, the above formula can be expressed as:

$$F_B = \frac{l_g}{l_b}\left[\frac{18 - 3l_1 \sin\alpha}{18 - 2l_1 \sin\alpha}ql_1 + \frac{1}{2}ql_g\right] \tag{2}$$

Then, the expression of L1 is obtained as follows:

$$l_1 = \frac{2k\sin\alpha + 18q + \sqrt{4k^2\sin^2\alpha + 342q^2 - 114k\sin\alpha}}{69\sin\alpha} \tag{3}$$

Combined with the z-direction displacement of coal pillars in different stages of mining, it can be well explained that the coal pillar in the upper coal seam will have stepped subsidence when the coal pillars are staggered outside. Combined with the z-direction displacement of coal pillars in different stages of

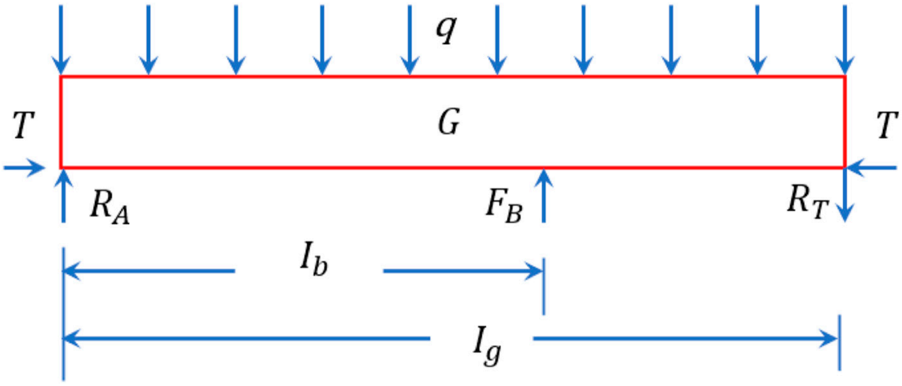

FIGURE 12
Mechanical model of broken coal G column.

TABLE 3 Coal pillar state at different stages.

Stage	Maximum z stress/MPa	Maximum Z displacement/m	Width of plastic zone/m	Pillar state
A	8.5	0.25	1.4	Stable
B	11.4	0.43	3.54	Stable
C	3.8	4	40	Breaking and stability
D	7	4.2	40	Compaction after breaking

mining, it can be well explained that when the coal pillars are staggered outside, mining below the adjacent coal seam will make the coal pillar of the upper coal seam sink step by step, which will lead to the relative cutting of coal pillars along the strike, which can also explain that at mining stage C, the load of the coal pillar is less than the original rock stress, but the coal pillar has a large area of plastic failure and instability. The status of coal pillars in different stages of mining is shown in Table 3 below:

3.5 Determination of hazardous area of coal pillar

According to the above analysis, different from the traditional coal pillar, which is broken and unstable because of the load exceeding the bearing limit, under the research conditions of this paper, the mining of the lower coal seam leads to the collapse of the bedrock under the coal pillar of the upper coal seam. After the completion of mining face C, the distribution diagram of displacement and stress on the top of the coal pillar is as follows:

According to the displacement, the coal pillar area is divided. Area A and C at both ends of the coal pillar along the strike are defined as the “step sinking area”. The difference of the top surface is mainly concentrated in areas A and C. As shown in Figure 13 (1), due to the existence of a *z*-direction displacement difference, fractures along the dip are mostly developed in areas A and C, and the length of A and C is approximately 50 m, which is also consistent with the ultimate fracture length along the strike derived in this paper. B in the middle of the coal pillar is defined as “compaction after breaking”. According to Figure 13 (1), the *z*-direction displacement difference of the coal pillar in this area can be ignored after compaction by overburdening. Area B is in the compaction state after breaking, and the fracture development degree and quantity in area B are far less than those in areas A and C. As shown in Figure 13 (2), area D is defined as the “reverse stress area”. In area D, the stress on the top of the coal pillar appears to be vertical upward along the *z*-direction, which is opposite to the stress direction of other areas of the coal pillar, which is downward along the *z*-direction; the maximum *z*-direction stress difference between the coal body in area D and the middle of the coal pillar is 4 MPa, and the relative shear action of the coal pillar is obvious.

(Pan et al., 2017) conducted a temperature programmed test on unloading coal bodies with different initial stresses and concluded that unloading coal bodies are easier to oxidize than

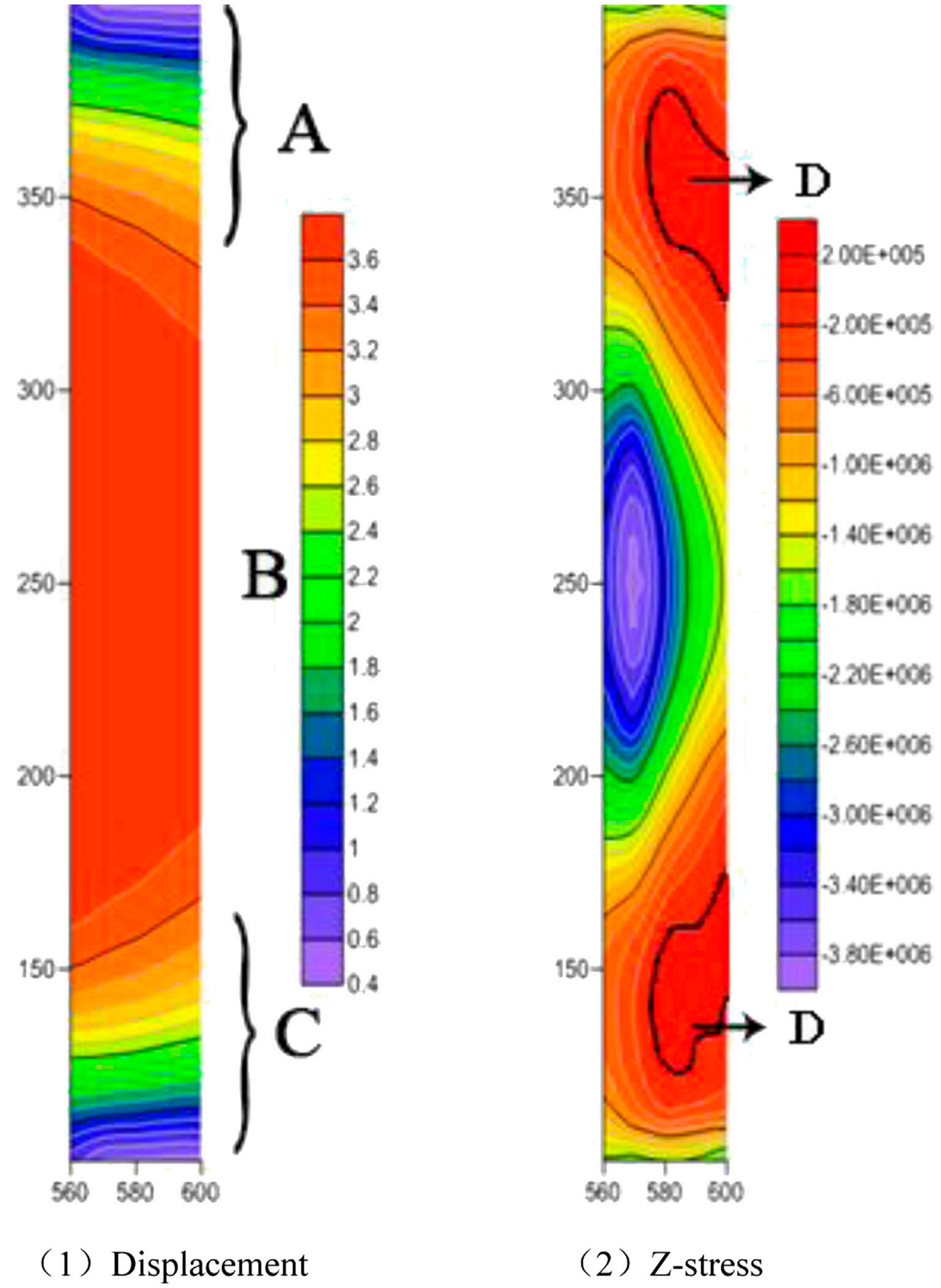

（1） Displacement （2） Z-stress

FIGURE 13
Distribution diagram of displacement and z-stress on top of coal pillar in old goaf after completion of stope D.

the original coal samples under different initial stresses. Under the research conditions in this paper, the stress on the coal pillar experienced three states: the original rock stress state, the stress concentration state and the stress release state. The load of the coal body in area D is only 0.05 times that of its original rock stress, which is approximately the state of complete unloading. In addition, most of area D coincides with area A with a fully developed fracture, so it can be determined that area D is a high-risk area for the spontaneous combustion of coal pillars in the upper coal seam under the condition of repeated mining of shallow buried coal seams.

4 Conclusion

In this paper, FLAC^{3D} numerical simulation software is used to simulate the repeated mining process of shallow buried and close-seam groups. Based on the analysis of the dynamic evolution process of the stress displacement of the upper coal pillar in different stages of mining, the mechanism of the instability and fracture of the upper coal pillar under the condition of the repeated mining of the shallow buried andxclose coal seam group is obtained. The conclusions are as follows:

1) In the process of repeated mining of a close coal seam group, the mining of the lower adjacent layer is a pressure relief process for the upper coal pillar. Compared with the traditional coal pillar, which is broken and unstable due to the load exceeding the ultimate strength, the main reason for the fracture and instability of the upper coal pillar is the difference distribution of the stress on the upper coal pillar caused by the mining of the lower coal seam.
2) The " block structure of voussoir beam " is used to calculate the ultimate fracture length of the coal pillar along the strike under this working condition, which is consistent with the numerical simulation.
3) According to the dynamic evolution characteristics of displacement stress on coal pillars, the coal pillar of the upper coal seam is divided into “step subsidence area”, “compaction after broken area” and “reverse stress area”, and the high spontaneous combustion risk area of coal pillars is determined and identified by combining with previous studies, which is of great practical significance for understanding the spontaneous combustion of coal pillars of upper coal seams under the condition of repeated mining.

Data availability statement

The original contributions presented in the study are included in the article/Supplementary Material, further inquiries can be directed to the corresponding author.

Author contributions

All authors listed have made a substantial, direct, and intellectual contribution to the work and approved it for publication.

Funding

This work was financially supported by the research fund provided by the National Key Research and Development Program of China (2018YFC0807900), the National Scientific Foundation of China (51574111, 52004084), the Henan Province Key R&D and Promotion Special (Technology Tackling Key) Project (222102320124, 22210232006, 212102310388, 22210232006), The Key scientific research projects plan of colleges and universities in Henan Province (22A440005).

Conflict of interest

The authors declare that the research was conducted in the absence of any commercial or financial relationships that could be construed as a potential conflict of interest.

Publisher’s note

Supplementary material

The Supplementary Material for this article can be found online at: https://www.frontiersin.org/articles/10.3389/feart.2022.991304/full#supplementary-material

References

Asadi, A., Shahriar, K., and Goshtasbi, K. (2005). Development of a new mathematical model for prediction of surface subsidence due to inclined coal-seam mining[J]. *Journal- South Afr. Inst. Min. Metallurgy* 105 (1), 15–20.

Bi, Y., Xie, L., Wang, J., Zhang, Y., and Wang, K. (2019). Impact of host plants, slope position and subsidence on arbuscular mycorrhizal fungal communities in the coal mining area of north-central China. *J. Arid Environ.* 163, 68–76. doi:10.1016/j.jaridenv.2018.11.011

Changchun, H., and Jialin, X. (2018). Subsidence prediction of overburden strata and surface based on the Voussoir beam structure theory[J]. *Advances in Civil Engineering* 2018, 1–13. doi:10.1155/2018/2606108

Chen, C., Hu, Z., Wang, J., and Jia, J. (2019). Dynamic surface subsidence characteristics due to super-large working face in fragile-ecological mining areas: A case study in shendong coalfield, China. *Adv. Civ. Eng.* 2019, 1–16. doi:10.1155/2019/8658753

Cheng, W., Hu, X., Xie, J., and Zhao, Y. (2017). An intelligent gel designed to control the spontaneous combustion of coal: Fire prevention and extinguishing properties. *Fuel* 210, 826–835. doi:10.1016/j.fuel.2017.09.007

Genc, B., and Cook, A. (2015). Spontaneous combustion risk in South African coalfields. *J. South Afr. Inst. Min. Metallurgy* 115 (7), 563–568. doi:10.17159/2411-9717/2015/V115N7A1

Guo, H., Yuan, L., Shen, B., Qu, Q., and Xue, J. (2012). Mining-induced strata stress changes, fractures and gas flow dynamics in multi-seam longwall mining. *Int. J. Rock Mech. Min. Sci. (1997).* 54, 129–139. doi:10.1016/j.ijrmms.2012.05.023

Hao, M., Li, Y., Song, X., Kang, J., Su, H., and Zhou, F. (2019). Hazardous areas determination of coal spontaneous combustion in shallow-buried gobs of coal seam group: A physical simulation experimental study. *Environ. Earth Sci.* 78 (1), 39. doi:10.1007/s12665-018-8010-5

Huang, Q., and Cao, J. (2019). Research on threefield evolution and rational coal pillar staggered distancein shallow buried closely spaced multi-seam mining[J]. *J. China Coal* 44 (3), 681–689.

Huang, Q., and Du, J. (2018). Coupling control of pillar stress and surface cracks in shallow coal seam group mining[J]. *J. China Coal* 43 (3), 591–598.

Jaiswal, A., and Shrivastva, B. K. (2009). Numerical simulation of coal pillar strength. *Int. J. Rock Mech. Min. Sci.* 46 (4), 779–788. doi:10.1016/j.ijrmms.2008.11.003

Ju, J. F., and Xu, J. L. (2015). Surface stepped subsidence related to top-coal caving longwall mining of extremely thick coal seam under shallow cover. *Int. J. Rock Mech. Min. Sci. (1997).* 78, 27–35. doi:10.1016/j.ijrmms.2015.05.003

Kidybinski, A., and Babcock, C. O. (1973). Stress distribution and rock fracture zones in the roof of longwall face in a coal mine. *Rock Mech.* 5 (1), 1–19. doi:10.1007/BF01246754

Li, H., Li, H., and Song, G. (2016). Physical and mechanical properties of the coal-bearing strata rock in shendong coal field. *J. China Coal Soc.* 41 (11), 2661–2671.

Li, S., He, X., and Li, S. (2013). Experimental research on strata movement and fracture dynamic evolution of double pressure-relief mining in coal seams group[J]. *J. China Coal Soc.* 38 (127), 2146–2152.

Li, Y., Wang, J., Chen, Y., and Wang, Z. (2019). Overlying strata movement with ground penetrating radar detection in close-multiple coal seams mining. *Int. J. Distrib. Sens. Netw.* 15 (8), 155014771986985. doi:10.1177/1550147719869852

Liu, Y. (2019). Experimental analysis of coal permeability evolution under cyclic loading[J]. *J. China Coal* 44 (8), 2579–2588.

Liu, Y., Hou, J., and Zhang, L. (2016). Permeability experiments of pore structure in coal matrix[J]. *J. China Coal* 41 (2).

Lu, Y., and Qin, B. (2015). Identification and control of spontaneous combustion of coal pillars: A case study in the qianyingzi mine, China. *Nat. Hazards (Dordr).* 75 (3), 2683–2697. doi:10.1007/s11069-014-1455-2

Ma, L., Du, X., and Wang, F. (2013). Water-preserved mining technology for shallow buried coal seam in ecologically-vulnerable coal field: A case study in the shendong coal field of China [J]. *Disaster Adv.* 6, 268–278.

Majdi, A., Hassani, F. P., and Nasiri, M. Y. (2012). An estimation of the height of fracture zone in longwall coal mining[J]. *J. Am. Chem. Soc.* 107 (14), 4343–4345.

Pan, R., Chen, L., and Yu, M. (2017). Oxidation characteristics of unloaded coal under different initial stress[J]. *J. China Coal* 42 (9).

Prucz, J. C., and Fu, S. H. (1989). Prediction of dynamic fracture modes in coal mining. *Int. J. Rock Mech. Min. Sci. Geomechanics Abstr.* 26 (2), 161–167. doi:10.1016/0148-9062(89)90004-1

Przylucka, M., Graniczny, M., and Kowalski, Z. (2015). *Identification and changes of subsidence basins caused by coal mining activity in upper silesia using satellite interferometeric data[C]*, Fringe Workshop (University of the Witwatersrand).

Ramani, R. V. (1997). A numerical simulation of spontaneous combustion of coal in goaf[M]. *Int. Mine Vet.Congr.* 6, 313–316. doi:10.1016/S0140-6701(97)85372-6

Wactawik, J. (1998). A numerical simulation of spontaneous combustion of coal in goaf[J]. *Fuel Energy Abstr.* 39 (1), 15–19. doi:10.1016/S0140-6701(97)85372-6

Wang, H., Dlugogorski, B. Z., and Kennedy, E. M. (2003). Analysis of the mechanism of the low-temperature oxidation of coal. *Combust. Flame* 134 (1-2), 107–117. doi:10.1016/S0010-2180(03)00086-5

Wang, K., Tang, H., Wang, F., Miao, Y., and Liu, D. (2019). Research on complex air leakage method to prevent coal spontaneous combustion in longwall goaf. *PLoS ONE* 14 (3), e0213101. doi:10.1371/journal.pone.0213101

Wang, Z., Fu, X., * Hao, M., Li, G., Pan, J., Niu, Q., et al. (2021). Experimental insights into the adsorption-desorption of CH4/N2 and induced strain for medium-rank coals. *J. Petroleum Sci. Eng.* 204, 108705. doi:10.1016/j.petrol.2021.108705

Wang, Z., Pan, J., * Hou, Q., Niu, Q., Tian, J., Wang, H., et al. (2018a). Changes in the anisotropic permeability of low-rank coal under varying effective stress in Fukang mining area, China. *Fuel* 234, 1481–1497. doi:10.1016/j.fuel.2018.08.013

Wang, Z., Pan, J., * Hou, Q., Yu, B., Li, M., and Niu, Q. (2018b). Anisotropic characteristics of low-rank coal fractures in the Fukang mining area, China. *Fuel* 211, 182–193. doi:10.1016/j.fuel.2017.09.067

Wattimena, R. K., Kramadibrata, S., Sidi, I. D., and Azizi, M. (2013). Developing coal pillar stability chart using logistic regression. *Int. J. Rock Mech. Min. Sci.* 58, 55–60. doi:10.1016/j.ijrmms.2012.09.004

Xie, H., and Zhou, H. (1999). Application of FLAC to predict gound surface displacements due to coal extraction and its comparative analysis[J]. *Chin. J. Rock Mech. And Eng.* 5 (4), 29–33.

Zhu, L., Jialin, X., Jinfeng, J., Zhu, W., and Xu, J. (2018). The effects of the rotational speed of voussoir beam structures formed by key strata on the ground pressure of stopes. *Int. J. Rock Mech. Min. Sci.* 108, 67–79. doi:10.1016/j.ijrmms.2018.04.041

Zhuo, H., Qin, B., Qin, Q., and Su, Z. (2019). Modeling and simulation of coal spontaneous combustion in a gob of shallow buried coal seams. *Process Saf. And Environ. Prot.* 131, 246–254. doi:10.1016/j.psep.2019.09.011

frontiers | Frontiers in Earth Science

TYPE Original Research
PUBLISHED 17 January 2023
DOI 10.3389/feart.2022.1031419

OPEN ACCESS

EDITED BY
Mingjun Zou,
North China University of Water Resources and Electric Power, China

REVIEWED BY
Guofa Ji,
Yangtze University, China
Yanyan Chen,
Research Institute of Petroleum Exploration and Development (RIPED), China
Jingyi Zhu,
Southwest Petroleum University, China

*CORRESPONDENCE
Jinxuan Han,
hanjx@ysu.edu.cn

SPECIALTY SECTION
This article was submitted to Economic Geology, a section of the journal Frontiers in Earth Science

RECEIVED 30 August 2022
ACCEPTED 24 October 2022
PUBLISHED 17 January 2023

CITATION
Lu Y, Han J, Zhang H, Xu Z, Yang Z, Yang M, Guo J, Zhu H and Qi Y (2023), Study on coal seam physical characteristics and influence on stimulation: A case study of coal seams in zhengzhuang block.
Front. Earth Sci. 10:1031419.
doi: 10.3389/feart.2022.1031419

Study on coal seam physical characteristics and influence on stimulation: A case study of coal seams in zhengzhuang block

Yanjun Lu[1], Jinxuan Han[1]*, Hua Zhang[2], Zhenping Xu[3], Zhaozhong Yang[4], Manping Yang[1], Junfeng Guo[5], Hongjian Zhu[1] and Yu Qi[1]

[1]School of Vehicle and Energy, Yanshan University, Qinhuangdao, China, [2]CNPC Bohai Drilling Engineering Company Limited, Tianjin, China, [3]Exploration and Development Research Institute of Changqing Oilfield Company, PetroChina, Xi'an, China, [4]State Key Laboratory of Oil and Gas Reservoir Geology and Exploitation, Southwest Petroleum University, Chengdu, China, [5]Shanxi CBM Exploration and Development Co., PetroChina, Jincheng, China

Coalbed Methane (CBM) is an unconventional form of natural gas which is self-generated and self-stored in coal seams. In order to realize the effective exploitation of CBM in Zhengzhuang block, microstructure, wettability, permeability, rock mechanics and *in-situ* stress of coal were studied in this research. It is found that high rank anthracite characterized by high vitrinite content and low inorganic mineral content, is abundant in CBM. More than 96% of inorganic minerals are clays dominated by kaolinite and illite. Various types of pores are developed on the coal. The wettability of coal differs from high to low to surface water, active water, and foam fracturing fluid; and contact angles of coal with active water and foam fracturing fluid decrease with the increase of burial depth. Gradients of fracture pressure and closure pressure in No.3 coal seam are higher than that of No.15 coal seam. The elastic modulus of coal is lower than that of sandstone. The construction curve of hydraulic fracturing shows that, when the construction flow rate and sand quantity are similar, the construction pressure of prepad in No.3 coal seam is lower than the pumping pressure of No.15 coal seam, but the propagated pressure is higher than that of No.15 coal seam. The drainage effect of No.3 coal seam with large pore volume, shallow burial depth and obvious fracture pressure is better than that of No.15 coal seam. The comprehensive understanding of coal physical properties and engineering practice in the block provide certain guiding significance to the CBM exploitation in Qinshui Basin.

KEYWORDS

coalbed methane, anthracite, pore-fissure of coal, coal physical properties, hydraulic fracturing

1 Introduction

Compared with conventional oil and gas reservoirs, CBM reservoir is characterized by low porosity, low pressure, and low permeability; the production of coalbed methane has to undergo the process of desorption, diffusion and seepage (Balan and Gumrah, 2009; Liu and Harpalani, 2013). Most coal seams must be fractured before they can be put into production (Wang et al., 2014). Through hydraulic fracturing, natural fracture system can be communicated, pollution near wellbore can be removed, and high seepage channel can be established for CBM desorption (Lu et al., 2018; Li et al., 2021). The final effect of fracturing is not only closely related to the characteristics of coal porosity and permeability, microstructure, rock mechanics, *in-situ* stress and other geological factors (Zhang et al., 2018; Xue et al., 2019; Salmachi et al., 2021; Min et al., 2022), but also affected by fracturing engineering factors (Li et al., 2020). Therefore, comprehensive reservoir geology analyzes and employ of fracturing engineering are necessary during CBM exploitation by provide developing guidance.

In the process of fracturing, fracturing fluid certainly will bring damage to coal seam, resulting in the permeability reduction and affecting the exploiting effect. Coal has high adsorption capacity for guar gum and broken organic polymer fracturing fluid (Cong et al., 2007; Gao, 2016). The damage rate of activate water to coal permeability is relatively low, and its damage to coal seam mainly comes from water sensitivity and water lock (Li et al., 2021). The contact between active water and coal matrix will produce wetting on the coal surface, and the micropore wetting will affect the desorption and seepage of gas. The decrease of contact angle indicates that the active water has good spreading effect on the coal surface, which is beneficial to the treatment of coal powder (Xu et al., 2021). The formation and propagation of fractures are controlled by surrounding rock to a certain extent. With the increase of the elastic modulus difference between coal and surrounding rock, the length of fractures formed by fracturing increases, the height decreases, and the fracture width increases. The longitudinal heterogeneity of mechanical properties of coal and surrounding rock increases the difficulty in vertical propagation of fractured fractures, which makes them easier to be confined in the coal seam and form long and wide fractures (Gao et al., 2020). In-site stress, tensile strength and cohesion are the important factors affecting the fracture propagation in coal (Teufel and Clark, 1984; Behnia et al., 2015). Whether hydraulic fracture penetrates the bedding plane depends not only on the mechanical properties difference between productive strata and interlayer, but also on the interface properties, vertical stress difference, horizontal stress difference, fracturing fluid pressure, fracture geometry and other factors (Huang and Liu, 2017). The shale—coal interface has a hindering effect on fracture propagation, and the fracture mainly extends in the horizontal direction, never crossing the rock interface (Yu et al., 2019).

In previous researches, mineral composition, macerals, mechanics and metamorphism degree of coal in Qinshui Basin have been thoroughly studied, but specific understanding of the effects of these characteristics on CBM exploitation is still a gap in the industry. In this paper, the No.3 and No.15 coal seams in Zhengzhuang block, southern Qinshui Basin are taken as examples. The influence of coal geology and engineering on CBM exploiting is comprehensively analyzed on the basis of laboratory experiments, combined with fracturing construction and on-site drainage data. The research results are expected to provide guiding significance for fracturing design.

2 Geological setting

Qinshui Basin, located in southeast Shanxi Province, is one of the areas with the most abundant carboniferous and Permian coal resources in North China. The coal seams of Taiyuan and Shanxi Formations are the targets of CBM exploration in this area. Coal measure strata are well developed and well preserved; and the tectonic structure is relatively simple and stable in Qinshui Basin. The total reserve of CBM in the basin is 3.97 × $10^{12}m^3$, accounting for 10.8% of total geological resources of CBM in China. At present, Qinshui Basin is an area with the largest investment, the highest degree of exploration, the most active exploitation and the most significant gas recovery, so it has become one of the two CBM industrialization bases in China (Liu et al., 2019). Zhengzhuang block is in southeast Qinshui Basin (Figure 1), which has many favorable conditions for CBM exploration and exploitation, and has been an important site for CBM exploration in recent years (Li et al., 2016; Zhu et al., 2018).

3 Experimental methods

Using scanning electron microscope (SEM), X-ray diffraction (XRD), energy dispersive spectrometer (EDS), optical microscope, HARKE-SPCA contact Angle tester, permeability test, injection/pressure drop well testing and *in-situ* stress test, and triaxial mechanical test, based on micro and macro structure-composition analysis, the physical properties of CBM occurrence in No.3 and 15 coal seams in Zhengzhuang block, Qinshui Basin were analyzed: including coal structure, composition, wettability, porosity, permeability, *in-situ* stress and mechanics of coal and surrounding rock. The differences between No.3 and No.15 coal seams were discussed, and the physical characteristics of two in the block were emphatically compared and analyzed to illustrate the influence of coal physical characteristics on CBM fracturing.

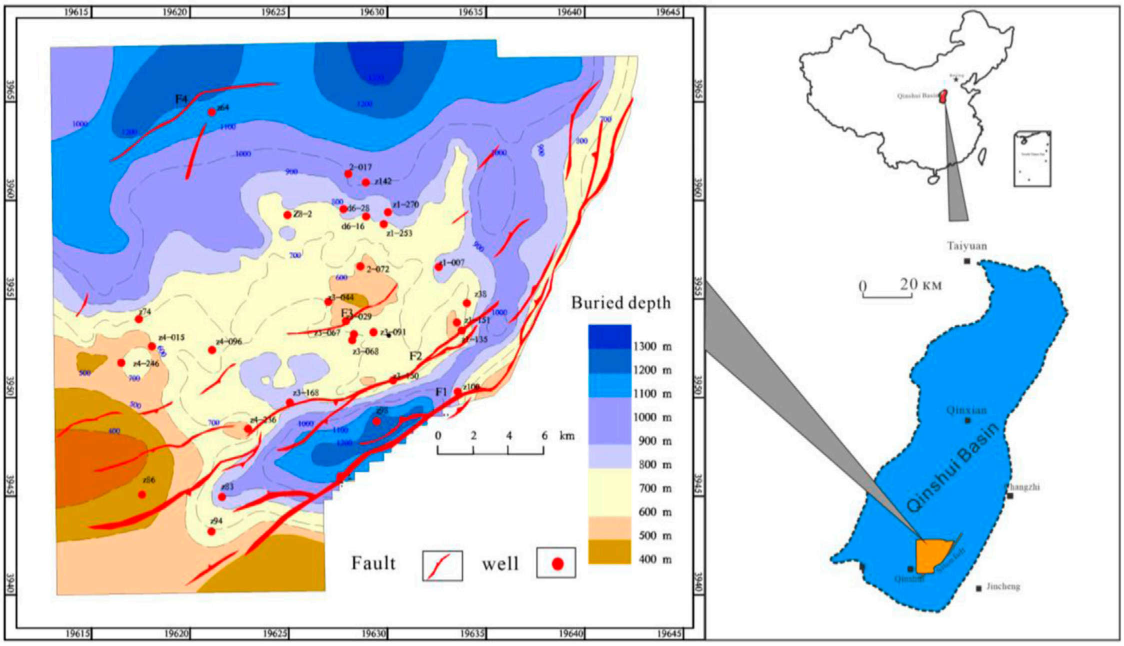

FIGURE 1
Location map of Zhengzhuang Block (modified according to Zhu and Li according to the literatures Li et al., 2016 and Zhu et al., 2018).

Coal sample from CBM Well in No.3 coal seam-ZM74

Coal sample from CBM Well in No.15 coal seam-ZM98

Coal sample from roadway located in No.3 coal seam-SM1

FIGURE 2
Different coal samples.

4 Sample characteristics

4.1 Apparent

Experimental core samples were collected from Zhengzhuang CBM Wells and Sihe coal mine, as shown in Figure 2. The color of coal in the area is black or gray-black, and the striation color is dark black, showing glass-strong glass luster. Endogenous fissures are not well developed; and irregular and conchoidal fractures can be observed. The natural fractures of roadway coal samples mainly exist in the form of horizontal fractures, while the natural micro-fractures of coal in CBM Wells mainly develop along the vertical direction, parallel to the wellbore direction, which is related to the coal sedimentary

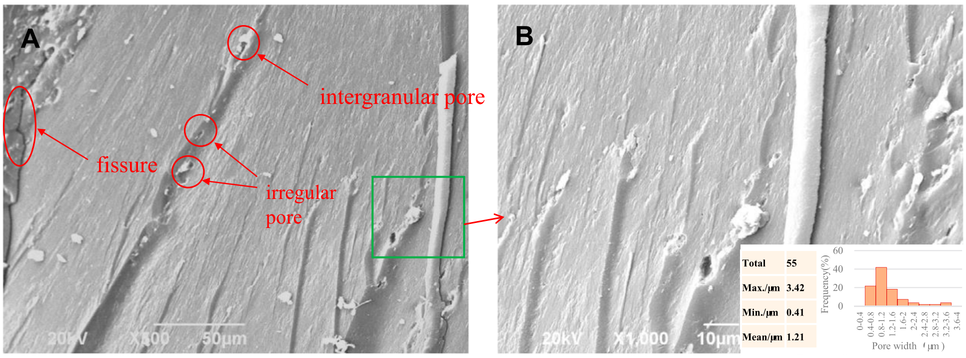

Roadway coal sample SM-1

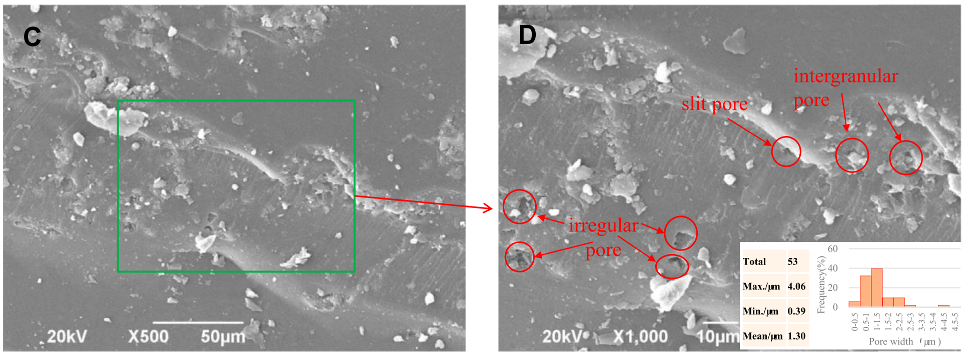

ZM98 Well located in No.3 coal seam

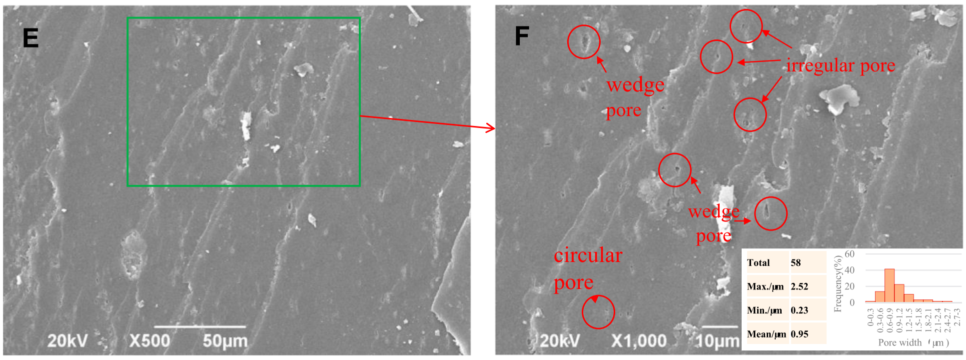

ZM74 Well located in No.15 coal seam

FIGURE 3
SEM of coal samples.

environment, tectonic movement and other factors. Compared with the coal samples in the roadway, the natural fractures in CBM Wells are more developed, and the coal has obvious metallic luster.

4.2 Microstructure

The microstructure of the samples was analyzed by SEM (Figure 3). It can be observed that there are different forms of pores and fissures on the coal surface, mainly pores by SEM. Most of the pores are uneven and partially filled or inlaid with clay. Types of pores include wedge, circular, irregular and slit. Point counting and measurements of pores in SEM images were done using Nano Measurer 1.2 software, and maximum pore size, minimum pore size, average pore size and pore size distribution in coal samples were obtained (Figure 3). The results show that under the same magnification (×1,000 times), the average pore size of roadway coal sample (No.3 coal) is 1.21 μm, the average pore size of No.3 coal seam is 1.30 μm, and the average pore size of No. 15 coal seam is 0.95 μm. It can be seen that the average pore size of No.3 coal seam is larger than that of No. 15 coal seam. According to Hodot's classification of pore size, coal pore can be divided into micropore (<10 nm), transition pore (10–100 nm),

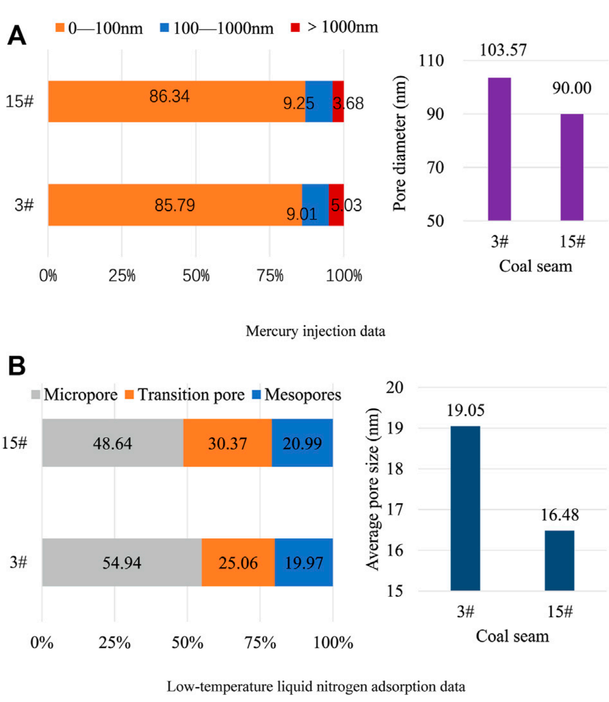

FIGURE 4
Pore characteristics of No. 3 and No. 15 coal seams (Hu et al., 2015).

mespore (100–1000 nm) and macropore (>1000 nm) (Hodot, 1966). Mercury injection can be used to study the distribution of transition pores, mesopores and macropores. Mercury injection data show that the pore size of No. 3 and No. 15 coal seams is mainly concentrated in 0–100 nm (as shown in Figure 4A). The proportion of pore size with 0–100 nm in No. 15 coal seam is higher than that in No. 3 coal seam, while the proportion of pore size over 1000 nm is lower than that in No. 3 coal seam. The mean pore diameter of No. 3 coal seam (103.57 nm) is larger than that of No. 15 coal seam (90 nm). This is consistent with the SEM results that No. 3 coal seam has more large pores, while No. 15 coal seam has more small pores. Low-temperature liquid nitrogen adsorption can be used to analyze the distribution of micropores, transition pores and mesopores. The adsorption data show that the average pore size of No. 15 coal seam is lower than that of No. 3 coal seam, but the proportion of transition pores and mesopores in No. 15 coal seam is slightly higher than that in No. 3 coal seam, indicating that the pore diameter of No. 15 coal seam is generally smaller in the same pore size segment (Figure 4B) (Hu et al., 2015).

In summary, the data of SEM, mercury injection and low-temperature liquid nitrogen adsorption show that the proportion of large pores, pore throat radius and average pore size of No. 3 coal seam are larger than those of No. 15 coal seam, and the pore structure is generally better, which is conducive to CBM exploitation.

4.3 Maceral and mineral analysis

Macerals are the smallest organic particles of coal which can be observed under microscope. Because they are composed of vegetation from different regions, they have different optical properties and chemical composition. The test results show that the vitrinite reflectance (R_o) of coal samples is 3.72–3.93%. The maceral is composed of vitrinite and inertinite without exinite. Mineral content is relatively low, accounting for 1–3.1% (Table 1). The vitrinite reflectance and mineral content of coal samples from coal mines and Wells are close to each other, indicating that the coal in this area all belong to high rank anthracite.

The organic residues of plants constitute the main part of coal, but inorganic substances (minerals) are involved in the whole process of converting vegetation into coal without exception. It is not only a part of coal, but also affects the conversion process of organic materials. The inorganic components in coal are mainly clay minerals, which are the main source of ash content. The distribution of carbonate minerals in coal is second only to clay minerals, including calcite, siderite and dolomite, etc. The most common sulfide mineral is pyrite, which is mostly found in shallow sea or coastal coal. Silica is mainly from quartz, mostly in the form of a single particle or larger block. By XRD experiments, the inorganic minerals of coal in Zhengzhuang block are mainly clay, quartz, potash feldspar, calcite and dolomite, of which clay accounts for 95%–98% (Table 1).

The mineral composition of the samples was analyzed by EDS. The white particles distributed on the coal surface are clay minerals, mainly kaolinite and illite. Kaolinite is a relatively stable non-swelling clay mineral which is not easy to be hydrated, it discontinuously distributes in the pore wall or fills in the pore space (Figure 5A), narrowing the pore. However, due to poor mechanical resistance of kaolinite, it is easy to cause cleavage cracking and disperse into scaly particles under external force, which damages the permeability of CBM reservoir. Illite is also a kind of non-expanding clay mineral, mostly dispersed in pores in a thin film shape, which is easily broken into discrete particles migrated with the fluid under the impact of high-speed fluid (Figure 5B), blocking the pore throat channel and affecting the diffusion and seepage of methane in coal seam.

The existence of clay minerals will have adverse effects on fracturing and drainage gas recovery of coal seam. On one side, the permeability of reservoir decreases and the fluid flow is affected due to the blockage of pores and fissures in coal. On the other side, it can weaken the mutual support strength of coal particles, lead to the production of coal powder, and affect the fracture conductivity and drainage effect after fracturing.

TABLE 1 Component analysis of coal samples.

Sample	Depth (m)	Maceral content (%)			Mineral content (%)	Mineral type and proportion (%)					Vitrinite reflectance R_o (%)
		Vitrinite	Inertinite	Exinite		Clay	Quartz	Potash feldspar	Calcite	Dolomite	
3#SM1	300–305	81.6	16.8	-	1.6	96	0	1	0	3	3.93
15#ZM74	958–959	84.3	14.2	-	1.5	95	1	2	0	2	3.85
3#ZM94	687–692	85.6	11.3	-	3.1	97	2	1	1	0	3.89
3#ZM98	1,232–1,233	77.8	21.2	-	1	98	1	1	0	0	3.72

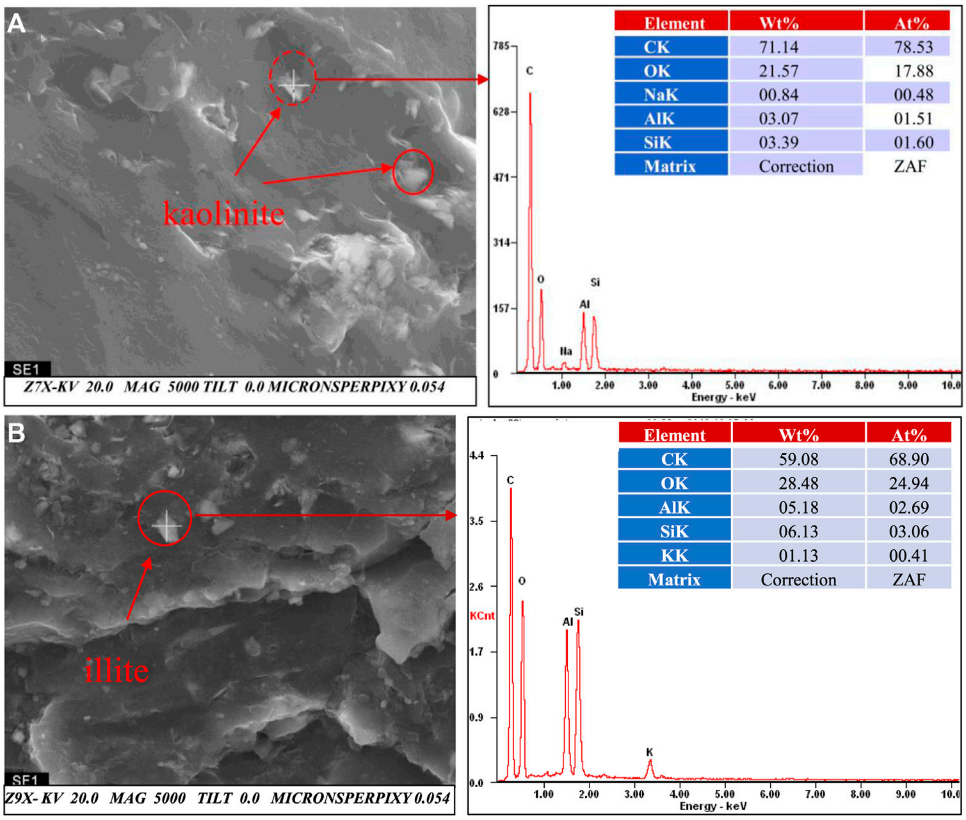

Element	Wt%	At%
CK	71.14	78.53
OK	21.57	17.88
NaK	00.84	00.48
AlK	03.07	01.51
SiK	03.39	01.60
Matrix	Correction	ZAF

Element	Wt%	At%
CK	59.08	68.90
OK	28.48	24.94
AlK	05.18	02.69
SiK	06.13	03.06
KK	01.13	00.41
Matrix	Correction	ZAF

FIGURE 5
EDS of coal.

5 Discussion

5.1 Surface wettability

Wettability of coal can be affected by coal rank, chemical composition, oxygen-containing functional groups, composition and porosity (Li and Li, 2016). In the formation of high rank coal, the side chains and functional groups of coal fall off continuously, resulting in the increasing number of aromatic rings, closer arrangement of aromatic lamella, reduced spacing, decreased porosity, weakened hydrophilicity of coal and enhanced adsorption gas.

In this research, the wettability of coal was studied by HARKE-SPCA contact Angle tester, and the study liquids were surface water, active water fracturing fluid and foam fracturing fluid. The results are shown in Figure 6. By experiments, wetting angles of the three coal samples to surface water are 44°, 57° and 29° respectively, indicating

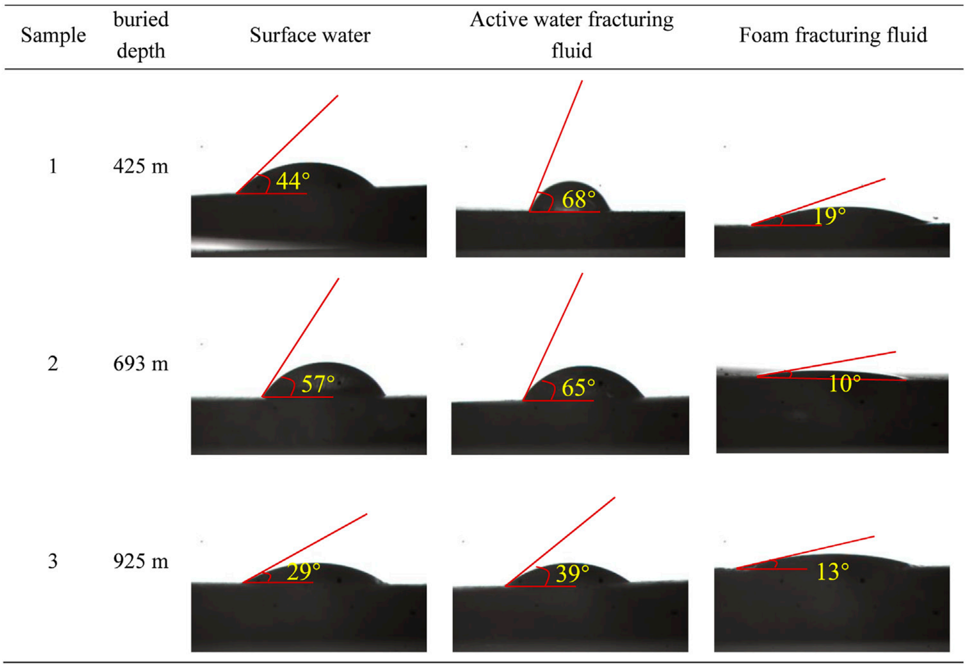

FIGURE 6
Wetting angle measurement results.

hydrophilicity. by adding surfactants into surface water, the contact angles become larger, respectively 68°, 65° and 39°, and the wettability becomes worse. However, after adding foaming agent into surface water, the contact angles between coal and foam fracturing fluid are 19°, 16° and 13°, respectively, and the wettability becomes better. It can be seen that coal heterogeneity results in differences in wettability of coal samples to the same liquid, and with the increase of sample depth, the contact angle with active water and foam fracturing fluid presents a trend of decrease, that is, increases in hydrophilicity.

The influence of wettability on CBM fracturing is multifaceted. When the contact angle is large, the coal powder has strong hydrophobicity and poor dispersion in water, make it easy to accumulate at the end of fractures to form blockage. When the contact angle is small, the liquid has good wettability on the coal surface, and the coal powder is discharged with the flow back fluid, which reduces the damage to the reservoir. In addition, at a low contact angle, water molecules will form adsorption water film on the surface of pores and fissures, narrowing the channel of methane diffusion and seepage, thus affecting the production of CBM (Li et al., 2016). Therefore, the system of fracturing fluid needs to be selected according to the actual situation. For the Well with serious pulverized coal, the liquid with good wettability can be used as far as possible, and conversely, the hydrophobic liquid system can be used.

5.2 Permeability

The permeability test of coal samples in roadway shows that the permeability is generally very low, and the value ranges from 0.003mD to 0.068mD (Table 2). Under similar external conditions, different permeability reflects the difference of fissure and pore distribution. According to the data, the permeability of CBM Wells in the study area is 0.015–0.29mD, and the porosity is 3.33–6.53% (Table 2) (Zhang, 2018).

Although the pores of coal matrix have certain permeability, it is far less than the cleat permeability of coal. Fluid only flows in the cleats, so the permeability reflected in the test is the comprehensive permeability dominated by cleat permeability. The coal of Zhengzhuang block belongs to ultra-low permeability and low porosity reservoir. Permeability statistics show that permeability and porosity of coal seam are affected by depth to a certain extent. As is shown in Figure 7, the inflection point of porosity and permeability appears near 800 m and 720 m depth respectively, and then decreases with the increase of depth. Significant changes in gas content and permeability can be observed with depth. This change is related to coal rank, sealing ability of overlying strata, measurement method, thermal effect of magmatic intrusion, geological structure and stress state (Salmachi et al., 2021).

TABLE 2 Permeability and porosity of coal samples in Zhengzhuang block.

Sample/Well	Depth (m)	Permeability (mD)	Porosity (%)
Coal samples in Sihe coal mine			
1	/	0.068	/
2	/	0.018	/
3	/	0.010	/
4	/	0.003	/
5	/	0.043	/
Coal samples from CBM Wells (Zhang, 2018)			
ZS19	562.85	0.085	5.26
ZS27	749.70	0.300	6.5
ZS30	641.06	0.290	6.49
ZS39	995.29	0.094	5.63
ZS64	1,245.26	0.047	3.33
ZS102	1,104.30	0.015	6.53

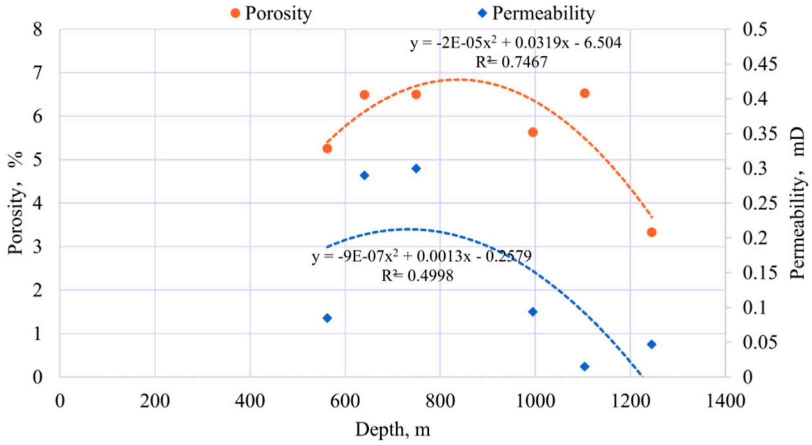

FIGURE 7
Porosity and permeability in relation to depth (Zhang, 2018).

TABLE 3 Injection/pressure drop well testing and *in-situ* stress test of Well—Z38.

Coal seam	Thickness (m)	Middle depth (m)	Geothermal gradient (°C/ 100 m)	Reservoir pressure coefficient	Breakdown pressure (MPa)	Permeability (mD)	Closure pressure (MPa/100 m)
3#	5.30	662.4	4.31	1.05	19.59	0.02	2.85
15#	2.27	753.0	4.51	9.22	14.17	3.13	1.61

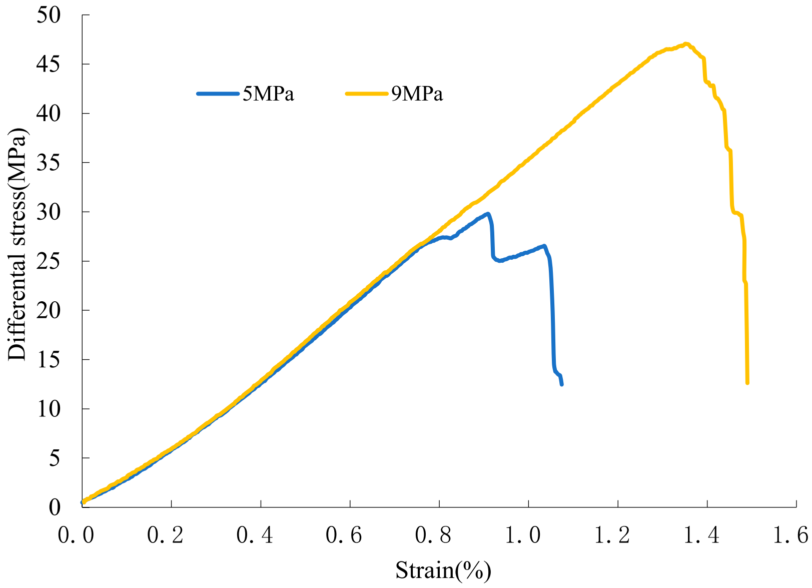

FIGURE 8
Stress-strain curves of coal samples at different confining pressures.

TABLE 4 Mechanical parameters obtained at different confining pressures.

Coal seam	Sample	Confining pressure (MPa)	Poisson's ratio	Elastic modulus (MPa)	Maximum differential stress (MPa)	Cohesion (MPa)	Internal friction angle (°)
Coal seam							
3#	A901	5	0.285	3,114.9	29.8	1.77	43.16
	A903	9	0.178	3,443.8	47.1		
Roof and floor							
3#	3-46-1	11.9	0.198	13013.2	72.3	6.61	40.35
	3-46-2	7	0.259	13451.3	54.3		
15#	15-100-1	14.7	0.207	9,997.3	58.3	19.59	13.29
	15-100-2	8	0.146	9,712.7	54.3		

5.3 *In situ* stress characteristic of coalbed methane reservoir

The intensity and direction of *in-situ* stress not only dominate the morphology of hydraulic fractures, but also have great influence on reservoir permeability during drainage. Injection/pressure drop well testing and *in-situ* stress test were carried out on the No.3 and No.15 coal seams of Well - Z38 (Table 3) to obtain reservoir parameters (permeability, reservoir pressure and temperature, breakdown pressure and closure pressure, etc.), providing reliable parameter basis for production potential evaluation and exploitation test of surrounding areas.

According to Table 3, compared with No.15 coal seam, No.3 coal seam has higher reservoir pressure and closure pressure gradient, but the geothermal gradient and

TABLE 5 Fracturing geology and operation parameters.

Number	M1	M2
Depth	840.6–846.5	1,095.45–1,099.3 m
Exploited coal seam	No.3	No.15
Thickness (m)	5.9	3.85
Gas content (m^3/t)	20.95	22.19
Fracturing fluid volume (m^3)	813.78	726.11
Fracturing fluid type	Clear water+0.5%KCl +0.1% discharge aiding agent	Clear water+0.5%KCl +0.1% discharge aiding agent
Proppant type	Quartz sand	Quartz sand
Proppant volume (m^3)	40.03	40.00
Proppant mesh (mm)	0.425–0.85	0.425–0.85
	0.85–1.18	0.85–1.18

permeability is lower than No.15 coal seam. It can be seen that the higher the minimum horizontal principal stress (approximately equal to the closure pressure) is, the permeability is lower, and the breakdown pressure is positively correlated to the closure pressure.

The lower sealing pressure gradient, breakdown pressure and higher permeability of No.15 coal seam provides more advantages in fracturing operation and gas production compared with No.3 coal seam.

5.4 Mechanical characteristics of coal

1) Coal seam

In order to determine the mechanical parameters of coal, triaxial mechanical tests were carried out on samples from No.3 coal seam. Differential stress-strain curves at different confining pressures are shown in Figure 8. When the confining pressure rises from 5 MPa to 9MPa, the slope of the differential stress-strain curve increases and the pressure at the fracture point increases.

In the triaxial experiment, fractures in coal determine the uniaxial compressive strength, which is very sensitive to the heterogeneity and fracture distribution of samples, resulting in uncertainty in the experiment. In order to reduce the occurrence of the uncertainty, the triaxial compressive strength test was carried out at lower confining pressure. The results show that the stress-strain curve has a concave shape in general, which is caused by the closure phenomenon of cleats in coal at compressive stress. The degree of concave in the initial time indicates the closure stiffness of gaping fracture under certain conditions.

Young's elastic modulus, Poisson's ratio, internal friction angle and other parameters obtained from rock mechanics experiments are shown in Table 4. The density of coal is much lower than that of conventional sandstone and carbonate, averaging 1.440 g/cm^3, Poisson's ratio averaging 0.223, and elastic modulus averaging 3,251.05 MPa.

2) Roof and floor

The roof and floor of Zhengzhuang block are mostly tight sandstone and shale. According to the triaxial mechanical experiments of the roof and floor, the average Poisson's ratio is 0.20, the average elastic modulus is 11.74 GPa (Table 4), the average cohesion is 9.95MPa, and the average internal friction angle is 26.63°, indicating that the roof and floor have good sealing ability, reflecting the low or medium development of tectonic fissures in this area. The gas content of coal reservoir is generally higher in the stable tectonic zone, far from fold axis and fault zone. In addition, the mechanical strength of reservoir roof and floor is higher than that of coal, which leads to increased resistance of formed hydraulic fracture when it expands in surrounding rock, and local distortion occurs in the path of hydraulic fracture propagation, but the fracture can still maintain a certain opening, providing a channel for fluid migration.

The permeability of No.15 coal seam is higher than that of No.3 coal seam, and the sealing pressure gradient and breakdown pressure are lower, which has advantages in fracturing operation and gas production.

6 Effect analysis of field application

6.1 Hydraulic fracturing

In order to increase CBM production, some stimulation measures need to be taken, among which hydraulic fracturing is the key technology of CBM stimulation in this area (Cao et al., 2020). Well M1 and Well M2 are two CBM Wells exploited in No.3 coal seam and No.15 coal seam respectively, both are completed by casing perforation. Preliminary laboratory experiments show that the clay content in Zhengzhuang block

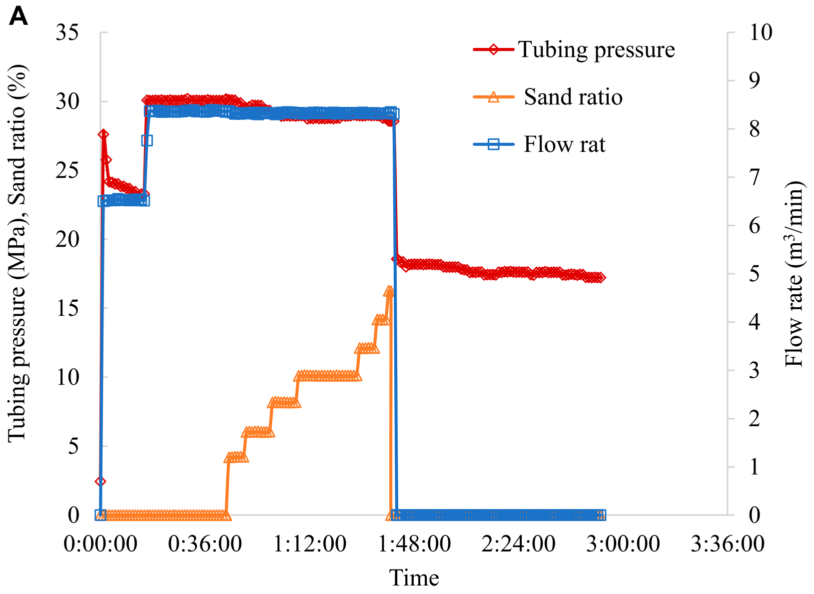

Well M1 located in No.3 coal seam

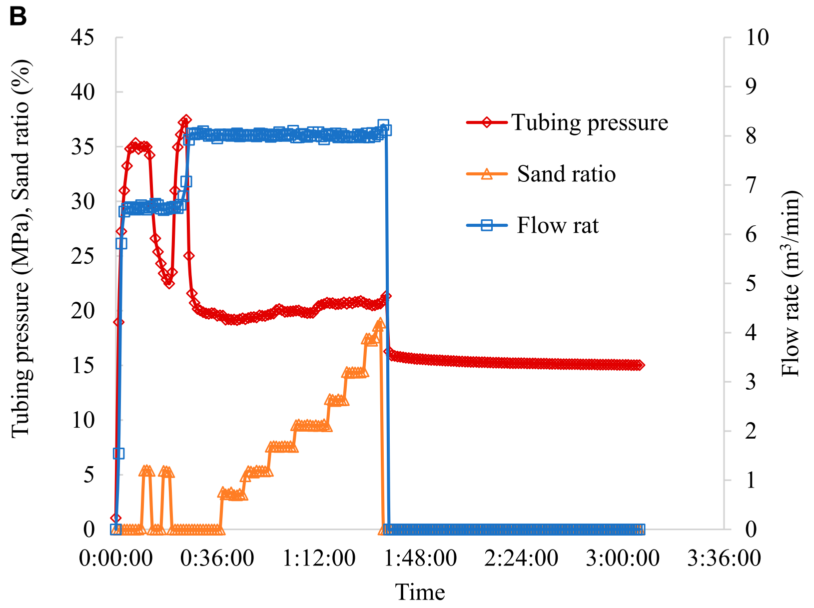

Well M2 located in No.15 coal seam

FIGURE 9
Fracturing curves of the Wells.

is low, so clear water or active water with a large contact angle with coal can be used for fracturing, and quartz sand can be selected for construction according to the closure pressure of the block. The geological parameters and fracturing data of the two Wells are shown in Table 5.

Well M2 is located at a depth of 1,095.45–1,099.3 m. The depth and gas content of Well M2 is larger than that of Well M1, but thinner than that of Well M1. The actual sand addition was equal in both, but the total fluid volume in Well M1 was slightly higher than that in Well M2. Fracturing operations were completed on both, as shown in Figure 9.

As can be seen from the fracturing construction curve, the breakdown pressure (27.59 MPa) of Well M1 is more obvious than that of Well M2. The flow rate of prepad fluid is 6.5–8.39 m^3/min with an average of 7.75 m^3/min. As the flow rate increases, the construction pressure increases significantly, which is caused by the increased friction of the string and fracture at high flow rate, so that the maximum injection pressure has reached 30.17 MPa. The

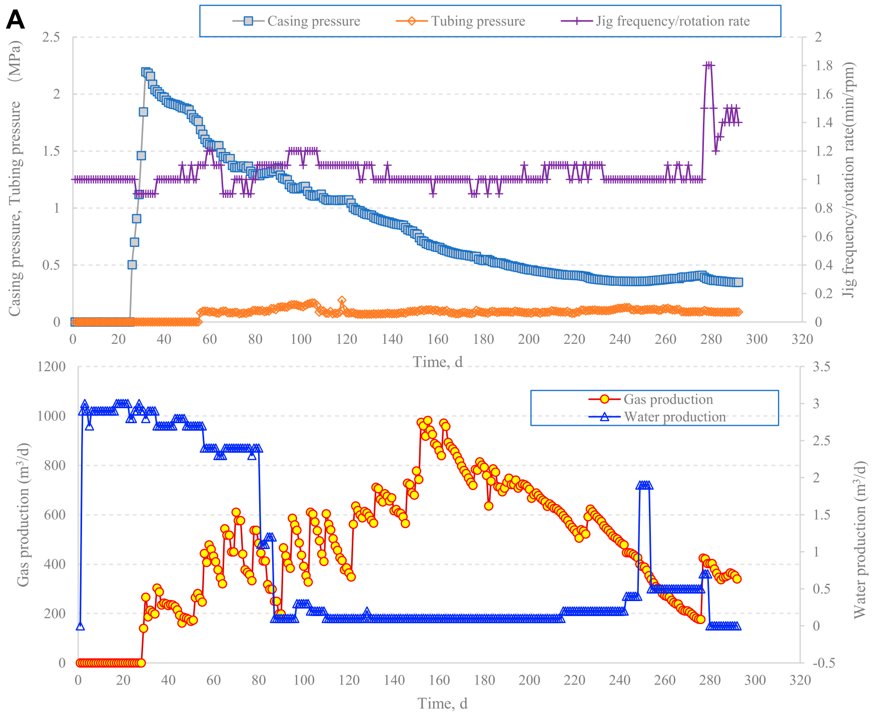

Well M1 located in No.3 coal seam

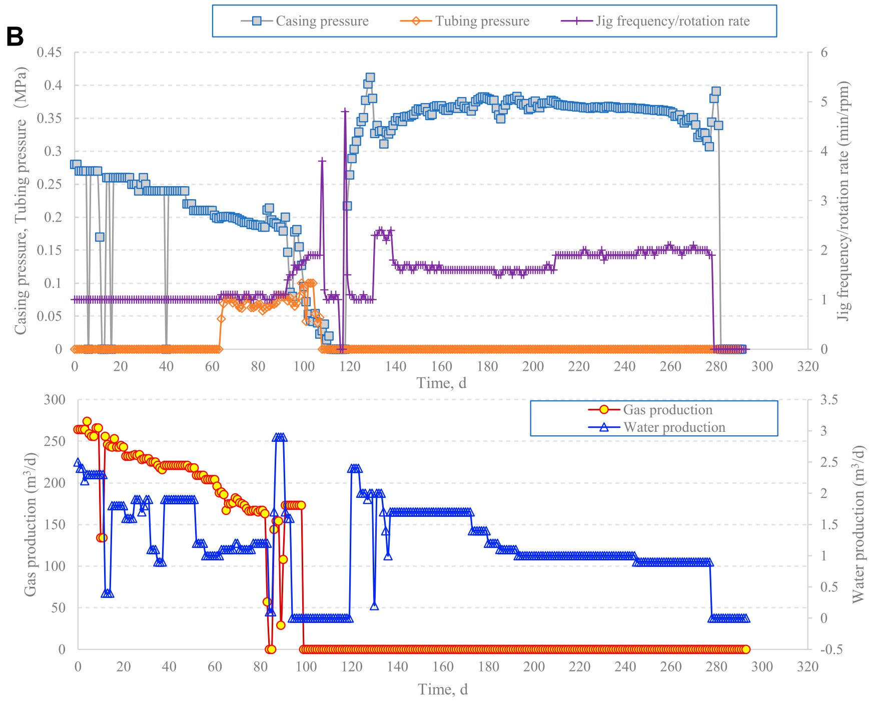

Well M2 located in No.15 coal seam

FIGURE 10
Production curves of the Wells.

average flow rate of carrying fluid is 8.32 m^3/min. With fracture propagation and proppant addition, fluid column pressure of wellbore increases, and fracture propagation pressure shows a downward trend, but it is higher than that of Well M2. The pressure of pump stopping is 18.56MPa, and the pressure after pressure fall-off test is 16.8 MPa. The actual injection volume of Well M1 is 813.78 m^3, quartz sand addition is 40.03 m^3 (0.425–0.85 mm quartz sand—20 m^3, 0.85–1.18 mm quartz sand - 20.03 m^3), and the average sand ratio is 8.45%.

In the construction stage of Well M2, the flow rate of prepad fluid is 6.5–8.0 m^3/min, the average flow rate is 6.88 m^3/min, the highest construction pressure is 37.47MPa, and the total injection volume of prepad fluid is 250.8 m^3. In the prepad stage, the slug is injected twice with 5% sand ratio. The particle size of quartz sand in the slug is 0.425–0.85 mm, and 2.0 m^3 is injected in total. In the sand-carrying stage, the average flow rate is 8.01 m^3/min, and 461.9 m^3 of carrying fluid is injected accumulatively, of which 38 m^3 of sand is injected, and the average sand ratio is 8.23%.According to the results of *in-situ* stress test, the closure pressure of No.15 coal seam is lower than that of No.3 coal seam, so the average fracture propagation pressure of Well M2 is lower than that of Well D6-18 located in No.3. The pressure fall-off test is carried out after the fracturing construction, and the pressure drops from 16.5 MPa to 15.0MPa, which is close to the formation pressure. It is further verified that the pressure coefficient of No.15 coal seam is lower than that of No.3 coal seam.

6.2 Drainage gas recovery after fracturing

Gas drainage of pumping well is performed in Wells M1 and M2 after hydraulic fracturing, with a total of 292 days. The drainage data are shown in Figure 10A and Figure 10B. The results show that the average daily gas and water production of Well M1 are 458.51 m^3 and 0.91 m^3 respectively, and the gas production is significantly higher than that of Well M2. As the drainage reduces the pressure, the pressure relief area of coal seam increases, coal seam water is discharged from the wellbore, and the effective desorption area gradually expands. The produce of gas begins when the critical desorption pressure is reached, and the gas production increases slowly and steadily with the growth of exploiting time. The peak of gas production occurred in Well M1 about 160 days after drainage. With the continuous decrease of casing pressure, the water production is almost zero, and the gas production also shows a decreasing trend. The average gas production of Well M2 is 67.56 m^3/d, and the average water production is 1.18 m^3/min. In the early stage of drainage, the gas production reaches the highest point, but with the progress of drainage, the gas production declines. In about 100 days, production stops, and the corresponding casing pressure also reaches its lowest value. In the later stage, the water production gradually decreases from 2 m^3/d to 0 m^3/d. Gas production is mainly affected by reservoir reserves and stimulation. Due to the high number of micropores in No.15 coal seam, the gas content of No.15 coal seam is larger than that of No.3 coal seam, but the smaller the pores are, the greater the adsorption potential energy of methane is, and the more difficult it is to desorb. Therefore, the actual gas production of No.15 coal seam is lower than that of No.3 coal seam. In addition, the thickness of No.15 coal seam is thin, and the strength of roof and floor rock is weak, which is easier to crush through adjacent aquifers, leading to high water production in the process of drainage.

According to the results of drainage gas recovery, the gas production of No.3 coal seam is better than that of No.15 coal seam, but it is not enough to meet the requirements of industrial exploiting. It is considered that the main causes of deficiency are from two aspects: First, the coal seam in this area has a large burial depth, and the compaction of gas-bearing reservoir under pressure is characterized by low porosity and low permeability; Secondly, the coal elastic modulus is low, and the fractures generated by fracturing are relatively short, and the fractures have the possibility of closure at high stress after a period of drainage. Beyond that, the thickness of the coal seam is relatively thin, and the coal seam may be crushed at high pressure, resulting in fractures connecting the upper and lower aquifers, causing serious water invasion, affecting the CBM desorption.

7 Conclusion

Zhengzhuang block of Qinshui Basin is the main area of CBM production in China in the future. Through the comprehensive study on the microstructure, composition, porosity, permeability and mechanical characteristics of coal in the study area, the following conclusions are drawn:

1) No.3 coal seam in Zhengzhuang block belongs to high rank anthracite, with an average vitrinite reflectance of 3.82%, which belongs to the same type of coal from the roadway in this area. There are circular, wedge-shaped and irregular pores and micro-fissures in coal, and the pores are the main space for CBM occurrence. Compared with No.3 coal seam, No.15 coal seam has smaller aperture, more pores per unit area and higher gas content.
2) Causing by differences in components, the surface of coal has different wettability to different liquids, and weak hydrophilicity is expected because it facilitates the flowback of fracturing fluids. In Zhengzhuang block, in order to control the cost of fracturing fluid and reduce the damage of coal seam effectively, clear water is commonly used during coal seam fracturing. Quartz sand is selected as proppant based on the burial depth and closure pressure of the study area. Mechanical experiments show that the Poisson’s ratio of coal is 0.175–0.285, with an average of 0.209; and the elastic modulus is 2,593.5–3,443.8MPa, with an average of 3,147.3 MPa. Low Young’s modulus indicates that wide artificial fractures are easily formed in coal seam.
3) The coal in Zhengzhuang block has the characteristics of low porosity and low permeability, so stimulation technology has

to be put into production. According to the field fracturing construction curve, the fracture initiation pressure is not obvious, the construction pressure is greatly affected by the flow rate, and the fracture propagation pressure is significantly affected by the *in-situ* stress. The drainage data after fracturing show that the production of No.3 and No.15 coal seams does not exceed 1000 m^3. From the perspective of industrial production, the exploitation of the two Wells is not successful, mainly because of the low permeability of CBM reservoir, and the effective of communication range of artificial fractures, which is not conducive to the desorption and seepage of CBM. For Wells with low production from initial fracturing, refracturing technology is suggested in later stage of production to increase the stimulated reservoir volume and desorption area for further enhancing gas recovery.

Data availability statement

The datasets presented in this study can be found in online repositories. The names of the repository/repositories and accession number(s) can be found in the article/supplementary material.

Author contributions

YL—Writing the article; JH—Reviewing the article; HuZ and ZX—Data analysis; ZY—Project management; MY—Supervisor; HoZ—Methodology; YQ—Resources. All authors contributed to the article and approved the submitted version.

Acknowledgments

The authors gratefully acknowledge the support of National Natural Science Funds of China (grant number: 52104041, 42102186), Natural Science Funds of Hebei (grant numbers: E2021203219, E2021203203) and Basic Innovation and Scientific Research Cultivation Project of Yanshan University (grant number: 2021LGQN010).

Conflict of interest

HuZ was employed by CNPC Bohai Drilling Engineering Company Limited. ZX was employed by Exploration and Development Research Institute of Changqing Oilfield Company, PetroChina. JG was employed by Shanxi CBM Exploration and Development Co., PetroChina.

The remaining authors declare that the research was conducted in the absence of any commercial or financial relationships that could be construed as a potential conflict of interest.

Publisher's note

References

Balan, H. O., and Gumrah, F. (2009). Assessment of shrinkage-swelling influences in coal seams using rank-dependent physical coal properties. *Int. J. Coal Geol.* 77, 203–213. doi:10.1016/j.coal.2008.09.014

Behnia, M., Goshtasbi, K., Marji, M. F., and Golshani, A. (2015). Numerical simulation of interaction between hydraulic and natural fractures in discontinuous media. *Acta Geotech.* 10, 533–546. doi:10.1007/s11440-014-0332-1

Cao, L., Yao, Y., Cui, C., and Sun, Q. (2020). Characteristics of *in-situ* stress and its controls on coalbed methane development in the southeastern Qinshui Basin, North China. *Energy Geosci.* 1, 69–80. doi:10.1016/j.engeos.2020.05.003

Cong, L. Z., Chen, J. F., Li, Z. P., and Zhang, S. A. (2007). Adsorption features of fracturing fluid by coal substrate during the fracturing process in coalbed methane well. *Coal Geol. Explor.* 35, 27–30.

Gao, X. D., Wang, Y. B., Ni, X. M., Tao, C. Q., and Zhao, S. H. (2020). Mechanical properties of deep coal and rock in Linxing area and its influences on fracturing of deep coal reservoir. *J. China Coal Soc.* 45, 912–921.

Gao, X. (2016). Evaluation of fracturing-fluid damage for permeability in coal seam, Liulin Area, Ordos Basin. *Nat. Gas. Explor. Dev.* 39, 53–56.

Hodot, B. B. (1996). *Outburst of coal and coalbed gas (Chinese translation).* Beijing, China: China Industry Press.

Hu, Z. Z., Huang, W. H., Lu, X. X., Xu, Q. L., Zhang, Q., and Chen, Y. P. (2015). Correlation analysis on pore characteristics of No. 3 and No. 15 coal seams in southern Qinshui Basin. *Coal Sci. Tech.* 43, 173–178.

Huang, B., and Liu, J. (2017). Experimental investigation of the effect of bedding planes on hydraulic fracturing under true triaxial stress. *Rock Mech. Rock Eng.* 50, 2627–2643. doi:10.1007/s00603-017-1261-8

Li, C., Liu, D., Cai, Y., and Yao, Y. (2016). Fracture permeability evaluation of a coal reservoir using geophysical logging: A case study in the Zhengzhuang area, southern Qinshui Basin. *Energy Explor. Exploitation* 34, 378–399. doi:10.1177/0144598716631664

Li, J. Y., and Li, K. Q. (2016). Influence factors of coal surface wettability. *J. China Coal Soc.* 41, 448–453.

Li, M., Chen, L., Bao, W. H., Zhao, J., Shen, J. W., Sun, H. T., et al. (2021). Study on fracturing fluid adaptability in unconventional multi-target reservoir. *Petrochem. Indus Appl.* 40, 72–75.

Li, P., Ma, D. M., Zhang, H., Li, W. B., and Yang, F. (2016). Influence of high and low rank coal wettability and methane adsorption/desorption characteristics. *Coal Geo. Explor.* 44, 80–85.

Li, P., Zhang, X., Li, J., Zhao, J., Huang, J., Zhang, S., et al. (2020). Analysis of the key factors affecting the productivity of coalbed methane wells: A case study of a high-rank coal reservoir in the central and southern Qinshui Basin, China. *ACS omega* 5, 28012–28026. doi:10.1021/acsomega.0c03540

Li, X., Zhang, J., Li, R., Qi, Q., Zheng, Y., Li, C., et al. (2021). Numerical simulation research on improvement effect of ultrasonic waves on seepage characteristics of coalbed methane reservoir. *Energies* 14, 4605. doi:10.3390/en14154605

Liu, S., and Harpalani, S. (2013). Permeability prediction of coalbed methane reservoirs during primary depletion. *Int. J. Coal Geol.* 113, 1–10. doi:10.1016/j.coal.2013.03.010

Liu, S. T., Zheng, Z. H., Geng, M., Jiao, J., Gao, Y., and Wu, J. P. (2019). Resources potential and exploration prospect of coalbed methane in Qinshui basin. *China Min. Mag.* 28, 37–43.

Lu, Y., Shelepov, V. V., Yang, Z., Liu, J., Han, J., Guo, J., et al. (2018). Research on initial pressure of fracture in the technique of staged fracturing of a horizontal well. *J. Appl. Mech. Tech. Phy.* 59, 1111–1117. doi:10.1134/s0021894418060172

Min, C., Zhang, X. H., Yang, Z. Z., Li, X. G., and Dai, B. R. (2022). Identification of main controlling factors of fracturing performance in coalbed methane wells based on CBFS-CV algorithm. *Pet. Geol. Rec. Eff.* 29, 168–174.

Salmachi, A., Rajabi, M., Wainman, C., Mackie, S., McCabe, P., Camac, B., et al. (2021). History, geology, *in situ* stress pattern, gas content and permeability of coal seam gas basins in Australia: A review. *Energies* 14, 2651. doi:10.3390/en14092651

Teufel, L. W., and Clark, J. A. (1984). Hydraulic fracture propagation in layered rock: Experimental studies of fracture containment. *Soc. Petroleum Eng. J.* 24, 19–32. doi:10.2118/9878-pa

Wang, S., Zhang, Y., Guo, J., Lai, J., Wang, D., He, L., et al. (2014). A study of relation between suspension behavior and microstructure and viscoelastic property of guar gum fracturing fluid. *J. Pet. Sci. Eng.* 124, 432–435. doi:10.1016/j.petrol.2014.09.016

Xu, T., Mao, J., Zhang, Q., Lin, C., Yang, X., Zhang, Y., et al. (2021). Synergistic polymer fracturing fluid for coal seam fracturing. *Colloids Surfaces A Physicochem. Eng. Aspects* 631, 127648. doi:10.1016/j.colsurfa.2021.127648

Xue, H. F., Zhu, G. H., Wang, W., Lu, X. X., Wang, M. H., and Wang, Y. B. (2019). Analysis and application of key influencing factors of CBM well fracturing effects in Shizhuang area, Qinshui basin. *Coal Geol. Explor.* 47, 76–81.

Yu, Y. J., Zhu, W. C., Li, L. C., Wei, C. H., Zhang, X. F., Qin, C., et al. (2019). Simulations on hydraulic fracture propagation of coal-rock combination in deep underground. *Hazard Control Tunn. Und. Eng.* 1, 96–108.

Zhang, X. Y. (2018). "Optimization model of quantitative drainage system for CBM vertical wells in Zhengzhuang block," ([Xuzhou (Jiangsu)]: China University of Mining and Technology) ([Dissertation/doctoral thesis].

Zhang, Z., Wang, H., Deng, B., Li, M., and Zhang, D. (2018). Field investigation of hydraulic fracturing in coal seams and its enhancement for methane extraction in the Southeast Sichuan Basin, China. *Energies* 11, 3451. doi:10.3390/en11123451

Zhu, Q. Z., Zhang, X. D., Yang, Y. H., Hu, X. F., Zhang, Y. P., Yang, Y. L., et al. (2018). Geological factors affecting desorption pressure of CBM wells in the southern and central-southern Qinshui Basin and their influencing mechanism. *J. China Univ. Pet.* 42, 41–49.

Frontiers in
Earth Science

Investigates the processes operating within the major spheres of our planet

Advances our understanding across the earth sciences, providing a theoretical background for better use of our planet's resources and equipping us to face major environmental challenges.

Discover the latest Research Topics

See more →

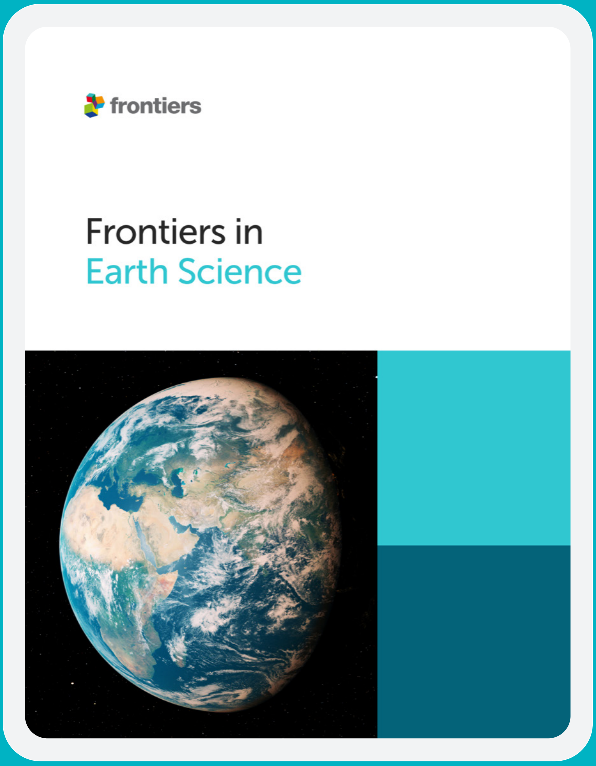

frontiers

Frontiers in
Earth Science

Frontiers

Avenue du Tribunal-Fédéral 34
1005 Lausanne, Switzerland
frontiersin.org

Contact us

+41 (0)21 510 17 00
frontiersin.org/about/contact